A NEW ELASTO_PLASTICITY CONSTITUTIVE MODEL FOR CONCRETE UNDER MULTIAXIAL COMPRESSION BASED ON EXPERIMENTAL OBSERVATIONS

KEHLAN SALMAN

Ph.D July 2007

THE UNIVERSITY OF SHEFFIELD

I dedicate this work to
my late parents and
my late brother Dayan

Acknowledgements

I would like to express my deep gratitude and thanks to those who supervised me during this work. In particular, I sincerely thank my first supervisor Professor Roger Crouch for his guidance, support and help. He was the one who initiated this research and provided many suggestions and invaluable advice. I found him to be a real scholar of the highest standard who inspired us to strive for unique scientific contributions. His office and indeed house was opened for us at all times whether night or day. From his kindness was his continued support even when he left the University of Sheffield for the University of Durham.

I thank my second supervisor Professor Kypros Pilakoutas who accepted taking over as the official supervisor after the departure of my first supervisor. He was as we know him always a teacher, a helper and a kind supporter. I thank my third supervisor Dr. Mihail Petkovski, who took over during the write-up of this thesis. During this period he gave me much help and support.

I would like to sincerely thank Dr Benabdellah Tahar for his encouragement, support and help throughout this work. He is another example of extreme generosity.

I wish to give my thanks to all the staff and researchers at the Department of Civil and Structural Engineering at the University of Sheffield for all their help and for the facilities provided to me for the duration of this work. I also thank my colleagues in the same research group, in particular Dr Tianbai Li.

Special thanks go to my family, in particular my wife for her patience and support throughout this research, to my three daughters for their love and perseverance with me during this work and all those who helped me directly or indirectly to complete this thesis.

Finally, I acknowledge that my Ph.D. study was partially supported by the Engineering and Physical Science Research Council (EPSRC).

Abstract

This thesis comprises of two different kinds of work. The first part is focussed on existing experimental data. Investigations and observations of the behaviour of plain concrete under triaxial and multiaxial compression following cyclic loading and a variety of stress paths has been presented. The behaviour of concrete with different constituents was also investigated. The directions of the plastic strain vectors were identified. Two loading surface were also identified: (i) the Peak Nominal Stress surface (PNS) which was identified from the peak stresses recorded from stress control tests and (ii) the Volume Transition Stress surface (VTS) which determines the onset of the volumetric dilation. The plastic VTS is the surface which was identified from plastic strain components only. At this surface, the directions of the plastic strain vectors are purely deviatoric. A proposal for the shapes of the yield surface for concrete is given. These shapes were identified by the plastic work contours and also from the directions of the plastic strain vectors assuming the associated flow rule. This assumption has been verified by examining the normality of the plastic strain vectors to the PNS surface.

Following the investigation of the experimental data, an examination of various advanced plasticity models for concrete revealed the need to develop a new constitutive model with a suitable shape of the loading surfaces and with a better prediction for the stress-strain response. A new constitutive model for plain concrete has been developed using the previous work in this field at the University of Sheffield. The new yield surface was developed as a combination of a reflection of part of the peak nominal stress surface (PNS) and a quartic function. The continuity, the convexity and the normality of the yield surfaces were ensured. The model was calibrated and the optimum values of the thirteen material constants are presented. This is followed by a sensitivity study with simulations of a wide range of existing experimental data. Simulations of concrete with different constituents are also presented.

The formulation of the model was simplified and verified by using numerical derivatives. A comparative study between the analytical and numerical derivatives of the constitutive model is presented.

The sensitivity study and the simulations of experimental tests showed that the new constitutive model is: (i) easy to calibrate using only data from uniaxial compression tests and one triaxial compression test, and (ii) gives very good predictions of stress-strain response of different types of concrete under triaxial compression stresses and at different levels of confinement all the way to the peak stress state.

Contents

1 Introduction **1**

1.1 Introduction 1

1.2 Objective of the Thesis 5

1.3 The Original Contributions of the Thesis 6

1.4 The Features of the Model 7

1.5 The Limitations 7

1.6 The Organisation of the Thesis 8

1.7 References 9

2 The Deformation of Concrete under Compression **14**

2.1 Introduction 14

2.2 Definition of Cauchy Stress 16

2.3 The Structure of Concrete 21

2.4 The Behaviour of Concrete under Uniaxial Cyclic Compression Loading 23

2.4.1 Axial and Lateral Stress-strain Behaviour 24

2.4.2 Volumetric Strain 25

2.4.3 Poisson's Ratio, ν 27

2.4.4 Young's Modulus, E 29

2.4.5 Volumetric Plastic Strain 30

2.4.6 Peak Stress, f_c 31

2.4.7 Strain at Peak Stress 35

2.3.8 Plastic Work, W^p 35

2.4.9 Plastic Flow 36

2.4.9.1 Effect of E on Plastic Flow 39

2.4.9.2 Effect of ν on Plastic Flow 39

2.5 The Behaviour of Concrete under Triaxial Compression 39

2.5.1 Peak Axial Stress 43

2.5.2 Strain at Peak Stress 44

2.5.3 Volumetric Strain 45

2.5.4 Poisson's Ratio, ν 47

2.5.5 Young's Modulus, E 47

2.5.6 PNS Surface 49
2.5.7 VTS Surface 50
2.5.8 Plastic Flow 50
2.5.9 Plastic Work 54
2.6 Concluding Remarks 55
2.7 References 59

3 Development of the New Constitutive Model **64**
3.1 Introduction 64
3.2 Continuum Constitutive Modelling 65
3.2.1 Elasticity Models 66
3.2.2 Damage Models 66
3.2.3 Microplane Models 67
3.2.4 Plasticity Models 69
3.3 The Theory of Elasto-plasticity 70
3.3.1 Plasticity Basic Assumptions 70
3.3.2 Loading and Unloading 78
3.3.3 Drucker's Stability Postulate 80
3.3.4 Development of the Consistency Parameter and the Tangent Elasto-plasticity Matrix 81
3.3.5 Integration of the Infinitesimal Equations 83
3.3.6 Sheffield Model 88
3.4 The Development of the New Model 89
3.4.1 Elastic Behaviour 89
3.4.2 Peak Nominal Stress (PNS) Envelope 91
3.4.3 New Yield Function 98
3.4.4 The Hardening Function 104
3.4.5 Ductility Measure, ζ 106
3.4.6 Auxiliary Stress Surface 107
3.5 The Derivatives 111
3.5.1 The derivative of the Yield Function with respect to k_p 111
3.5.2 The Mixed Derivatives 116
3.5.3 Stress Derivatives 117
3.5.4 The Derivatives of the Hardening Function 119
3.6 Concluding Remarks 120
3.7 References 121

4 Calibration and Simulations **126**
4.1 Introduction 126
4.2 Material Constants 127

4.3 Calibration 127
4.3.1 Poisson's Ratio, ν 128
4.3.2 Young Modulus, E 129
4.3.3 Uniaxial Compression strength, f_c 130
4.3.4 Uniaxial Tensile strength, f_t 131
4.3.5 PNS Meridional Shape Constant, γ 132
4.3.6 PNS Deviatoric Shape Constant, α 132
4.3.7 Yield Surface Constant, α_1 133
4.3.8 Volumetric Transition Constant, α_2 133
4.3.9 Initial Hardening Surface Constant, k_0 and Hydrostatic Intersection Constant, A_k 134
4.3.10 Hardening Slope Constant, s_0 134
4.3.11 Hardening Constants, A_h and B_h 134
4.4 Sensitivity Study 135
4.4.1 Poisson's Ratio, ν 135
4.4.2 Young Modulus, E 137
4.4.3 Uniaxial Compression Strength, f_c 137
4.4.4 Uniaxial Tensile Strength, f_t 138
4.4.5 PNS Meridional Shape Constant, γ 140
4.4.6 PNS Deviatoric Shape Constant, α 140
4.4.7 Yield Surface Constant, α_1 143
4.4.8 Volumetric Transition Constant, α_2 143
4.4.9 Hardening Slope Constant, s_0 145
4.4.10 Initial Hardening Surface Constant, k_0 145
4.4.11 Hydrostatic Intersection Constant, A_k 147
4.4.12 Hardening Constants, A_h 147
4.4.13 Hardening Constants, B_h 150
4.5 Simulations 150
4.5.1 Sheffield Uniaxial and Triaxial Compression Tests 151
4.5.2 Colorado Multiaxial Compression Tests 156
4.6 The Error 177
4.7 Concluding Remarks 183
4.8 References 183

5 Investigations and Simulations of Concrete with Different Constituents 186
5.1 Introduction 186
5.2 Uniaxial Response 188
5.2.1 Stress-strain Response 188
5.2.2 Volumetric Strain 189
5.2.3 Peak Stress 192

5.2.4 Strain at Peak Stress 193
5.2.5 Young's Modulus 193
5.2.6 Poisson's Ration 194
5.2.7 Plastic Flow 194
5.3 Triaxial Response 196
5.3.1 Stress-strain Response 197
5.3.2 Peak Stress 198
5.3.3 Young's Modulus 198
5.3.4 Poisson's Ration 199
5.3.5 Plastic Strain at Peak Stress 199
5.3.6 Plastic Flow 201
5.3.7 Peak Nominal Stress, PNS 203
5.3.8 Volume Transition Stress, VTS 205
5.4 Yield Surfaces 207
5.5 Simulations 208
5.6 Concluding Remarks 215
5.7 References 216

6 Numerical Verification and Simplification 217
6.1 Introduction 217
6.2 The Formulation of the Numerical Derivatives 218
6.2.1 Romberg's Method 220
6.2.2 The Algorithm 221
6.2.3 The Derivatives of the Yield Function 222
6.2.4 Verifications 224
6.3 The Model Calibration 224
6.4 The Simulations 226
6.5 The Time Consumption 235
6.6 Concluding Remarks 238
6.7 References 238

7 Conclusions and Suggestions for Further Research 240
7.1 Introduction 240
7.2 Conclusions 240
7.2.1 Experimental Observations 240
7.2.2 The New Constitutive Model 243
7.3 Suggestions for Further Research 246

A Derivatives of the Stress Invariants and the Deviatoric Shape Function **248**

A.1 Derivatives of the Stress Invariants 248

A.2 Derivatives of the Deviatoric Shape Function 252

List of Tables

2.1 The values of Poisson's ratio from three uniaxial compression tests . . . 29
2.2 The values of Young's modulus for the three uniaxial tests from Sheffield tests calculated for two loading cycles 29
2.3 The values of peak stresses and strains for three uniaxial compression tests 34
3.1 The relationship between different elastic moduli for linear isotropic elasticity 90
3.2 PNS values for uniaxial and biaxial states 91
4.1 The model material constants classified into three groups 128
4.2 Model constants with typical ranges and default values for concrete . . 135
4.3 Material constants used for the triaxial simulations 152
4.4 The root mean square of the error recorded for series 1, Colorado tests 181
4.5 The root mean square of the error recorded for series 2, Colorado tests 181
4.6 The root mean square of the error recorded for series 3, Colorado tests 182
4.7 The root mean square of the error recorded for series 4, Colorado tests 182
4.8 The root mean square of the error recorded for series 5, Colorado tests 182
4.9 The root mean square of the error recorded for series 6, Colorado tests 182
5.1 The mix proportions (by weight), for the three mixes, normalised with respect to cement content 188
5.2 The percentages of the VTS to f_c for the three mixes tested under uniaxial compression tests 192
5.3 The peak stresses for the three mixes tested under uniaxial compression tests 193
5.4 The peak axial strains for the three mixes tested under uniaxial compression tests 193
5.5 The peak lateral strains for the three mixes tested under uniaxial compression tests 194
5.6 The average values of Young's modulus for the three mixes tested under uniaxial compression tests 194
5.7 The average values of Poisson's ratio for the three mixes tested under uniaxial compression tests 195

5.8 The optimised values of m, the numerical values for $\bar{f}_t$, the experimental values of f_c and f_t for the three mixes 204
5.9 The model material constants for the three mixes 210
6.1 The minimum error between experimental data and model predictions and the hardening parameters A_h and B_h with the hydrostatic intersection constantA_k for series 1, Colorado tests 226
6.2 The minimum error and the hardening parameters A_h and B_h with the hydrostatic intersection constantA_k for series 2, Colorado tests 228
6.3 The minimum error and the hardening parameters A_h and B_h with the hydrostatic intersection constantA_k for series 3, Colorado tests 230
6.4 The minimum error and the hardening parameters A_h and B_h with the hydrostatic intersection constantA_k for series 4, Colorado tests 230
6.5 The minimum error and the hardening parameters A_h and B_h with the hydrostatic intersection constantA_k for series 5, Colorado tests 234
6.6 The minimum error and the hardening parameters A_h and B_h with the hydrostatic intersection constantA_k for series 6, Colorado tests 234
6.7 The time consumption of the analytical and numerical codes, series 1, Colorado tests 235
6.8 The time consumption of the analytical and numerical codes, series 2, Colorado tests 236
6.9 The time consumption of the analytical and numerical codes, series 3, Colorado tests 236
6.10 The time consumption of the analytical and numerical codes, series 4, Colorado 237
6.11 The time consumption of the analytical and numerical codes, series 5, Colorado 237
6.12 The time consumption of the analytical and numerical codes, series 6, Colorado 237

List of Figures

2.1 Cut-away view of the triaxial testing cell designed by Hoek and Franklin 15
2.2 Element of stress tensor and three principal stresses 17
2.3 Eight stress regions in principal stresses space 18
2.4 Normalised Haigh-Westergaard stress space 21
2.5 The concrete composite [Mehta] 22
2.6 Axial, lateral and volumetric stress-strain for the uniaxial compression test from Sheffield University, sample 5_3a 25
2.7 Axial stress versus axial and lateral strains with cyclic loading, Sheffield tests, sample 5_3a_R_0 28
2.8 Axial stress versus total and plastic volumetric strain, uniaxial test, sample 5_3*a*, Sheffield University 31
2.9 Effect of loading rate on the stress-strain behaviour in uniaxial compression [Fumagalli] 33
2.10 Uniaxial compression strength variation: (a) with anti-friction materials between loading platens and specimen, (b) without anti-friction materials [Fumagalli]. 34
2.11 Uniaxial compression stress-strain variations for three tests 35
2.12 Plastic work versus $\bar{\xi}$ for uniaxial test, Sheffield tests 36
2.13 Plastic strain directions, stress path, and volumetric transition stress point for the uniaxial compression test, Sample 5_3a, Sheffield tests . 38
2.14 The sensitivity of plastic flow to Young's modulus, sample 5_3*a*, Sheffield tests 40
2.15 The sensitivity of plastic flow to Poisson's ratio, sample 5_3*a*, Sheffield tests 40
2.16 Axial stress versus axial and lateral strain for different level of confinement, Sheffield tests 41
2.17 Stress path for triaxial compression under 60 MPa confinement, Sheffield test, sample 5_2*c* 42
2.18 Peak axial stresses for different levels of confinement, Sheffield tests . 44
2.19 Lateral stress versus axial and Lateral strains at Peak Stresses 45

2.20 Equivalent plastic strain at peak stresses for different levels of confinement, Sheffield tests 46
2.21 Axial stress versus volumetric plastic strain with different level of confinement 46
2.22 Poisson's ratio versus the hydrostatic stress 47
2.23 Young's modulus for different levels of confinement calculated at each loading cycle, Sheffield tests. 48
2.24 Peak nominal stress surface, Sheffield tests 50
2.25 PNS and VPT surfaces 51
2.26 Plastic strain directions, stress path, PNS and VTS for different levels of confinement, Sheffield tests. 52
2.27 Schematic draw for the proposed shapes of the yield surfaces assuming associated flow rule 53
2.28 Proposed shapes of the yield surfaces assuming associated flow rule . 53
2.29 Plastic work for different level of confinement, Sheffield tests 54
2.30 Peak plastic work for different levels of confinement, Sheffield tests . . 55
2.31 Plastic work contour for different levels of confinement, Sheffield tests 56
2.32 Proposed yield surfaces based on plastic work contour, Sheffield tests 56
2.33 Proposed yield surfaces based on plastic work contour superimposed on the plastic strain vectors, Sheffield tests 57
3.1 Classic yield surfaces and yield surface for concrete 74
3.2 Idealised stress strain models 77
3.3 Loading and unloading for work-hardening materials 80
3.4 The Peak Nominal Stress surface (PNS) determined by equation (3.62) and compared against triaxial data from Sheffield tests for f_c =58 MPa 95
3.5 Bhowmik-Long deviatoric plane 96
3.6 The PNS and VTS surfaces from the Sheffield experiments and the model predictions for the compression meridian 99
3.7 The general shape of the four equations that formulate the yield surface 100
3.8 The general shape of a yield surface with PNS and VTS surfaces . . . 104
3.9 The initial and subsequent yield surfaces 105
3.10 Plastic strain directions and yield surfaces for the new model 105
3.11 The relationship between hardening measure k and the hardening internal variable k_p 107
3.12 The ductility measure ζ versus $\bar{\xi}$ 108
3.13 Auxiliary stress state and the six zones 109
3.14 The continuity of the first derivative of the yield function with respect to k 116

4.1 The sensitivity of the stress-strain response to Poisson's ratio ν . . . 136
4.2 The sensitivity of the stress-strain response to E . . . 136
4.3 The sensitivity of the PNS to f_c . . . 137
4.4 The sensitivity of the stress-strain to f_c . . . 138
4.5 Sensitivity of the model to f_t . . . 139
4.6 The sensitivity of the stress-strain to f_t . . . 139
4.7 The relation between m and $\bar{f}_t$ . . . 140
4.8 Sensitivity of the model to γ . . . 141
4.9 Sensitivity of the stress-strain response to γ . . . 141
4.10 The deviatoric sections of the smooth PNS criterion at ten levels of normalised hydrostatic pressure ($\bar{\xi} = 0$ to -2) for two different α values , (a) $\alpha = 0.005$ and (b) $\alpha = 0.6$ ($\gamma = 1$)[Tahar] . . . 142
4.11 Sensitivity of the model to α_1 . . . 143
4.12 Sensitivity of the stress-strain response to the change of α_1 . . . 144
4.13 Sensitivity of the model to α_2 . . . 144
4.14 Sensitivity of the stress-strain response to the change of α_2 . . . 145
4.15 The sensitivity of the hardening variable k to s_0 . . . 146
4.16 The sensitivity of the yield surface to k_0 . . . 146
4.17 The effect of k_0 on the stress-strain response . . . 147
4.18 The sensitivity of the model to A_k . . . 148
4.19 The effect of A_k on the stress-strain prediction . . . 148
4.20 Effect of constant A_h on the ductile measure ζ . . . 149
4.21 The effect of A_h on the stress-strain prediction . . . 149
4.22 Effect of constant B_h on the ductile measure, ζ . . . 150
4.23 The effect of B_h on the stress-strain response . . . 151
4.24 The predictions of the model for six different levels of confinement for Sheffield triaxial compression tests using fixed values for A_h and B_h . 153
4.25 The predictions of the model for six different levels of confinement for Sheffield triaxial compression tests using different values for A_h and B_h 154
4.26 Plastic flow, stress paths and stress-strain simulations for Colorado tests, sample 1-1, 1-2, 1-3 and 1-4 . . . 159
4.27 Plastic flow, stress paths and stress-strain simulations for Colorado tests, sample 1-5, 1-6, 1-7 and 1-8 . . . 160
4.28 Plastic flow, stress paths and stress-strain simulations for Colorado tests, sample 1-9, 1-10, 1-11 and 1-12 . . . 162
4.29 Plastic flow, stress paths and stress-strain simulations for Colorado tests, sample 2-1,2-2, 2-3, and 2-4 . . . 163
4.30 Plastic flow, stress paths and stress-strain simulations for Colorado tests, sample 2-5, 2-6, 2-7 and 2-8 . . . 165

4.31 Plastic flow, stress paths and stress-strain simulations for Colorado tests, sample 3-1, 3-2, 3-3 and 3-4 166
4.32 Plastic flow, stress paths and stress-strain simulations for Colorado tests, sample 3-5, 3-6, 3-7 and 3-8 167
4.33 Plastic flow, stress paths and stress-strain simulations for Colorado tests, sample 3-9, 3-10, 3-11 and 3-12 168
4.34 Plastic flow, stress paths and stress-strain simulations for Colorado tests, sample 3-13, 3-14, 3-15 and 3-16 170
4.35 Plastic flow, stress paths and stress-strain simulations for Colorado tests, sample 3-17, 4-1, 4-2 and 4-3 171
4.36 Plastic flow, stress paths and stress-strain simulations for Colorado tests, sample 4-4, 4-5, 4-6 and 4-7 172
4.37 Plastic flow, stress paths and stress-strain simulations for Colorado tests, sample 4-8, 4-9, 4-10 and 4-11 174
4.38 Plastic flow, stress paths and stress-strain simulations for Colorado tests, sample 4-12, 4-13, 4-14 and 4-15 175
4.39 Plastic flow, stress paths and stress-strain simulations for Colorado tests, sample 4-16, 4-17, 4-18 and 4-19 176
4.40 Plastic flow, stress paths and stress-strain simulations for Colorado tests, sample 4-20, 4-21, 4-22 and 5-1 178
4.41 Plastic flow, stress paths and stress-strain simulations for Colorado tests, sample 5-2, 5-3, 5-4 and 5-5 179
4.42 Plastic flow, stress paths and stress-strain simulations for Colorado tests, sample 5-6, 6-1 and 6-2 180
5.1 Three stress-strain curves for uniaxial compression test of Mix 1, Sheffield tests 190
5.2 Three stress-strain curves for uniaxial compression test of Mix 2, Sheffield tests 190
5.3 Three stress-strain curves for uniaxial compression test of Mix 3, Sheffield tests 191
5.4 The variation of the stress-strain response of the three mixes under uniaxial compression loading 191
5.5 The volumetric strains versus the axial stresses for the three mixes . . 192
5.6 Plastic strain directions of concrete under uniaxial compression for Mix 1, sample M1A3_00_1 195
5.7 Plastic strain directions of concrete under uniaxial compression for Mix 2, sample M1D3_00_2 196
5.8 Plastic strain directions of concrete under uniaxial compression for Mix 3, sample M3A6_00_1 197

5.9 The axial stress versus axial and lateral strains for two levels of confinement 198
5.10 The peak axial stress versus lateral stress for the three mixes 199
5.11 Young's modulus for the three mixes with different levels of confinement 200
5.12 Poisson's ratio for the three mixes with different levels of confinement 200
5.13 The equivalent plastic strain at peak stress for the three mixes 201
5.14 The plastic flow and stress path for Mix 1 202
5.15 The plastic flow and stress path for Mix 2 202
5.16 The plastic flow and stress path for Mix 3 203
5.17 Experimental PNS and model fit for the three mixes 205
5.18 Experimental PNS and VTS, ρ_c and ρ_{vts} for Mix 1 206
5.19 Experimental PNS and VTS, ρ_c and ρ_{vts} for Mix 2 206
5.20 Experimental PNS and VTS, ρ_c and ρ_{vts} for Mix 3 207
5.21 Yield surfaces, plastic strain directions, experimental PNS and VTS, ρ_c and ρ_{vts} for mix 1 208
5.22 Yield surfaces, plastic strain directions, experimental PNS and VTS, ρ_c and ρ_{vts} for mix 2 209
5.23 Yield surfaces, plastic strain directions, experimental PNS and VTS, ρ_c and ρ_{vts} for mix 3 209
5.24 Experimental and model predictions for stress-strain curves of Mix 1, with 0, 10, 20, 30 and 50 MPa confinement 211
5.25 Experimental and model predictions for stress-strain curves of Mix 2, with 0, 10, 20 and 30 MPa confinement 213
5.26 Experimental and model predictions for stress-strain curves of Mix 3, with 0, 10, 20, 30, 40 and 50 MPa confinement 214
6.1 Experimental and model stress-strain curves for the Colorado tests, Series 1 227
6.2 Experimental and model stress-strain curves for the Colorado tests, Series 2 229
6.3 Experimental and model stress-strain curves for the Colorado tests, Series 3 231
6.4 Experimental and model stress-strain curves for the Colorado tests, Series 4 232
6.5 Experimental and model stress-strain curves for the Colorado tests, Series 5 and 6 233

Chapter 1

Introduction

1.1 Introduction

Proper understanding and characterisation of engineering materials and implementation of these models in modern computational solution procedures is a vital component for safe, economical and competitive design of industrial and public work systems. Unless constitutive models for the materials composing these systems, based on sound scientific principles, laboratory testing and verification, are employed in the analysis, the computer results will have only limited validity, if at all. This recognition has encouraged significant activities towards research for the constitutive modelling and testing for wide range of engineering materials. As a result, great number of models have been developed for a wide range of materials. In addition to the theoretical developments, it is also essential to calibrate the models based on appropriate laboratory tests and identify and evaluate the material constants [Desai *et al.*, 1991].

Concrete under compression is of significant importance in many special structures such as reactor containment vessels, off-shore structures, columns for high-rise buildings, bridges, prestressed concrete elements, gravity dams and other structures. Therefore, efforts have been made to develop constitutive models to analyse the response of plain concrete under multiaxial compression.

The behaviour of concrete on the macro-level is highly complicated due to its heterogeneous multi-phase nature. It exhibits nonlinear and complex mechanical behaviour. It is a cohesive-frictional material in which the stress transfer in many loading cases is accomplished by frictional forces. The three-dimensional stress-strain behaviour of concrete is highly pressure-sensitive ranging from quasi-brittle in tension to almost ductile response in highly confined compression.

With the acknowledgment of this difficulty, many constitutive models have been proposed and used for the analysis of concrete. These include the elasticity-based models [Kupfer, 1973; Elwi and Murray, 1979; Kotsovos and Newman, 1977], which no longer appear quite so prominent as they fail to address the irrecoverable deformations observed under load.

Fracture and damage models have been developed to deal with the stiffness degradation. This theory was first proposed by Kachanov (1958) to describe creep rupture in metals. The theory further developed to describe the isotropic and anisotropic damaging behaviour of concrete [Krajcinovic and Fonseca, 1981; Li and Ansari, 1999].

The microplane model is one of the recent advanced models [Bažant and Prat (1988a; 1988b)]. This model does not satisfactorily simulate degradation in the unloading stiffness and in its current explicit form it possesses a very high sensitivity to the values (and calibration) of the material constants [Qiu, 1999]. The numerical integration procedure required by this model is also costly in terms of computer disk space and CPU time [Tahar, 2000].

Most of the other models have been cast within the plasticity framework [Willam and Warnke, 1974; Ohtani and Chen, 1988; Chen and Saleeb, 1994b]. Attempts have been made to use elastoplastic modeling for prepeak behaviour and fracture energy for postpeak behaviour [Frantziskonis and Desai , 1987; Etse and Willam, 1994; Meschke *et al.*, 1998; Lee and Willam, 1997; Hansen and Willam, 2001]. Some efforts have concentrated on introducing an appropriate unified framework for modelling crack development through the use of strain softening and specific fracture energy concepts [Willam *et al.*, 1986; Smith, 1987]. Other work has examined approaches to provide a robust integration algorithm and the consistent tangent operator for plasticity models [Krieg and Krieg, 1977; Ortiz and Simo, 1986; Simo and Hughes 1987; Runesson *et al.*, 1988; Li, 2005].

A number of peak nominal stress (PNS) surfaces have been proposed to model the response of plain concrete. Mohr-Coulomb (1800) and the Drucker-Prager (1952) were the two first criteria. These criteria were developed to describe the response of materials such as rock, sand and concrete for which hydrostatic pressure affects the material yield and failure strengths. The Mohr-Coulomb criterion is rarely utilized in current concrete models in part because of the discontinuity of the surface which

causes numerical complications and in part because recent investigations show the Mohr-Coulomb criterion to be only a moderate fit to experimentally observed material response.

The Drucker-Prager criterion represents moderately well the response of plain concrete subjected to multiaxial compression and provides a smooth yield surface. This criterion is incorporated into some currently proposed concrete material models [Imran and Pantazopoulou, 1996]. The response of concrete subjected to biaxial compressive loading [Kupfer *et al.*, 1969] is characterized well by this criterion. Comparison of the Drucker-Prager criterion with experimental data shows that while the criterion may be used to represent the response of concrete subjected to multiaxial compression, the model over-estimates the capacity of concrete for high confinement if the calibration is based on the uniaxial compression and uniaxial tensile strengths.

A number of researchers have addressed the response of plain concrete under various load regimes through the use of multi-surface plasticity models. Murray *et al.* (1979) proposed a three surface model to characterise the response of plain concrete subjected to biaxial loading. This approach was extended to concrete loaded in three-dimensions by Chen and Chen (1975), and Lubliner et al. (1989). Experimental investigations of concrete subjected to severe hydrostatic pressure loading show that the material does not respond elastically as is implied by some models [Drucker-Prager, 1952; Murray *et al.*, 1979; Vermeer and De Borst, 1984] in which the failure surface is linear in Haigh-Westergaard space. This issue has been addressed by other models where a non-linear relationship is proposed [Han and Chen, 1985].

The evolution of yield surface is another important topic when the theory of plasticity is adopted. This evolution is typically defined by a hardening rule. Some models assume that the shape of the yield surface remains the same with the elastic region expanding and contracting as a function of load history [Kupfer *et al.*, 1969; Chen and Chen, 1975; Murray *et al.*, 1979]. In this case the hardening function is a scalar. There are few data defining the way the concrete elastic domain expands and contracts under multiaxial loading. Hence, it is reasonable to calibrate the hardening function on the basis of the well-defined uniaxial concrete response [Murray *et al.*, 1979; Lubliner *et al.*, 1989].

The hardening law in some models is based on the plastic strain as hardening pa-

rameter [Grassl, 2004]. Some researchers [Lade and Kim, 1988] used plastic work as a hardening parameter.

Models that propose variable shaped yield surfaces include that proposed by Han and Chen (1985), Ohtani and Chen (1988) and de Boer and Dresenkamp (1988). The model proposed by Han and Chen incorporates many of the techniques currently used in the development of a concrete yield surface that evolves under a variable load history.

Some models have been formulated assuming nonassociated flow rule where the yield function is chosen independently from the plastic potential function [Lee and Willam, 1997; Imran and Pantazopoulou, 2001; Grassl, 2004]. The evolution of the plastic strain is given as a function of the plastic potential, which depends on the stress vector and possibly other internal variables. Others modelled concrete using associated flow rule [Ohtani and Chen, 1988; Najjar *et al.*, 1993, Tahar, 2000; Li, 2005].

Although all the up-to-date constitutive models have been developed to give insight into a fundamental response of concrete, it is generally believed that the complexity of behaviour displayed by concrete is beyond the reach of these conceptualised approaches. The behaviour of plain concrete subjected to multiaxial stresses is the subject of an intensive experimental research programme in the Department of Civil and Structural Engineering at the University of Sheffield. The aim of this research is to obtain a detailed picture of the mechanical behaviour of plain concrete with different constituents under variety of load paths. This is to be used for the material in nuclear reactor vessels by extending the range of stresses in which it can be safely employed.

Examination of some advanced plasticity models developed for concrete revealed some previously un-reported features associated with the shape of the loading surfaces and the manner in which hardening is incorporated into these models. In particular the attractive model for concrete proposed by Etse and Willam [Etse and Willam, 1994] has a difficulty associated with the form of the hardening surfaces. Under moderate levels of hydrostatic confinement, the model can exhibit a loading direction oriented towards, rather than away from, the hydrostatic axis. This produces dilative plastic strains if an associated flow rule is adopted. Even without this undesirable feature, the Etse-Willam model shows a complex dependency of the shape of the deviatoric sections on the mean stress level and the degree

of hardening. Many of the other models exhibit vertices in the tension and compression regions. These difficulties can lead to instability (failure to converge) in a finite element analysis [Tahar, 2000].

Given these difficulties, an improved version of Etse-Willam model has been proposed by Tahar where the proposed hardening yield surface function is constructed such that the meridians always intersect the hydrostatic axis normally in the compression and tension quadrants. However, there are some shortcomings associated with this model. The model overestimates the axial strain in the pre-peak region for the uniaxial compression tests and for concrete under low level of confinement. The model also lacks the flexibility needed to identify the onset of plastic dilation.

1.2 Objective of the Thesis

The aim of this thesis is to develop a constitutive model for plain concrete with different constituents subjected to multiaxial compression loading. The model is to be flexible, extendable and based on experimental observations rather than abstract mathematical principles. The simulations are to be carried out over large number of tests with different stress paths, sample shapes and constituents. Beside the evaluation of the validity of the model, these simulations will offer a step forward in developing a comprehensive model which will be constituent dependent. The model is to be developed within the framework of plasticity and should take in consideration the fundamental behaviour of concrete and the advances which have been achieved in this field. The new yield surface is to be smooth and convex, and defined by a simple mathematical expression.

The newly developed model should have the following features:

1. Provide a realistic description of concrete behaviour in the full range of compression loading; both uniaxial and multiaxial, monotonic and cyclic loading, including proportional and nonproportional stress paths.

2. Take into account the apparent contraction and dilation of the material under load.

3. Offer a simple formulation which is easy to calibrate and is consistent with the fundamental laws of thermodynamics.

4. Satisfy Drucker's stability postulate to insure uniqueness, continuity, and stability of a solution

5. It will be suitable for use in computation (in particular the model should lend itself to a straightforward and efficient implementation in finite element codes).

1.3 The Original Contribution of the Thesis

The original contribution of the thesis can be summarised as follows:

1. Development of a new constitutive model to describe the behaviour of concrete under multiaxial compression. The new model has been created by using meridional reflection of the PNS envelope along with another quartic equation about symmetrical axis in the meridional plane. Special care has been given to the determination of the directions of the plastic strain vectors. This is then used to identify the yield surfaces assuming associated flow rule. The model is then fully validated under complex loading histories.

2. Proposal of a new hardening function based on the equivalent plastic strain.

3. Proposal of a new ductility measure to scale the equivalent plastic strain.

4. Introduction of an auxiliary formulation to deal with the stresses that fall out side the zones covered by the model.

5. A new formulation to identify the onset of plastic dilation.

6. Determination of the directions of the plastic strain vectors for concrete with different load paths, strengths and constituents, from existing experimental data.

7. Proving the validity of associated flow rule for concrete based on experimental identification. This has been achieved in two ways:

   (a) Identification of the peak nominal stress envelope and the plastic strain vectors at that envelope.

   (b) Using the plastic work contours.

8. Proposal for the shapes of the yield surfaces based on experimental observations. Two ways have been used to identify these surfaces (i) the plastic strain vectors, assuming associated plasticity, and (ii) the plastic work contours.

1.4 The Features of the Model

1. The adoption of the peak nominal stress reflection gives the model the flexibility to be used by any PNS formulation. This formulation also helps in the reduction of material constants.

2. The capability of the model to predict the plastic dilation.

3. The good performance of the model over a large number of multiaxial compression tests and different stress paths, cyclic loading, and for different types of concrete.

1.5 The Limitations

The newly developed model has the following limitations:

1. It deals with plain concrete.

2. The study is focused on the response of concrete in multiaxial compression only (no tensile states).

3. Only hardening response is modelled here (no softening).

4. Isotropic hardening is assumed in the initial and subsequent loading process (no anisotropy due to damage).

5. Associated flow rule has been assumed.

6. The model is time independent (no rate effect). In the experiments used here, the concrete is subjected to quasistatic short-term loading.

7. The investigation is restricted to the isothermal (temperature independent) case.

8. The concrete is subjected to quasistatic monotonic short-term loading.

9. The model is a phenomenological model, which relates average stresses to average strains (macroscopic level).

10. Only concrete and mortar with normal-to-high strength (f_c =20-60 MPa) is considered in this study (no high performance concrete).

1.6 Organisation of the Thesis

Chapter 2 presents an experimental observation of concrete under compression loading. The chapter starts with the definition of stress, and an introduction to the stress invariants and the Haigh-Westergaard stress space. The chapter then describes the structure of plain concrete. The uniaxial behaviour of concrete is discussed. This includes the axial and lateral stress-strain response, elasticity parameters, total and plastic volumetric strain, peak strength, the peak strain, plastic flow and plastic work. The behaviour of concrete under triaxial loading is investigated by the same topics that have been discussed in the uniaxial loading, with an addition of the peak nominal stress surface (PNS) and the volume transition stress (VTS) surface, and a discussion on the validity of the associated flow assumption. A proposal for the shape of the yield surfaces is introduced based on the identification of the plastic work contours and the directions of the plastic strain vectors.

Chapter 3 presents the formulation of the new constitutive model. The continuum constitutive modelling of concrete is briefly presented. This includes elasticity, damage, microplane and elasto-plastic models. The main characteristics of these models along with their advantages and disadvantages are introduced. The main topics associated with the theory of elasto-plasticity are then presented. These include the additive decomposition of the strain vector, the yield condition, the flow rule, and the hardening law. The loading and unloading states, the Drucker's stability postulate and the isotropic hardening are then discussed. The development of the consistency parameter and the tangent elasto-plastic matrix are also presented. The numerical integration algorithm needed for the infinitesimal equations along with a stable stress return algorithm, the closest point projection (CPP) needed to integrate the proposed elasto-plastic constitutive model at the material level is subsequently presented. The main features of the Sheffield model are also discussed with some observations and reservations. The formulation of the new model is also given. The isotropic hardening function which controls the evolution of the yield surfaces, and thereby the expanding elastic domain is then described. A new auxiliary stress surface has been formulated. The model first and second derivatives with respect to the stress (σ) and the internal variable k_p are presented in detail.

In Chapter 4, calibration and simulation of the model at a material level using triaxial and multiaxial compression test data are presented. The chapter presents the full set of material constants which are divided into three groups; elastic, PNS and hardening constants. The calibration process for these material constants is

subsequently discussed. This process enables the user to identify near-optimum value for each constant. The sensitivity analysis of each material constant reveals its influence on the response of the model. This has been done at two levels, local and global. The local level addresses the influence of each constant on the part of the model which it controls, while the global level addresses the influence on the stress-strain response. The simulations of the model for two sets of experimental data are presented; triaxial compression tests conducted at the University of Sheffield and a set of multiaxial compression tests carried out at Colorado University. Finally, a comparative study using an error measure based on the Root Mean Square method is presented.

Chapter 5 presents the investigations and simulations of concrete with different constituents. Three mixes were used for this purpose; the first was normal mix similar in mix design to that presented in Chapter 2, the second was made with no coarse aggregates and the third with double amount of coarse aggregates. The chapter begins with the examination of the uniaxial compression response of the three mixes. This includes stress-strain response, the volumetric strain, peak stress, peak strain, Young's modulus, Poisson's ratio and the plastic flow vectors. The same topics are discussed for the triaxial response with an additional study of the peak nominal stress envelope, the volume transition stress envelope and the yield surfaces. The simulations of the three mixes are then presented.

In Chapter 6, the general formulation of the numerical derivatives is introduced along with Romberg's optimisation method. Ridder's algorithm is presented with a verification study to evaluate the algorithm performance and the calculations of the derivatives. In order to explore the performance of the model using numerical derivatives, the Colorado multiaxial data set is re-visited. The calibration of the model is discussed and the simulations of a number of tests are presented. A comparative study of the time consumption for the numerical and analytical formulations is presented.

Finally, Chapter 7 summarizes the major findings of the thesis and suggests possible topics to be explored in further research work.

1.7 References

Bažant Z. P. and Prat P. C., 1988a, Microplane model for brittle-plastic material. I: Theory, *Journal of Engineering Mechanics.ASCE*, Vol. **114**, No. 10, pp. 1672-

1687.

Bažant Z. P. and Prat P. C., 1988b, Microplane model for brittle-plastic material. II: Verification, *Journal of Engineering Mechanics.ASCE*, Vol. **114**, No. **10**, pp. 1689-1702.

Chen A. C. T. and Chen W. F., 1975, Constitutive relations for concrete, *Journal of Engineering Mechanics Division, ASCE*, Vol. **101**, No. EM4, pp. 465-485.

Chen W. F. and Saleeb A. F., 1994 b, Constitutive equations for engineering materials, Vol. 2: Plasticity and Modeling, Elsevier.

de Boer R. and Dresenkamp H. T., 1989, Constitutive equations for Concrete in failure state, *ASCE Journal of Engineering Mechanics Division* , Vol. **115**, pp. 1591-1608.

Desai C. S., Krempl E., Frantziskonis G. and Saadatmanesh H., 1991, Constitutive laws for engineering materials, Proceedings of the third International Conference on Constitutive Laws for Engineering Materials: Theory and Applications, Tucson, Arizona, USA.

Drucker D. C. and Prager, W., 1952, Soil mechanics and plastic analysis or limit design, *Quar. Appl. Math*, Vol. **10**, pp. 157-165.

Elwi A. and Murray D. W., 1979, Hypoelastic concrete constitutive relationship, *Journal of Engineering Mechanics*, Vol. **105**, No. 4, pp. 623-641.

Etse G., and Willam K. J., 1994, Fracture energy formulation for inelastic behaviour of plain concrete, *ASCE, Journal of Engineering Mechanics*, Vol. **120**, No. 9, pp. 1983-2011.

Frantziskonis G. and Desai C. S., 1987, Constitutive model with strain softening, *International Journal of Solids and Structures*, Vol. **23**, No. 6, pp. 733-750.

Grassl P., 2004, Plasticity and damage mechanics for modelling concrete failure, Doctoral thesis, Chalmers University of Technology, Göteborg, Sweden.

Han D. J. and Chen W. F., 1985, A Nonuniform hardening plasticity model for

concrete materials, *Journal of Mechanics of Materials*, Vol. 4, No. 4, pp. 283-302.

Hansen E. and Willam K., 2001, A two-surface anisotropic damage/plasticity model for plain concrete, Proceeding of Framcos-4 Conference Paris, *Fracture Mechanics of Concrete Materials*, pp. 549-556.

Imran I., and Pantazopoulou S. J., 1996, Experimental study of plain concrete under triaxial stress, *ACI Materials Journal*, Vol. **93**, No. 6, pp. 589-601.

Imran I. and Pantazopoulou S. J., 2001, Plasticity model for concrete under triaxial compression, *ASCE, Journal of Engineering Mechanics*, Vol. **127**, No. 3, pp. 281-290.

Kachanov L.M., 1958, Time of the rupture process under creep conditions, Izvestia Akademii Nauk, USSR, Otdelenie Teknicheskikh Nau Izvestiya, Vol. 8, pp. 26-31.

Kotsovos M. D. and Newman J. B, 1977, Generalised stress-strain relations for concrete, *ACI Journal*, Vol. **74**, No. 9, pp. 443-446.

Krajcinovic D. and Fonseka G. U., 1981, The Continuous damage theory of brittle materials, Part I and Part II, *ASME, Journal of Applied Mechanics*, Vol. 48, pp. 809-824.

Krieg R. D. and Krieg D. B., 1977, Accuracies of numerical solution methods for the elastic-perfectly plastic model, Transactions of the ASME, pp. 510-515.

Kupfer H., Hilsdorf H. K. and Rusch H., 1969, Behaviour of concrete under biaxial stresses, ACI Journal, Vol. **66**, No. 52, pp. 656-666.

Kupfer, H., 1973, Das Verhalten des Betons unter mehrachsiger Kurzzeitbelastung unter besonderer Berücksichtigung der zweiachsiger Beanspruchung. In: Deutcher Ausschluss für Stahlbeton, Vol. 229, Berlin.

Lade P. V. and Kim M. K., 1988, Single hardening constitutive model for frictional materials, II. Yield criterion and plastic work contours, *Computers and Geotechnics*, Elsevier, Vol. **6**, No. 1, pp. 13-29.

Lee Y. and Willam K. J., 1997, Anisotropic vertex plasticity formulation for con-

crete in-Plane stress, *Journal of Engineering Mechanics*, Vol. **123**, No. 7, pp. 714-726.

Li Q. and Ansari F., 1999, Mechanics of damage and constitutive relationships for high-strength concrete in triaxial compression, *Journal of Engineering Mechanics*, Vol. **125**, No. 1, pp. 1-10.

Li T., 2005, Stress integration strategies for a new hardening/softening elasto-plasticity model for structural concrete, Doctorate thesis, The University of Sheffield.

Lubliner J., Oliver J., Oller S. and Onate E., 1989, A plastic-damage model for concrete, *International Journal of Solids and Structures*, Vol. 25, No. 3, pp. 299-326.

Meschke R., Lackner R. and Mang A., 1998, An Anisotropic elastoplastic-damage model for plain concrete, *International Journal for Numerical Methods in Engineering*, Vol. **42**, pp. 703-727.

Murray D. W., Chitnuyanondh L., Rijub-Agha K. Y. and Wong C., 1979, Concrete plasticity theory for biaxial stress analysis, *Journal of the Engineering Mechanics Division*, ASCE, Vol. **105**, pp. 989-1005.

Najjar Y. M., Zaman M. and Faruque M. O., 1993, Modelling of stress-strain behavior of plain concrete using a plasticity framework, *Materials and Structures*, Vol. **26**, pp. 129-135.

Ohtani Y. and Chen W. F, 1988, Multiple hardening plasticity for concrete materials, *ASCE, Journal of Engineering Mechanics*, Vol. 114, No. 11, pp. 1890-1910.

Ortiz M. and Simo J. C., 1986, Analysis of a new class of integration algorithms for elasto-plastic constitutive relations, *International Journal for Numerical Methods in Engineering*, Vol. **23**, pp. 353-366.

Qiu Y, 1999, An Investigation into the microplane model for concrete, Doctoral Thesis, Department of Civil & Structural Engineering, University of Sheffield, UK.

Runesson K., Sture S. and Willam K., 1988, Integration in computational plasticity, *Computer and Structures*, Vol. **30**, pp. 119-130.

Simo J. C., and Hughes T. J. R., 1987, General return mapping algorithms for rate independent plasticity, In Constitutive Equations for Engineering Materials, Desai(Ed.), Elsevier, pp. 221-231.

Smith S., 1987, On fundamental aspects of concrete behaviour, MSc. Thesis, University of Colorado.

Tahar B., 2000, C_2 Continuous hardening/softening elasto-plasticity model for concrete, Doctoral thesis, The University of Sheffield, UK.

Vermeer P. A. and De Borst R., 1984, Non-associated plasticity for soils, *Concrete and Rock*, Heron, Vol. **29**, No. 3.

Willam K. J. and Warnke E. P., 1974, Constitutive model for the triaxial behaviour of concrete, *IABSE Seminar on Concrete Structures Subjected to Triaxial Stresses III-1*, **184**.

Willam K. J., Hurlbut B. and Sture S., 1986, Experimental and constitutive aspects of concrete failure, Proc US-Japan Seminar FEA Reinforced Concrete Structs, ASCE Special Publication, pp. 226-254.

Chapter 2

The Deformation of Concrete under Compression

2.1 Introduction

The testing of concrete under multiaxial stresses provides vital information for the development and validation of a constitutive model. The first step in such modelling could be the adoption of the theory of elastoplasticity to simulate the ductile behaviour of confined concrete [for example Smith *et al.* 1989], although other approaches exist.

Since the pioneering work of Balmer (1949), many researchers have captured the experimental multiaxial deformation of concrete [Kotsovos and Newman, 1978; van Mier, 1986; Wang *et al.*, 1987; Smith *et al.*, 1989; Bellotti and Rossi, 1991; Chern *et al.*, 1992; Dahl, 1992; Imran and Pantazopoulou, 1996; Li and Ansari, 1999].

The present chapter reports on the experimental testing by others, to determine the mechanical properties of concrete subjected to triaxial loading. The experimental program was conducted at the Department of Civil and Structural Engineering at the University of Sheffield during 1998. The intention was to observe the behaviour of moderate strength concrete under triaxial compression with cyclic loading. As part of her taught MSc. degree, Papatheodorou carried out the tests under the supervision of Professor Crouch. The work was reported in a document to British Energy (UK) plc [Crouch *et al*; 2001]. The tests were carried out in a Hoek cell. This is a triaxial cell in which the axial forces are applied on the flat ends of a cylindrical specimen, and radial compressive forces are applied by pressurising the fluid in the reservoir of the cell. Figure 2.1 shows a cutaway view of this cell. The tests were performed by using stress control in the axial direction. As a result,

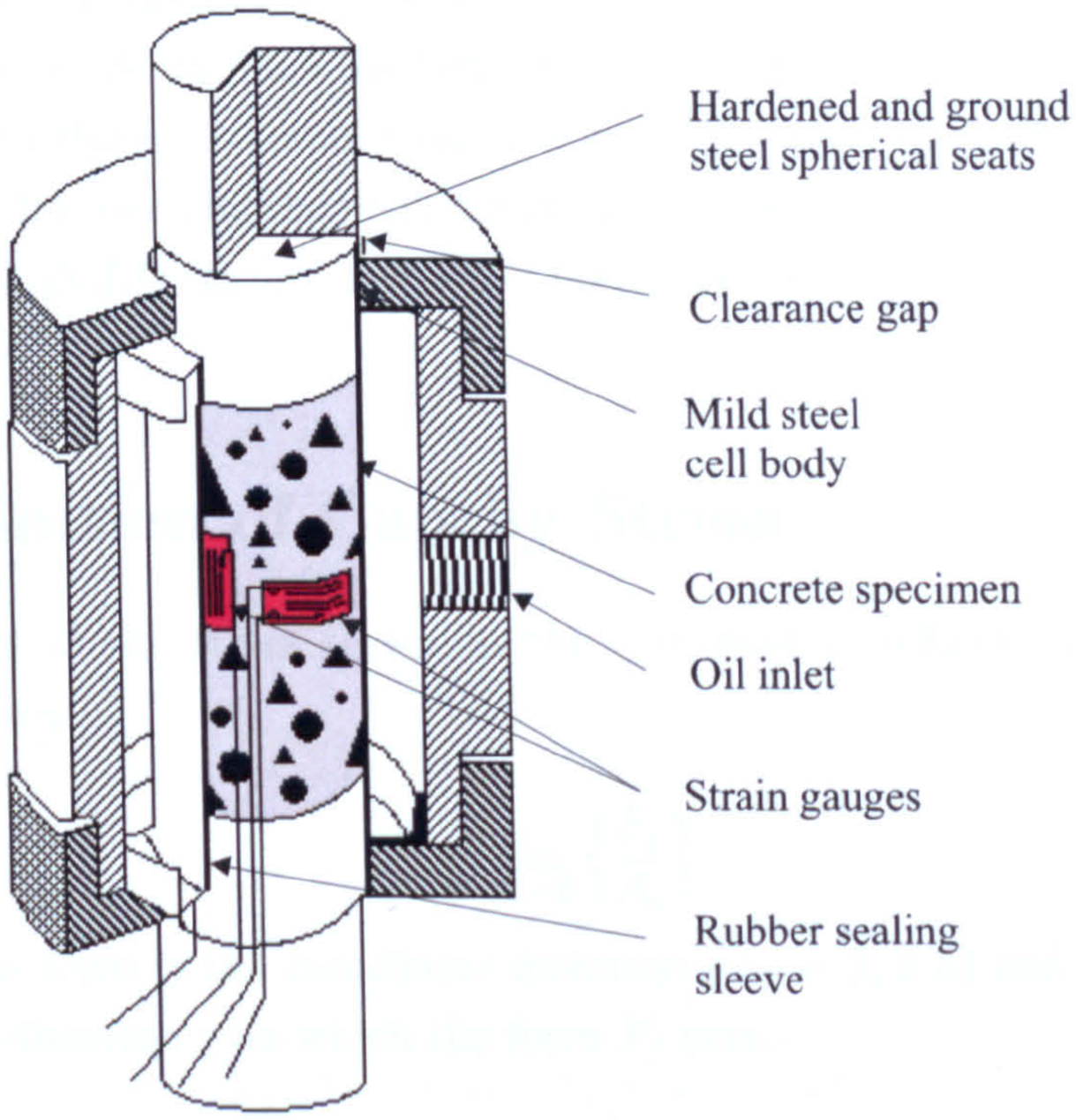

Figure 2.1: Cut-away view of the triaxial testing cell designed by Hoek and Franklin

the softening post-peak response was not recorded. The data stored in the results files contain the readings of two strain gauges measuring the axial strains and two strain gauges measuring the lateral strains. The average values of the axial and lateral strains, the time, the load, the axial and lateral stresses were also recorded. The concrete cylinders were 60 mm in diameter and 120 mm in height.

The raw output data needed to be prepared into common format with a few negative stress values removed from the beginning of some tests. The post peak readings were also ignored (see Chapter 1). The average readings from the two axial and lateral strain gauges were taken. If one gauge is broken before reaching peak, then the reading of the other gauge is taken as an average value. The signs of the compression stresses and strains are taken as negative, while the tensile stresses and strains are taken as positive. The test has been performed at ambient temperature.

In Section 2.2 the definition of stress, the stress invariants and the Haigh-Westergaard stress space, respectively are introduced. In Section 2.3 the structure of concrete is briefly described. In Section 2.4 the uniaxial behaviour of concrete is discussed. This includes the axial and lateral stress-strain response, elasticity parameters, the

total and plastic volumetric , the peak strength, the peak strain, plastic flow and the plastic work. In Section 2.5 the behaviour of concrete under triaxial loading is investigated with the same topics that have been discussed in Section 2.4 with an addition of the discussion of the peak nominal stress surface (PNS) and the volume transition stress (VTS) surface and a discussion on the validity of the associated flow assumption.

2.2 Definition of Cauchy Stress

The component of the stress tensor in the Cartesian coordinate system can be defined as follows:

$$\sigma_{ij} = \lim_{A_i \to 0} \left\{ \frac{F_j}{A_i} \right\} \tag{2.1}$$

where F_j is the force in the coordinate direction j $(j = 1, 2, 3)$ and A_i is the area normal to the direction j on which the force F_j acts.

There are, in total, nine stress components on the three faces of a cubic continuum under equilibrium (Figure 2.2 A).

$$\sigma_{ij} = \begin{bmatrix} \sigma_{xx} & \sigma_{xy} & \sigma_{xz} \\ \sigma_{yx} & \sigma_{yy} & \sigma_{yz} \\ \sigma_{zx} & \sigma_{zy} & \sigma_{zz} \end{bmatrix} \tag{2.2}$$

Only six components are unique due to symmetry in the absence of body moments (that is σ_{xy}=σ_{yx}, σ_{yz}=σ_{zy} and σ_{zx}=σ_{xz}). In engineering use, components of stress are often expressed in vector form as

$$\{\sigma\}^T = [\sigma_{xx} \quad \sigma_{yy} \quad \sigma_{zz} \quad \tau_{xy} \quad \tau_{yz} \quad \tau_{zx}] \tag{2.3}$$

where the component with identical subscripts are the direct (or normal) stresses and those with different subscripts are the shear stresses. This vector can be simplified into three principal direct stresses as acting seen in Figure 2.2 B. The principal stresses are defined as normal stresses on planes of such orientation that the associated shear stresses vanish. This condition of principal stresses can be stated without reference to any particular coordinate system (that is, they are coordinate invariant).

The principal stresses σ_1, σ_2, and σ_3 can be expressed in a three-dimensional space of principal stresses. If we take the tensile stress to be positive, the stress state

divides the stress space into eight different zones with differently signed values. Figure 2.3 shows the eight stress regions in principal stresses space.

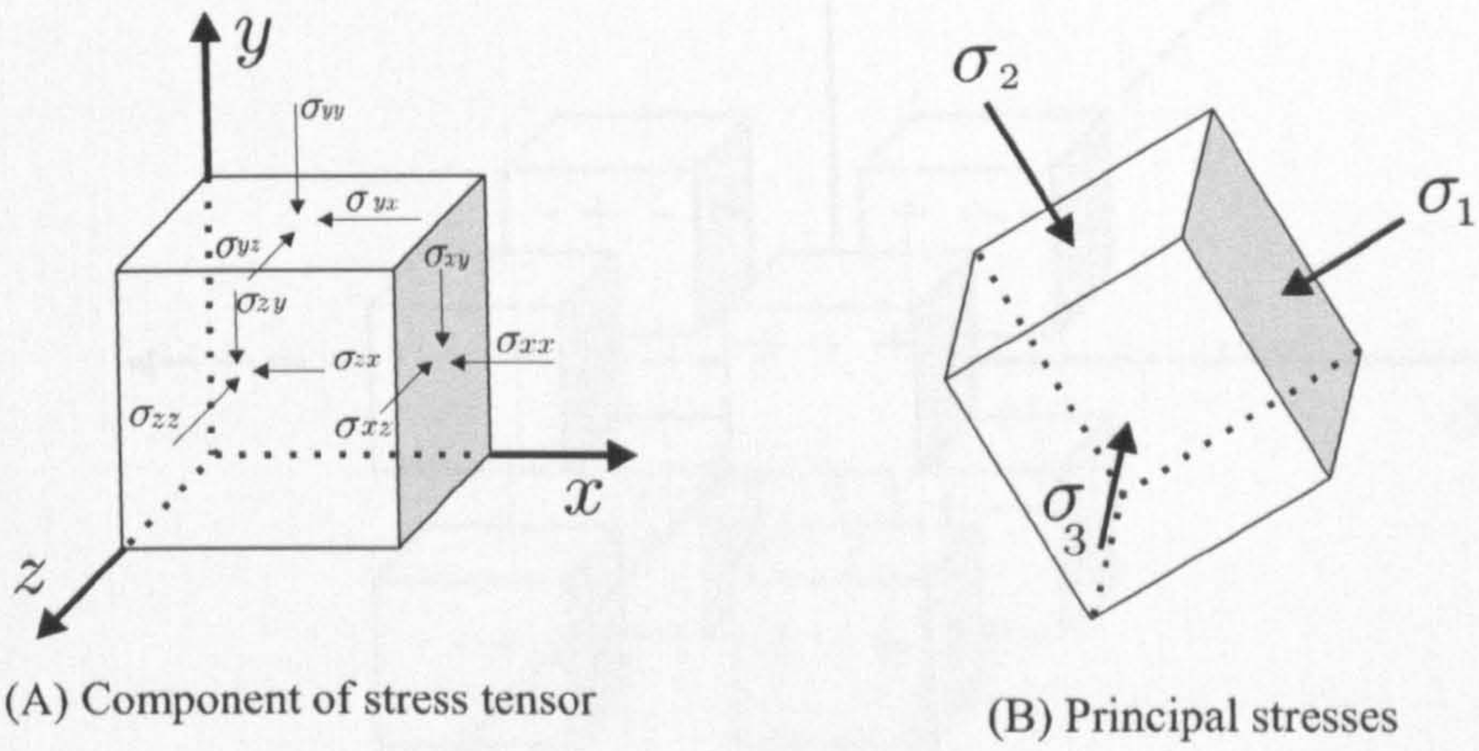

(A) Component of stress tensor

(B) Principal stresses

Figure 2.2: Element of stress tensor and three principal stresses

The principal stresses are not the only invariants . Alternative invariants can be defined in a number of ways [Desai and Siriwardane]; one way is to use the Cayley-Hamilton theorem which states that every square matrix over the real or complex field, satisfies its own characteristic equation. This implies the following:

If [A] is the given square n×n matrix and $[I]$ is the n×n identity matrix, then the characteristic polynomial of [A] is defined as:

$$F(\lambda) = det\,(\lambda\,[I] - [A]) \tag{2.4}$$

where *det* is the determinant function. The Cayley-Hamilton theorem states that the characteristic polynomial results in a zero matrix for any matrix [A]

$$F(\lambda) = 0 \tag{2.5}$$

If the stress tensor σ_{ij} is considered, the characteristic equation can be written as

$$\lambda^3 - I_1\lambda^2 + I_2\lambda - I_3 = 0 \tag{2.6}$$

where

$$I_1 = \sigma_{ii} = \sigma_{xx} + \sigma_{yy} + \sigma_{zz} = tr(\sigma) \tag{2.7}$$

$$I_2 = \begin{vmatrix} \sigma_{xx} & \sigma_{xy} \\ \sigma_{xy} & \sigma_{yy} \end{vmatrix} + \begin{vmatrix} \sigma_{yy} & \sigma_{yz} \\ \sigma_{yz} & \sigma_{zz} \end{vmatrix} + \begin{vmatrix} \sigma_{xx} & \sigma_{zx} \\ \sigma_{zx} & \sigma_{zz} \end{vmatrix} = \frac{1}{2}\,tr(\sigma)^2 \tag{2.8}$$

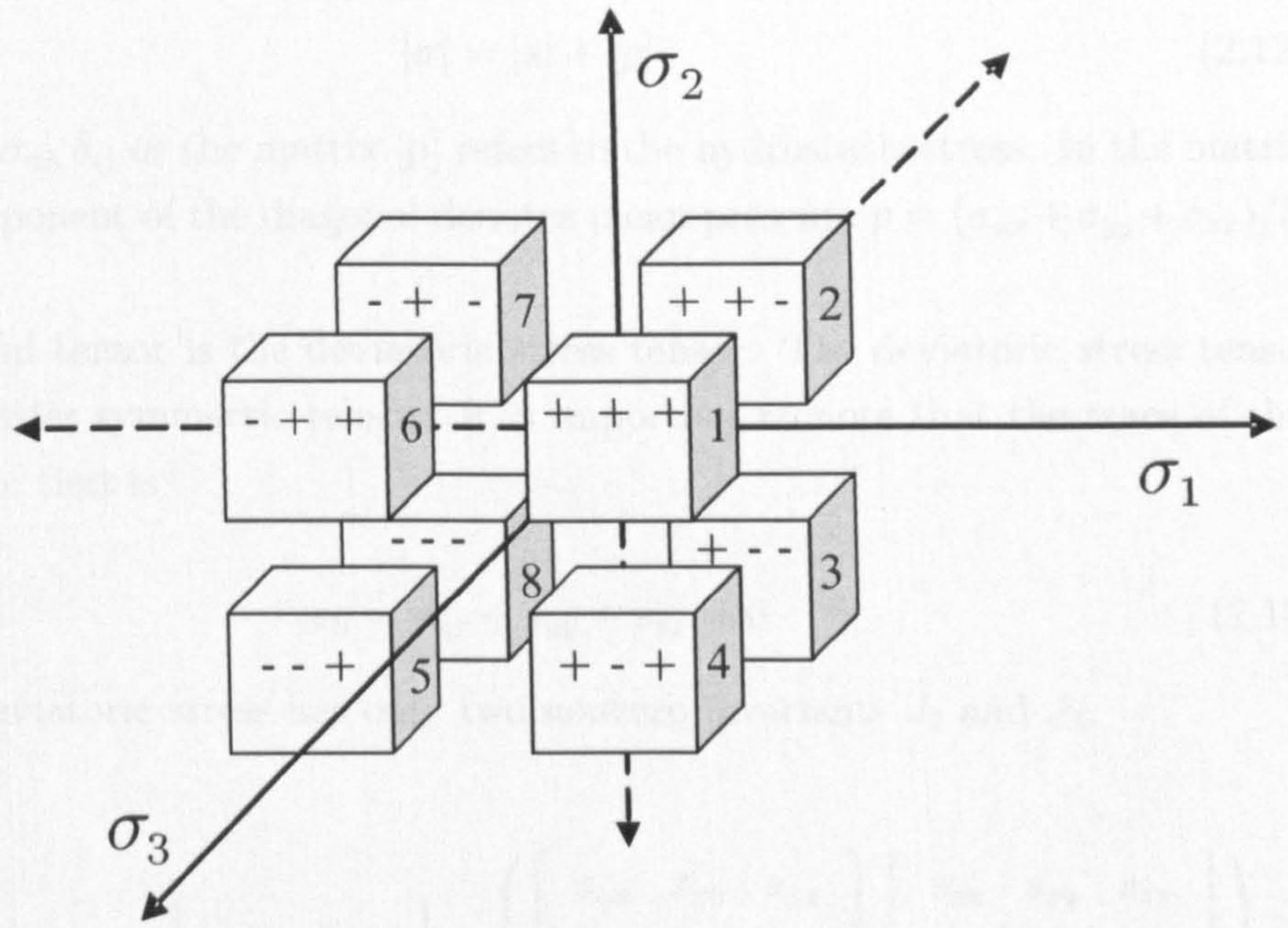

Figure 2.3: Eight stress regions in principal stresses space

$$I_3 = |\sigma_{ij}| = \frac{1}{3}\, tr(\sigma)^3 \tag{2.9}$$

These three quantities, I_1, I_2, I_3, are invariants of the stress tensor. According to the Cayley-Hamilton theorem equation 2.6 will be satisfied when σ_{ij} is substituted for λ.

In terms of the principal stresses, the three invariants can be written as

$$\begin{aligned} I_1 &= \sigma_1 + \sigma_2 + \sigma_3 \\ I_2 &= \sigma_1\sigma_2 + \sigma_2\sigma_3 + \sigma_3\sigma_1 \\ I_3 &= \sigma_1\sigma_2\sigma_3 \end{aligned} \tag{2.10}$$

The symmetric stress tensor σ_{ij} can be decomposed into two symmetric tensors; hydrostatic tensor and deviatoric tensor. The decomposition is given by

$$\sigma_{ij} = s_{ij} + \frac{1}{3}\,\sigma_{nn}\,\delta_{ij} \tag{2.11}$$

where s_{ij} is the deviatoric stress tensor, δ_{ij} is the Kronecker delta and repeated suffix implies summation.

Equation (2.11) can be written in matrix notation as

$$[\sigma] = [s] + [p] \tag{2.12}$$

The tensor $\frac{1}{3}\sigma_{nn}\delta_{ij}$ or the matrix [p] refers to the hydrostatic stress. In the matrix [p], each component of the diagonal denotes mean pressure $p = (\sigma_{xx} + \sigma_{yy} + \sigma_{zz})/3$.

Another useful tensor is the deviatoric stress tensor. The deviatoric stress tensor is a second-order symmetric tensor. It is important to note that the trace of this tensor is zero; that is

$$s_{ii} = s_{xx} + s_{yy} + s_{zz} = 0 \tag{2.13}$$

Hence the deviatoric stress has only two nonzero invariants J_2 and J_3.

$$J_2 = \frac{1}{2}s_{ij}\,s_{ij} = \frac{1}{2}\,tr(s)^2 = \frac{1}{2}tr\left(\begin{bmatrix} s_{xx} & s_{xy} & s_{zx} \\ s_{xy} & s_{yy} & s_{yz} \\ s_{zx} & s_{yz} & s_{zz} \end{bmatrix}\begin{bmatrix} s_{xx} & s_{xy} & s_{zx} \\ s_{xy} & s_{yy} & s_{yz} \\ s_{zx} & s_{yz} & s_{zz} \end{bmatrix}\right) \tag{2.14}$$

expanding (2.14)

$$J_2 = \frac{1}{2}[s_{xx}^2 + s_{xy}^2 + s_{zx}^2 + s_{xy}^2 + s_{yy}^2 + s_{yz}^2 + s_{zx}^2 + s_{yz}^2 + s_{zz}^2] \tag{2.15}$$

Substitute (2.12) into (2.15) and from the definition we have $s_{xx} = \sigma_{xx} - p$, $s_{yy} = \sigma_{yy} - p$, $s_{zz} = \sigma_{zz} - p$, $s_{xy} = \sigma_{xy}$, $s_{yz} = \sigma_{yz}$, $s_{zx} = \sigma_{xy}$, the forgoing expression is simplified to

$$J_2 = \frac{1}{6}[(\sigma_{xx} - \sigma_{yy})^2 + (\sigma_{yy}^2 - \sigma_{zz})^2 + (\sigma_{xx} - \sigma_{zz})^2] + \sigma_{xy}^2 + \sigma_{yz}^2 + \sigma_{zx}^2 \tag{2.16}$$

In terms of the principal stresses

$$J_2 = \frac{1}{6}[(\sigma_1 - \sigma_2)^2 + (\sigma_2 - \sigma_3)^2 + (\sigma_1 - \sigma_3)^2] \tag{2.17}$$

The third invariant of the deviatoric tensor (J_3) can be expressed as

$$\begin{aligned} J_3 &= \tfrac{1}{3}\,s_{ij}\,s_{jm}\,s_{mi} = \tfrac{1}{3}\,tr(s)^3 \\ &= \tfrac{1}{3}\,tr\left(\begin{bmatrix} s_{xx} & s_{xy} & s_{zx} \\ s_{xy} & s_{yy} & s_{yz} \\ s_{zx} & s_{yz} & s_{zz} \end{bmatrix}\begin{bmatrix} s_{xx} & s_{xy} & s_{zx} \\ s_{xy} & s_{yy} & s_{yz} \\ s_{zx} & s_{yz} & s_{zz} \end{bmatrix}\begin{bmatrix} s_{xx} & s_{xy} & s_{zx} \\ s_{xy} & s_{yy} & s_{yz} \\ s_{zx} & s_{yz} & s_{zz} \end{bmatrix}\right) \end{aligned} \tag{2.18}$$

expanding 2.18

$$\begin{aligned} J_3 = \; & \tfrac{1}{3}((s_{xx}^2 + s_{xy}^2 + s_{zx}^2)s_{xx} + 2(s_{xx}s_{xy} + s_{xy}s_{yy} + s_{zx}s_{yz})s_{xy} + \\ & 2(s_{xx}s_{zx} + s_{xy}s_{yz} + s_{zx}s_{zz})s_{zx} + (s_{xy}^2 + s_{yy}^2 + s_{yz}^2)s_{yy} + \\ & 2(s_{xy}s_{zx} + s_{yy}s_{yz} + s_{yz}s_{zz})s_{yz} + (s_{zx}^2 + s_{yz}^2 + s_{zz}^2)s_{zz}) \end{aligned} \tag{2.19}$$

$$= \tfrac{1}{3}(s_{xx}^3 + s_{yy}^3 + s_{zz}^3)$$

In terms of the principal stresses

$$J_3 = \frac{1}{27}(2\sigma_1 - \sigma_2 - \sigma_3)(2\sigma_2 - \sigma_1 - \sigma_3)(2\sigma_3 - \sigma_1 - \sigma_2) \tag{2.20}$$

For isotropic materials, the values of three principal stresses are sufficient to describe the state of stress uniquely as do the values of the three stress invariants, I_1, J_2, J_3.

This study will be restricted to isotropic behaviour, therefore the Haigh-Westergaard representation of the yield function is employed [Hill]. The use of these coordinates leads to an attractive geometric interpretation [Chen and Saleeb 1994a]. Figure 2.4 shows the Haigh-Westergaard stress space. In the Haigh-Westergaard representation, the hydrostatic and deviatoric stress components are defined by the stress invariants as follows

$$\xi = \frac{I_1}{\sqrt{3}} \tag{2.21}$$

$$\bar{\xi} = \frac{\xi}{f_c} \tag{2.22}$$

$$\rho = \sqrt{2\,J_2} \tag{2.23}$$

$$\bar{\rho} = \frac{\rho}{f_c} \tag{2.24}$$

where f_c is the uniaxial compression strength of concrete.

The position of the stress point in the deviatoric plane is identified by the Lode angle. It is the angle measured from the projection the major principal stress (σ_1) on the deviatoric plane to ρ and can be defined as

$$cos\,(3\,\theta) = \frac{3\sqrt{3}}{2}\frac{J_3}{J_2^{\frac{3}{2}}} \tag{2.25}$$

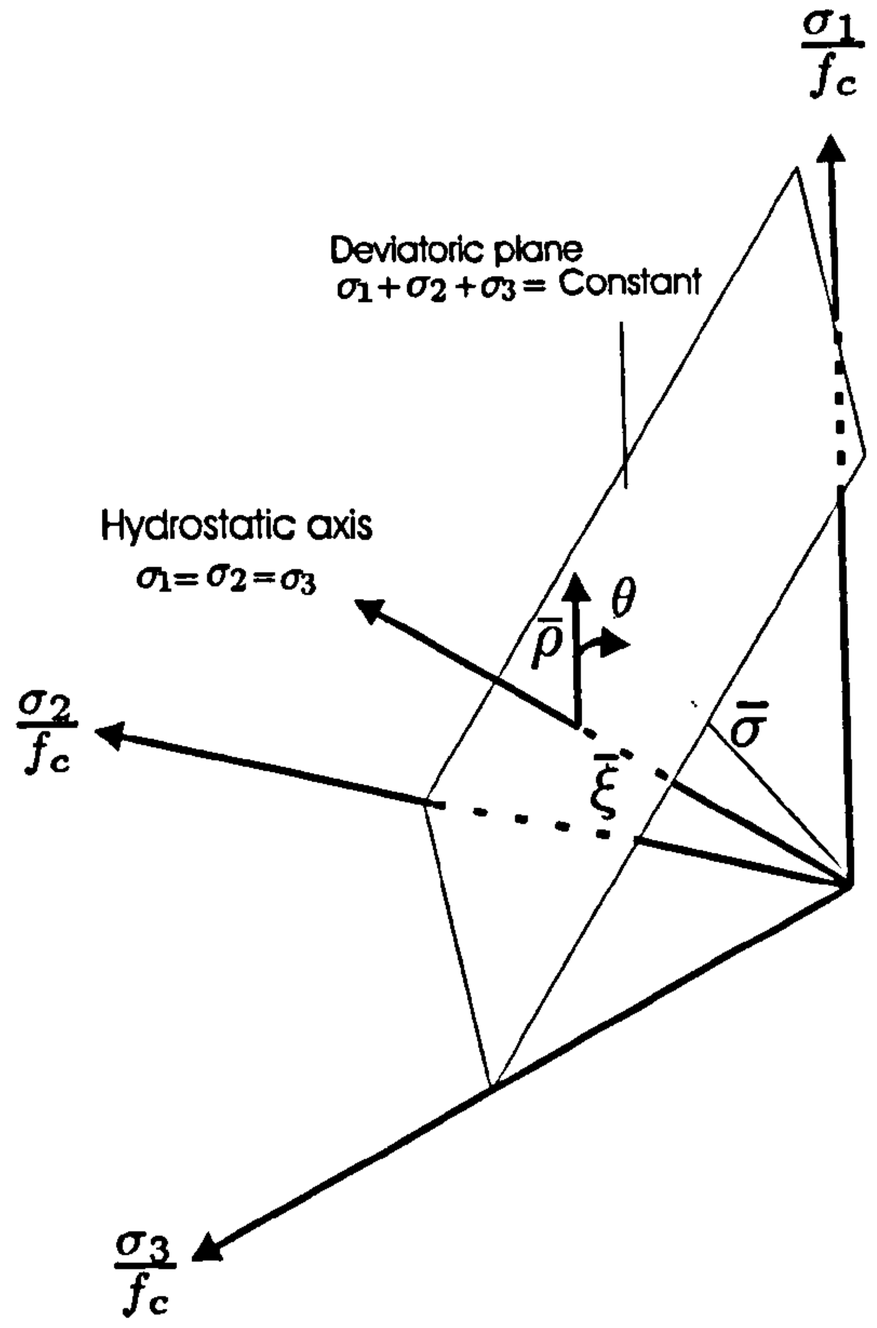

Figure 2.4: Normalised Haigh-Westergaard stress space

2.3 The Structure of Concrete

Plain concrete is a heterogeneous mixture of coarse aggregate, sand and hydrated cement paste (Figure 2.5). For normal-weight concrete mixes, coarse aggregate is usually gravel or crushed rock that is larger than 4.75 mm in diameter whereas sand is aggregate compromising particles with diameters between 4.75 mm and 0.75 mm. Hydrated cement paste (HCP) refers to the hydration products of Portland cement and water. The transition zone refers to the HCP located in the immediate vicinity of the coarse aggregate particles. Because the transition zone typically has a slightly higher water to cement ratio than is observed in the bulk HCP and because of the physical boundary between the different materials, the transition zone is generally weaker than the bulk HCP.

Schematically, concrete can be seen as either aggregates embedded in the cement matrix or a stack of aggregates of many different sizes. This means that concrete is highly heterogeneous. Despite its heterogeneous nature, concrete is often assumed to be isotropic.

In computational material science, concrete is characterised as a multi-phase material with several different representative scales. At the macroscopic scale, concrete

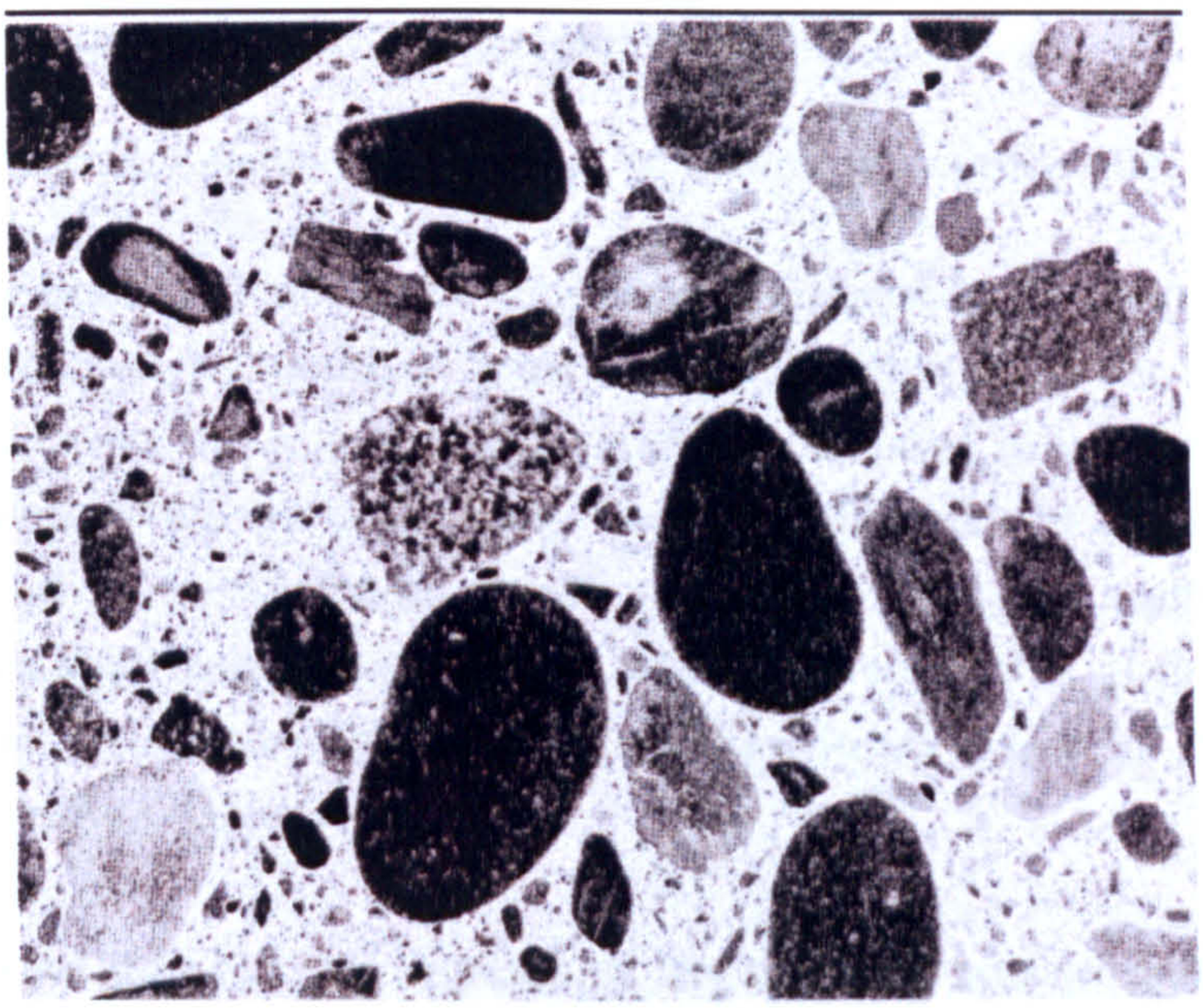

Figure 2.5: The concrete composite [Mehta and Monteiro]

could be regarded as a homogeneous material while at mesoscopic scale it is treated as consisting of coarse aggregates and mortar matrix. Further subdivisions of the mortar matrix produce fine aggregates and hardened cement paste with pores embedded within [Wriggers and Moftah].

One of the most important factors which affects the behaviour of concrete at any load state is the existence of large numbers of microcracks in the transition zone between the cement paste matrix and the aggregate. The microcracks are exist even before any load has been applied. In the following text, consideration of the causes of these microcracks is given.

It is generally accepted that the cause of fracture and failure of concrete is the propagation of flaws or microcracks which exist within the body of the material. Kotsovos (1979) has attributed these pre-existing flaws to a number of causes, the main ones being

1. Discontinuities in the cement paste matrix due to its complex morphology. Such flaws range in size from a number of angstrom units at the gel lattice level, to several microns, or above, for isolated or continuous capillary pores

2. Voids caused by shrinkage or thermal movements due to incompatibility between the properties of the various phases present in concrete

3. Discontinuities at the boundary between the aggregate particles and the paste

or mortar matrix caused by segregation

4. Voids present in concrete as a result of incomplete compaction

The above pre-existing flaws can be considered as randomly distributed and orientated within the material and to exhibit a range of shapes and sizes. The presence of these microcracks has a great effect on the mechanical behaviour of concrete, since their propagation during loading leads to the nonlinear behaviour at low stress levels and causes volume expansion near failure. Since the aggregate-mortar interface has a significantly lower tensile strength than mortar, it constitutes the weakest link in the composite system. This is the primary reason for the low tensile strength of concrete [Grassl].

Under moderate loading, the response of the concrete mixture is controlled by microcracking in the transition zone between the aggregate and the HCP. Under increased loading, microcracks in the transition zone grow and merge and therefore microcracks initiate in the HCP. Eventually, a continuous crack system forms which traverses the transition zone and the HCP, resulting in the loss of load capacity. Under compression loading, the continuous crack system may include cracks that transverse the coarse aggregate. Under tensile loading, the increased load acts directly to increase the stress at the crack tip and thus drive crack propagation. As a result, for tensile loading, the sequence of cracking leading up to the development of a continuous crack system and loss of strength occurs very rapidly. Increased compressive loading indirectly increases the stress at the crack tip, driving crack propagation at a slower rate. For compressive loading, the stages of crack initiation and propagation are readily identified in the observed stress-strain response of the concrete and loss of load capacity occurs more slowly.

2.4 The Behaviour of Concrete under Uniaxial Cyclic Compression Loading

The response of concrete subjected to uniaxial compression provides useful data for use in characterising the response of concrete to general loading. The mechanical behaviour is presented here in the form of stress-strain response, so that the material description becomes less dependent on the dimensions of the specimen tested.

2.4.1 Axial and Lateral Stress-strain Behaviour

The stress or strain state applied to a composite material such as concrete, generates a strain field within the material which is dependent on the distribution of the component phases (i.e. the aggregate particles and the cement paste matrix), and the size, shape and distribution of flaws. Local strain concentrations therefore develop throughout the material due to the incompatible deformation of the constituent phases. Such strain concentrations are further intensified due to the presence of flaws, particularly those with high aspect ratios. These flaws are considered to be the potential sources of any load-induced cracking.

Over the last thirty years a picture of the progressive fracture in concrete has emerged. The following notes collect together the descriptions from many tests. Newman (1973), in particular, has introduced the notions of stable and unstable crack growth in concrete.

Figure 2.6 shows a plot of the stress-strain response of a concrete sample subjected to uniaxial cyclic loading undertaken at Sheffield University. The sign of the axial compression and the lateral strain are taken as positive while the axial strain remained negative. This has been done for the sake of illustration but the signs used for all calculations throughout this thesis are taken as positive for tension and negative for compression.

From the shape of the stress-strain curves it seems that in the first part of the loading process, the curve shows an almost linear response up to about 30 percent of the peak stress (f_c). This is because at this level of loading the transition zone remains relatively undamaged and the pre-existing cracks do not propagate significantly.

At the end of this stage, the stress-strain curve exhibits its first visible nonlinear response. However, the crack process is stable and the debonding cracks are not interacting with each other. The nonlinearity then increases gradually with the tangent slope becomes increasingly flat until it becomes parallel to the strain axis at the peak stress. The increase of nonlinearity with increased loading is attributed to the irregularities and the different mechanical stiffness of the components that may lead to stress concentrations and, thereby, to further crack growth.

To clarify this, the stiffness of the aggregates is significantly greater than the stiffness of the surrounding matrix (for normal strength concrete). Hence, in com-

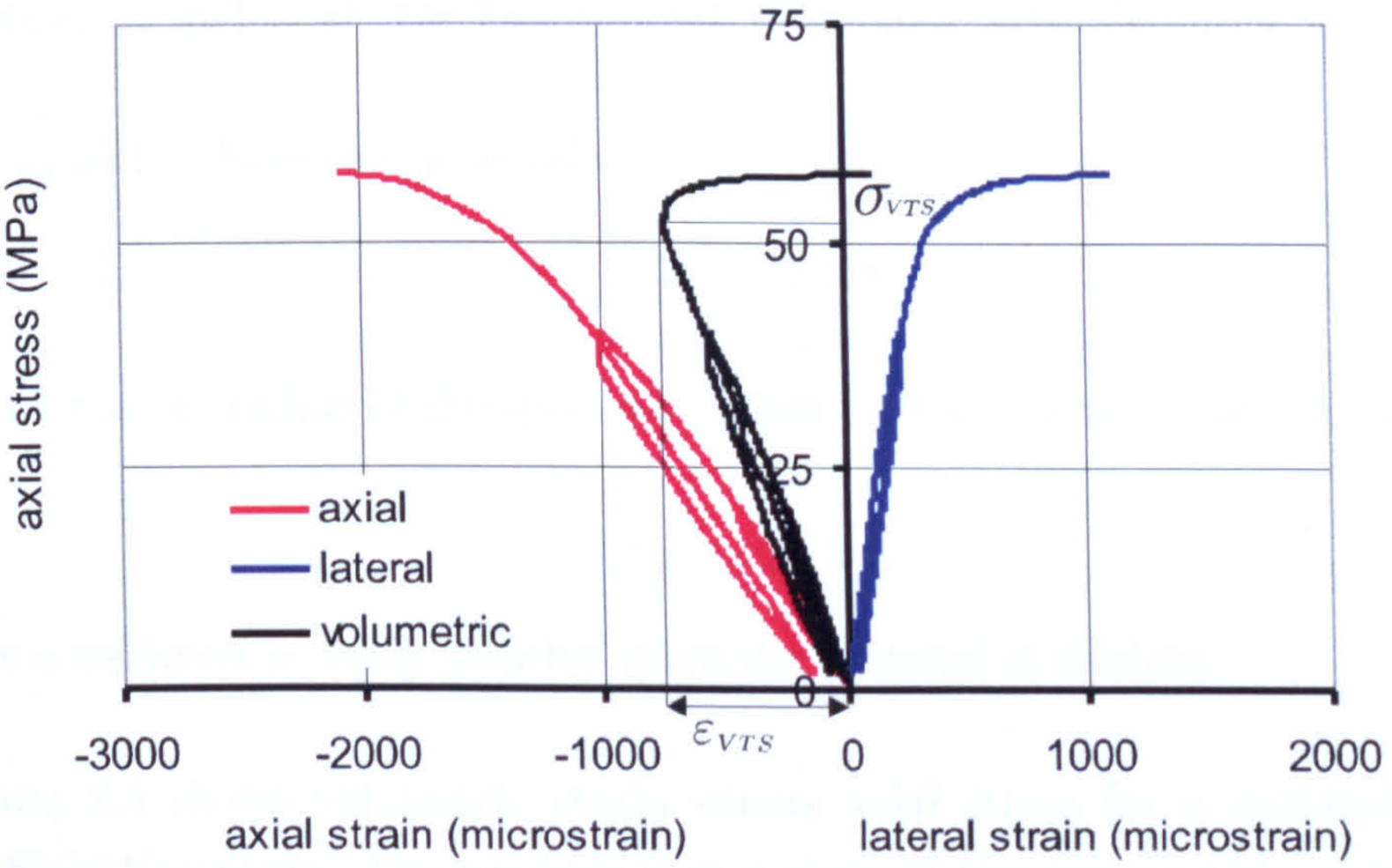

Figure 2.6: Axial, lateral and volumetric stress-strain for uniaxial compression test from Sheffield University, sample 5_3a

pression the lateral deformations of the softer matrix are greater than those of the aggregates, so the bond between aggregate and matrix is broken. Furthermore, due to the difference in lateral deformations, shear stresses are activated at the top and the bottom of the aggregate, leading to triaxial compression regions. When the external load increases, these cracks propagate into the matrix. This crack process is initially stable and the inclined cracks resist increasing load, while the cracks in the load direction open. The response in this stage is strongly non-linear. Due to crack opening, the lateral strains increase faster than the axial strains.

2.4.2 Volumetric Strain

The Volumetric strain (ε_v) is the ratio of the change in volume that occurs when a body placed under pressure to the original volume of the body. This is equal to the first invariant of the strain, $I_{1\varepsilon}$ or in other words, the trace of the strain tensor

$$\varepsilon_v = I_{1\varepsilon} = \varepsilon_1 + \varepsilon_2 + \varepsilon_3 \tag{2.26}$$

where ε_1, ε_2 and ε_3 are the principal strains. In cylindrical specimens, the principal strains, ε_1, ε_2 and ε_3 are equal to ε_l, ε_r and ε_c therefore

$$\varepsilon_v = \varepsilon_l + \varepsilon_r + \varepsilon_c \tag{2.27}$$

where ε_l, ε_r and ε_c are the longitudinal, radial and circumferential strains.

But ε_r and ε_c have the same value

$$\varepsilon_r = \frac{\Delta r}{r} = \frac{2\pi\Delta r}{2\pi r} = \varepsilon_c \tag{2.28}$$

where r is the radius of the specimen. Thus for this cases ε_v may be written as

$$\varepsilon_v = \varepsilon_l + 2\,\varepsilon_c \tag{2.29}$$

ε_v is considered as being positive when the material is dilating.

Figure 2.6 shows volumetric strain versus axial stress for a uniaxial test from Sheffield University. The concrete is in a state of compaction throughout the pre-peak range but close to the peak, the sample recovers its original volume. The volumetric strain exhibits an almost linear response for about 40% of the peak stress. Arrival at this stage has been termed by some researchers [Newman] onset of stable fracture propagation (OSFP), and has been linked with the stress level at which the volumetric strain becomes nonlinear. It should be noted that the detection of this point has been based on approximation, because the linearity of concrete itself is an issue of discussion.

The compaction continues with an increasing rate in nonlinearity. At about 90% of the peak, the size of the sample reaches its minimum. The cracks grow again at the transition zone and also in the cement paste matrix. When the two groups of cracks assemble, the system becomes unstable. The stress at this level is called by some researchers the *critical stress* [Chen and Saleeb, 1994b], while some call it the *onset of unstable fracture propagation* (OUFP) [Newman], and in this study it will be called *volume transition stress* (VTS). This is because the previous two names associated the behaviour of concrete with fractures which might bring some reservations when concrete is treated as continuum media. At this level of stress, concrete shows a time dependance fracture; that is, under sustain stress conditions cracks bridging between the transition zone and the matrix would lead to failure at a stress level lower than the peak strength f_c [Price].

The dilation response then starts, where the rate of dilation is significantly greater than the earlier contraction. The lateral displacements increase to such an extent

that the volume of the specimen starts to increase again.

Concrete loaded to more than the VTS responds with an increased compressive strain under constant loading. This results from spontaneous crack growth in the transition zone and HCP as well as from the consolidation of microcracks into continuous crack systems. Finally, loading to compressive strains beyond that corresponding to the compressive strength, results in reduced compressive stress. This response is a result of the development of multiple continuous crack systems and thereby the softening occurs.

For model development, the pre-peak behaviour may be simplified into three levels of response

1. Elastic: Concrete initially responds as an elastic material.
2. Nonlinear with volume contraction: Under increased loading, the response becomes none linear with volumetrical contraction.
3. Nonlinear with volume dilation: Further increase in compressive stress increases the nonlinearity with volumetric dilation and the sample retains its original volume close to the peak stress.

2.4.3 Poisson's ratio, ν

When concrete is loaded in uniaxial compression, it will shorten and at the same time develop a lateral strain. The ratio of lateral to axial strain is called Poisson's ratio. A common value measured for concrete is 0.20 to 0.21, but that value may vary from 0.15 to 0.25 depending upon the aggregate, moisture content, concrete age, and compressive strength [Neville].

In the case of uniaxial compression, Poisson's ratio is given by

$$\nu = \frac{-\Delta\varepsilon_2}{\Delta\varepsilon_1} \tag{2.30}$$

For the more general case (considered subsequently) we make use of the incremental 3D isotropic form of Hook's law

$$\Delta\varepsilon_1^e = \frac{\Delta\sigma_1 - \nu(\Delta\sigma_2 + \Delta\sigma_3)}{E} \tag{2.31}$$

$$\Delta\varepsilon_2^e = \frac{\Delta\sigma_2 - \nu(\Delta\sigma_1 + \Delta\sigma_3)}{E} \tag{2.32}$$

$$\Delta\varepsilon_3^e = \frac{\Delta\sigma_3 - \nu(\Delta\sigma_2 + \Delta\sigma_1)}{E} \tag{2.33}$$

Where ν is Poisson's ratio, E is the modulus of elasticity, $\Delta\sigma_1, \Delta\sigma_2, \Delta\sigma_3$, are the corresponding changes in the principal stresses and $\Delta\varepsilon_1, \Delta\varepsilon_2, \Delta\varepsilon_3$, are the changes in principal strains. In Sheffield's triaxial data (as has been mentioned) $\sigma_2 = \sigma_3$.

Solving Poisson's ratio, we obtain

$$\nu = \frac{(\Delta\sigma_2\Delta\varepsilon_1) - (\Delta\sigma_1\Delta\varepsilon_2)}{(\Delta\varepsilon_1\Delta\sigma_1) + (\Delta\sigma_2\Delta\varepsilon_1) - (2\Delta\sigma_2\Delta\varepsilon_2)} \tag{2.34}$$

$\Delta\sigma_1$, $\Delta\sigma_2$, $\Delta\varepsilon_1$ and $\Delta\varepsilon_2$ are taken from the loading and unloading points on the stress-strain curve as shown in Figure 2.7. The values of Poisson's ratio for two loading cycles in three tests of uniaxial compression are shown in Table 2.1. The values for the first cycle is slightly higher than the second cycle by approximately 5 %. The average value of the ratio for all cycles is found to be 0.21, which is a common value normally assumed for concrete analysis.

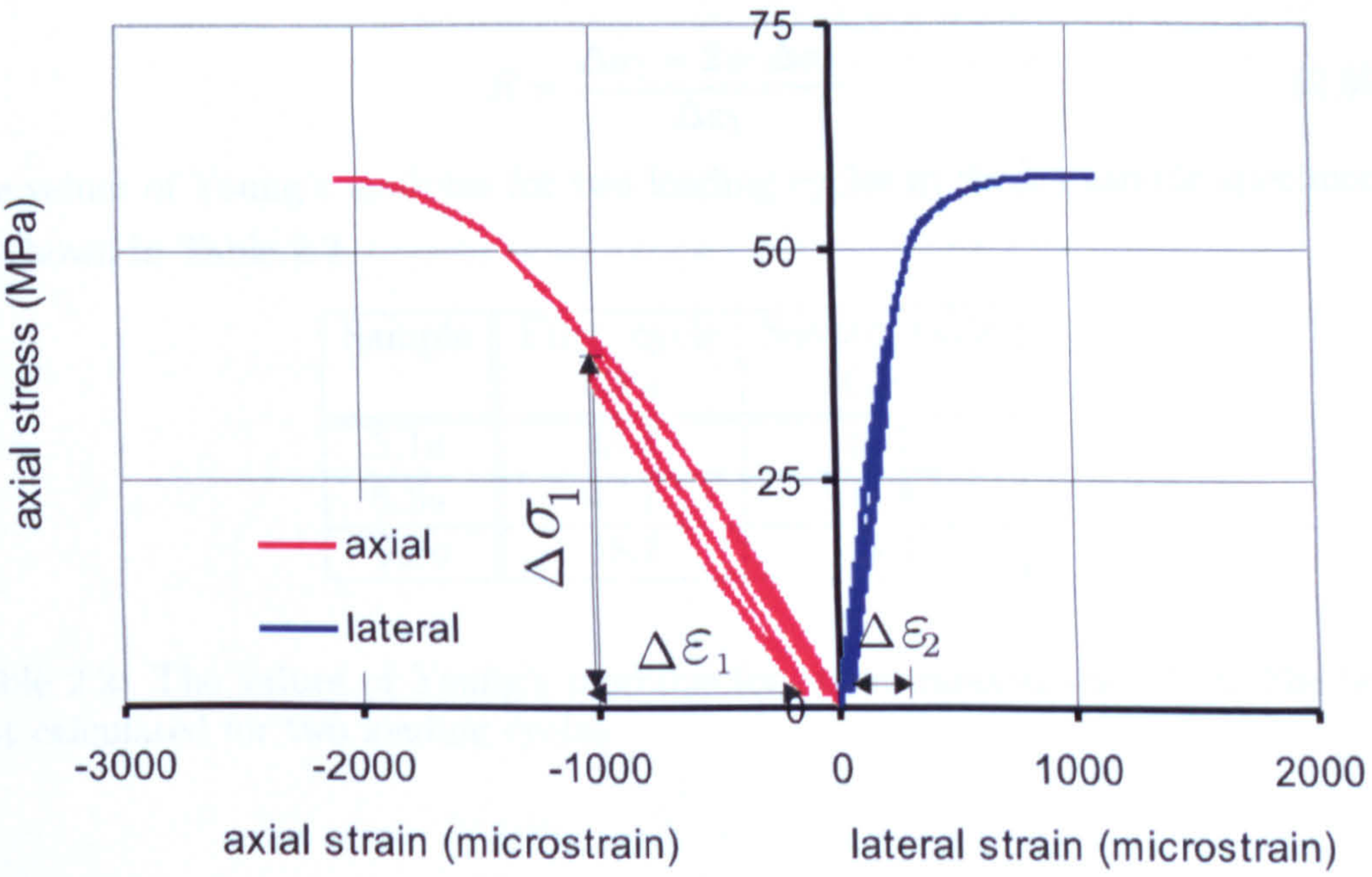

Figure 2.7: Axial tress versus axial and lateral strains with cyclic loading, Sheffield tests, sample 5_3a_R_0

Sample	First cycle	Second cycle
5_1a	0.22	0.21
5_3a	0.22	0.21
5_8c	0.21	0.2

Table 2.1: The values of Poisson's ratio from three uniaxial compression tests

2.4.4 Young's Modulus

The common way to define the Youngs modulus, E_c, is to assume it to be equal to the tangent ratio of the initial, approximately linear, part of the uniaxial stress-strain curve and is determined by the ratio of the average stress and the average strain in this region. However, the stress-strain curve is rarely perfectly linear, even at the initial part of the curve. In fact, sometimes concavity occurs at the initial part due to the closure of the pre-existing cracks. Therefore, there are different methods for computing the modulus; tangent, secant and chord moduli. In this study, the unloading chord modulus is used, which is the modulus calculated from the unloading reloading points on the stress strain curves as shown in Figure 2.7. The modulus is estimated as follows

$$E = \frac{\Delta\sigma_1 - 2\nu\,\Delta\sigma_2}{\Delta\varepsilon_1} \tag{2.35}$$

The values of Young's modulus for two loading cycles in three example specimens are shown in Table 2.2.

Sample	First cycle GPa	Second cycle GPa
5_1a	48.4	45.7
5_3a	47.1	44.4
5_8c	48.7	43.4

Table 2.2: The values of Young's modulus for three uniaxial tests from Sheffield test calculated for two loading cycles

The average value of the modulus for all of the loading cycles is found to be 46.3 GPa.

It is clear that the values of the modulus in the second loading cycle decreases by about 8 %. This degradation of stiffness is attributed to the damage that has

been encountered during the cyclic loading. The first value is thought to be more appropriate, since it represents the value before the damage has occurred.

It is of interest to compare the values found here with some empirical formulas that have been suggested in the literatures. The value of Young's modulus that has been recommended by ACI 318-95 (revised 1992) for structural calculations, applicable to normal weight concrete, is

$$E_c = 4.73\,(f_c)^{0.5} \tag{2.36}$$

where f_c is the uniaxial peak stress in MPa.

Using (2.36) with $f_c = 58$MPa, the value of E_c is found to be 36 GPa, which is about 22 % lower than the experimental value.

For concrete with strengths up to 83 MPa, ACI 363 R -92 quotes

$$E_c = 3.32\,(f_c)^{0.5} + 6.9 \tag{2.37}$$

The value calculated form this expression is found to be 32.2 GPa, which is about 30 % lower than the experimental value. These expressions are proposed for practical uses and the safety precautions taken may explain the conservative values for these expressions.

2.4.5 Volumetric Plastic Strain

Plastic strain is defined as the deformation that is not recovered upon unloading to zero stress. The total strain increment can be considered to be decomposed into elastic and plastic components, denoted by $\Delta\varepsilon^e{}_{ij}$ and $\Delta\varepsilon^p{}_{ij}$, respectively,

$$\Delta\varepsilon_{ij} = \Delta\varepsilon^e{}_{ij} + \Delta\varepsilon^p{}_{ij} \tag{2.38}$$

After calculating the linear elastic isotropic constants (E, υ), from (2.34) and 2.35), the elastic strain from (2.31), (2.32), and (2.33), the principal plastic strain from (2.38), then the volumetric plastic strain can be calculated as follow

$$\Delta\varepsilon^p_v = \Delta\varepsilon^p{}_a + 2\,\Delta\varepsilon^p{}_l \tag{2.39}$$

for the cylindrical specimens.

Figure 2.8 shows the volumetric plastic strain (ε^P_v) versus the uniaxial stress for a

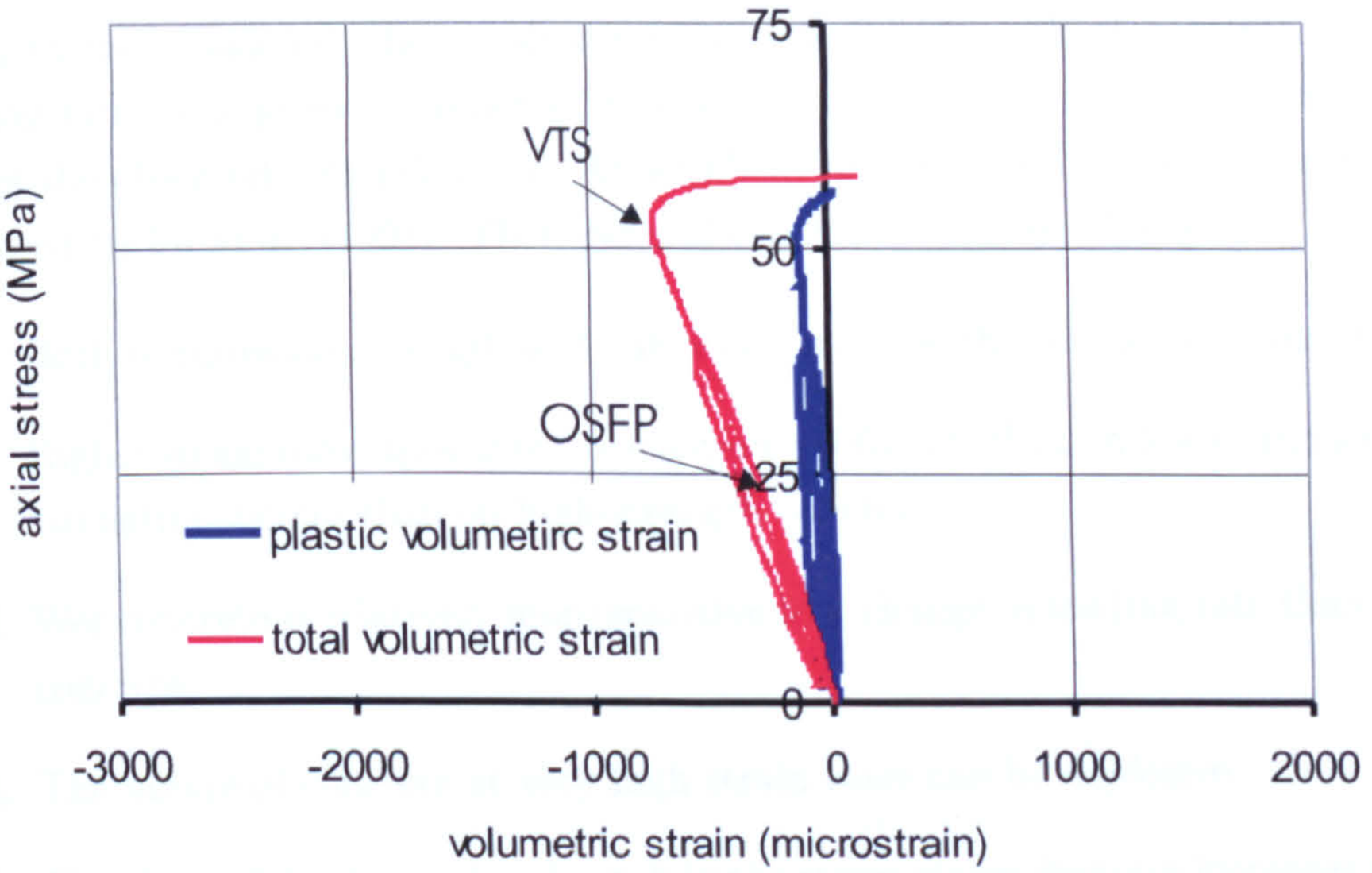

Figure 2.8: Axial stress versus total and plastic volumetric strain, uniaxial test, sample 5_3*a*, Sheffield University

uniaxial compression test from Sheffield University. Despite the appearance of very little volumetric plastic strain, considerable plastic deformation has occurred in the pre-peak region; yet the axial and lateral plastic strain oppose each other result in very little plastic volume change. It may be noted that no significant volumetric plastic strain is recorded for about 40% of the peak loading. This is a confirmation of the elastic response of the volumetric strain. ε_v^P is then increased at small but continuous rate up to about 0.9 f_c where the plastic VTS is reached. The stress level at this level has a significant importance. At this point the direction of the plastic strain vector is purely deviatoric. If an associated flow is assumed, this point could be used to identify the yield surface.

2.4.6 Peak Stress, f_c

The uniaxial compressive strength is defined as the average axial stress carried by the specimen at peak load, F_{max}:

$$f_c = \sigma_{max} = \frac{F_{max}}{A_c} \tag{2.40}$$

where A_c is the area on which the load is applied.

The uniaxial compression strength is used to normalise the multiaxial stress to obtain a non-dimensional representation of the data. An important factor which needs to be considered when evaluating the uniaxial strength of concrete is the loading rate. It is generally reported that the more rapid the rate of loading, the higher the observed strength value. An excellent review of the literature has been prepared by Fu *et al.* (1991). Their general conclusions are as follows:

1. Both compressive strength and stiffness increase with increasing strain rates.
2. Higher strain rates appear to have a more profound effect on low to moderate strength concrete than on high-strength concrete.
3. Wet concrete is relatively more sensitive to a change in loading rate than dry concrete.
4. The failure of concrete at very high strain rates can be explosive.
5. The slope of the descending branch in the stress-strain diagram increases with increasing rate of straining [Zia *et al.*].

However, Jones and Richart (1936) found that within the range of customary testing, the effect of rate of loading on strength is not that large. For example, compared with the data from the standard compression test (ASTM C 469), which requires the rate of uniaxial compression loading to be 0.25 ± 0.034 MPa/sec, a loading rate of 0.007 MPa/sec reduced the indicated strength of 150 × 300 mm concrete cylinders by about 12%. On the other hand, a loading rate of 7 MPa/sec increased the indicated strength by a similar amount [Mehta and Monteiro]. Figure 2.9 shows the effect of loading rate on the stress-strain behaviour of a uniaxial compression test.

The specimen size also needs attention in order to evaluate the present experimental results. Many studies [Tanigawa *et al.*, 1990; Baalbaki *et al.*, 1992; French and Mokhtarzadeh, 1993; Aitcin *et al.*, 1994] have been conducted to investigate the specimen size effect on the compressive strength. Comparisons were usually made between the compressive strength of 100 × 200 mm cylinders and that of 150 × 300 mm cylinders. Generally, 100 × 200 mm cylinders exhibit higher strengths than 150 × 300 mm cylinders. The difference may vary from 2 to 10 % with a common value being 5 %, and the difference is lower for higher strength concrete. Burg and Ost (1992) reported, however, that their test data showed that the strength of 100×200 mm cylinders was within 1 % of the strength of 150×300 mm cylinders. A contradiction to this trend is the study reported by Carrasquillo and Carrasquillo

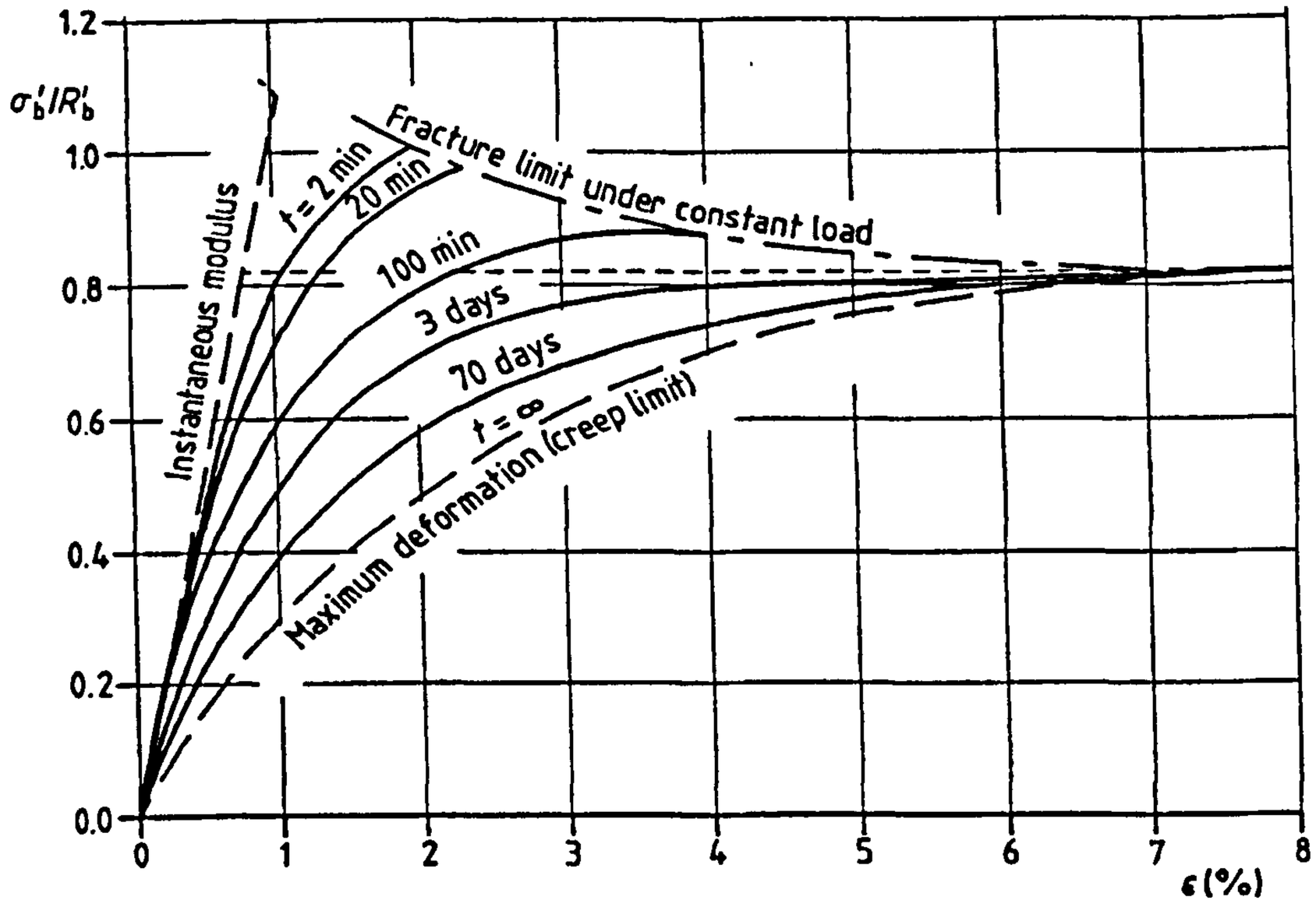

Figure 2.9: Effect of loading rate on the stress-strain behaviour in uniaxial compression [Fumagalli]

(1988a) which showed that the compressive strength of 100 × 200 mm cylinders were approximately 7 % lower than 150 × 300 mm cylinders.

The preparation of the end conditions (capping) of the concrete cylinder can significantly affect the measured compressive strength. Many studies [Pistilli and Willems, 1993; Boulay *et al.*, 1992; Lessard *et al.*, 1993; Johnson and Mirza, 1993] have been conducted to investigate the end condition effect. The standard sulphur mortar capping is found to be suitable for concrete strength up to about 52 MPa. For higher strength concrete, different procedures are used to prepare the end conditions of cylinders for compressive testing. One procedure is the parallel grinding of the ends of the cylinder, thereby eliminating the need for end caps. While grinding is regarded as the best procedure, it entails expensive equipment and longer preparation time so that it is not practical for many laboratory applications. Another procedure is the use of an un-bonded cap which is far more cost-effective and can be easily equipped by any laboratory and used in the field [Zia *et al*].

Ipatti (1993) compared untreated mold surface, sulphur capping, and ground surface for cube specimens, and sawn surface, sulfur capping, and ground surface for cylindrical specimens. The test results indicated that for the cylindrical specimens, the highest average strengths were obtained with ground or sulphur capped sur-

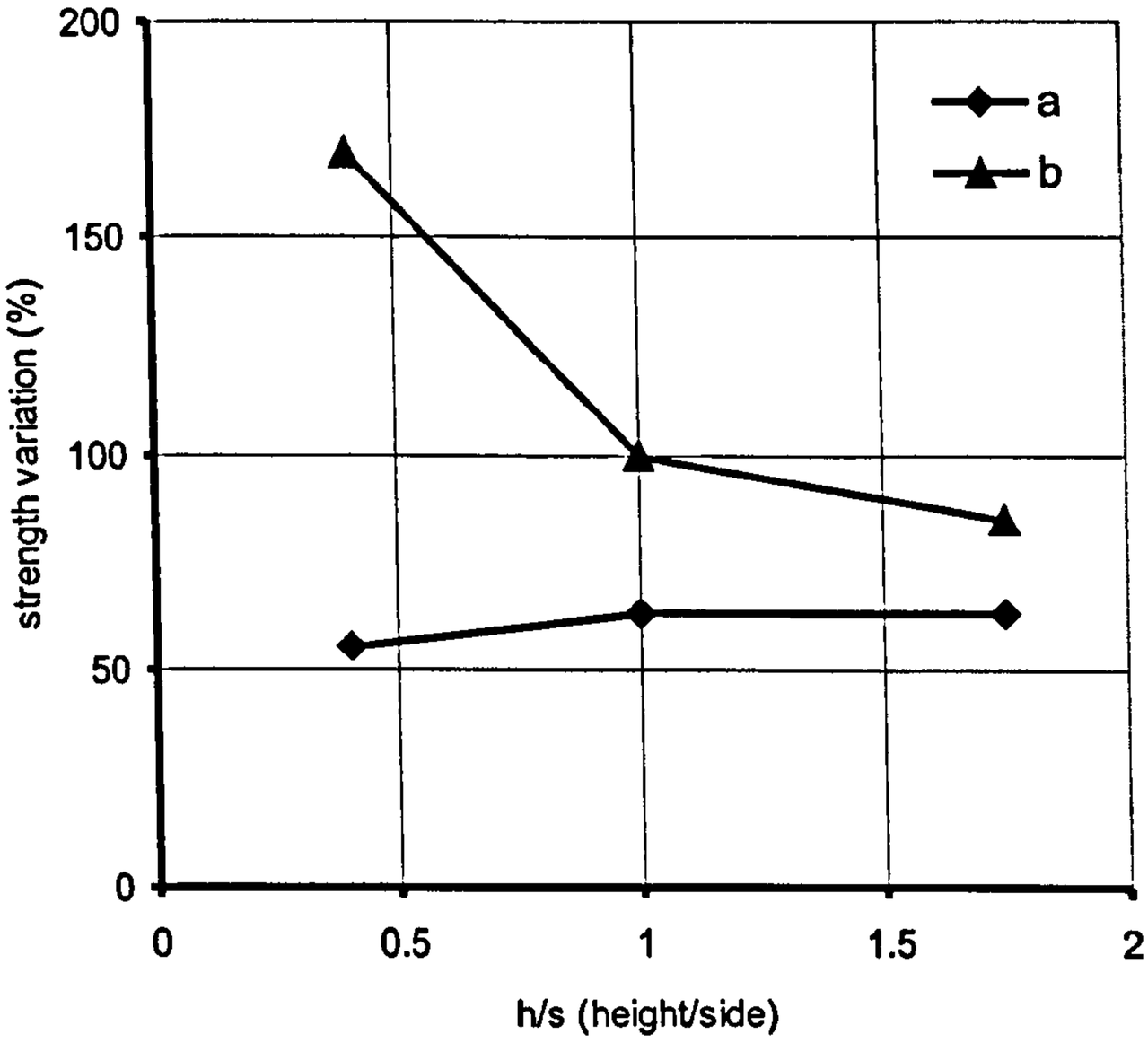

Figure 2.10: Uniaxial compression strength variation: (a) with antifriction materials between loading platens and specimen, (b) without anti-friction materials [Fumagalli].

faces. The coefficient of variation averaged 1 % for ground surfaces, 1.5 % for sulphur capped surfaces and 7.9 % for sawn surfaces. Figure 2.10 shows uniaxial compression strength variation with antifriction materials between loading platens and specimen, and without anti-friction materials.

Sample	Peak stress MPa	Peak axial strain $\mu\varepsilon$	Peak lateral strain $\mu\varepsilon$
5_1a	58.16	-1766.85	751.23
5_3a	58.01	-2085.77	1106.64
5_8c	53.93	-1679.08	904.21

Table 2.3: The values of peak stresses and strains for three uniaxial compression tests

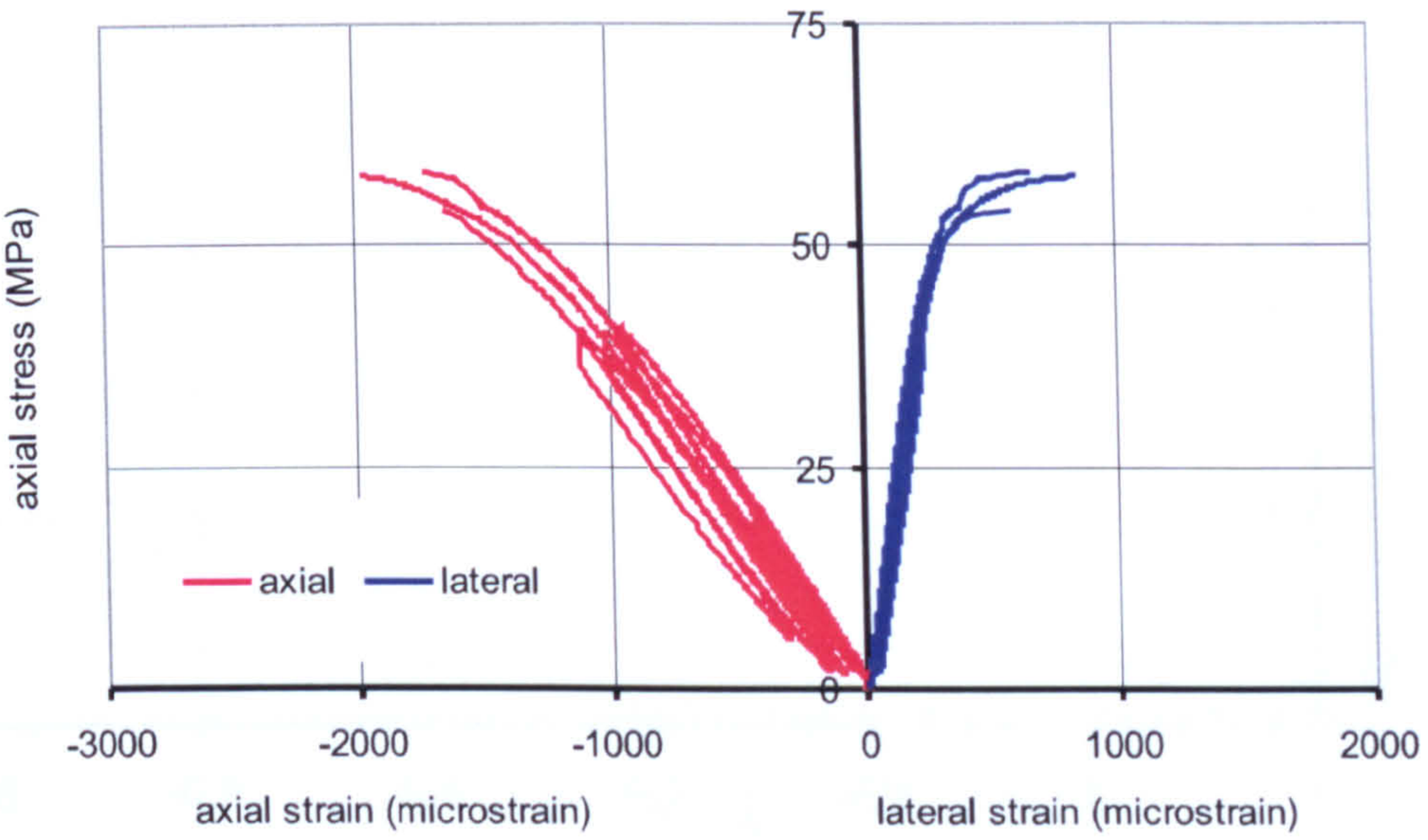

Figure 2.11: Uniaxial compression stress-strain variations for three tests

2.4.7 Strain at Peak Stress

The axial strain capacity, (i.e. the strain at maximum stress), similarly to the strength response, depends on various factors. Table 2.3 and Figure 2.11 show the stress-strain results for three different uniaxial tests from the Sheffield data. The average value of the first two samples is found to be -1926.31 $\mu\varepsilon$ and the lateral is 928.94 $\mu\varepsilon$. Even with nominally identical concrete mix and test arrangement, variations in peak strains have been recorded. The axial variation of the first two samples is around 20% and the variation in the lateral strain even higher. This is due to the rapid formation of multiple cracks especially in the lateral direction which makes the accurate recording of lateral strain at peak challenging. The heterogenous nature of concrete, the end preparation of the sample and the loading rate all play roles in these variations.

2.4.8 Plastic Work, W^p

Plastic work identifies the irrecoverable part of energy expended during a loading cycle, which may be obtained from the area enclosed in the loading cycle multiplied by the specimen volume. The incremental plastic work per unit volume is given by

$$W^p = \int \{\sigma\}^T \{d\varepsilon^P\} \tag{2.41}$$

For some constitutive models, cast within the framework of plasticity, the yield

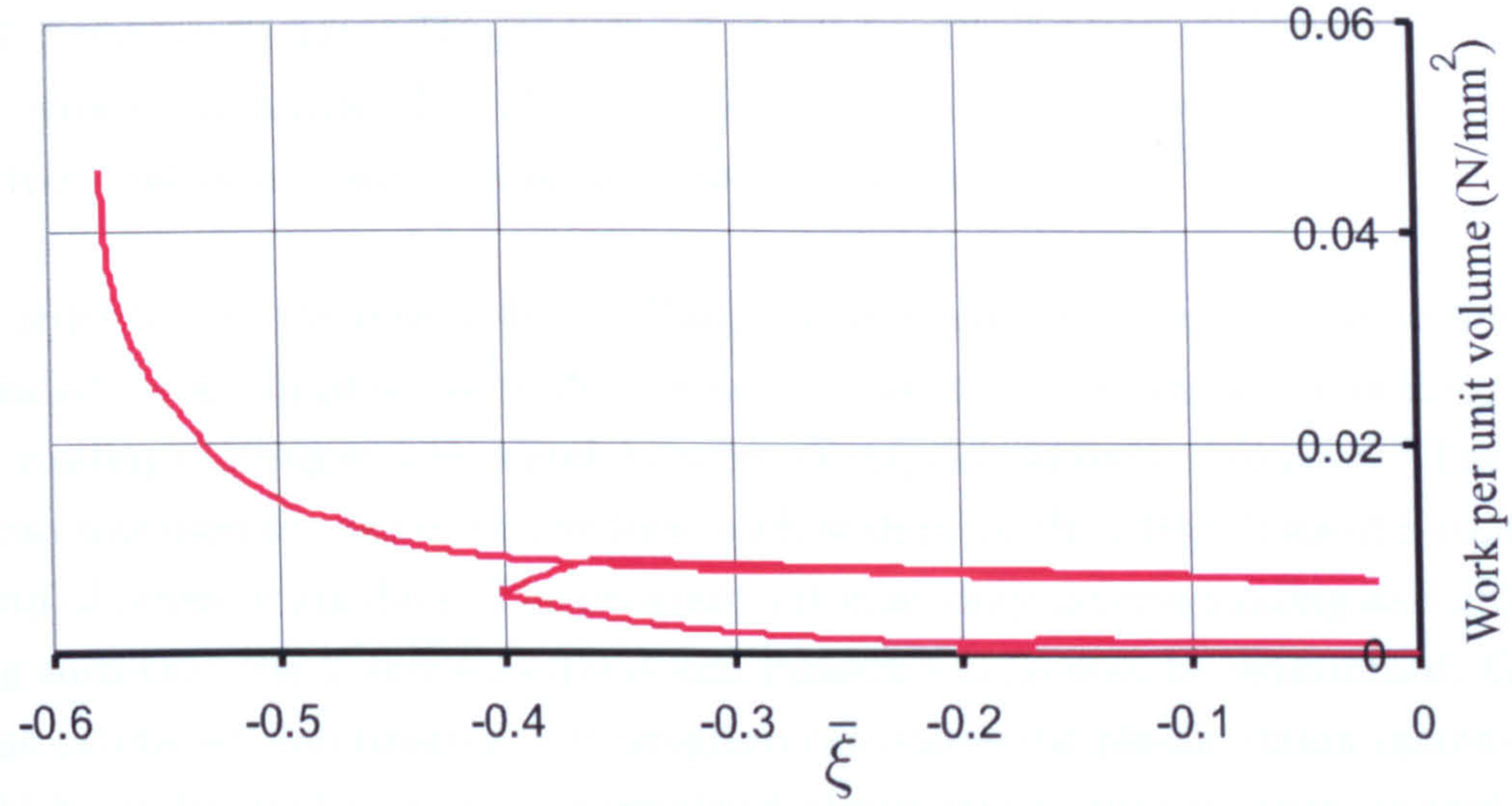

Figure 2.12: Plastic work versus $\bar{\xi}$ for uniaxial test, Sheffield tests

surface is defined as a contour of constant plastic work. The correlation between plastic work and yield surfaces is based on the experimentally observed behaviour of frictional materials [Sinan and Lade]. Some researchers [Lade and Kim] see advantages in using plastic work as a hardening parameter instead of plastic strain as the former avoids difficulties in determination of yield points on stress-strain curves. Computation of plastic work is relatively straight forward. The plastic work contours capture yielding in terms of shear strains as well as volumetric strains.

Figure 2.12 shows the plastic work for a uniaxial test from Sheffield University. The general shape of the response follows an exponential function. The response is concave, with loading to approximately 30% f_c showing no significant plastic work. Close to the peak, significant plastic work has been recorded. During the loading-unloading cycles, the plastic work does not appear to change. Plastic work represents the consumption of energy which can not be recovered. The concept of plastic work might prove to be an interesting way of defining the shape of the yield surfaces. Further discussion on this concept will be presented in Subsection 2.5.9

2.4.9 Plastic Flow

The plastic strain directions or the plastic flow is a kinematic assumption of the plastic deformation. It defines the direction and thus could be treated as a vector

in the six dimensional strain space or three dimensional space in principal coordinates. The component which is parallel to the hydrostatic axis, represents the volumetric strain rate. The component parallel to the deviatoric axis represents the deviatoric strain rate. The identification of the plastic flow gives direct indication of the yield surface when associated flow rule is assumed.

In order to plot the plastic flow in Haigh-Westergaard stress space, the author has created a Fortran program to determine the change in the plastic strain directions by reading existing experimental data from compression tests of concrete. The program was used to read in 81 test files, each with more than 1000 lines of 8-columns data of stress-strain data. The program automatically detects loading and unloading such that the Young's modulus and Poisson's ratio may be determined. Given this (averaged) information, the program calculates the plastic strain increments, which can be used to plot the normalised plastic strain vectors superimposed on a stress path diagram.

The algorithm for the calculation of the plastic flow operates as follows

1. It identifies the loading-unloading turning points on the stress-strain curves.

2. It calculates the Poisson's ratio (ν) for every cycle using (2.34).

3. It selects the appropriate ν value, the value of the first cycle, the last, or the average value (depending on the user control).

4. It calculates the Young's modulus for each cycle using (2.35).

5. It selects the appropriate value for the Young's modulus.

6. It calculates the axial elastic strain from (2.31), and the lateral elastic strain from (2.32).

7. It calculates the axial plastic strain, ε_a^p

$$\varepsilon_a^p = \varepsilon_a - \varepsilon_a^e \tag{2.42}$$

and the lateral plastic strain, ε_l^p

$$\varepsilon_l^p = \varepsilon_l - \varepsilon_l^e \tag{2.43}$$

8. The hydrostatic strain invariant increment, $\Delta\xi_\varepsilon^p$, is calculated from

$$\Delta\xi_{\varepsilon}^{p} = (\Delta\varepsilon_{a}^{p} + (2\,\Delta\varepsilon_{l}^{p}))/\sqrt{3} \tag{2.44}$$

9. The deviatoric strain invariant increment, $\Delta\rho_{\varepsilon}^{p}$, is defined from

$$\Delta\rho_{\varepsilon}^{p} = \sqrt{\frac{2}{3}}\,|\Delta\varepsilon_{a}^{p} - \Delta\varepsilon_{l}^{p}| \tag{2.45}$$

10. It calculates the norm of the plastic strain invariant increment

$$|\Delta\varepsilon^{p}| = \sqrt{(\Delta\xi_{\varepsilon}^{p})^{2} + (\Delta\rho_{\varepsilon}^{p})^{2}} \tag{2.46}$$

11. The program normalises ξ_{ε}^{p} and ρ_{ε}^{p} with respect to this norm

12. From (2.22) the code calculates the normalised hydrostatic stress invariant $\bar{\xi}$ and from (2.24) it calculates the normalised deviatoric stress invariant $\bar{\rho}$

13. Finally, the code superimpose the strain invariants on the stress path.

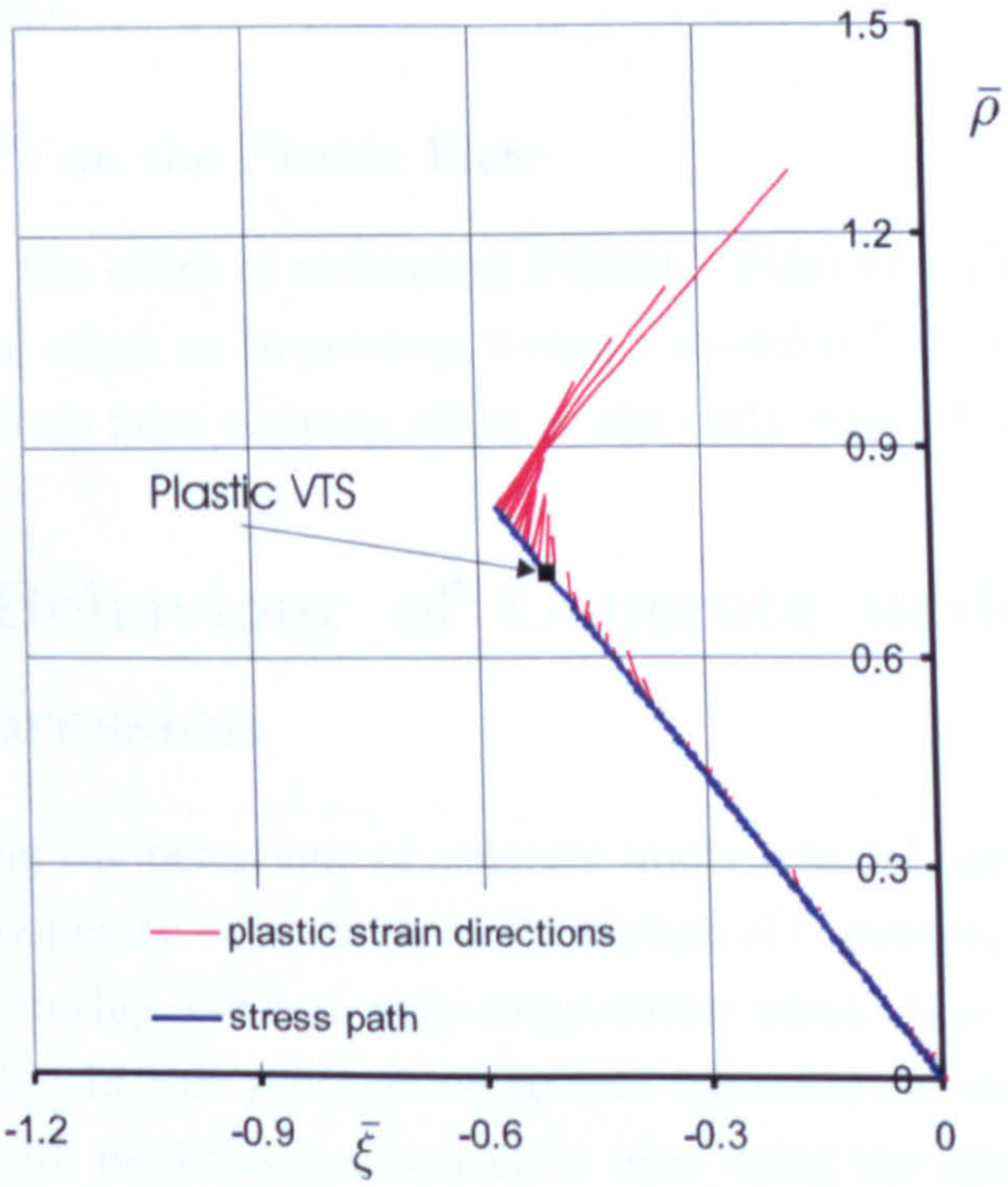

Figure 2.13: Plastic strain directions, stress path, and volumetric transition stress point for uniaxial compression test, Sample 5_3a, Sheffield tests

Figure 2.13 shows the plastic strain direction for one uniaxial test from Sheffield University. The magnitude of the plastic strain is seem to increase with continuation of loading. During the initial part of loading, the plastic strain directions (of very small magnitude) seem to have an almost random directions. This is due to the cyclic loading where some plastic strains appear, although, theoretically for an un-coupled elasto-plastic material, the unloading should be purely elastic. The plastic strain directions are predominantly in the negative hydrostatic direction during the initial loading. This indicates plastic compaction in the specimen. The direction then becomes increasingly rotated towards the deviatoric direction, becoming purely deviatoric at the plastic volumetric transition stress point. Beyond this point, the direction of the plastic strain becomes increasingly volumetric but in the positive direction which indicates that the specimen is undergoing plastic dilation in this phase of the test.

2.4.9.1 Effect of E on the Plastic Flow

Figure 2.14 shows the sensitivity of the plastic strain directions following increase of Young's modulus by 20%. Increasing the modulus increases the elastic strains which delays the occurrence of the plastic strains. This effect decreases as the peak is approached. The later is due to the plastic strains becoming the dominant part of the strain response.

2.4.9.2 Effect of ν on the Plastic Flow

Figure 2.15 shows the effect of increasing Poisson's ratio by 20%. Increasing this ratio has a similar effect to increasing Young's modulus but with less intensity. Both elastic constants have a strong effect in the early stage of loading.

2.5 The Behaviour of Concrete under Triaxial Compression

When investigating the behaviour of concrete under triaxial compression, one can not neglect the Cooperative Research on Properties of Concrete, promoted by Gerstle in the 1970s, during which a wide comparative research programme was performed [Fumagalli]. In this programme several laboratories, the most active and qualified in the field, performed comparative tests using the same concrete from a central source, prepared at the University of Colorado in Boulder. The laboratories used advanced but quite different testing methodologies. The large variation in experimental results suggests that basic research is not yet able to explore in an

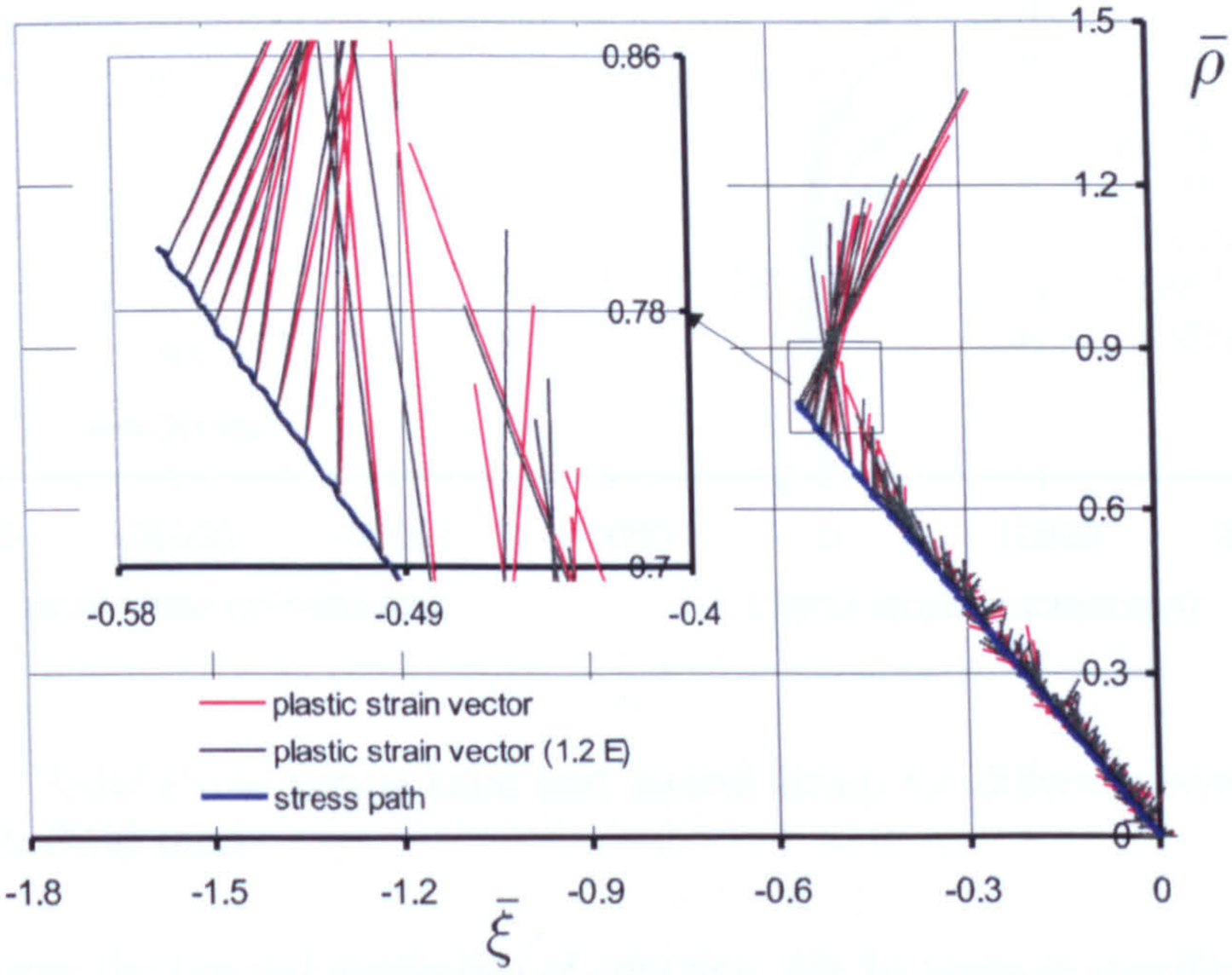

Figure 2.14: The sensitivity of plastic flow to Young's modulus, sample 5_3*a*, Sheffield tests

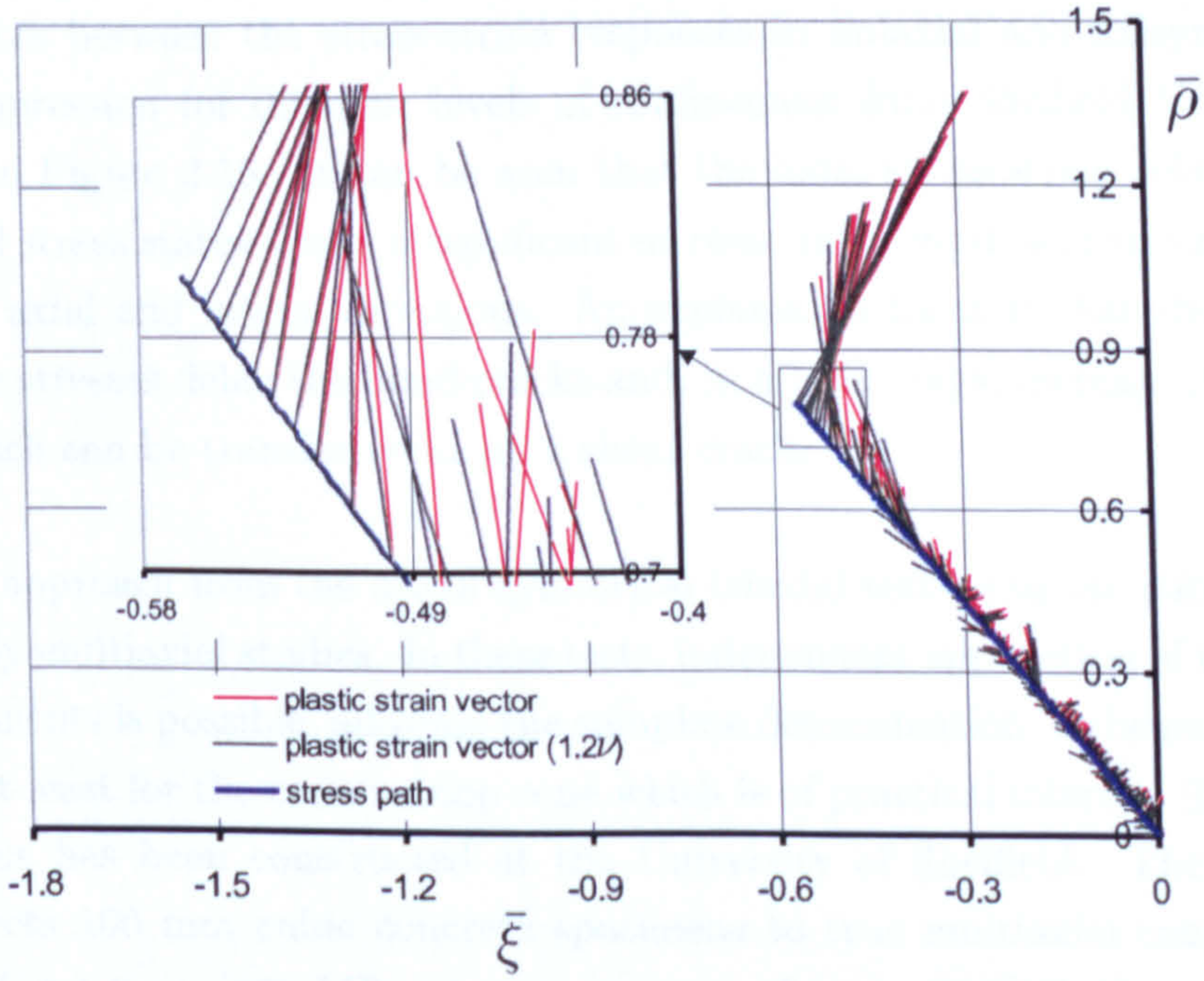

Figure 2.15: The sensitivity of plastic flow to Poisson's ratio, sample 5_3*a*, Sheffield tests

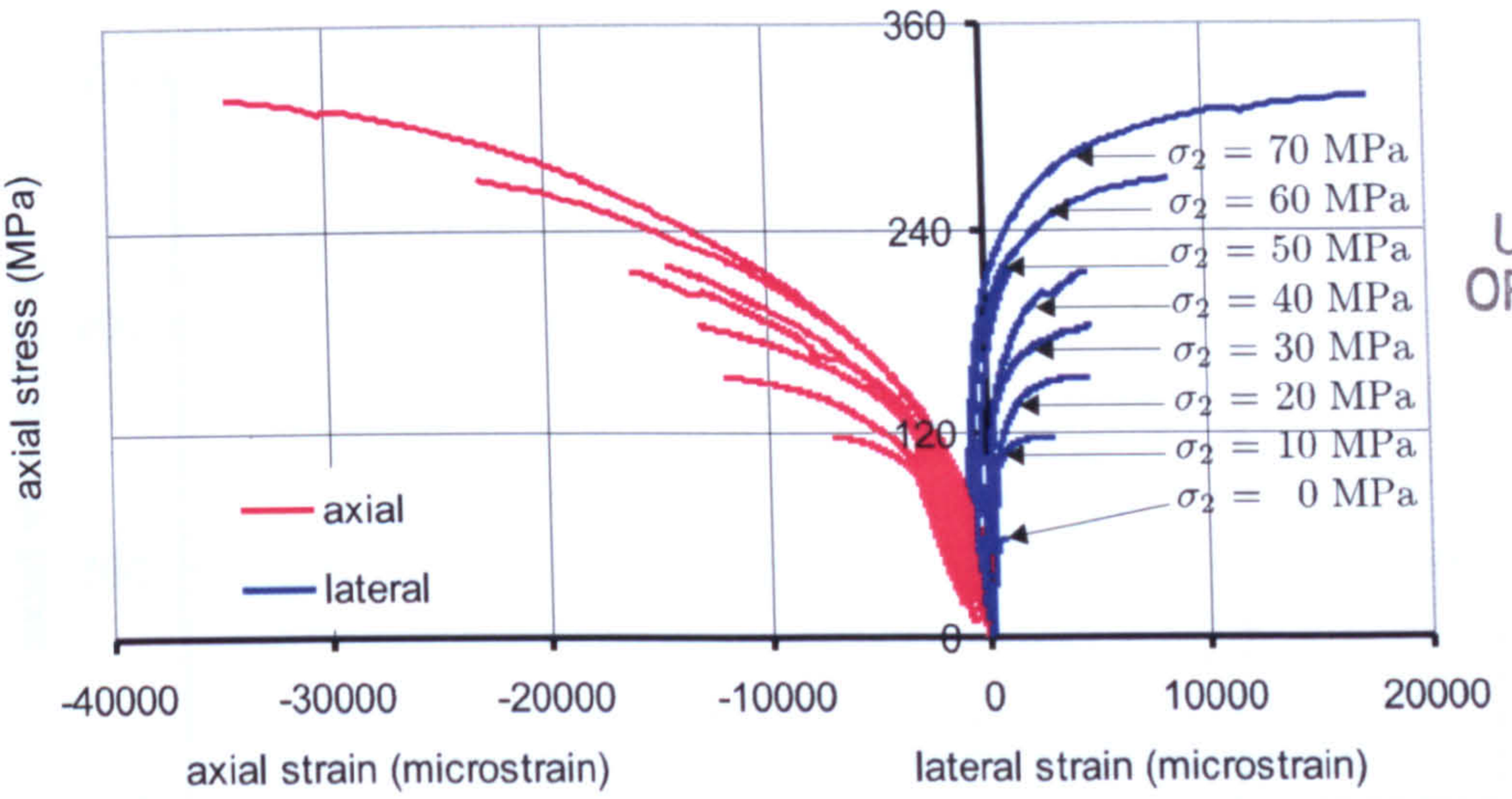

Figure 2.16: Axial stress versus axial and lateral strain for different level of confinement, Sheffield tests

exhaustive way the triaxial properties of concrete, nor to propose specifications in order to perform tests in a complete systematic way.

Under triaxial compression stress states, the non-linear response depends very much on the load path followed. Also, it is well known that the stress-strain response in the pre-peak region depends significantly on the stress state applied. For instance, the differences between the stress-strain responses in uniaxial and axisymmetric triaxial compression for different levels of confinement from Sheffield University are shown in Figure 2.16. It can be seen that the axial stress-strain relation for the confined stress states shows a significant increase in strength and strain capacity in both axial and lateral directions. An explanation for it is that the lateral compressive stresses delay the bond cracks and, in a later stage, increase the shear stresses which can be transferred along a shear crack.

A different approach from the use of cylindrical triaxial tests is to use cubic specimens in fully multiaxial studies. In these tests, independent application of the three load components is possible, allowing the complete determination of the peak stress envelope, at least for the compression zone which is of practical interest. This kind of apparatus has been constructed at the University of Sheffield. The new facility subjects 100 mm cubic concrete specimens to true multiaxial compression ($\sigma_1 \neq \sigma_2 \neq \sigma_3$) up to 400 MPa at temperatures of up to 300^0 C. Forces are delivered through three independent loading frames equipped with servo-controlled

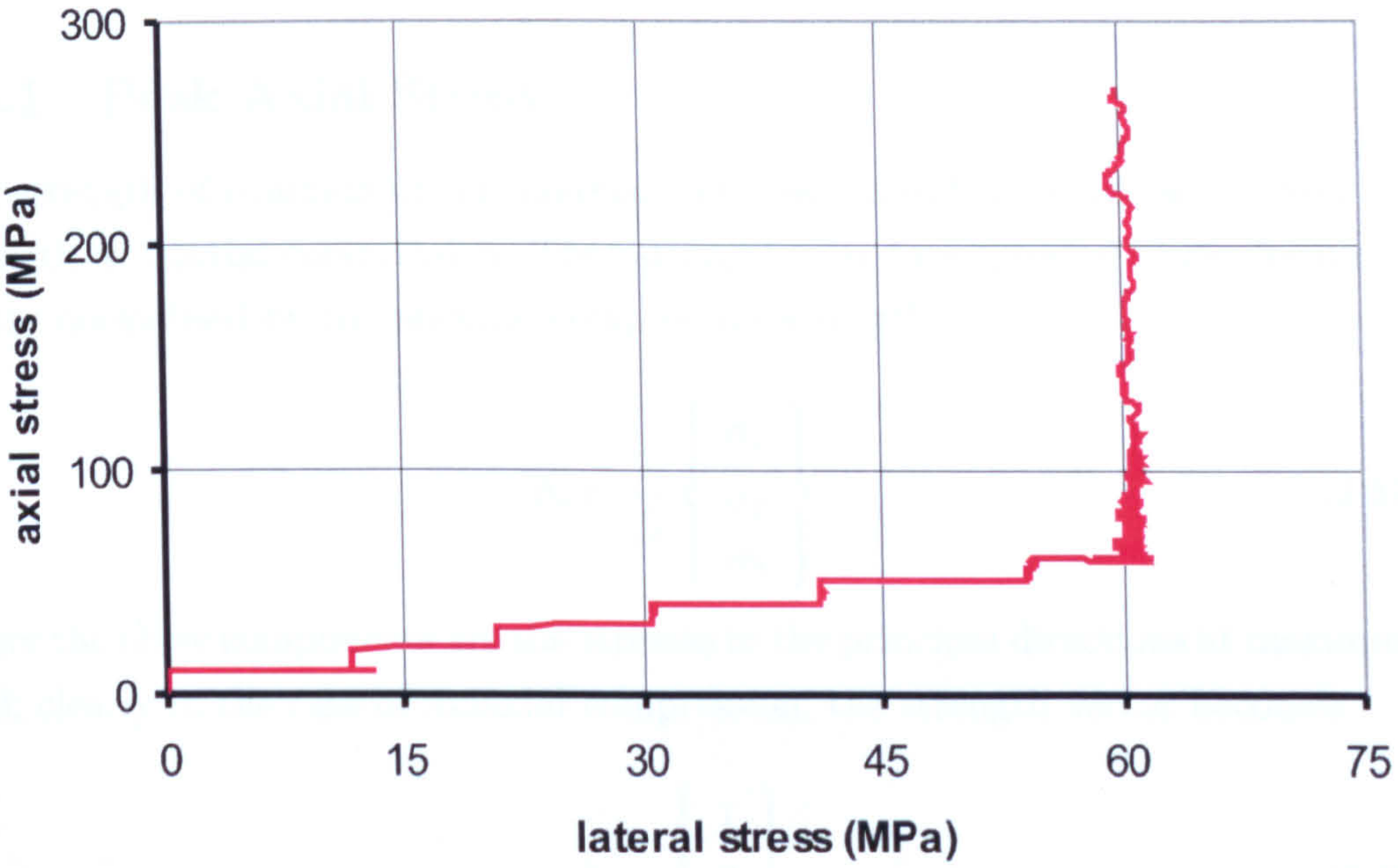

Figure 2.17: Stress path for triaxial compression under 60 MPa confinement, Sheffield test, sample 5_2*c*

hydraulic actuators creating uniform displacement boundary conditions via rigid platens. Specimen deformation is calculated from displacements measured to an accuracy of 10^{-6} m using a system of six laser interferometers [Petkovski *et al.*].

The investigations on the concrete response in this chapter were carried out using the triaxial tests in Sheffield University where the major principal stress (σ_1) was greater than the other two principal stresses (σ_2, σ_3), which are equal to each other ($\sigma_1 > \sigma_2 = \sigma_3$). For this stress condition the stresses σ_1 were applied in steps of 10 MPa, and then held constant while ($\sigma_2 = \sigma_3$) increased until it became equal to σ_1. This operation was repeated for the higher confinement until it reached the specified level and held constant whereupon σ_1 was increased until the peak. Figure 2.17 shows a stress path of one of Sheffield's triaxial test with 60 MPa confinement. Note that in this plot the compressive stresses are taken as positive and the scale of the two axis are not the same. To observe the behaviour of concrete in more complex loading histories, the specimens were tested under cyclic loading paths.

Strain data obtained from some relatively high level confinement tests are incomplete due to rupture of strain gauges before reaching the peak. Tests at 50 and 70 MPa have only one result each where sufficient data was captured. Tests at 40

MPa confinement exhibited some irregularities as can be seen in Figure 2.16.

2.5.1 Peak Axial Stress

The strength of concrete under uniaxial compression differs significantly from the strength in triaxial compression. That strength may be expressed in the form of a vector normalised by the uniaxial compressive strength

$$\bar{\sigma}_i = \frac{1}{f_c} \left\{ \begin{array}{c} \sigma_1 \\ \sigma_2 \\ \sigma_3 \end{array} \right\} \tag{2.47}$$

where the three components are the stresses in the principal directions at maximum load; clearly in the case of uniaxial compression, the strength vector becomes

$$\bar{\sigma}_i = \left\{ \begin{array}{c} 1 \\ 0 \\ 0 \end{array} \right\} \tag{2.48}$$

The normalised strength vectors can be presented as points in principal stress space; a combination of all such points results in a strength surface. The stresses σ_1, σ_2 and σ_3 may be transformed from Cartesian co-ordinates into Haigh-Westergaard co-ordinates. The axis in the deviatoric plane for which the Lode angle $\theta = -\frac{\pi}{6}$, is referred to as the extension meridian. A stress state on this meridian is equivalent to a hydrostatic stress state with a tensile stress superimposed in one direction. Analogously, a stress state on the compressive meridian ($\theta = \frac{\pi}{6}$) is defined as a hydrostatic stress state with a compressive stress superimposed in one direction.

The increase in confining pressure leads to an increase in the maximum axial load-carrying capacity as can be seen in Figure 2.16. The highest level of normalised confinement for Sheffield data was $1.17 f_c$. At low level of confinement ($0.17 f_c$), the load carrying capacity increases to $2 f_c$. At medium level of confinement ($0.5 f_c$), the load carrying capacity increases to reach $2.3 f_c$. For high level of confinement ($1.17 f_c$), the load carrying capacity increases to reach $4.6 f_c$.

The relationship between the level of confinement and maximum peak axial stress seems to be linear as shown in Figure 2.18. In the absence of more data between uniaxial and 10 MPa level of confinement, the response can be modeled with two linear equations. For the first zone between 0 to 10 MPa confinement

$$\sigma_1 = A \sigma_{(2=3)} + f_c \tag{2.49}$$

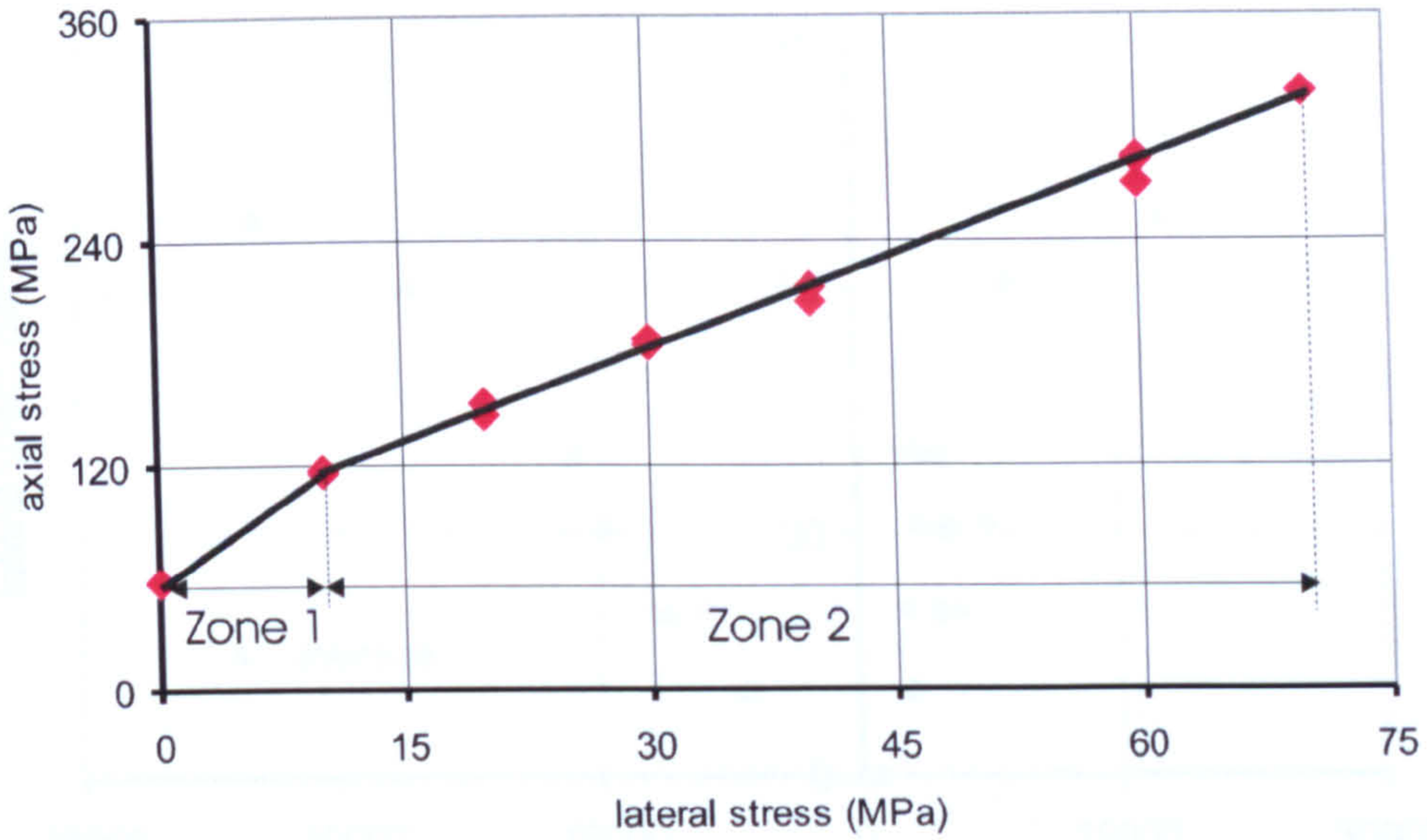

Figure 2.18: Peak axial stresses for different levels of confinement, Sheffield tests

where A is constant and its value is 5.8.

The second zone from 10 to 70 MPa confinement can be modelled as follows

$$\hat{\sigma}_1 = B\,\sigma_{(2=3)} + C\,f_c \tag{2.50}$$

where B and C are constants and their values are 3.25 and 1.5 respectively.

2.5.2 Strains at Peak Stress

The axial and lateral strains at peak stress both increase significantly with increasing confinement, as can be seen in Figure 2.19. The average increase in axial strain for low level confinement is $2.6\,\varepsilon_{uxa}$ and the average increase in the lateral strain is $2\,\varepsilon_{uxl}$, where ε_{uxa} and ε_{uxl} are the axial and lateral uniaxial peak strain respectively. For medium level of confinement, the average increase in peak axial strain is $6.9\,\varepsilon_{uxa}$ and the average increase for the peak lateral strain is $4.5\,\varepsilon_{uxl}$. For high level of confinement, the average increase in peak axial strain is $17.7\,\varepsilon_{uxa}$ and the average increase for the lateral strain is $17.7\,\varepsilon_{uxl}$.

Figure 2.20 shows the equivalent plastic strain $\left(\varepsilon^p_{eq} = \sqrt{(\varepsilon^p_a)^2 + 2\,(\varepsilon^p_l)^2}\right)$ at peak axial stresses for different levels of confinement, versus the normalised hydrostatic pressure ($\bar{\xi}$). The peak equivalent plastic strain increases with the increase in the level of confinement. The response is nonlinear and follows an exponential form.

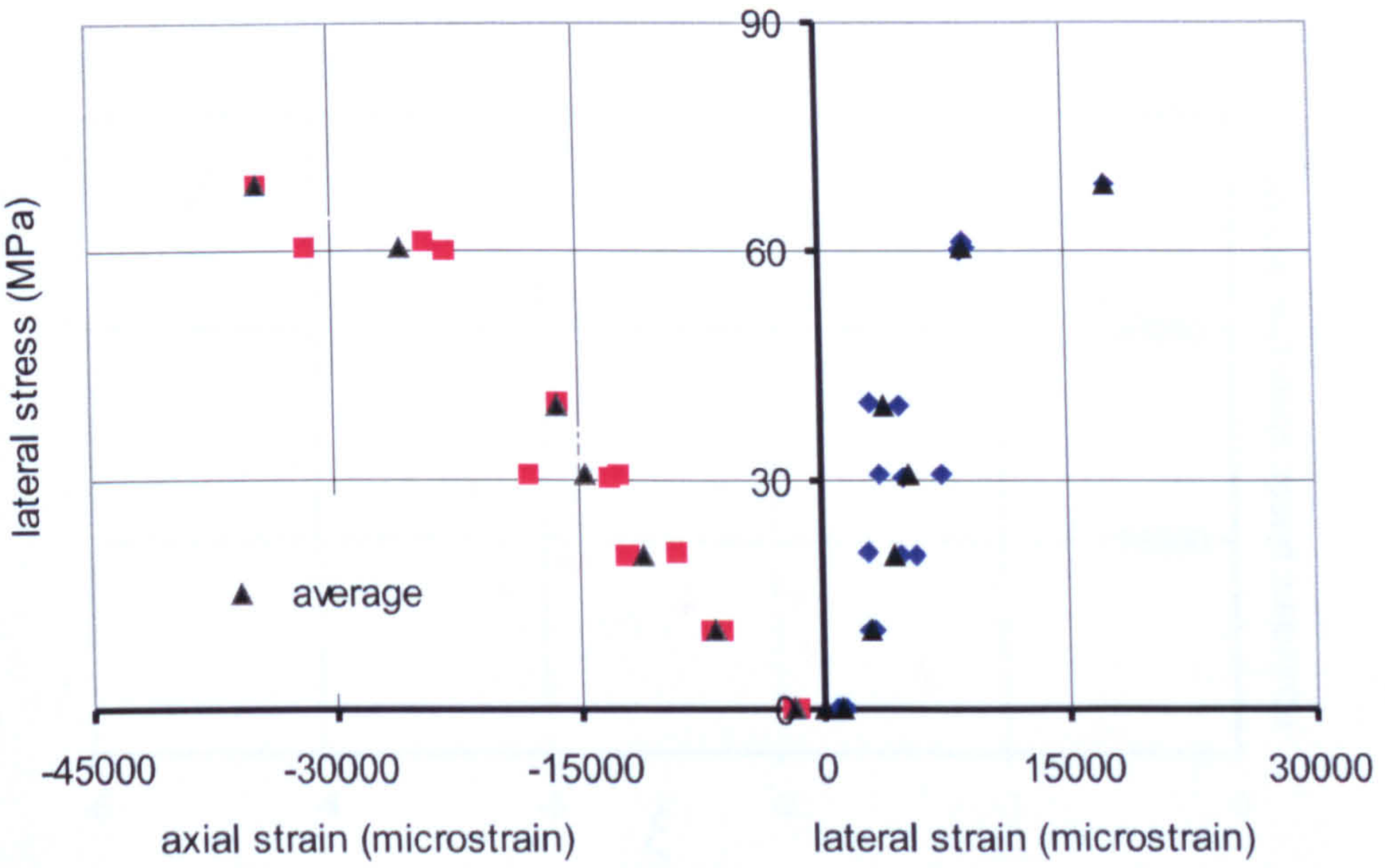

Figure 2.19: Lateral stress versus axial and lateral strains at Peak Stresses

2.5.3 Volumetric Strain

Figure 2.21 shows the volumetric strain for different levels of confinement. It may be noted that for medium ($\sigma_2 = 30\,MPa$) and high ($\sigma_2 = 60\,MPa$) levels of confinement the initial change in the volume is almost linear up to 0.4 of the peak axial stress ($\hat{\sigma}_1$). The stress at this level is referred to as the *onset of stable fracture propagation* (OSFP). The behaviour then becomes nonlinear up to about 0.9 $\hat{\sigma}_1$. At this point the volumetric strain changes from compaction to dilation. The stress at this transition level is referred to as *volume transition stress* (VTS).

The volumetric plastic strain is also shown in Figure 2.21. Up to about $0.2\hat{\sigma}_1$, concrete shows no plastic strain. During unloading-reloading the volumetric plastic strain remains relatively constant, this shows that the response is essentially elastic. The behaviour then becomes increasingly nonlinear until the volumetric plastic strain reaches its minimum value near the stress level at the onset of total volumetric strain dilation (VTS). It can be seen that the total VTS and the plastic VTS are close to each other especially with high levels of confinement. This is because the plastic strain is dominant at this region.

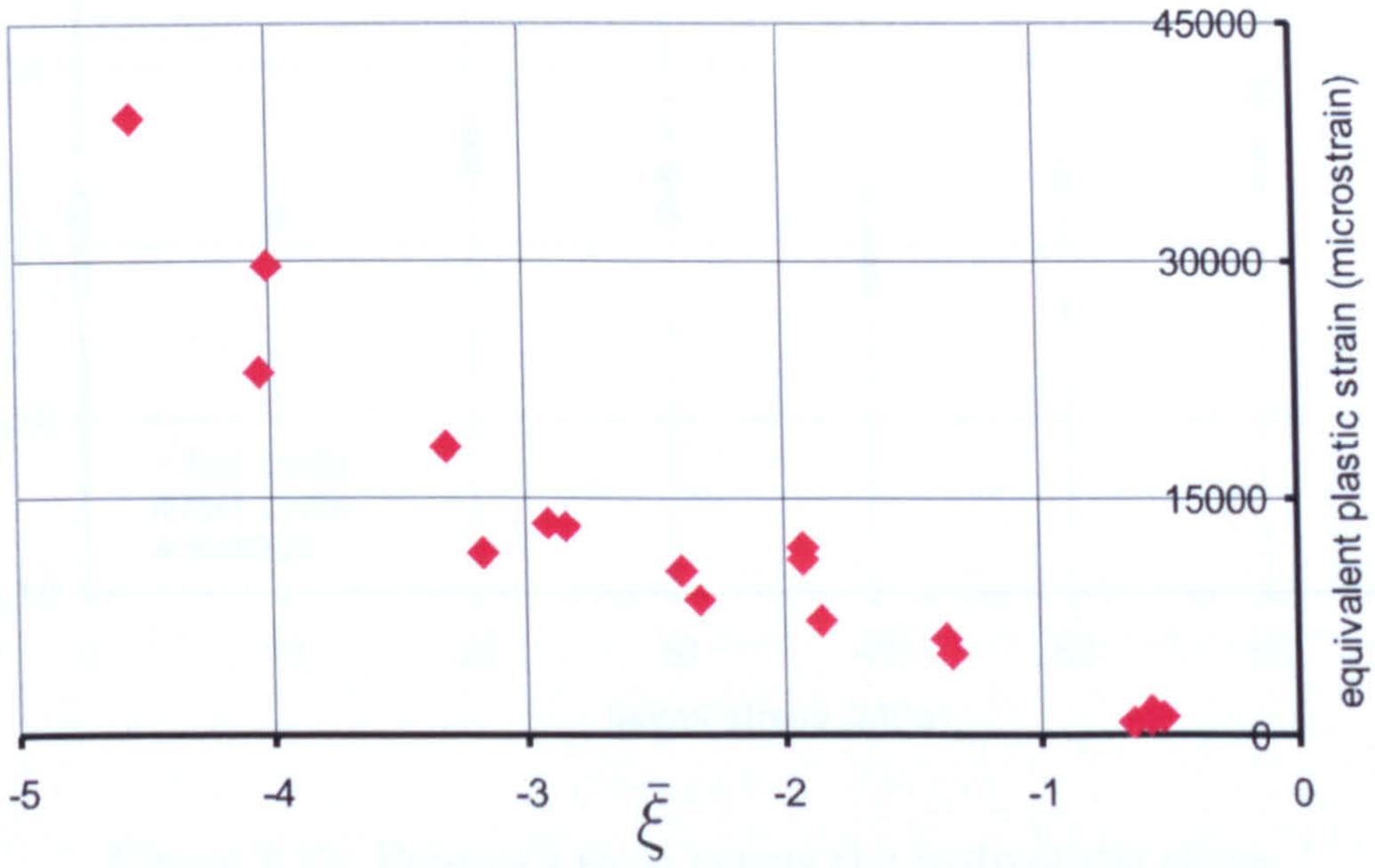

Figure 2.20: Equivalent plastic strain at peak stresses for different levels of confinement, Sheffield tests

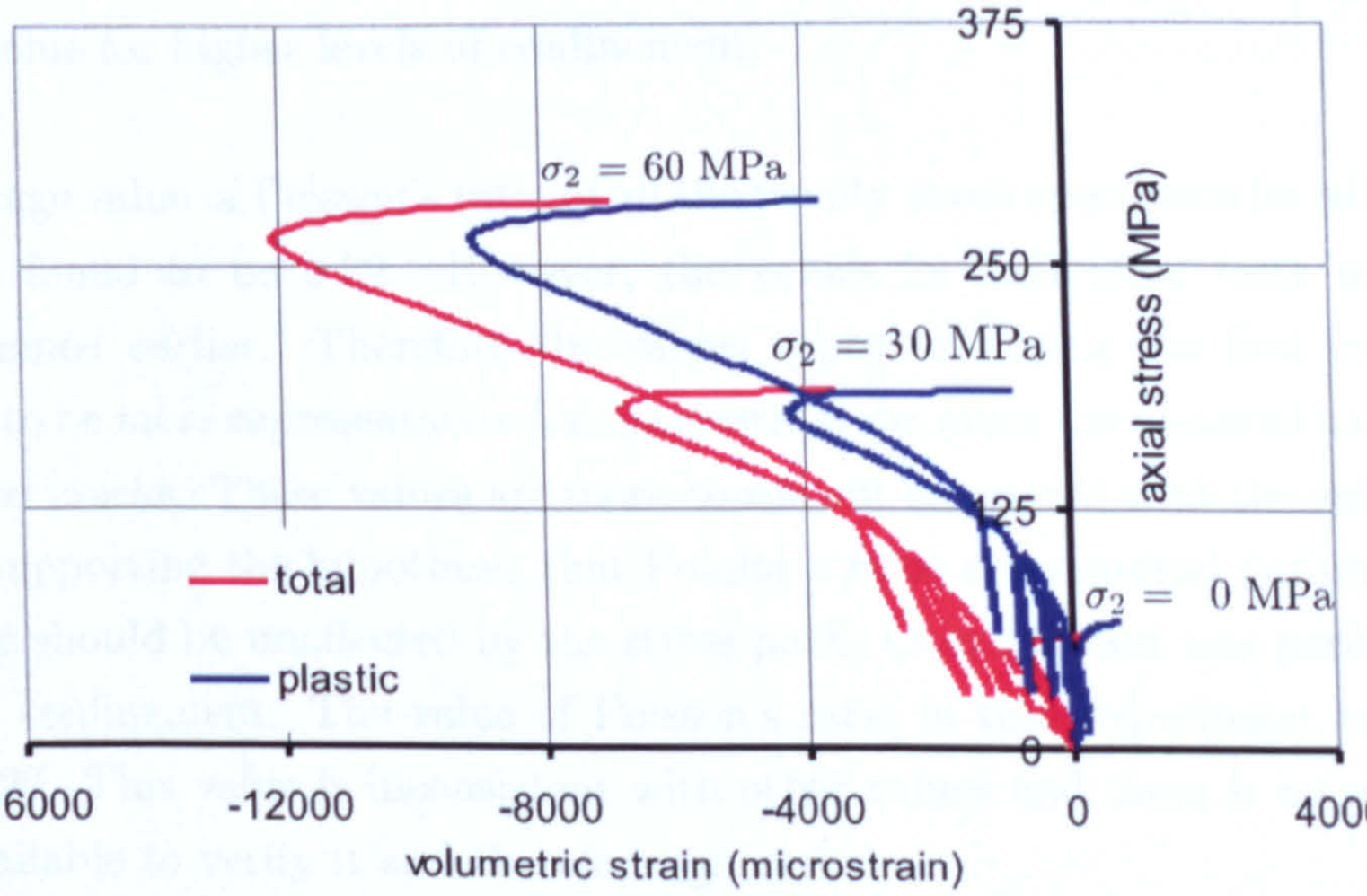

Figure 2.21: Axial stress versus volumetric plastic strain with different level of confinement

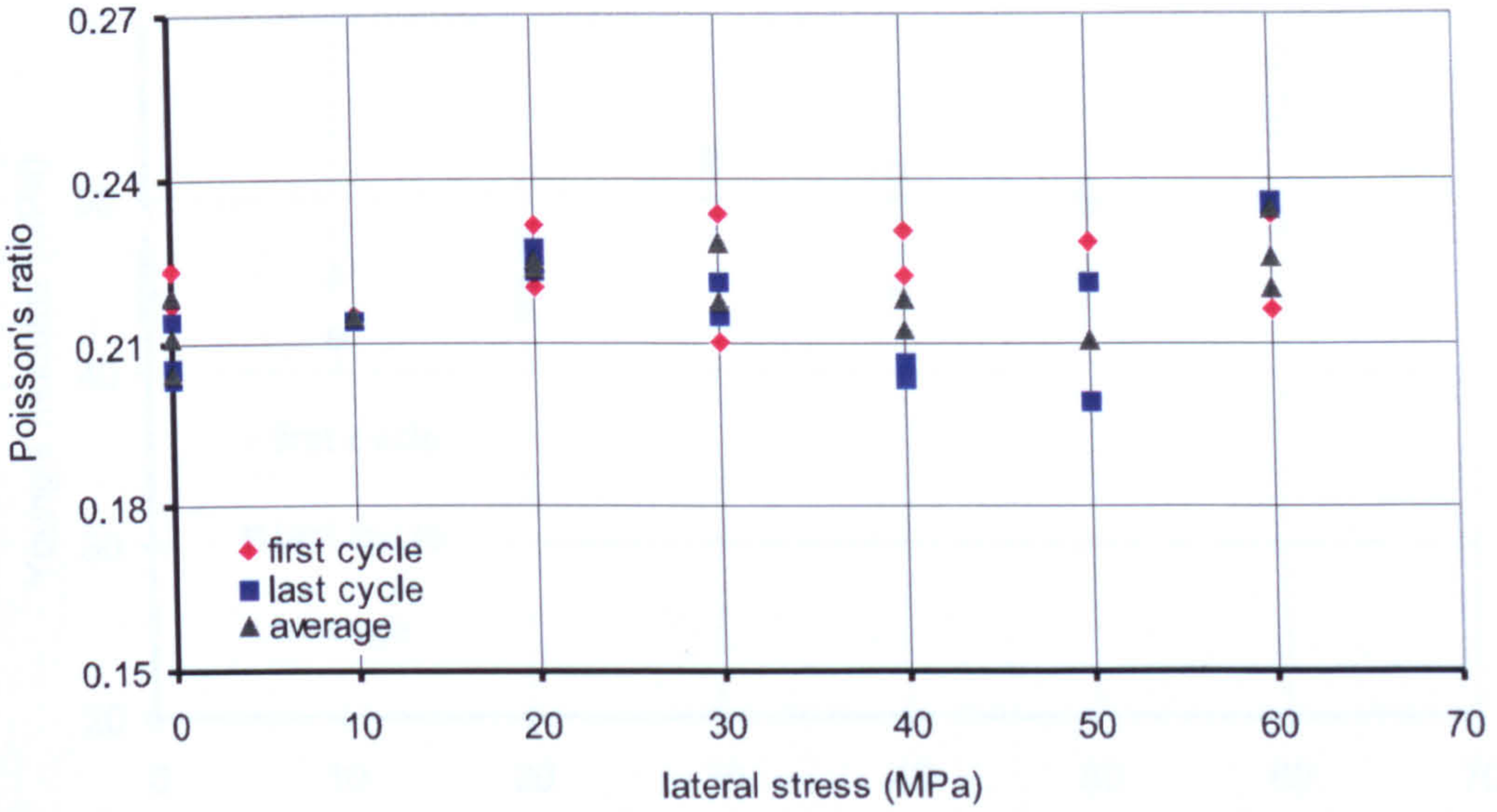

Figure 2.22: Poisson's ratio versus the hydrostatic stress

2.5.4 Poisson's Ratio

Figure 2.22 shows the values of Poisson's ratio for different levels of confinement. The value of the ratio for the first cycle appears to be greater than the values recorded in the last cycles for most of the samples. This could be due to closure of the initial cracks during the first cycle. The average value of the ratio seems to increase during low level of confinement ($0.17\ f_c \leq \sigma_2 \leq 0.35\ f_c$), but maintains a similar value for higher levels of confinement.

The average value of Poisson's ratio of all the twenty seven specimens for all loading cycles is found to be 0.22. However, the values for individual tests may vary as mentioned earlier. Therefore the values captured during the first cycles are thought to be more representative for the elastic state, since the material has not yet developed cracks. These values are more consistent compared with the subsequent values, supporting the hypothesis that Poisson's ratio is a material parameter and therefore should be unaffected by the stress path. Only one test was performed at 70 MPa confinement. The value of Poisson's ratio in that experiment was found to be 0.27. This value is inconsistent with other values and there is no other test data available to verify it and therefore ignored.

2.5.5 Young's Modulus

The Young's modulus from each cycle has been calculated. Figure 2.23 shows the values of the modulus for every cycle at different levels of confinement. The value

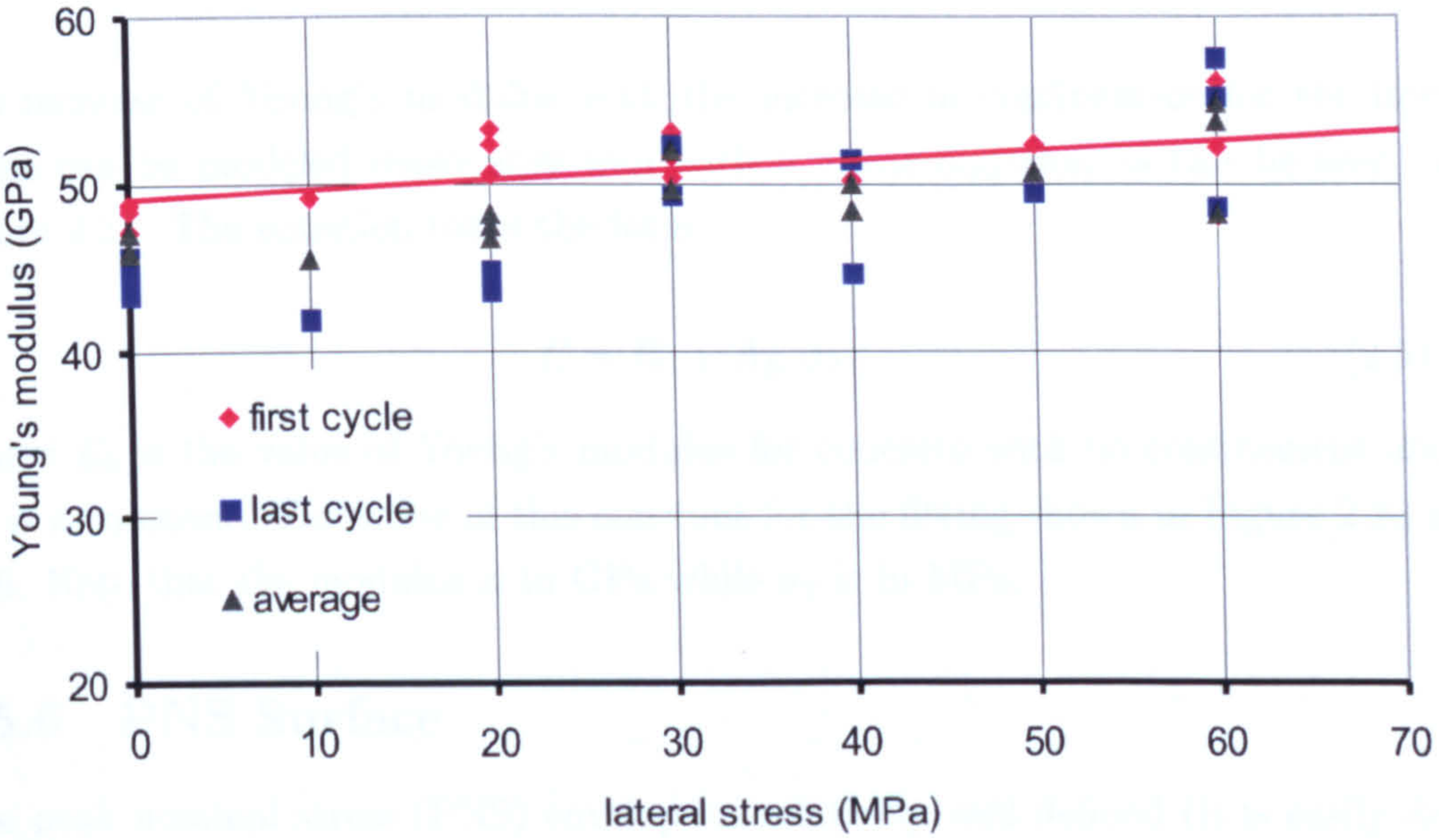

Figure 2.23: Young's modulus for different levels of confinement calculated at each loading cycle, Sheffield tests.

of the modulus for the first cycles of loading appear to be greater than those in the last under low confinement, the degradation of stiffness is attributed to the damage that have been encountered during the cyclic loading.

The values of the modulus for the first cycles seem to increase slightly with the increase of the level of confinement. This is thought to be a result of compaction of the specimen due to the closure of the microcracks and the collapse of voids in the material invoked by hydrostatic pressure. The average value of the modulus for all cycles is found to be 50.5 GPa. The average value of the modulus for the first cycles of loading is 51.1 GPa and the value for the last loading cycles is 50.0 GPa. The average difference between the first and last cycles is around 2 %.

The values of Young's modulus calculated from the first loading cycles is thought to be more representative to the modulus of elasticity. This is because firstly, it represent the material before the propagation of the fractures. Secondly, the modulus is thought to be a material parameter and should be independent from the stress path. Therefore, the modulus for the first cycle has been adopted in this study. The values of the modulus for the test under 70 MPa confinement for three cycles are found to be 80.2, 66.2 and 53.3 GPa. These values are found to be inconsistent with other values and there is no other test to verify them. Therefore they are

ignored.

The increase of Young's modulus with the increase in confinement for the first cycles can be modeled reasonably well with a linear equation as can be seen in Figure 2.23. The equation takes the form

$$E = E_0 + A_E \, \sigma_2 \tag{2.51}$$

Where E_0 is the value of Young's modulus for concrete with no confinement and A_E is a constant. The value of this constant for the fitting shown in Figure 2.23 is 0.06. Note that the modulus is in GPa while σ_2 is in MPa.

2.5.6 PNS Surface

The peak nominal stress (PNS) envelope is relatively well defined (it is easily detected) in concrete under biaxial, triaxial and even truly multiaxial stress states [Crouch]. In Figure 2.24, data is presented from Sheffield's results to illustrate the PNS in the compression meridian using the Haigh-Westergaard $\bar{\xi}$ and $\bar{\rho}$ coordinates. These results show that the PNS envelope is open-ended along the hydrostatic axis in the compression region but intuitively, the hypothesis can be made that such a surface closes itself on the hydrostatic tensile region close to the origin. This is confirming the well known fact of the weakness of concrete in tension and also the fact that the PNS envelope is pressure-sensitive. The results show sharp nonlinearity near the origin. This nonlinearity decreases and the envelope becomes almost linear with high hydrostatic stress. This contradicts the reports of other researchers [Launay and Gachon] which suggest that the meridians of the PNS envelope are curved.

The following are the characteristics of the PNS envelope that have been reported by others (for example Launay and Gachon, 1972):

1. The strength is significantly smaller on the extension meridian than on the compressive meridian.

2. The difference between the deviatoric lengths on the compressive and extension meridians decreases with increasing pressure.

3. The envelope is sensitive to the intermediate stress component. This means that strength in equibiaxial compression is greater than the strength in uniaxial compression.

These findings are well documented but due to the limited data that have been used here, these findings can not be verified.

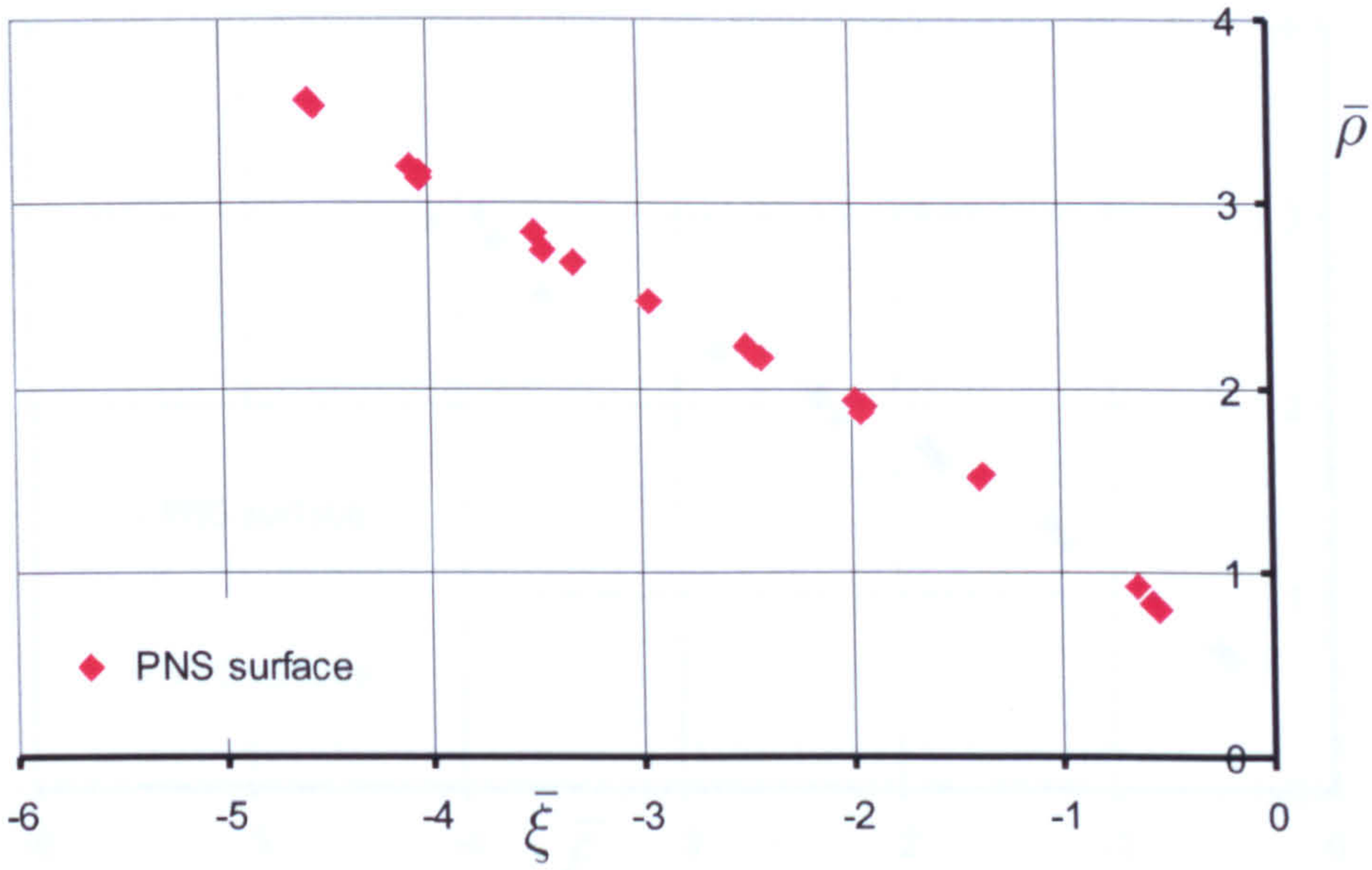

Figure 2.24: Peak nominal stress surface, Sheffield tests

2.5.7 VTS Surface

A second stress surface that could be identified is that corresponding to the plastic VTS. Figure 2.25 shows the experimental values of this surface obtained from the Sheffield tests. From examining the experimental results it seems that this surface for concrete has a similar shape to that of the peak nominal stress surface but with a reduced size. The ratio α_{vts} of the stresses at this surface to that at the PNS surface appears to be almost constant. For the Sheffield tests this value is found to be approximately 0.92. This surface is therefore identified by the following expression

$$\bar{\rho}_{vts} = \alpha_{vts}\, \bar{\rho}_c \tag{2.52}$$

where $\bar{\rho}_{vts}$ is the normalised deviatoric stress invariant for VTS and $\bar{\rho}_c$ is the normalised deviatoric stress invariant for the PNS.

2.5.8 Plastic Flow

Figure 2.26 shows the plastic flow vectors for six Sheffield tests with different levels of confinement. The stress paths for the sample with 30 and 70 MPa confinements suffered control problems during the hydrostatic loading stages but returned to the intended paths subsequently. It seems that these path diversions have not af-

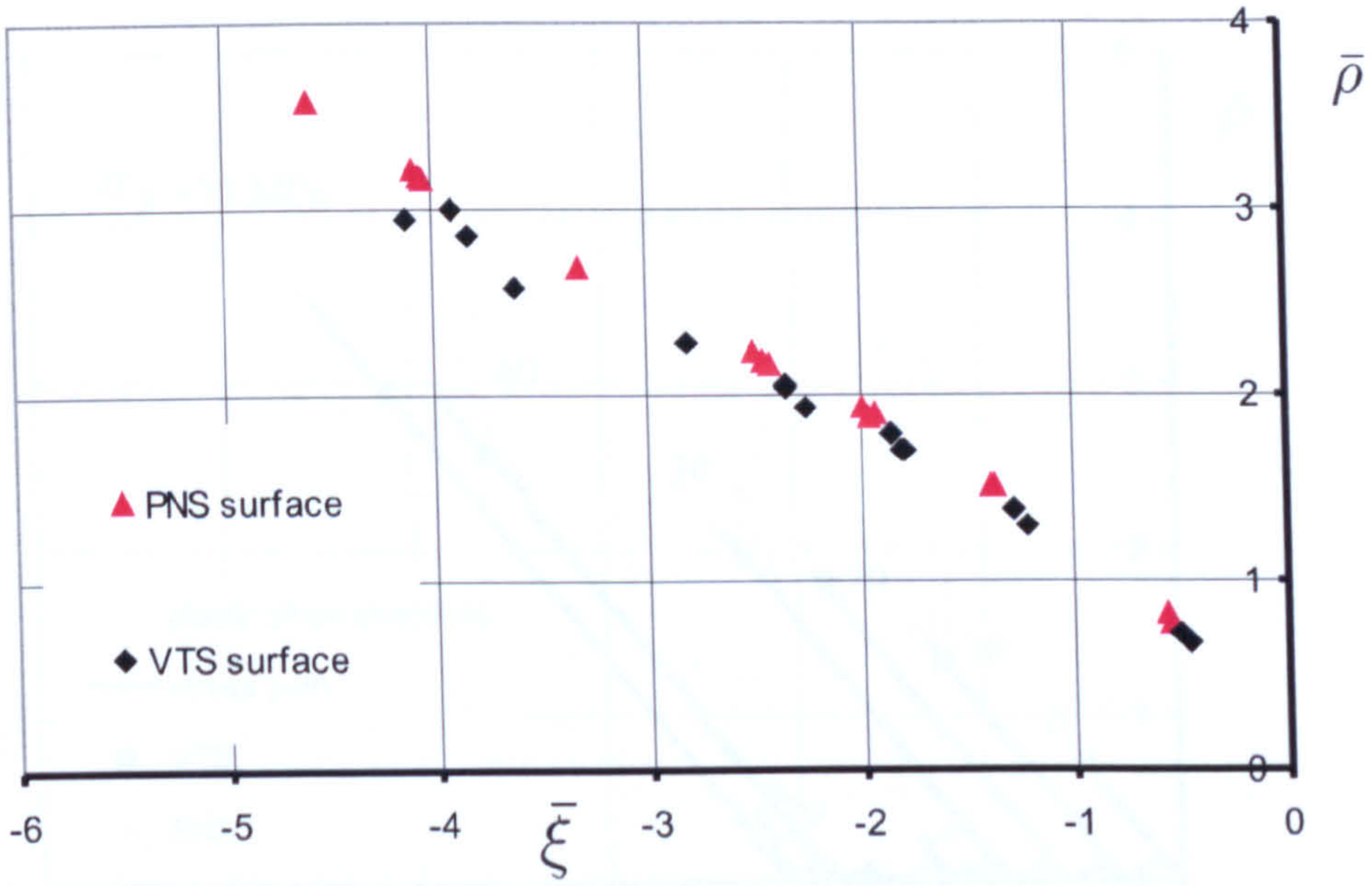

Figure 2.25: PNS and VTS surfaces

fected the plastic flow results. The strain gauges for the test with 20 and 60 MPa confinement had ruptured before reaching the peak as can be seen in Figure 2.26 (red triangles). Tests under 40 and 50 MPa confinement, encountered an early failure of the strain gauges and thus the plastic strain vectors have not been presented.

The general trends of the triaxial plastic strain directions are similar to those seen in uniaxial compression test. The initial parts of these tests show limited plastic strains. Then plastic strains increase and reach the maximum values at peak. Note that the results have been considered up to the peak stress and if the tests are to be continued after the peak, more plastic strains would have been recorded.

The initial vectors are mostly in the hydrostatic negative direction which indicate that the samples undergo compaction. The deviatoric component increases as the axial loading increases and the direction becomes purely deviatoric at about 90 % of the peak stresses where the total volume of the sample reaches its minimum (VTS). Then the directions rotates with an increasing rate towards the hydrostatic positive direction which is an indication that the sample undergoes plastic dilation.

At peak, the directions of the plastic strain vectors appear normal to the PNS surface. This is most interesting, since it suggests that the plastic flow for concrete at PNS is associated. This observation will be used to support the argument for

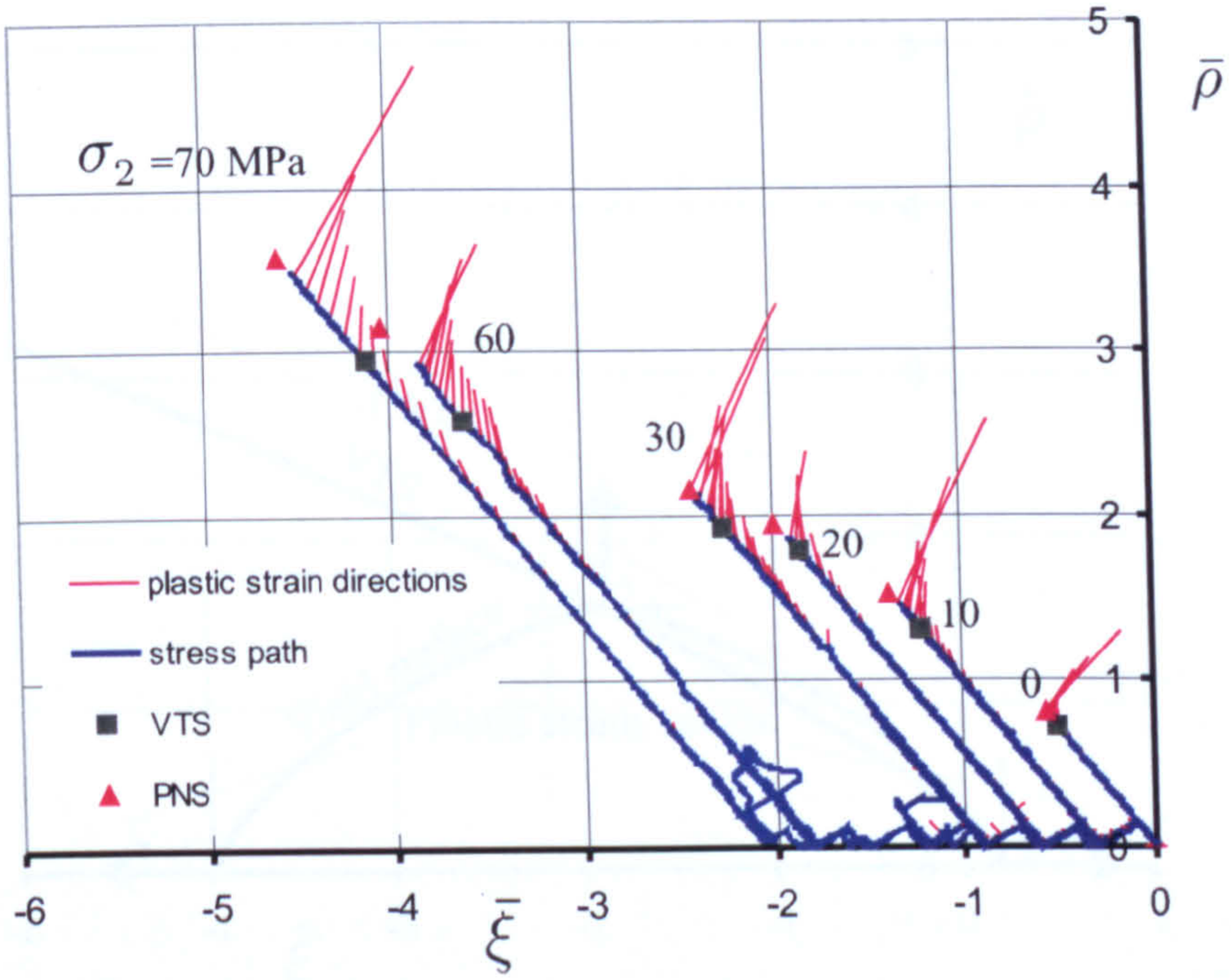

Figure 2.26: Plastic strain directions, stress path, PNS and VTS for different levels of confinement, Sheffield tests.

associated plasticity when modelling the behaviour of concrete under multiaxial compression is considered. There are now three stress states and the corresponding plastic strain directions are clearly identified:

1. The plastic VTS and the directions of the plastic strain vectors which is purely deviatoric

2. The plastic strain directions on the hydrostatic intersection point in the tensile region where the plastic strain is in the hydrostatic positive direction

3. The intersection point on the hydrostatic axis in the compression region where the plastic strain is purely hydrostatic and the negative direction

These three points along with the directions of the plastic vectors could be used to identify the shape of the yield surfaces. A schematic draw of the proposed surface is shown in Figure 2.27. An initial attempt has been made to identify the shape of the yield surfaces for the Sheffield tests is shown in Figure 2.28.

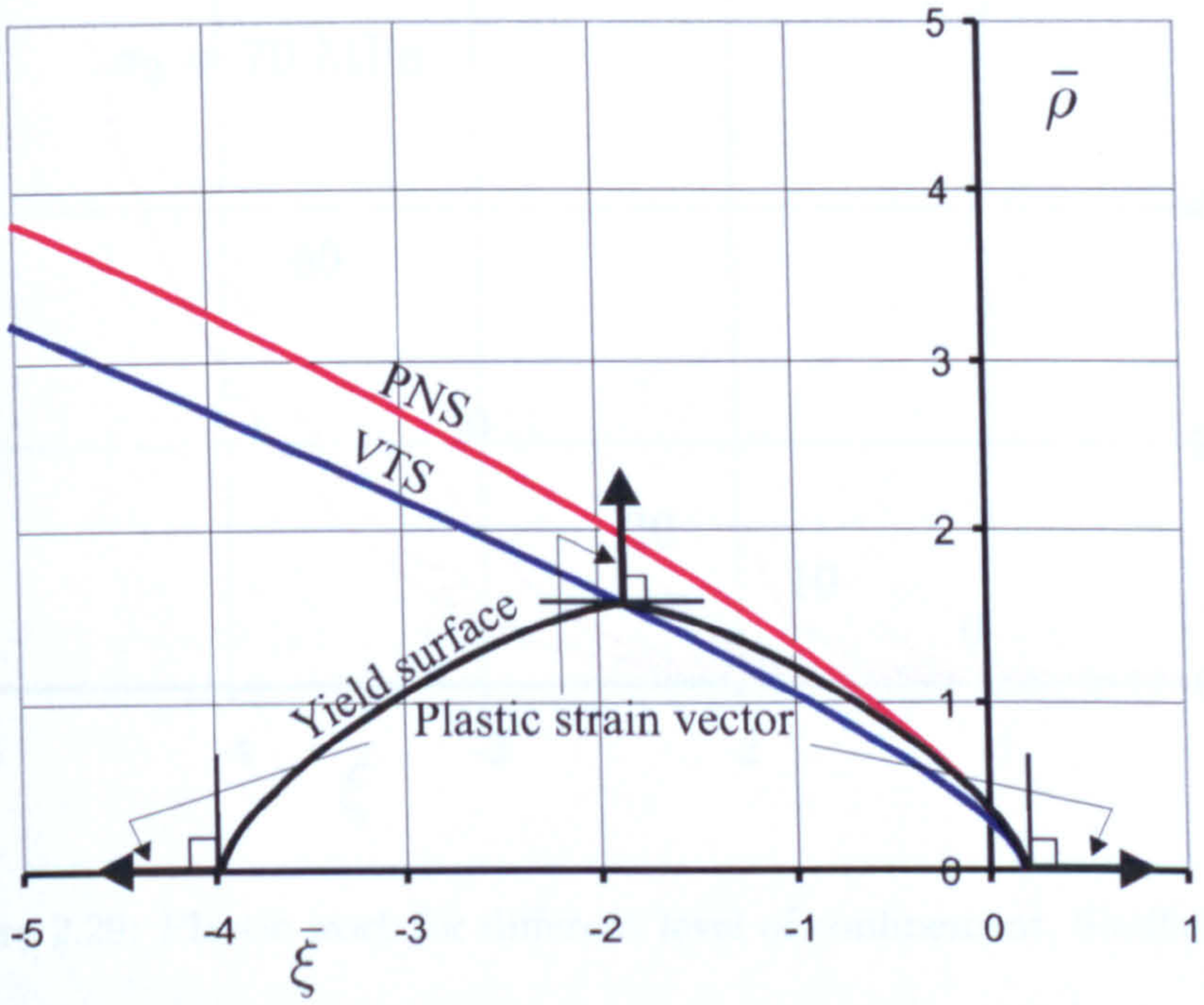

Figure 2.27: Schematic draw for the proposed shapes of the yield surfaces assuming associated flow rule

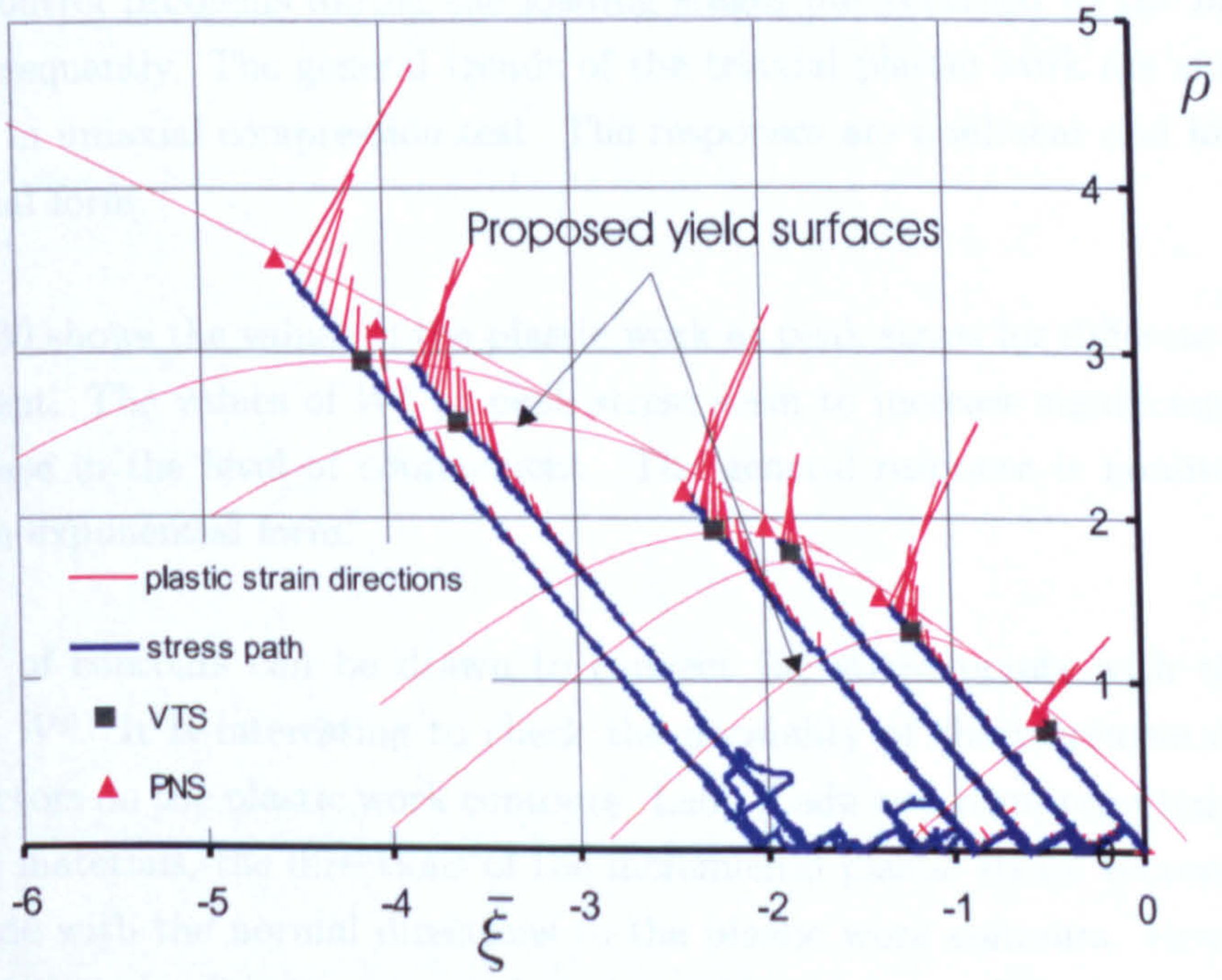

Figure 2.28: Proposed shapes of the yield surfaces assuming associated flow rule

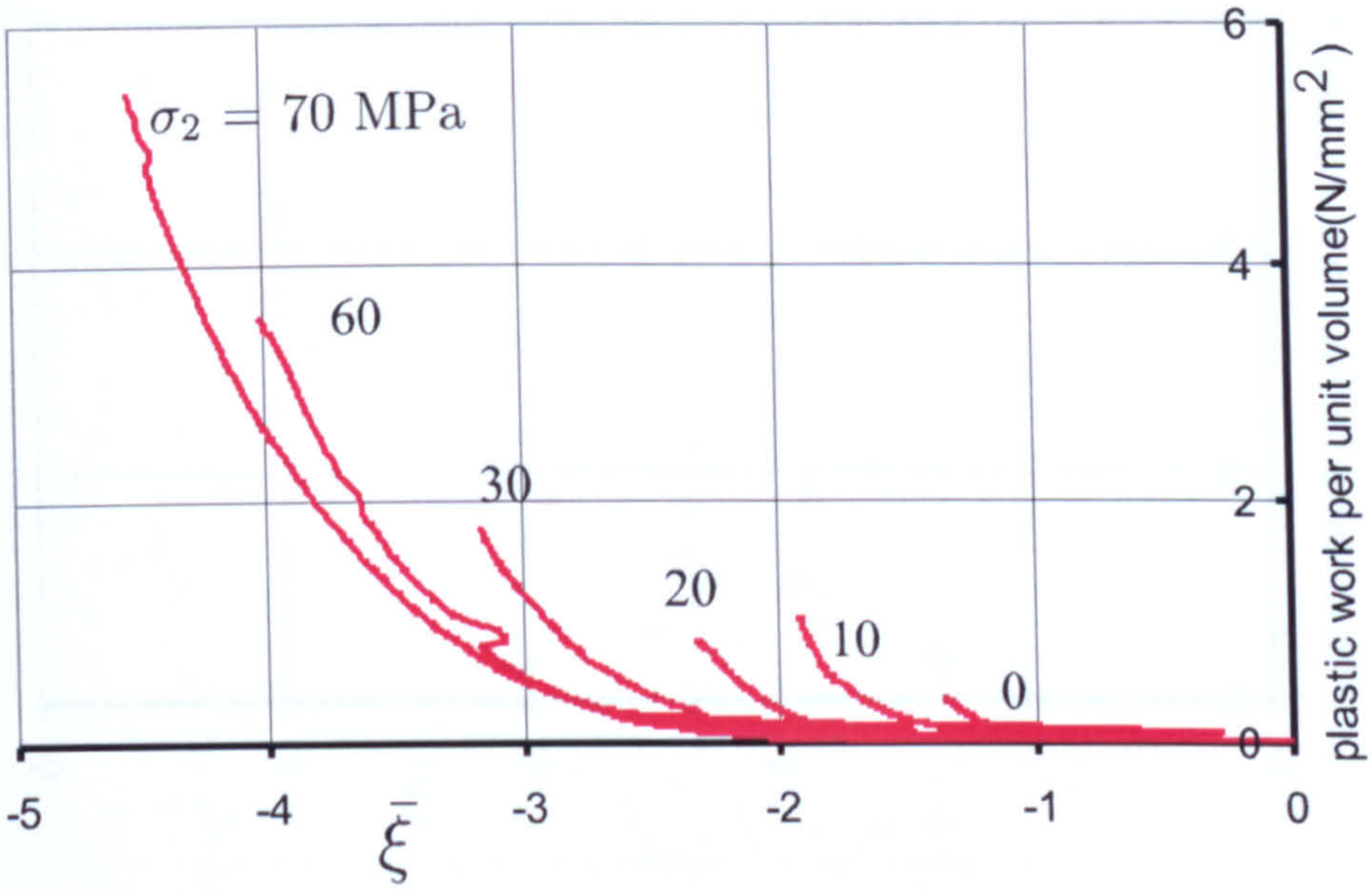

Figure 2.29: Plastic work for different level of confinement, Sheffield tests

2.5.9 Plastic Work, W^p

Figure 2.29 shows a family of plastic work curves obtained from six triaxial compression tests on plain concrete from the Sheffield tests under confining pressures of 0, 10, 20, 30, 60 and 70 MPa. The test for the sample with 60 MPa confinements suffered control problems during the loading stages but returned to the intended paths subsequently. The general trends of the triaxial plastic work are similar to that seen in uniaxial compression test. The responses are nonlinear and follow an exponential form.

Figure 2.30 shows the values of the plastic work at peak stress for different level of confinement. The values of W^p at peak stress seem to increase significantly with the increase in the level of confinement. The general response is nonlinear and follows an exponential form.

A family of contours can be drawn to connect the stress points with the same values of W^p. It is interesting to check the normality of the incremental plastic strain vectors on the plastic work contours. Lade [Lade and Kim] reported that for frictional materials, the directions of the incremental plastic strain vectors appear to coincide with the normal directions to the plastic work contours. However, he suggested that the directions normal to the yield surfaces at failure correspond to more dilation of the material than measured in experiments. This conclusion makes

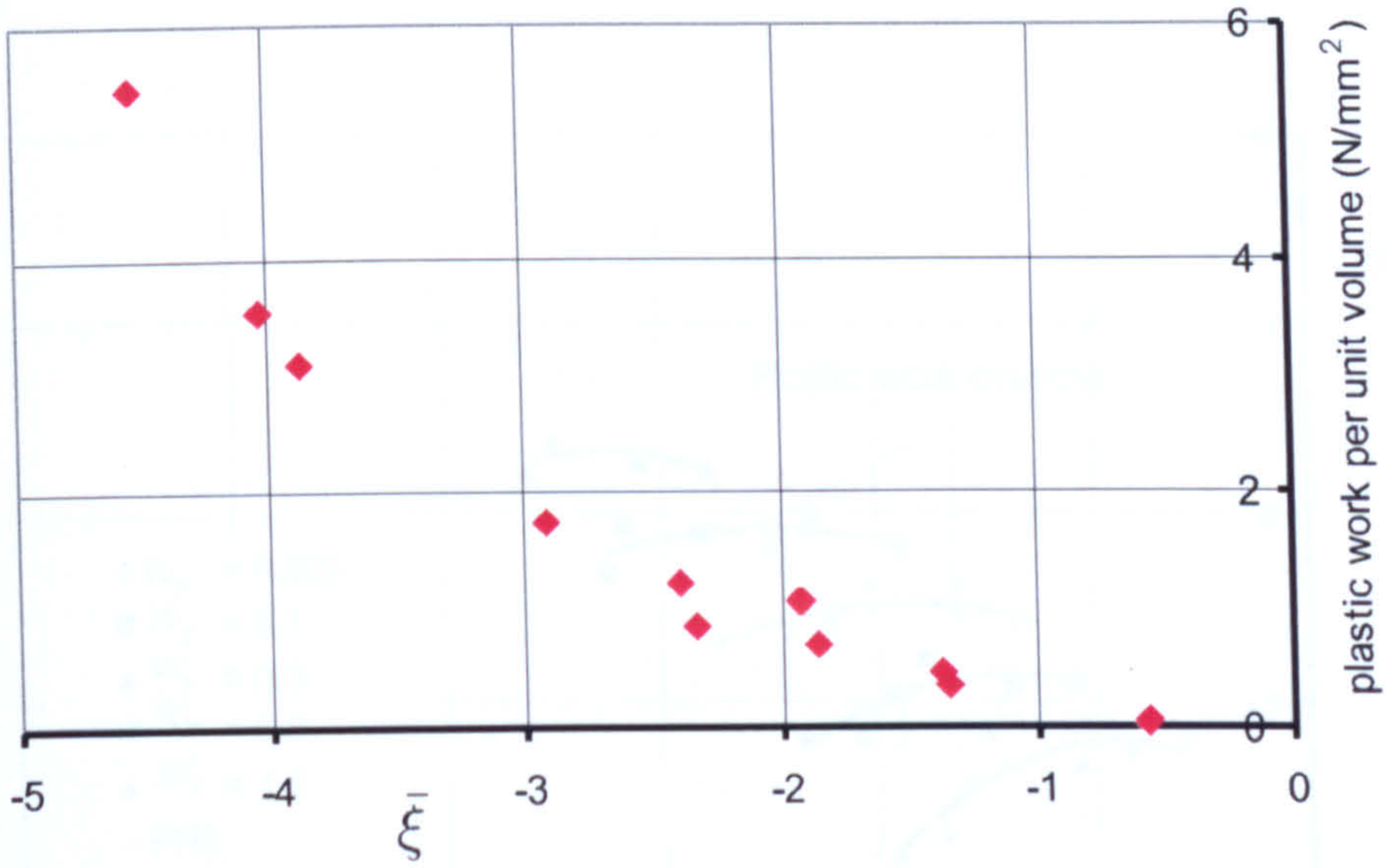

Figure 2.30: Peak plastic work for different level of confinement, Sheffield tests

it necessary to employ a nonassociated flow rule. However, Figure 2.27 shows the plastic strain vectors appear to be normal to the PNS which is in disagreement with his findings.

Figure 2.31 shows the plastic work contours for the Sheffield tests. These contour lines have been identified by using parabolic equations and the least square optimisation technique. Figure 2.32 shows the proposed yield surfaces based on the plastic work contours. Figure 2.33 shows the suggested yield surface superimposed on the plastic strain vectors. It appears that the plastic strain vectors are normal to the plastic work contours. Therefore the assumption of associated flow for concrete is valid.

2.6 Concluding Remarks

1. The PNS envelope is open-ended along the hydrostatic axis in the compression region. With no or low confinement the surface is nonlinear but the shape becomes increasingly linear with high confinement.

2. At peak, the directions of the plastic strain increments appear to be normal to the PNS surface. This is an important point, since it suggests that the plastic flow for concrete at PNS is associated.

3. It appears that the plastic strain vectors are normal to the plastic work

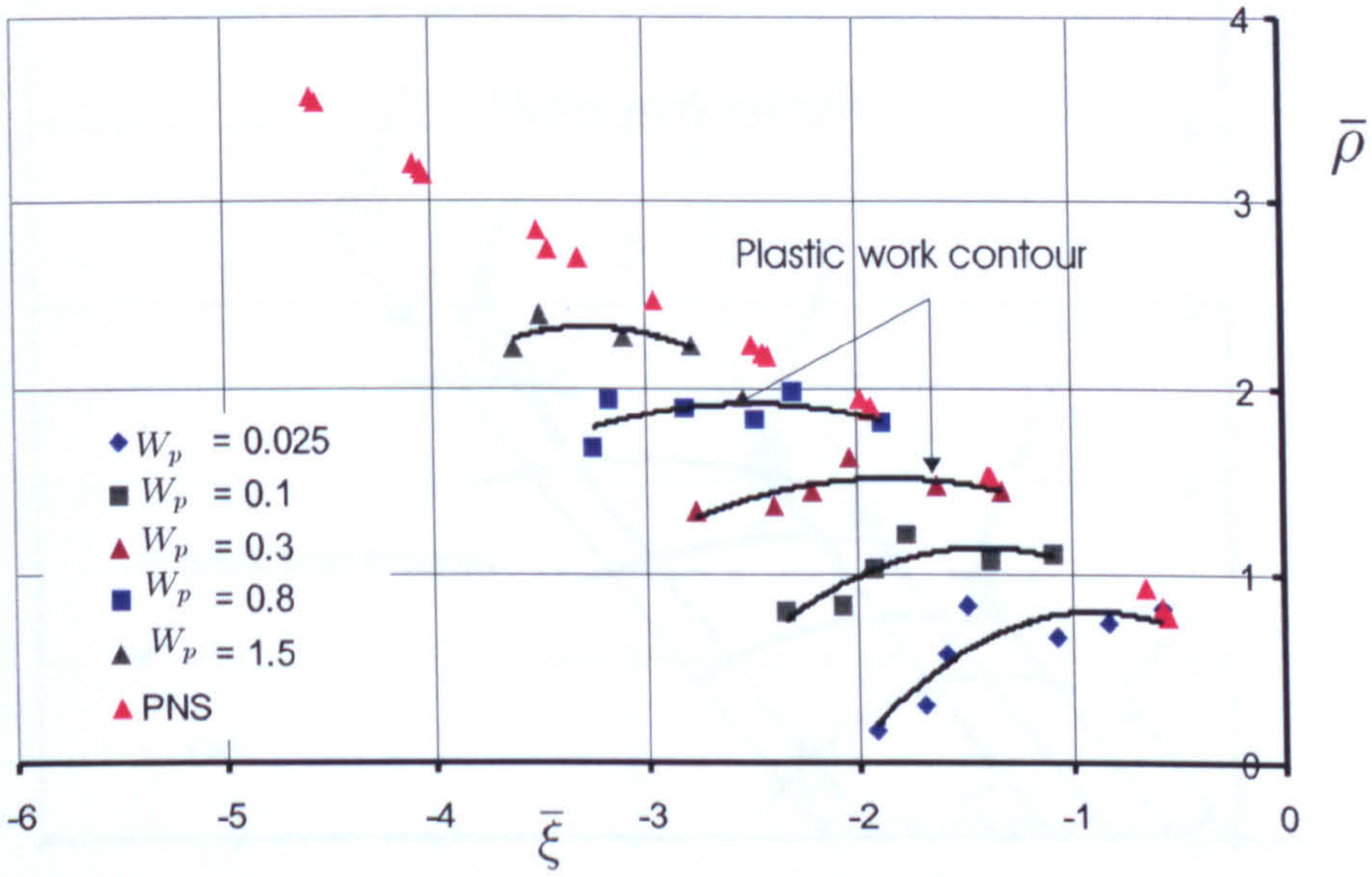

Figure 2.31: Plastic work contour for different level of confinement, Sheffield tests

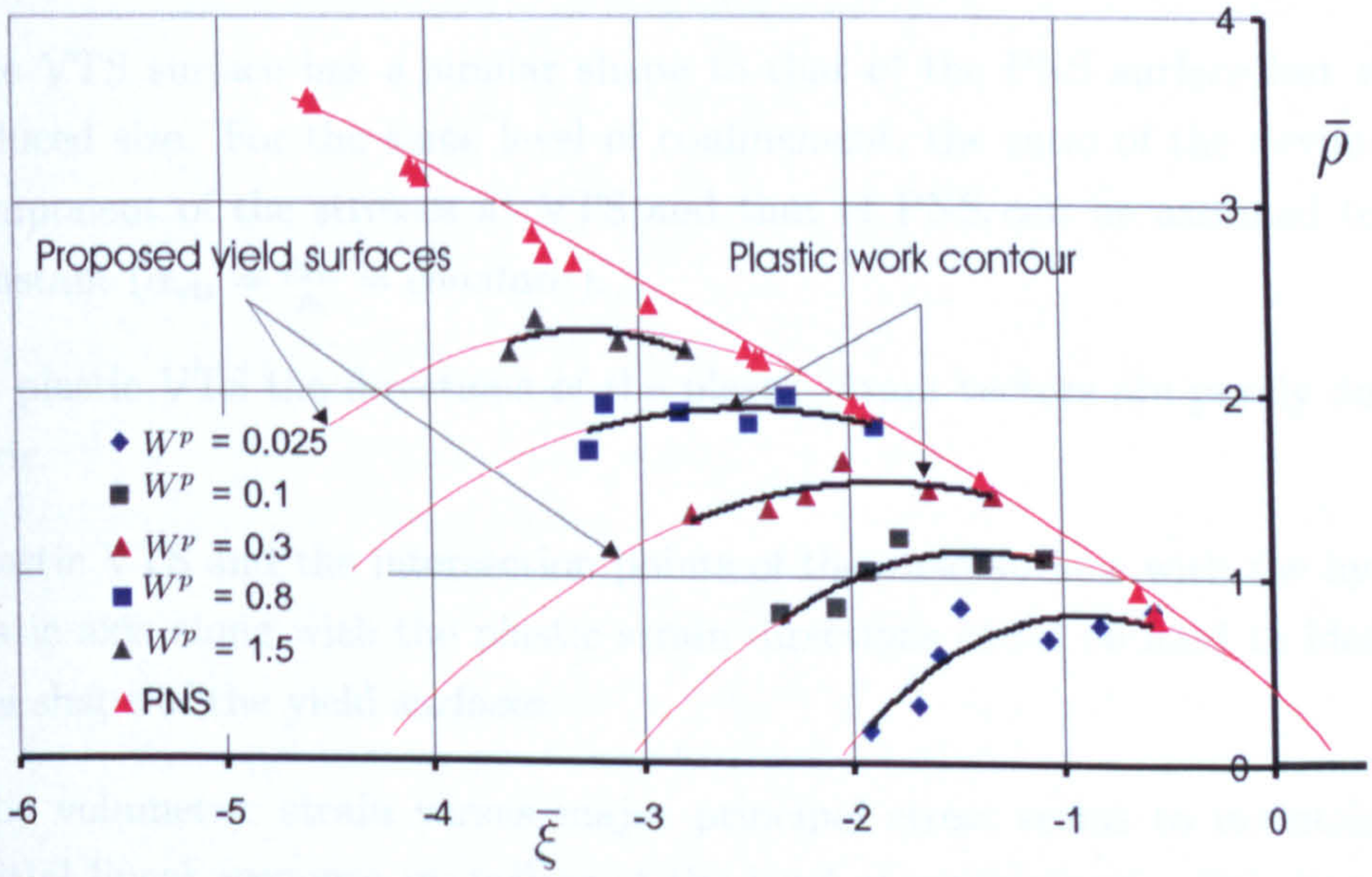

Figure 2.32: Proposed yield surfaces based on plastic work contour, Sheffield tests

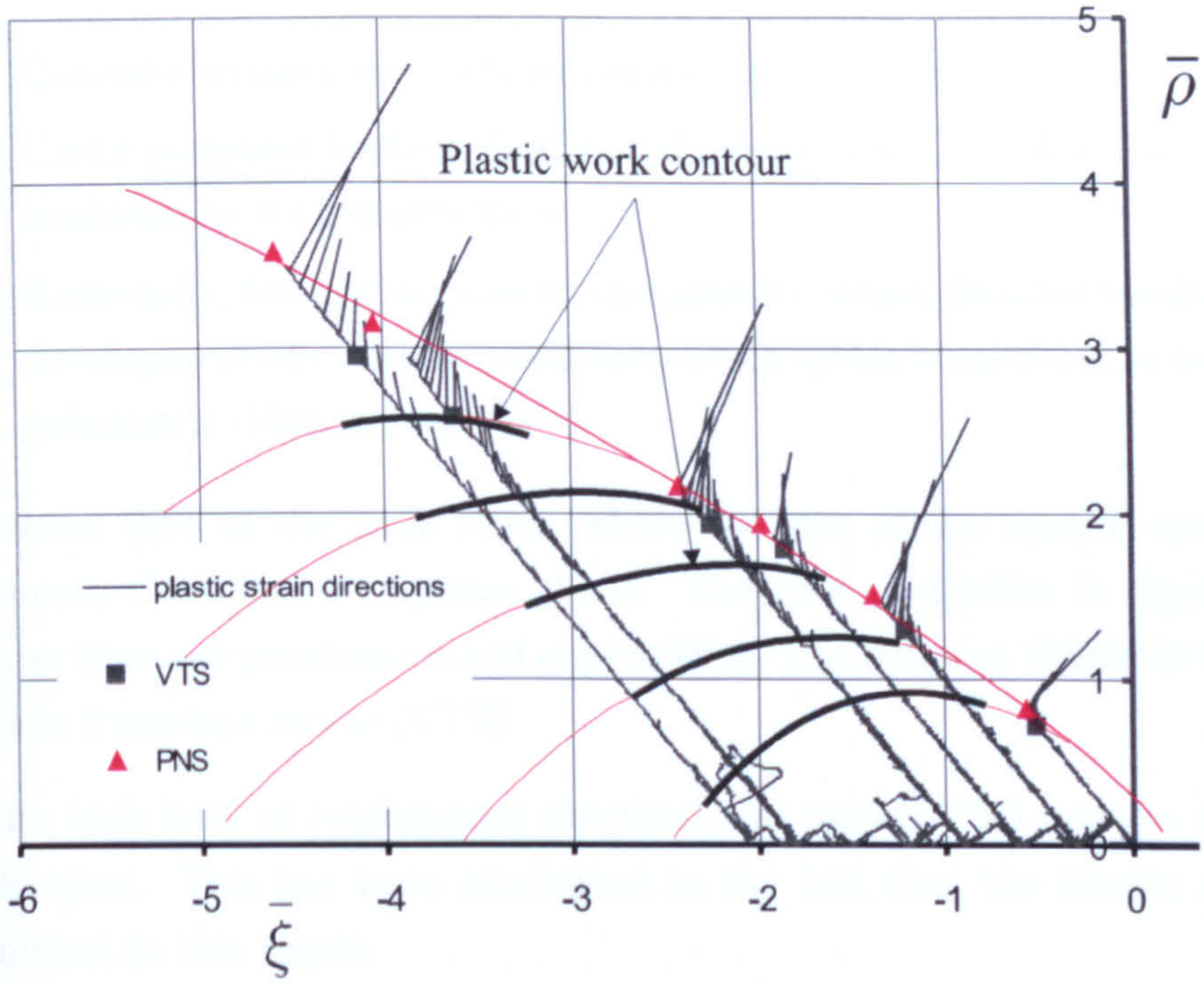

Figure 2.33: Proposed yield surfaces based on plastic work contour superimposed on the plastic strain vectors, Sheffield tests

contours. This gives further support to the assumption of associated flow for concrete.

4. The VTS surface has a similar shape to that of the PNS surface but with reduced size. For the same level of confinement, the ratio of the deviatoric component of the stresses at VTS and that of PNS can be assumed to be constant ($\alpha_{vts} = \frac{\rho_{vts}}{\rho_c} = constant$).

5. At plastic VTS the directions of the plastic strain vectors are purely deviatoric.

6. Plastic VTS and the intersection points of the yield surface with the hydrostatic axis along with the plastic strain directions could be used to identify the shape of the yield surfaces.

7. The volumetric strain versus major principal stress seems to maintain an initial linear response regardless of the level of confinement. This linearity then turn to nonlinearity at a point referred to as the onset of stable fracture propagation (OSFP).

8. The pre-peak behaviour of concrete under compression may be simplified into three levels of response:

   (a) Concrete initially responds as purely elastic material.

   (b) Under increased loading, distributed microcracking results in volumetric nonlinearity with contraction.

   (c) Eventually, further increase in compressive strain demand results in the development of multiple continuous crack systems resulting in nonlinear volumetric dilation response.

9. At about 90% of the peak stress where the size of the sample reaches its minimum the dilation response starts. The rate of dilation is significantly greater than the previous rate of contraction. The stress at this level is called *volume transition stress* (VTS).

10. Under high level of confinement the total and plastic VTS become closer to each other. This has been attributed to the fact that the plastic strain is dominant in this region.

11. Concrete seems to be in a state of compaction throughout the compression loading but at peak, it seems that concrete sample retains its initial size.

12. The values of Young's modulus in the second and subsequent loading cycles is less than the first cyclic loading. This degradation of stiffness is attributed to the damage that have been encountered during the cyclic loading.

13. The average values of Young's modulus seems to increase slightly with the increase of the confinement. This is due to the compaction of the material caused by closing of cracks and collapse of voids.

14. Poisson's ratio is effectively independent of the loading path.

15. The influence of the elastic parameters (E and ν) on the plastic flow is more evident close to the elastic region.

16. The peak axial and lateral stresses and corresponding strains increase significantly with the increase of confinement. This supports the well known fact of the higher strain capacity of confined concrete.

17. The axial strain capacity increases more than the lateral one.

18. The equivalent plastic strain at peak stress increase significantly with the increase of confinement. The general relationship is nonlinear and follows an exponential form.

19. The values of peak plastic work also increases significantly with the increase of confinement. The general relationship is nonlinear and follows an exponential form.

2.7 References

ACI 318-95 Building code requirements for structural concrete, ACI manual of concrete practice Part 3: Use of concrete in buildings - Designs, specifications and related topics, p. 345, (Detroit, Michigan, 1996).

ACI 363 R-92, State-of-the-art report on high-strength concrete, ACI manual of concrete practice Part 1: Material and general properties of concrete, p. 55, (Detroit, Michigan, 1994).

Aitcin P-C., Miao B., Cook W. D., and Mitchell D., 1994, Effects of size and curing on cylinder compressive strength of normal and high-strength concretes, *ACI Materials Journal*, Vol. **91**, No. 4, pp. 349-354.

ASTM Standards, ASTM C 469, Standard test method for static modulus of elasticity and Poisson's Ratio of concrete in compression.

Baalbaki W., Baalbaki M., Benmokrane B. and Aitcin P-C., 1992, Influence of specimen size on compressive strength and elastic modulus of high-performance concrete, Cement, Concrete and Aggregates, Vol. **14**, No. 2, pp. 113-117.

Balmer G.G., 1949, Shearing strength of concrete under high triaxial stress-computation of Mohrs envelope as a curve, Structural Research Laboratory Report SP-23, US Bureau of Reclamation, Denver, Colorado.

Bellotti R. and Rossi P., 1991, Cylinder tests: experimental technique and results, *Materials and Structures*, Vol. **24**, pp. 45-51.

Boulay C., Belloc A. , de Larrard F. and Torrenti J-M., 1992, New method of surfacing test samples of high and very high performance concrete, Bulletin de Liaison des Laboratoires des Ponts et Chaussees, No. 179, pp. 43-55.

Burg R. G. and Ost. B. W., 1992, Engineering properties of commercially available high-strength concretes, Research and Development Bulletin, No. RD104.01T,

Portland Cement Association, Skokie, IL, p. 55.

Carrasquillo P. M. and Carrasquillo R. L., 1988a, Evaluation of the use of current concrete practice in the production of high-strength concrete, *ACI Materials Journal*, Vol. **85**, No. 1, pp. 49-54.

Chen W. F. and Saleeb A. F., 1994a,Constitutive equations for engineering materials, Volume 1: Elasticity and Modeling, Elsevier.

Chen W. F. and Saleeb A. F., 1994b, Constitutive equations for engineering materials, Vol. 2: Plasticity and Modeling, Elsevier.

Chern J. C., Yang H. J.and H. W. Chen, 1992, Behavior of steel fiber reinforced concrete in multiaxial loading, *ACI Material Journal*, Vol. **89**, No. 1, pp. 3240.

Crouch R., 1990, Nonlinear deformation of concrete subjected to multiaxial compression, Doctoral thesis, The University of Manchester.

Crouch R. S., Petkovsi M. and Fernandez-Vega J., 2001, PCPV and PCCV materials behaviour under multiaxial loading conditioned with elevated temperature, CETWG BB/E/40835.

Dahl K. K. B., 1992, A constitutive model for normal and high strength concrete, Report No. 287, Department of structural Engineering, Technical University of Denmark.

Desai C. S. and Siriwardane H. J., 1984, Constitutive laws for engineering Materials: With Emphasis on Geologic Materials, Prentice Hall, Inc., Englewood Cliffs, New Jersey.

Fumagalli M., 1991, Behaviour of concrete under multiaxial stress states: some observations on the state of the art, *Materials and Structures*, Vol. **24**, pp. 42-44.

French C. W. and Mokhtarzadeh A., 1993, High strength concrete: effects of materials, curing and test procedures on short-term compressive strength, *PCI Journal*, Vol. **38**, No. 3, pp. 76-87.

Fu H. C., Erki M. A. and Seckin M., 1991, Review of effects of loading rate on

concrete in compression, *ASCE, Journal of Structural Engineering*, Vol. **117**, No. 12, pp. 3645-3659.

Hill R., 1956, The mathematical theory of plasticity, Clarendon Press, Oxford.

Grassl P., 2004, Plasticity and damage mechanics for modelling concrete failure, Doctoral thesis, Chalmers University of Technology, Göteborg, Sweden.

Imran I., and Pantazopoulou S.J., 1996, Experimental study of plain concrete under triaxial stress, *ACI Materials Journal*, Vol. **93**, No. 6, pp. 589-601.

Ipatti A., 1993, Effect of specimen size and capping method on apparent compressive strength of high-strength concrete, Nordic Concrete Research, Publication No. 13, pp. 56-69.

Jones P. G. and Richart F. E., 1936, *ASTM Proc*, Vol **36**, pp. 380-91.

Johnson C. D. and Mirza S. A., 1993, Compressive strength testing of HPC cylinders utilizing confined caps, Civil Engineering Research Series, Report No. CE-93-2, Department of Civil Engineering, Lakehead University, Ontario, Canada.

Kotsovos M. D. and Newman J. B., 1978, Generalised stress-strain relations for concrete, *ACI Journal*, Vol. **74**, No. 9, pp. 443-446.

Kotsovos M. D., 1979, Fracture processes of concrete under generalised stress states, *Materials and Structures*, Vol. **12**, No. 6.

Lade P. V. and Kim M. K., 1988, Single Hardening constitutive Model for Frictional Materials II. Yield Criterion and Plastic Work Contour, *Computers and Geotechnics*, Vol. **6**, pp. 13-29.

Launay P. and Gachon H., 1972, Strain and ultimate strength of concrete under triaxial stress, Paper 13. ACI Special Publication-34.

Lessard M., Chaallal O. and Aitcin P-C., 1993, Testing high-strength concrete compressive strength, *ACI Materials Journal*, Vol. **90**, No. 4, pp. 303-308.

Li Q. and Ansari F., 1999, Mechanics of damage and constitutive relationships for

high-strength concrete in triaxial compression, *Journal of Engineering Mechanics*, Vol. **125**, No. 1, pp. 1-10.

Mehta P.K., and Monteiro P. J. M., 1993, Concrete: microstructure, properties, and materials. Prentice-Hall, Inc. Eaglewood Cliffs, New Jersey.

Newman J. B., 1973, Criterion for concrete strength, PhD Thesis, London University.

Neville A. M., 1995, Properties of Concrete, Forth edition, Longman.

Pistilli M. F. and Willems T., 1993, Evaluation of cylinder size and capping method in compression strength testing of concrete cement, *Concrete and Aggregates*, Vol. **15**, No. 1, pp. 59-69.

Petkovski M., Crouch R. S. and Waldron P., 2006, Apparatus for testing concrete under multiaxial compression at elevated temperature (mac^{2T}), *Experimental Mechanics*, Vol. **46**, No. 3.

Price W. H., 1951, Factors influencing concrete strength, *ACI Journal*, Vol. **22**, pp. 417-432.

Sinan I. and Lade P. V, 1997, Rotational kinematic hardening model for sand. Part II characteristic work hardening law and predictions, *Computers and Geotechnics*, Vol. **21**, No. 3, pp. 211-234.

Smith S. S., Willam K. J., Gerstle K. H. and Sture S., 1989, Concrete over the top, or: is there life after peak, *ACI Materials Journal*, No. 86-M45, pp. 491-497.

Tanigawa H., Mori H., Watanabe K. and Miwa M., 1990, Testing methods and statistical aspects of compressive strength of high-strength concrete, Transactions of the Japan Concrete Institute, Vol. **12**, pp. 69-76.

van Mier J. G. M., 1986, Multiaxial strain-softening of concrete, Part II: Load-Histories, Materials and Structures (RILEM), Vol.**19**, No.111, pp. 190-200.

Wang C.-Z., Guo Z.-H. and Zhang X.-Q., 1987, Experimental investigation of biaxial and triaxial compressive strength, *ACI Materials Journal*, Vol. **84**, No. 2,

pp. 92-100.

Wriggers P. and Moftah S.O., 2006, Mesoscale models for concrete: Homogenisation and damage behaviour, *Finite Elements in Analysis and Design*, Vol. **42** , pp. 623-636.

Zia P., Ahmad S., and Leming M., 1989-1994, High-performance concretes, A State-of-Art Report.

Chapter 3

Development of the New Constitutive Model

3.1 Introduction

This chapter deals with the modelling of the behaviour of plain concrete under multiaxial compression using the theory of plasticity. The aim is to model the stress strain behaviour in uniaxial, biaxial and multiaxial compression by means of few parameters utilizing the advances that have been achieved in this field and maintaining the simplicity of the mathematical approaches.

The model formulation is based on the experimental observations discussed in Chapter 2, of which the behaviour of concrete under triaxial loading has been investigated. The observations include the plastic flow and the directions of the plastic strain vectors. One of the most easily detectable characteristic features is the state at which plastic dilation commences. This point has been referred to as the plastic volume transition stress (VTS). It is the state associated with the minimum volumetric plastic strain. Note that at this point the response is purely deviatoric.

The model is then constructed assuming associated plasticity in which the plastic strain increment is normal to the yield surface. Three points on the yield surface are identified; the hydrostatic tensile intersection point ($\bar{\xi}_{ht}$), the hydrostatic compression intersection point ($\bar{\xi}_{hc}$) and the plastic VTS point (ξ_{vts}, ρ_{vts}). The directions of the plastic strains at these points are also known; for ($\bar{\xi}_{ht}$) and ($\bar{\xi}_{hc}$), the direction is in the hydrostatic sense while at the plastic VTS point is in the deviatoric direction.

An important point which should be considered is the convexity of the yield surface

needed to fulfill the stability requirement of Drucker's postulate. In the newly developed model, the convexity has been ensured within the range of the material parameter that has been suggested. A novel hardening law has been used with a new ductility measure introduced. The yield surface is expressed in Haigh-Westergaard stress space which is based on the cylindrical coordinate stress invariants ξ and ρ and the Lode angle θ.

The continuum constitutive modelling of concrete is briefly presented in Section 3.2. This includes elasticity, damage, microplane and elasto-plastic models. The main characteristics of these models along with their advantages and disadvantages are introduced. In Section 3.3, the main topics associated with the theory of elasto-plasticity are presented. These include, additive decomposition of the strain vector, the yield condition, the flow rule, and the hardening law. In the same section the loading and unloading states, the Drucker's stability postulate and the isotropic hardening are discussed. The development of the consistency parameter and the tangent elasto-plastic matrix is also presented. The numerical integration algorithm needed for the infinitesimal equations along with a stable stress return algorithm, the closest point projection (CPP) needed to integrate the proposed elasto-plastic constitutive model at the material level is presented in this section. The main features of the Sheffield model are also discussed with some observations and reservations.

The formulation of the new model is given in section 3.4. The isotropic hardening function which controls the evolution of the yield surfaces, and thereby the expanding elastic domain is described in the same section. A new auxiliary stress surface has been formulated. The first and second derivatives of the yield surface with respect to σ and the internal variable k_p are presented in section 3.5. Finally, concluding remarks are given in section 3.6.

3.2 Continuum Constitutive Modelling

Many constitutive models have been proposed and used for the analysis of concrete structures. These models may be classified into two groups

1. The group of macroscopic models, based on a representative volume element relating average strain states to average stress states.

2. The group of microscopic models, based on discrete modelling of the interaction between the components of concrete (e.g. the aggregates and the

cement matrix). These models are often used to simulate fracture initiation and processes [Vonk, 1992; Carol *et al.*, 2001b].

Common macroscopic models for plain concrete are the elasticity models, plasticity models, continuum damage mechanics models, and microplane models. Grassl has reported on the later three groups [Grassl]. In this section a summarised overview of these models is presented along with their main advantages and disadvantages.

3.2.1 Elasticity Models

The linear theory of elasticity combined with criteria defining failure of concrete is the most commonly used material law for concrete in reinforced concrete analysis [Chen and Saleeb, 1994a]. The simplest constitutive model for a strain recoverable material is provided by the hyperelastic formulation, for which the stress response is characterised in terms of a stored energy function. Linear elasticity is normally expressed in terms of the classical constitutive equations, referred to as the generalised Hook's law. The elasticity based models [Kupfer, 1973; Kotsovos and Newman, 1978] no longer appear so prominent to model the deformation of plain concrete as they fail to address the irrecoverable deformation observed under load. From a physical point of view, the elastic models bears only a faint resemblance to the internal mechanism proper to concrete in the stress range of interest. The reason for their previous adoption is clearly a matter of practical convenience, not of physical belief.

3.2.2 Damage Models

Damage theory is developed to deal with the stiffness degradation. This theory was first proposed by Kachanov (1958) to describe creep rupture in metals. The theory further developed to describe the isotropic and anisotropic damaging behaviour of concrete [Krajcinovic and Fonseca, 1981]. The basic assumptions used of the theory are:

1. The response of the material depends only on the current state of the microstructural arrangement.
2. The current state of the microstructural arrangement can be described by a finite set of internal variables, termed "damage variables".

As a damage measure, damage variable may be a scalar or a tensorial quantity. Most of the early damage models were using a scalar as damage variable since the scalar implies that the damage is isotropic, independent of the orientation of the

microdefects. To describe flat planar microcracks, a vector normal to the plane of crack and of magnitude equal to the area of the crack is needed [Chen and Saleeb, 1994b].

The models based on this theory are often used to describe the mechanical behaviour of concrete in tension [Mazars and Pijaudier-Cabot, 1996; Peerlings, 1999; Carol et al., 2001c]. The fundamental assumption for these models is that the local damage in the material can be averaged and represented in the form of damage variables, which are related to the tangential stiffness tensor of the material. The main components are the damage loading function, the evolution law and the relation of the damage variables to the tangential stiffness tensor.

The advantages of using damage mechanics models can be summarised as follows

1. The use of explicit algorithm. That is for a given strain increment, the corresponding secant stiffness modulus and stress state can be determined without iterative calculation procedures.

2. The elastic stiffness degradation observed in experiments in the case of tensile loading can be accounted for.

The disadvantages are as follows

1. These models cannot describe the remaining deformations observed in experiments with concrete in compression.

2. The loading function is formulated in the strain space, which is difficult to calibrate to experimental results.

3. The evolution law cannot be directly related to a stress-strain curve, and hence cannot be determined easily from experiments, unlike the hardening law used in the theory of plasticity.

3.2.3 Microplane Model

The microplane model is a highly simplified model of the microstructure in which the adjacent grains forming the material exchange forces on planes passing through their contact points. The number of force components assumed to act on these planes and the stress-stain laws attributed to each of them determine the behaviour of the model at the macroscale level [Qui].

The microplane model was presented for concrete in its classical form based on kinematic constraints by Bažant and Prat [1988a; 1988b]. It can describe brittle cracking in tension and the behaviour of concrete under triaxial compression and shear. It was subsequently extended to cyclic loading by Ožbolt and Bažant [1992] and its numerical implementation was improved through an explicit algorithm by Carol *et al.* [1992]. The microplane model in this form showed a pathological behaviour in uniaxial tension, in the form of unrealistic lateral expansion. To overcome this problem, Bažant et al. [1996a; 1996b] introduced stress-strain boundaries, i.e. the microplane components have stress limits which are a function of the macroscopic stress state. The model was further developed by Bažant et al. [2000], and a thermodynamic formulation was presented by Carol *et al.* [2001a] and Kuhl *et al.* [2001]. An alternative approach to overcome the pathological behaviour in tension was proposed by Ožbolt et al. [2001] by using a relaxed kinematic approach in the case of dominant tensile loading.

The advantages of the microplane models can be summarised as follows:

1. Their capability to fit a large set of experimental data.
2. The explicit calculation flow of these models where the stress state can be directly determined for a given strain state.

The disadvantages can be summarised as follows:

1. There are many parameters on the microplane level which are required to be calibrated in order to obtain agreement with experimental results.
2. An explicit calibration by means of results of material tests is not possible. Instead, it is necessary to obtain the parameter required by means of reanalysis. Hereby, it is difficult to distinguish between material properties and structural properties, and the extrapolation of the calibration parameters obtained is doubtful.
3. The earlier versions of the microplane models do not fulfil the thermodynamic laws.
4. The very high computational cost, which is mainly caused by the split of the strain tensors onto the microplanes.
5. These models do not satisfactory simulate degradation in the unloading stiffness and in its current explicit form it possessed very high sensitivity to the values of material constants [Qui].

3.2.4 Plasticity Models

The physical model behind elastic-plastic theories involves the occurrence of irreversible slips within the crystalline structure of the material. As such, the model is certainly a more appropriate start point for describing the macroscopic behaviour of metal, rather than concrete. However, the theory of plasticity when not narrowly interpreted, provides a very flexible mathematical model that can be used to describe the behaviour of concrete [Chen and Saleeb, 1994b].

This theory has now been widely used in modeling the non-linear stress strain behaviour of concrete in multiaxial stress state. Many models have been classified as plasticity based models [Willam and Warnke, 1974; Ohtani and Chen, 1987; Chen and Saleeb, 1994b; Tahar 2000; Li, 2005]. The stress-strain behaviour of concrete consists of a linear elastic regime, corresponding to the first stage of deformation, and a nonlinear hardening corresponding to the second stage. In the nonlinear regime, the total strain is decomposed into an elastic part and a plastic part. Then the multiaxial stress-strain relations can be developed based on the theory of plasticity.

The advantages of the plasticity theory can be summarised as follows

1. The simplicity and direct calibration of the stress state.
2. The yield surface corresponds at a certain stage of hardening to the strength envelope of concrete, and thus has, a strong physical meaning.
3. The split of the strains into elastic and plastic parts corresponds to the observed remaining deformations of concrete in compression, so that unloading and path dependency can be accounted for in a realistic way.
4. The theory of plasticity has a very long tradition; hence the implementation of the formulation is efficient and thermodynamic validity is assured.

The disadvantages can be summarised as follows

1. Unable to account for the stiffness degradation during loading process.
2. The indirect calibration of the deformation behaviour by means of the plastic potential if associated plasticity is used.
3. The number of invariants to describe the behaviour of plain concrete is limited and, therefore it is difficult to model the concrete behaviour with all its complexity.

4. The implicit calculation procedure where the stress state must be iterated so that, for a given strain state, the yield condition is fulfilled and that is computationally costly.

Comparing the advantages and disadvantages of models based on different theories, it can be seen that the plasticity models are well suited to describe the compression behaviour of concrete, whereas the strength of damage mechanics models lie in the modelling of the tensile behaviour.

3.3 The Theory of Elasto-Plasticity

In this section the main topics related to the theory of elasto-plasticity are presented. These include the basic assumptions of the theory, the loading-unloading states, Drucker's stability postulate and the isotropic hardening. The development of the consistency parameter and the tangent elasto-plastic matrix are also presented. The numerical integration of the infinitesimal equations is described along with the closest point projection algorithm. Finally, a brief introduction to the Sheffield model is presented.

3.3.1 Plasticity Basic Assumptions

Plasticity model of concrete must involve four basic assumptions:

1. The additive decomposition of the strain vector

2. There exist an initial yield surface and a failure surface in stress space, which define the elasticity region and the hardening region, respectively.

3. A hardening rule, which defines the change of the loading surface as well as the change of the hardening properties of the material during the course of the plastic flow.

4. A flow rule, which is related to a plastic potential function and leads to an incremental plastic stress strain relation [Chen and Saleeb, 1994b].

The yield surface (loading surface) limits the elastic domain. It depends on the stress state $\{\sigma\}$ and a hardening function k. It has the form

$$F(\sigma, k) = 0 \tag{3.1}$$

where k is a function of the hardening parameter k_p, expressed as

$$k = h\left(k_p\right) \tag{3.2}$$

The hardening parameter is given in the form

$$dk_p = d\lambda \; k_p(\sigma, \epsilon^p) \tag{3.3}$$

where $d\lambda$ is plastic multiplier.

If the yield function is equal to zero, plastic flow occurs. The flow rule prescribes in which way the plastic flow develops. The direction of the flow vector is determined by the gradient of the plastic potential function G. The amount of the plastic flow is determined by the plastic multiplier $d\lambda$

$$\{d\epsilon^p\} = d\lambda \left\{\frac{\partial G}{\partial \sigma}\right\} \tag{3.4}$$

Additive Decomposition of the Strain Vector

The strain vector is decomposed into its elastic and plastic components, denoted by $\{\epsilon^e\}$ and $\{\epsilon^p\}$, respectively, according to the infinitesimal relationship

$$\{d\epsilon\} = \{d\epsilon^e\} + \{d\epsilon^p\} \tag{3.5}$$

$\{d\epsilon\}$ is regarded as an independent vector variable. As noted above, the infinitesimal stress vector $\{d\sigma\}$ is related to the infinitesimal elastic strain vector $\{d\epsilon^e\}$ by means of a stored energy function χ according to the hyperelastic relationship. For linearised elasticity, χ is a quadratic function of the elastic strain ($\chi = \frac{1}{2}\{\epsilon^e\}\,[D]\,\{\epsilon^e\}$), where $[D]$ is the elasticity stiffness matrix which can be identified for an isotropic material by two material constants, Young's modulus (E) and Poisson's ratio (ν).

The relationship between the linear components is expressed as follows

$$\{\sigma\} = [D]\,\{\epsilon^e\} \tag{3.6}$$

Equations (3.5) and (3.6) may be combined to obtain

$$\{\sigma\} = [D]\,(\{\epsilon\} - \{\epsilon^p\}) \tag{3.7}$$

Note that it is possible to write (3.7) in terms of total stress and strain measures because of the linearity of the elastic components.

Yield Conditions

The yield criterion can be defined as the limit of elastic deformations expressed by combination of states of stresses [Desai and Siriwardane]. It is worth noting that the shape of the yield surface is still a matter of investigation amongst researchers. No consensus has been reached as what is the true shape of this surface or even if plasticity is an appropriate constitutive framework. The differences might continue as long as there is no experimental investigation into the real shape of the yield surface, which might be achieved by performing a sequence of small load-unload paths throughout the stress space to identify the plastic strain occurring at each stage. Note that the identifications of the initial and subsequent yield surfaces are not easy to achieve experimentally. However, a proposal for the shape of the yield surfaces assuming associated flow has been given in Chapter 2. The modelling of such surfaces is presented in Section (3.4.3).

One of the issues related to the shape of the yield surface is whether the plastic flow is associated or not. It has been argued by several workers that when plastic potential function is chosen independently from the yield function, the fit to the experimental observations is better [Bićanić and Pearce]. Others [Najjar *et al.*] have modelled concrete reasonably well using an associated flow rule. There is, however, a serious price to pay for the introduction of non-associativity, in that it results in a non-symmetric tangentional stiffness matrix. The latter is not convenient from a numerical point of view. It necessitates greater storage and a more general solution technique for large systems of equation. There is also a second physically unacceptable consequence of non-associated rule; the uniqueness of a solution is not guaranteed and energy may be created during a load-unload cycle [Tahar]. Therefore, the validity of introducing the associated flow is one of the questions examined in this study.

At any stage of plastic deformation the yield condition is given as a function of the stress state $\{\sigma\}$ and the internal variable k. For isotropic plasticity, the latter is considered as a scalar measure, which itself is a function of the accumulated plastic strains $\{\epsilon^p\}$, in the simple strain hardening formulation considered here

$$F = F\left(\sigma, k(\epsilon^p)\right) = 0 \tag{3.8}$$

For stress states inside the yield surface, $F < 0$. Points on the yield surface satisfy $F = 0$, whereas inadmissible states, outside the yield surface, are described by $F > 0$. When the yield surface expands as k evolves, hardening behaviour is observed. A hardening rule describes how the yield surfaces grow or move with

respect to k. Conversely, softening is associated with shrinking or translation of the yield surface.

At a stress point $\{\sigma\}$ on the yield surface, a stress increment $\{\Delta\sigma\}$ may have any direction for hardening plasticity. In the case of softening plasticity, it can only be directed inwards. Considering the hardening case, if the stress probe is directed inward then a purely elastic response will be generated. If it is directed outward, however, both elastic and plastic straining will occur. For a stress state lying within the loading surface ($F < 0$) the material will behave according to the constitutive relations of elasticity.

The yield surface at peak stress or the peak nominal stress surface (PNS) is easier to identify experimentally. There are many formulations in the literature for the PNS envelope. There are formulations proposed by Rankinee (1876), Mohr-Coulomb (1900), von Mises (1913), Leon (1935), Drucker-Prager (1952), Willam and Warnke (1974), Ottosen (1977), Hoek-Brown (1980), Etse-Willam (1994, Mentrey and Willam (1995), Bićanić-Pearce (1996), Tahar (2000), Li (2005). These formulations differ mainly in the number and kind of material parameters required for the calibration.

In commercial finite element codes it is still often common to use a Mohr-Coulomb or a Drucker-Prager yield surface . These surfaces do not represent the main properties of the failure surface of concrete in compression. In the case of the Mohr-Coulomb failure surface (see Figure 3.1), the meridians are straight and the yield surface is independent of the intermediate principal stress component, i.e. the strength in uniaxial compression is equal to the strength in biaxial compression. Furthermore, the relation of the strength on the compressive meridian to the strength on the tensile meridian stays constant with increasing hydrostatic pressure. The Drucker-Prager yield surface (Figure 3.1) is a generalisation of the Mohr-Coulomb yield surface. The meridians are straight, and the strength on the compressive meridian is equal to that on the tensile meridian, i.e. the strength in biaxial compression is highly overestimated. Calibrated for stress states on the compressive meridian, the Drucker-Prager yield surface leads to an equibiaxial compressive strength significantly higher than the uniaxial compressive strength [Grassl].

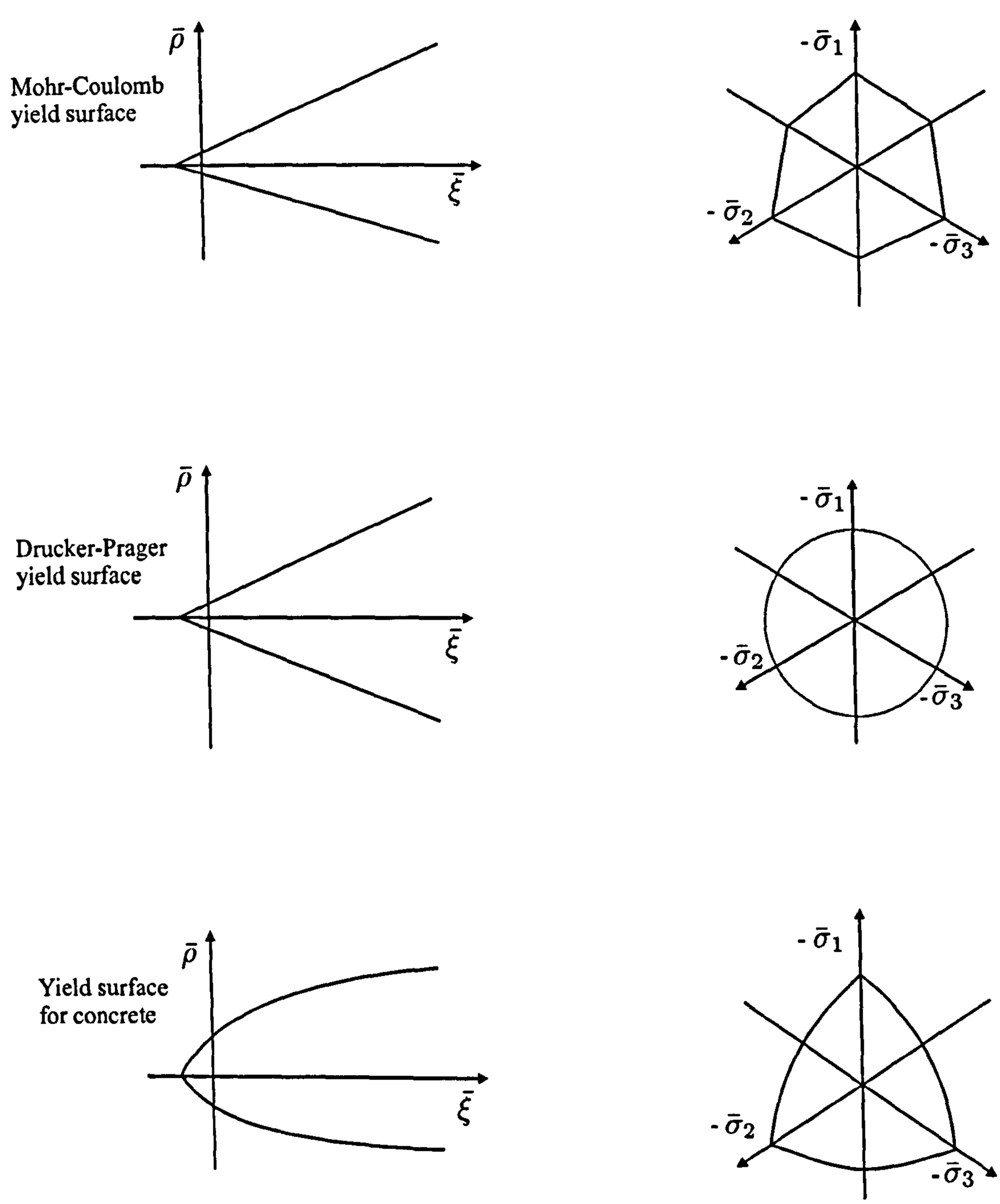

Figure 3.1: Classic yield surfaces and yield surface for concrete

Flow rule

The flow rule prescribes the evolution and the amount of the plastic strain. The evolution of the plastic strain is given as a function of the plastic potential, G, which depends on the stress vector and possibly other internal variables, $G(\sigma, r)$. The flow rule is defined by the following expression

$$\{d\epsilon^p\} = d\lambda \frac{\partial G}{\partial \sigma} \tag{3.9}$$

where $\frac{\partial G}{\partial \sigma}$ defines the direction of the plastic flow and the parameter $d\lambda \geq 0$ is a non-negative scalar factor, called the plastic multiplier (or consistency parameter), which obeys the following Kuhn-Tucker complementarily conditions [Simo and Hughes, 1987]

$$d\lambda \geq 0, \qquad F(\sigma, k_p) \leq 0 \quad \text{and} \quad d\lambda F(\sigma, k_p) = 0 \tag{3.10}$$

In addition, the following consistency requirement must be satisfied

$$d\lambda \; dF(\sigma, k_p) = 0 \tag{3.11}$$

In its most general case, the flow is said to be non-associated. When the yield function is used as a plastic potential ($G = F$) then the resulting theory is referred to as associated plasticity. This implies that the plastic strain rate develops in a direction normal to the yield surface hence (3.9) is often referred to as a normality rule. Experimental observations show that the plastic deformation of metals can be characterised quite well by the associated flow rule, but for many frictional, porous materials such as rocks, concrete and soils, some researchers think that the use of an associated flow rule overestimates the volumetric expansion reported in experiments [Tahar]. Hence non-associated flow rule is often thought to provide a better representation of behaviour [Khan and Huang]. However, it has been shown in Chapter 2 that the plastic flow of concrete at PNS and during hardening can be characterised as associated. The plastic work contours also thought to be normal to the plastic strain vectors. Therefore the associated flow rule is adopted to model the response of concrete in this thesis.

Hardening law

There are certain ways to idealise the stress-strain behaviour of different materials; these idealisation are:

1. Perfectly elastic

2. Rigid, perfectly plastic

3. Rigid, linear strain hardening

4. Elastic, perfectly plastic

5. Elastic, linear strain hardening, linear strain softening

6. Elastic, nonlinear strain hardening, nonlinear strain softening

The elastic deformations do not depend on how and along what stress path the state of stress was reached. They depend only on the final state of stress. However, in the case of plastic deformations, the strains depend on the history of the stress state, and the stress-strain relationships are generally nonlinear. If the material is assumed to experience no hardening, then it is called perfectly plastic. Figure 3.2 shows graphical representation of different idealised models.

If the material characteristics are not affected by the orientation, the material is called isotropic. A material that is initially isotropic may remain isotropic during the deformation process or it may become anisotropic.

The isotropic hardening (adopted here) assumes that the subsequent yield surface is a uniform expansion of the initial yield surface. In other words, the shape and orientation do not change. It is also assumed that the material's isotropic response to yielding remains unchanged during plastic deformation. It neglects the anisotropic effect on the subsequent yielding induced by the deformation.

For isotropic materials, the yield surface F may be expressed in terms of the principal stresses:

$$F(\sigma_1, \sigma_2, \sigma_3) = 0, \tag{3.12}$$

or the stress invariants:

$$F(I_1, J_2, J_3) = 0 \tag{3.13}$$

The assumption of isotropy will be shown to offer a reasonable compromise for concrete provided that the material does not undergo significant stress reversals or changes in the principal stress directions. Note that the hardening parameter k reflects the effects of the past loading events on the material fabric. If the yield surfaces were anisotropic then k would be represented by a higher order matrix.

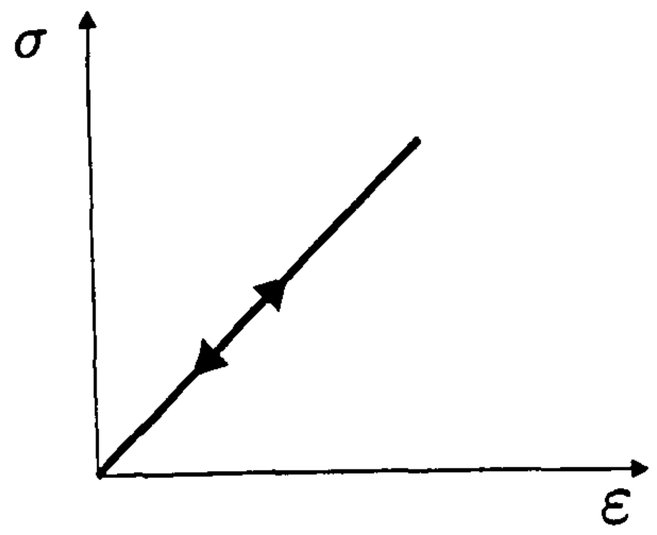

Perfectly elastic

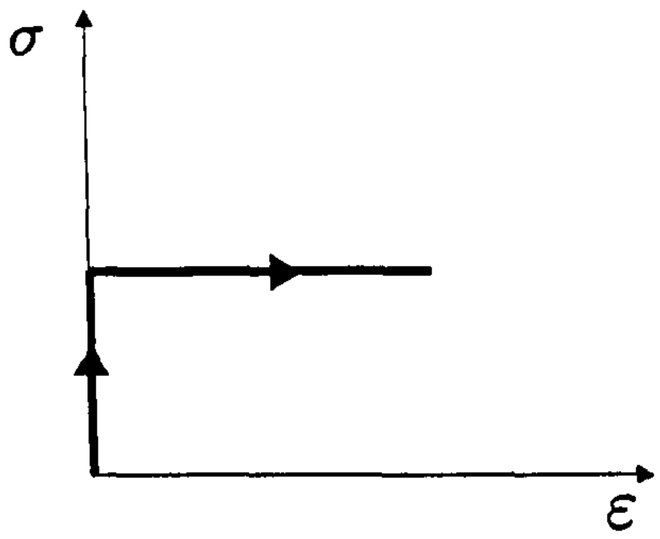

Rigid, perfectly plastic

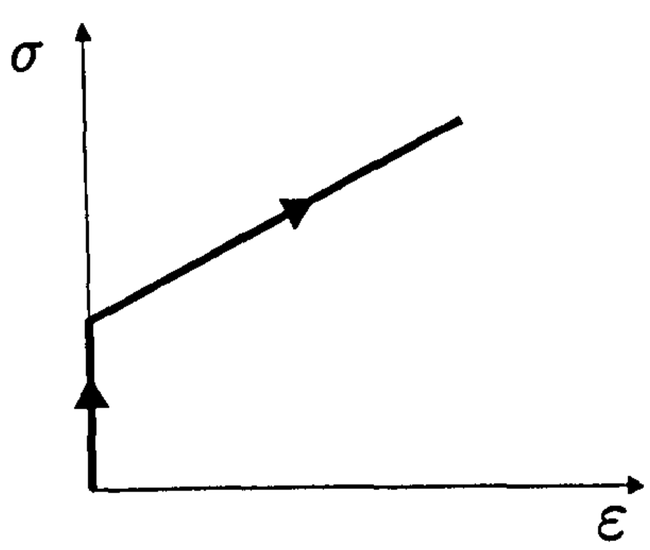

Rigid, linear elastic hardening

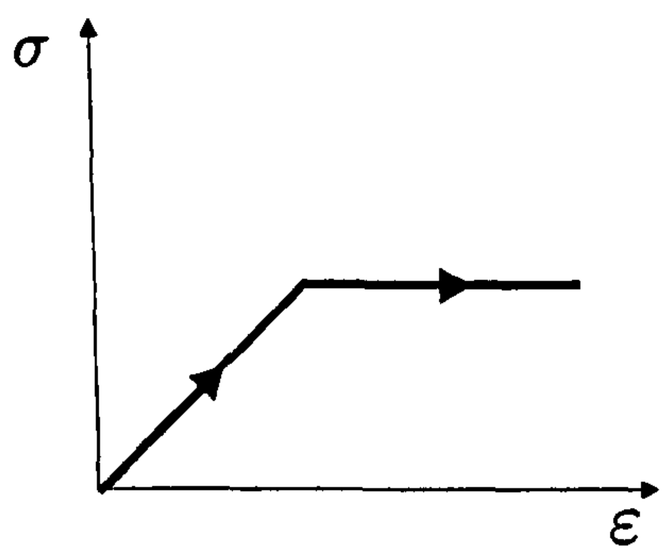

Elastic, perfectly plastic

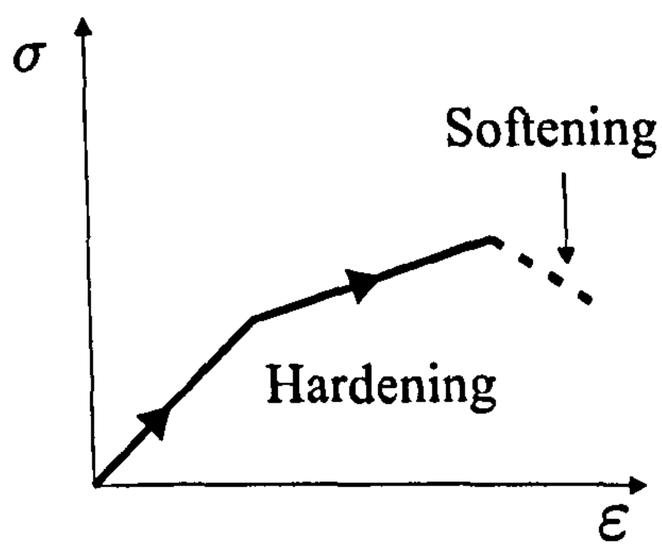

Elastic, linear hardening, softening

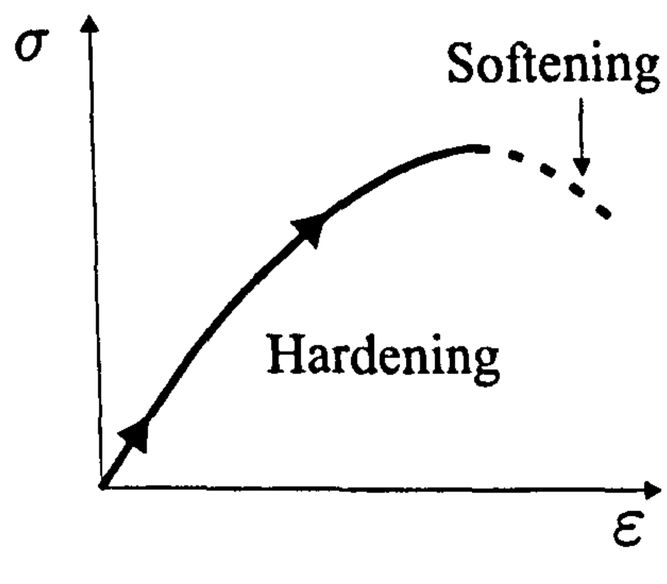

Elastic, nonlinear hardening, softening

Figure 3.2: Idealised stress strain models

The isotropic hardening implies the existence of a universal function between a certain measure of stress, called equivalent stress, and a certain measure of strain called equivalent strain or equivalent plastic strain. The definitions of these measures depend on the yield criteria to be used. The function is called universal because it holds true for any stress and strain state and loading path.

The hardening law, given by equation (3.2), controls the shape and size of the yield surface and the plastic potential by means of the function k. Hence, it determines the amount of plastic deformation at a certain stress state. The function k is often a form of the relation of the uniaxial compressive stress to the equivalent plastic strain (ϵ^p), which is a scalar defined as the length of the plastic strain

$$\epsilon^p = \sqrt{\{\epsilon^p\}\{\epsilon^p\}} \tag{3.14}$$

where the plastic strain vector, $\{\epsilon^p\}$, is determined according to the flow rule in equation (3.4).

The influence of the confinement on the axial and lateral inelastic deformation capacities was presented in Chapter 2. It was seen that with increasing of the confinement the deformation capacity increases significantly. A way to incorporate this increase into the hardening law may be achieved by introducing a ductility measure. The hardening parameter k_p from equation (3.3) is hereby scaled with a function of the hydrostatic stress, ζ, also called the ductility measure [Etse and Willam, 1994]. Then the hardening parameter becomes a function of the stress state and the plastic strain state:

$$k_p(\sigma, \epsilon_p) = \frac{\epsilon^p}{\zeta(\bar{\xi})} \tag{3.15}$$

3.3.2 Loading and Unloading

The yield surface can be used to identify the elastic and plastic regions and loading and unloading criteria to identify the characteristics of the deformation. For perfectly plastic materials the subsequent yield surface at any instant is exactly the same as the initial yield surface. Loading occurs when the stress state point is on the yield surface and remains there, and the plastic strain can increase indefinitely. If the stress point moves to the inside of the yield surface, it causes unloading. This can be summarised as follows

$$\begin{aligned} &\mathrm{F}<0 && && \text{(elastic deformation)} \\ &F=0 && \text{and} \quad dF>0 && \text{(loading)} \\ &F=0 && \text{and} \quad dF<0 && \text{(unloading)} \end{aligned}$$

For the work-hardening materials the Kuhn-Tucker complementary loading/unloading conditions summarize the consistency condition which conform with our intuitive notions of plastic loading and elastic unloading.

1. If $F(\sigma, k_p) < 0$ then, from condition (3.11), $d\lambda\ F(\sigma, k_P) = 0$ infers that $d\lambda = 0$. Then, it follows that $\{d\epsilon^p\} = 0$ and $dk_P = 0$. This case corresponds to the elastic loading case $\{d\epsilon\} = \{d\epsilon^e\}$, and the infinitesimal form leads to

$$\{d\sigma\} = [D]\ \{d\epsilon\} \tag{3.16}$$

   hence the response is instantaneously elastic.

2. When the stress path has reached the yield condition $F(\sigma, k_p) = 0$. Two situations can be obtained, depending on whether $d\lambda$ is zero or positive

   (a) If $dF(\sigma, k_p) < 0$ and $d\lambda\ dF(\sigma, k_p) = 0$ this implies that $d\lambda = 0$, resulting in $\{d\epsilon^p\} = 0$ and $dk_p = 0$. This type of response is called elastic unloading from a plastic state

   (b) If $dF(\sigma, k_p) = 0$, this defines the differential form of the plastic consistency condition in which equation (3.11) is automatically satisfied. If $d\lambda > 0$, then $\{d\epsilon^p\} \neq 0$ and $dk_p \neq 0$; a situation called plastic loading. The case $d\lambda = 0$ and $dF(\sigma, k_p) = 0$ is termed neutral loading

These loading/unloading conditions are summarised below

$$\begin{aligned} &F<0 && && d\lambda=0 && \text{(elastic loading)} \\ &F=0 \begin{cases} \\ \\ \\ \end{cases} && dF<0 && d\lambda=0 && \text{(elastic unloading)} \\ & && dF=0 && d\lambda=0 && \text{(neutral loading)} \\ & && dF=0 && d\lambda>0 && \text{(plastic loading)} \end{aligned}$$

Figure 3.3 shows the loading and unloading conditions for work-hardening materials.

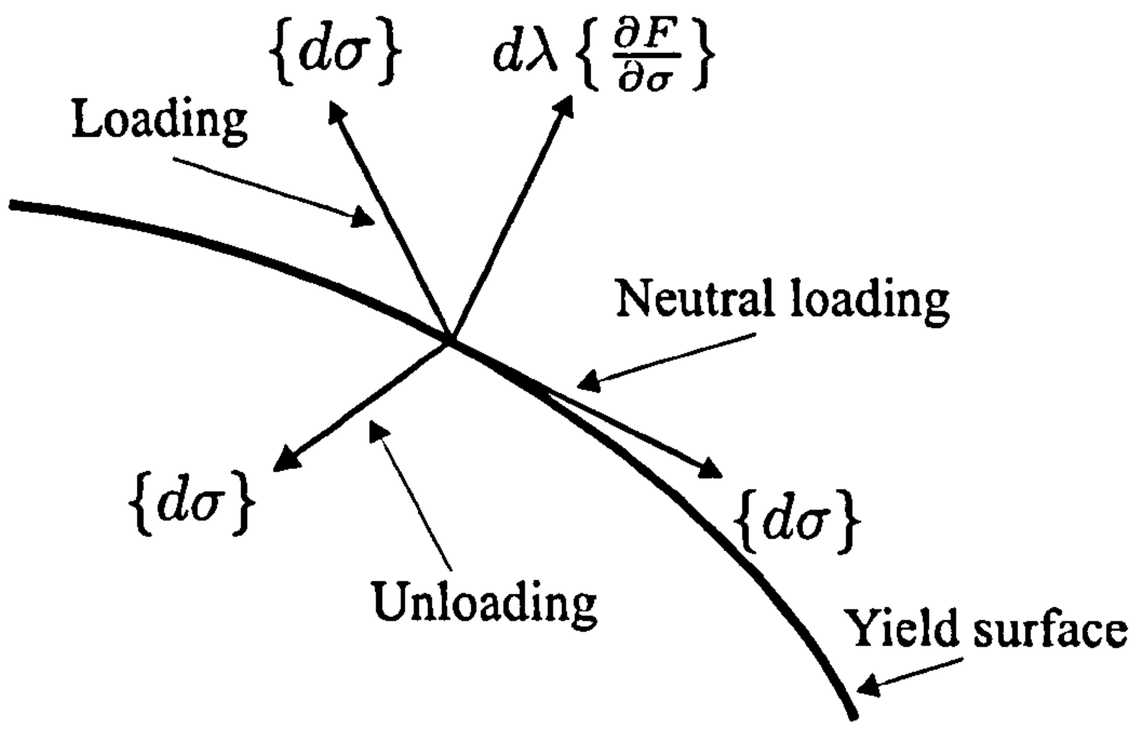

Figure 3.3: Loading and unloading for work-hardening materials

3.3.3 Drucker's Stability Postulate

In an effort to establish the general plastic stress-strain relations for any yield criterion, Drucker proposed a unified approach based on his stability postulate. In a series of papers [Drucker; 1950, 1951, 1959, 1964], he developed the postulates of *stability in the small* and of *stability in the large* for isothermal time independent materials. By means of these postulates it is possible to prove that for a work-hardening material the yield surface is convex and that the plastic strain-increment is normal to the yield surface. One major consequence of Drucker's postulate is that the flow rule for stable material is associated (i.e. G = F).

Drucker's stability postulate asserts that if a material is stable, the following inequality must be satisfied:

$$W = \int \{\Delta\sigma\}\{d\epsilon\} \geq 0 \tag{3.17}$$

The integral represents the work done by the external agency. It was shown by Drucker that any material that does not obey this inequality is unstable.

Drucker summarised these conditions by the following inequality

$$\{d\sigma\}\{d\epsilon^p\} \geq 0 \tag{3.18}$$

The above expression refers to stability in the small. Stability in the large is expressed by

$$\{\sigma\}\{d\epsilon^p\} \geq 0 \tag{3.19}$$

The Drucker's stability postulate is a fairly strong requirement that can be satisfied

only by hardening materials whose subsequent yield strength increase with deformation. Any material on which an external agency does positive work during an elastic-plastic stress cycle is considered as hardening material. Drucker's postulate does not apply to softening materials, and it needs to be modified for perfectly plastic materials [Khan and Huang].

The postulate has the following implications:

1. The yield surface should be convex in stress space.
2. The yield surface and the plastic potential surface should coincide, implying an associated flow rule is necessary.
3. Work softening is not permissible.

Some researchers feel Drucker's postulate is more a means of identifying material classes rather than a strict requirement for all constitutive models [Tahar].

3.3.4 Development of the Consistency Parameter and the Tangent Elasto-Plastic Matrix

Recall the four infinitesimal general elasto-plastic constitutive relations:

1. The additive decomposition of the strain vector

$$\{d\varepsilon\} = \{d\varepsilon^e\} + \{d\varepsilon^p\} \tag{3.20}$$

2. The hypoelastic law

$$\{d\sigma\} = [D^e]\{d\varepsilon^e\} \tag{3.21}$$

3. The flow rule for associated flow (F = G)

$$\{d\varepsilon^p\} = d\lambda \left\{\frac{\partial F}{\partial \sigma}\right\} \tag{3.22}$$

4. The hardening rule

$$dk_p = d\lambda\, h \tag{3.23}$$

where

$$dk_p = \frac{\sqrt{\{d\varepsilon^p\}^T\{d\varepsilon^p\}}}{\zeta} \tag{3.24}$$

and ζ is a ductility measure.

Following standard Voigt notation $\{\varepsilon\}$, $\{\varepsilon^e\}$ and $\{\varepsilon^p\}$ denote the total, elastic and plastic strain tensor, $\{\sigma\}$ is the Cauchy stress, and k_p signifies a suitable internal variable. Equation (3.20) expresses the commonly assumed additive decomposition of the infinitesimal strain tensor into elastic and plastic parts. Equation (3.21) represents the generalized Hooke's law which linearly relates stress and elastic strain rates through a stiffness matrix $[D^e]$. Equation (3.22) expresses an associated flow rule for the plastic strains whereas (3.23) governs the evolution of the plastic variable. In these equations, $\left\{\frac{\partial F}{\partial \sigma}\right\}$ is the plastic flow direction, h is the plastic modulus and $d\lambda$ is a plastic consistency parameter to be determined with the aid of the loading-unloading criterion, which can be expressed in terms of the Kuhn-Tucker conditions.

Substitute (3.22) into (3.24)

$$dk_p = \frac{\sqrt{d\lambda\left\{\frac{\partial F}{\partial \sigma}\right\}^T d\lambda\left\{\frac{\partial F}{\partial \sigma}\right\}}}{\zeta} \tag{3.25}$$

$$dk_p = d\lambda\frac{\sqrt{\left\{\frac{\partial F}{\partial \sigma}\right\}^T\left\{\frac{\partial F}{\partial \sigma}\right\}}}{\zeta} \tag{3.26}$$

from (3.23) and (3.26)

$$h = \frac{\sqrt{\left\{\frac{\partial F}{\partial \sigma}\right\}^T\left\{\frac{\partial F}{\partial \sigma}\right\}}}{\zeta} \tag{3.27}$$

The yield surface is identified as follows

$$F(\sigma, k_p) = 0 \tag{3.28}$$

where F gives the yield function.

Using the chain rule, the derivative of F at (σ, k_p) is given as

$$dF = \left\{\frac{\partial F}{\partial \sigma}\right\}^T \{d\sigma\} + \frac{\partial F}{\partial k_p}\, dk_p = 0 \tag{3.29}$$

By substituting (3.26) into (3.29)

$$dF = \left\{\frac{\partial F}{\partial \sigma}\right\}^T [D^e]\{d\varepsilon\} - \left\{\frac{\partial F}{\partial \sigma}\right\}^T [D^e]\{d\varepsilon^p\} + \frac{d\lambda}{\zeta}\frac{\partial F}{\partial k_p}\sqrt{\left\{\frac{\partial F}{\partial \sigma}\right\}^T \left\{\frac{\partial F}{\partial \sigma}\right\}} = 0 \quad (3.30)$$

Substitute (3.22) in (3.30)

$$dF = \left\{\frac{\partial F}{\partial \sigma}\right\}^T [D^e]\{d\varepsilon\} - \left\{\frac{\partial F}{\partial \sigma}\right\}^T [D^e]\, d\lambda \left\{\frac{\partial F}{\partial \sigma}\right\} + \frac{d\lambda}{\zeta}\frac{\partial F}{\partial k_p}\sqrt{\left\{\frac{\partial F}{\partial \sigma}\right\}^T \left\{\frac{\partial F}{\partial \sigma}\right\}} = 0 \quad (3.31)$$

and solve (3.31) for $d\lambda$

$$d\lambda = \frac{\left\{\frac{\partial F}{\partial \sigma}\right\}^T [D^e]\{d\varepsilon\}}{\left\{\frac{\partial F}{\partial \sigma}\right\}^T [D^e] \left\{\frac{\partial F}{\partial \sigma}\right\} - \frac{1}{\zeta}\frac{\partial F}{\partial k_p}\sqrt{\left\{\frac{\partial F}{\partial \sigma}\right\}^T \left\{\frac{\partial F}{\partial \sigma}\right\}}} \quad (3.32)$$

Substitute (3.32) into (3.22) and using this with (3.20)in (3.21) gives

$$\{d\sigma\} = [D^e]\{d\varepsilon\} - \frac{[D^e]\left\{\frac{\partial F}{\partial \sigma}\right\}^T [D^e]\{d\varepsilon\}\left\{\frac{\partial F}{\partial \sigma}\right\}}{[D^e]\left\{\frac{\partial F}{\partial \sigma}\right\}^T \left\{\frac{\partial F}{\partial \sigma}\right\} - \frac{1}{\zeta}\frac{\partial F}{\partial k_p}\sqrt{\left\{\frac{\partial F}{\partial \sigma}\right\}^T \left\{\frac{\partial F}{\partial \sigma}\right\}}} \quad (3.33)$$

Substituting 3.27 into 3.33 gives the constitutive equation:

$$\{d\sigma\} = [D^e]\{d\varepsilon\} - \frac{[D^e]\left\{\frac{\partial F}{\partial \sigma}\right\}^T [D^e]\{d\varepsilon\}\left\{\frac{\partial F}{\partial \sigma}\right\}}{[D^e]\left\{\frac{\partial F}{\partial \sigma}\right\}^T \left\{\frac{\partial F}{\partial \sigma}\right\} - \frac{\partial F}{\partial k_p}\, h} \quad (3.34)$$

$$\{d\sigma\} = \underbrace{\left[[D^e] - \frac{[D^e]\left\{\frac{\partial F}{\partial \sigma}\right\}^T [D^e]\left\{\frac{\partial F}{\partial \sigma}\right\}}{[D^e]\left\{\frac{\partial F}{\partial \sigma}\right\}^T \left\{\frac{\partial F}{\partial \sigma}\right\} - \frac{\partial F}{\partial k_p}\, h}\right]}_{[D^{ep}]}\{d\varepsilon\} \quad (3.35)$$

where $[D^{ep}]$ is the elasto-plastic stiffness matrix.

3.3.5 Integration of the Infinitesimal Equations

The constitutive relations for a general elasto-plastic material relate an infinitesimal stress rate to an infinitesimal strain rate at a given stress state and a plastic deformation state, as has been shown in the previous section (3.3.5). However,

in a conventional finite element analysis, one applies a finite load increment (or displacement) instead of an infinitesimal one. Therefore, the constitutive relations have to be integrated. In most cases this must be done numerically. The precision with which the constitutive relations are integrated has a direct impact on the overall accuracy of the analysis. The efficiency of the integration algorithm has a significant effect on the overall computational cost of the analysis. There are a large number of integration algorithms which may be used for this purpose [Ortiz and Simo, 1986; Runesson *et al*, 1988; Pramono and Willam, 1989]. One of the simplest implicit computational techniques is the cutting-plane method. With this approach the derivative of the hardening law and the second derivatives of the yield function need not be determined [Tahar].

There are two classes of stress return algorithm: explicit and implicit. Explicit methods have recently fallen out of favour in view of their conditional stability, poor accuracy and the fact that the updated solution may not even exist if the strain increment is too large [Runesson *et al.*]. Among the implicit methods, there exist the backward Euler (or Closest Point Projection method, CPP), the generalised midpoint rule (GMPR) and the generalised trapezoidal rule (GTR). In general, implicit predictor-corrector schemes are widely accepted as being most appropriate for the integration of elasto-plastic constitutive relations. The Closest Point Projection is known to be superior for large increments, providing smaller errors compared with other methods. This scheme has also been identified as being particularly suitable when the yield surfaces have regions of high curvature [Simo and Hughes].

Closest Point Projection (CPP) Method

In the displacement-based finite element (FE) method, the closest point projection approach first considers the total strain increment $\{\Delta\epsilon\}$ as producing a purely elastic response, thereby arriving at an initial predictor trial stress state, $\{\sigma^{tr}\}$ [Li, Tahar]. If this lies inside the yield surface

$$F(\{\sigma^{tr}\},\{k_p\}) \leq 0, \tag{3.36}$$

no plastic deformation will have occurred during that strain increment; otherwise, an elasto-plastic response must have taken place.

Given the stress state and the hardening parameter at step n plus the newly calculated elastic predictor stresses, the central tasks of the CPP algorithm are to find the following values at step $n+1$:

1. the corrective up-dated (return) stress $\{_{n+1}\sigma\}$
2. the converged plastic strains $\{_{n+1}\varepsilon^p\}$
3. the plastic multiplier $_{n+1}\lambda$ that simultaneously
   (a) results in zero residual strains $\{_{n+1}r\} = \{0\}$ (see below the definition of {r})

   and

   (b) satisfies the consistency condition $_{n+1}F(\{_{n+1}\sigma\}, \{_{n+1}k_p\}) = 0$
4. the algorithmic tangent corresponding to the final converged state.

The following expression $\{r\}$, identifies the *residual plastic strains and hardening internal variable* calculated in CCP iteration i during the global time increment from n to $n+1$

$$\{^i_{n+1}r\} = \left\{ \begin{array}{c} -\{^i_{n+1}\varepsilon^p\} + \{\varepsilon^p\} \\ -^i_{n+1}k_p + _n k_p \end{array} \right\} + ^i_{n+1}\Delta\lambda \left\{ \begin{array}{c} \{^i_{n+1}\frac{\partial F}{\partial \sigma}\} \\ ^i_{n+1}h \end{array} \right\} \tag{3.37}$$

If $i = 0$, we set

$$\{^0_{n+1}\varepsilon_p\} = \{_n\varepsilon_p\} \qquad ^0_{n+1}k_p = _n k_p \qquad ^0_{n+1}\Delta\lambda = 0 \tag{3.38}$$

Linearising (3.37) at stress state $\{^i_{n+1}\sigma\}$, which is equivalent to expanding $\{_{n+1}r\}$ via a Taylor's series at stress state $\{^i_{n+1}\sigma\}$, ignoring the second and higher derivative terms and then equating $\{_{n+1}r\}$ to zero and noting that both F and h are functions of $\{\sigma\}$ and k_p, leads to:

$$\begin{aligned} &\{^i_{n+1}r\} - \left\{ \begin{array}{c} \{^i_{n+1}\Delta\varepsilon^p\} \\ ^i_{n+1}\Delta k_p \end{array} \right\} + ^i_{n+1}\Delta\lambda \left[\begin{array}{cc} [^i_{n+1}\frac{\partial^2 F}{\partial\sigma^2}] & \{^i_{n+1}\frac{\partial^2 F}{\partial F \partial k_p}\} \\ \{^i_{n+1}\frac{\partial h}{\partial\sigma}\}^T & ^i_{n+1}\frac{\partial h}{\partial k_P} \end{array} \right] \left\{ \begin{array}{c} \{^i_{n+1}\Delta\sigma\} \\ ^i_{n+1}\Delta k_p \end{array} \right\} \\ &+ ^i_{n+1}\delta\lambda \left\{ \begin{array}{c} \{^i_{n+1}\frac{\partial F}{\partial\sigma}\} \\ ^i_{n+1}h \end{array} \right\} = \{0\} \end{aligned} \tag{3.39}$$

Since the sum of the corrective elastic and plastic strains from the *trial* state to the final *converged* state is zero during the corrective return:

$$\{^i_{n+1}\Delta\varepsilon^e\} + \{^i_{n+1}\Delta\varepsilon^p\} = \{0\}, \tag{3.40}$$

the plastic strain increment is:

$$\{{}^{i}_{n+1}\Delta\varepsilon^{p}\} = -[D^{e}]^{-1}\{{}^{i}_{n+1}\Delta\sigma\} \tag{3.41}$$

Substituting (3.41) into (3.39) gives

$$\{{}^{i}_{n+1}r\} + [{}^{i}_{n+1}A]^{-1}\begin{Bmatrix} \{{}^{i}_{n+1}\Delta\sigma\} \\ {}^{i}_{n+1}\Delta k_p \end{Bmatrix} + {}^{i}_{n+1}\delta\Delta\begin{Bmatrix} \{{}^{i}_{n+1}\frac{\partial F}{\partial\sigma}\} \\ {}^{i}_{n+1}h \end{Bmatrix} = \{0\} \tag{3.42}$$

where

$$[{}^{i}_{n+1}A]^{-1} = \begin{bmatrix} [D^{e}]^{-1} + {}^{i}_{n+1}\Delta\lambda[{}^{i}_{n+1}\frac{\partial^2 F}{\partial\sigma^2}] & {}^{i}_{n+1}\Delta\lambda\{{}^{i}_{n+1}\frac{\partial^2 F}{\partial\sigma\partial k_p}\} \\ {}^{i}_{n+1}\Delta\lambda\{{}^{i}_{n+1}\frac{\partial h}{\partial\sigma}\}^{T} & -1 + {}^{i}_{n+1}\Delta\lambda\,{}^{i}_{n+1}\frac{\partial h}{\partial k_p} \end{bmatrix} \tag{3.43}$$

The dimension of $[{}^{i}_{n+1}A]^{-1}$ is seven by seven but it can be decreased to four by four by using three component principal stresses rather than the six component form. The principal form is adopted in this study to simulate the experimental data where only principal components were recorded and no rotation of the principal axes occurred. If the algorithmic elasto-plastic tangent is to be calculated then the general form with six component needs to be used [Borja *et al.*].

Solving (3.42) for $\{{}^{i}_{n+1}\sigma\}$ and ${}^{i}_{n+1}k_p$ gives:

$$\begin{Bmatrix} \{{}^{i}_{n+1}\sigma\} \\ {}^{i}_{n+1}k_p \end{Bmatrix} = [{}^{i}_{n+1}A]\left(\{{}^{i}_{n+1}r\} + {}^{i}_{n+1}\delta\Delta\begin{Bmatrix} \{{}^{i}_{n+1}\frac{\partial F}{\partial\sigma}\} \\ {}^{i}_{n+1}h \end{Bmatrix}\right) \tag{3.44}$$

Likewise, linearisation of the consistency condition

$$F(\{{}_{n+1}\sigma\}, {}_{n+1}k_p) = 0 \tag{3.45}$$

at the stress state $\{{}_{n+1}\sigma\}$ gives

$${}^{i}_{n+1}F + \left[\left\{{}^{i}_{n+1}\frac{\partial F}{\partial\sigma}\right\}^{T} \quad {}^{i}_{n+1}\frac{\partial F}{\partial k_p}\right]\begin{Bmatrix} \{{}^{i}_{n+1}\Delta\sigma\} \\ {}^{i}_{n+1}\Delta k_p \end{Bmatrix} = 0 \tag{3.46}$$

Substituting (3.44) into (3.46) and then solving for $\delta\lambda$ leads to:

$${}^{i}_{n+1}\delta\lambda = \frac{{}^{i}_{n+1}F - [\{{}^{i}_{n+1}\frac{\partial F}{\partial\sigma}\}^{T} \quad {}^{i}_{n+1}\frac{\partial F}{\partial k_p}][{}^{i}_{n+1}A]\{{}^{i}_{n+1}r\}}{[\{{}^{i}_{n+1}\frac{\partial F}{\partial\sigma}\}^{T} \quad {}^{i}_{n+1}\frac{\partial F}{\partial k_p}][{}^{i}_{n+1}A]\begin{Bmatrix} \{{}^{i}_{n+1}\frac{\partial F}{\partial\sigma}\} \\ {}^{i}_{n+1}h \end{Bmatrix}} \tag{3.47}$$

The stress increment and the hardening internal variable are then obtained from (3.44), and the incremental plastic strain from (3.41). These are used in-turn to update the current state.

CPP algorithm

We are now in position to define the CPP algorithm. Given $\{_{n+1}\varepsilon\}$, $\{_n\varepsilon^P\}$ and $_nk_p$, the task is to find $\{_{n+1}\varepsilon^p\}$, $\{_{n+1}\sigma\}$ and $_{n+1}k_p$ using the following stages. These stages have been illustrated graphically by Li [Li] and a thorough investigation of the CPP method can be found there.

1. Set the CPP iterative counter $i = 0$.

2. Let the plastic strains and the internal variables equal their values obtained from the converged state at the end of the previous time-step.

$$\{^0_{n+1}\varepsilon^p\} = \{_n\varepsilon^p\}$$

$$\{^0_{n+1}k_p\} = \{_nk_p\}$$

3. Set the plastic multiplier to zero

$$^0_{n+1}\Delta\lambda = 0$$

4. Determine the current stress state

$$\{^i_{n+1}\sigma\} = [D^e](\{_{n+1}\varepsilon\} - \{^i_{n+1}\varepsilon^p\})$$

5. Calculate the first derivative of the yield function $\{^i_{n+1}\frac{\partial F}{\partial \sigma}\}$

6. Calculate the residual plastic strain and internal hardening variable

$$\{^i_{n+1}r\} = \left\{ \begin{array}{c} -\{^i_{n+1}\varepsilon^p\} + \{\varepsilon^p\} \\ -^i_{n+1}k_p + _n k_p \end{array} \right\} + ^i_{n+1}\Delta\lambda \left\{ \begin{array}{c} \{^i_{n+1}\frac{\partial F}{\partial \sigma}\} \\ ^i_{n+1}h \end{array} \right\}$$

If $|^i_{n+1}F| < tol_F$ and $\|\{^i_{n+1}r\}\| < tol_r$ then the solution is deemed to have converged and the algorithm may be exited; otherwise move to step 7.

7. Calculate the following derivatives:

   (a) The second derivatives of the yield function with respect to the stresses $[^i_{n+1}\frac{\partial^2 F}{\partial \sigma^2}]$.

   (b) The mixed derivatives of the yield function with respect to the stresses and the hardening internal variable $\{^i_{n+1}\frac{\partial^2 F}{\partial \sigma \partial k_p}\}$.

   (c) The derivatives of the hardening function with respect to the stresses $\{^i_{n+1}\frac{\partial h}{\partial \sigma}\}$.

(d) The derivatives of the hardening function with respect to the internal hardening variable ${}^{i}_{n+1}\frac{\partial h}{\partial k_p}$.

8. Calculate $[{}^{i}_{n+1}A]$ from (3.43).

9. Calculate the first derivatives of yield function with respect to the hardening internal variable $\frac{\partial F}{\partial k_p}$.

10. Calculate the iterative change in the plastic multiplier ${}^{i}_{n+1}\delta\lambda$ using (3.47).

11. Calculate $\{{}^{i}_{n+1}\Delta\sigma\}$ and ${}^{i}_{n+1}\Delta k_p$ from (3.44).

12. Calculate $\{{}^{i}_{n+1}\Delta\varepsilon^p\}$ from (3.41).

13. Update the plastic strains $\{{}^{i+1}_{n+1}\varepsilon^p\}$ using

$$\{{}^{i+1}_{n+1}\varepsilon^p\} = \{{}^{i}_{n+1}\varepsilon^p\} + \{{}^{i}_{n+1}\Delta\varepsilon^p\}$$

14. Update the internal hardening variable ${}^{i+1}_{n+1}k_p$ using

$${}^{i+1}_{n+1}k_p = {}^{i}_{n+1}k_p + {}^{i}_{n+1}\Delta k_p$$

15. Update the plastic multiplier ${}^{i+1}_{n+1}\Delta\lambda$ using

$${}^{i+1}_{n+1}\Delta\lambda = {}^{i}_{n+1}\Delta\lambda + {}^{i}_{n+1}\delta\lambda$$

16. Increment the iterative counter $i = i+1$ then return to step 1 and repeat the loop.

3.3.6 Sheffield Model

A C_2 continuous hardening / softening elasto plasticity model for concrete has been developed at the University of Sheffield by Tahar [Tahar]. In its most general form this model is defined by sixteen material constants. In many cases it is only necessary to define eleven of the material constants as the remaining can assume defaults values. This model is based on earlier work carried out at the University of Colorado [Pramono and Willam, 1989; Etse and Willam, 1994]. Restricting the formulation to the common case of isotropy, the peak nominal stress (PNS) surfaces are formulated in a way which provides a continuous, smooth surface, intersecting the hydrostatic axis normally in the tension region.

In order to describe the shape of the PNS surface not only on the compression and extension meridians, but also for any Lode angle θ, the Bhomik-Long deviatoric shape function r is used to define smooth convex traces [Bhowmik and Long], which ensure a stable material behaviour according to Drucker Stability Postulate, having unique gradients to define the direction of the plastic strain rate. Unlike the original elliptic function of Willam and Warnke [Willam and Warnke], this formulation introduces an addition control point on this shear meridian. The proposed hardening yield surface function is constructed such that the meridians always intersect the hydrostatic axis normally in the compression and tension quadrants.

There are some shortcomings associated with this model. These can be summarised as follows:

1. The model overestimates the axial strain in the pre-peak region for the uniaxial compression test. The same can be said for concrete under low level of confinement.

2. The model lacks the flexibility needed to identify the onset of plastic dilation.

3. The ductility measure which should represent the values of the plastic strain at peak, does not take the true material response under confinement.

The newly formulated model has adopted the same PNS formulation of the Sheffield model both in the meridional and deviatoric sections. A new yield function is introduced assuming associated flow rule. A new hardening function along with a new ductility measure is also proposed.

3.4 The Development of the New Model

In this section the formulation of the new model is described. This includes the description of the the elastic behaviour, the peak nominal stress envelope (PNS) in meridional and deviatoric sections, the yield surface, and the hardening function incorporating new ductility measure.

3.4.1 Elastic Behaviour

If the trial stress state lies inside the yield surface that is ($F < 0$), the response is considered as purely elastic. In this case, the classical constitutive equations, referred to as the generalised Hooke's law is to be used

$$\{\sigma\} = [D^e]\,\{\epsilon\} \tag{3.48}$$

where $[D^e]$ is the elastic matrix. If $[D^e]$ is constant, the material is said to be linearly elastic.

The isotropic linear elastic stress-strain relation can be re-written using the Lamé constants as

$$\{\sigma\} = \lambda[I]\{\epsilon\} + 2\mu\{\epsilon\} \tag{3.49}$$

where λ and μ are Lamé constants and $[I]$ is the identity matrix. Table 3.1 shows the relationships between Young's Modulus, E, Poisson's ratio, ν, the elastic bulk modulus, K, the elastic shear modulus, μ, and λ.

	E	ν	K	λ	μ
E, ν	-	-	$\frac{E}{3(1-2\nu)}$	$\frac{\nu E}{(1+\nu)(1-2\nu)}$	$\frac{E}{2(1+\nu)}$
E, K	-	$\frac{3K-E}{6K}$	-	$\frac{K(9K-3E)}{9K-E}$	$\frac{3KE}{9K-E}$
K, μ	$\frac{9\mu K}{3K+\mu}$	$\frac{3K-2\mu}{2(3K+\mu)}$	-	$K - \frac{2\mu}{3}$	-

Table 3.1: The relationship between different elastic moduli for linear isotropic elasticity

The linear, isotropic elastic stiffness matrix may finally be written as:

$$[D^e] = \frac{E}{(1+\nu)(1-2\nu)} \begin{bmatrix} 1-\nu & \nu & \nu & 0 & 0 & 0 \\ \nu & 1-\nu & \nu & 0 & 0 & 0 \\ \nu & \nu & 1-\nu & 0 & 0 & 0 \\ 0 & 0 & 0 & \frac{1}{2}(1-2\nu) & 0 & 0 \\ 0 & 0 & 0 & 0 & \frac{1}{2}(1-2\nu) & 0 \\ 0 & 0 & 0 & 0 & 0 & \frac{1}{2}(1-2\nu) \end{bmatrix} \tag{3.50}$$

and the corresponding compliance matrix as:

$$[D^e]^{-1} = \frac{1}{E} \begin{bmatrix} 1 & -\nu & -\nu & 0 & 0 & 0 \\ -\nu & 1 & -\nu & 0 & 0 & 0 \\ -\nu & -\nu & 1 & 0 & 0 & 0 \\ 0 & 0 & 0 & 2(1+\nu) & 0 & 0 \\ 0 & 0 & 0 & 0 & 2(1+\nu) & 0 \\ 0 & 0 & 0 & 0 & 0 & 2(1+\nu) \end{bmatrix} \tag{3.51}$$

For the case of principal stresses and strains the stiffness matrix is:

$$[D^e] = \frac{E}{(1+\nu)(1-2\nu)} \begin{bmatrix} 1-\nu & \nu & \nu \\ \nu & 1-\nu & \nu \\ \nu & \nu & 1-\nu \end{bmatrix} \tag{3.52}$$

and the corresponding compliance matrix as

$$[D^e]^{-1} = \frac{1}{E} \begin{bmatrix} 1 & -\nu & -\nu \\ -\nu & 1 & -\nu \\ -\nu & -\nu & 1 \end{bmatrix} \tag{3.53}$$

3.4.2 Peak Nominal Stress (PNS) Envelope

After some initial uncertainty [Wastiels], there now appears a consensus as to the proper form for the triaxial strength envelope (PNS) [Crouch]. Many of the new models offer a satisfactory fit to the peak stress compression meridian experimental data. The peak nominal stress achievable by an isotropic concrete specimen under multi-axial loading may be expressed in terms of the three principal stress components. The envelope of points corresponding to the PNS states may also be defined in terms of normalised Haigh-Westergaard co-ordinates $\bar{\xi}$, $\bar{\rho}$ and θ. The Lode angle, θ, equals $-\frac{\pi}{6}$, 0 and $+\frac{\pi}{6}$ on the extension, shear and compression meridians respectively, whilst ρ_c, ρ_s and ρ_e refer to the values of the deviatoric invariant on the compression, shear and extension meridians. Although the convention adopted here is one of tension positive, the uniaxial compressive strength f_c (used to normalise the invariants) is treated as a positively-valued quantity.

Given that the symbols $\bar{f}_t$ and $\bar{f}_{bc}$ represent the positively-valued normalised PNS magnitudes under uniaxial tension and equal biaxial compression respectively, Table 3.2 shows the values for the normalised principal stresses and invariants.

Loading case	$\bar{\sigma}_1$	$\bar{\sigma}_2$	$\bar{\sigma}_3$	$\bar{\xi}$	$\bar{\rho}$	θ
Uniaxial tension	$\bar{f}_t$	0	0	$\frac{\bar{f}_t}{\sqrt{3}}$	$\sqrt{\frac{2}{3}}\bar{f}_t$	$\frac{-\pi}{6}$
Uniaxial compression	0	0	-1	$\frac{-1}{\sqrt{3}}$	$\sqrt{\frac{2}{3}}$	$\frac{\pi}{6}$
Equal biaxial compression	0	$-\bar{f}_{bc}$	$-\bar{f}_{bc}$	$\frac{-2\bar{f}_{bc}}{\sqrt{3}}$	$\sqrt{\frac{2}{3}}\bar{f}_{bc}$	$\frac{-\pi}{6}$

Table 3.2: PNS values for uniaxial and biaxial states

Meridional Laws

Many concrete PNS meridional (that is θ = constant) criteria can be expressed in a common mixed-polynomial form, encompassing the Rankine (1876), von Mises (1913), Mohr-Coulomb (1900), Drucker-Prager (1952), Leon (1935), Willam-Warnke (1974), Hoek-Brown (1980), Etse-Willam (1994), Menétry-Willam (1995), Bićanić-Pearce (1996) and the Tahar (2000) criteria. The generalised expression is given as follows

$$F = \alpha_0 (\bar{\rho} r)^{n_1} + \alpha_1 (\bar{\rho} r)^{\frac{n_1}{2}} + \beta_0 (\bar{\xi})^{n_2} + \beta_1 (\bar{\xi})^{\frac{n_2}{2}} - 1 = 0 \qquad (3.54)$$

where r is a deviatoric shape function and α_0, α_1, β_0 and β_1 are material constants. For some of the common PNS criteria $n_1 = n_2 = 2$ [Tahar].

The Hoek-Brown criterion [Hoek and Brown], which was originally developed for rocks, is based on the combined considerations of the Griffith fracture criterion and the Mohr-Coulomb slip criterion. This empirical criterion was first defined in terms of the normalised major and minor principal stresses as follows:

$$F_{\text{HB}}(\bar{\sigma}_1, \bar{\sigma}_3) = (\bar{\sigma}_1 - \bar{\sigma}_3)^2 + m_{\text{HB}} \bar{\sigma}_1 - c_{\text{HB}} = 0 \qquad (3.55)$$

The material parameters c_{HB} and m_{HB} represent measurements of cohesive and frictional strength, respectively.

One of the real attractions of this criterion is that it can be calibrated by using just two material constants; uniaxial tension and uniaxial compression. It is appealing because it provides a limiting tensile stress condition (similar to that of Rankine) and a compression criterion sharing the features of the Mohr-Coulomb criterion. Researchers at the University of Colorado successfully used the Hoek-Brown criterion to characterise the triaxial strength of structural concrete [Willam and Warnke].

Using (3.55) and the following relationships between the principal stresses and the (Haigh-Westergaard) cylindrical co-ordinate invariants

$$\begin{aligned}\bar{\sigma}_1 &= \tfrac{1}{\sqrt{3}}\bar{\xi} + \sqrt{\tfrac{2}{3}}\bar{\rho}\sin(\theta - \tfrac{2\pi}{3}) \\ \bar{\sigma}_2 &= \tfrac{1}{\sqrt{3}}\bar{\xi} + \sqrt{\tfrac{2}{3}}\bar{\rho}\sin(\theta) \\ \bar{\sigma}_3 &= \tfrac{1}{\sqrt{3}}\bar{\xi} + \sqrt{\tfrac{2}{3}}\bar{\rho}\sin(\theta + \tfrac{2\pi}{3})\end{aligned} \tag{3.56}$$

(where $\sigma_1 > \sigma_2 > \sigma_3$), the Hoek-Brown criterion may be re-expressed as:

$$F_{\text{HB}}(\bar{\xi}, \bar{\rho}, \theta) = 2\cos^2\theta\bar{\rho}^2 + \sqrt{\frac{2}{3}}\,\bar{\rho}m_{\text{HB}}\cos(\theta + \frac{\pi}{6})\bar{\rho} + \frac{m_{\text{HB}}}{\sqrt{3}}\bar{\xi} - 1 = 0 \tag{3.57}$$

The expression for the compression meridian is obtained by inserting the value of $\theta = \frac{\pi}{6}$ in equation (3.57).

$$F_{\text{HB}_c}(\bar{\xi}, \bar{\rho}) = \frac{3}{2}(\bar{\rho}_c)^2 + \frac{m_{\text{HB}}}{\sqrt{6}}\bar{\rho}_c + \frac{m_{\text{HB}}}{\sqrt{3}}\bar{\xi} - 1 = 0 \tag{3.58}$$

Similarly, the extension meridian is obtained by inserting $\theta = -\frac{\pi}{6}$ into (3.57):

$$F_{\text{HB}_e}(\bar{\xi}, \bar{\rho}) = \frac{3}{2}(\bar{\rho}_e)^2 + m_{\text{HB}}\sqrt{\frac{2}{3}}\bar{\rho}_e + \frac{m_{\text{HB}}}{\sqrt{3}}\bar{\xi} - 1 = 0 \tag{3.59}$$

Re-arranging (3.58) one obtains:

$$\bar{\rho}_c = \frac{1}{6}\sqrt{\frac{2}{3}}\left(-m_{\text{HB}} + \sqrt{{m_{\text{HB}}}^2 - 12\sqrt{3}m_{\text{HB}}\bar{\xi} + 36}\right) \tag{3.60}$$

and re-arranging (3.59) one obtains:

$$\bar{\rho}_e = \frac{1}{3}\sqrt{\frac{2}{3}}\left(-m_{\text{HB}} + \sqrt{{m_{\text{HB}}}^2 - 3\sqrt{3}m_{\text{HB}}\bar{\xi} + 9}\right) \tag{3.61}$$

In the form presented here, the Hoek-Brown criterion exhibits deviatoric sections which are similar to those of the Mohr-Coulomb criterion. That is, they reproduce the experimental results well, but introduce corners at the compression and extension meridians. Despite being somewhat less flexible than the Wilam-Warnke criterion, the Hoek-Brown surface deserves attention because of its ease of calibration.

All the above criteria which intersect the hydrostatic axis in the tension region exhibit a vertex at this point. If these PNS surfaces define yield surfaces (and plastic potential surfaces) in an elasto-plastic model then the surface normal will be non-unique and the surface undefined for zones outside this region. The latter will lead to problems when a hydrostatic trial stress states passes beyond the vertex. To remove this discontinuity, a modification to the expressions defining the PNS meridians has been proposed by Tahar [Tahar].

In all that follows, the Hoek-Brown criterion has been adopted as the basic criterion as it offers a good balance between physical relevance, ease of calibration and accuracy. However, it should be pointed out that the same procedures proposed by Tahar could be applied to many of the other PNS criteria. The Tahar modification has been achieved by raising certain terms of Hoek-Brown criterion to a power γ which is typically $0.9 \leq \gamma < 1$. This provides a continuous, simple, smooth surface, intersecting the hydrostatic axis normally in the tension region. The modification is as follows:

$$\bar{\rho}_c = (\frac{1}{6})^\gamma \sqrt{\frac{2}{3}} \left(-m + \sqrt{m^2 - 12\sqrt{3}m\bar{\xi} + 36}\right)^\gamma \tag{3.62}$$

$$\bar{\rho}_e = (\frac{1}{3})^\gamma \sqrt{\frac{2}{3}} \left(-m + \sqrt{m^2 - 3\sqrt{3}m\bar{\xi} + 9}\right)^\gamma \tag{3.63}$$

Consider the case when $\bar{\xi} = -\frac{1}{\sqrt{3}}$:

$$\bar{\rho} = (\frac{1}{6})^\gamma \sqrt{\frac{2}{3}} \left(-m + \sqrt{m^2 + 12\sqrt{3}m\frac{1}{\sqrt{3}} + 36}\right)^\gamma = \sqrt{\frac{2}{3}} \tag{3.64}$$

This formulation ensures that the surface passes through the uniaxial compression point. In the case $\bar{\xi} = \frac{\bar{f}_t}{\sqrt{3}}$ and $\bar{\rho} = \sqrt{\frac{2}{3}}\bar{f}_t$ (corresponding to the peak uniaxial tensile stress), we obtain:

$$\sqrt{\frac{2}{3}}\bar{f}_t = (\frac{1}{3})^\gamma \sqrt{\frac{2}{3}} \left(-m + \sqrt{m^2 - 3\sqrt{3}m\frac{1}{\sqrt{3}}\bar{f}_t + 9}\right)^\gamma \tag{3.65}$$

After rearranging, we can express m as:

$$m = \frac{3\left(1 - (\bar{f}_t)^{\frac{2}{\gamma}}\right)}{\bar{f}_t + 2(\bar{f}_t)^{\frac{1}{\gamma}}} \tag{3.66}$$

Since the new PNS surface is formulated on the basis that it passes through both f_c and f_t, it follows that the material constant m is controlled by both the normalised tensile strength and the constant γ. When γ is taken equal to 1, an m identical to that used in the Hoek-Brown expression is recovered.

Now consider the case of equal biaxial compression, where $\bar{\xi} = -\frac{2\bar{f}_{bc}}{\sqrt{3}}$, $\bar{\rho} = \sqrt{\frac{2}{3}}\bar{f}_{bc}$ and $\theta = -\frac{\pi}{6}$:

$$\sqrt{\frac{2}{3}}\bar{f}_{bc} = (\frac{1}{3})^\gamma \sqrt{\frac{2}{3}} \left(-m + \sqrt{m^2 + 6\sqrt{3}m\frac{1}{\sqrt{3}}\bar{f}_{bc} + 9}\right)^\gamma \tag{3.67}$$

After simplifying, we obtain:

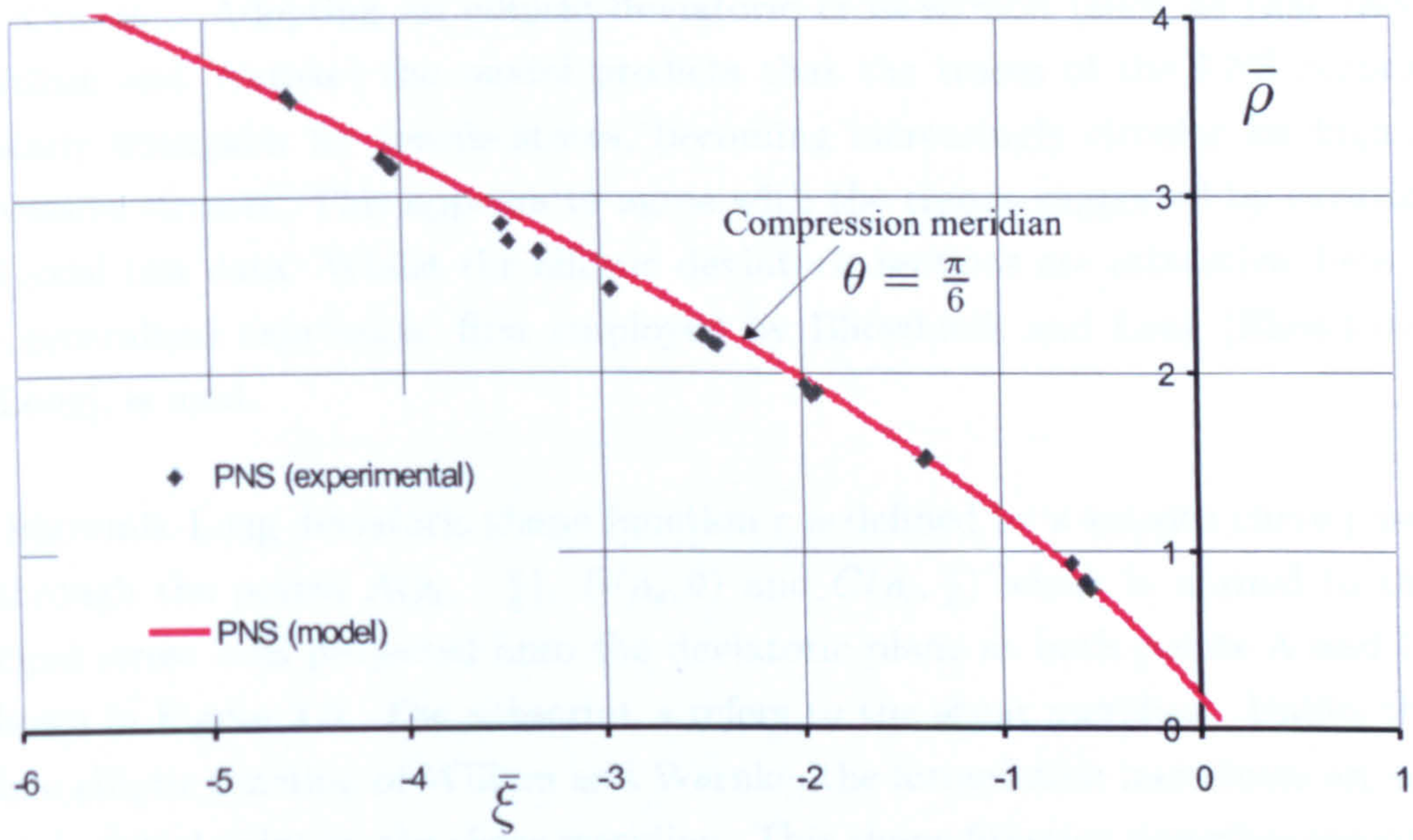

Figure 3.4: The Peak Nominal Stress surface (PNS) determined by (3.62) and compared against triaxial data from Sheffield tests for f_c =58 MPa

$$9(\bar{f}_{bc})^{(\frac{2}{\gamma})} + 6m(\bar{f}_{bc})^{(\frac{1}{\gamma})} - 6m\bar{f}_{bc} - 9 = 0 \tag{3.68}$$

It can be shown that for any γ (in the range defined above), $\bar{f}_{bc}$ will always equal 1.

This criteria seems to preform well with Sheffield experimental data presented in Chapter 2. Figure 3.4 shows the PNS surface predicted by the model compared with the test data for a normal concrete mix with f_c =58 MPa. The model has been calibrated as follows:

1. assume default value for γ of 0.99,
2. use the experimental mean value for f_c,
3. identify the best value of m using least squares fit procedure, and
4. solve equation (3.66) numerically to identify f_t.

Deviatoric Behaviour

Experimental observations show that for a given value of hydrostatic stress there is a considerable variation of peak deviatoric stress with Lode angle (θ) . For

large values of hydrostatic stress, the PNS deviatoric section tend to a circular form [Crouch]. Adopting an elliptic deviatoric cross-section (such as that used by Willam and Warnke) the model predicts that the traces of the PNS surface are nearly triangular for tensile states, becoming increasingly circular for higher compressive stresses. This appears to agree with the trends suggested by existing multi-axial test data. Whilst the elliptic deviatoric sections are attractive, here a more generalised expression, first employed by Bhowhmik and Long [Bhowhmik and Long], is used.

The Bhowmik-Long deviatoric shape function r is defined by a smooth curve passing through the points $A(\rho_e, -\frac{\pi}{6})$, $B(\rho_s, 0)$ and $C(\rho_c, \frac{\pi}{6})$ which is normal to the principal stress axes projected onto the deviatoric plane at both points A and C, as shown in Figure 3.5. The subscript s refers to the shear meridian. Unlike the original elliptic function of Willam and Warnke, the formulation introduces an additional control point on the shear meridian. This shape function describes smooth convex PNS traces. In the context of a plasticity model, these imply convex yield surfaces which ensure a stable material behaviour according to Drucker's Stability Postulate, having unique gradients to define the direction of plastic strain increments (in an associated flow formulation).

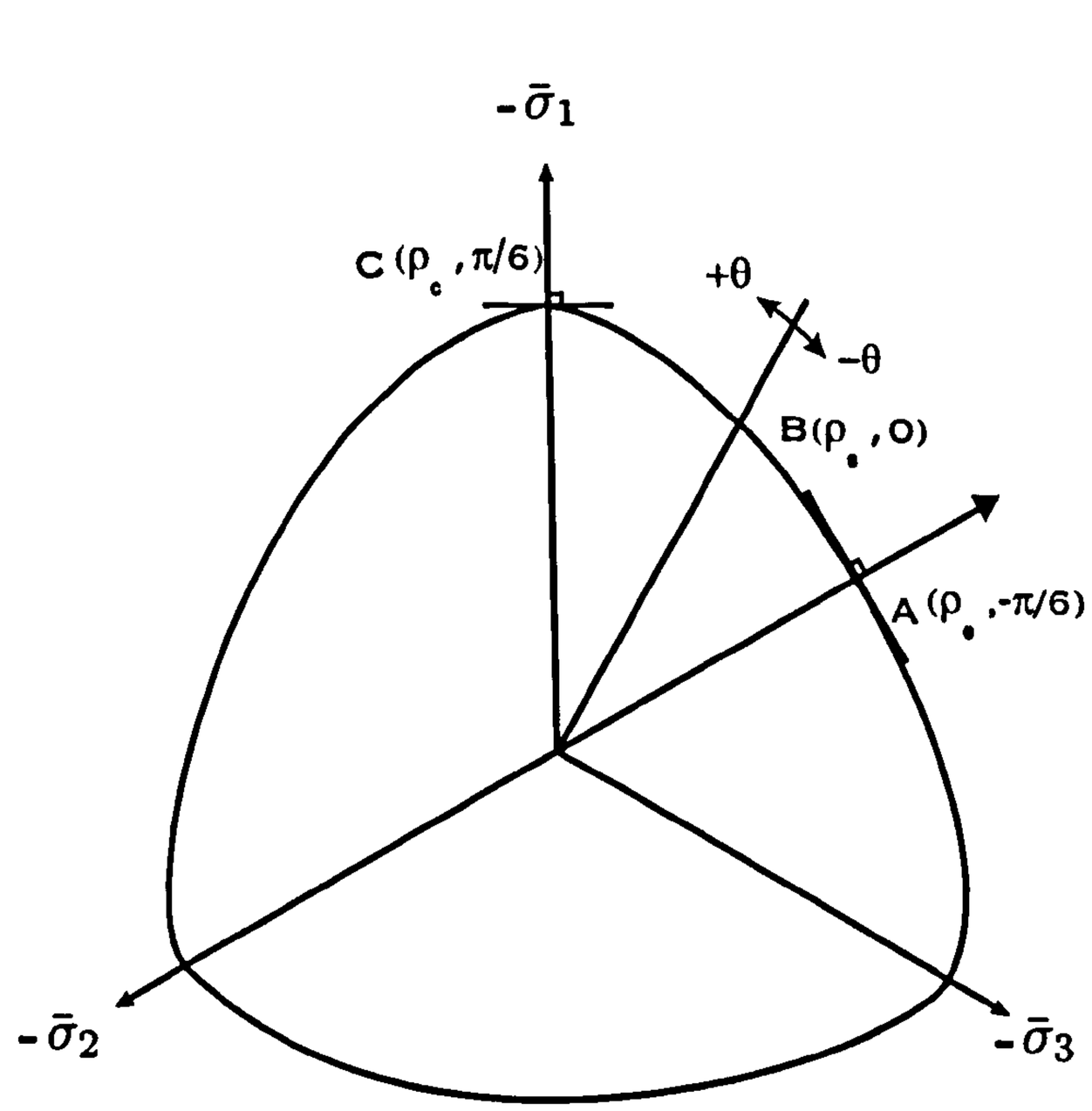

Figure 3.5: Bhowmik-Long deviatoric plane

The deviatoric shape function is expressed in the first sextant of principal stress

space ($-\frac{\pi}{6} \leq \theta \leq \frac{\pi}{6}$) as:

$$r = \frac{2d_0}{d_1 - \sqrt{((d_1)^2 - 4d_0d_2)}} \tag{3.69}$$

where

$$\begin{aligned} d_0 &= c_1\cos^2\theta - c_2\sin^2\theta + c_3\sin\theta\cos\theta \\ d_1 &= 2(c_4\sqrt{3}\cos\theta - c_5\sin\theta) \\ d_2 &= B_0(4 - 3B_0c_0) \end{aligned} \tag{3.70}$$

$$\begin{aligned} c_0 &= \frac{(2-\sqrt{3}B_1)(2B_0-\sqrt{3}B_1)}{(B_1(1+B_0)-\sqrt{3}B_0)^2} \\ c_1 &= 3 - c_0(1+B_0)^2 \\ c_2 &= 1 + 3c_0(1-B_0)^2 \\ c_3 &= 2c_0\sqrt{3}(1-{B_0}^2) \\ c_4 &= (1+B_0)(1-B_0c_0) \\ c_5 &= (1-B_0)(1-3B_0c_0) \end{aligned} \tag{3.71}$$

subject to the following restrictions

$$\begin{aligned} &\tfrac{1}{2} < B_0 \leq 1 \\ &\tfrac{\sqrt{3}B_0}{1+B_0} < B_1 < \tfrac{2B_0}{\sqrt{3}} \end{aligned} \tag{3.72}$$

where

$$B_0 = \frac{\rho_e}{\rho_c} \tag{3.73}$$

and

$$B_1 = \frac{\rho_s}{\rho_c}. \tag{3.74}$$

The portions of the trace in the other sextants are obtained from symmetry. B_1 can be expressed as a function of B_0 in terms of its upper and lower limits

$$B_1 = \frac{\sqrt{3}B_0}{1+B_0} + \alpha(\frac{2B_0}{\sqrt{3}} - \frac{\sqrt{3}B_0}{1+B_0}) \tag{3.75}$$

where α takes a value between 0 and 1.

As α approaches 0, r degenerates to a linear form between the compression and extension meridians. The Tresca form is obtained when $B_0 = 1$ and $\alpha = 1$.

Note that the Bhowmik-Long deviatoric shape function includes the original elliptic form as a special case. Clearly at $\theta = -\frac{\pi}{6}$, 0 and $\frac{\pi}{6}$, r equals $\frac{1}{B_0}$, $\frac{1}{B_1}$ and 1

respectively.

3.4.3 New Yield Function

In this study associated plasticity has been assumed. On that basis and with the help of the plastic strain directions calculated in Chapter 2, the shape of the yield surface can be identified. We may begin by considering the PNS surface as one of the yield surfaces. Figure 3.4 shows the results from the University of Sheffield tests on 60 mm diameter cylindrical specimens at confining levels of 0, 10, 20, 30, 50, 60 and 70 MPa (see Chapter 2). The proposed formulation of the new yield surface has to fulfill the following basic requirements;

1. smoothness,
2. convexity,
3. normality with respect to the plastic strain vectors
4. validity of the function for a broad class of experimental data for different concrete mixes.

Plastic Volumetric Transition Stress Surface, VTS

The plastic volumetric transition stress (VTS) is one of the key components in the formulation of this model. The identification of this state has been discussed in Chapter 2. Examination of experimental results has indicated that under compressive loadings, dilation begins at about 90 percent of the peak stress. This is also supported by the findings from other researchers [Chen and Saleeb, 1994b]. The plastic volumetric transition stress (VTS) locus could be expressed as follow

$$\bar{\rho}_{vts} = \alpha_2 \, \bar{\rho}_c \tag{3.76}$$

where ρ_c identifies the deviatoric stress on the PNS surface and α_2 is a material constant which can be identified for example from uniaxial compression tests. In Chapter 2 (for a normal concrete mix with a uniaxial compression stress of 58 MPa) this parameter was found to be 0.927. The value has been identified by the method of least squares. Figure 3.6 shows this surface at the compression meridian for confinements ($\sigma_1 = \sigma_2$) of 0, 10, 20, 30, 40 , 50 and 60 MPa.

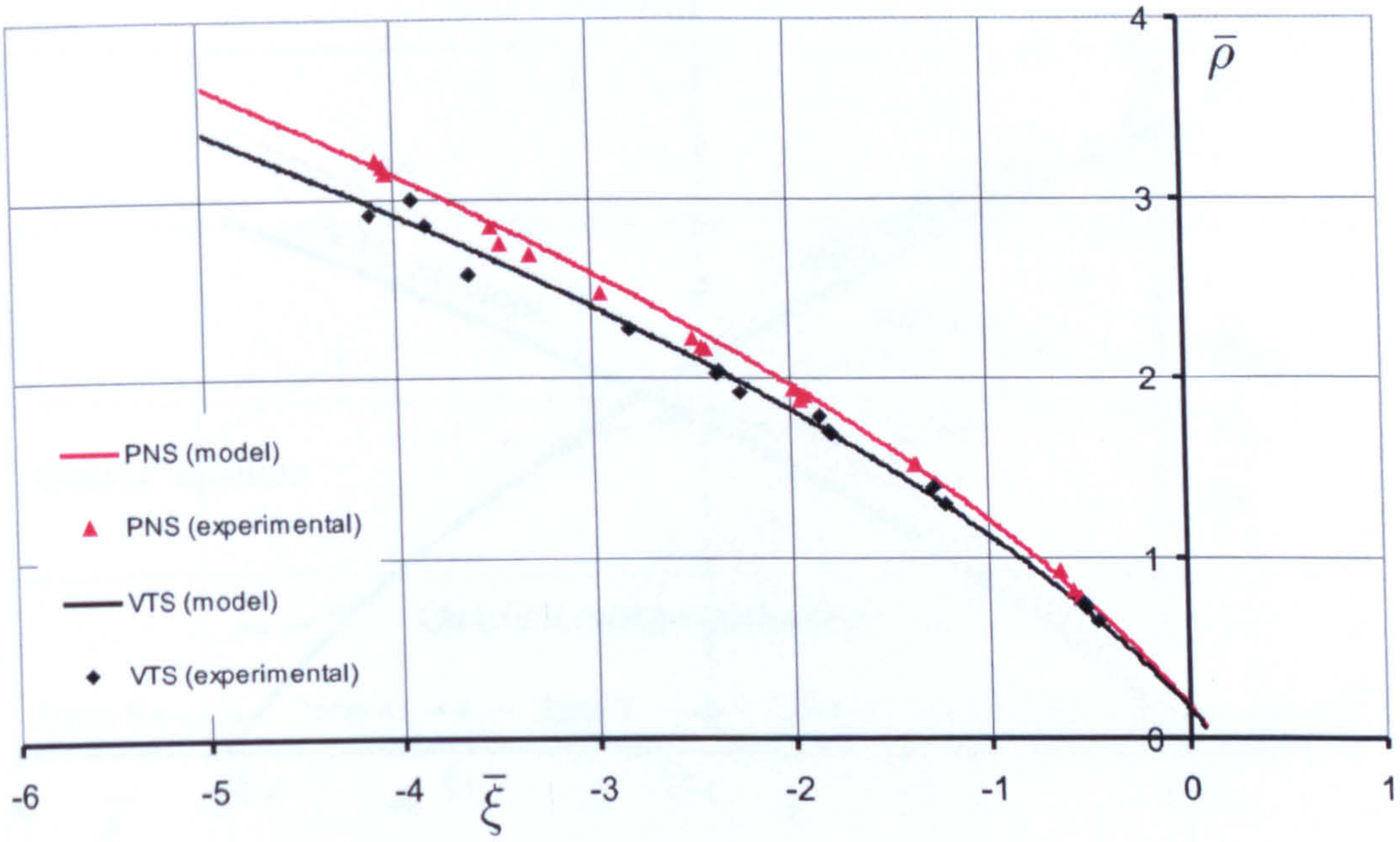

Figure 3.6: The PNS and VTS surfaces from Sheffield experiments and the model predictions for the compression meridian

The Formulation of the New Yield Function

The yield function of the proposed model has been formulated in four zones (Zone 1 to zone 4) by four equations (see Figure 3.7) as follows

1. In the first zone $(\bar{\xi}_{ht} - \xi_1)$ the yield function takes the form of the PNS surface as expressed by (3.62).

2. The second zone $(\xi_1 - \xi_2)$ has been represented by polynomial equation that fulfills five conditions:

   (a) The curve passes through the common point (ξ_1, ρ_1) on the PNS surface

   (b) The equation is to have the same value of the first derivative of the PNS with respect to $\bar{\xi}$ at the converging point (ξ_1, ρ_1) in order to ensure continuity of the first derivatives.

   (c) The equation is to have the same value of the second derivative of the PNS with respect to $\bar{\xi}$ at the common point (ξ_1, ρ_1) in order to ensure continuity of the second derivatives.

   (d) The equation is to pass through the volumetric transition stress (VTS) point identified by (ξ_2, ρ_2).

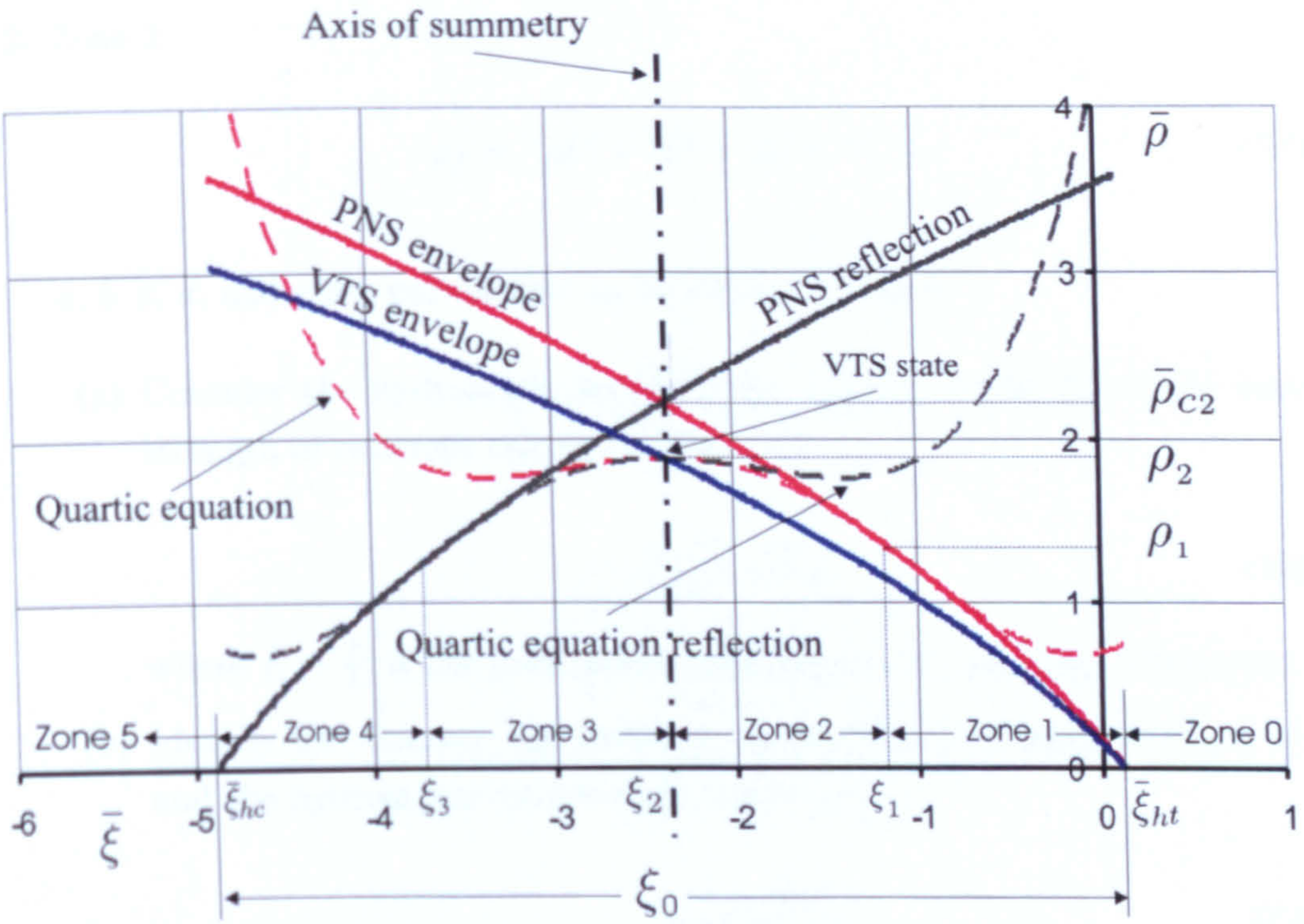

Figure 3.7: The general shape of the four equations that formulate the yield surface

(e) The first derivative of the equation with respect to $\bar{\xi}$ at point (ξ_2, ρ_2) is to be equal to zero. This will ensure normality of the plastic strain vector at the plastic volumetric transition point.

3. In the third zone $(\xi_2 - \xi_3)$ the equation is the reflection of the second zone about a symmetry plane normal to $\bar{\xi}$ axis at the point ξ_2.

4. In the fourth zone $(\xi_3 - \bar{\xi}_{hc})$ the function is the reflection of the first zone about a symmetry plane normal to $\bar{\xi}$ axis at the point ξ_2.

The general yield function , F, takes the form

$$F(\sigma, k_p) = r\,\bar{\rho} - \rho_f = 0 \tag{3.77}$$

where r is the deviatoric shape function and ρ_f is the deviatoric stress at a mean stress ξ calculated in each zone as follows:

1. Zone 1

$$\rho_f = (1/6)^\gamma \sqrt{\frac{2}{3}}(-m + \sqrt{(m^2 - 12\sqrt{3}\,m\,\bar{\xi} + 36)})^\gamma \tag{3.78}$$

This equation is identical to the PNS formulation.

2. Zone 2

$$\rho_f = a\bar{\xi}^4 + b\bar{\xi}^3 + c\bar{\xi}^2 + d\bar{\xi} + e \tag{3.79}$$

a, b, c, d, and e are parameters to be identified below.

(a) Consider the hydrostatic tensile point $(\bar{\xi}_{ht}, 0)$, where $\bar{\xi}_{ht}$ is the tensile strength of concrete taking the form

$$\bar{\xi}_{ht} = \sqrt{3}\,\bar{f}_t \tag{3.80}$$

where $\bar{f}_t = \frac{f_t}{f_c}$ is the normalised uniaxial tensile strength of concrete.

(b) Identify the distance (ξ_0) between the hydrostatic tensile strength $(\bar{\xi}_{ht})$ and the hydrostatic compression stress $(\bar{\xi}_{hc})$

$$\xi_0 = \frac{A_k}{1-k} \tag{3.81}$$

where A_k is a material parameter and k is the hardening scalar.

(c) Identify the common point (ξ_1, ρ_1). There are two ways to achieve this:

i. Calculate ξ_1

$$\xi_1 = \bar{\xi}_{ht} - \alpha_1\,\xi_0 \tag{3.82}$$

where α_1 is a material parameter. Then define ρ_1 form

$$\rho_1 = (1/6)^\gamma \sqrt{\frac{2}{3}} \left(-m + \sqrt{m^2 - 12\sqrt{3}m\xi_1 + 36}\right)^\gamma \tag{3.83}$$

ii. Identify ρ_1 and then calculate ξ_1

$$\rho_1 = \alpha_1\,\rho_2 \tag{3.84}$$

where ρ_2 is the ρ of the plastic volumetric transition stress calculated as follow

$$\rho_2 = \alpha_2\,\rho_{c2} \tag{3.85}$$

where the ρ_{c2} is the PNS value associated with ξ_2 calculated as follows:

$$\rho_{c_2} = (1/6)^\gamma \sqrt{\frac{2}{3}} \left(-m + \sqrt{m^2 - 12\sqrt{3}m\xi_2 + 36}\right)^\gamma \tag{3.86}$$

and

$$\xi_2 = \bar{\xi}_{ht} - \frac{\xi_0}{2} \tag{3.87}$$

After calculating ρ_2, ξ_1 can be calculated form

$$\xi_1 = \frac{-1}{36\,m}\left(-36\,(2)^{\frac{2}{\gamma}} + \left(\frac{\rho_{c1}\sqrt{6}}{(1/6)^{\gamma}}\right)^{\frac{2}{\gamma}} + 2\left(\frac{\rho_{c1}\sqrt{6}}{(1/6)^{\gamma}}\right)^{\frac{1}{\gamma}} m(2)^{\frac{1}{\gamma}}\right)\sqrt{3}(2)^{-\frac{2}{\gamma}} \tag{3.88}$$

The first approach has been adopted for this study because it is simpler and easier to code. This approach requires an extra care when choosing the parameter α_1, but the sensitivity study (Chapter 4) will show that the model is not very sensitive to α_1 within the range discussed there.

(d) Identify the first derivative of the PNS at point (ξ_1, ρ_1) with respect to ξ_1:

$$\frac{\partial F}{\partial \xi_1} = \frac{-2\,(1/6)^{\gamma}\sqrt{6}\left(-m+\sqrt{\beta_1}\right)^{\gamma}\gamma\sqrt{3}m}{\sqrt{\beta_1}\left(-m+\sqrt{\beta_1}\right)} \tag{3.89}$$

where

$$\beta_1 = m^2 - 12\sqrt{3}\,m\,\xi_1 + 36 \tag{3.90}$$

(e) Identify the second derivative of the PNS at point (ξ_1, ρ_1) with respect to ξ_1:

$$\frac{\partial^2 F}{\partial \xi_1^2} = \frac{36\,(1/6)^{\gamma}\sqrt{6}\left(-m+\sqrt{\beta_1}\right)^{\gamma}\gamma^2 m^2}{\beta_1\left(-m+\sqrt{\beta_1}\right)^2} - \frac{36\,(1/6)^{\gamma}\sqrt{6}\left(-m+\sqrt{\beta_1}\right)^{\gamma}\gamma\,m^2}{{\beta_1}^{3/2}\left(-m+\sqrt{\beta_1}\right)} - \frac{36\,(1/6)^{\gamma}\sqrt{6}\left(-m+\sqrt{\beta_1}\right)^{\gamma}\gamma\,m^2}{\beta_1\left(-m+\sqrt{\beta_1}\right)^2} \tag{3.91}$$

(f) Solve equation (3.79) for the five unknowns a, b, c, d, and e using the five known pair of values, (ξ_1, ρ_1), $(\xi_1, \frac{\partial F}{\partial \xi_1})$, $(\xi_1, \frac{\partial^2 F}{\partial \xi_1^2})$, (ξ_2, ρ_2), and $(\xi_2, \frac{\partial F}{\partial \xi_2})$

$$a = \frac{-6\,\rho_2 + {\xi_1}^2\,\frac{\partial^2 F}{\partial {\xi_1}^2} + 4\,\xi_2\,\frac{\partial F}{\partial \xi_1} - 2\,\xi_2\,\xi_1\,\frac{\partial^2 F}{\partial {\xi_1}^2} - 4\,\xi_1\,\frac{\partial F}{\partial \xi_1} + {\xi_2}^2\,\frac{\partial^2 F}{\partial {\xi_1}^2} + 6\,\rho_1}{2\,({\xi_2}^4 - 4\,\xi_2\,{\xi_1}^3 + 6\,{\xi_2}^2\,{\xi_1}^2 + {\xi_1}^4 - 4\,\xi_1\,{\xi_2}^3)} \tag{3.92}$$

$$b = -(\frac{\partial^2 F}{\partial \xi_b^2}\xi_1^3 - \xi_1^2\xi_2\frac{\partial^2 F}{\partial \xi_1^2} - 5\xi_1^2\frac{\partial F}{\partial \xi_1} - \xi_1\xi_2^2\frac{\partial^2 F}{\partial \xi_1^2} - 8\xi_1\rho_2 + 8\xi_1\rho_1 + 2\xi_1\xi_2\frac{\partial F}{\partial \xi_1} + 3\xi_2^2\frac{\partial F}{\partial \xi_1} + 4\xi_2\rho_1 + \xi_2^3\frac{\partial^2 F}{\partial {\xi_1}^2} - 4\xi_2\rho_2)/(\xi_2^4 - 4\xi_2\xi_1^3 + 6\xi_2^2\xi_1^2 + \xi_1^4 - 4\xi_1\xi_2^3) \tag{3.93}$$

$$c = (-12{\xi_1}^2\rho_2 + {\xi_1}^4\frac{\partial^2 F}{\partial \xi_1^2} - 12\xi_2{\xi_1}^2\frac{\partial F}{\partial \xi_1} + 2{\xi_1}^3\xi_2\frac{\partial^2 F}{\partial \xi_1^2} - 6{\xi_1}^3\frac{\partial F}{\partial \xi_1} - 6\xi_2^2{\xi_1}^2\frac{\partial^2 F}{\partial \xi_1^2} + 12{\xi_1}^2\rho_1 + 18\xi_2^2\xi_1\frac{\partial F}{\partial \xi_1} + 24\xi_1\xi_2\rho_1 + 2\xi_2^3\xi_1\frac{\partial^2 F}{\partial \xi_1^2} - 24\xi_1\xi_2\rho_2 + \xi_2^4\frac{\partial^2 F}{\partial \xi_1^2})/(2(\xi_2^4 - 4\xi_2{\xi_1}^3 + 6\xi_2^2{\xi_1}^2 + {\xi_1}^4 - 4\xi_1\xi_2^3)) \tag{3.94}$$

$$d = -\xi_2(\xi_1^4\frac{\partial^2 F}{\partial \xi_1^2} - \xi_1^3\xi_2\frac{\partial^2 F}{\partial \xi_1^2} + 3\xi_2\xi_1^2\frac{\partial F}{\partial \xi_1} - 6\xi_1^3\frac{\partial F}{\partial \xi_1} - \xi_2^3\frac{\partial F}{\partial \xi_1} - \xi_2^2\xi_1^2\frac{\partial^2 F}{\partial \xi_1^2} + \xi_2^3\xi_1\frac{\partial^2 F}{\partial \xi_1^2} + 4\xi_2^2\xi_1\frac{\partial F}{\partial \xi_1} - 12\xi_1^2\rho_2 + 12\xi_1^2\rho_1)/(\xi_2^4 - 4\xi_2\xi_1^3 + 6\xi_2^2\xi_1^2 + \xi_1^4 - 4\xi_1\xi_2^3) \tag{3.95}$$

$$e = (-6\xi_1^3\xi_2^2\frac{\partial F}{\partial \xi_1} + \xi_1^4\xi_2^2\frac{\partial^2 F}{\partial \xi_1^2} + 2\xi_1^4\rho_2 + 2\rho_1\xi_2^4 - 2\xi_1^3\xi_2^3\frac{\partial^2 F}{\partial \xi_1^2} - 8\xi_1^3\xi_2\rho_2 - 2\xi_1\frac{\partial F}{\partial \xi_1}\xi_2^4 + 8\xi_1^2\frac{\partial F}{\partial \xi_1}\xi_2^3 + \xi_1^2\frac{\partial^2 F}{\partial \xi_1^2}\xi_2^4 + 12\rho_1\xi_2^2\xi_1^2 - 8\rho_1\xi_1\xi_2^3)/(2(\xi_2^4 - 4\xi_2\xi_1^3 + 6\xi_2^2\xi_1^2 + \xi_1^4 - 4\xi_1\xi_2^3)) \tag{3.96}$$

3. Zone 3

In this zone the reflection of the quartic equation of zone 2 about a symmetry plane normal to the ξ axis at ξ_2 has been used

$$\rho_f = a\,\bar{\xi}_3^4 + b\,\bar{\xi}_3^3 + c\,\bar{\xi}_3^2 + d\,\bar{\xi}_3 + e \tag{3.97}$$

where

$$\bar{\xi}_3 = -\bar{\xi} + 2\,\xi_2 \tag{3.98}$$

4. Zone 4

The reflection of the PNS equation about a symmetry plane normal to the ξ axis at ξ_2 has been used

$$\rho_f = (1/6)^\gamma \sqrt{\frac{2}{3}}(-m + \sqrt{(m^2 - 12\sqrt{3}\, m\, \bar{\xi}_3 + 36)})^\gamma \tag{3.99}$$

Figure 3.7 shows the general shape of the four equations. Figure 3.8 shows a sample of a yield surface that has been produced from the four equations. Figure 3.9 shows the yield surface for different level of hardening and Figure 3.10 shows the plastic strain direction with the yield surfaces. The results suggest that the proposed model is capable of fulfilling the normality condition and convexity needed for associated plasticity.

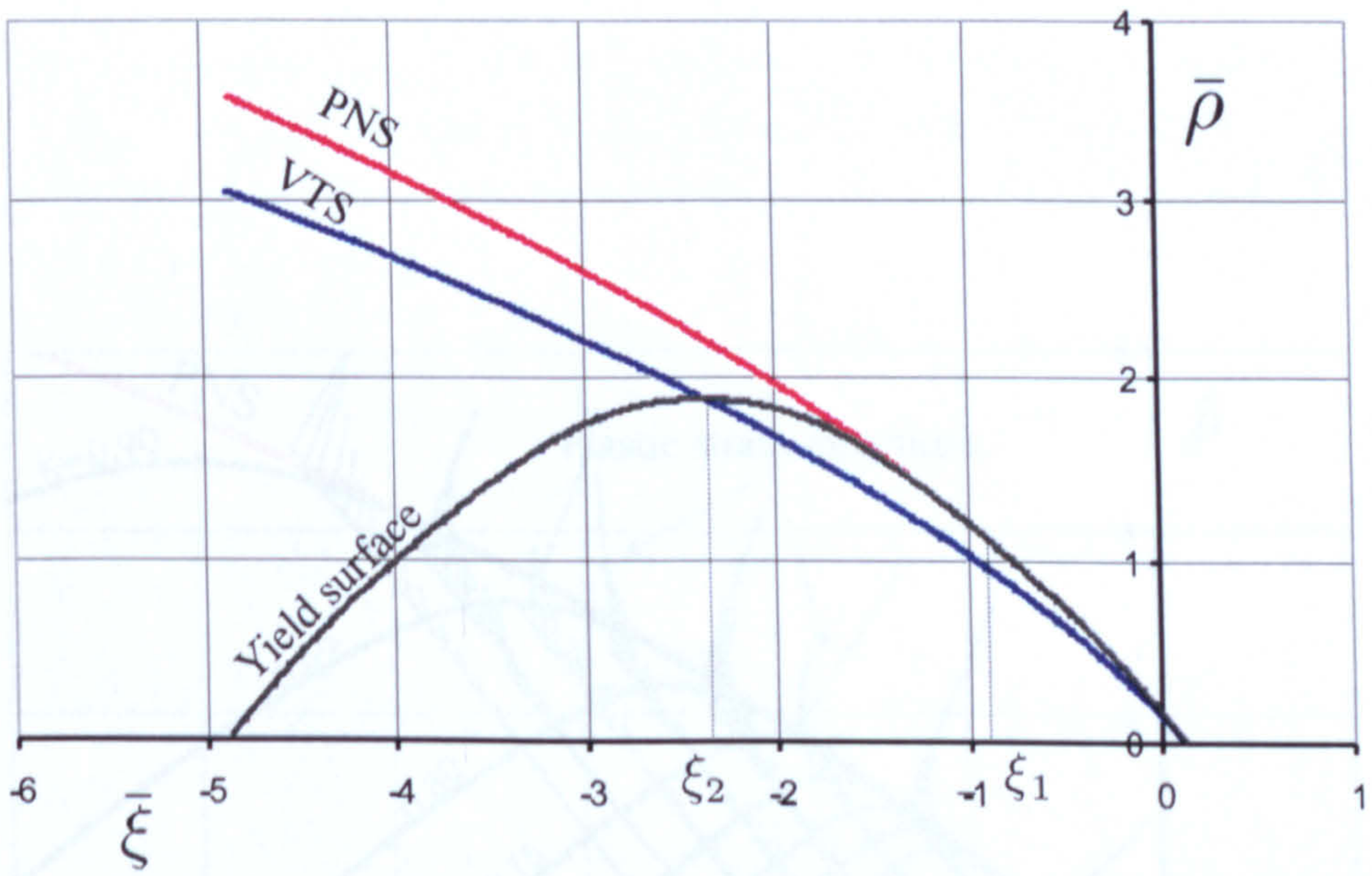

Figure 3.8: The general shape of a yield surface with PNS and VTS surfaces

3.4.4 The hardening function

The hardening function k controls the evolution of the yield surfaces, and thereby the elastic domain. In isotropic plasticity, the internal variable (k_p) is considered as a scalar measure, which itself is a function of accumulated plastic strains, $\{\varepsilon^p\}$.

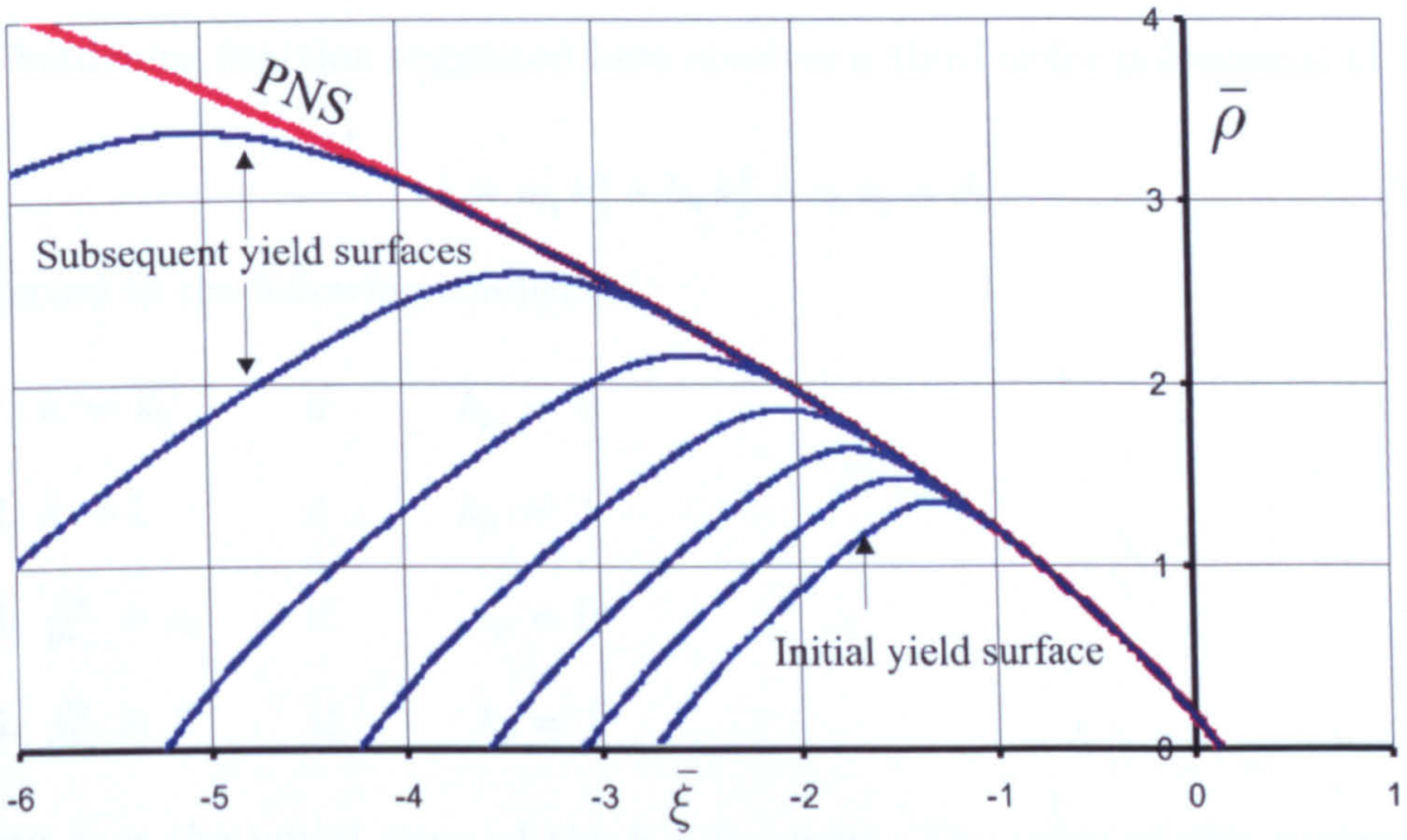

Figure 3.9: The initial and subsequent yield surfaces

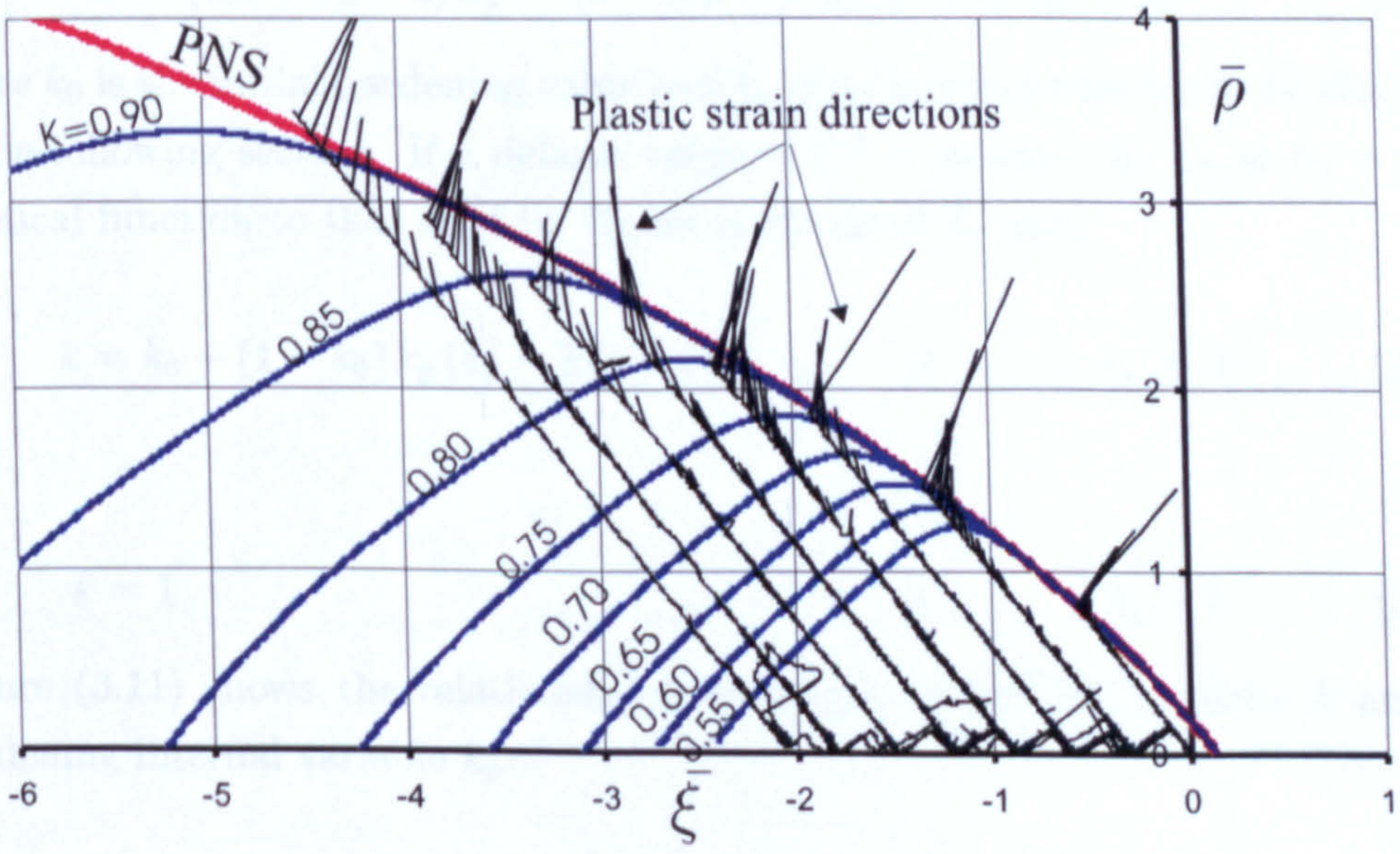

Figure 3.10: Plastic strain directions and yield surfaces for the new model

If the yield surfaces are anisotropic then k would be represented by a higher order tensor.

The hardening function suggested here involves a third order polynomial of k_p

$$k = a_h\, k_p^3 + b_h\, k_p^2 + c_h\, k_p + d_h \tag{3.100}$$

subjected to the following conditions

1. $k = k_0$ if $k_p = 0$
2. $k = 1$ if $k_p = 1$
3. $\frac{\partial k}{\partial k_p} = s_0$ if $k_p = 0$
4. $\frac{\partial k}{\partial k_p} = 0$ if $k_p = 1$

where s_0 is the initial slope of the $k - k_p$ curve. The value of this parameter is finite and positive.

After solving equation (3.100) for the four unknown constants, $a_h = 2\ k_0 + s_0 - 2$, $b_h = 3 - 2\ s_0 - 3\ k_0$, $c_h = s_0$ and $d_h = k_0$, and substituting these values in equation 3.100, the hardening function takes the form

$$k = (2k_0 + s_0 - 2)\, k_p^3 + (3 - 2s_0 - 3k_0)\, k_p^2 + s_0\, k_p + k_0 \tag{3.101}$$

where k_0 is the initial hardening value and k_p is an internal variable to be discussed in the following section. If a default value of 2.7 is assumed for s_0 at $k_p = 0$, an identical function to that used by Grassl is obtained [Grassl]

$$k = k_0 + (1 - k_0)\, k_p\, (k_p^2 - 3\, k_p + 3) \qquad \text{if} \qquad k_p \leq 1 \tag{3.102}$$

and

$$k = 1 \qquad \text{if} \qquad k_p > 1 \tag{3.103}$$

Figure (3.11) shows the relationship between the hardening measure k and the hardening internal variable k_p.

3.4.5 Ductility Measure ζ

The evolution of the hardening variable k_p depends on the rate of the plastic strain and the stress state. The infinitesimal increment of the hardening function ($d\kappa_p$)

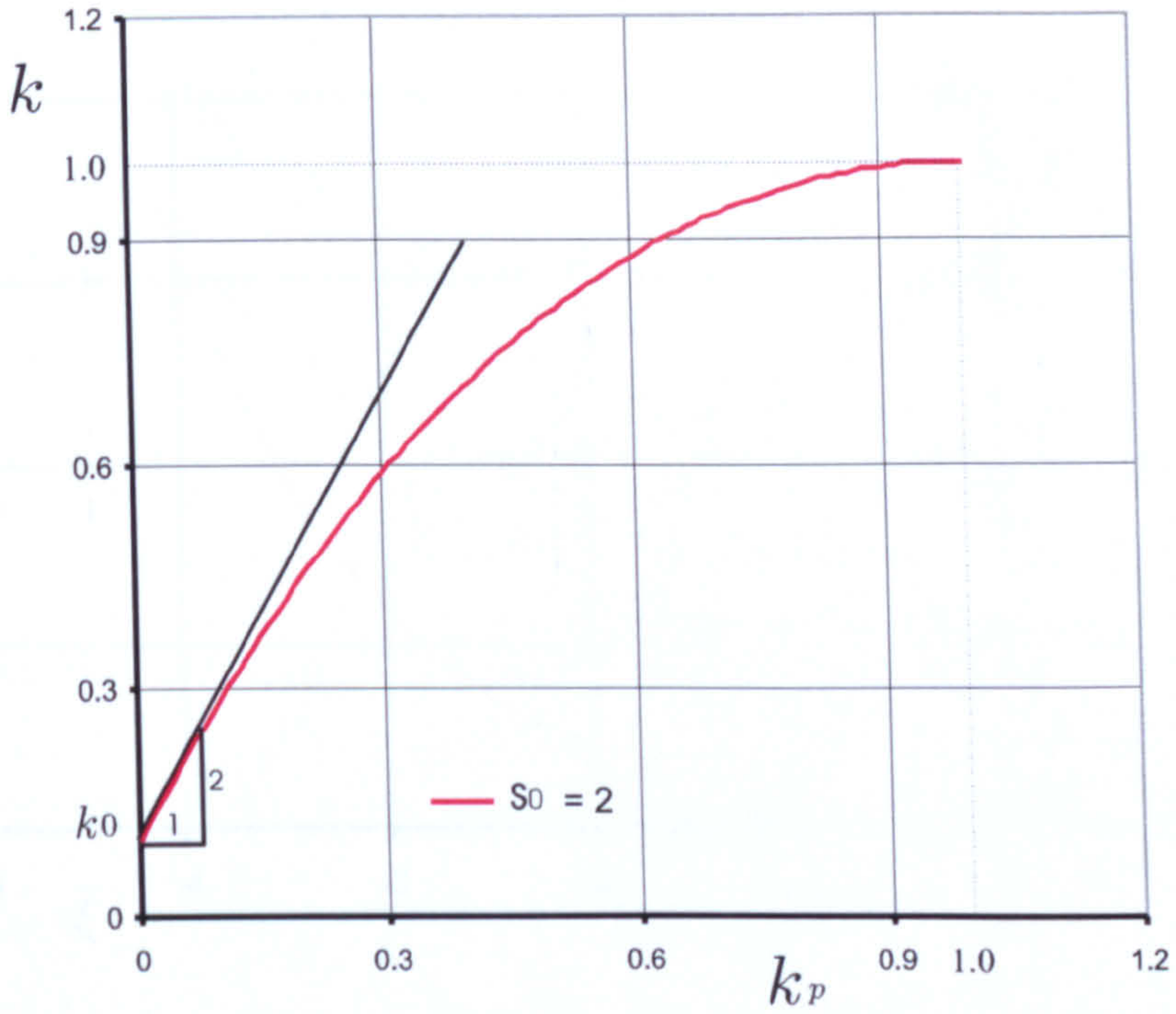

Figure 3.11: The relationship between hardening measure k and the hardening internal variable k_p

is the norm of the plastic strain scaled by the hardening ductility measure ζ. The function suggested in this study for ζ is a single exponential function with only two material parameters A_h and B_h. The equation takes the form:

$$\zeta = A_h \exp\left(-\bar{\xi}/B_h\right) \tag{3.104}$$

Figure 3.12 shows the general shape of the ζ function with the values of material parameters A_h and B_h taken as 0.003 and 0.99 respectively. These values have been identified from the calibration process which will be presented in Chapter 4.

3.4.6 Auxiliary Stress Surface

The model is capable of dealing with the stresses that fall inside the zones between the hydrostatic tensile strength ($\bar{\xi}_{ht}$) and the hydrostatic compressive stress ($\bar{\xi}_{hc}$). These zones are referred to here as zone 1, 2, 3, and 4. The zone that is greater than $\bar{\xi}_{ht}$ is zone 0, and less than $\bar{\xi}_{hc}$ is zone 5 as shown in Figure 3.13. If the stress trial state falls in zones 0 and 5; an auxiliary stress is to be introduced to ensure that the stress state remains inside the zone covered by the model. The value of the auxiliary stress state suggested here is defined by the intersection point between a circular arc passing through the hydrostatic compression stress state $\bar{\xi}_{hc}$ and having

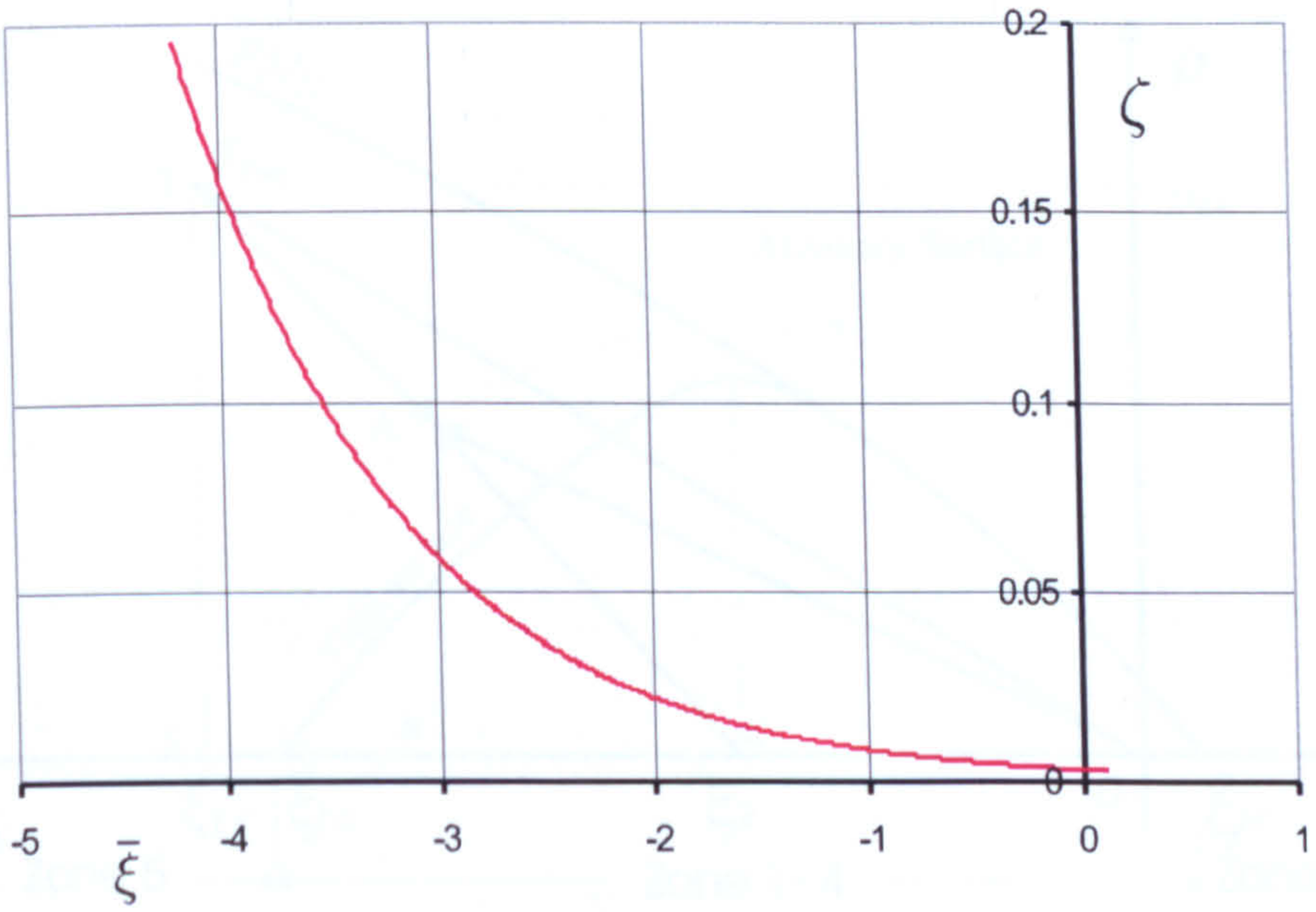

Figure 3.12: The ductility measure ζ versus $\bar{\xi}$

its center on the hydrostatic axis at ξ_2, and a radial projection passing ξ_2 on the hydrostatic axis to the trial stress $(\xi_{tr}\ ,\ \rho_{tr})$ as shown in Figure 3.13.

The procedure to identify the auxiliary stress state is as follows:
The linear equation of CT takes the form

$$\rho = a_x\,\xi + b_x \tag{3.105}$$

Subjected to the following conditions:

$$\text{If} \quad \xi = \xi_2 \quad \text{then} \quad \rho = 0$$
$$\text{and}$$
$$\text{if} \quad \xi = \xi_{tr} \quad \text{then } \rho = \rho_{tr}$$

where a_x and b_x are constants determined as follows:
Substitute the above values in (3.105) and solve the equation for a_x and b_x and re-insert the values into equation 3.105

$$\rho = \frac{\rho_{tr}\ (\xi - \xi_2)}{\xi_{tr} - \xi_2} \tag{3.106}$$

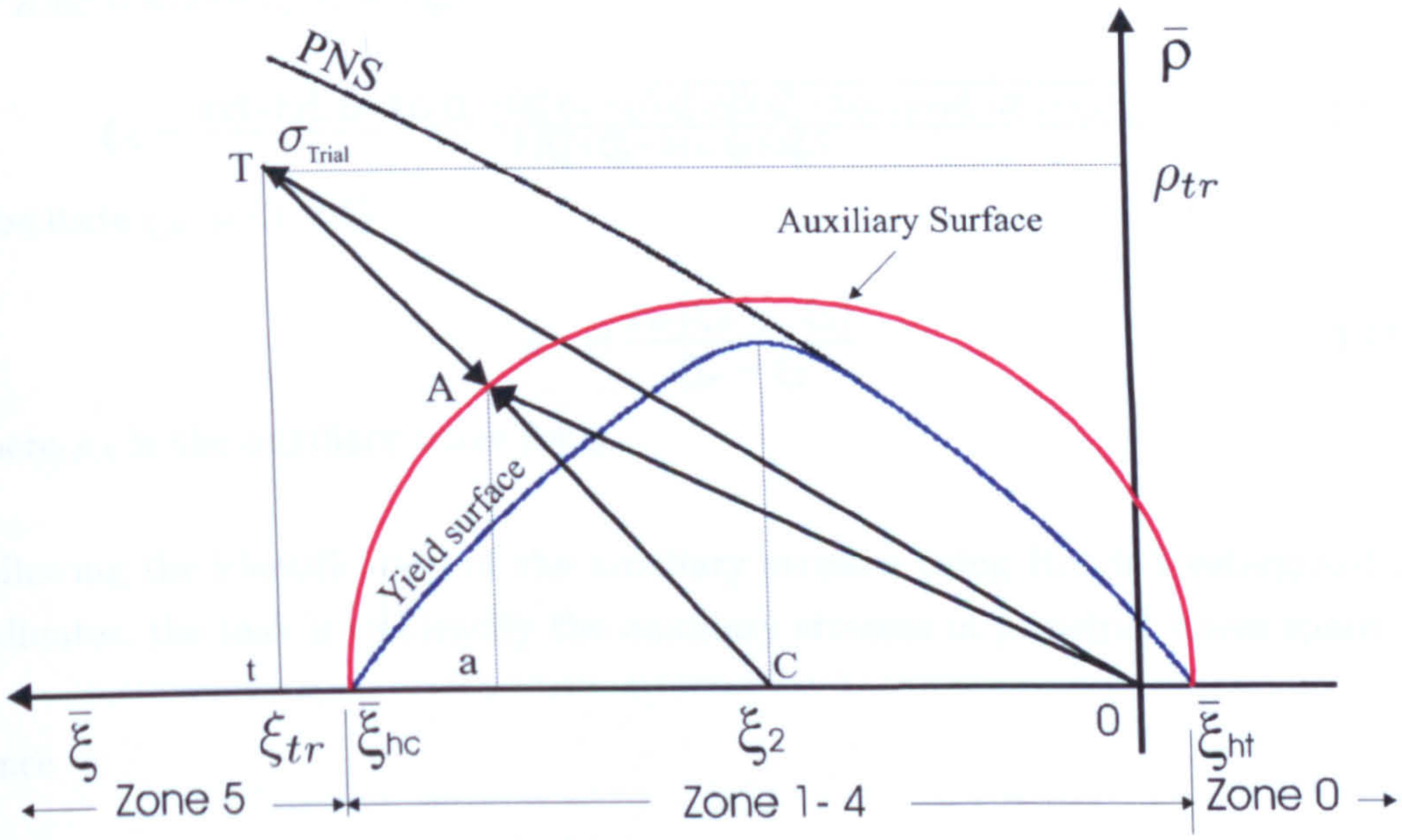

Figure 3.13: Auxiliary stress state and the six zones

The equation of the circular arc is given as

$$(\xi - c_x)^2 + \rho_2^2 = \frac{\xi_0^2}{4} \tag{3.107}$$

subjected to the following condition: if $\xi = \xi_{hc}$ then $\rho = 0$

Substituting the above into (3.107) and solving for c_x gives two solutions of the equation for (c_x):

$$c_x = \xi_{hc} + \frac{\xi_0}{2} \tag{3.108}$$

and

$$c_x = \xi_{hc} - \frac{\xi_0}{2} \tag{3.109}$$

The first solution identifies the value we seek and the other solution is valid for the extension meridian.

Substituting (3.108) in (3.107) and solving for ξ also gives two roots. For zone 0 where $(\xi >= \xi_{ht})$

$$\xi_A = \frac{2\,\xi_2^3 + 2\,\rho_{tr}^2\,\xi_2 + 2\,\xi_2\,\xi_{tr}^2 - 4\,\xi_2^2\,\xi_{tr} + \sqrt{(\xi_0^2\,(\xi_2^2 + \xi_{tr}^2 - 2\,\xi_{tr}\,\xi_2 + \rho_{tr}^2)\,(\xi_{tr} - \xi_2)^2)}}{2\,(\xi_2^2 + \xi_{tr}^2 - 2\,\xi_{tr}\,\xi_2 + \rho_{tr}^2)} \tag{3.110}$$

where ξ_A is the auxiliary value of ξ.
For zone 5 where ($\xi <= \xi_{hc}$)

$$\xi_A = \frac{2\xi_2^3+2\rho_{tr}^2\xi_2+2\xi_2\xi_{tr}^2-4\xi_2^2\xi_{tr}-\sqrt{(\xi_0^2(\xi_2^2+\xi_{tr}^2-2\xi_{tr}\xi_2+\rho_{tr}^2)(\xi_{tr}-\xi_2)^2)}}{2(\xi_2^2+\xi_{tr}^2-2\xi_{tr}\xi_2+\rho_{tr}^2)} \tag{3.111}$$

Substitute ξ_A in (3.106)

$$\rho_A = \frac{\rho_{tr}(\xi_A - \xi_2)}{\xi_{tr} - \xi_2} \tag{3.112}$$

where ρ_A is the auxiliary value for ρ.

Following the identification of the auxiliary stresses using Haigh-Westergaard coordinates, the task is to identify the auxiliary stresses in principal stress space.

Since

$$\vec{OA} = \vec{OC} + \vec{CA} \tag{3.113}$$

and

$$\xi = \frac{\sigma_1 + \sigma_2 + \sigma_3}{\sqrt{3}} \tag{3.114}$$

and on the hydrostatic axis, $\sigma_1 = \sigma_2 = \sigma_3$. Therefore 3.114 can be written as follows

$$\xi_2 = \sqrt{3}\{\sigma\} \tag{3.115}$$

or

$$\vec{OC} = \left\{\frac{\xi_2}{\sqrt{3}}\right\} \tag{3.116}$$

Since the triangles CAa and CTt are *similar*. That is

$$\Delta\, CAa \sim \Delta\, CTt \tag{3.117}$$

It is possible to establish that

$$\vec{CA} = \frac{\rho_A}{\rho_T}\vec{CT} \tag{3.118}$$

where

$$\vec{CT} = \vec{OT} - \vec{OC} \tag{3.119}$$

Substituting 3.116 into 3.119 and then into 3.118 and then into 3.113 the auxiliary stress vector can be identified

$$\{\sigma\} = \frac{\xi_2 f_c}{\sqrt{3}} + \frac{\rho_A}{\rho_T}\left(\{\sigma_{tr}\} - \frac{\xi_2 f_c}{\sqrt{3}}\right) \tag{3.120}$$

3.5 The Derivatives

The linearisation of the *residual plastic strains and hardening parameter* $\{r\}$, which is required as part of the CPP method, necessitates the calculations of four sets of derivatives:

1. The derivatives of the yield surface (F) with respect to the internal hardening parameter k_p, that is $\frac{\partial F}{\partial k_p}$.

2. The derivatives of the yield function with respect to the stress tensor, which include the first derivative $\left\{\frac{\partial F}{\partial \sigma}\right\}$ and the second derivative $\left[\frac{\partial^2 F}{\partial \sigma^2}\right]$

3. Mixed derivative of the yield surface with respect to the internal hardening parameter and the stress tensor $\left\{\frac{\partial^2 F}{\partial k_p \partial \sigma}\right\}$.

4. The derivatives of the hardening function (h), which include the derivative with respect to the stress tensor $\left\{\frac{\partial h}{\partial \sigma}\right\}$, and to the internal hardening parameter $\frac{\partial h}{\partial k_p}$

3.5.1 The Derivative of Yield Function with Respect to k_p

The yield function (F) is presented here as a function of stress (σ) and hardening internal variable k_p

$$F(\sigma, k_p) = r\,\bar{\rho} - \rho_f = 0 \tag{3.121}$$

The derivative of the yield surface may be written using the chain rule,

$$\frac{\partial F}{\partial k_p} = \frac{\partial F}{\partial k}\frac{\partial k}{\partial k_p} \tag{3.122}$$

The derivative takes the form

$$\frac{\partial k}{\partial k_p} = 3\,(2\,k_0 + s_0 - 2)\,{k_p}^2 + 2\,(3 - 2\,s_0 - 3\,k_0)\,k_p + s_0 \tag{3.123}$$

Here $\frac{\partial F}{\partial k}$ is calculated from the chain rule as

$$\frac{\partial F}{\partial k} = \frac{\partial F}{\partial \xi_0}\frac{\partial \xi_0}{\partial k} \tag{3.124}$$

Since the hardening parameter k is a function of ξ_0 (expressed in equation (3.81)) the first derivative of k with respect to ξ_0 can be calculated as follows

$$\frac{\partial \xi_0}{\partial k} = \frac{A_k}{(1-k)^2} \tag{3.125}$$

Note that the term of the yield equation that is dependant on k is ρ_f, while the deviatoric shape function (r) and ρ are independent of k. Therefore the first derivative of the yield function with respect to k takes the following form:

$$\frac{\partial F}{\partial \xi_0} = -\frac{\partial \rho_f}{\partial \xi_0} \tag{3.126}$$

The expressions for ρ_f in each of the four zones are different, therefore for each of these zones the $\frac{\partial F}{\partial \xi_0}$ is to be determined independently.

In Zone 1, the formulation of ρ_f adopts the same form as the PNS, and it is independent of ξ_0. Therefore:

$$\frac{\partial \rho_f}{\partial \xi_0} = 0 \tag{3.127}$$

In Zone 2, ρ_f takes the form expressed in (3.79), where all the five parameters (a, b, c, d, and e) which appear in the equations are variables dependant on ξ_0. The $\bar{\xi}$ are independent variables of ξ_0. Therefore the first derivative of ρ_f with respect to ξ_0 can be expressed as follows:

$$\frac{\partial \rho_f}{\partial \xi_0} = \frac{\partial a}{\partial \xi_0}\bar{\xi}^4 + \frac{\partial b}{\partial \xi_0}\bar{\xi}^3 + \frac{\partial c}{\partial \xi_0}\bar{\xi}^2 + \frac{\partial d}{\partial \xi_0}\bar{\xi} + \frac{\partial e}{\partial \xi_0} \tag{3.128}$$

where $\frac{\partial a}{\partial \xi_0}$, $\frac{\partial b}{\partial \xi_0}$, $\frac{\partial c}{\partial \xi_0}$, $\frac{\partial d}{\partial \xi_0}$, and $\frac{\partial e}{\partial \xi_0}$ are presented in the equations from (3.133) to (3.138). These derivatives have been calculated using mathematics tool MAPLE 8 [MAPLE]. These derivatives have also been verified numerically using the central difference approximation

$$y'(x) \sim \frac{y(x+h) - y(x-h)}{2\,h} \tag{3.129}$$

where h, is a small increment (of the order of 1×10^{-6} in most cases here). The results are then presented graphically as shown in Figure 3.14. It can be noticed that the first derivative of the yield surface with respect to k, shows graphical continuity in all zones.

In Zone 3, ρ_f takes the form expressed in (3.97) and (3.98). All the terms that appear in the equations are dependant on ξ_0. Therefore, the first derivative of ρ_f with respect to ξ_0 can be expressed as follows:

$$\frac{\partial \rho_f}{\partial \xi_0} = \frac{\partial a}{\partial \xi_0}\bar{\xi}_3^4 + 4a\bar{\xi}_3^3\frac{\partial \bar{\xi}_3}{\partial \xi_0} + \frac{\partial b}{\partial \xi_0}\bar{\xi}_3^3 + 3b\bar{\xi}_3^2\frac{\partial \bar{\xi}_3}{\partial \xi_0} + \frac{\partial c}{\partial \xi_0}\bar{\xi}_3^2 + 2c\bar{\xi}_3\frac{\partial \bar{\xi}_3}{\partial \xi_0} + \frac{\partial d}{\partial \xi_0}\bar{\xi}_3 + d\frac{\partial \bar{\xi}_3}{\partial \xi_0} + \frac{\partial e}{\partial \xi_0} \tag{3.130}$$

and from equation (3.98) the derivatives of ξ_3 with respect to ξ_0 can be expressed as follows:

$$\frac{\partial \xi_3}{\partial \xi_0} = -1 \tag{3.131}$$

In Zone 4, ρ_f is given by (3.99). The first derivative of ρ_f with respect to ξ_0 is given by

$$\frac{\partial \rho_f}{\partial \xi_0} = 2\,\frac{(1/6)^\gamma\sqrt{6}\left(-m+\sqrt{\beta_3}\right)^\gamma\gamma\sqrt{3}m}{\sqrt{\beta_3}\left(-m+\sqrt{\beta_3}\right)} \tag{3.132}$$

where β_3 is a dependant variable given by (3.140).

The derivatives of the five parameters (a, b, c, d, and e) with respect to ξ_0 are

$$\begin{aligned}\frac{\partial a}{\partial \xi_0} = {} & 1/2\left(-\frac{\alpha_2\sqrt{6}\sqrt{3}m}{\sqrt{\beta_2}} - 12\,\frac{\xi_1\sqrt{6}m^2\alpha_1}{{\beta_1}^{3/2}} + 108\,\frac{{\xi_1}^2\sqrt{6}m^3\sqrt{3}\alpha_1}{{\beta_1}^{5/2}} + 2/3\,\frac{\sqrt{6}\sqrt{3}m}{\sqrt{\beta_1}} + \right.\\ & 12\,\frac{\xi_2\sqrt{6}m^2\alpha_1}{{\beta_1}^{3/2}} - 6\,\frac{\xi_1\sqrt{6}m^2}{{\beta_1}^{3/2}} - 216\,\frac{\xi 2\xi_1\sqrt{6}m^3\sqrt{3}\alpha_1}{{\beta_1}^{5/2}} + 2/3\,\frac{\alpha_1\sqrt{6}\sqrt{3}m}{\sqrt{\beta_1}} + \\ & \left.6\,\frac{\xi_2\sqrt{6}m^2}{{\beta_1}^{3/2}} + 108\,\frac{{\xi_2}^2\sqrt{6}m^3\sqrt{3}\alpha_1}{{\beta_1}^{5/2}}\right){\beta_6}^{-1} - 1/2\left(-1/3\,\alpha_2\sqrt{6}\left(-m+\sqrt{\beta_2}\right) - \right.\\ & 6\,\frac{{\xi_1}^2\sqrt{6}m^2}{{\beta_1}^{3/2}} - 4/3\,\frac{\xi_2\sqrt{6}\sqrt{3}m}{\sqrt{\beta_1}} + 12\,\frac{\xi_2\xi_1\sqrt{6}m^2}{{\beta_1}^{3/2}} + 4/3\,\frac{\xi_1\sqrt{6}\sqrt{3}m}{\sqrt{\beta_1}} - 6\,\frac{{\xi_2}^2\sqrt{6}m^2}{{\beta_1}^{3/2}} + \\ & \left.1/3\,\sqrt{6}\left(-m+\sqrt{\beta_1}\right)\right){\beta_4}{\beta_6}^{-2}\end{aligned} \tag{3.133}$$

$$\begin{aligned}\frac{\partial b}{\partial \xi_0} = {} & -\left(1/9\,\alpha_2\sqrt{6}\left(-m+\sqrt{\beta_2}\right) - 1/9\,\sqrt{6}\left(-m+\sqrt{\beta_1}\right) - 3\,\frac{{\xi_1}^2\sqrt{6}m^2}{{\beta_1}^{3/2}} + \right.\\ & 4/9\,\alpha_1\,\alpha_2\sqrt{6}\left(-m+\sqrt{\beta_2}\right) + 9\,\frac{{\xi_2}^2\sqrt{6}m^2}{{\beta_1}^{3/2}} - 4/9\,\alpha_1\sqrt{6}\left(-m+\sqrt{\beta_1}\right) + \\ & 108\,\frac{\sqrt{6}m^3{\xi_1}^3\sqrt{3}\alpha_1}{{\beta_1}^{5/2}} - 12\,\frac{{\xi_1}^2\sqrt{6}m^2\alpha_1}{{\beta_1}^{3/2}} - 108\,\frac{{\xi_1}^2\xi_2\sqrt{6}m^3\sqrt{3}\alpha_1}{{\beta_1}^{5/2}} - 2/3\,\frac{\xi_1\sqrt{6}\sqrt{3}m\alpha_1}{\sqrt{\beta_1}} + \\ & 12\,\frac{\alpha_1{\xi_2}^2\sqrt{6}m^2}{{\beta_1}^{3/2}} - 6\,\frac{\xi_2\xi_1\sqrt{6}m^2}{{\beta_1}^{3/2}} - 108\,\frac{\xi_1{\xi_2}^2\sqrt{6}m^3\sqrt{3}\alpha_1}{{\beta_1}^{5/2}} - 4/3\,\frac{\xi_1\alpha_2\sqrt{6}\sqrt{3}m}{\sqrt{\beta_2}} + \\ & 2\,\frac{\alpha_1\xi_2\sqrt{6}\sqrt{3}m}{\sqrt{\beta_1}} + 1/3\,\frac{\xi_1\sqrt{6}\sqrt{3}m}{\sqrt{\beta_1}} + \frac{\xi_2\sqrt{6}\sqrt{3}m}{\sqrt{\beta_1}} + 108\,\frac{{\xi_2}^3\sqrt{6}m^3\sqrt{3}\alpha_1}{{\beta_1}^{5/2}} - \\ & \left.2/3\,\frac{\xi_2\alpha_2\sqrt{6}\sqrt{3}m}{\sqrt{\beta_2}}\right){\beta_6}^{-1} + \left(-6\,\frac{\sqrt{6}m^2{\xi_1}^3}{{\beta_1}^{3/2}} + 6\,\frac{{\xi_1}^2\xi_2\sqrt{6}m^2}{{\beta_1}^{3/2}} + 5/3\,\frac{{\xi_1}^2\sqrt{6}\sqrt{3}m}{\sqrt{\beta_1}} + \right.\\ & 6\,\frac{\xi_1{\xi_2}^2\sqrt{6}m^2}{{\beta_1}^{3/2}} - 4/9\,\xi_1\,\alpha_2\sqrt{6}\left(-m+\sqrt{\beta_2}\right) + 4/9\,\xi_1\sqrt{6}\left(-m+\sqrt{\beta_1}\right) - \\ & 2/3\,\frac{\xi_2\xi_1\sqrt{6}\sqrt{3}m}{\sqrt{\beta_1}} - \frac{{\xi_2}^2\sqrt{6}\sqrt{3}m}{\sqrt{\beta_1}} + 2/9\,\xi_2\sqrt{6}\left(-m+\sqrt{\beta_1}\right) - 6\,\frac{{\xi_2}^3\sqrt{6}m^2}{{\beta_1}^{3/2}} - \\ & \left.2/9\,\xi_2\,\alpha_2\sqrt{6}\left(-m+\sqrt{\beta_2}\right)\right){\beta_4}{\beta_6}^{-2}\end{aligned} \tag{3.134}$$

$$\frac{\partial c}{\partial \xi_0} = 11/2\left(-2/3\,\xi_1\sqrt{6}\left(-m+\sqrt{\beta_1}\right)-4/3\,\alpha_1\,\xi_2\sqrt{6}\left(-m+\sqrt{\beta_1}\right)-4/3\,\xi_1\sqrt{6}\left(-m+\sqrt{\beta_1}\right)\alpha_1+6\,\frac{\xi_1\xi_2\sqrt{6}\sqrt{3}m}{\sqrt{\beta_1}}+18\,\frac{\xi_1{\xi_2}^2\sqrt{6}m^2}{{\beta_1}^{3/2}}+4/3\,\xi_1\,\alpha_2\sqrt{6}\left(-m+\sqrt{\beta_2}\right)\alpha_1+108\,\frac{{\xi_1}^4\sqrt{6}m^3\sqrt{3}\alpha_1}{{\beta_1}^{5/2}}-12\,\frac{{\xi_1}^3\sqrt{6}m^2\alpha_1}{{\beta_1}^{3/2}}-2\,\frac{{\xi_1}^2\alpha_2\sqrt{6}\sqrt{3}m}{\sqrt{\beta_2}}-2\,\frac{{\xi_1}^2\sqrt{6}\sqrt{3}m\alpha_1}{\sqrt{\beta_1}}-36\,\frac{\xi_2{\xi_1}^2\sqrt{6}m^2\alpha_1}{{\beta_1}^{3/2}}+36\,\frac{\xi_1{\xi_2}^2\sqrt{6}m^2\alpha_1}{{\beta_1}^{3/2}}+12\,\frac{{\xi_2}^3\alpha_1\sqrt{6}m^2}{{\beta_1}^{3/2}}+6\,\frac{{\xi_2}^2\alpha_1\sqrt{6}\sqrt{3}m}{\sqrt{\beta_1}}+108\,\frac{{\xi_2}^4\sqrt{6}m^3\sqrt{3}\alpha_1}{{\beta_1}^{5/2}}+4/3\,\alpha_1\,\xi_2\,\alpha_2\sqrt{6}\left(-m+\sqrt{\beta_2}\right)+6\,\frac{{\xi_1}^3\sqrt{6}m^2}{{\beta_1}^{3/2}}+2/3\,\xi_1\,\alpha_2\sqrt{6}\left(-m+\sqrt{\beta_2}\right)+12\,\frac{{\xi_2}^3\sqrt{6}m^2}{{\beta_1}^{3/2}}-36\,\frac{\xi_2{\xi_1}^2\sqrt{6}m^2}{{\beta_1}^{3/2}}-2\,\frac{{\xi_1}^2\sqrt{6}\sqrt{3}m}{\sqrt{\beta_1}}+216\,\frac{{\xi_1}^3\xi_2\sqrt{6}m^3\sqrt{3}\alpha_1}{{\beta_1}^{5/2}}-4\,\frac{\xi_1\xi_2\,\alpha_2\sqrt{6}\sqrt{3}m}{\sqrt{\beta_2}}+216\,\frac{{\xi_2}^3\xi_1\sqrt{6}m^3\sqrt{3}\alpha_1}{{\beta_1}^{5/2}}-648\,\frac{{\xi_2}^2{\xi_1}^2\sqrt{6}m^3\sqrt{3}\alpha_1}{{\beta_1}^{5/2}}\Big)\,{\beta_6}^{-1}-1/2\,(-2/3\,{\xi_1}^2\alpha_2\sqrt{6}\left(-m+\sqrt{\beta_2}\right)-6\,\frac{{\xi_1}^4\sqrt{6}m^2}{{\beta_1}^{3/2}}+4\,\frac{\xi_2{\xi_1}^2\sqrt{6}\sqrt{3}m}{\sqrt{\beta_1}}-12\,\frac{{\xi_1}^3\xi_2\sqrt{6}m^2}{{\beta_1}^{3/2}}+2\,\frac{{\xi_1}^3\sqrt{6}\sqrt{3}m}{\sqrt{\beta_1}}+36\,\frac{{\xi_2}^2{\xi_1}^2\sqrt{6}m^2}{{\beta_1}^{3/2}}+2/3\,{\xi_1}^2\sqrt{6}\left(-m+\sqrt{\beta_1}\right)-6\,\frac{\xi_1{\xi_2}^2\sqrt{6}\sqrt{3}m}{\sqrt{\beta_1}}+4/3\,\xi_1\,\xi_2\sqrt{6}\left(-m+\sqrt{\beta_1}\right)-12\,\frac{{\xi_2}^3\xi_1\sqrt{6}m^2}{{\beta_1}^{3/2}}-4/3\,\xi_1\,\xi_2\,\alpha_2\sqrt{6}\left(-m+\sqrt{\beta_2}\right)-6\,\frac{{\xi_2}^4\sqrt{6}m^2}{{\beta_1}^{3/2}}\Big)\,\beta_4{\beta_6}^{-2} \tag{3.135}$$

$$\frac{\partial d}{\partial \xi_0} = 1/2\,\frac{\beta_5}{\beta_6}-\xi_2\Big(-3\,\frac{{\xi_1}^3\sqrt{6}m^2}{{\beta_1}^{3/2}}-4/3\,\xi_1\sqrt{6}\left(-m+\sqrt{\beta_1}\right)\alpha_1-12\,\frac{{\xi_1}^3\sqrt{6}m^2\alpha_1}{{\beta_1}^{3/2}}+108\,\frac{{\xi_1}^4\sqrt{6}m^3\sqrt{3}\alpha_1}{{\beta_1}^{5/2}}-108\,\frac{{\xi_1}^3\xi_2\sqrt{6}m^3\sqrt{3}\alpha_1}{{\beta_1}^{5/2}}+1/2\,\frac{{\xi_1}^2\sqrt{6}\sqrt{3}m}{\sqrt{\beta_1}}+2\,\frac{\xi_2\xi_1\sqrt{6}\sqrt{3}m\alpha_1}{\sqrt{\beta_1}}-2\,\frac{{\xi_1}^2\sqrt{6}\sqrt{3}m\alpha_1}{\sqrt{\beta_1}}-1/2\,\frac{{\xi_2}^2\sqrt{6}\sqrt{3}m}{\sqrt{\beta_1}}-6\,\frac{{\xi_1}^2\xi_2\sqrt{6}m^2}{{\beta_1}^{3/2}}+12\,\frac{{\xi_2}^2\xi_1\sqrt{6}m^2\alpha_1}{{\beta_1}^{3/2}}-108\,\frac{{\xi_2}^2{\xi_1}^2\sqrt{6}m^3\sqrt{3}\alpha_1}{{\beta_1}^{5/2}}+9\,\frac{{\xi_2}^2\xi_1\sqrt{6}m^2}{{\beta_1}^{3/2}}+108\,\frac{{\xi_2}^3\xi_1\sqrt{6}m^3\sqrt{3}\alpha_1}{{\beta_1}^{5/2}}+4/3\,\frac{\xi_2\xi_1\sqrt{6}\sqrt{3}m}{\sqrt{\beta_1}}+4/3\,\frac{{\xi_2}^2\alpha_1\sqrt{6}\sqrt{3}m}{\sqrt{\beta_1}}+4/3\,\xi_1\,\alpha_2\sqrt{6}\left(-m+\sqrt{\beta_2}\right)\alpha_1-2\,\frac{{\xi_1}^2\alpha_2\sqrt{6}\sqrt{3}m}{\sqrt{\beta_2}}\Big)\,{\beta_6}^{-1}+\frac{\xi_2\,\beta_5\,\beta_1}{{\beta_6}^2} \tag{3.136}$$

$$\begin{aligned}\frac{\partial e}{\partial \xi_0} = \; & 1/2\left(-18\frac{{\xi_1}^3{\xi_2}^2\sqrt{6}m^2}{{\beta_1}^{3/2}} - 2/9\sqrt{6}\left(-m+\sqrt{\beta_1}\right){\xi_2}^3 + 2/9\,{\xi_1}^3\alpha_2\sqrt{6}(-m+\right.\\ & \left.\sqrt{\beta_2}\right) - 2/3\sqrt{6}\left(-m+\sqrt{\beta_1}\right)\xi_2{\xi_1}^2 + 4/9\sqrt{6}\left(-m+\sqrt{\beta_1}\right)\alpha_1{\xi_2}^3 + \\ & 2/3\sqrt{6}\left(-m+\sqrt{\beta_1}\right)\xi_1{\xi_2}^2 - 2\frac{{\xi_1}^2{\xi_2}^2\sqrt{6}\sqrt{3}m\alpha_1}{\sqrt{\beta_1}} - 2\frac{{\xi_1}^3\xi_2\sqrt{6}\sqrt{3}m}{\sqrt{\beta_1}} - \\ & 12\frac{{\xi_1}^3{\xi_2}^2\sqrt{6}m^2\alpha_1}{{\beta_1}^{3/2}} + 6\frac{{\xi_1}^4\xi_2\sqrt{6}m^2}{{\beta_1}^{3/2}} + 108\frac{{\xi_1}^4{\xi_2}^2\sqrt{6}m^3\sqrt{3}\alpha_1}{{\beta_1}^{5/2}} - 4/9\,{\xi_1}^3\alpha_2\sqrt{6}(- \\ & m+\sqrt{\beta_2}\left)\alpha_1 + 1/3\frac{{\xi_1}^4\alpha_2\sqrt{6}\sqrt{3}m}{\sqrt{\beta_2}} + 12\frac{{\xi_1}^2{\xi_2}^3\sqrt{6}m^2\alpha_1}{{\beta_1}^{3/2}} - 216\frac{{\xi_1}^3{\xi_2}^3\sqrt{6}m^3\sqrt{3}\alpha_1}{{\beta_1}^{5/2}} + \right.\\ & 4/3\,{\xi_1}^2\xi_2\alpha_2\sqrt{6}\left(-m+\sqrt{\beta_2}\right)\alpha_1 - 4/3\frac{{\xi_1}^3\xi_2\alpha_2\sqrt{6}\sqrt{3}m}{\sqrt{\beta_2}} - 4/3\frac{\xi_1\sqrt{6}\sqrt{3}m{\xi_2}^3}{\sqrt{\beta_1}} + \\ & 8/3\frac{\xi_1\sqrt{6}\sqrt{3}m{\xi_2}^3\alpha_1}{\sqrt{\beta_1}} + 4\frac{{\xi_1}^2{\xi_2}^2\sqrt{6}\sqrt{3}m}{\sqrt{\beta_1}} + 108\frac{{\xi_1}^2\sqrt{6}m^3{\xi_2}^4\sqrt{3}\alpha_1}{{\beta_1}^{5/2}} + 12\frac{{\xi_1}^2{\xi_2}^3\sqrt{6}m^2}{{\beta_1}^{3/2}} - \\ & 4/3\sqrt{6}\left(-m+\sqrt{\beta_1}\right){\xi_2}^2\xi_1\alpha_1\Big){\beta_6}^{-1} - 1/2\left(2\frac{{\xi_1}^3{\xi_2}^2\sqrt{6}\sqrt{3}m}{\sqrt{\beta_1}} - 6\frac{{\xi_1}^4{\xi_2}^2\sqrt{6}m^2}{{\beta_1}^{3/2}} + \right.\\ & 1/9\,{\xi_1}^4\alpha_2\sqrt{6}\left(-m+\sqrt{\beta_2}\right) + 1/9\sqrt{6}\left(-m+\sqrt{\beta_1}\right){\xi_2}^4 + 12\frac{{\xi_1}^3{\xi_2}^3\sqrt{6}m^2}{{\beta_1}^{3/2}} - \\ & 4/9\,{\xi_1}^3\xi_2\alpha_2\sqrt{6}\left(-m+\sqrt{\beta_2}\right) + 2/3\frac{\xi_1\sqrt{6}\sqrt{3}m{\xi_2}^4}{\sqrt{\beta_1}} - 8/3\frac{{\xi_1}^2\sqrt{6}\sqrt{3}m{\xi_2}^3}{\sqrt{\beta_1}} - \\ & 6\frac{{\xi_1}^2\sqrt{6}m^2{\xi_2}^4}{{\beta_1}^{3/2}} + 2/3\sqrt{6}\left(-m+\sqrt{\beta_1}\right){\xi_2}^2{\xi_1}^2 - 4/9\sqrt{6}\left(-m+\sqrt{\beta_1}\right)\xi_1 \\ & {\xi_2}^3\Big){\beta_4}{\beta_6}^{-2}\end{aligned} \tag{3.137}$$

where β_1, β_2, β_3, β_4 and β_4 are five dependant variables given by

$$\beta_1 = m^2 - 12\sqrt{3}m\xi_1 + 36 \tag{3.138}$$

$$\beta_2 = m^2 - 12\sqrt{3}m\xi_2 + 36 \tag{3.139}$$

$$\beta_3 = m^2 - 12\sqrt{3}m\xi_3 + 36 \tag{3.140}$$

$$\begin{aligned}\beta_4 = \; & 2(-{\xi_2}^3 + \xi 1^3 + 6\,\xi_2{\xi_1}^2\alpha_1 - 3\,{\xi_1}^2\xi_2 - 6\,{\xi_2}^2\xi_1\alpha_1 - 2\,{\xi_1}^3\alpha_1 + \\ & 2\,\alpha_1{\xi_2}^3 + 3\,{\xi_2}^2\xi_1)\end{aligned} \tag{3.141}$$

$$\begin{aligned}\beta_5 = \; & -6\frac{{\xi_1}^4\sqrt{6}m^2}{{\beta_1}^{3/2}} + 6\frac{{\xi_1}^3\xi_2\sqrt{6}m^2}{{\beta_1}^{3/2}} - \frac{{\xi_1}^2\xi_2\sqrt{6}\sqrt{3}m}{\sqrt{\beta_1}} + 2\frac{{\xi_1}^3\sqrt{6}\sqrt{3}m}{\sqrt{\beta_1}} + 1/3\frac{{\xi_2}^3\sqrt{6}\sqrt{3}m}{\sqrt{\beta_1}} + \\ & 6\frac{{\xi_2}^2{\xi_1}^2\sqrt{6}m^2}{{\beta_1}^{3/2}} - 6\frac{{\xi_2}^3\xi_1\sqrt{6}m^2}{{\beta_1}^{3/2}} - 4/3\frac{{\xi_2}^2\xi_1\sqrt{6}\sqrt{3}m}{\sqrt{\beta_1}} - 2/3\,{\xi_1}^2\alpha_2\sqrt{6}\left(-m+\sqrt{\beta_2}\right) + \\ & 2/3\,{\xi_1}^2\sqrt{6}\left(-m+\sqrt{\beta_1}\right)\end{aligned} \tag{3.142}$$

$$\beta_6 = {\xi_2}^4 - 4\,{\xi_1}^3\xi_2 + 6\,{\xi_2}^2{\xi_1}^2 + {\xi_1}^4 - 4\,{\xi_2}^3\xi_1 \tag{3.143}$$

The derivatives for the parameters are rather lengthly. This is unfortunate but unavoidable given the constraints acting on the expressions (common tangents

between zones).

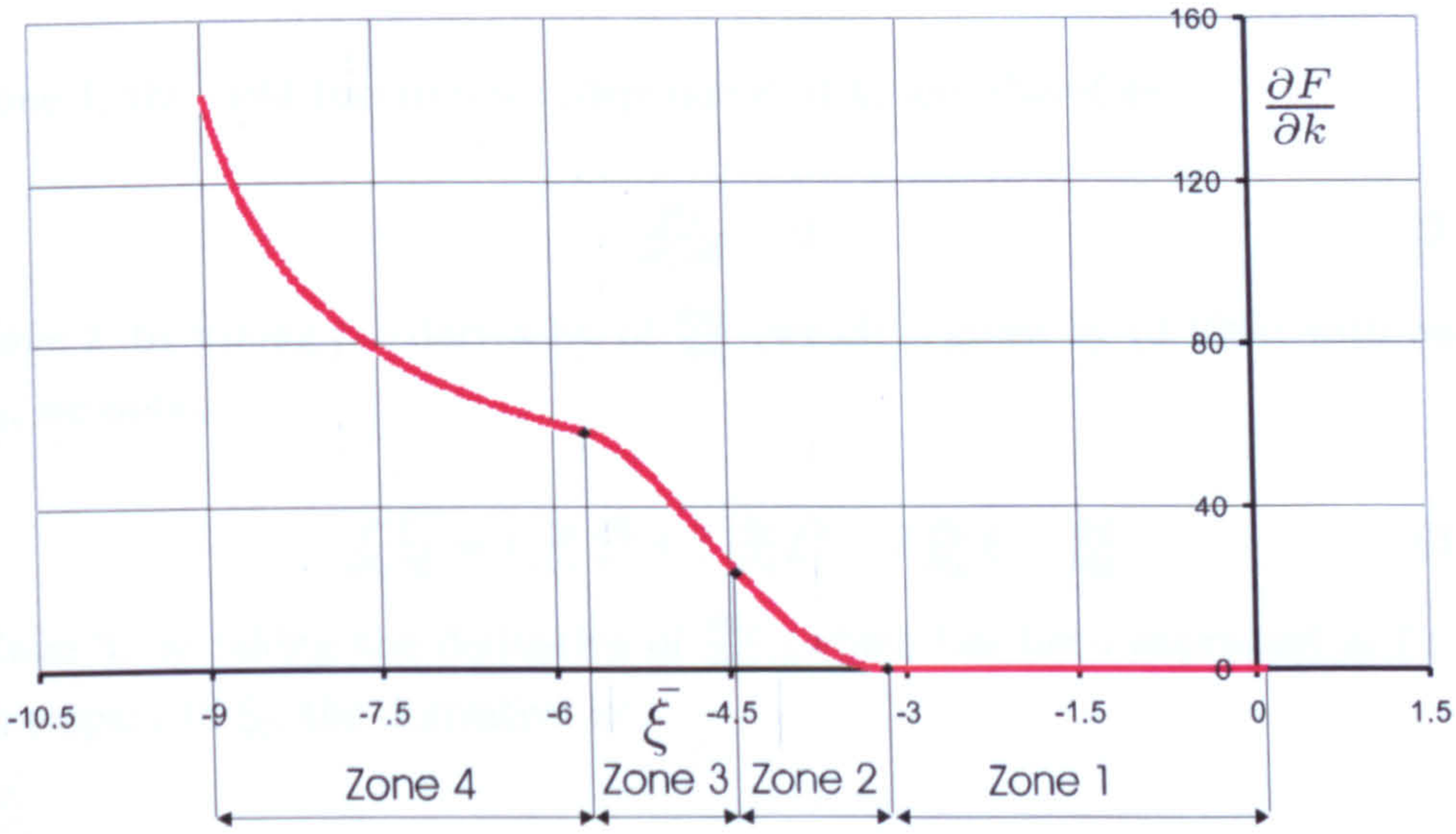

Figure 3.14: The continuity of the first derivative of the yield function with respect to k

3.5.2 The Mixed Derivatives

The mixed derivatives of the yield function with respect to the internal hardening parameter k_p and the stresses are given as

$$\left\{\frac{\partial^2 F}{\partial k_p \partial \sigma}\right\} = \frac{\partial^2 F}{\partial k_p \, \partial \xi}\left\{\frac{\partial \bar{\xi}}{\partial \sigma}\right\} \tag{3.144}$$

$\left\{\frac{\partial \bar{\xi}}{\partial \sigma}\right\}$ can be determined directly from

$$\bar{\xi} = \frac{\sigma_1 + \sigma_2 + \sigma_3}{f_c} \tag{3.145}$$

thus

$$\left\{\frac{\partial \bar{\xi}}{\partial \sigma}\right\} = \left\{\frac{1}{\sqrt{3} f_c}\right\} \tag{3.146}$$

while

$$\frac{\partial^2 F}{\partial k_p \partial \xi} = \frac{\partial^2 F}{\partial k \partial \xi}\frac{\partial k}{\partial k_p} \tag{3.147}$$

This derivative can be determined using (3.126)

$$\frac{\partial^2 F}{\partial k \partial \xi} = -\frac{\partial^2 \rho_f}{\partial \xi_0 \partial \xi}\frac{\partial \xi_0}{\partial k} \tag{3.148}$$

where $\frac{\partial \xi_0}{\partial k}$ is given by (3.125), while $\frac{\partial^2 \rho_f}{\partial \xi_0 \partial \xi}$ is to be calculated independently for each zone.

In Zone 1, the yield function is independent of k, and therefore:

$$\frac{\partial^2 F}{\partial \xi_0 \partial \xi} = 0 \tag{3.149}$$

In Zone 2, by taking the derivative of $\frac{\partial \rho_f}{\partial \xi_0}$ (which is given by (3.128)) with respect to ξ_0, we obtain:

$$\frac{\partial^2 F}{\partial \xi_0 \partial \xi} = 4\frac{\partial a}{\partial \xi_0}\bar{\xi}^3 + 3\frac{\partial b}{\partial \xi_0}\bar{\xi}^2 + 2\frac{\partial c}{\partial \xi_0}\bar{\xi} + \frac{\partial d}{\partial \xi_0} \tag{3.150}$$

In Zone 3, by taking the derivative of $\frac{\partial \rho_f}{\partial \xi_0}$ (which has been expressed in (3.130)) with respect to ξ_0, the derivative is:

$$\frac{\partial^2 F}{\partial \xi_0 \partial \xi} = 4\frac{\partial a}{\partial \xi_0}{\xi_3}^3 + 12\,a{\xi_3}^2\frac{\partial \xi_3}{\partial \xi_0} + 3\frac{\partial b}{\partial \xi_0}{\xi_3}^2 + 6\,b\xi_3\frac{\partial \xi_3}{\partial \xi_0} + 2\frac{\partial c}{\partial \xi_0}\xi_3 + 2\,c\frac{\partial \xi_3}{\partial \xi_0} + \frac{\partial d}{\partial \xi_0} \tag{3.151}$$

Finally, for Zone 4, by taking the derivative of $\frac{\partial \rho_f}{\partial \xi_0}$ (which is given by (3.132)) with respect to ξ_0:

$$\frac{\partial^2 F}{\partial \xi_0 \partial \xi} = \frac{-36\,(1/6)^\gamma\sqrt{6}\left(-m+\sqrt{\beta_3}\right)^\gamma\gamma^2 m^2}{\beta_3\left(-m+\sqrt{\beta_3}\right)^2} + \frac{36\,(1/6)^\gamma\sqrt{6}\left(-m+\sqrt{\beta_3}\right)^\gamma\gamma\,m^2}{{\beta_3}^{3/2}\left(-m+\sqrt{\beta_3}\right)} + \frac{36\,(1/6)^\gamma\sqrt{6}\left(-m+\sqrt{\beta_3}\right)^\gamma\gamma\,m^2}{\beta_3\left(-m+\sqrt{\beta_3}\right)^2} \tag{3.152}$$

3.5.3 Stress Derivatives

The partial derivatives of the yield function with respect to the stress tensor is obtained by applying the chain rule of differentiation. Recall (3.77); each term which appears in the equation is dependant on the stress state. Therefore the first derivative of the yield function with respect to the stresses is expressed as follows:

$$\left\{\frac{\partial F}{\partial \sigma}\right\} = \bar{\rho}\left\{\frac{\partial r}{\partial \sigma}\right\} + r\frac{\partial \bar{\rho}}{\partial J_2}\left\{\frac{\partial J_2}{\partial \sigma}\right\} - \frac{\partial \rho_f}{\partial \bar{\xi}}\left\{\frac{\partial \bar{\xi}}{\partial \sigma}\right\} \tag{3.153}$$

where J_2 is the second deviatoric stress invariant.

The second derivatives of the yield function with respect to the stresses are given by

$$\left[\frac{\partial^2 F}{\partial \sigma^2}\right] = \left[\frac{\partial^2 r}{\partial \sigma^2}\right] \bar{\rho} + \frac{\partial \bar{\rho}}{\partial J_2}\left\{\frac{\partial J_2}{\partial \sigma}\right\}\left\{\frac{\partial r}{\partial \sigma}\right\} + \frac{\partial^2 \bar{\rho}}{\partial J_2}\left\{\frac{\partial J_2}{\partial \sigma}\right\}\left\{\frac{\partial J_2}{\partial \sigma}\right\} r + \left[\frac{\partial^2 J_2}{\partial \sigma^2}\right]\frac{\partial \bar{\rho}}{\partial J_2} r + \left\{\frac{\partial r}{\partial \sigma}\right\}\frac{\partial \bar{\rho}}{\partial J_2}\left\{\frac{\partial J_2}{\partial \sigma}\right\} - \frac{\partial^2 \rho_f}{\partial \xi^2}\left\{\frac{\partial \bar{\xi}}{\partial \sigma}\right\}\left\{\frac{\partial \bar{\xi}}{\partial \sigma}\right\} \tag{3.154}$$

The first derivative of r with respect to the stress tensor is given as:

$$\left\{\frac{\partial r}{\partial \sigma}\right\} = \frac{\partial r}{\partial \xi}\left\{\frac{\partial \bar{\xi}}{\partial \sigma}\right\} + \frac{\partial r}{\partial \theta}\left\{\frac{\partial \theta}{\partial \sigma}\right\} \tag{3.155}$$

The second derivative is

$$\left[\frac{\partial^2 r}{\partial \sigma^2}\right] = \frac{\partial^2 r}{\partial \xi^2}\left\{\frac{\partial \bar{\xi}}{\partial \sigma}\right\}\left\{\frac{\partial \bar{\xi}}{\partial \sigma}\right\} + \frac{\partial^2 r}{\partial \xi \partial \theta}\left\{\frac{\partial \theta}{\partial \sigma}\right\}\left\{\frac{\partial \bar{\xi}}{\partial \sigma}\right\} + \frac{\partial^2 r}{\partial \theta \partial \xi}\left\{\frac{\partial \bar{\xi}}{\partial \sigma}\right\}\left\{\frac{\partial \theta}{\partial \sigma}\right\} + \left[\frac{\partial^2 r}{\partial \theta^2}\right]\left\{\frac{\partial \theta}{\partial \sigma}\right\} + \left[\frac{\partial^2 \theta}{\partial \sigma^2}\right]\frac{\partial r}{\partial \theta} \tag{3.156}$$

The details of derivations of $\frac{\partial r}{\partial \theta}$, $\frac{\partial^2 r}{\partial \xi^2}$, $\frac{\partial^2 r}{\partial \xi \partial \theta}$, $\left\{\frac{\partial \theta}{\partial \sigma}\right\}$, $\left[\frac{\partial^2 r}{\partial \theta^2}\right]$, $\left[\frac{\partial^2 \theta}{\partial \sigma^2}\right]$ can be found in the appendix.

The first and second partial derivatives of F with respect to ξ have been calculated separately for each zone.

In Zone 1 and from (3.78):

$$\frac{\partial \rho_f}{\partial \xi} = \frac{-2\,(1/6)^\gamma \sqrt{6}\left(-m+\sqrt{\beta}\right)^\gamma \gamma \sqrt{3} m}{\sqrt{\beta}\left(-m+\sqrt{\beta}\right)} \tag{3.157}$$

$$\frac{\partial^2 \rho_f}{\partial \xi^2} = \frac{36\,(1/6)^\gamma \sqrt{6}\left(-m+\sqrt{\beta}\right)^\gamma \gamma^2 m^2}{\beta\left(-m+\sqrt{\beta}\right)^2} - \frac{36\,(1/6)^\gamma \sqrt{6}\left(-m+\sqrt{\beta}\right)^\gamma \gamma m^2}{\beta^{3/2}\left(-m+\sqrt{\beta}\right)} - \frac{36\,(1/6)^\gamma \sqrt{6}\left(-m+\sqrt{\beta}\right)^\gamma \gamma m^2}{\beta\left(-m+\sqrt{\beta}\right)^2} \tag{3.158}$$

In Zone 2, from (3.79):

$$\frac{\partial \rho_f}{\partial \xi} = 4a\bar{\xi}^3 + 3b\bar{\xi}^2 + 2c\bar{\xi} + d \tag{3.159}$$

$$\frac{\partial^2 \rho_f}{\partial \bar{\xi}^2} = 12a\bar{\xi}^2 + 6b\bar{\xi} + 2c \tag{3.160}$$

In Zone 3, from (3.97):

$$\frac{\partial \rho_f}{\partial \xi} = -\left(4a\bar{\xi_3}^3 + 3b\bar{\xi_3}^2 + 2c\bar{\xi_3} + d\right) \tag{3.161}$$

$$\frac{\partial^2 \rho_f}{\partial \bar{\xi}^2} = 12\,a\,\bar{\xi_3}^2 + 6\,b\,\bar{\xi_3} + 2\,c \tag{3.162}$$

In Zone 4, from (3.99):

$$\frac{\partial \rho_f}{\partial \xi} = \frac{2\,(1/6)^\gamma \sqrt{6}\left(-m+\sqrt{\beta_3}\right)^\gamma \gamma \sqrt{3} m}{\sqrt{\beta_3}\left(-m+\sqrt{\beta_3}\right)} \tag{3.163}$$

$$\frac{\partial^2 \rho_f}{\partial \xi^2} = \frac{36\,(1/6)^\gamma \sqrt{6}\left(-m+\sqrt{\beta_3}\right)^\gamma \gamma^2 m^2}{\beta_3\left(-m+\sqrt{\beta_3}\right)^2} - \frac{36\,(1/6)^\gamma \sqrt{6}\left(-m+\sqrt{\beta_3}\right)^\gamma \gamma m^2}{{\beta_3}^{3/2}\left(-m+\sqrt{\beta_3}\right)} - \frac{36\,(1/6)^\gamma \sqrt{6}\left(-m+\sqrt{\beta_3}\right)^\gamma \gamma m^2}{\beta_3\left(-m+\sqrt{\beta_3}\right)^2} \tag{3.164}$$

The first and second derivatives of $\bar{\rho}$ with respect to the second deviatoric stress invariant J_2 are given from

$$\bar{\rho} = \frac{\sqrt{2J_2}}{f_c} = \frac{\sqrt{(\sigma_1-\sigma_2)^2+(\sigma_2-\sigma_3)^2+(\sigma_3-\sigma_1)^2}}{\sqrt{3} f_c} \tag{3.165}$$

thus

$$\frac{\partial \bar{\rho}}{\partial J_2} = \frac{1}{f_c\,\rho} \tag{3.166}$$

and

$$\frac{\partial^2 \bar{\rho}}{\partial J_2^2} = \frac{-1}{f_c\,\rho^3} \tag{3.167}$$

The first and second derivatives of J_2 with respect to the stress tensor are given in the appendix.

3.5.4 The Derivatives of the Hardening Function

Recall (3.27)

$$h = \frac{\sqrt{\left\{\frac{\partial F}{\partial \sigma}\right\}^T \left\{\frac{\partial F}{\partial \sigma}\right\}}}{\zeta} \tag{3.168}$$

The first derivative of h with respect to the stress tensor is

$$\left\{\frac{\partial h}{\partial \sigma}\right\} = \frac{\left(\left[\frac{\partial^2 F}{\partial \sigma^2}\right]\cdot\left\{\frac{\partial F}{\partial \sigma}\right\}\right) + \left(\left\{\frac{\partial F}{\partial \sigma}\right\}\cdot\left[\frac{\partial^2 F}{\partial \sigma^2}\right]\right)}{2\,h\,\zeta^2} - \frac{h\,\left\{\frac{\partial \zeta}{\partial \sigma}\right\}}{\zeta} \tag{3.169}$$

and

$$\frac{\partial h}{\partial k_p} = \frac{\partial h}{\partial k}\frac{\partial k}{\partial k_p} \tag{3.170}$$

where

$$\frac{\partial h}{\partial k} = \frac{\left(\left\{\frac{\partial^2 F}{\partial \sigma \partial k}\right\} \cdot \left\{\frac{\partial F}{\partial \sigma}\right\}\right) + \left(\left\{\frac{\partial F}{\partial \sigma}\right\} \cdot \left\{\frac{\partial^2 F}{\partial \sigma \partial k}\right\}\right)}{2\, h\, \zeta^2} \tag{3.171}$$

which can be simplified to:

$$\frac{\partial h}{\partial k} = \frac{\left\{\frac{\partial^2 F}{\partial \sigma \partial k}\right\} \cdot \left\{\frac{\partial F}{\partial \sigma}\right\}}{h\, \zeta^2} \tag{3.172}$$

3.6 Concluding Remarks

The newly proposed constitutive model for plain concrete under multiaxial compression has the following features:

1. The new formulation of the yield surfaces captures the fundamental requirements of simulating plastic compaction and dilation.

2. The yield surfaces are convex, smooth, C_2 continuous and intersect the hydrostatic axis in the compression and tension regions without vertices.

3. The model is constructed within a classical isotropic elasto-plastic framework, based on a study of the plastic strain rate vectors and the assumption of an associated flow rule.

4. The proposed model is capable of fulfilling the normality condition needed for associated plasticity.

5. The deviatoric cross-sections of the yield surface have a general elliptic form which includes a control point on the shear meridian, in addition to control points on the compression and extension meridians.

6. The hardening function has been formulated to introduce a control of the initial slope of the k-k_p curve. This enables the nonlinear multiaxial deformation to be simulated in a realistic way.

7. The ductility measure is expressed using an exponential function using just two parameters.

8. An auxiliary stress surface has been introduced to deal with stress states which fall outside the zone where the yield function is undefined.

9. The concept of the reflected yield surface and the ductility dependent hardening function could be introduced into other formulations with different PNS descriptions.

10. In total, thirteen material constants are available to calibrate the model. Some of these may take default values, if experimental data has not been captured for a particular concrete. The calibration, sensitivity study, and simulation procedures are described in Chapter 4.

3.7 References

Bažant Z. P., Caner F. C., Carol I., Adley M. D. and Akers S. A., 2000, Microplane model M4 for concrete, I: Formulation with work- conjugate deviatoric stress, *Journal of Engineering Mechanics. ASCE*, Vol. 126, No. 9, pp. 944-953.

Bažant Z. P. and Prat P. C., 1988a, Microplane model for brittle-plastic material. I: Theory, *Journal of Engineering Mechanics.ASCE*, Vol. 114, No. 10, pp. 1672-1687.

Bažant Z. P. and Prat P. C., 1988b, Microplane model for brittle-plastic material. II: Verification, *Journal of Engineering Mechanics.ASCE*, Vol. 114, No. 10, pp. 1689-1702.

Bažant Z. P., Xiang Y. and Prat P. C., 1996a, Microplane model for concrete. I: stress-strain boundaries and finite strain, *Journal of Engineering Mechanics*, Vol. 122, No. 3, pp. 245-254.

Bažant Z. P., Xiang Y. Y., Adley M. D., Prat P. C. and Akers S. A., 1996b, Microplane model for concrete. II: Data delocalization and verification, *Journal of Engineering Mechanics.ASCE*, Vol. 122, No. 3, pp. 255-262.

Bićanić N. and Pearce C. J., 1996, Computational aspects of a softening plasticity model for plain concrete, *Mechanics of Cohesive-Frictional Materials*, Vol. 1, pp. 75-93.

Bhowmik S. K. and Long J. H., 1990, A general formulation for the cross-sections of yield surfaces in octahedral planes, NUMENTA 90, Pande and Middleton (Eds.), Elsevier, 795-803.

Borja R.I., Sama, K.M., and Sanz, P.F., 2003, On the numerical integration of three-invariant elastoplastic constitutive models, *Computer Methods in Applied Mechanics and Engineering* ,**192**, pp. 1227-1258.

Carol I., Jirasek M. and Bažant Z., 2001a, A thermodynamically consistent approach to microplane theory. Part I: Free energy and consistent microplane stresses, *International Journal of Solids and Structures*, Vol. **38**, No. 17, pp. 2921-2931.

Carol I., Lopez C. M. and Roa O., 2001b, Micromechanical analysis of quasi-brittle materials using fracture-based interface elements. *International Journal for Numerical Methods in Engineering*, Vol. **52**, No. 1-2, pp. 193-215.

Carol I., Prat P. C. and Bažant Z. P., 1992, New explicit microplane model for concrete - theoretical aspects and numerical implementation, *International Journal of Solids and Structures*, Vol. **29**, No. 9, pp. 1173-1191.

Carol I., Rizzi E. and Willam K., 2001c, On the formulation of anisotropic elastic degradation. I: Theory based on a pseudo-logarithmic damage tensor rate, *International Journal of Solids and Structures*, Vol. **38**, No. 4, pp. 491-518.

Chen W. F., and Saleeb A. F., 1994 a, Constitutive equations for engineering materials, Volume 1: Elasticity and Modelling, Elsevier.

Chen W. F., and Saleeb A. F., 1994 b, Constitutive equations for engineering materials, Volume 1: Plasticity and Modelling, Elsevier.

Crouch R., 1990, Nonlinear deformation of concrete subjected to multiaxial compression, Doctoral thesis, The University of Manchester.

Desai C.S. and Siriwardane, H.J., 1984, Constitutive laws for engineering materials, with emphasis on geologic materials, Prentice-Hall, Englewood Cliffs, New Jersey.

Drucker D. C. and Prager, W., 1952, Soil mechanics and plastic analysis or limit design, *Quar. Appl. Math*, Vol. **10**, pp. 157-165.

Drucker D. C., 1950, Some implications of work-hardening and ideal plasticity, *Quart. Applied Math*, Vol. **7**, pp. 411-418.

Drucker D. C., 1951, A more fundamental approach to stress-strain relations, *Proc. First U. S. National Congress on Applied Mechanics*, ASME, pp. 487-491.

Drucker D. C., 1959, A definition of stable inelastic material, *Journal of Applied Mechanics*, Vol. **26**, pp. 101-106.

Drucker D. C., 1964, On the postulate of stability of material in the mechanics of continua, *Journal de Mecanique*, Vol. **3**, pp. 235-249.

Etse G., and Willam K. J., 1994, Fracture energy formulation for inelastic behaviour of plain concrete, *ASCE, Journal of Engineering Mechanics*, Vol. **120**, 9, pp. 1983-2011.

Grassl P., 2004, Plasticity and damage mechanics for modelling concrete failure, Doctoral thesis, Chalmers University of Technology, Göteborg, Sweden.

Hoek E. and Brown E. T., 1980, Empirical strength criterion for rock masses, *ASCE J Geotech Eng*, Vol. 106, No. 9, pp. 1013-1035.

Kachanov L.M., 1958, Time of the rupture process under creep conditions, Izvestia Akademii Nauk, USSR, Otdelenie Teknicheskikh Nau Izvestiya, Vol. 8, pp. 26-31.

Khan and Huang S. A. and Huang S., 1995, Continuum theory of plasticity, John Wiley.

Kotsovos M. D., Newman J. B., 1978, Generalised stress-strain relations for concrete, Journal of Engineering Mechanics, ASCE, Vol. 104, No. EM4, pp. 845-856.

Krajcinovic D. and Fonseca G. U., 1981, The continuous damage theory of brittle materials part 1: general theory, J*ournal of Applied Mechanics*, vol. 48, pp. 809-815.

Kuhl E., Steinmann P. and Carol I., 2001, A thermodynamically consistent approach to microplane theory, Part II, Dissipation and inelastic constitutive modeling, *International Journal of Solids and Structures*, Vol. **38**, No. 17, pp. 2933-2952.

Kupfer, H., 1973 Das Verhalten des Betons unter mehrachsiger Kurzzeitbelastung unter besonderer Berücksichtigung der zweiachsiger Beanspruchung. In: Deutcher

Ausschluss für Stahlbeton, Vol. 229, Berlin.

Li T., 2005, Stress integration strategies for a new hardening/softening elasto-plasticity model for structural concrete, Doctorate thesis, The University of Sheffield.

Leon A., 1935, Uber die Scherfestigkeit des Betons, *Beton und Eisen*, Vol. **34**, pp. 130-135.

MAPLE, www.maplesoft.com/whatismaple.aspx

Mazars J. and Pijaudier-Cabot G., 1996, From damage to fracture mechanics and conversely: A combined approach, *International Journal of Solids and Structures*, Vol. **33**, No. 20-22, pp. 3327-3342.

Menétry Ph. and Willam K. J., 1995, Triaxial failure criterion for concrete and its generalization, *ACI, J. Struct.*, Vol. **92, 3**, pp. 311-318.

Mohr O., 1900, Welche umstande bedingen die elastizitatsgrenze und den bruch eines materials, *Z Veriens Dtsch. Ing.*, Vol. 44, pp. 1525-1572.

Najjar, Y. M., Zaman, M., and Faruque M. O., 1993 ,Modelling of stress-strain behavior of plain concrete using a plasticity framework, *Materials and Structures*, Vol. **26**, pp. 129-135.

Ohtani Y, and Chen W. F., 1987, Multiple hardening plasticity for concrete materials,ASCE, *Journal of Engineering Mechanics*, Vol. **114**, No. 11, pp. 1890-1910.

Ortiz M. and Simo J. C., 1986, Analysis of a new class of integration algorithms for elasto-plastic constitutive relations, *International Journal for Numerical Methods in Engineering,* Vol. **23**, pp. 353-366.

Ottosen N.S., 1977, A failure criterion for concrete, *Journal of Engineering Mechanics*, ASCE, Vol. **103**, pp. 527535.

Ožbolt J. and Bažant Z. P., 1992, Microplane model for cyclic triaxial behaviour of concrete, *Journal of Engineering Mechanics-ASCE*, Vol. **118**, No. 7, pp. 1365-1386.

Ožbolt J., Li Y. J. and Kožar I., 2001, Microplane model for concrete with relaxed kinematic constraint, *International Journal of Solids and Structures*, Vol. **38**, No. 16, pp. 2683-2711.

Peerlings R. H. J., 1999, Enhanced damage modelling for fracture and fatigue, Doctoral Thesis, Eindhoven University of Technology, Eindhoven, The Netherlands.

Pramono E. and Willam K J, 1989, Implicit integration of composite yield surfaces with corners, *International Journal of Engineering Computations*, Vol. **6**, pp. 186-198.

Qui Y., 1999, An investigation into the microplane model for concrete, Doctoral thesis, Department of Civil and Structural Engineering, University of Sheffield, UK.

Runesson K., Sture S. and Willam K., 1988, Integration in computational plasticity, *Computer and Structures*, Vol. **30**, pp. 119-130.

Simo J. C., and Hughes T. J. R., 1987, General return mapping algorithms for rate independent plasticity, In Constitutive Equations for Engineering Materials, Desai (Ed.), Elsevier, pp. 221-231.

Tahar B., 2000, C_2 Continuous hardening/softening elasto-plasticity model for concrete, Doctoral thesis, The University of Sheffield, UK.

Von Mises, R., 1913, Mechanik der festen Körper im plastsch deformablen Zustand, *Götting Nachr. Math. Phys*, **K1**, pp. 582-592.

Vonk R., 1992, Softening of concrete loaded in compression, Doctoral thesis, Eindhoven University of Technology, Eindhoven, The Netherlands, p. 197.

Wastiels J., 1979, Failure criteria for concrete under multiaxial stress states, Plasticity in Reinforced Concrete, IABSE 29, pp. 63-10.

Willam K. J. and Warnke E. P., 1974, Constitutive model for the triaxial behaviour of concrete, *IABSE Seminar on Concrete Structures Subjected to Triaxial Stresses III-1*, **184**.

Chapter 4

Calibration and Simulations

4.1 Introduction

Reliability of constitutive models for any material depends on their performance to simulate the stress-strain response of the material under various loading histories. In the previous chapter, the mathematical formulation of the model has been described. Although the construction of the model is based on the experimental observation which has been presented in Chapter 2, the validation of the model relies on its performance against all possible stress histories consisting of arbitrary load paths, unloading, stress reversal, and reloading. Any element of a real structure could be expected to be exposed to such load sequences during its life-time.

In this chapter, calibration and simulation of the model at a material level using triaxial and multiaxial compression test data are presented. The model contains thirteen material constants that need careful value selection in order to attain close agreement with experimental observation.

Section 4.2 presents the full set of these material constants which are divided into three groups: elastic, PNS and hardening constants. The calibration process for these material constants is discussed in Section 4.3. This process enables the user to identify near optimum value for each constant. The sensitivity analysis of each material constant reveals its influence on the response of the model. This has been done at two levels, local and global. The local level addresses the influence of each constant on the part of the model which it controls, while the global level addresses the influence on the stress-strain response. This work is presented in section 4.4. In the last section, the simulations of the model for two sets of experimental data are presented;

(i) triaxial compression tests conducted at the University of Sheffield

(ii) a set of multiaxial compression tests carried out at Colorado University.

Concluding remarks are appended at the end of the chapter.

4.2 Material Constants

As noted in the introduction to this chapter, the full set of material constants for the new elasto-plastic model consists of thirteen constants. However, nine of these constants can be fixed with a default values. These material constants can be grouped into the following three categories:

1. The elastic constants (which control the initial stiffness): Young's modulus (E) and Poisson's ratio (ν). By using these two constants alone, an isotropic linear elastic behaviour may be described.

2. The PNS constants: the uniaxial compressive strength f_c, the uniaxial tensile strength f_t, the deviatoric shape factor α and the meridional shape factor γ. Adding this set of constants to the elastic constants allows an elastic-perfectly plastic behaviour to be described.

3. The hardening constants: the yield surface constant α_1, the plastic volume transition constant α_2, the initial hardening variable k_0, the hydrostatic intersection factor A_k, the initial slope factor s_0 and the hardening factors A_h and B_h. Adding this set of constants to the previous two sets describes an elastic-hardening plastic behaviour.

Table 4.1 shows a list of the constants classified according to the three categories, elastic, PNS and hardening. Ten of these constants are dimensionless, with units required only for E, f_c, and f_t.

4.3 Calibration

The calibration process for the material constants is discussed such that the optimum values may be obtained by examining laboratory data. The experimental results used for the calibration process here are those of Hoek cell tests undertaken in the Department of Civil and Structural Engineering at the University of Sheffield during 1999. In the triaxial cell tests, the axial forces are applied on the specimen by means of an axial load system, and the radial compressive forces are applied by pressurising the fluid in the reservoir of the cell. Cyclic loading with different

Group	Symbol	Material constant
Elastic	ν	Poisson's ratio
	E	Young's modulus
PNS	f_c	Uniaxial compressive strength
	f_t	Uniaxial tensile strength
	γ	PNS meridional shape constant
	α	PNS deviatoric shape constant
Hardening	α_1	Yield surface constant
	α_2	Volume transition constant
	k_0	Initial hardening surface constant
	s_0	Hardening meridional shape constant
	A_k	Hydrostatic intersection constant
	A_h	Ductility constant
	B_h	Ductility constant

Table 4.1: The model material constants classified into three groups

level of confinements have been reported [Crouch *et. al.*, 2001]. Another set of data was produced by a test program undertaken at the University of Colorado during 1981 and 1982 using multiaxial compression on cubic specimens [Scavuzzo, 1982; Stankowski, 1983]. The constants are now discussed in the same order as they appear in Table 4.1.

4.3.1 Poisson's Ratio, ν

The ratio of lateral to axial strain is called Poisson's ratio. A common value used is 0.20 to 0.21, although the value may vary from 0.15 to 0.25 depending upon the aggregate, moisture content, concrete age, and compressive strength [Neville].

From the elementary isotropic form for Hooke's law

$$\Delta\varepsilon_1 = \frac{1}{E}(\Delta\sigma_1 - \nu(\Delta\sigma_2 + \Delta\sigma_3)) \tag{4.1}$$

$$\Delta\varepsilon_2 = \frac{1}{E}(\Delta\sigma_2 - \nu(\Delta\sigma_1 + \Delta\sigma_3)) \tag{4.2}$$

$$\Delta\varepsilon_3 = \frac{1}{E}(\Delta\sigma_3 - \nu(\Delta\sigma_2 + \Delta\sigma_1)) \tag{4.3}$$

where ν is poisson's ratio; E is the modulus of elasticity, σ_1, σ_2, and σ_3, are principle stresses and $\varepsilon_1, \varepsilon_2$, and ε_3, are principal strains.

For the set of Sheffield triaxial experimental data with cylindrical specimens, the intermediate and minor principal stresses are equal ($\sigma_2 = \sigma_3$).

Solving the above equations for Poisson's ratio,

$$\nu = \frac{(\Delta\sigma_2\Delta\varepsilon_1) - (\Delta\sigma_1\Delta\varepsilon_2)}{(\Delta\varepsilon_1\Delta\sigma_1) + (\Delta\sigma_2\Delta\varepsilon_1) - (2\Delta\sigma_2\Delta\varepsilon_2)} \tag{4.4}$$

Where $\Delta\sigma_2$ is the change in the lateral stress; $\Delta\varepsilon_1$ is the change in the axial strain and $\Delta\sigma_1$ is the change in the axial stress; $\Delta\varepsilon_2$ is the change in the lateral strain. The change (Δ) is taken from the unloading and reloading points on the stress-strain curve as shown in Figure 2.7. The procedure to calculate Poisson's ratio is as follows:

1. Identify the loading unloading points on the experimental stress strain curves.
2. Identify the change in the principal stresses ($\Delta\sigma_1$, $\Delta\sigma_2$ and $\Delta\sigma_3$) and the principal strains ($\Delta\varepsilon_1$, $\Delta\varepsilon_2$, and $\Delta\varepsilon_3$).
3. Calculate Poisson's ratio for each cycle using the formula 4.4
4. Select the appropriate value or take the average of all the cycles (see Chapter 2).

The overall average value of Poisson's ratio of all twenty seven specimens from Sheffield experiments for all loading cycles is found to be 0.23 and the standard deviation is 0.02.

4.3.2 Young's Modulus, E

Since the stress-strain curve for concrete is not linear, the modulus may be taken from different parts of the σ-ε curve as discussed in Chapter 2. In this study, the unloading chord modulus has been used to represent Young's modulus. It is the modulus calculated from the unloading to the loading points on the stress strain curves (see Figure 2.7). In Chapter 2, the Young's modulus from the Sheffield tests for each cycle has been calculated using the following formula

$$E = \frac{\Delta\sigma_1 - 2\,\nu\,\Delta\sigma_2}{\Delta\varepsilon_1} \tag{4.5}$$

For the concrete mix with $f_c = 58$ MPa the average value of the modulus for all cycles is found to be 50.5 GPa, the average value of the modulus for the first cycles of loading is 51.1 GPa and the average value for the last loading cycles is 50 GPa.

The values of Young's modulus calculated from the first loading cycles is thought to be more representative for the modulus of elasticity. This is because firstly, it represents the material before the propagation of microcracks, secondly, the modulus is thought to be a material constant and should be independent from the stress path. Therefore, the modulus for the first cycle has been selected in this study.

4.3.3 Uniaxial Compressive Strength, f_c

The uniaxial compressive strength is the most common test preformed on concrete. However, it is surprising that with the advanced methods and techniques today available, the reliable determination of concrete strength is still a very difficult tasks. Uniaxial compression test results are subject to several causes of variation owing to the different test methodologies and apparatus used. Among the different causes of variation we can consider, for example, the sample size; the method of load application; the rate of loading [Riisch]; and in particular the boundary conditions (confinement conditions, the kind of contact between specimen surface and loading plate, and the type of loading system) [Fumagalli]. Various ways to carry out the test are described in different codes of practice. There are in general three different ways:

1. ASTM C 39 (Cylinder Test): The normal compressive specimen in North America is a cylinder with length to diameter ratio of 2:1. Since strength is dependent on loading rate, the specimen should be loaded at a controlled rate of 20 to 50 lb/in^2/s (0.14 to 0.34 MPa/sec) or a deformation rate of 0.05 in/min (1.27 mm/min).

2. Cube Test BS1881-120 (Cube test): Standard in Great Britain and Germany, uses a 6 in (152.4 mm) cubic mold, which is filled in three layers, rodded 35 times with a 25 mm square rod or compacted with a vibrator. The cube is tested at right angles to the position casted and therefore requires no capping or grinding. The loading rate is 33 lb/in^2/s (0.23 MPa/sec).

3. Prism Test (ASTM C 116): Developed to test compressive strength from broken portions of beams tested in flexure. This is a research test and is not an alternative to the cylinder test.

Cube tests - in general - provide higher values than the cylinder tests. The cylinder/cube ratio depends on various constants, including the compressive strength of the concrete. A number of studies have been carried out in order to express the variation of the ratio with cube strength. It is generally found that the ratio, which

is about 0.82 for ordinary concrete, approaches the value one when the strength increases. However, it has been known for a long time that the ratio, depends on other factors, for instance the maximum size of aggregate [Gyengo]. The sensitivity of the material to the curing process could be a relevant parameter also, because the surface/volume ratio is generally higher for cubes. Apart from these three factors related to the material itself, other factors, related to the specimen, are of importance. The size of the specimen, whatever the shape, influences the compressive strength (a bigger specimen leading to lower mean value and lower standard deviation). Finally, the end condition of a specimen plays a role, especially for cylinders, as cubes are generally tested directly by the lateral faces (as compared with the casting position), without any treatment (this is the main interest of the cube) [De Larrard *et al.*]. The mean value of the uniaxial compression strength in the Sheffield tests was found to be 58 MPa.

4.3.4 Uniaxial Tensile Strength, f_t

The value of the uniaxial tensile strength can be determined from three types of tests:

1. Direct tension test: This test is performed by the application of direct and pure tension force. However, the application of such a force free from eccentricity, is very difficult. A test using bonded end plates, is prescribed by the U.S. Bureau of Reclamation.

2. Flexure test: In these tests, a plain (unreinforced) concrete beam is subjected to flexure using symmetrical *two-point loading* until failure occurs. British Standards BS 1881:Part 118:1983 prescribes third-point loading on 150 by 150 by 750 mm beams supported over a span of 450 mm. 100 by 100 beams can also be used, provided the beam side is at least three times the maximum size of aggregate.

   The requirement of ASTM C 78-94 are similar to those of BS 1881:Part 118:1983. There exist also a test for flexural strength under *center-point* loading, prescribed in ASTM C 293-94, but no longer covered by a British Standard.

3. Splitting tension test: In this test, a concrete cylinder, of the type used for compression tests is placed with its axis horizontal between the platens of a testing machine, and the load is increased until failure by indirect tension

in the form of splitting along the vertical diameter takes place. This test is prescribed in BS 1881-117:1983 and ASTM C 496-90.

The value of f_t adopted here, was the value obtained from the triaxial compression tests by applying the following procedure:

1. Determine the values of the peak nominal stresses envelope (PNS) experimentally.
2. Identify the best value for the PNS constant m by the mean of the least square optimisation between the experimental values and the values calculated from the equation (3.62) using the existing value of f_c and γ.
3. Solve the equation (3.66) numerically for f_t.

The value of f_t for the tests carried out at the University of Sheffield is found to be 4.25 MPa ($0.07 f_c$).

4.3.5 PNS meridional Shape Constant, γ

The material constant γ has been introduced by Tahar to ensure continuity of the yield surface in the hydrostatic tensile region [Tahar]. On the basis of several investigations, Tahar recommends that a value of 0.99 be assumed for all structural concrete. The location of the PNS for $\gamma = 1$ and $\gamma = 0.99$ are almost identical. However, it is only when $\gamma < 1$ that C_- continuity of the surface is obtained. If the experimental data suggest that the PNS and residual surfaces are better simulated by lower values of γ, then a least squares error minimisation approach could be used to obtain the optimum value .

4.3.6 PNS Deviatoric Shape Constant, α

α may be determined on the basis of the biaxial compressive strength under a stress ratio of 1:0.5 assuming $\bar{f}_t$ and γ have already been found. The procedure is as follows:

1. Given the experimental result $\bar{\sigma}_1$ (knowing that $\bar{\sigma}_2 = 0.5\bar{\sigma}_1$ and $\bar{\sigma}_3 = 0$) find the corresponding value for $\bar{\xi}$ using equation (2.22)
2. Given $\bar{\xi}$ calculate the corresponding values for $\bar{\rho}_c$ (3.62) and $\bar{\rho}_e$ (3.63)
3. Calculate $\bar{\rho}_s$ using $\bar{\rho}_s = \sqrt{\frac{\bar{\sigma}_2^2}{2}}$

4. Insert the values of B_0 and B_1 into

$$\alpha = \frac{B_1 - \frac{\sqrt{3}B_0}{1+B_0}}{\frac{2B_0}{\sqrt{3}} - \frac{\sqrt{3}B_0}{1+B_0}} \tag{4.6}$$

Using this approach together with the classical biaxial data of Kupfer *et al.* (1969), Tahar obtained a value of $\alpha = 0.8$. It has been noticed that a slightly reduced value of α can provide a better fit to biaxial stress ratios less than 1:0.5. Note that an alternative method of calculating α could be to examine results from multi-axial compression testing in a given deviatoric plane for Lode angles $-\frac{\pi}{6}$, 0 and $\frac{\pi}{6}$. For the case where data is not available, a default value of 0.8 could be assumed.

4.3.7 Yield Surface Constant α_1

This is the constant which controls the common point at the PNS, or in other words the beginning of zone 2 of the yield surface. Two proposal have been introduced in Chapter 3. The first proposal is the one which has been used in this study for the reasons mentioned there (see Section 3.4.3). The value of this constant is found to be in the range between 0.2 and 0.4. Default value of 0.25 can be assumed.

4.3.8 Volumetric Transition Stress Constant α_2

This constant can be calibrated from the uniaxial compression tests as follows:

1. Calculate the volumetric plastic strain $\varepsilon_v^p = \varepsilon_1^p + \varepsilon_2^p + \varepsilon_3^p$.
2. Identify the stress state where ε_v^p value is at a minimum.
3. Calculate the $\bar{\xi}_{(VTS)}$ and $\bar{\rho}_{(VTS)}$ at this point
4. Identify $\bar{\rho}_{(PNS)}$ at the PNS that corresponds to the same point.
5. Calculate α_2

$$\alpha_2 = \frac{\bar{\rho}_{(VTS)}}{\bar{\rho}_{(PNS)}} \tag{4.7}$$

Experimental results from the previous chapter have indicated that under compressive loadings, dilation begins at about 90 percent of the peak stress. This is also supported by the findings of other researchers [Chen and Saleeb 1994b]. For Sheffield tests data, the overall value of this constant is found to be approximately 0.93.

4.3.9 Initial Hardening Surface constant, k_0, and Hydrostatic Intersection Constant, A_k

k_0 and A_k are the two constants that identify the initial yield surface which represent the limit of initial elasticity. To date, there have been no extensive experimental test programmes which have determined the size and shape of the initial yield surface for concrete in multi-axial stress space. This could be achieved by following small scale unloading-reloading stress probes in a multi-axial rig and monitoring when inelastic strains first appear after loading in different directions. Such a test programme has been undertaken at the University of Sheffield. Information of this kind is required in order to calibrate the material constants k_0 and A_k.

If hydrostatic compression test data are available and it is possible to detect the point at which non-linearity in the hydrostatic stress-strain curve first appears, then ξ_0 is known and A_k is given by

$$A_k = \xi_0 \, (1 - k_0) \tag{4.8}$$

The calibration of these two constants has been achieved by assuming a default value for $k_0 = 0.1$ and using the least square method to find the optimum value for A_k. This value is found to be in the range between 1.0 and 3.0.

4.3.10 Hardening Slope Constant, s_0

The role of this constant is to give an extra control over $k - k_p$ relationship by controlling the initial slope (Figure 3.11). This constant should take a finite positive value. The value which has been adopted throughout this study is 2.7.

4.3.11 Hardening Constants A_h and B_h

The hardening constants A_h and B_h (which control the value of the ductile measure ζ) are calibrated by means of the peak strains in uniaxial compression and triaxial compression (Figure 3.12). In the tensile region the variation in ζ is limited. The values for Sheffield tests for A_h and B_h are found to be 0.003 and 0.55 respectively, and for Colorado tests are 0.005 and 0.5. Typical ranges and default values of all constants for concrete are shown in Table 4.2.

	Material constant	Typical ranges	Default values
ν	Poisson's ratio	$0.15 \leftrightarrow 0.25$	0.2
E	Young's modulus	$15 \leftrightarrow 60$ GPa	NA
f_c	Uniaxial compressive strength	$20 \leftrightarrow 80$ MPa	NA
f_t	Uniaxial tensile strength	$2 \leftrightarrow 5$ MPa	$0.1 f_c$
γ	PNS meridional shape constant	$0.95 \leftrightarrow 0.999$	0.999
α	PNS deviatoric shape constant	$0.1 \leftrightarrow 0.9$	0.8
α_1	Yield surface constant	$0.2 \leftrightarrow 0.4$	0.25
α_2	Volume transition constant	$0.9 \leftrightarrow 0.95$	0.9
k_0	Initial hardening surface constant	$0 \leftrightarrow 0.3$	0.1
s_0	Hardening meridional shape constant	$1.0 \leftrightarrow 3.0$	2.7
A_k	Hydrostatic intersection constant	$0 \leftrightarrow 3$	1
A_h	Ductility constant	$0.003 \leftrightarrow 0.006$	NA
B_h	Ductility constant	$0.3 \leftrightarrow 1.5$	NA

Table 4.2: Model constants with typical ranges and default values for concrete

4.4 Sensitivity Study

In this section the sensitivity analysis of each constant is discussed, and how individual material constants affect the local and global response of the model. The local sensitivity illustrates the influence of each constant on that part of the model which is influenced by the constant, i.e the influence of the PNS constants on the PNS, the influence of the yield constants on the yield surface and the influence of the hardening constants on the hardening function.

The global study investigates the effect of changing the constants on the predictions of stress-strain results. The sensitivity is investigated for Sheffield tests data by fixing all but one of the material constants, then varying the constant by plus and minus the same value. In the following section, the sensitivity results from each of the material constants are discussed.

4.4.1 Poisson's ratio, ν

Figure 4.1 shows the stress-strain curves for sample 5-8a from the Sheffield tests with $\nu = 0.20$, 0.22 and 0.24. The model shows very little sensitivity to the change of ν. Higher value of ν results in only slight decrease in the stresses.

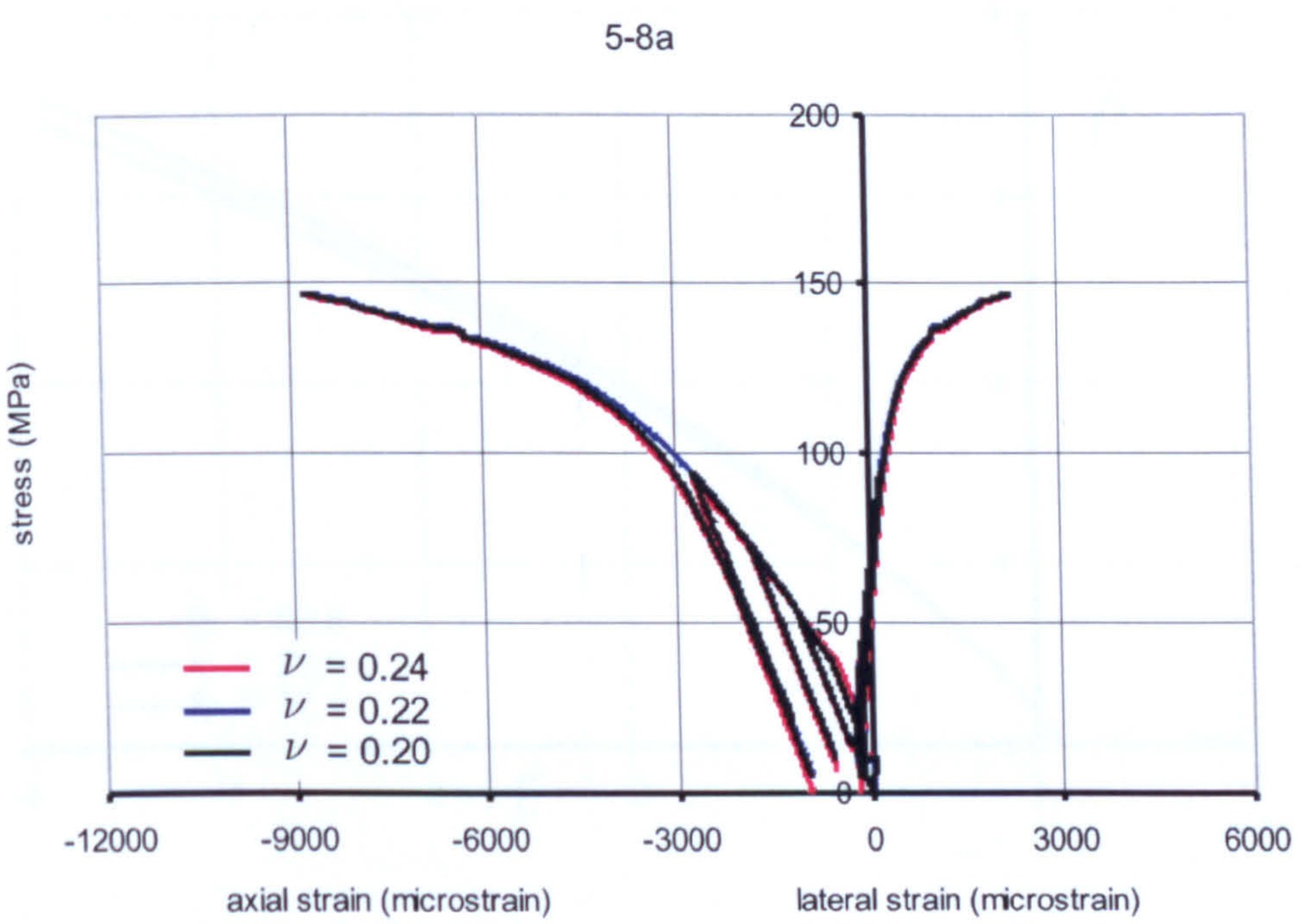

Figure 4.1: The sensitivity of the stress strain response to Poisson's radio ν

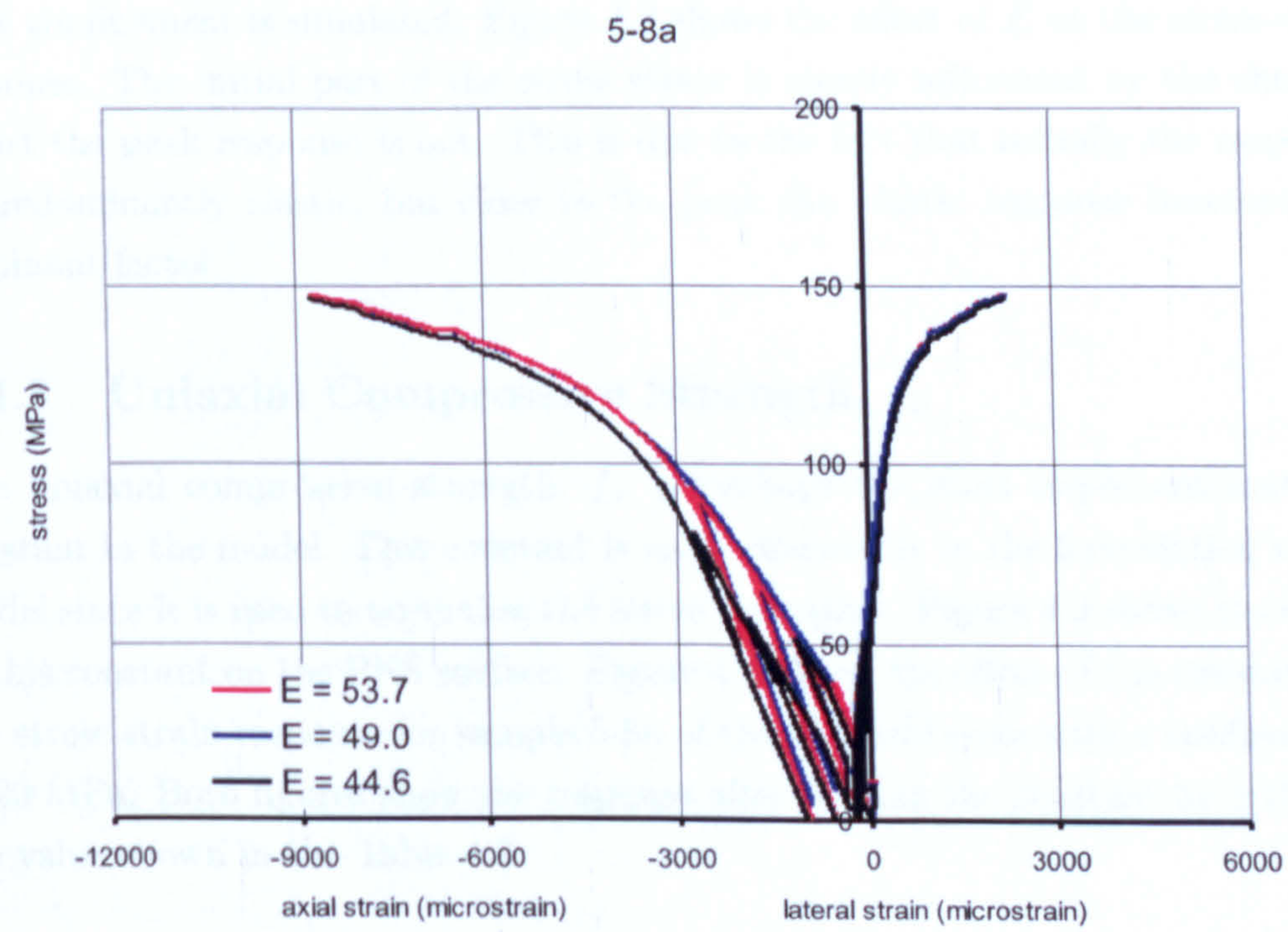

Figure 4.2: The sensitivity of the stress-strain response to E

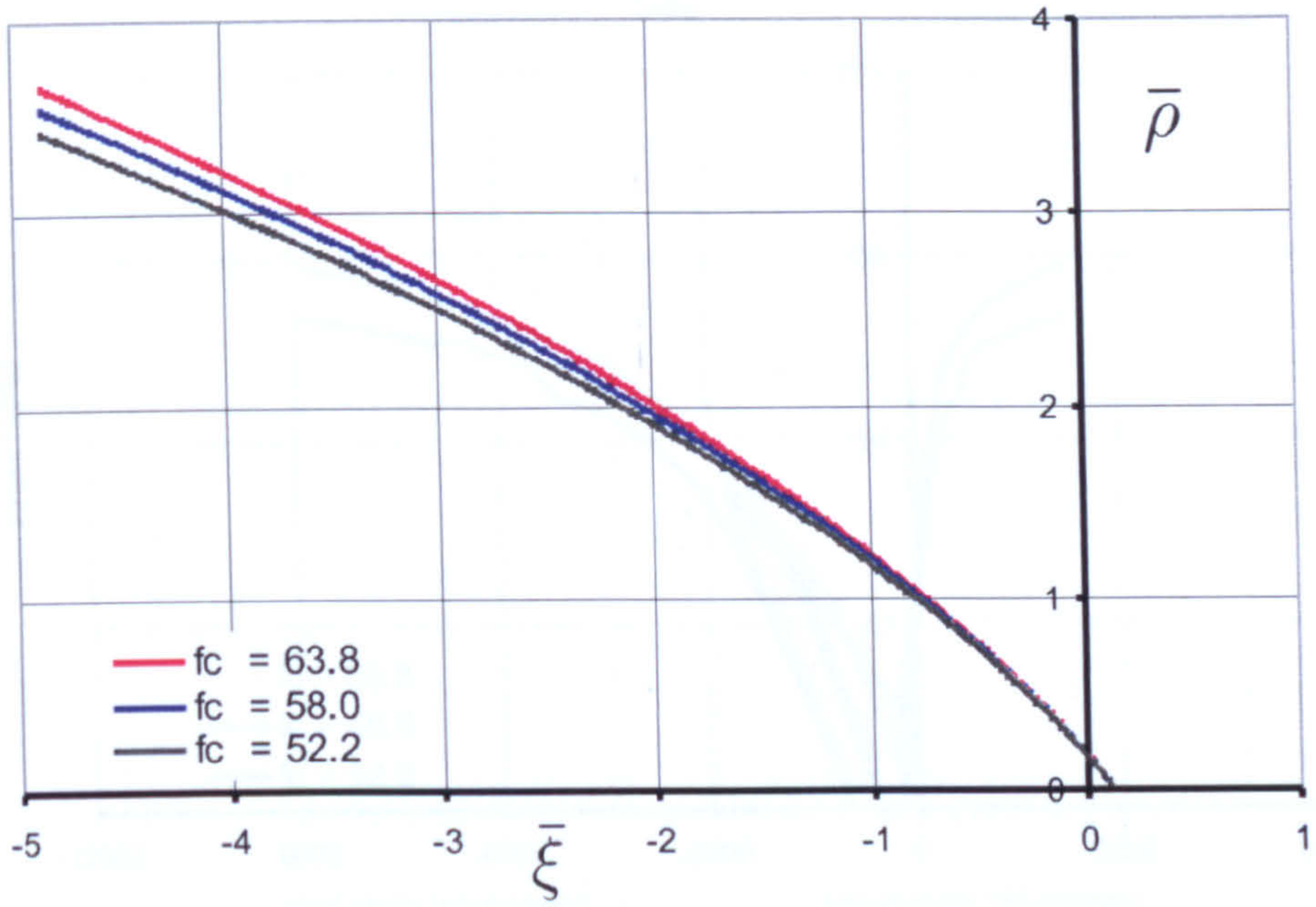

Figure 4.3: The sensitivity of the PNS to f_c

4.4.2 Young's Modulus, E

The sensitivity of the model to the Young's modulus (E) has been examined by using the values of 44.6, 49.0 and 53.7 GPa for E. Test sample 5-8a with 20 MPa confinement is simulated. Figure 4.2 shows the effect of E on the stress-stain response. The initial part of the stress strain is clearly influenced by the change, whilst the peak response is not. This is due to the fact that initially the response is predominantly elastic, but close to the peak the plastic response becomes the dominant factor.

4.4.3 Uniaxial Compressive Strength, f_c

The uniaxial compression strength, f_c, is perhaps the most important material constant in the model. This constant is used extensively in the formulation of the model since it is used to normalise the stress invariants. Figure 4.3 shows the effect of this constant on the PNS surface. Figure 4.4 shows the effect of the constant on the stress strain response for sample 5-8a of the Sheffield tests with a confinement of 20 MPa. Both figures show the response after varying the constant by $\pm 10\%$ of the value shown in the Table 4.3.

The formulation of the PNS is based on the condition that the equation passes through the uniaxial compression strength point, this results in enlarging the PNS

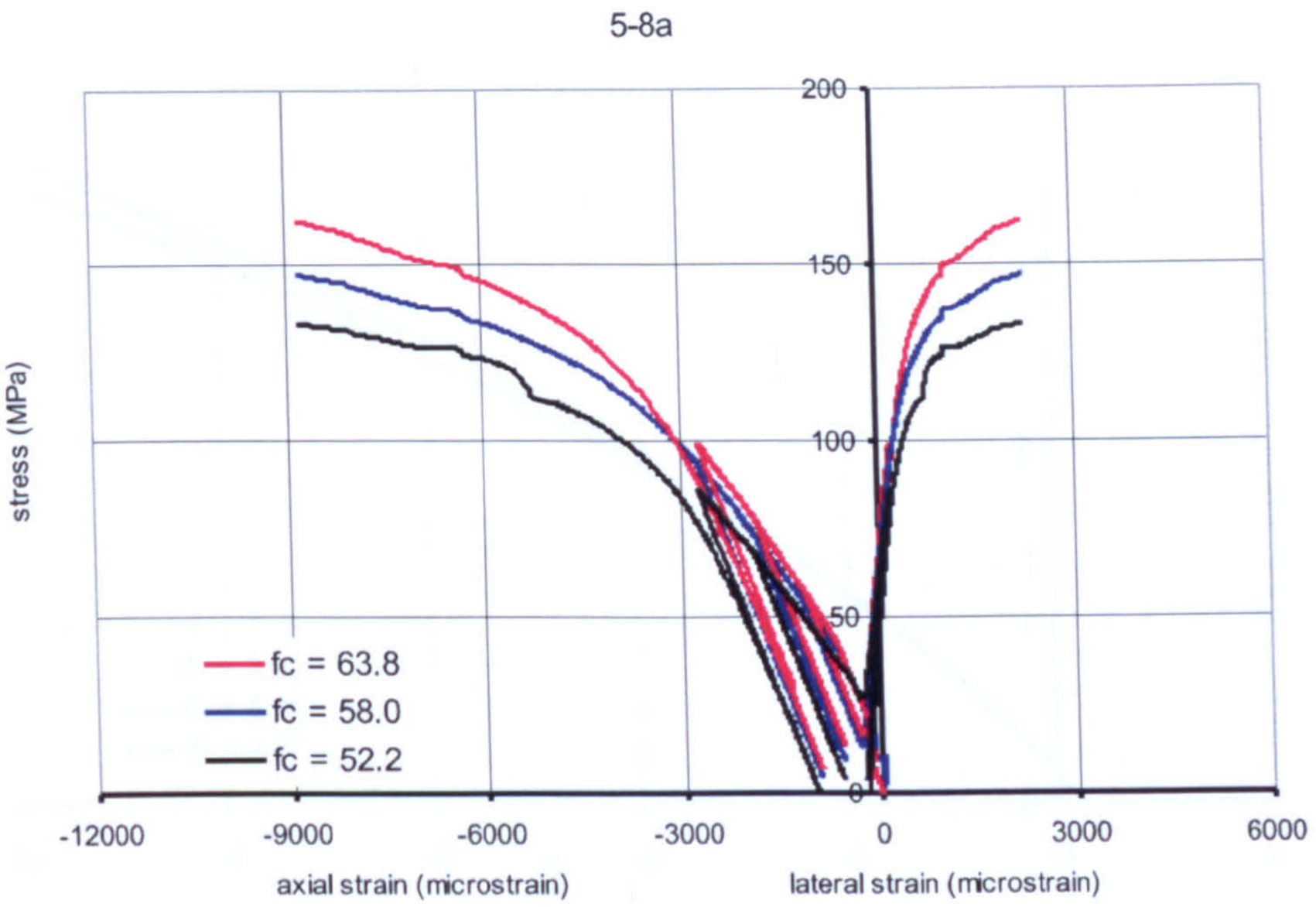

Figure 4.4: The sensitivity of the stress-strain to f_c

surface envelope away from the hydrostatic axis if the value of f_c increases. Globally, higher values of f_c cause the stress to increase for the same value of strains.

4.4.4 Uniaxial Tensile Strength, f_t

Figure 4.5 shows the effect of uniaxial tensile strength, f_t, on the PNS surface. Values of f_t of 3.82, 4.25, and 4.675 correspond to m values of 15.38, 13.82, and 12.54, respectively have been used. It is clear that decreasing the value of f_t has the effect of pushing the PNS surface away from the hydrostatic axis in the compression region and inward in the tensile region. This does not agree with the experimental evidences [Neville] which suggest that as compressive strength, f_c, increases, the tensile strength, f_t, also increases but with a decreasing rate. Therefore, further improvement is required to the performance of the model in the tensile region. Figure 4.6 shows the effect of this constant on the stress strain response for sample 5-8a of the Sheffield test with a confinement of 20 MPa. Decreasing the value of the constant increases the stresses predicted for the same values of strains. Both figures show the response after varying the constant by $\pm 10\%$ of the value shown in the Table 4.3. It can be seen that the effect is not proportional. This is due to the nonlinear relationship between constant m and f_t (See Figure 4.7).

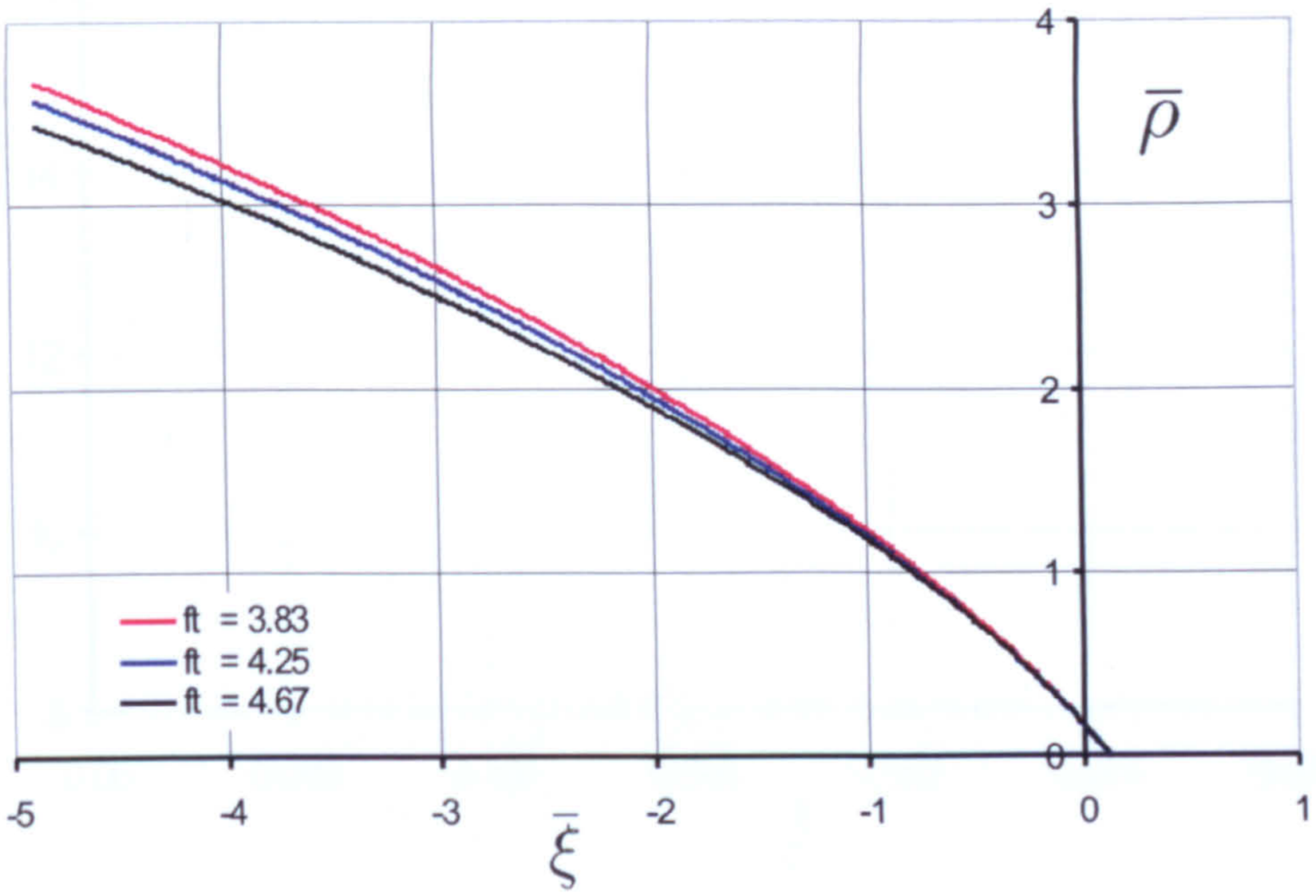

Figure 4.5: Sensitivity of the model to f_t

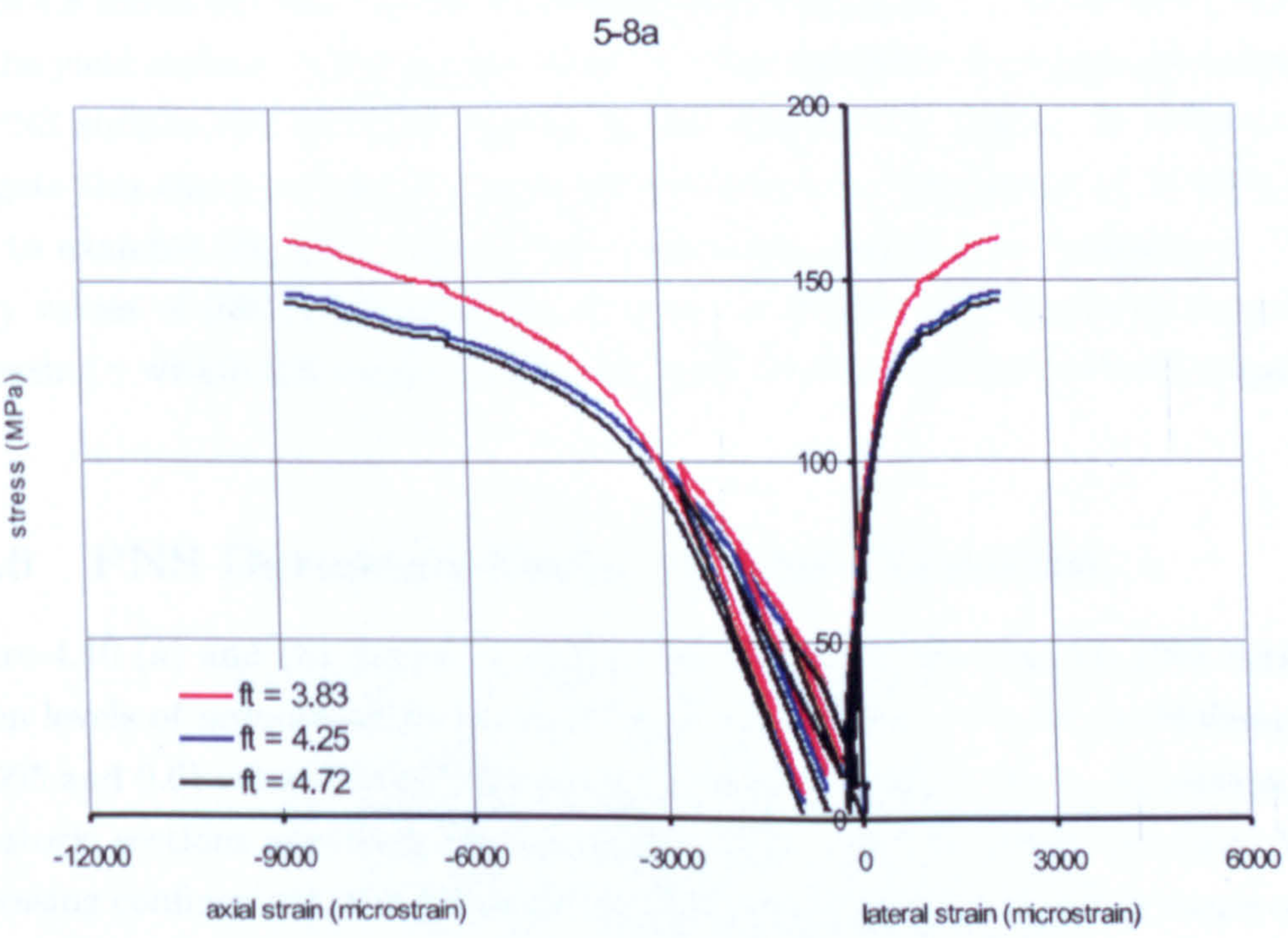

Figure 4.6: The sensitivity of the stress-strain response to f_t

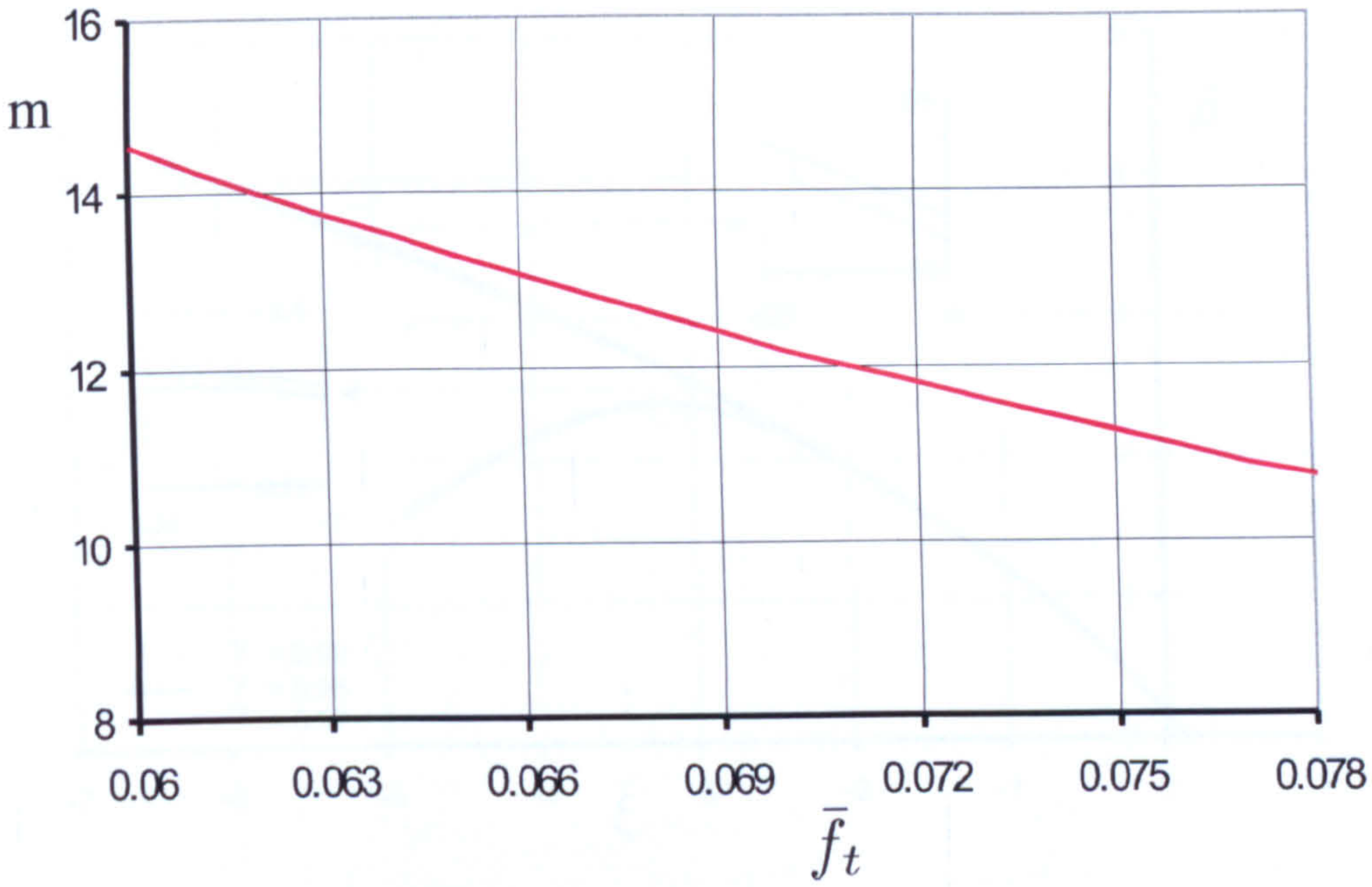

Figure 4.7: The relation between m and $\bar{f}_t$

4.4.5 PNS Meridional Shape Constant, γ

Figure 4.8 shows the effect of the meridional shape constant, γ, on the PNS surface and the yield surface. Reducing the value of γ has the effect of marginally reducing the PNS surface and the yield surface in the compression region. In order to investigate this effect, a triaxial compression test with a confinement of 20 MPa was used to examine the sensitivity of the stress-strain response to changing γ. This (for γ values of 0.97, 0.98 and 0.99) is shown in Figure 4.9. It can be seen that decreasing γ within this range has no noticeable effect on the stress-strain response.

4.4.6 PNS Deviatoric Shape Function Constant, α

Figure 4.10 (a) and (b) shows the deviatoric sections of the smooth PNS surfaces at ten levels of normalised hydrostatic pressure ($\bar{\xi} = 0$ to -2) for two different (α =0.005 and 0.6) values with PNS meridional shape constant $\gamma = 1$. In tension, the deviatoric sections approach the triangular shape of the Rankine envelope. With increasing confinement, the deviatoric sections resemble the hexagonal shape of the Mohr-Coulomb condition but under very high confinement they may approach the circular shape of the von-Mises criterion, depending on the value of α. Note that for $B_0 = 1$, the influence of the Lode angle disappears, and the deviatoric shape of

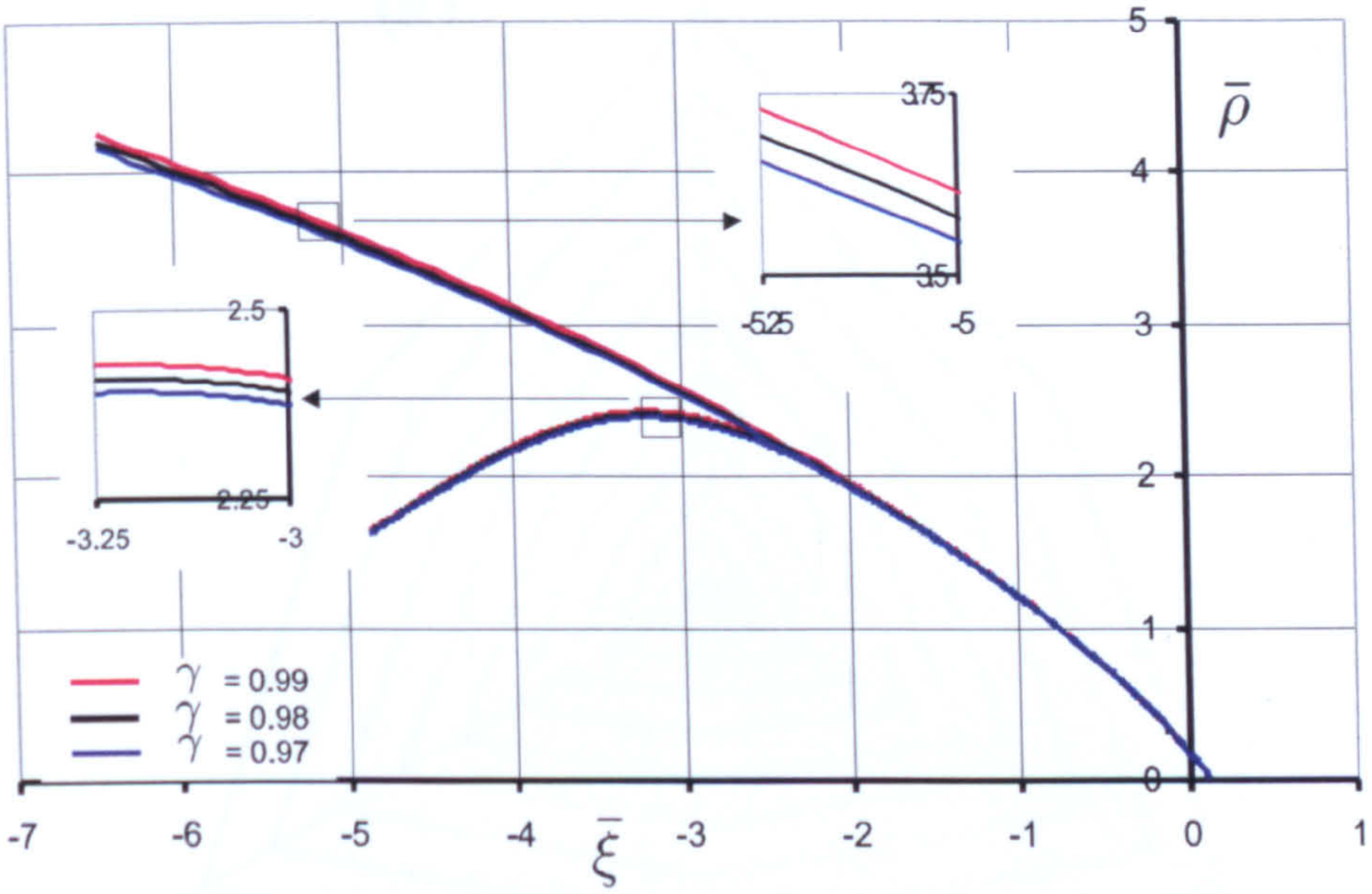

Figure 4.8: Sensitivity of the model to γ

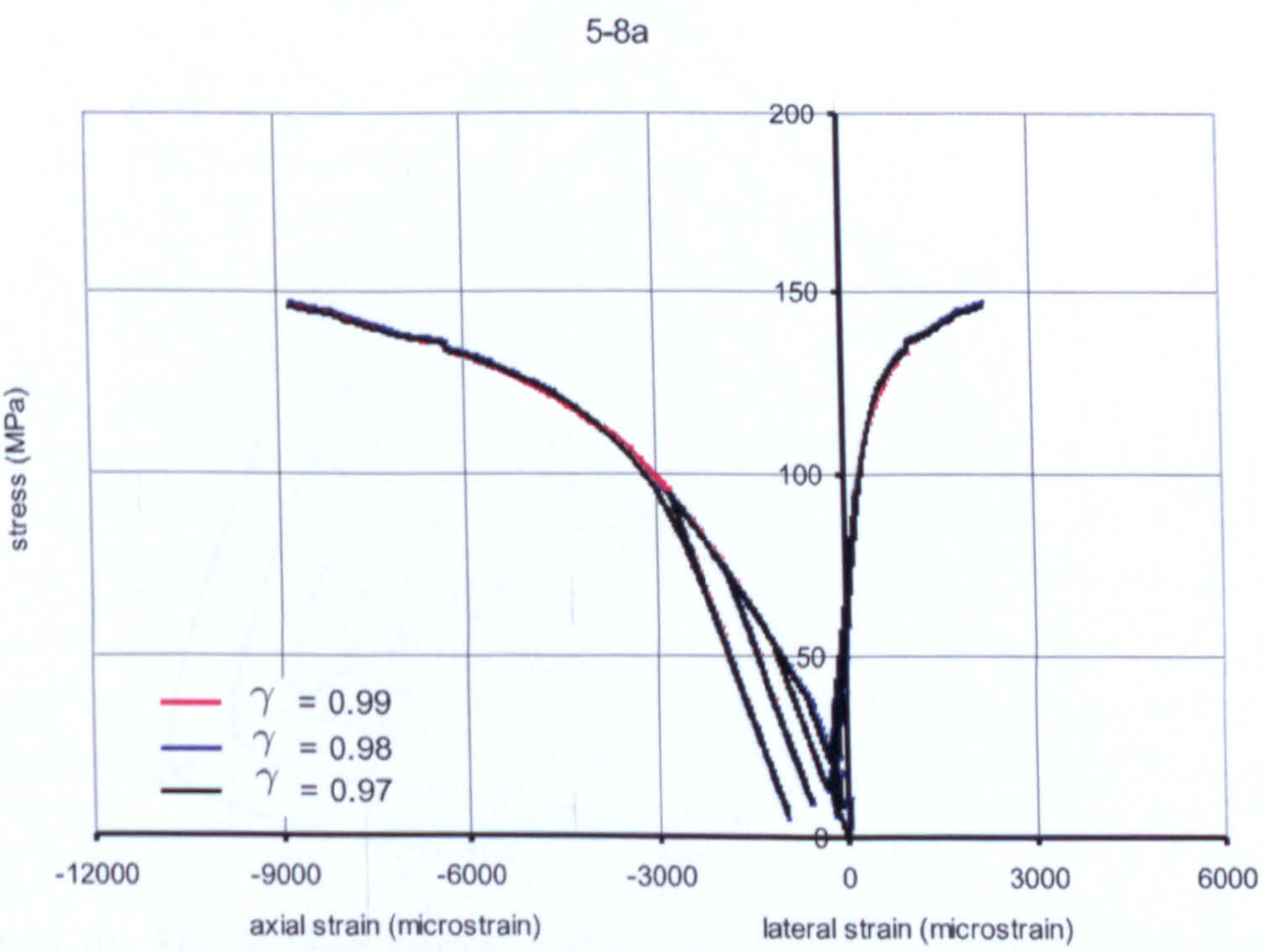

Figure 4.9: Sensitivity of the stress strain response to γ

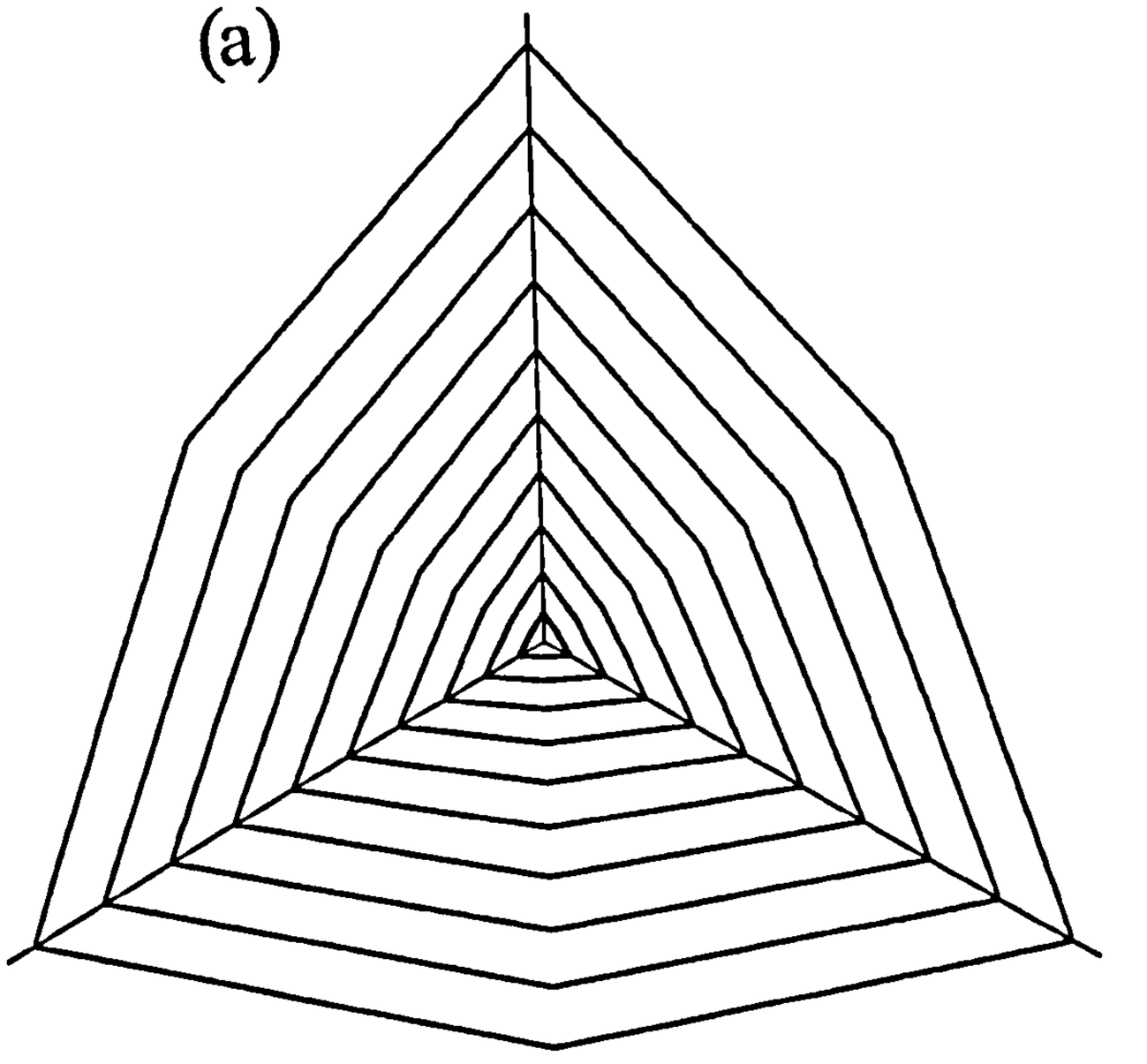

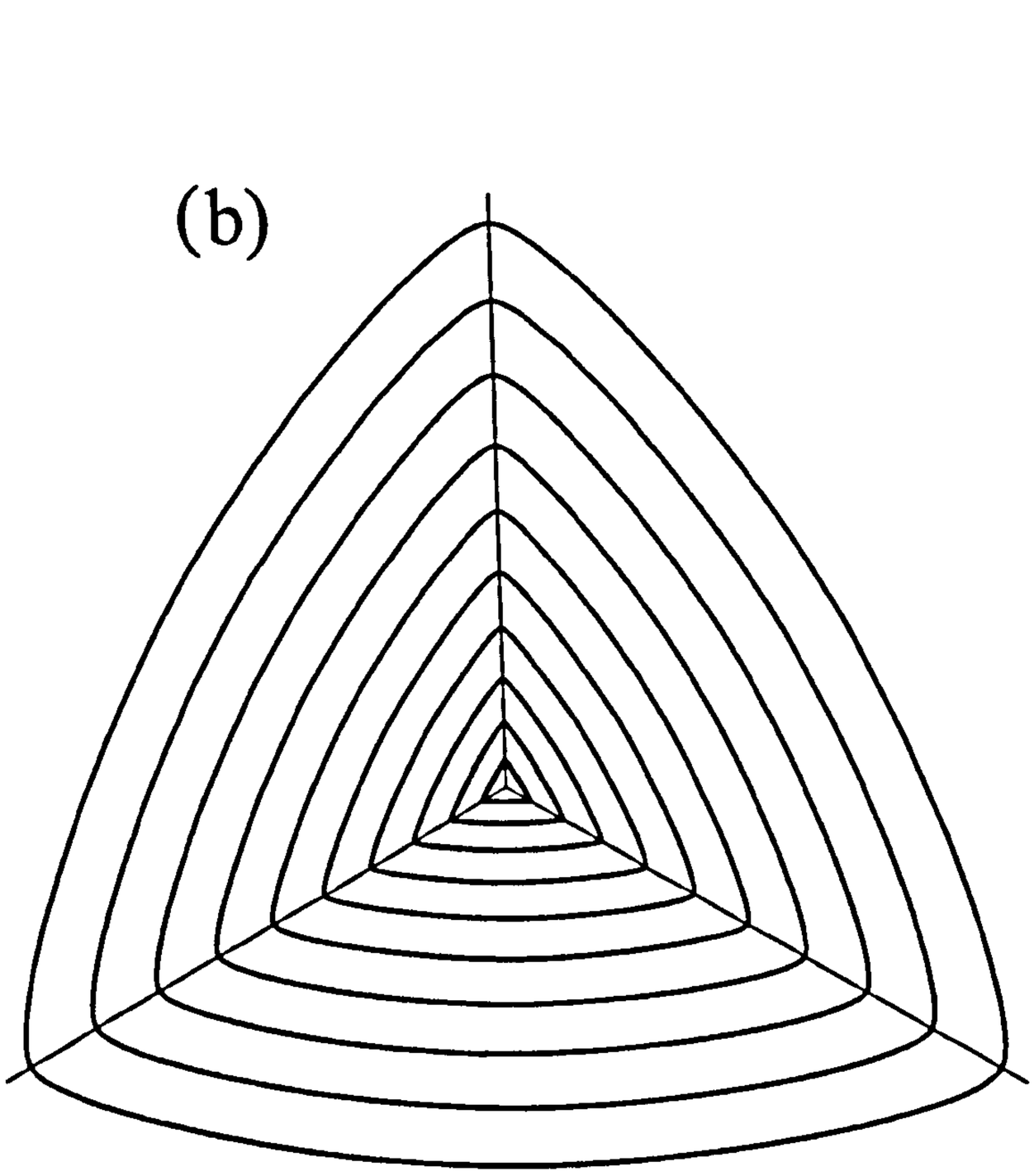

Figure 4.10: The deviatoric sections of the smooth PNS criterion at ten levels of normalised hydrostatic pressure ($\bar{\xi} = 0$ to -2) for two different α values , (a) $\alpha = 0.005$ and (b) $\alpha = 0.6$ ($\gamma = 1$)[Tahar]

the PNS surface becomes circular as in the generalised Drucker-Prager criterion.

The material constant α affects the shape of the PNS surface in a deviatoric plane. The model will show no change in the stress-strain curves under uniaxial compression and uniaxial tension as α is varied. The effect of α is only apparent when examining stress paths which lie away from the extension and compression meridians. That is, α only influences the behaviour when $\frac{-\pi}{6} < \theta < \frac{\pi}{6}$. Increasing α will lead to higher strengths in this region and will result in marginally higher strains at peak stress.

4.4.7 The Yield Surface Constant, α_1

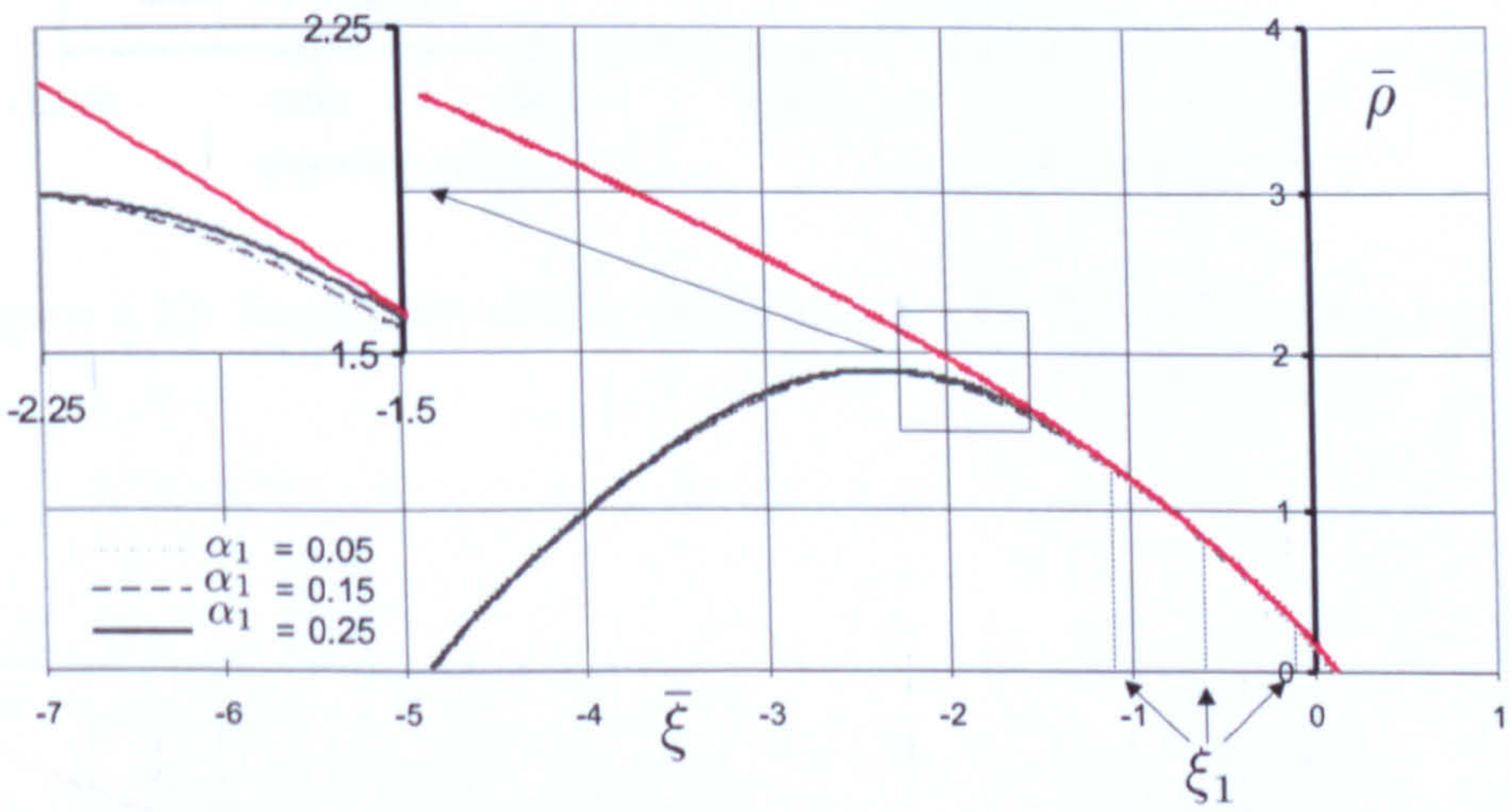

Figure 4.11: Sensitivity of the model to α_1

Figure 4.11 shows the effect of the yield surface constant α_1 on the yield surface. Values of α_1 of 0.05, 0.15, and 0.25 have been used. It is clear that within these values the effect is very limited. The global effect on the stress strain response also seems almost unnoticeable. Figure 4.12 shows the stress strain response of Sheffield test data with 20 MPa confinement to the increase and decrease of 10% of the value of the constant.

4.4.8 Plastic Volume Transition Constant, α_2

Figure 4.13 shows the effect of the plastic volume transition constant α_2 on the yield surface. Values of 0.7, 0.8 and 0.9 has been used to demonstrate the effect.

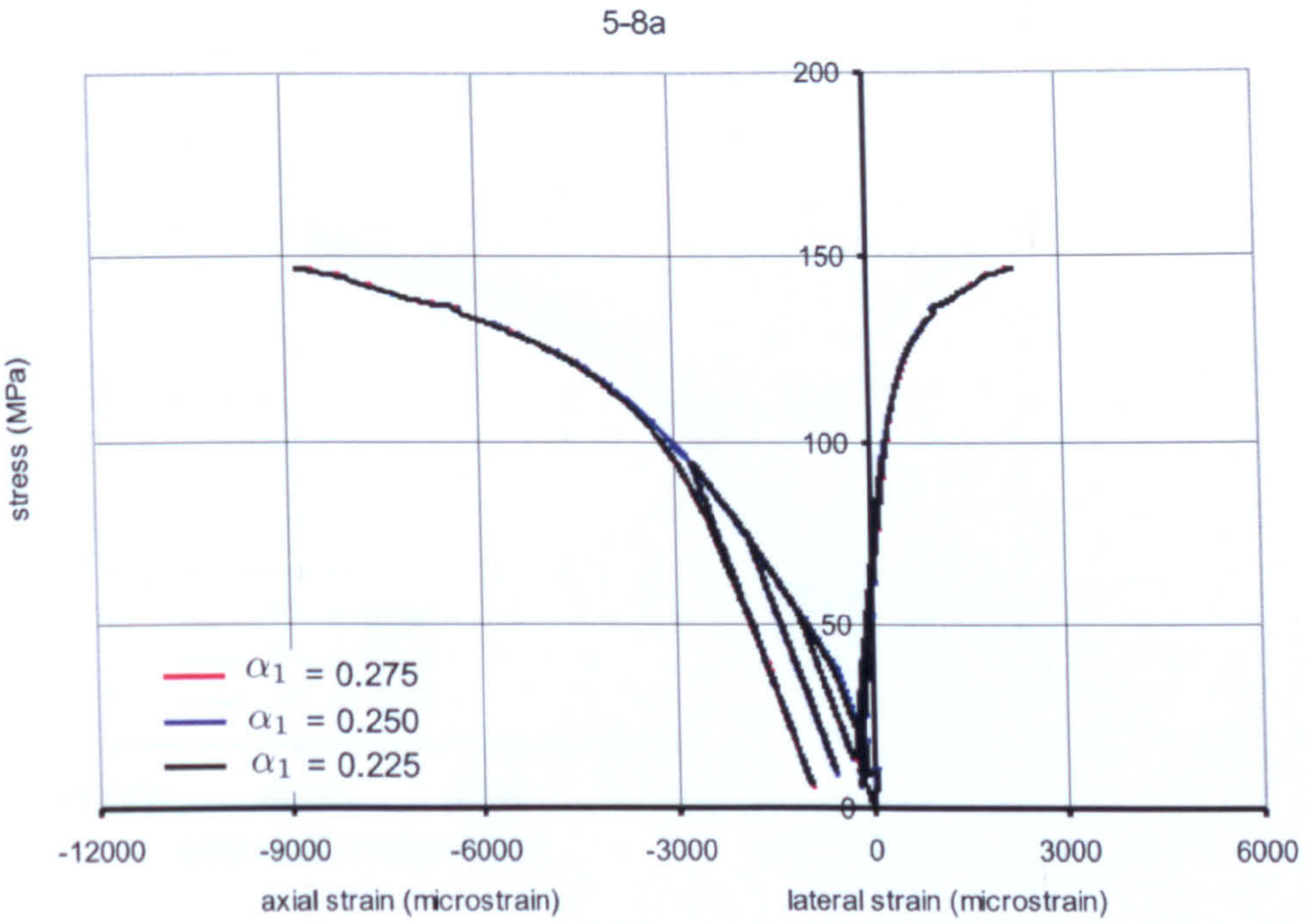

Figure 4.12: Sensitivity of the stress strain response to the change of α_1

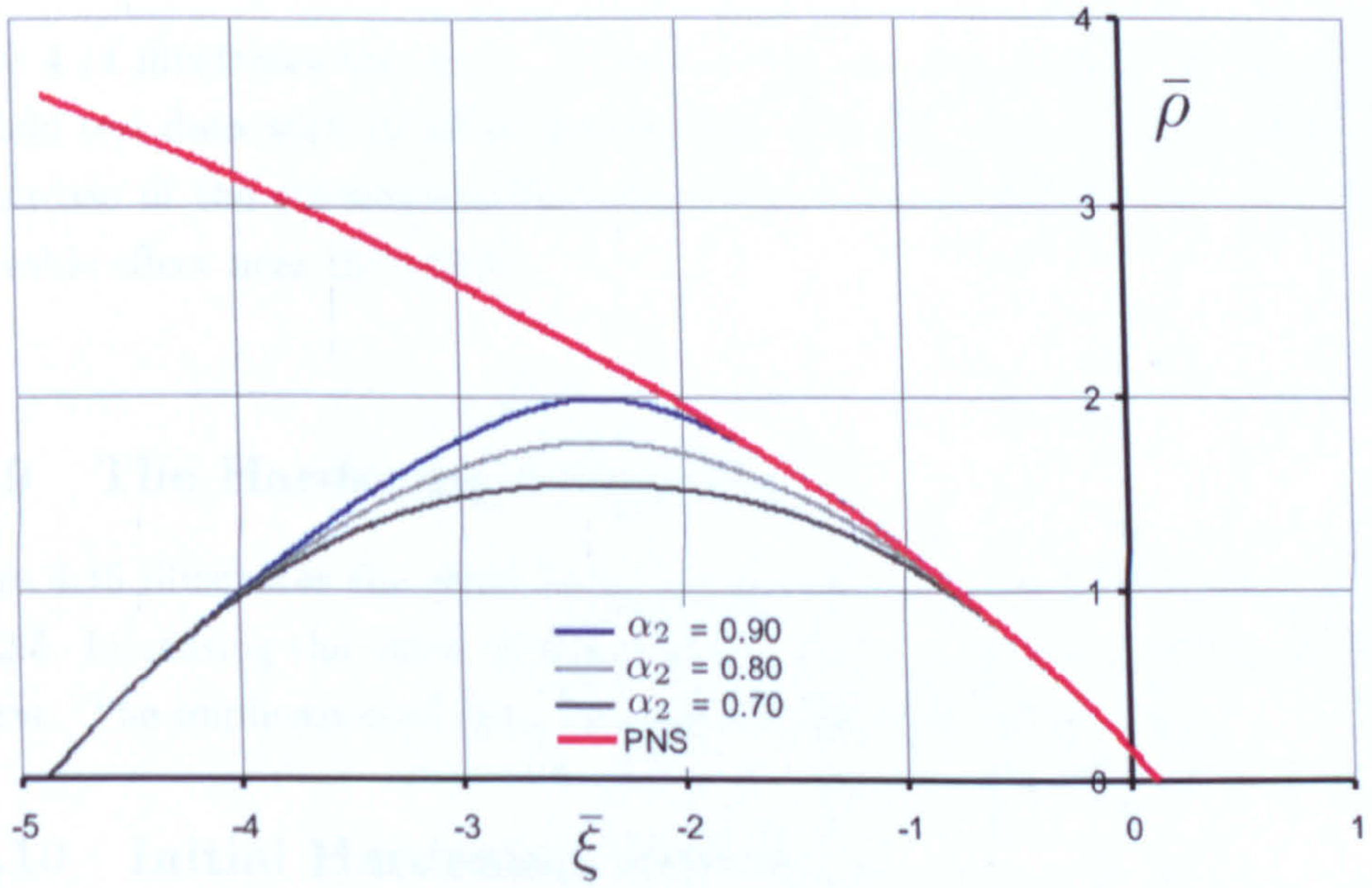

Figure 4.13: Sensitivity of the model to α_2

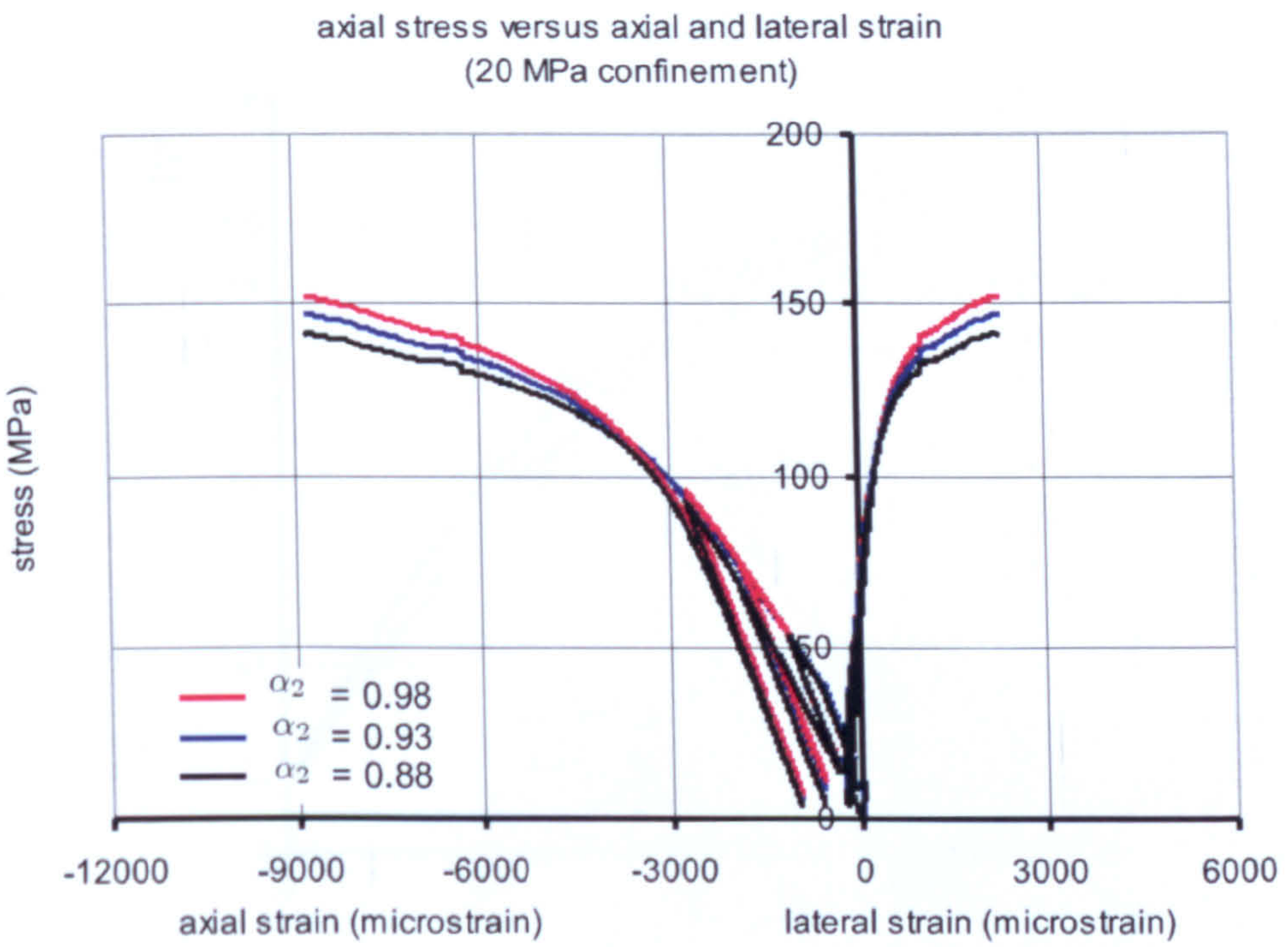

Figure 4.14: Sensitivity of the stress strain response to the change of α_2

Increasing the value of this constant pushes the yield surface towards the PNS surface without changing the value of the hydrostatic compression intersection point ξ_{hc} .

Figure 4.14 illustrates the effect of this constant on the stress strain response for Sheffield test data with 20 MPa confinement. The increase of this constant causes an increase of the stresses for the same values of strains near the peak with no noticeable effect near the origin.

4.4.9 The Hardening Constant, s_0

Figure 4.15 illustrates the effect of s_0 on the hardening variable k for $s_0 = 1.5$, 2 and 2.5. Increasing the value of this constant increases the initial slope of the k_p - k curve. The implication of that, is decreasing the initial hardening.

4.4.10 Initial Hardening Surface, k_0

The response of the yield surface to $k_0 = 0.1$, 0.15 and 0.2 is shown in Figure 4.16. The increase of this constant increases the size of the initial elastic domain and

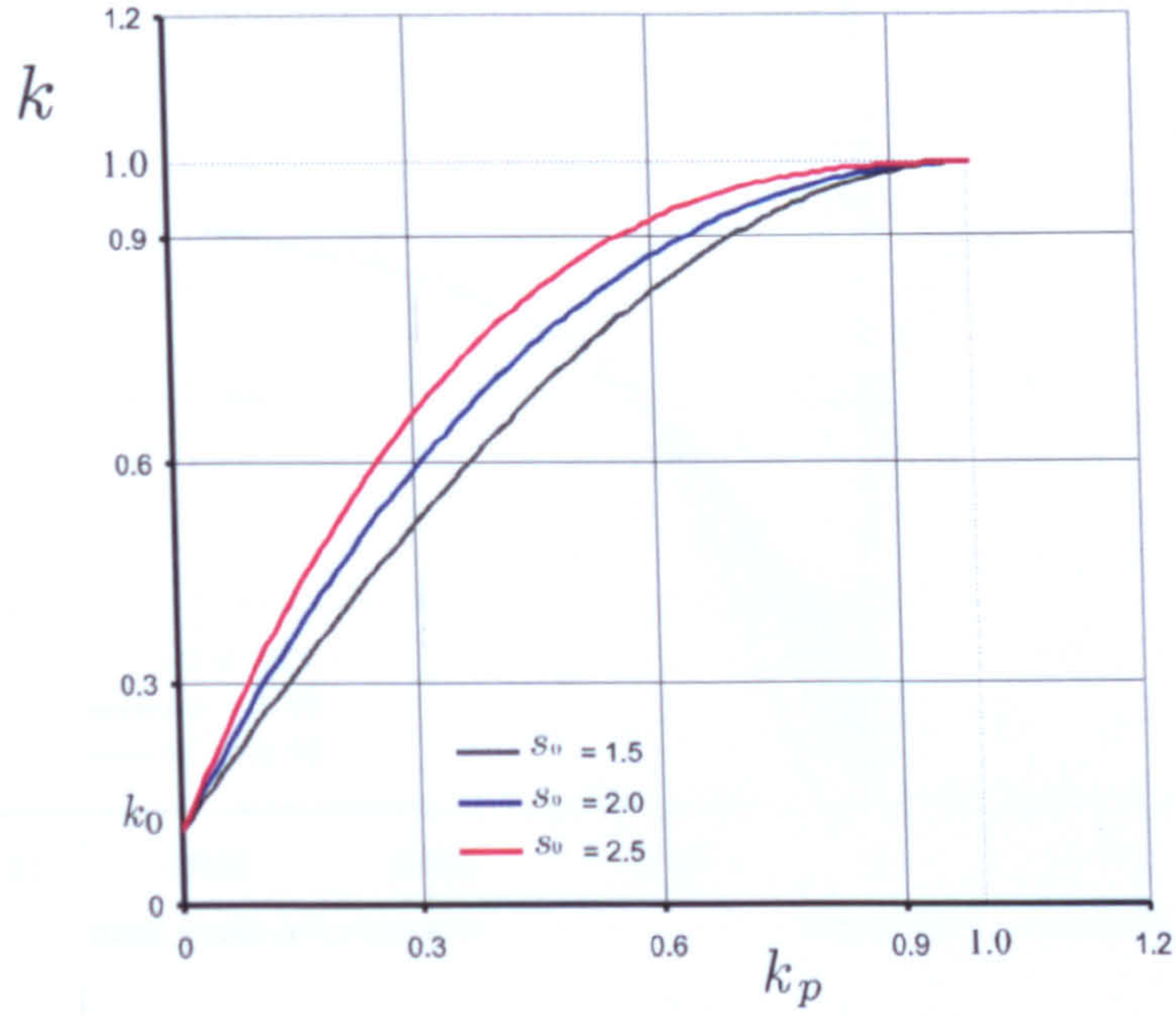

Figure 4.15: The sensitivity of the hardening variable k to s_0

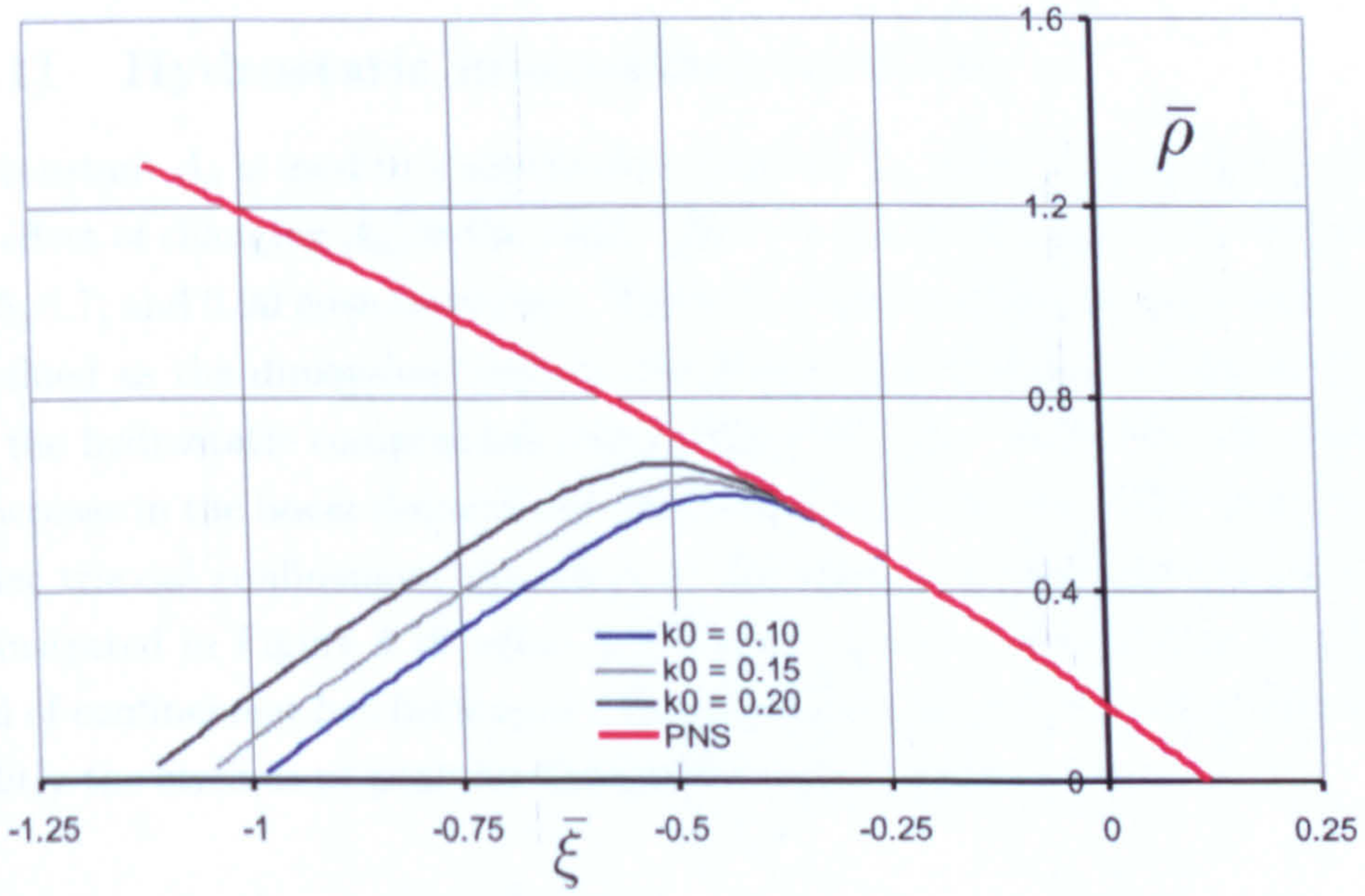

Figure 4.16: The sensitivity of the yield surface to k_0

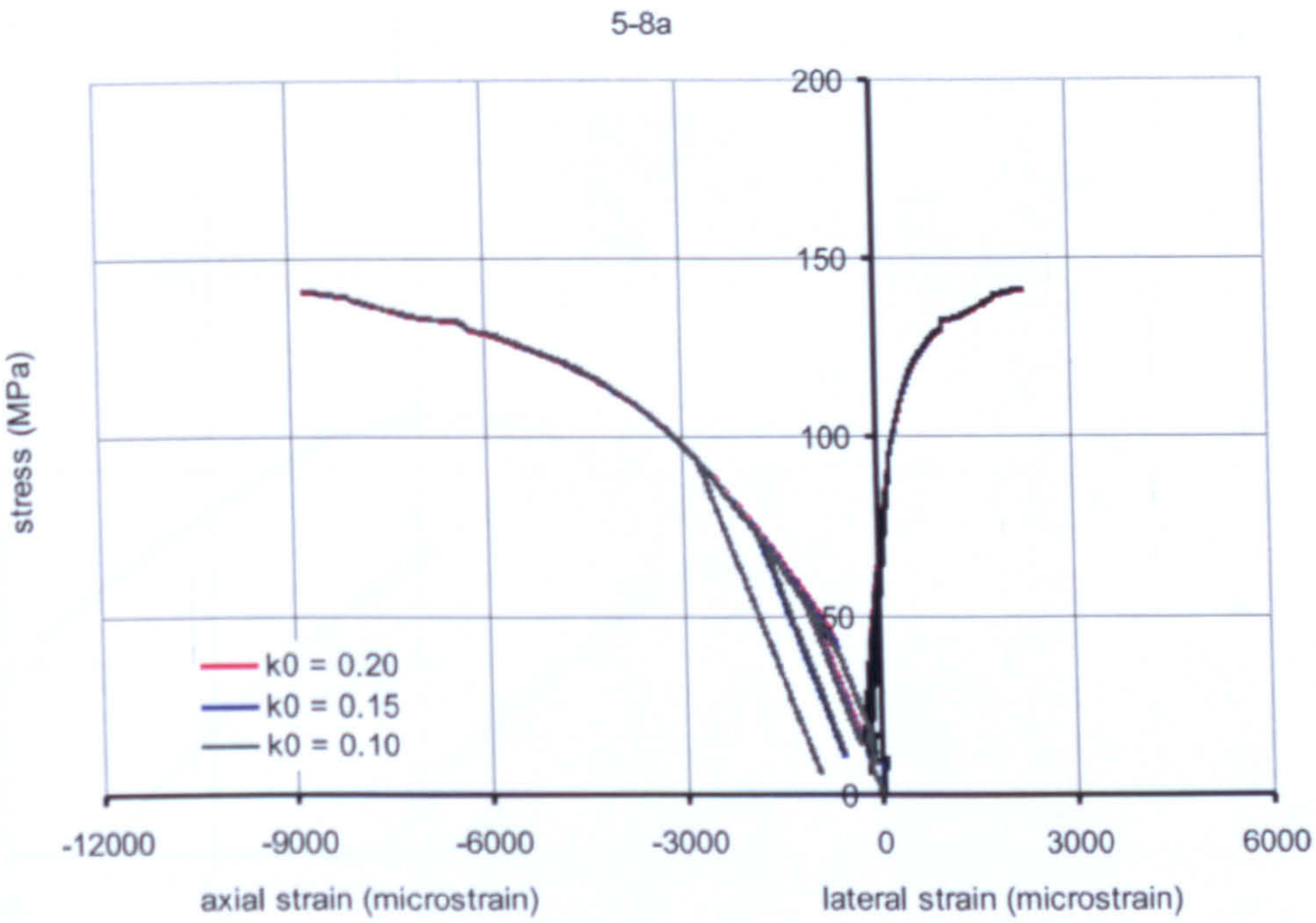

Figure 4.17: The effect of k_0 on the stress-strain response

hence, delays the onset of the nonlinear response. Figure 4.17 shows the effect of this constant on the triaxial test from Sheffield test data with 20 MPa confinement. The change of k_0 has no apparent effect on the response under this stress path.

4.4.11 Hydrostatic intersection constant, A_k

The constant A_k is used to scale the size of the elastic domain for a fixed value of k. The effect of changing A_k on the yield surface is shown in Figure 4.18. Values of A_k = 0.5, 0.7, and 0.90 have been used. The role of the constant is to increase ξ_0 which is defined as the dimension between the hydrostatic tensile intersection point ξ_{ht} and the hydrostatic compression intersection point ξ_{hc}. Increasing the value leads to increase in the linear domain and hence slightly delays the onset of non-linearity. Under triaxial confinement the effect of the change on the stress-strain response is illustrated in Figure 4.19 where test data from the Sheffield tests with 20 MPa level of confinement has been used . Decreasing the value of the constant, increases slightly the stresses at peak for the same level of strain.

4.4.12 Hardening constant, A_h

Increasing the value of A_h leads to increase in the value of the ductile measure ζ. Figure 4.20 shows the effect of A_h = 0.001, 0.003 and 0.005 on ζ. The sensitiv-

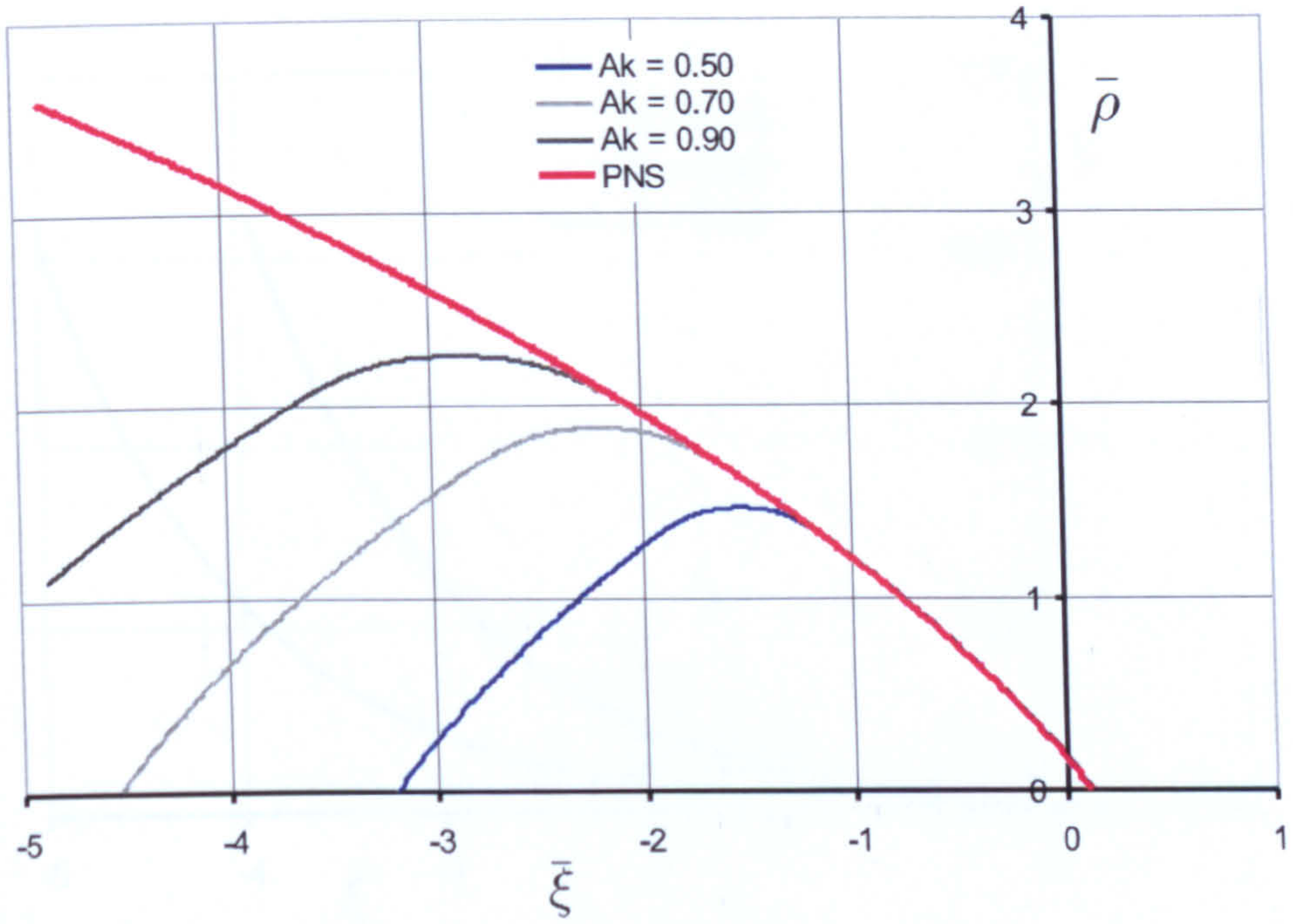

Figure 4.18: The sensitivity of the model to A_k

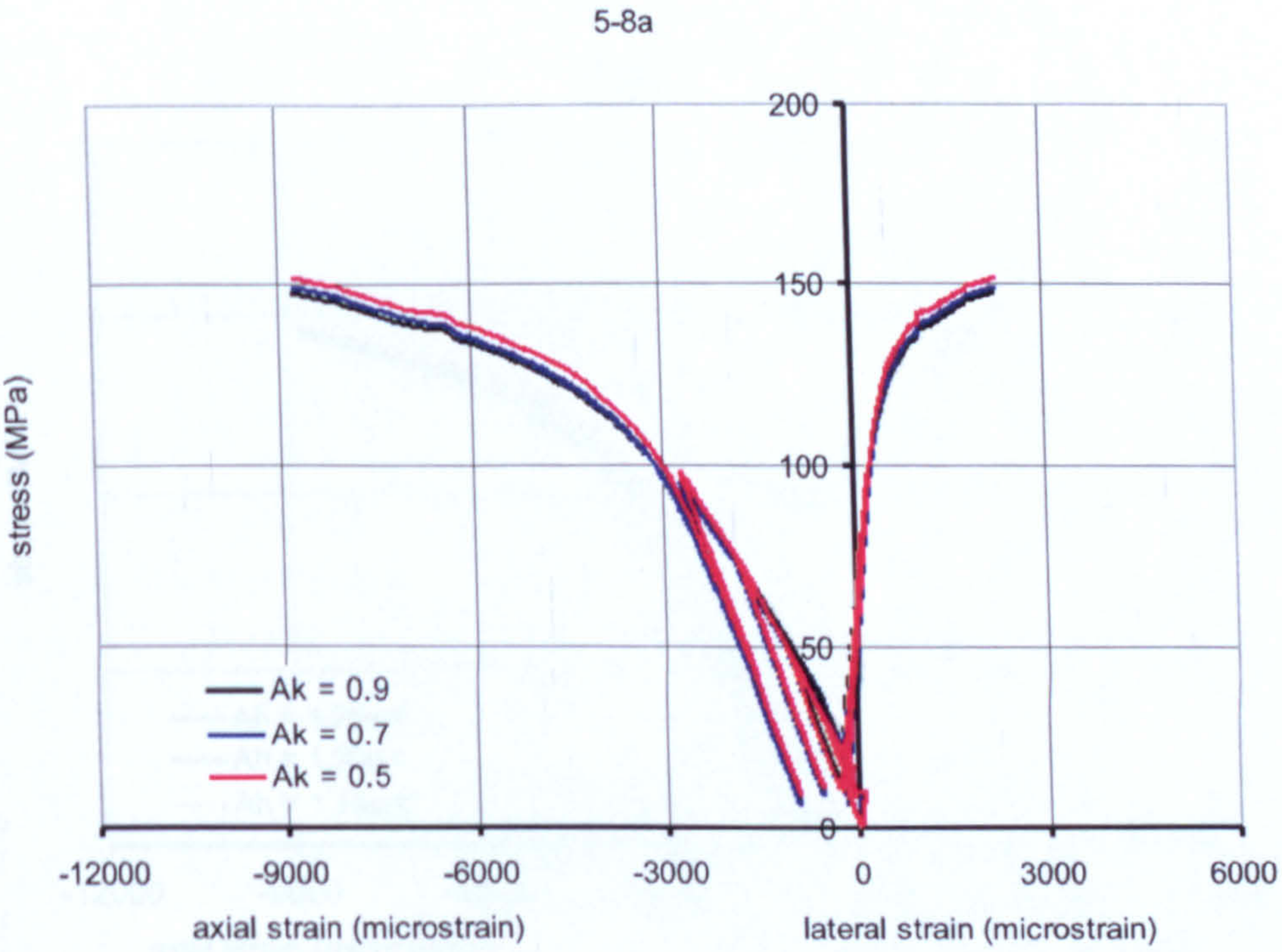

Figure 4.19: The effect of A_k on the stress strain prediction

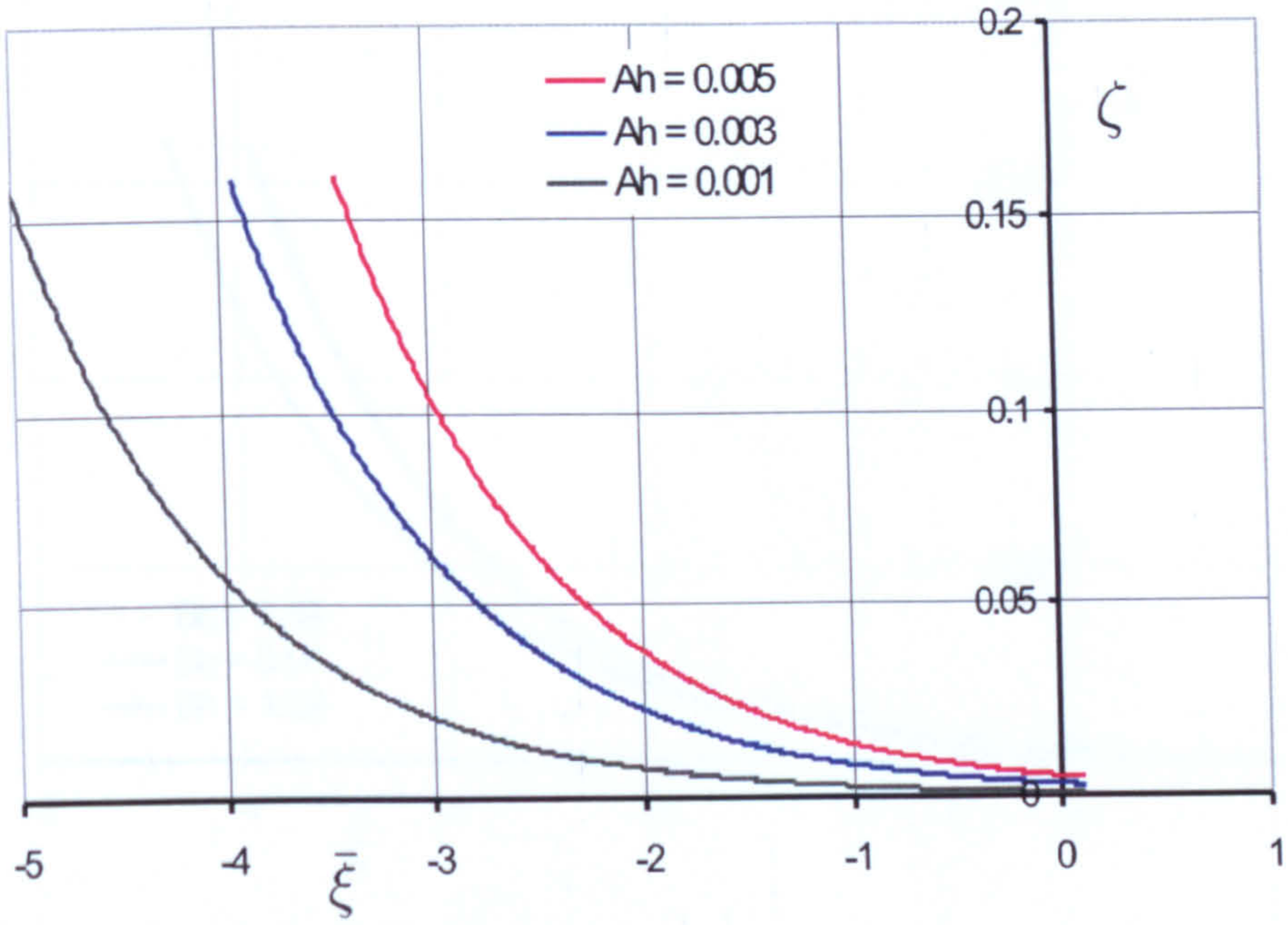

Figure 4.20: Effect of constant A_h on the ductile measure ζ

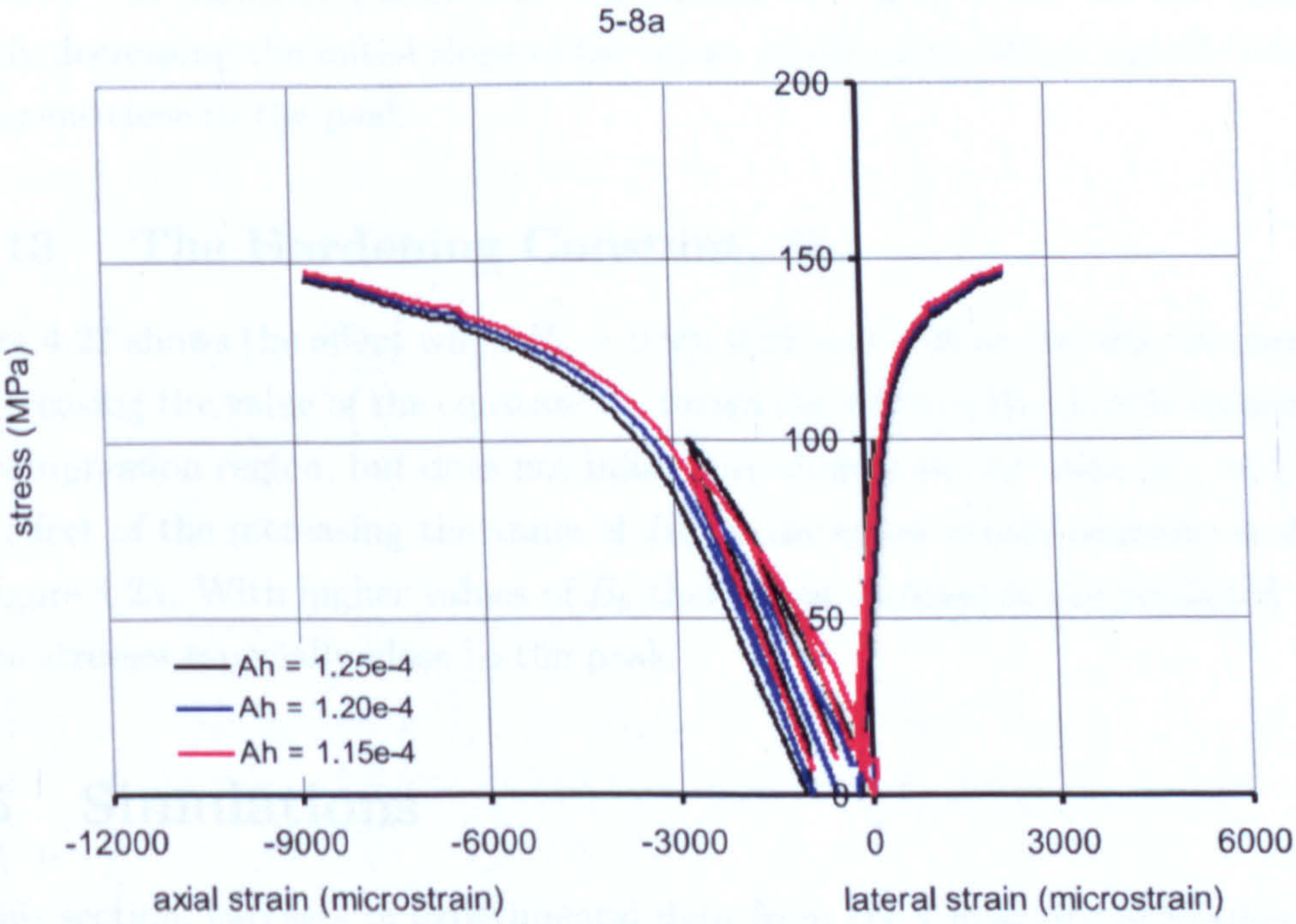

Figure 4.21: The effect of A_h on the stress strain prediction

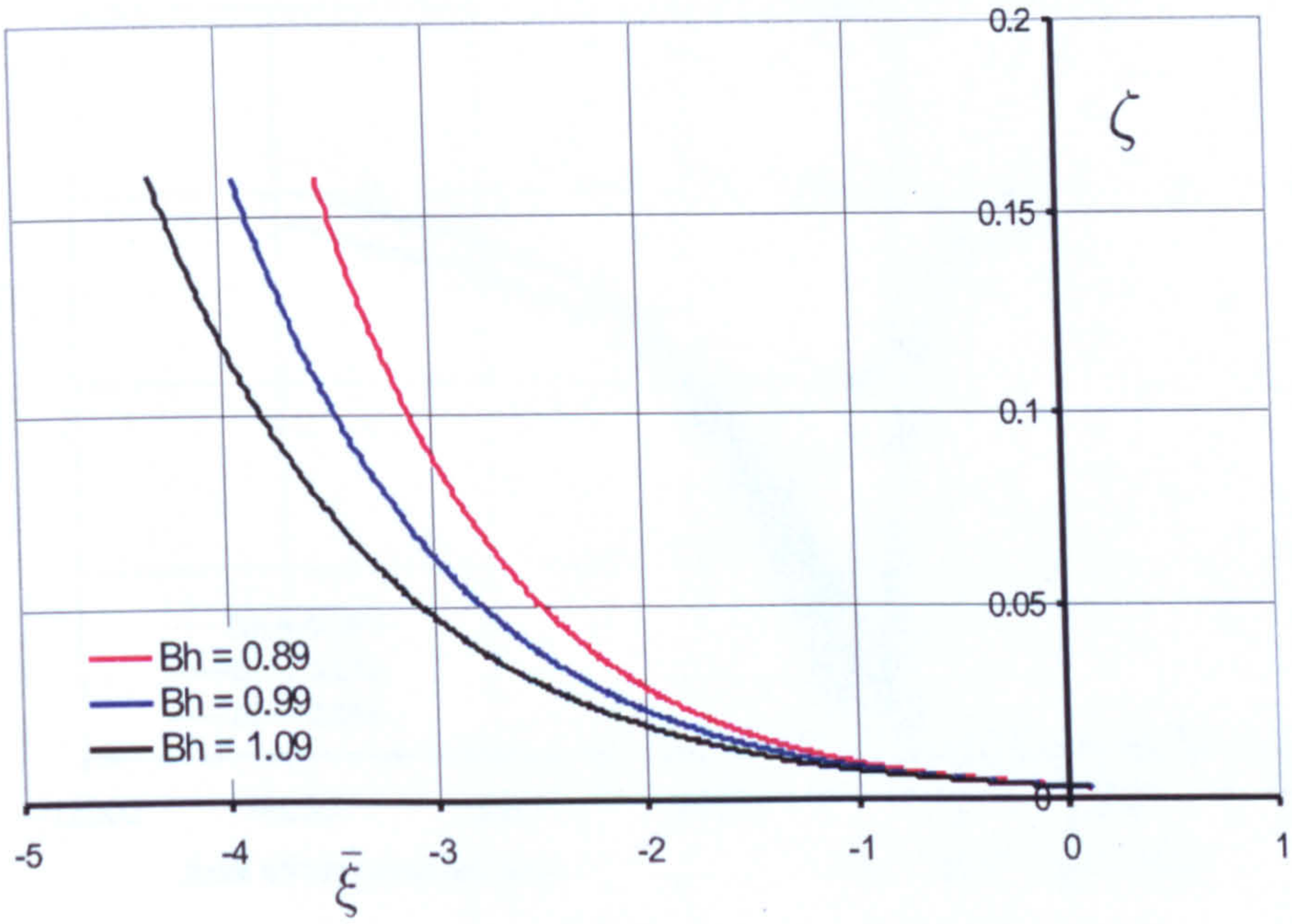

Figure 4.22: Effect of constant B_h on the ductile measure, ζ

ity of the hardening stress-strain response to $A_h = 1.15 \times 10^{-4}$, 1.20×10^{-4} and 1.25×10^{-4} is shown in Figure 4.21. Increasing the value of A_h has the effect of slightly decreasing the initial slope of the stress strain curve whilst the effect is less prominent close to the peak.

4.4.13 The Hardening Constant, B_h

Figure 4.22 shows the effect when $B_h = 0.89$, 0.99 and 1.09 on the ductile measure ζ. Increasing the value of the constant decreases the value of the ductile measure in the compression region, but does not inflict any change on the value of ζ at $\bar{\xi} = 0$. The effect of the increasing the value of B_h on the stress strain response is shown in Figure 4.23. With higher values of B_h there is an increase in the predicted value of the stresses especially close to the peak.

4.5 Simulations

In this section, two sets of experimental data from the University of Sheffield and the University of Colorado are used to examine the ability of the constitutive model to capture the material response of plain concrete. The first data set in-

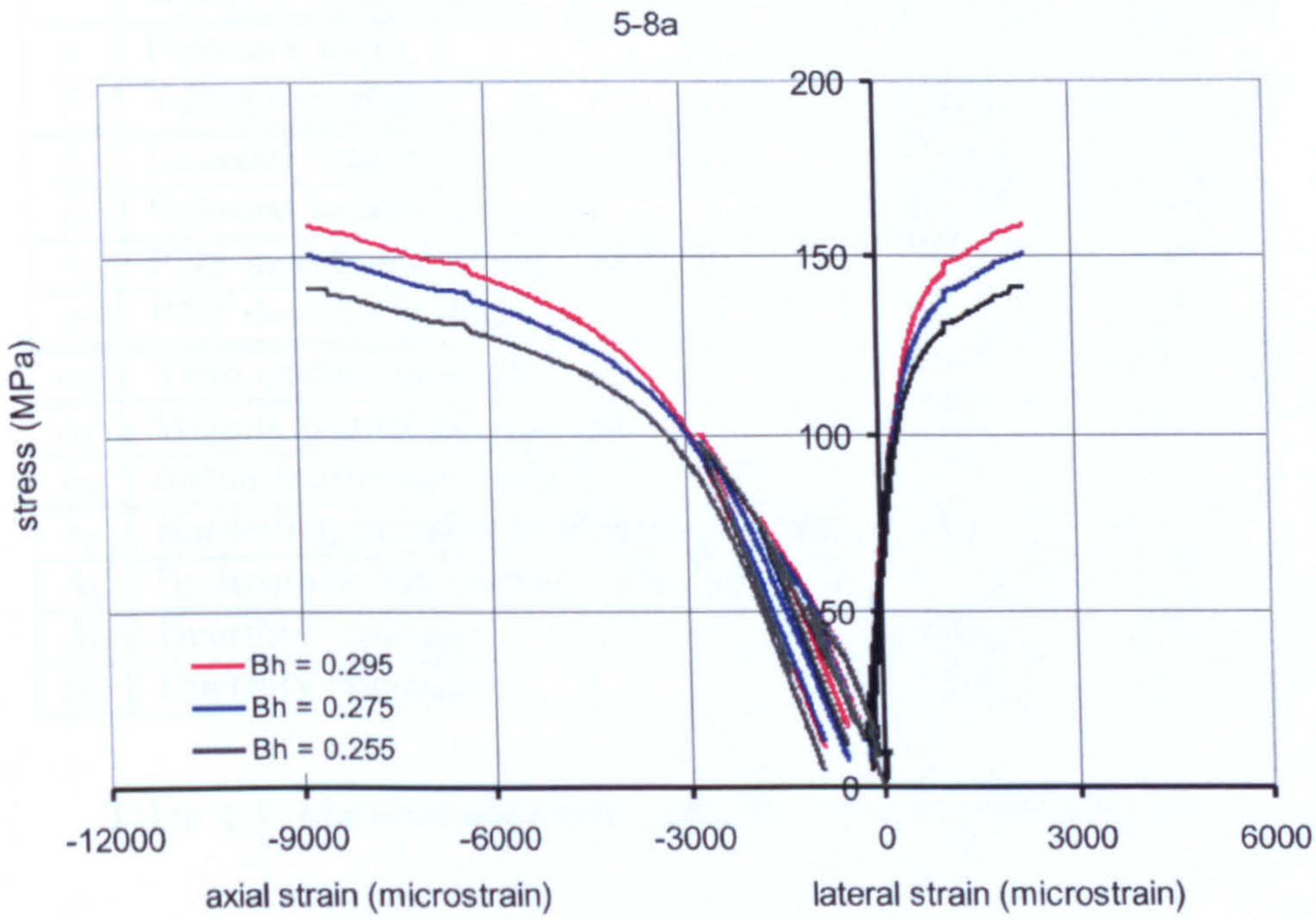

Figure 4.23: The effect of B_h on the stress-strain response

cludes cyclic triaxial compression loading tests performed by Papatheodorou as part of her taught MSc. degree, under the supervision of Professor Crouch. The work was reported in a document to British Energy (UK) plc [Crouch *et al*; 2001]. The second data set includes tests conducted by Robert Scavuzzo and Thomas Stankowski at the University of Colorado during 1981 and 1982 [Scavuzzo, 1982; Stankowski, 1983]. The tests consist of different multiaxial load paths, unloading, stress reversals and reloading.

The material constants used for the two sets of simulations are given in Table 4.3. The values for these constants were determined by the calibration procedure described in Section 4.3.

4.5.1 Sheffield Uniaxial and Triaxial Compression Tests

A series of six tests regimes are simulated. Each of these regimes was repeated at least once in the laboratory using nominally identical concrete. The repeat experiments give an indication of the scatter found when testing this heterogeneous material. The triaxial tests range from minimal confinement $\bar{\sigma}_2 = \bar{\sigma}_3 = 0$ to 70 MPa.

	Material Constant	Sheffield	Colorado
ν	Poisson's ratio	0.22	0.2
E	Young's modulus	50 GPa	20 GPa
f_c	Uniaxial compressive strength	58 MPa	22.6 MPa
f_t	Uniaxial tensile strength	4.28 MPa	2.26 MPa
γ	PNS meridional shape constant	0.999	0.999
α	PNS deviatoric shape constant	0.8	0.8
α_1	Yield surface constant	0.25	0.35
α_2	Volume transition constant	0.93	0.9
k_0	Initial hardening surface	0.1	0.1
s_0	Hardening meridional shape constant	2.7	2.7
A_k	Hydrostatic intersection constant	1	2.5
A_h	Ductility constant	0.003	0.005
B_h	Ductility constant	0.55	0.5

Table 4.3: Material constants used for the triaxial simulations

Figure 4.24 (a) shows the model simulation (in the red line) and the experimental stress-strain responses (blue) for the case of uniaxial compression test (test sample 5_1a_R_0). The simulation has been performed using the material constants illustrated in Table 4.3. In this test, the model simulates the stress-strain response of concrete very well for about eighty percent of the stress-strain curve. However, close to the peak, the model over-predicts the stresses. For the lateral stress, the shape of the curves are similar to that of the experimental. For the axial stress, the shape of the curve is almost linear initially and becomes increasingly nonlinear close to the peak. The simulation could be improved if an alternative values of A_h and B_h and A_k are used. Figure 4.25 (a) shows the simulation of the same test where the value of $A_h = 4 \times 10^{-5}$, $B_h = 0.12$ and $A_k = 1$ are used. The model predicts very well the behaviour of concrete and total agreement is achieved. However, the values of Figure 4.24 are chosen in order to maintain same values for all the material constants during the simulations. The simulations shown in Figure 4.25 have been performed using various values of the material constant B_h while other constants remained fixed. This has been performed in order to demonstrate the capability of the model for a much better simulations.

Figure 4.24 (b) shows the performance of the new model when compared with the results of triaxial compression tests under confinement of 10 MPa (sample 5_6a_R_10). With this level of confinement, the peak strength is increased to almost double the uniaxial strength and so are the peak strains. The model predictions

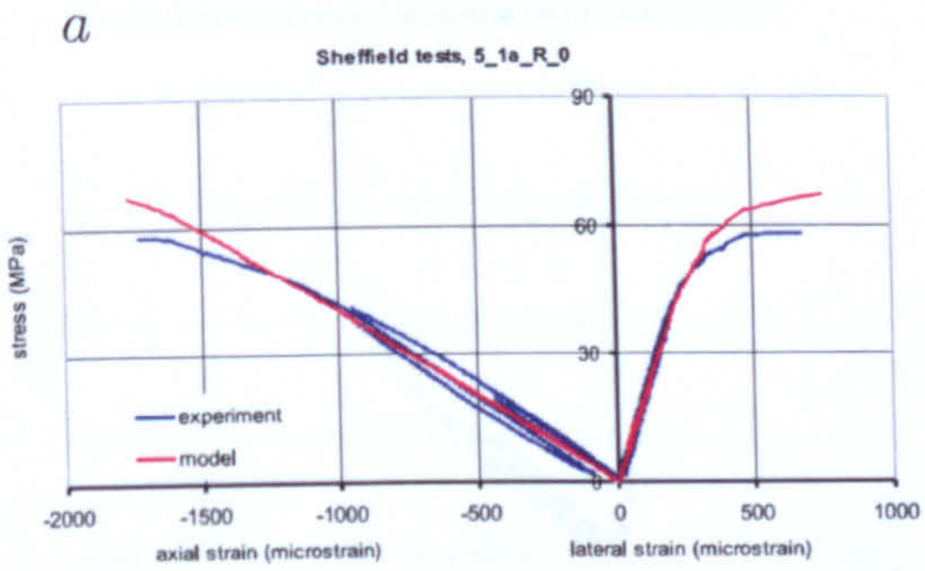

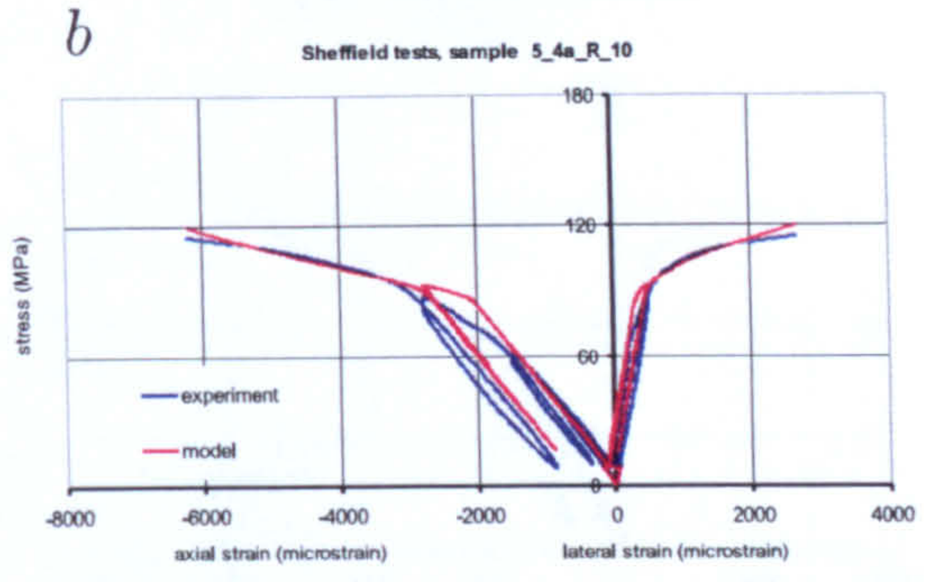

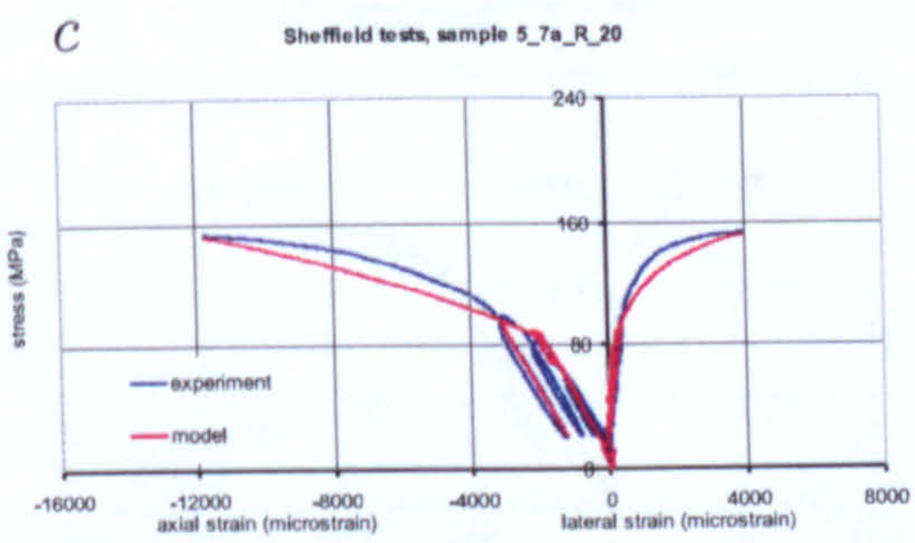

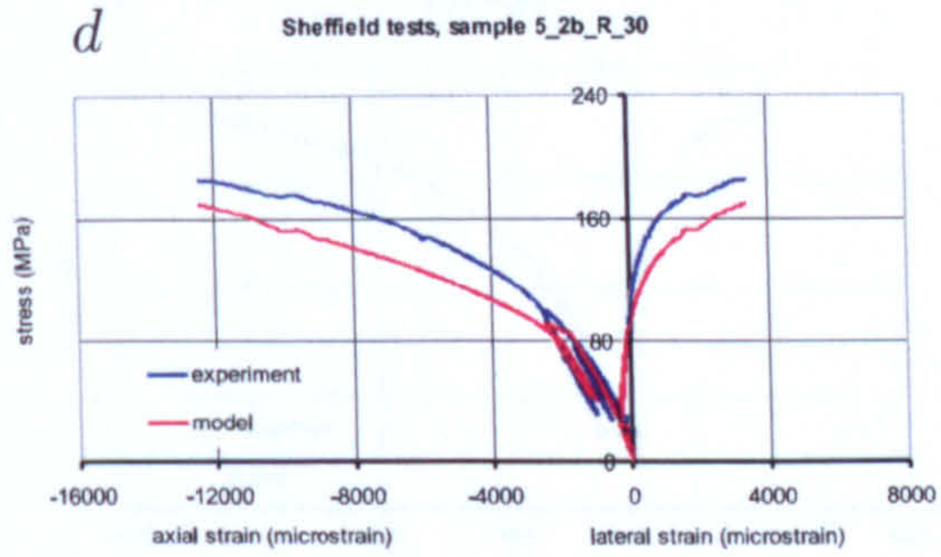

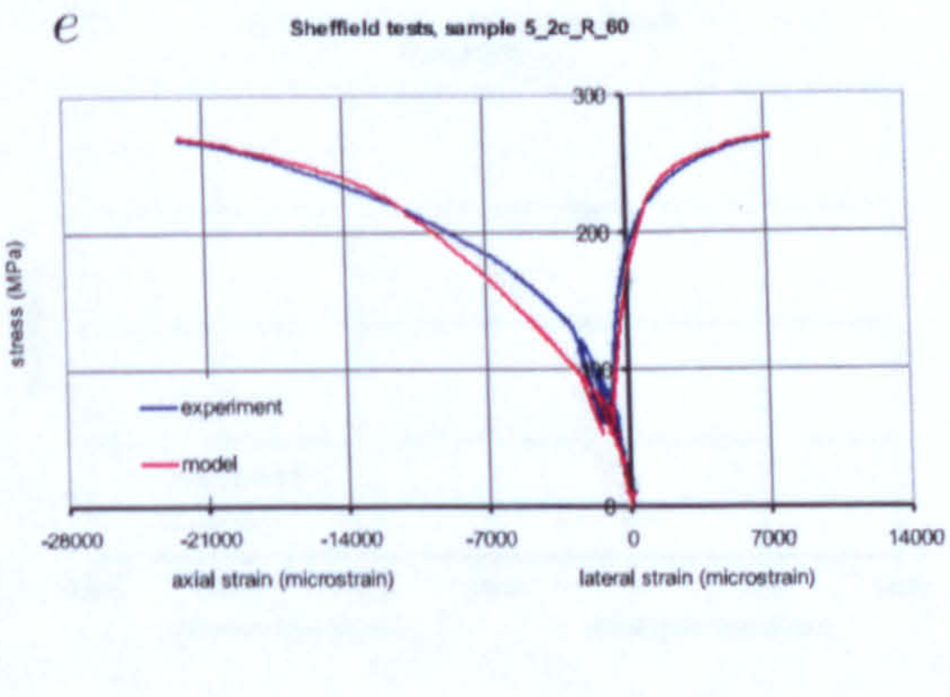

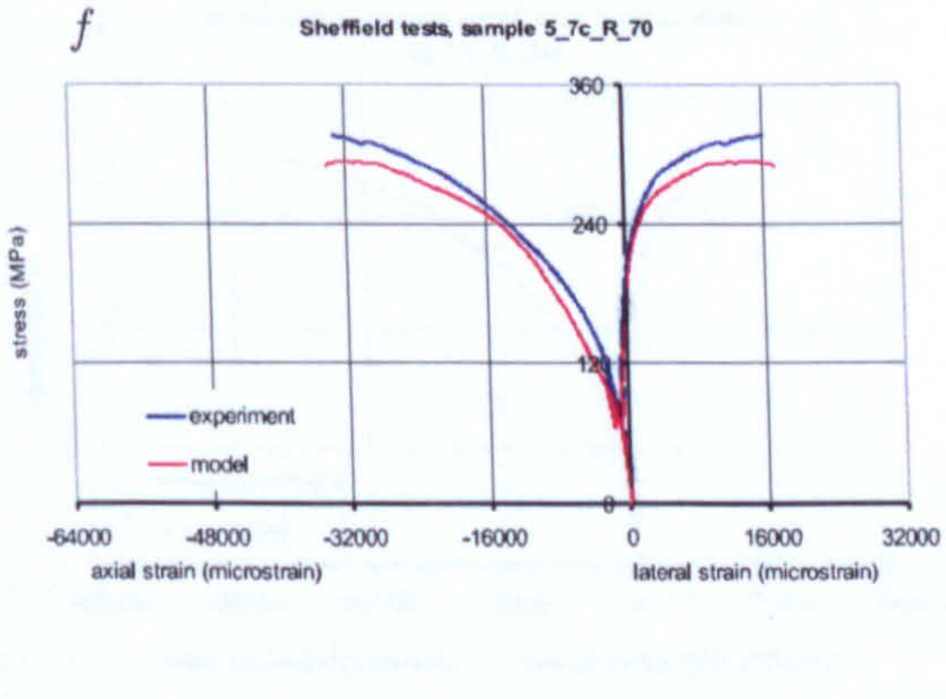

Figure 4.24: The predictions of the model for six different level of confinement for Sheffield triaxial compression tests using fixed values for A_h and B_h

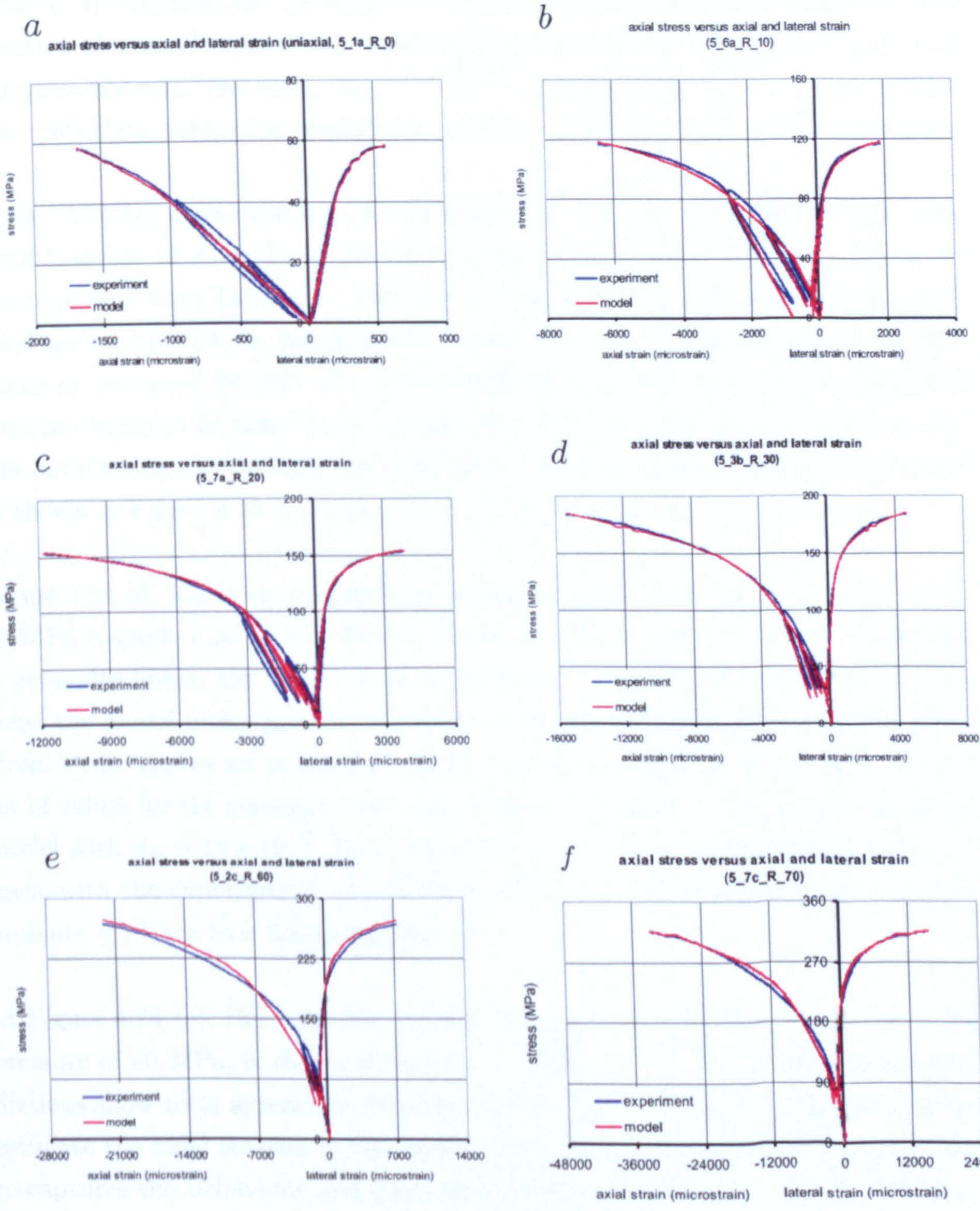

Figure 4.25: The predictions of the model for six different level of confinement for Sheffield triaxial compression tests using different values for A_h and B_h

for the lateral stresses seem to agree well with the experimental data and the shape of the curve is also in close agreement. The response of the model for the axial stresses seems to be linear in the first two cycles. The model does predict well the values of the stresses but the shape of the curve is close to a linear response. The selection of a small value of A_k could improve the shape of the curve. Figure 4.25 (b) shows the same test using $A_h = 7 \times 10^{-5}$, $B_h = 0.2$ and $A_k = 1$. It can be seen that with these values the prediction of the model is very close to the experiment.

Figure 4.24 (c) shows the model simulation for a triaxial compression test with a confinement of $\sigma_2 = \sigma_3 = 20$ MPa (sample 5_7a_R_20) using the values for the constants from Table 4.3. The lateral prediction of the model seems to be in good agreement with the experiments. As for the axial stresses the model response seems to be linear for part of the intermediate zone, then towards the peak the response tends to be none-linear and predicts well the peak stress of the concrete. The simulations can be improved if different values of material constants are used as shown in Figure 4.25 (c) where $A_h = 12 \times 10^{-5}$, $B_h = 0.265$, and $A_k = 1$.

Figure 4.24 (d) shows the results from a triaxial compression test where $\sigma_2 = \sigma_3 =$ 30 MPa (sample 5_3b_R_30). In the initial part of the tests, where the behaviour is generally linear, the model predicts well the stresses. After the cyclic loading zone, the model under-predicts the value of stresses but the general shapes of the stress-strain curves are maintained. The simulations could be improved if another set of values for the constants are used. Figure 4.25 (d) shows the prediction of the model with $A_h = 18 \times 10^{-5}$, $B_h = 0.25$, and $A_k = 1$. The model shows total agreement with the experiments. It can be seen that the improvement of the ductility measure (ζ) leads to a better simulation.

In Figure 4.24 (e), the behaviour of concrete under triaxial compression at a cell pressure of 60 MPa, is shown (sample 5_2c_R_60). Whilst the lateral stresses predictions show total agreement with the experiments, the model appears to underestimate the axial stresses in the intermediate part of the curve. The model then re-captures the behaviour and good agreement is achieved with the experiments. Figure 4.25 (e) shows the simulations of the same sample with $A_h = 29.5 \times 10^{-5}$, $B_h = 0.25$, and $A_k = 1$. The model predictions have been enhanced with the changing of the constants which give another confirmation of the significant role of the ductility measure ζ.

Finally, in Figure 4.24 (f), a triaxial compression test with a cell pressure of 70 MPa

(sample 5_7c_R_70) is simulated. The model slightly underestimates the values of stresses but the model captures the general shape of the stress-strain curve. Figure 4.25 (f) shows the simulations of the same sample with $A_h = 25 \times 10^{-5}$, $B_h = 0.25$, and $A_k = 1$. The simulations show very good agreement with the experiments.

The predictions of the model are compared with results from uniaxial and triaxial compression tests. It is shown that excellent predictions of the stress-strain responses for most of the compression tests are achieved. The predictions could be improved if different values for the ductility measure constants are used. Another set of simulations were performed by fixing all the material constants except the material constant B_h. These simulations have shown very good agreement with the experimental tests. The values of the material constant B_h were increased with the increase of the confinement. The relationship between B_h and ξ could be modelled with an exponential function. This requires an amendment to the model and an introduction of more derivatives and also leads to an increase in the number of material constants. However, this could open the way for further improvement to the model through the investigation of the properties of the ductility measure ζ. The simulations -in general- have shown that the assumption of associated flow is valid for modelling the behaviour of plain concrete under triaxial compression loading.

4.5.2 Colorado Multiaxial Compression Tests

In the previous section, results from triaxial compression Hoek cell tests have been simulated. In this section the performance of the model will be evaluated using multiaxial compression tests. Colorado data is used to verify the simulations. The data comprise sixty seven multiaxial loading tests. Stresses were applied in appropriate steps, and principal strains were measured and recorded for each load step, so that the complete stress-strain curves could be drawn. Details of the test program are contained in references [Scavuzzo] and [Stankowski].

The test program can be divided into the following series;

1. Series 1: Twelve cyclic triaxial tests, consisting of cyclic hydrostatic preloading to various stress levels, followed by proportional deviatoric stress cycles without reversal along the triaxial compression, simple shear, and triaxial extension paths.

2. Series 2: Eight cyclic triaxial tests consisting of hydrostatic pre-loading, followed by proportional deviatoric stress cycles with reversal along the same

deviator path as in series 1.

3. Series 3: Seventeen tests consisting of hydrostatic loading, followed by stress deviation, followed by a circular stress path within the deviatoric plane.

4. Series 4: Twenty two axisymmetric triaxial tests to explore load path effects; in addition to proportional and hydrostatic-deviatoric paths. This series contained stair-case type loadings to explore convergence to the proportional path, tests with hydrostatic stress increments with and without hydrostatic preloading, and tests under non-proportional loadings.

5. Series 5: Six tests within the deviatoric plane, as well as a number of other tests specifically designed to check the meaning of loading and unloading.

6. Series 6: Two tests of piecewise-uniaxial loadings.

For every test, the plastic flow has been presented using the same procedures described in Chapter 2. The average uniaxial compression strength is reported to be 22.6 MPa, the Young's modulus is 20.0 GPa and Poisson's ratio is 0.2.

In order to plot the results clearly in one figure, the first two strain readings are taken as negative and the third is taken as positive. Every stress is plotted against its associated strain.

The simulations of the first series of these tests are shown in Figures 4.26 to 4.28. Figure 4.26 shows the model simulation (red line) and the experimental stress-strain responses (black line) from test 1-1 to test 1-4. Test 1-1 is a cyclic triaxial extension (TE) test preformed by hydrostatic loading reaching a value of $\bar{\xi}$ = -3.8 in two loading-unloading cycles, followed by deviatoric loading reaching a value of ($\bar{\rho}$ = 2.3) in two loading-unloading cycles. The plastic flow in the hydrostatic zone shows scattered directions. This is due to the loading-unloading cycles where the the experiments suggested that there is an occurrence of plastic strains while theoretically the behaviour should be purely elastic. The plastic strains directions show consistency during the deviatoric loading. They suggest decreasing in compaction while the deviatoric loading increases. The results of the model simulations show that the model predicts well the general shape of the stress-strain curve but underestimates the stresses in the region close to the peak. This could be improved if different values for the ductility measure constants A_h and B_h are used.

In the same figure, the plastic flow and the model simulation for Test 1-2 is shown. This is a cyclic triaxial compression (TC) test which has been performed in the

same manner as the previous test with lower deviatoric loading. The model picks up the general shape of the stress-strain curves but slightly over estimates the stresses for one of the principal axes. At the end of one of the stress-strain curves there seems to be perfect plastic response where the model unable to capture. Test 1-3 is shown in the same figure. This is cyclic simple shear (SS) test with the same level of hydrostatic loading. The results are similar to the previous test. The results of both tests could be improved if the ductility measure (ζ) value increases slightly. This can be done by changing the values of the ductility constants A_h and B_h.

The performance of the model for test 1-4 is shown in the same figure. This is a cyclic triaxial compression (TC) test where the highest value of $\bar{\xi}$ = -2.8. The plastic flow takes the same trend with some vertical plastic strain vectors indicating that the test reached the volumetric transition stress (VTS) point. The model shows very good agreement with most of the test.

Figure 4.27 shows test 1-5 which is cyclic simple shear (SS) test where $\bar{\xi}$ = -2.8 is the deviatoric plane. The plastic flow also takes the same trend with some odd readings during the deviatoric loading, which could be due to the loading-unloading cycles. The model picks up the general trend of the behaviour, but close to the peak it slightly over predicts the stresses. This is due to the value of ζ which is controlled by the two constants A_h and B_h. In the same figure the performance of the model for test 1-6 is shown. This is cyclic triaxial extension (TE) test where the deviatoric plane is as in the previous test. The model slightly underestimates two principal stresses and overestimates the third. This could be improved by revisiting the values of the ductility constants. In the same figure, the test 1-7 is shown. This is a cyclic triaxial compression (TC) test in which the loading path in nominally identical to that of test 1-5. The model follows the general trend of the stress-strain behaviour and slightly over estimates the stresses. Test 1-8 is shown in the same figure. This test has been preformed in the same way of the previous tests. The model predictions is almost in total agreement with the experimental data.

The results for test 1-9 is shown in Figure 4.28. This a cyclic triaxial extension (TE) test with the deviatoric plane at $\bar{\xi}$ = -2.8. The plastic flow has the general directions as in the previous tests. The model predicts well the results for one principal stresses while slightly under predicts the other two. Test 1-10 shown in the same figure, is a cyclic triaxial compression (TC) with the deviatoric plane at $\bar{\xi}$ =

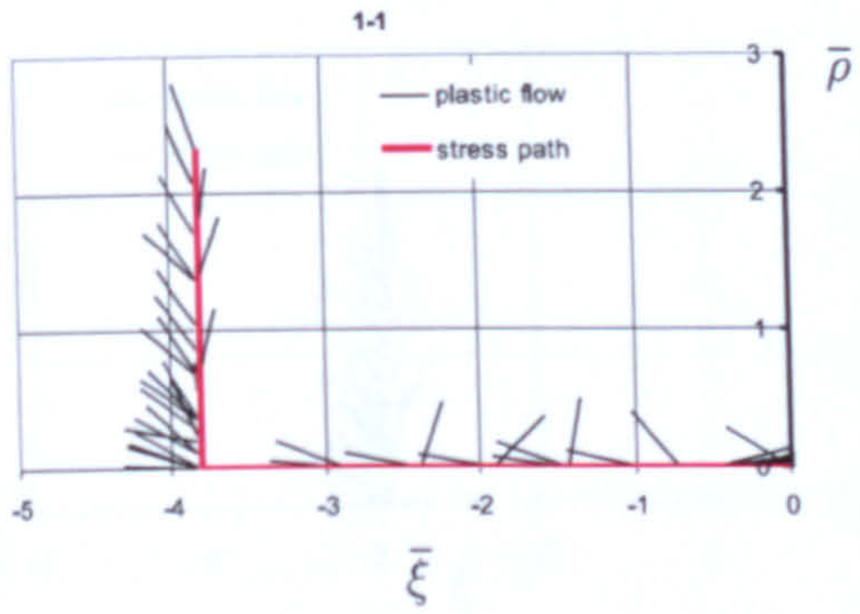

Figure 4.26: Plastic flow, stress paths and stress-strain simulations for Colorado tests, sample 1-1, 1-2, 1-3 and 1-4

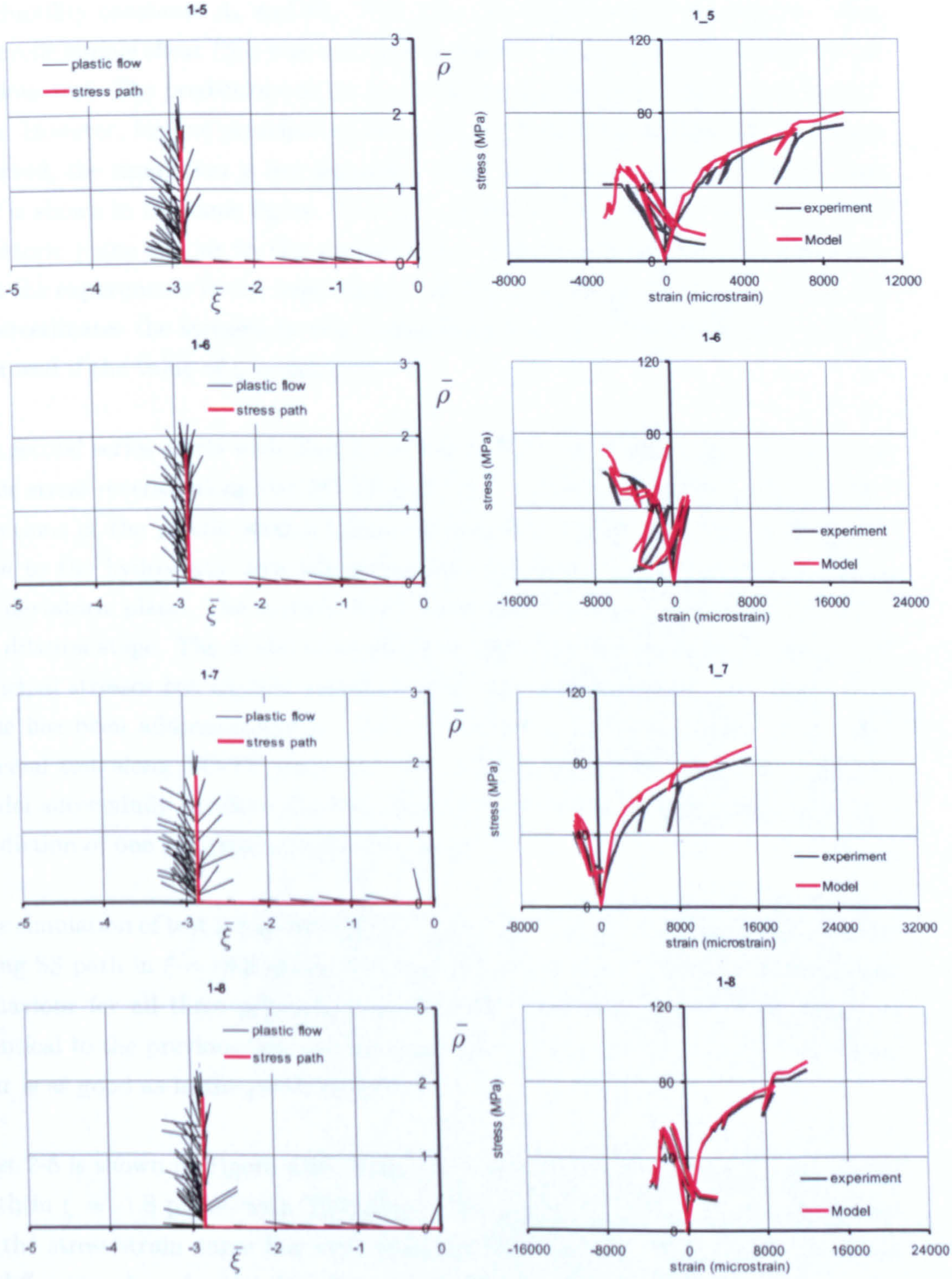

Figure 4.27: Plastic flow, stress paths and stress-strain simulations for Colorado tests, sample 1-5, 1-6, 1-7 and 1-8

-3.8. The model predicts the values of the stresses very well but, close to the peak the model underestimates slightly their values. This can be improved by changing the ductility constants A_h and B_h. Test 1-11 also shown in the same figure. This is a cyclic simple shear (SS) test with the deviatoric plane at $\bar{\xi}$ equal to that of the previous test. The predictions of the model agree almost totally with experimental data. However, for one principal stress at peak, where perfect plasticity has been observed, the simulation is not adequate. This has been noticed perviously. Test 1-12 is shown in the same figure. This is a cyclic triaxial extension (TE) test with deviatoric plane similar to the previous test. The results show good agreement with the experiments in the beginning of the test, but close to the peak the model underestimates the stresses in two principal directions. The prediction could be improved if the value of ζ is changed.

The second series starts with Test 2-1 which is shown in Figure 4.29. Test 2-1 is a cyclic stress reversal along the TC-TE path in $\bar{\xi}$ = -3.8 plane with TC failure. The directions of the plastic strains follow the expected trend indicating compaction close to the hydrostatic axis which decreases gradually as the test moves along the deviatoric plane. The vertical direction at the end is an indication of reaching the dilation stage. The model successfully predicts the experimental results for all principal stresses but slightly underestimates the stresses close to the peak. This issue has been addressed earlier. Test 2-2 shown in the same figure, is a cyclic reversal test along TC-TE path in $\bar{\xi}$ = -3.8 plane with TE failure. Initially, the model successfully predicts the stress-strain behaviour but close to the peak the prediction of one principal stress is not as good.

The simulation of test 2-3 is shown in the same figure. This is a cyclic stress reversal along SS path in $\bar{\xi}$ = -3.8 plane. The model successfully predicts the stress-strain behaviour for all three principal stresses. Test 2-4 shown in the same figure, is identical to the previous test and the model predictions of the stress-strain behaviour is as good as in the previous test.

Test 2-5 is shown in Figure 4.30. This test is a cyclic stress reversal along TC-TE path in $\bar{\xi}$ = -1.8 plane, with TC failure. The model picked up the general shape of the stress-strain curve but over estimated the stresses. This can be improved if different values for the ductility constants are used. Test 2-6 is shown in the same figure. This test is a cyclic stress reversal along TC-TE path in $\bar{\xi}$ = -1.8 with TE failure. The model predicts well the initial response but for stresses close to the peak the model overestimates the stresses. This can be improved by revisiting

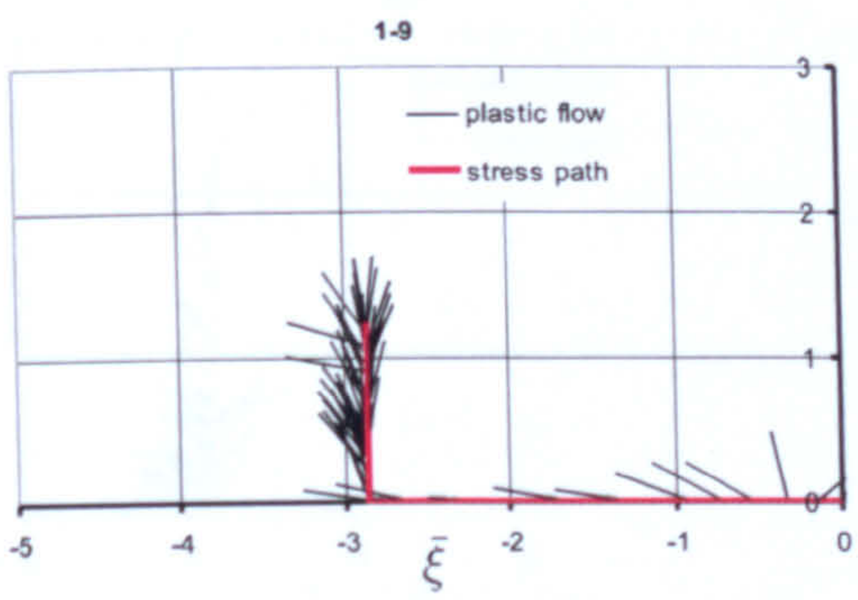

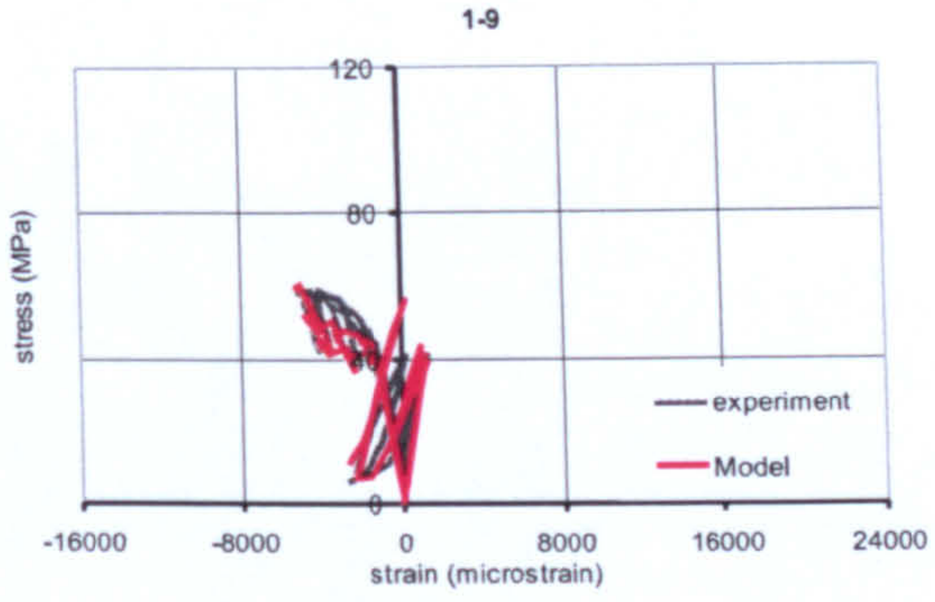

1-10

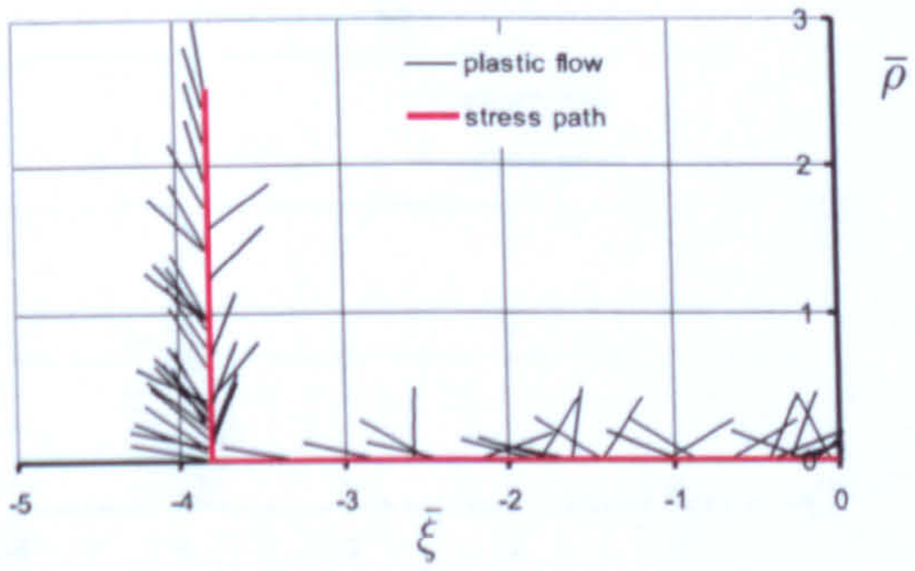

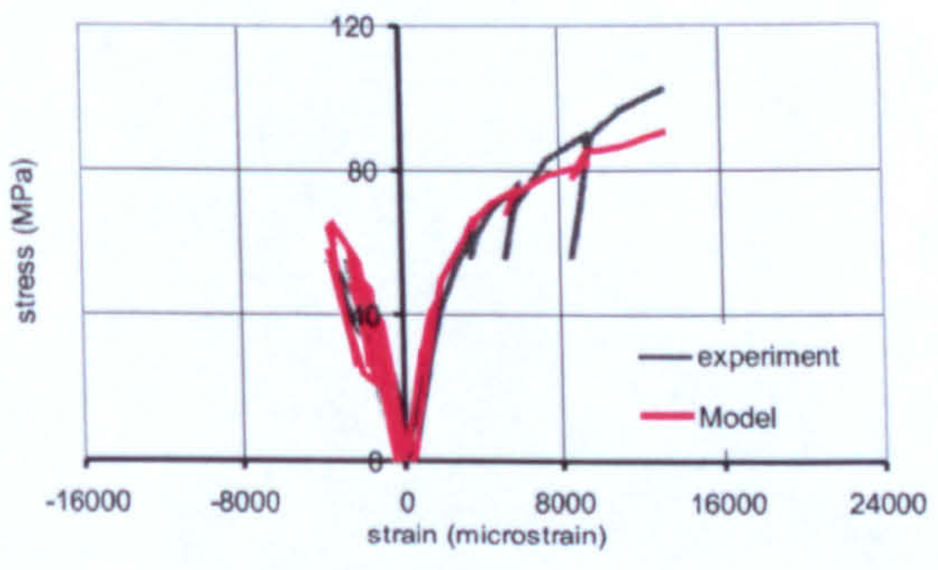

1-11

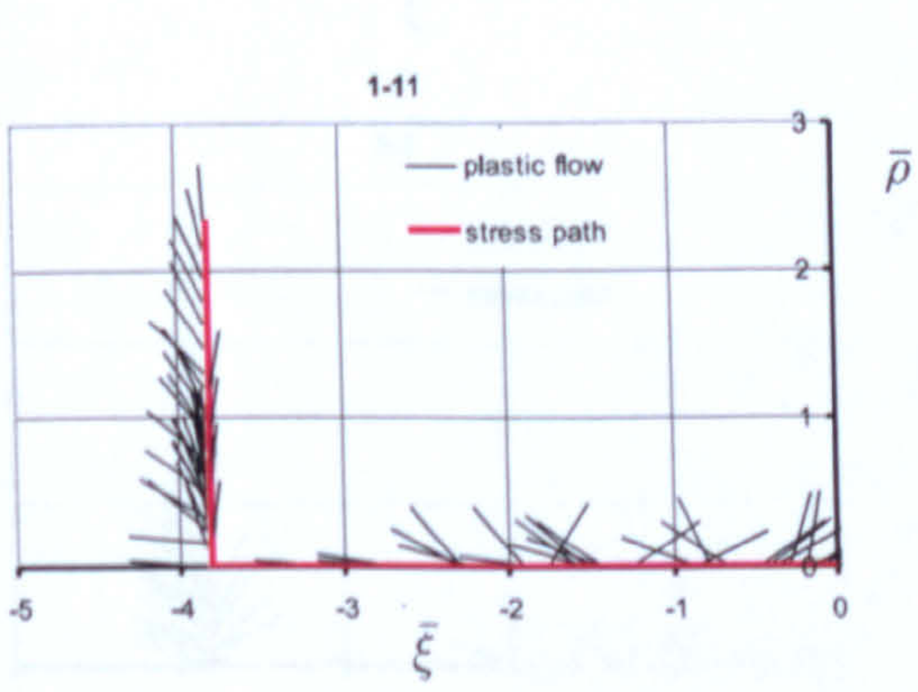

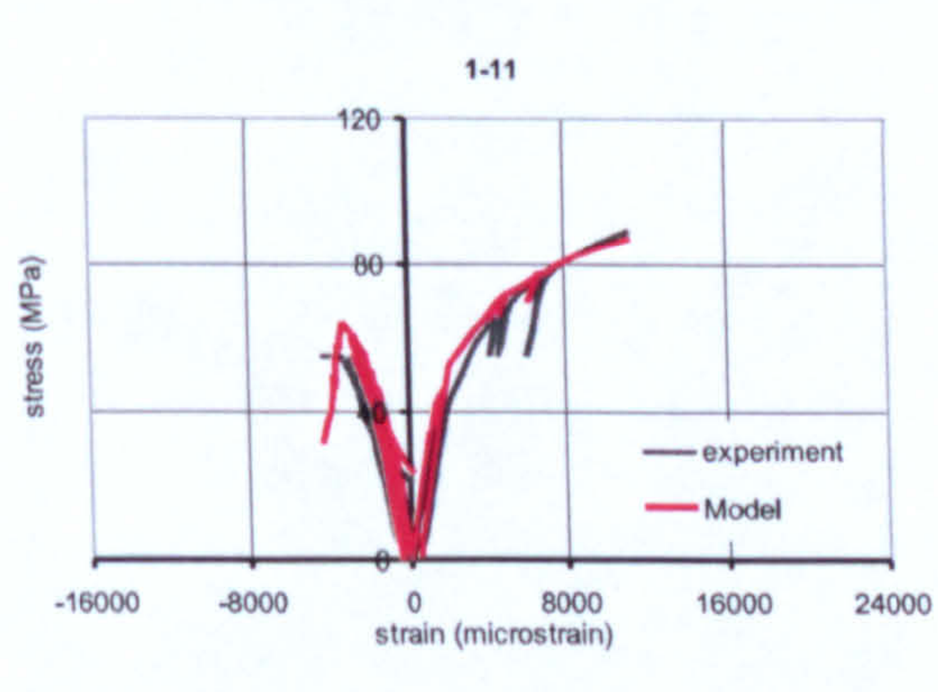

1-12

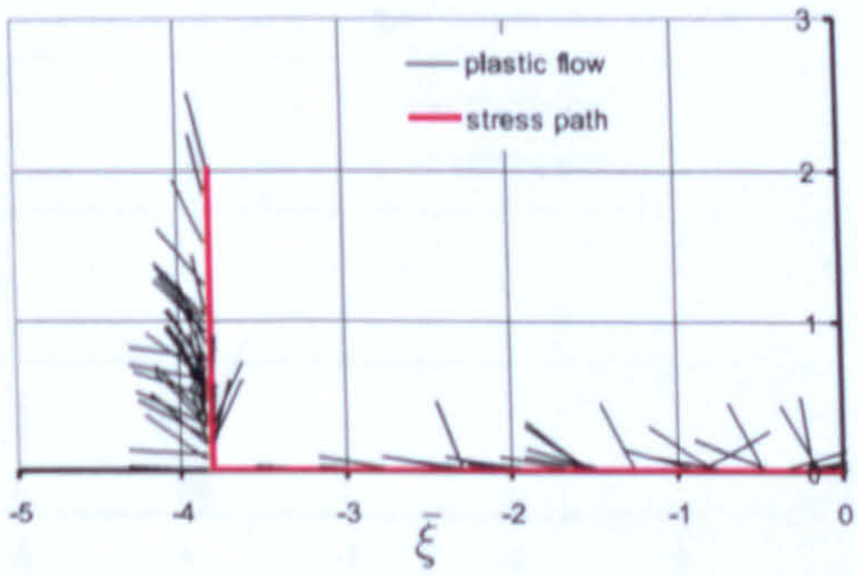

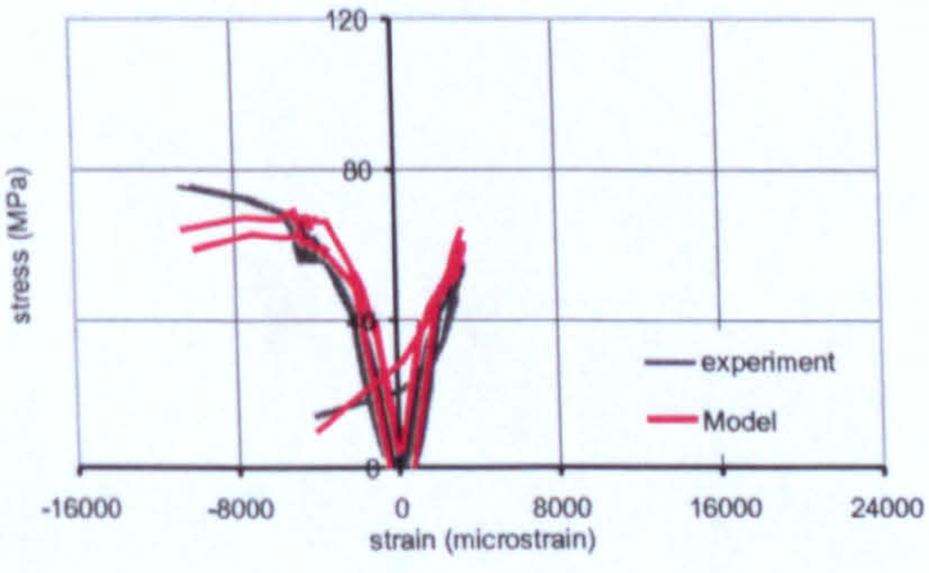

Figure 4.28: Plastic flow, stress paths and stress-strain simulations for Colorado tests, sample 1-9, 1-10, 1-11 and 1-12

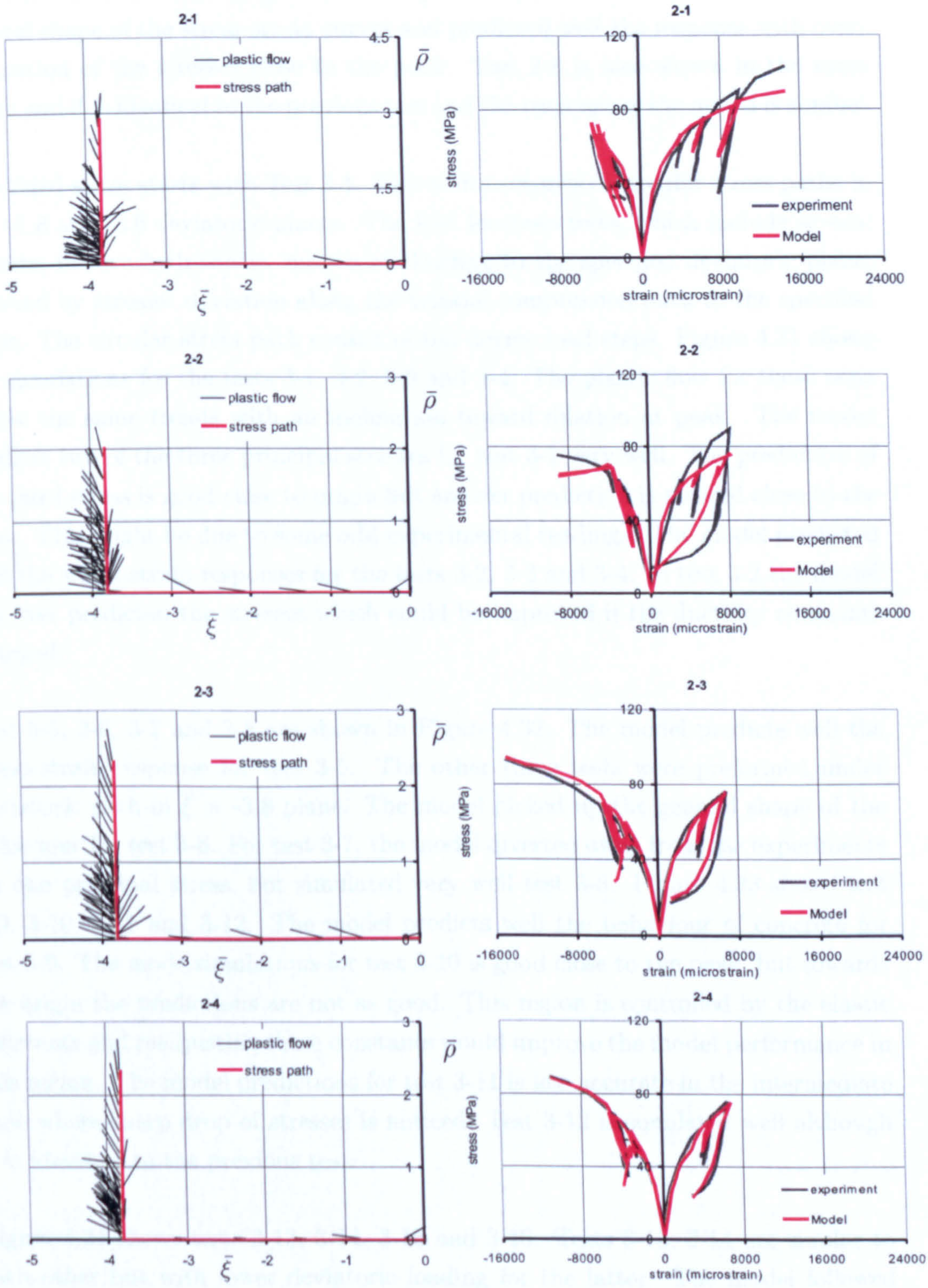

Figure 4.29: Plastic flow, stress paths and stress-strain simulations for Colorado tests, sample 2-1,2-2, 2-3, and 2-4

the values of the ductility constants. In the same figure test 2-7 is presented. It is cyclic stress reversal along SS path in $\bar{\xi}$ = -1.8 plane. The model followed the general shape of the stress-strain curves and predicted well the response with over-estimation of the stresses close to the peak. Test 2-8 is also shown in the same figure and it is identical to the previous test and the response of the model is similar.

The third series starts with Test 3-1. This series consists of circular stress paths in $\bar{\xi}$ = -1.8 and -3.6 deviatoric planes. The first fourteen tests, which include several repeats, involve hydrostatic, monotonic loading to the specified deviatoric plane, followed by stresses deviation along the triaxial compression path to the specified circle. The circular stress path consist of ten degree load steps. Figure 4.31 shows the simulations for the tests 3-1, 3-2, 3-3 and 3-4. The plastic flow for these tests follow the same trends with an inclination toward dilation at peak. The model predicts two of the three principal stresses for test 3-1 very well. The prediction of the third stress is good close to origin but an over prediction is noticed close to the peak. This might be due to some odd experimental readings. The model predicted well the stress-strain responses for the tests 3-2, 3-3 and 3-4. In test 3-2 the model has over predicted the stresses which could be improved if the ductility constants changed.

Test 3-5, 3-6, 3-7 and 3-8 are shown in Figure 4.32. The model predicts well the stress-strain response for test 3-5. The other three tests were preformed under deviatoric path in $\bar{\xi}$ = -3.8 plane. The model picked up the general shape of the behaviour for test 3-6. For test 3-7, the model diverted away from the experiments for one principal stress, but simulated very well test 3-8. Figure 4.33 shows test 3-9, 3-10, 3-11 and 3-12. The model predicts well the behaviour of concrete for test 3-9. The mode simulations for test 3-10 is good close to the peak, but towards the origin the predictions are not as good. This region is controlled by the elastic constants and readjusting these constants would improve the model performance in this region. The model predictions for test 3-11 is less accurate in the intermediate zone where sharp drop of stresses is noticed. Test 3-12 is simulated well although it is identical to the previous test.

Figure 4.34 shows tests 3-13, 3-14, 3-15 and 3-16. Tests 3-13, 3-14 are similar to each other but with lower deviatoric loading for the latter. The model followed well the general shape of the stress-strain response and the overall predictions are satisfactory.

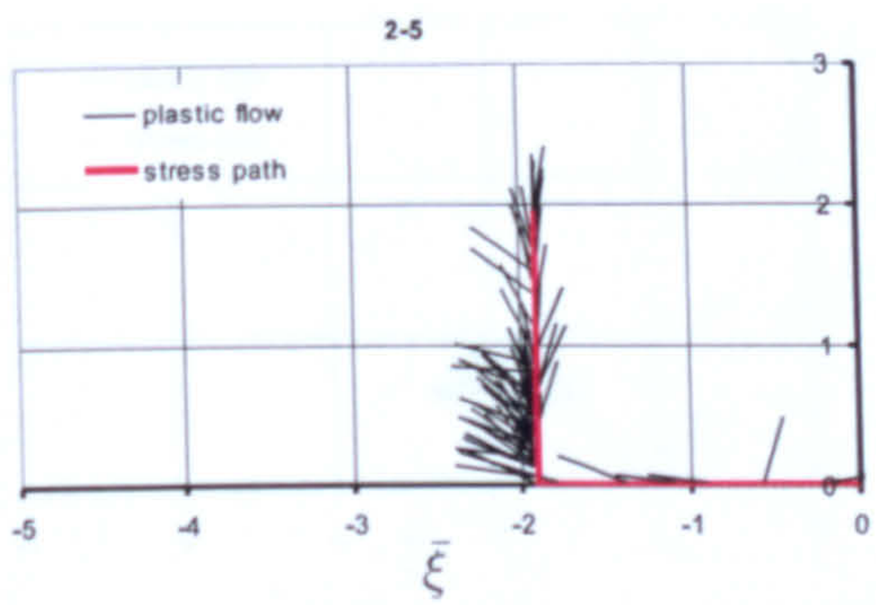

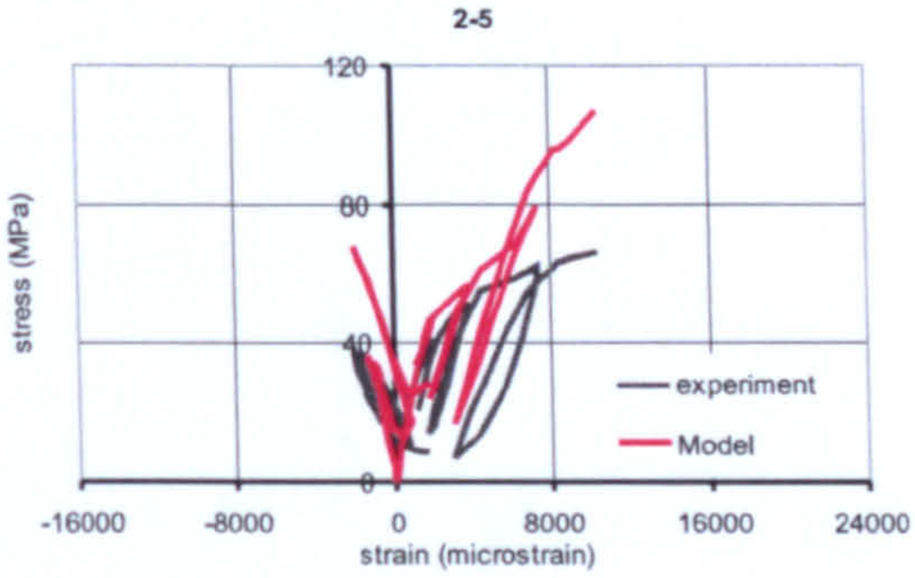

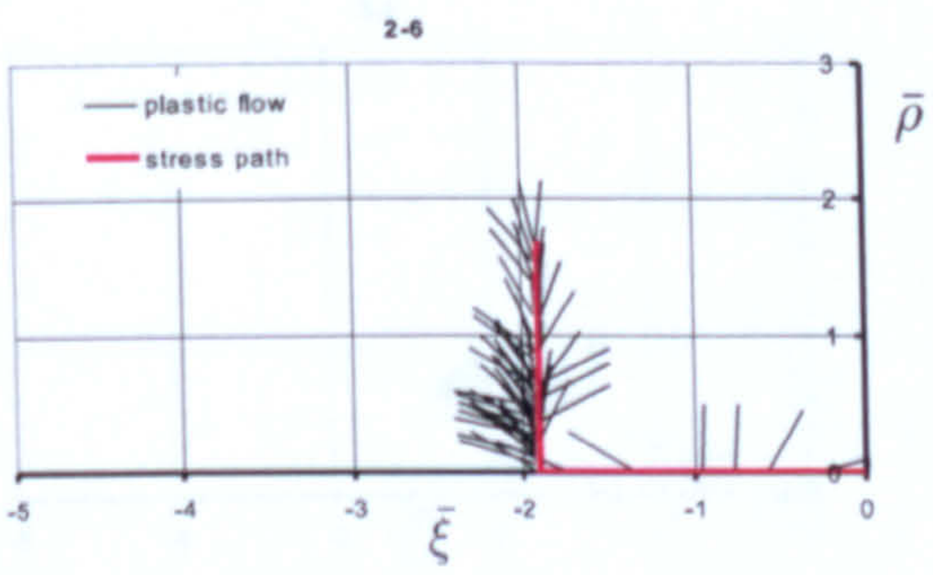

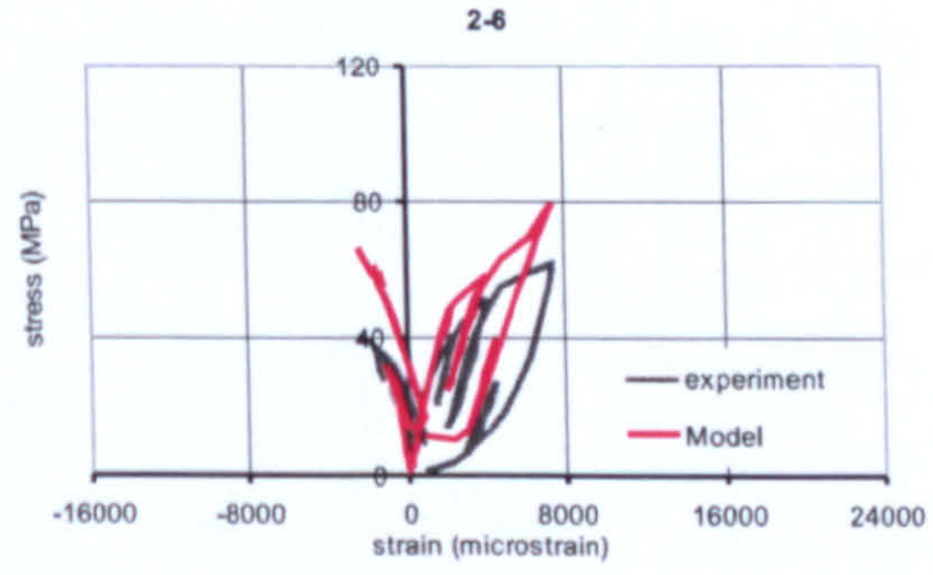

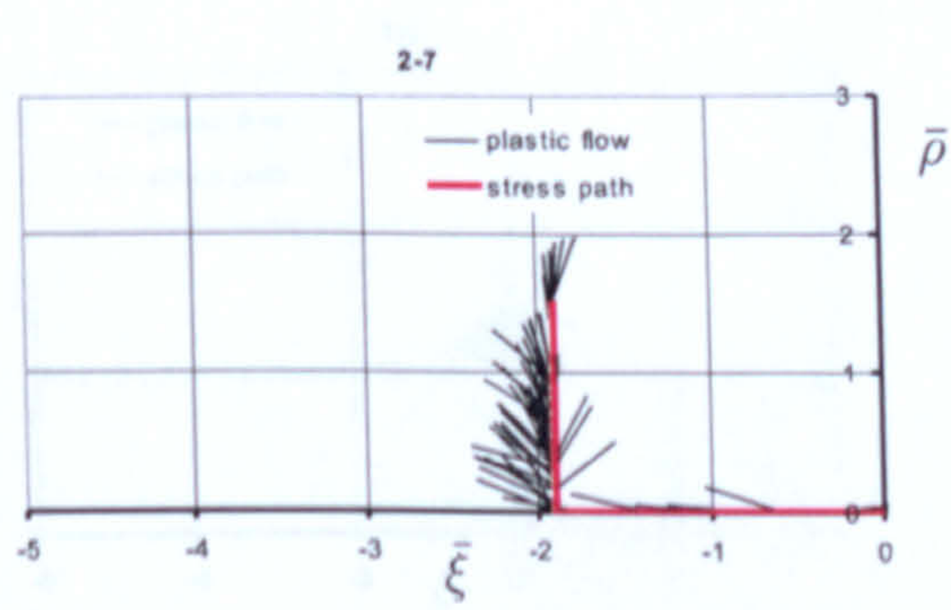

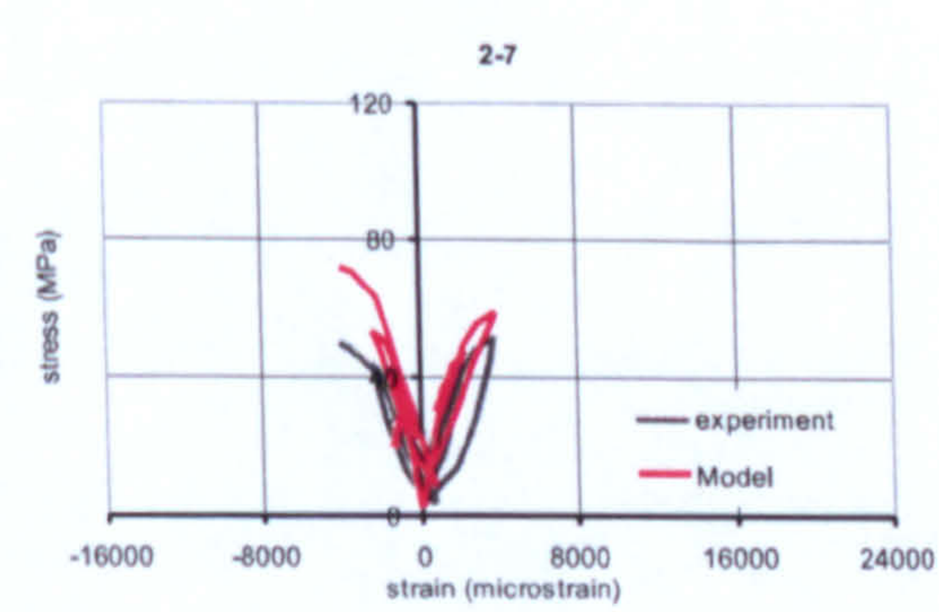

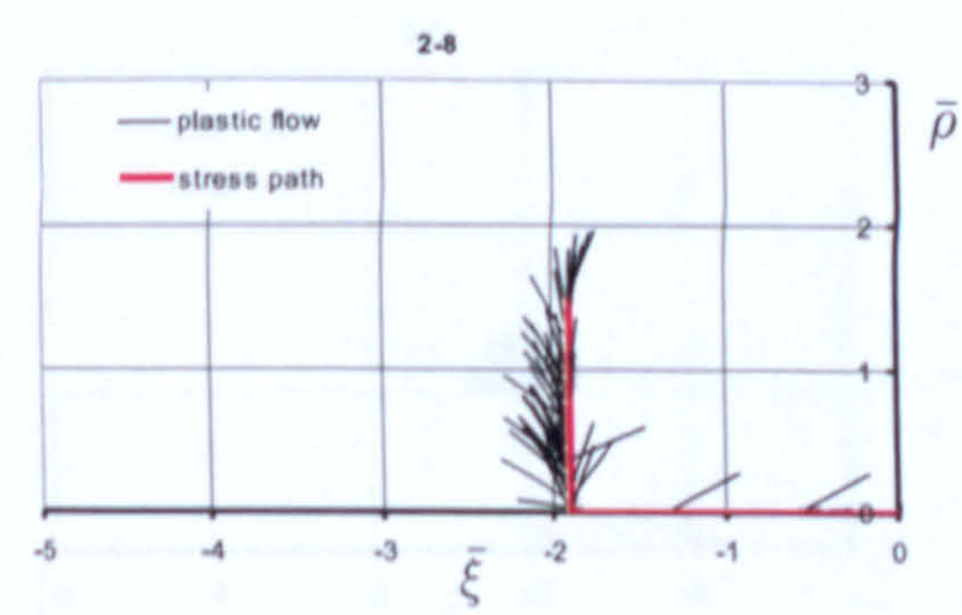

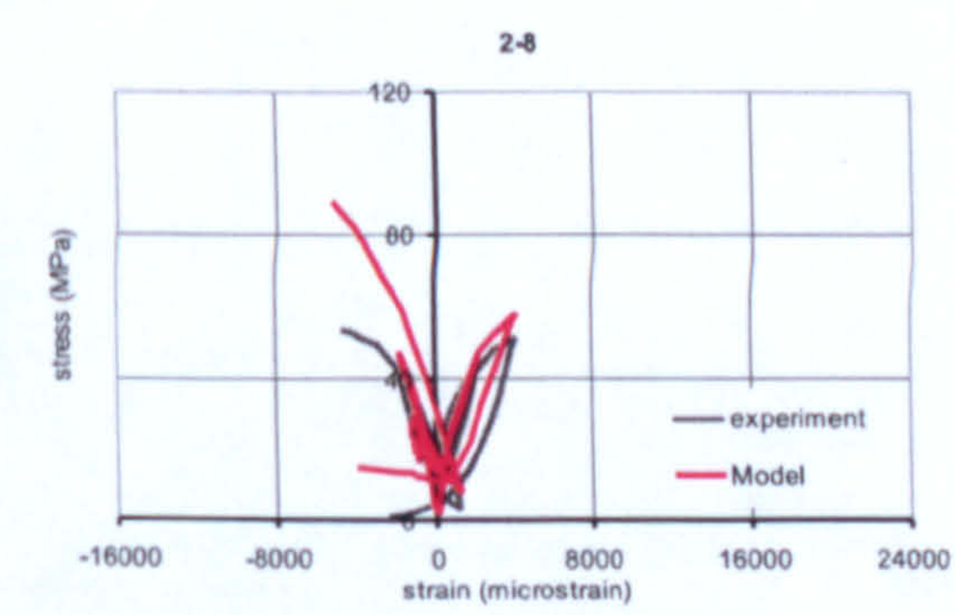

Figure 4.30: Plastic flow, stress paths and stress-strain simulations for Colorado tests, sample 2-5, 2-6, 2-7 and 2-8

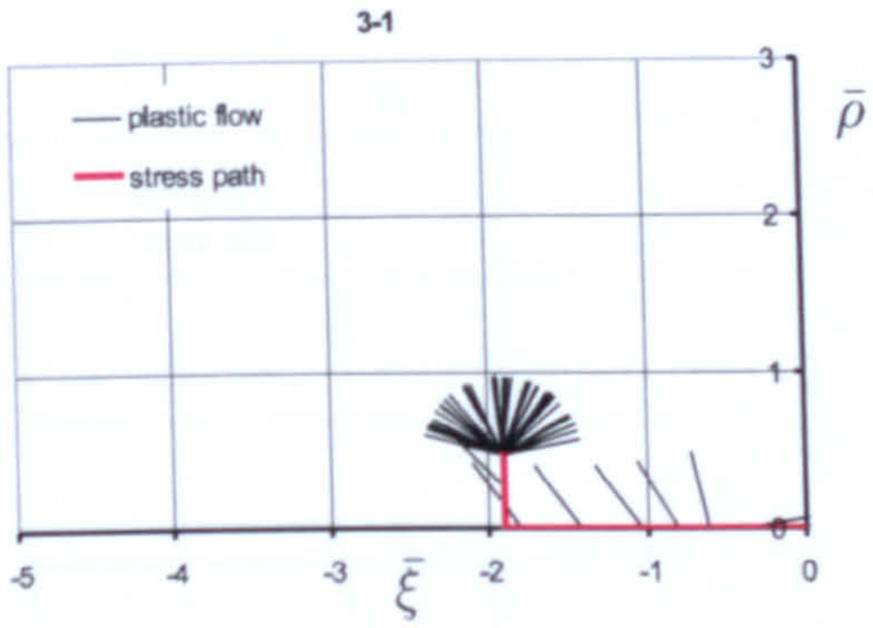

Figure 4.31: Plastic flow, stress paths and stress-strain simulations for Colorado tests, sample 3-1, 3-2, 3-3 and 3-4

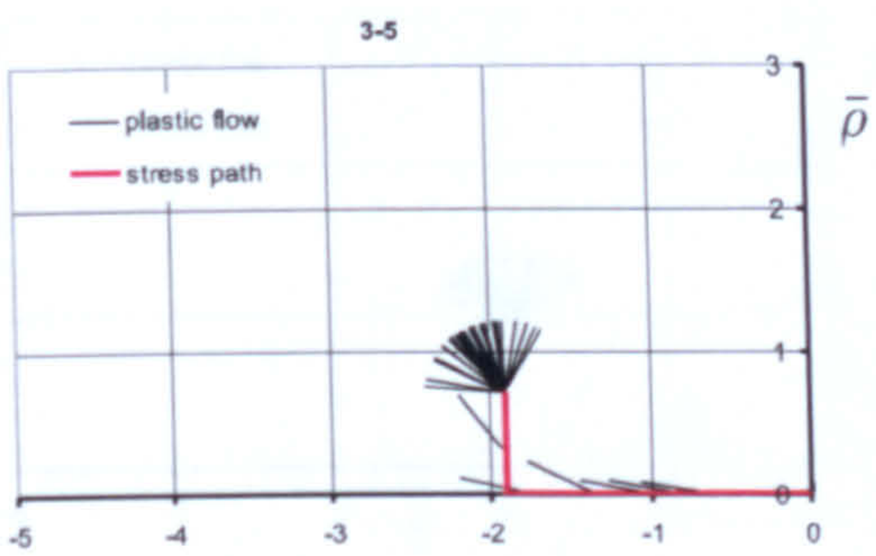

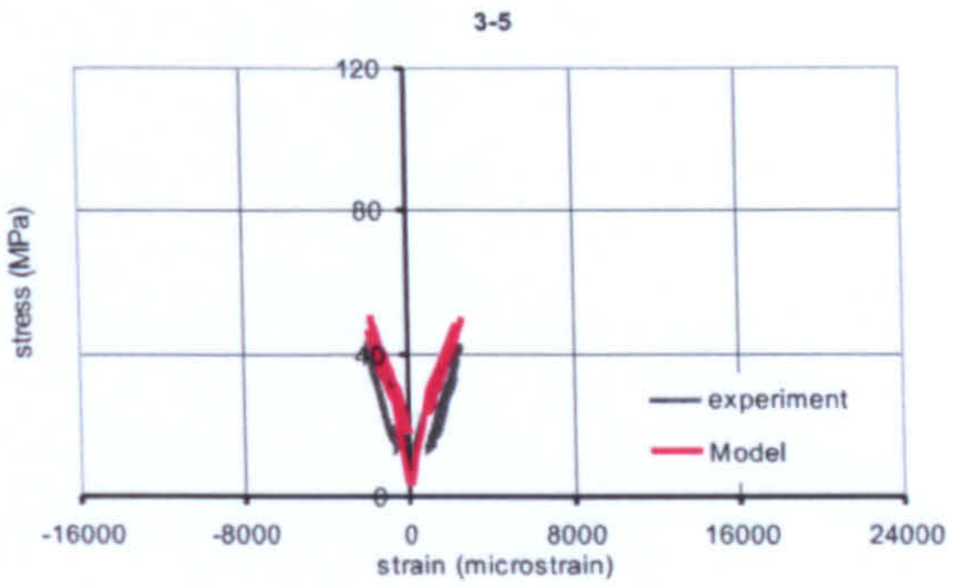

3-6

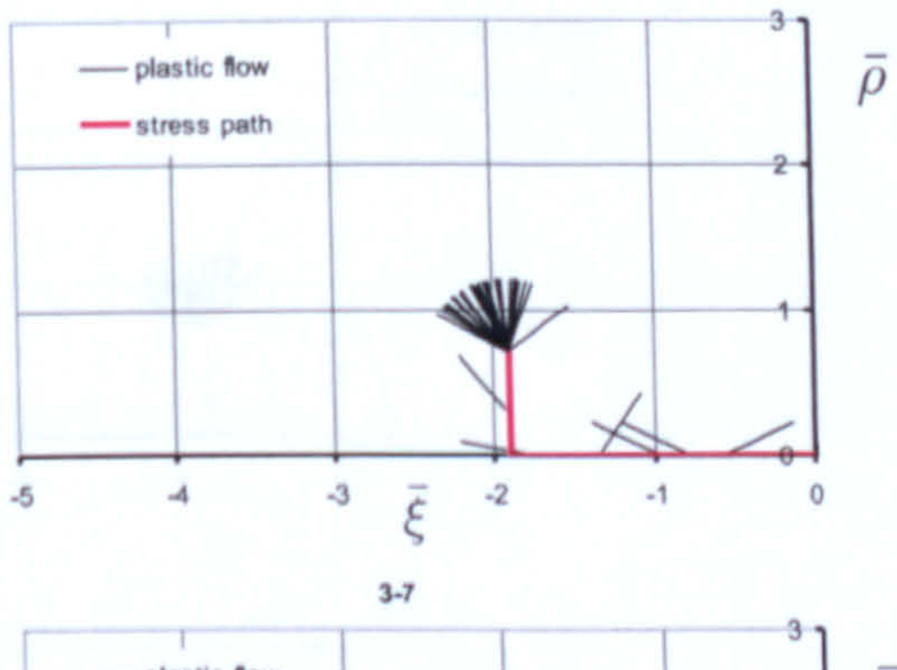

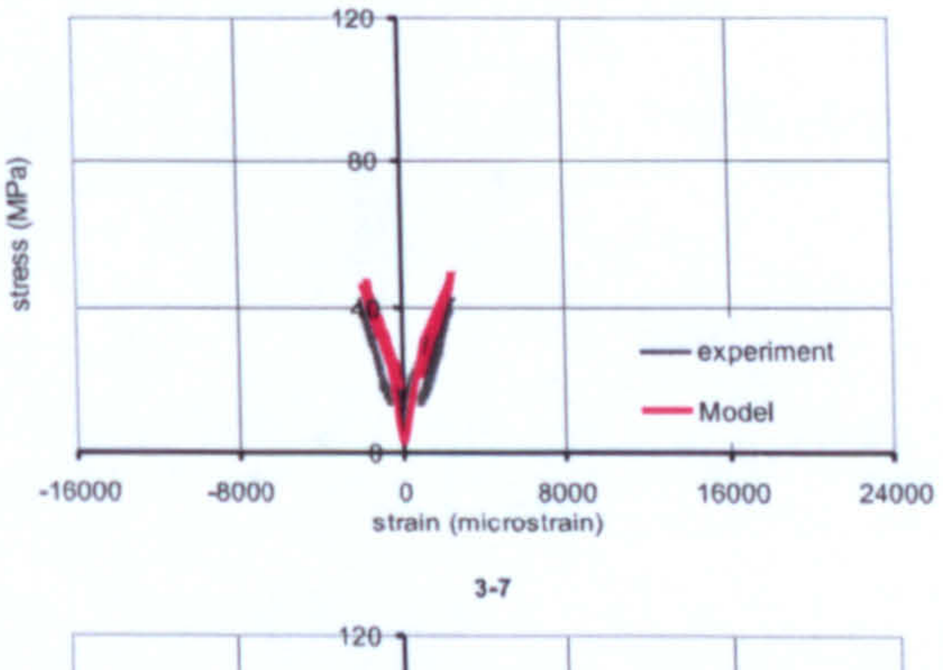

3-7

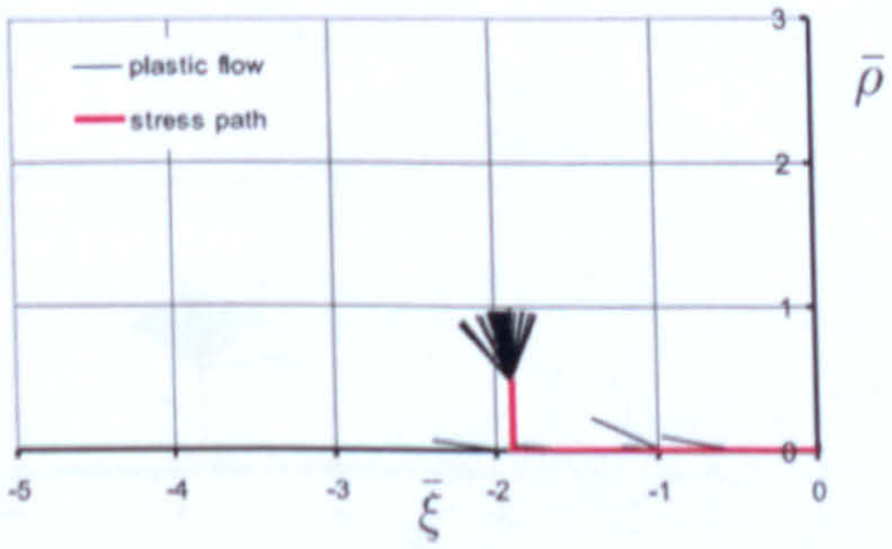

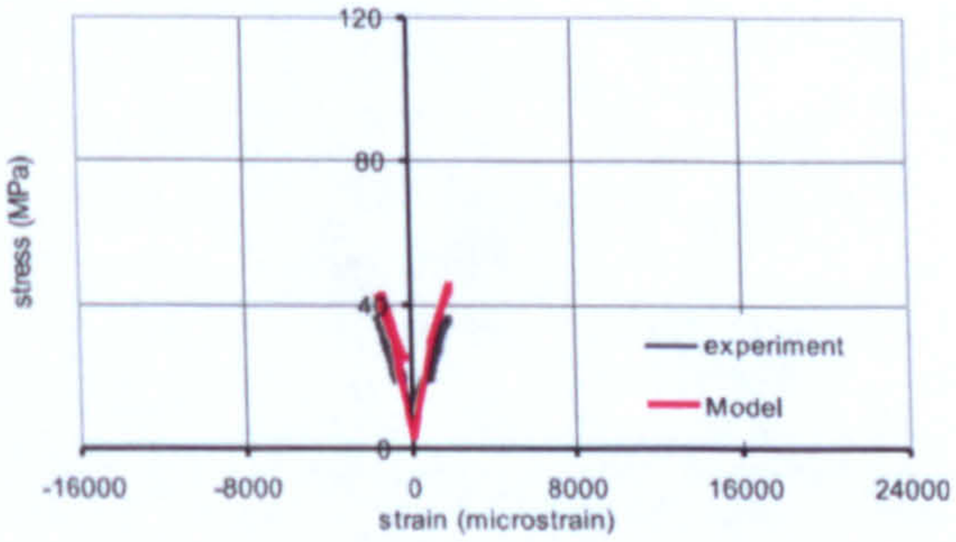

3-8

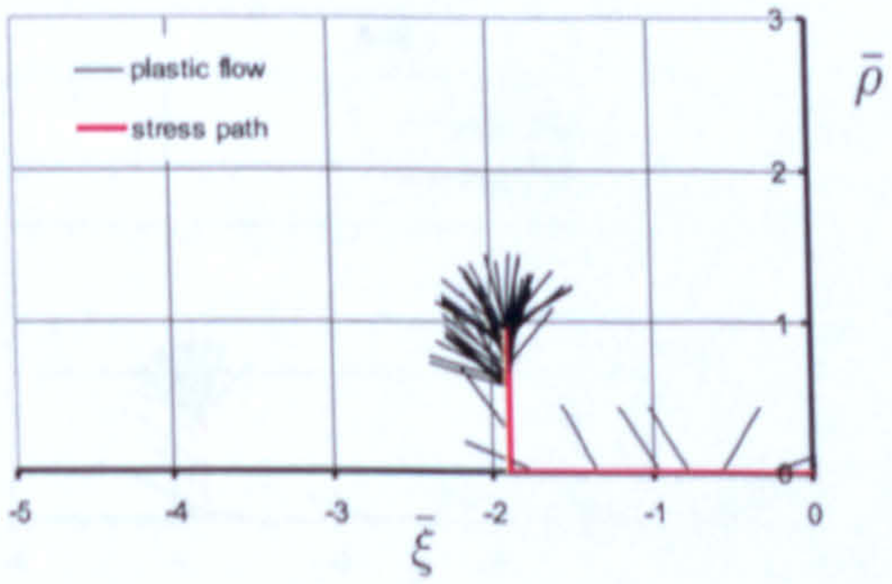

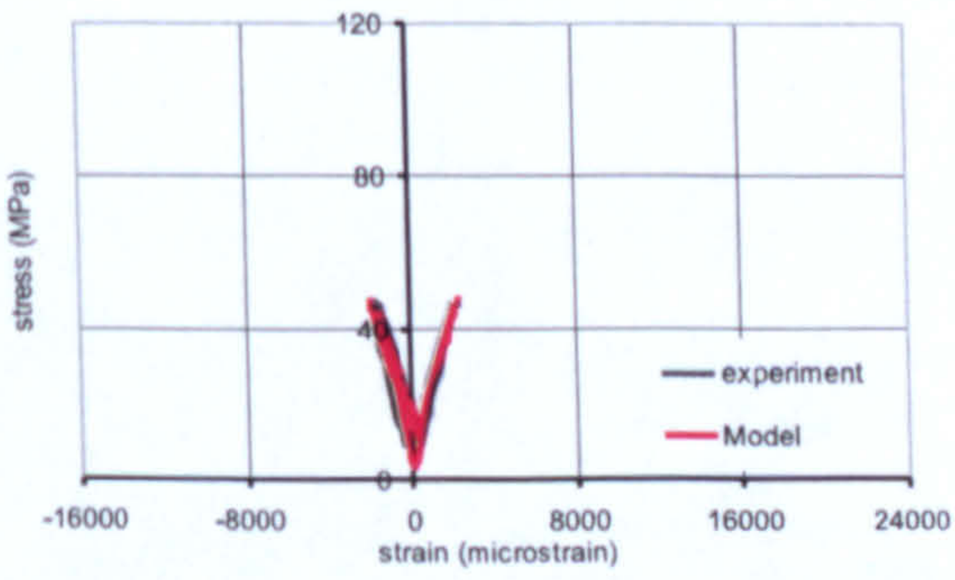

Figure 4.32: Plastic flow, stress paths and stress-strain simulations for Colorado tests, sample 3-5, 3-6, 3-7 and 3-8

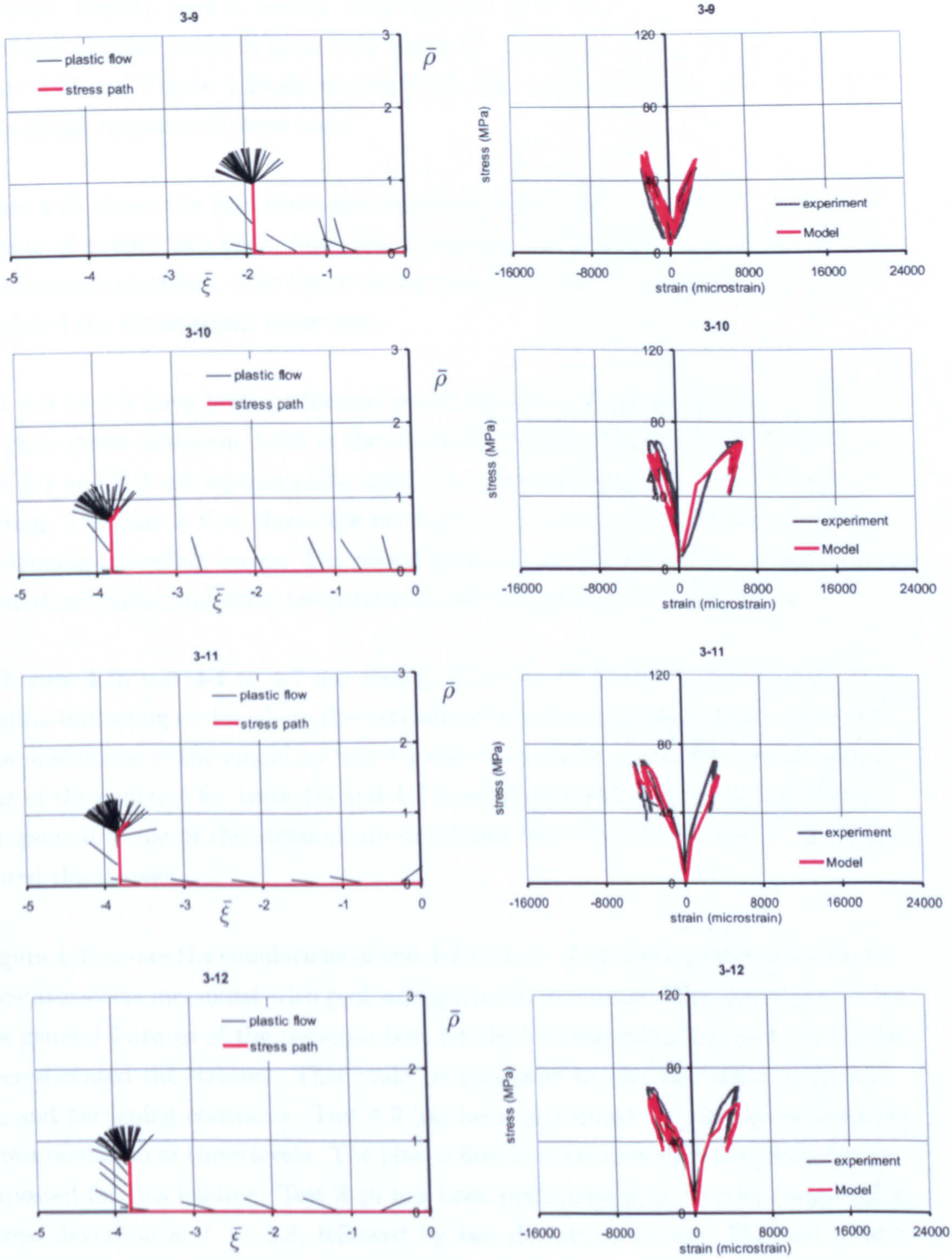

Figure 4.33: Plastic flow, stress paths and stress-strain simulations for Colorado tests, sample 3-9, 3-10, 3-11 and 3-12

Tests 3-15, 3-16 and 3-17 have been conducted using hydrostatic stress cycles up to various levels are applied in part A, followed in part B by circular stress paths as before. Finally, part C consist of hydrostatic post-loading in test 3-15, and of additional circular paths in tests 3-16 and 3-17. Tests 3-15 and 3-16 are shown in Figure 4.34 and Figure 4.35 shows test 3-17. The model predicts successfully the stress-strain response of these tests.

Figure 4.35 shows the first three simulations of the fourth series tests. This series consists of twenty two tests, intended to explore concrete response to loading at the extension meridian. The figure shows test 4-1 and 4-2, the model successfully simulated the stress-strain behaviour.

Test 4-3 to 4-8 have been performed under hydrostatic stress increments following prior stress deviation, both in the triaxially compressive and tensile directions. Test 4-1 and 4-2 are repeats while tests 4-4 to 4-8 involved prior hydrostatic preloading. The plastic flow shows the normal trends with some odd readings due to the loading-unloading cycles. The model picks up the behaviour of concrete under these stress paths and good predictions for all the stresses are observed.

In Figure 4.36 test 4-4 to 4-7 are shown. The plastic flow is inconsistent during loading-unloading cycles where theoretically should be no plastic strain occurrence. The predictions of the model for test 4-4 and 4-5 are very good. The overall behaviour of the concrete for tests 4-6 and 4-7 is simulated well and the model followed the general shape of the stress-strain behaviour but, close to the end, it overestimated the stresses.

Figure 4.37 shows the simulations of test 4-8 to 4-11. Test 4-8 is preformed with hydrostatic stress increment with preloading triaxial extension. The model picked up the general features of the response but, for the loading-unloading part the model overestimated the stresses. This could be improved by the alteration of the elastic and hardening constants. Test 4-9 has been preformed by triaxial compressive stress deviation at three levels. The plastic flow is consistent with the general shape expected for this loading. Test 4-10 has been preformed with triaxial compressive stress deviation at $\bar{\xi}$ = -2.8, followed by two deviatoric cycles. The odd plastic flow is attributed to the loading-unloading cycles. Test 4-11 has been preformed using triaxial compressive stress deviation at $\bar{\xi}$ = -3.8, followed by additional stress deviation. In these tests the predictions of the model does pick up the general trend of the behaviour of concrete but, the general fitting is not as good as the pre-

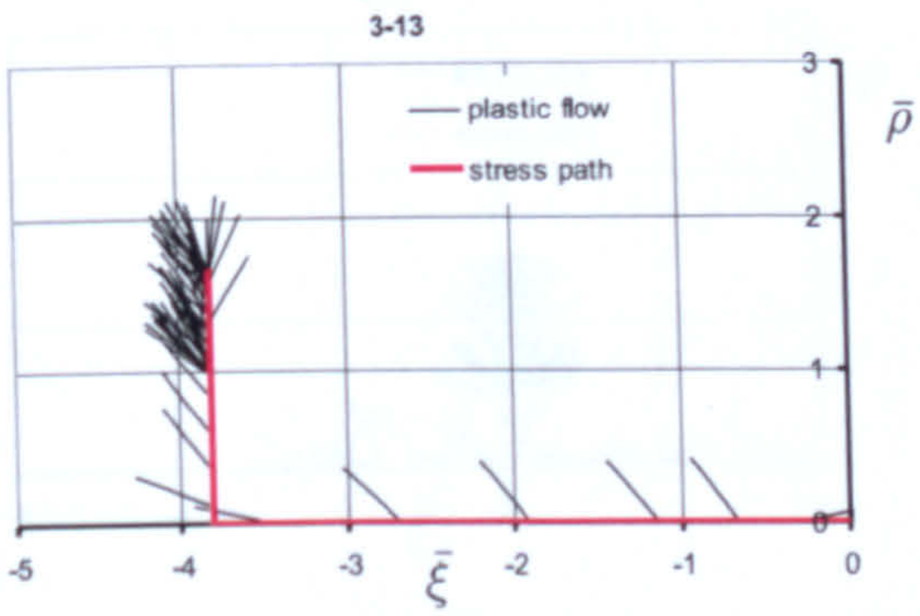

3-14

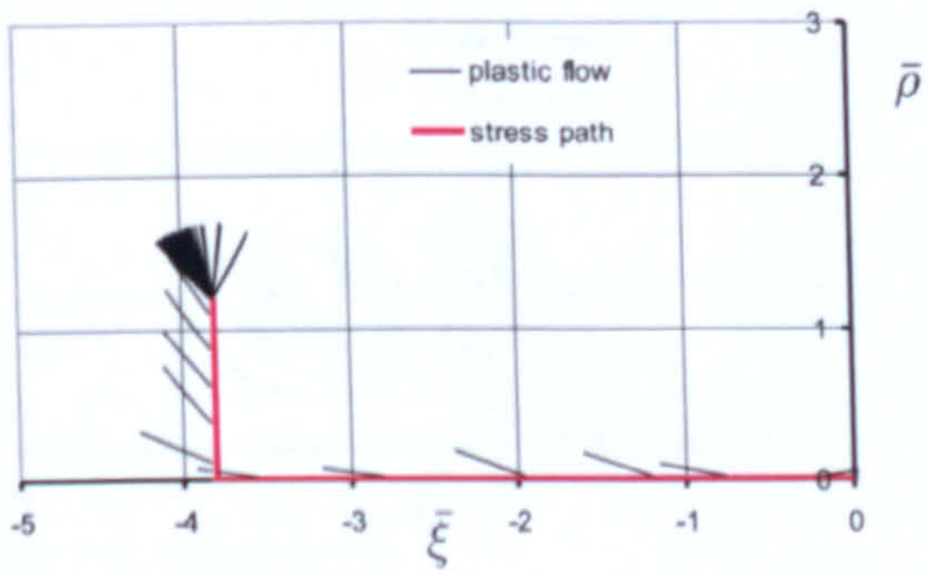

3-15

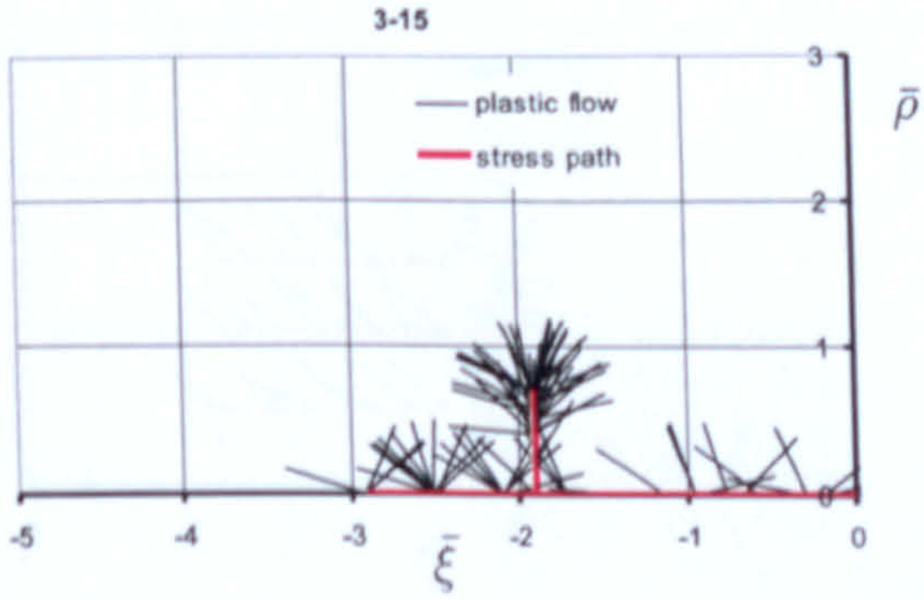

3-16

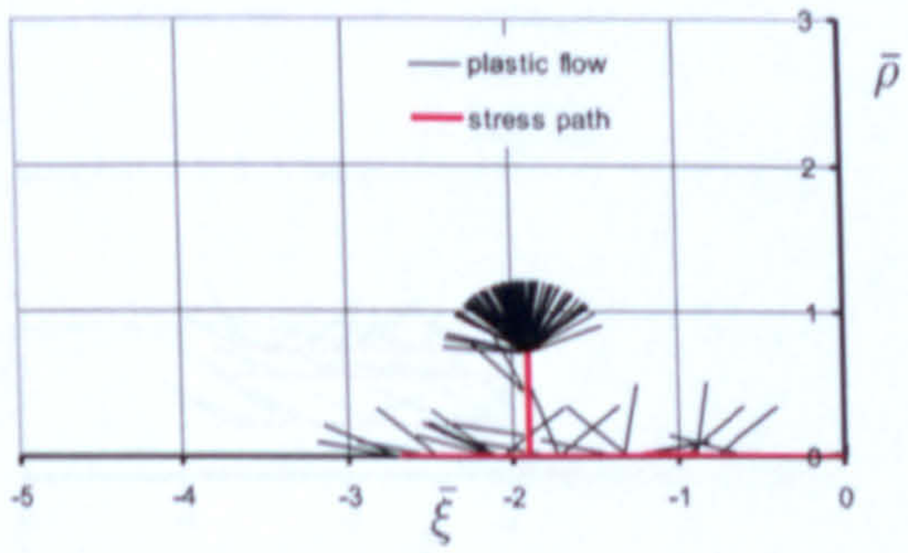

Figure 4.34: Plastic flow, stress paths and stress-strain simulations for Colorado tests, sample 3-13, 3-14, 3-15 and 3-16

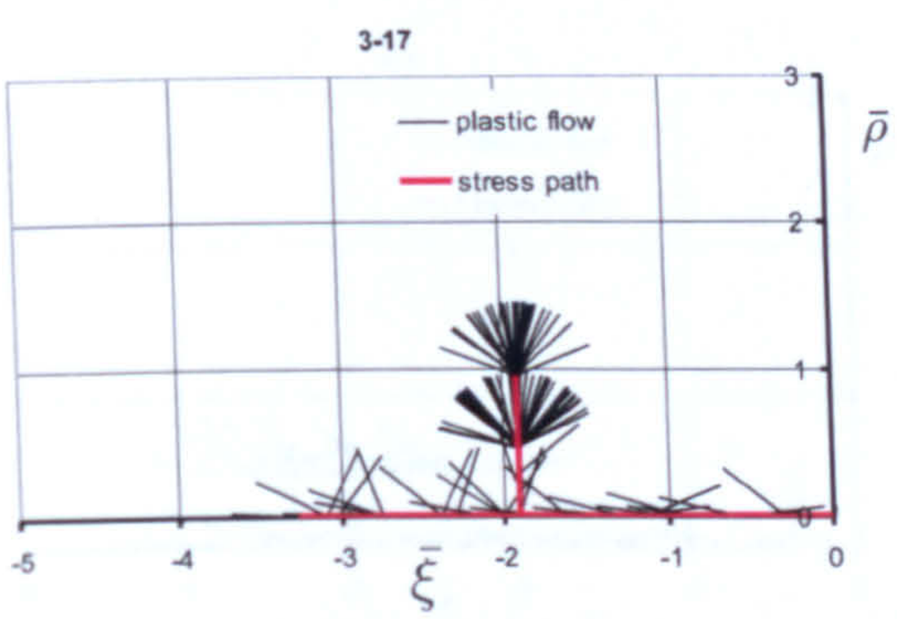

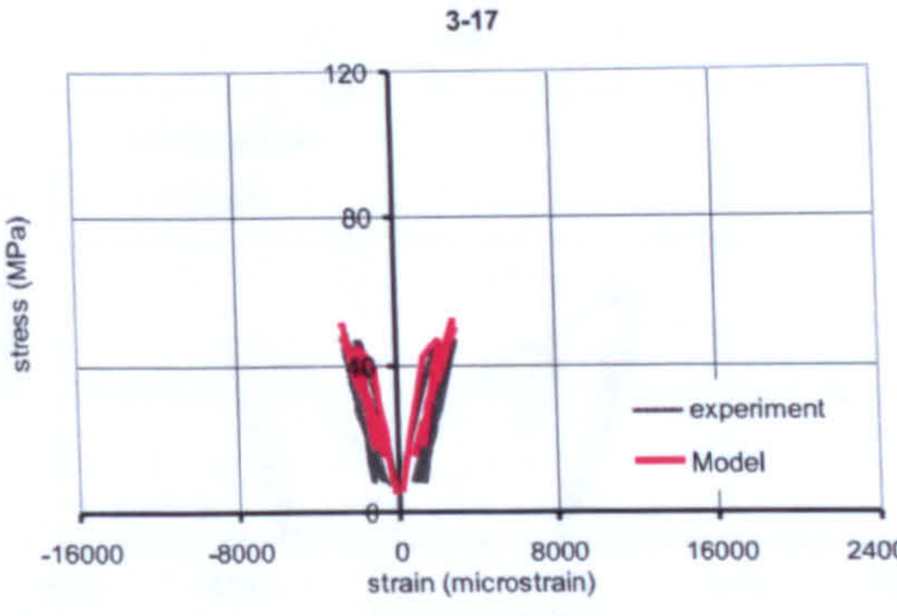

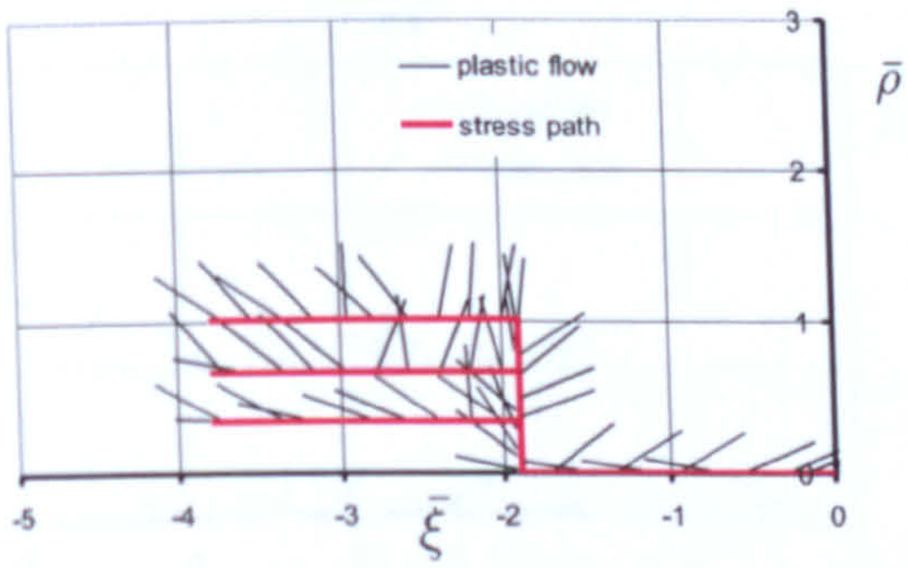

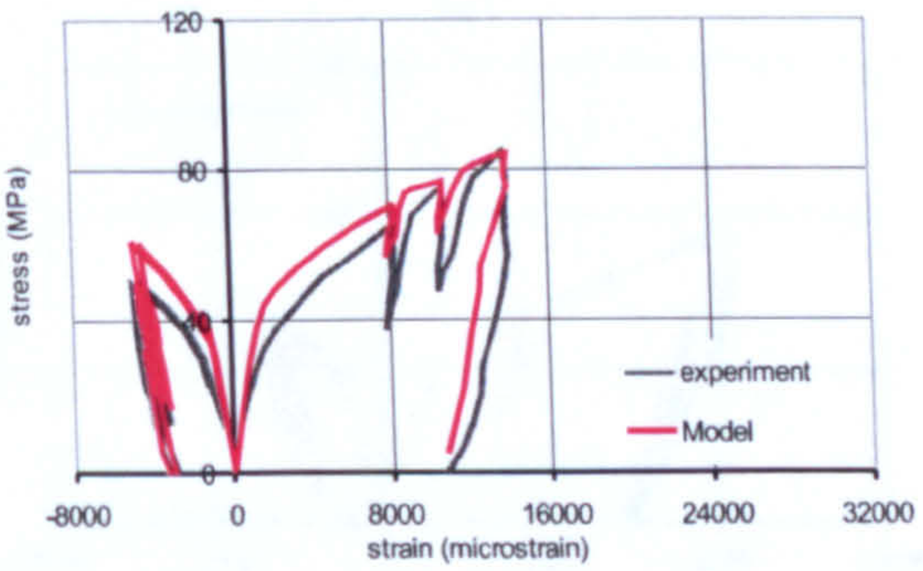

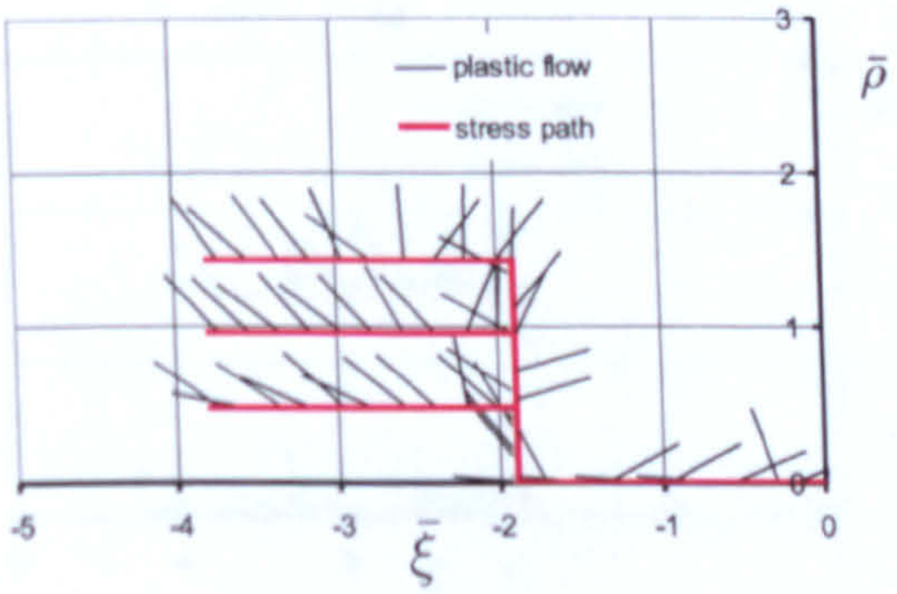

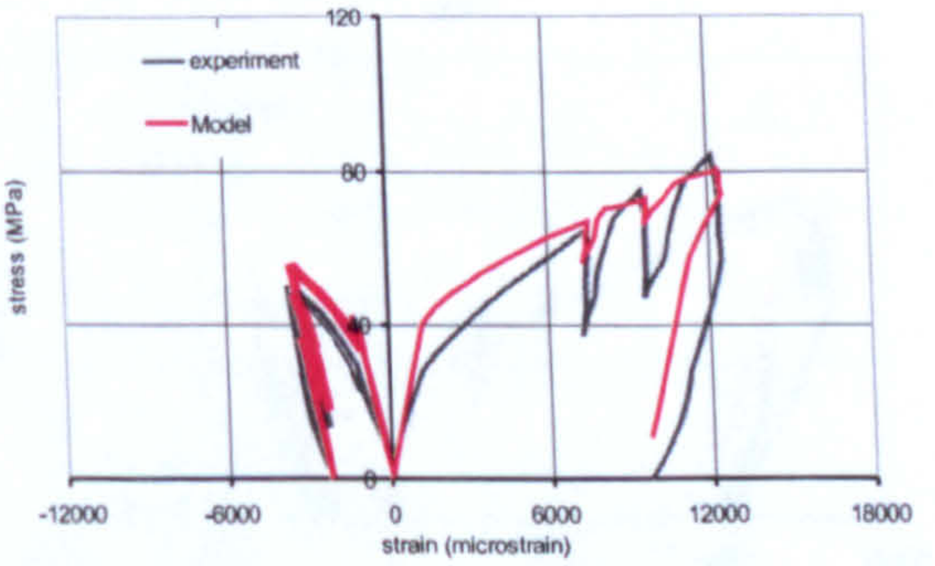

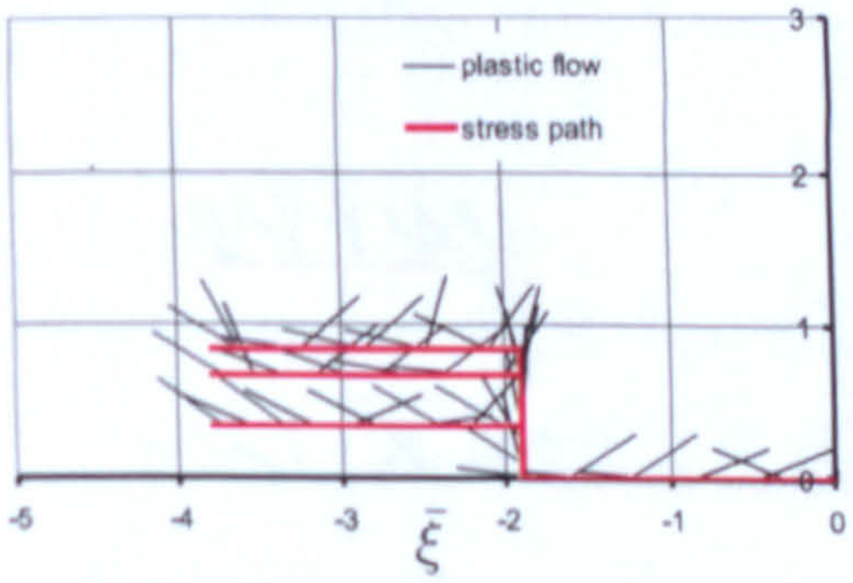

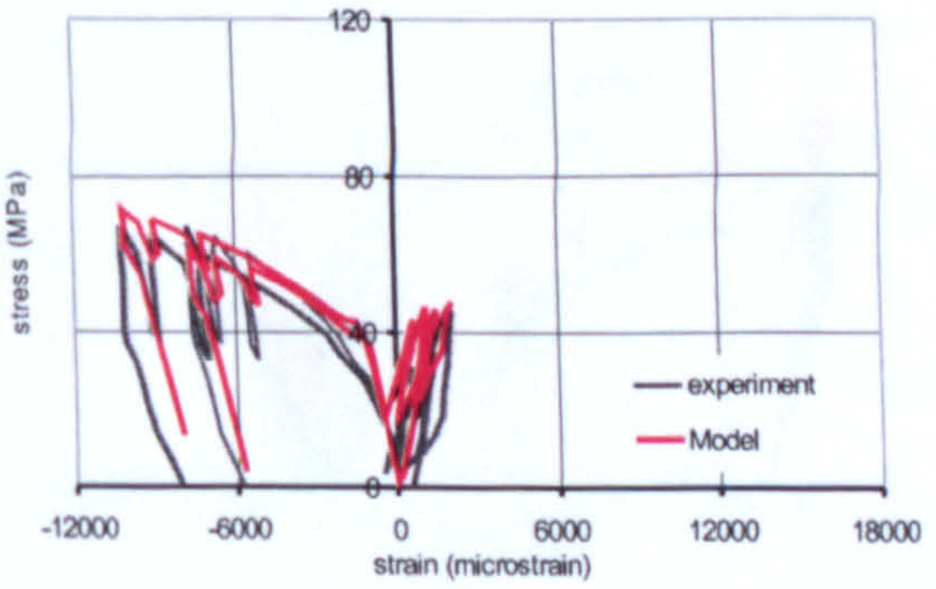

Figure 4.35: Plastic flow, stress paths and stress-strain simulations for Colorado tests, sample 3-17, 4-1, 4-2 and 4-3

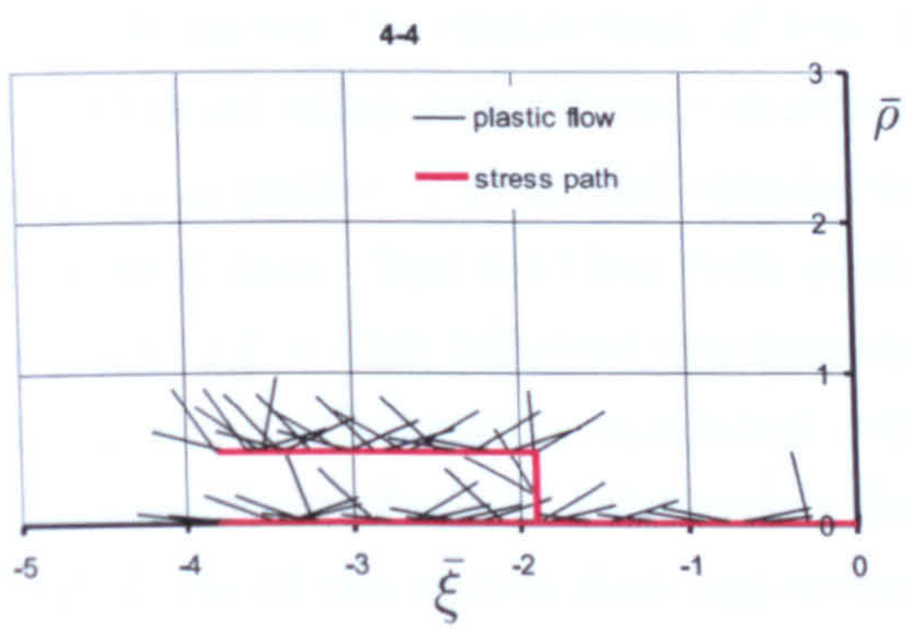

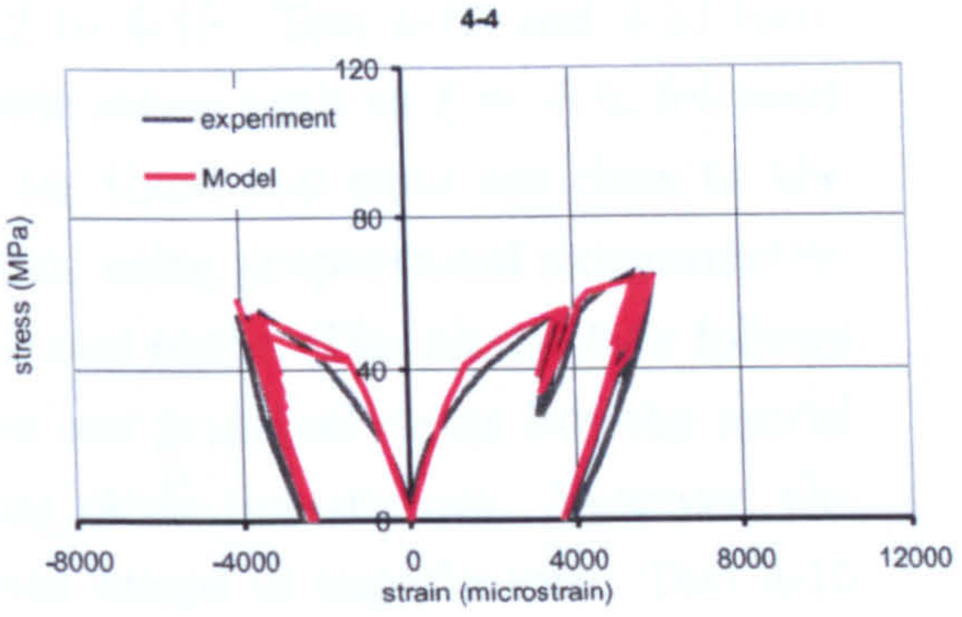

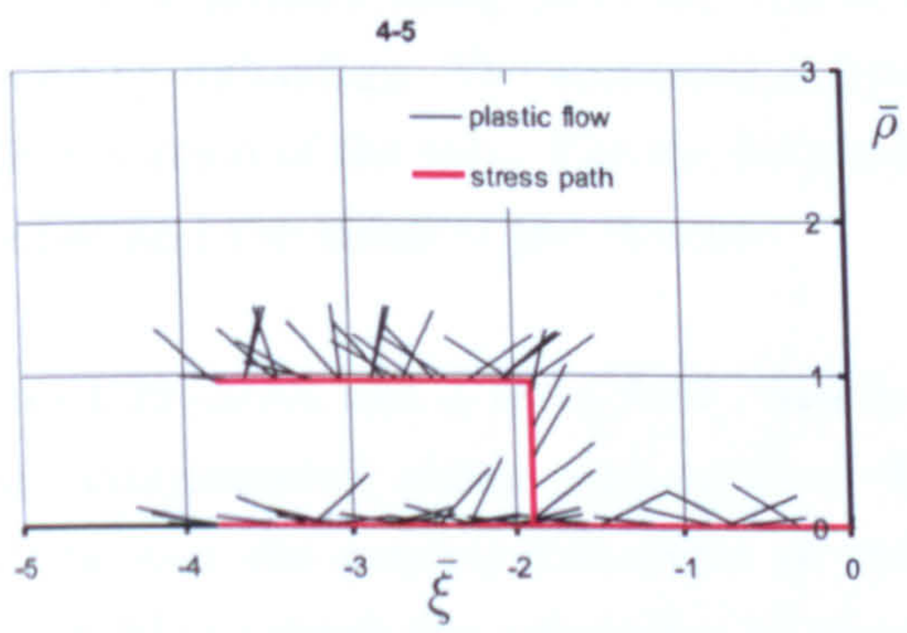

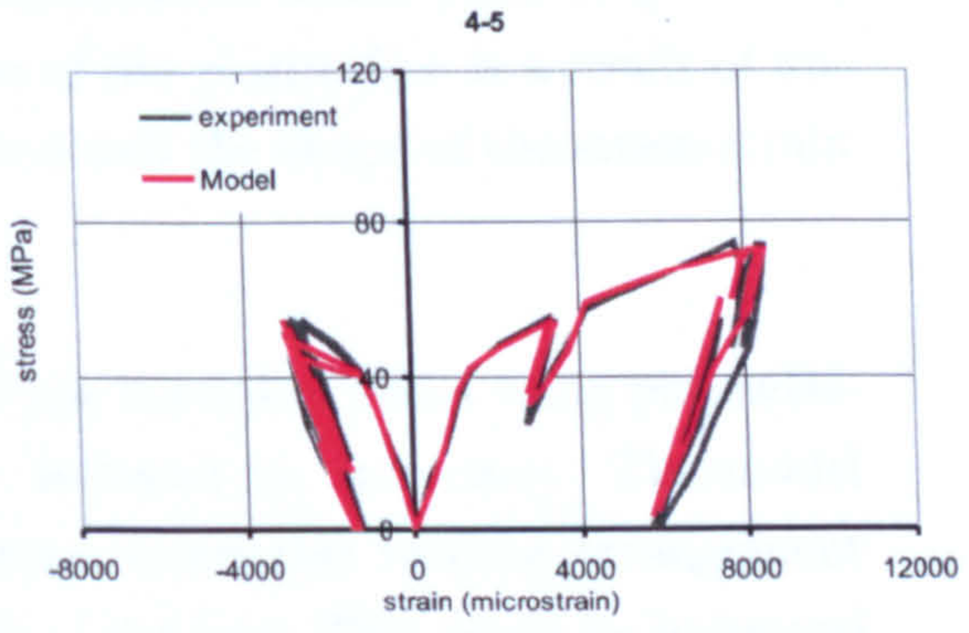

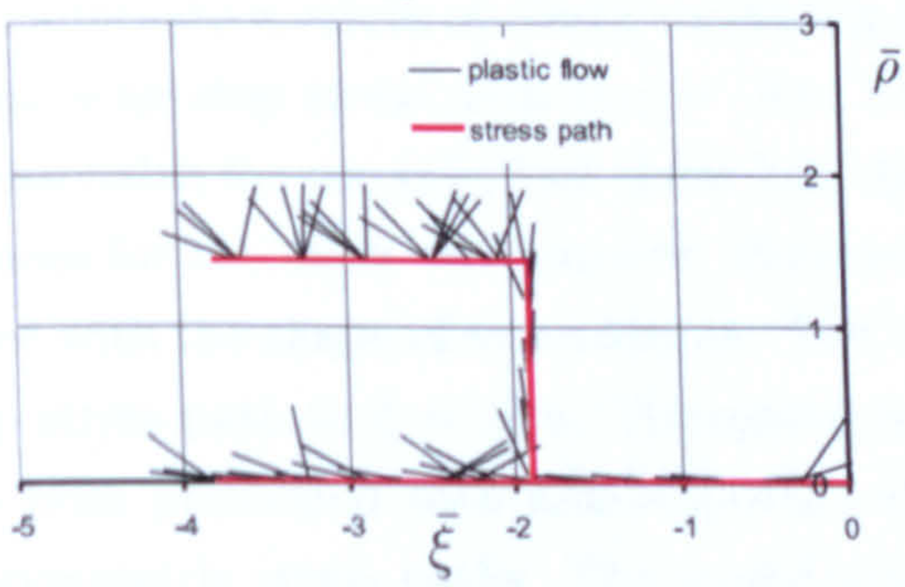

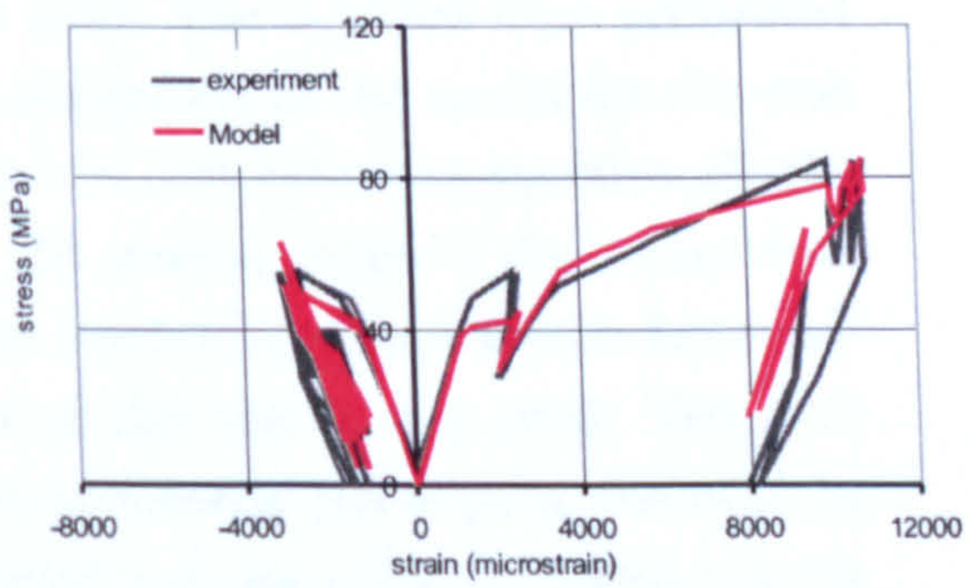

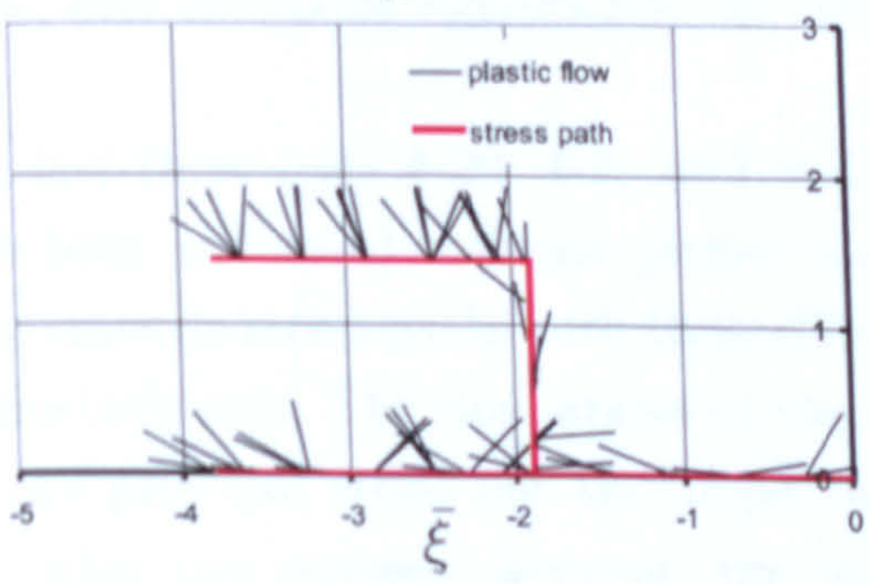

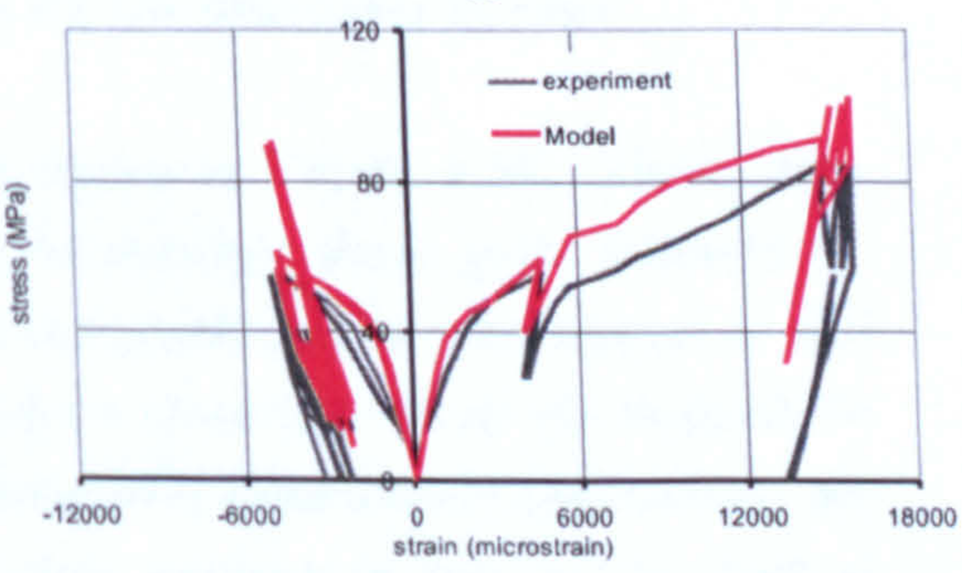

Figure 4.36: Plastic flow, stress paths and stress-strain simulations for Colorado tests, sample 4-4, 4-5, 4-6 and 4-7

vious simulations. This might be due to the complicated stress paths of these tests.

Figure 4.38 shows the simulations of test 4-12 to 4-15. Test 4-12 and 4-13 have been preformed using proportional axisymmetric stress path to $\bar{\xi}$ = -3.8, followed by additional paths. The model simulations for these two tests are close to the experimental data. Test 4-14 has been preformed using proportional axisymmetric stress path to $\bar{\xi}$ = -3.8, followed unsymmetric stress paths. The plastic flow follows the usual trend. This test is simulated well for one principal stress but the model over estimates significantly the stresses for the other two stresses. However, the general shape of the curves does agree with the shape of experiments. Test 4-15 has been preformed using piecewise-linear axisymmetric stress path to $\bar{\xi}$ = -3.8, followed by unloading. The scattered direction of the plastic flow is a result of unloading portion of the test. The model predicted well the shape of the stress-strain response and the value of the stresses.

Figure 4.39 shows test 4-16 to 4-19. Test 4-16 has been preformed using piecewise-linear axisymmetric stress path to $\bar{\xi}$ = -3.8, followed by unloading. The model predicts well the general behaviour of concrete under this loading arrangement but, unable to reach the zero value at the end of the test. This could be improved if an alternative values of elastic constants are used. Test 4-17 has been preformed coarse stair-step stress path to $\bar{\xi}$ = -3.8. The simulation of the model for this test is reasonable for one principal stress but the model over estimates significantly the stresses for the other two stresses. However, the general shape of the curves does agree with the shape of experiments. Test 4-18 has been preformed with fine stair-step stress path to $\bar{\xi}$ = -3.8. The simulations of this test is very good. Test 4-19 has been preformed with non-proportional axisymmetric stress path, followed by axisymmetric stress paths. The model simulated well one principal stress but the model over estimates significantly the stresses for the other two stresses.

The last three tests 4-20, 4-21 and 4-22 are shown in Figure 4.40. These tests have been preformed with non-proportional axisymmetric stress path, followed by axisymmetric stress paths with three different deviatoric angles with respect to the hydrostatic axis. The simulations of the model for these three tests are reasonable for one principal stress but the model over estimates significantly the stresses for the other two stresses; however, the model does capture in general the general trends of the stress-strain responses.

In the same figure, the first of the fifth series (test 5-1) is shown. This series con-

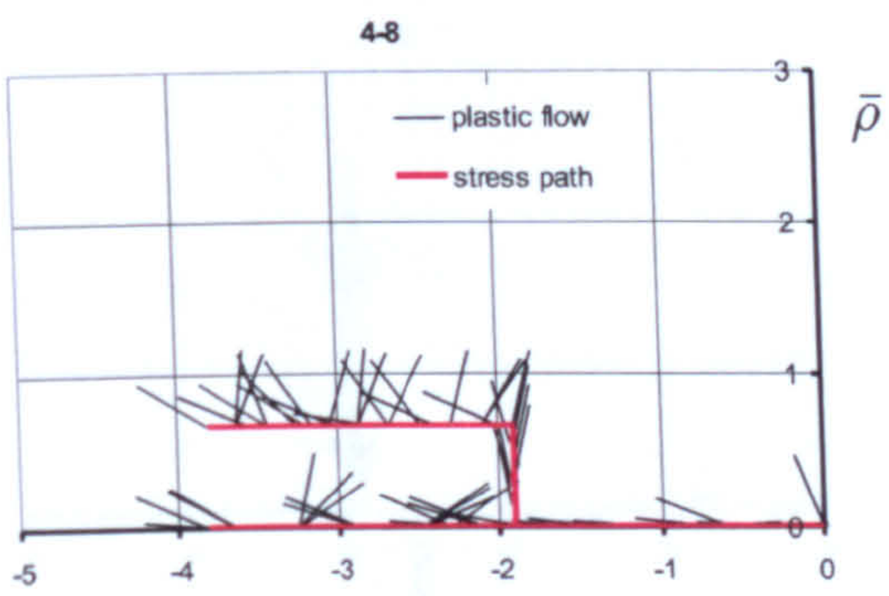

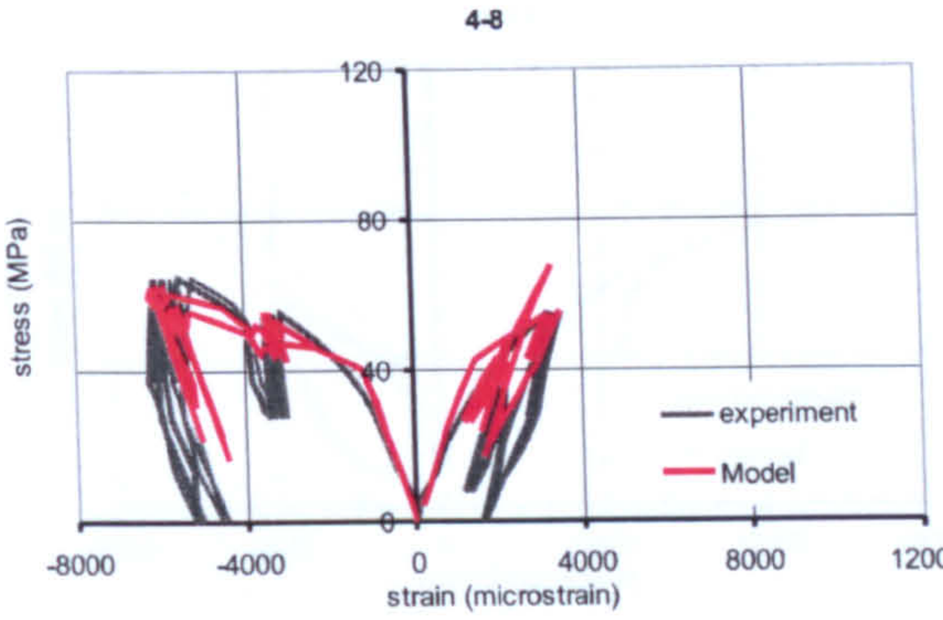

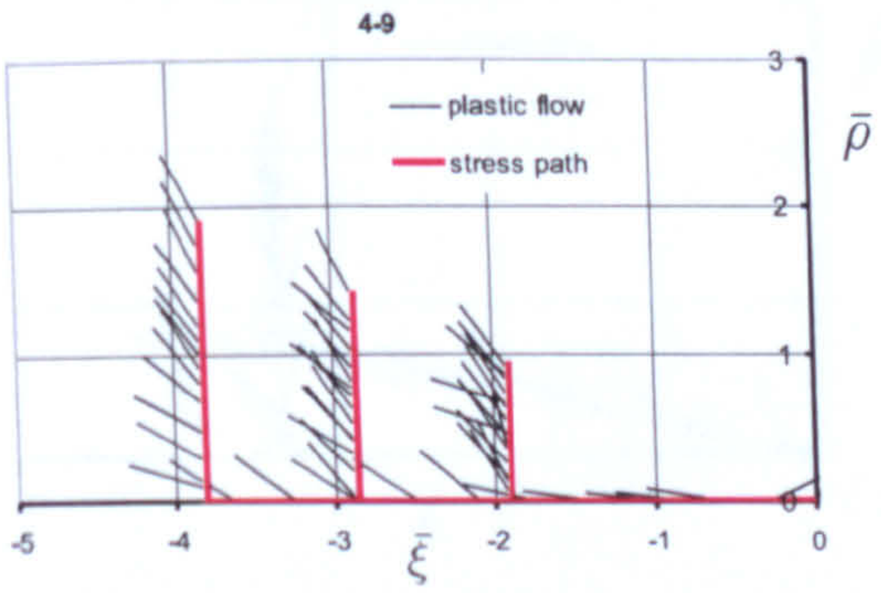

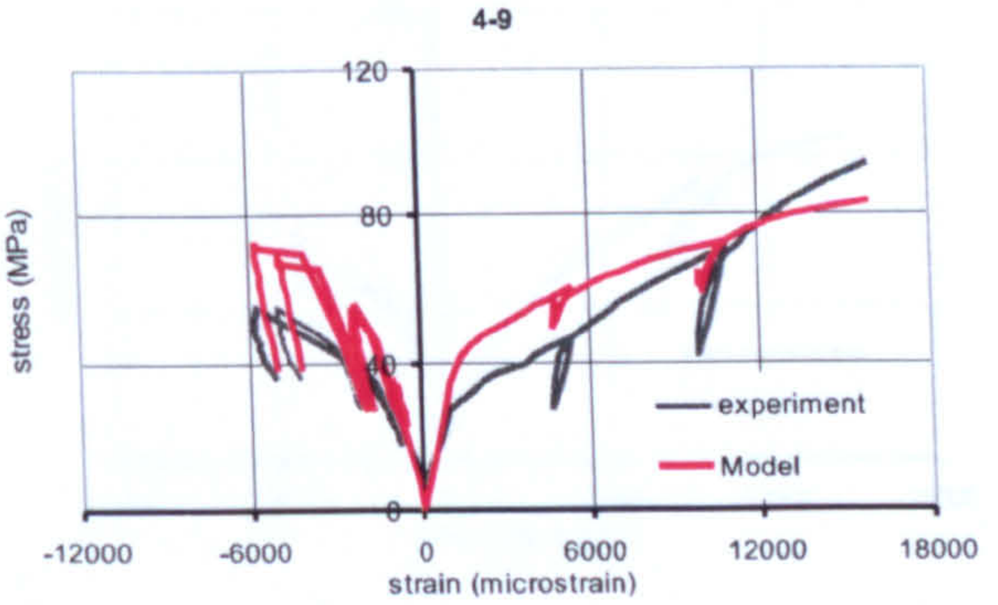

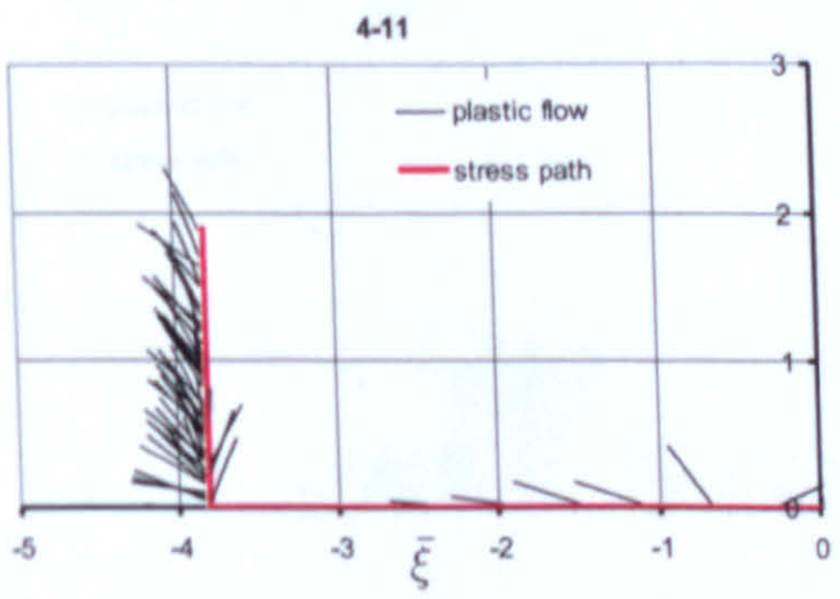

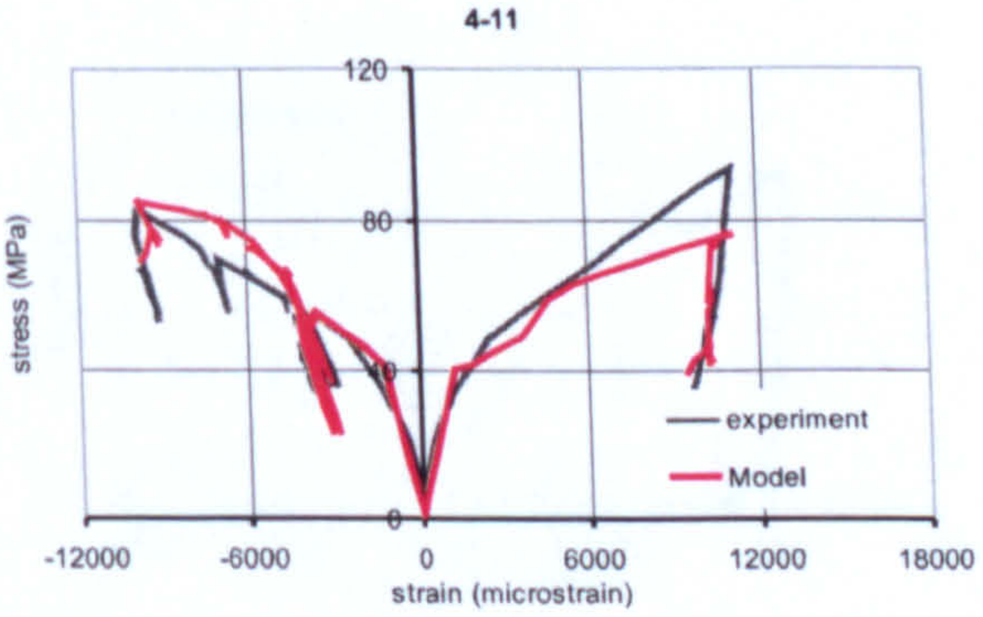

Figure 4.37: Plastic flow, stress paths and stress-strain simulations for Colorado tests, sample 4-8, 4-9, 4-10 and 4-11

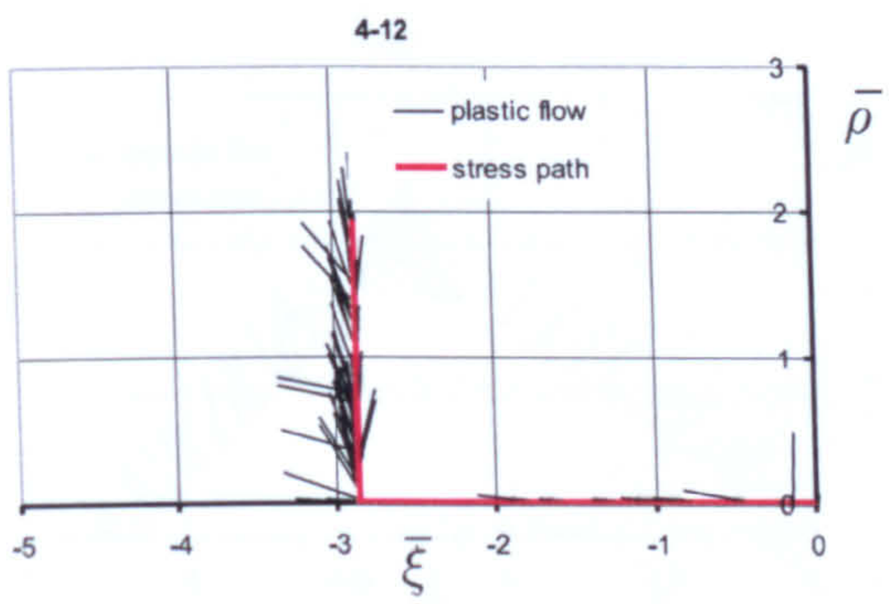

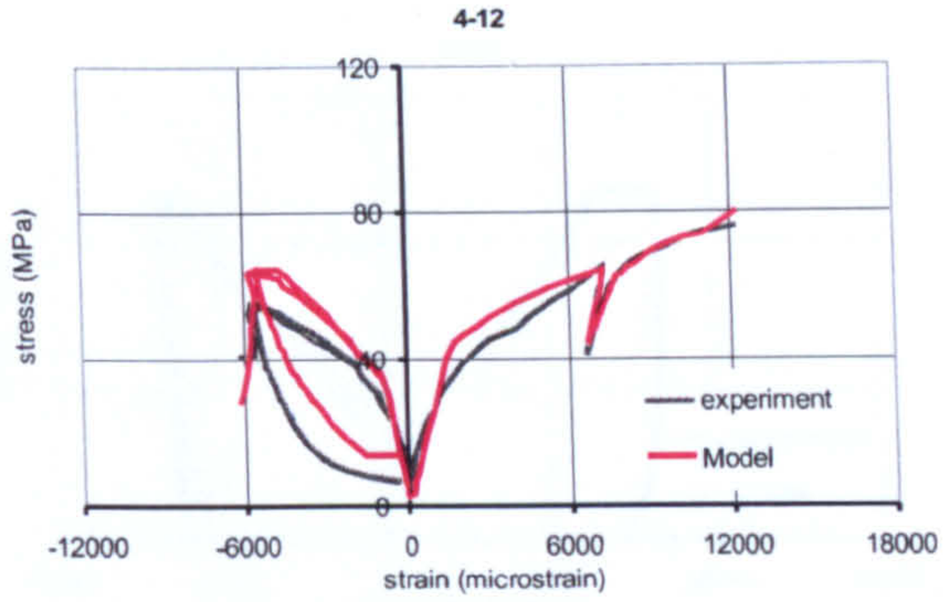

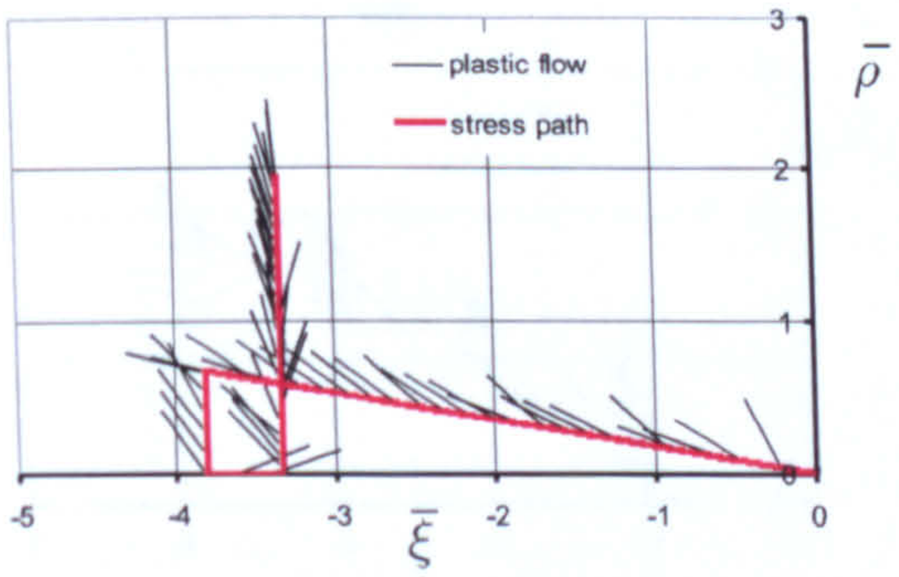

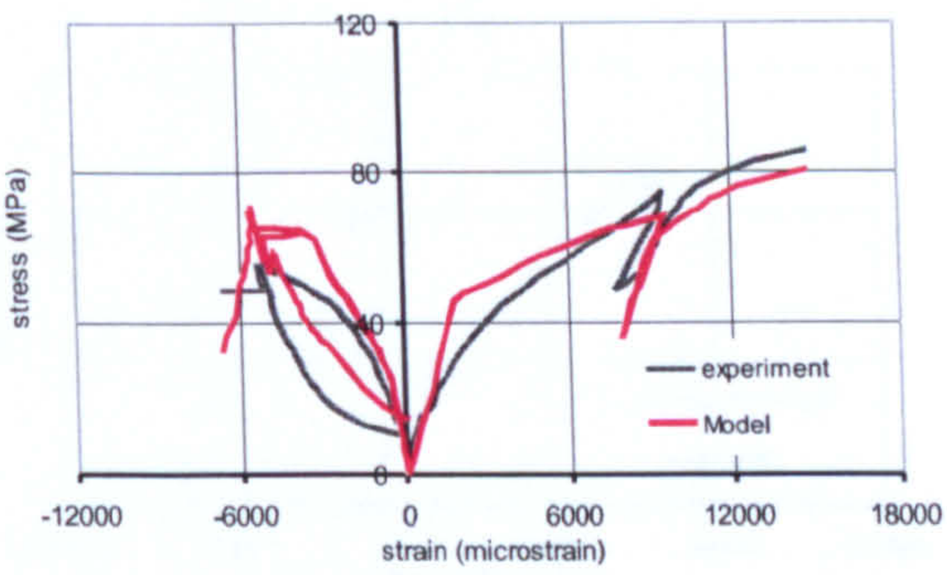

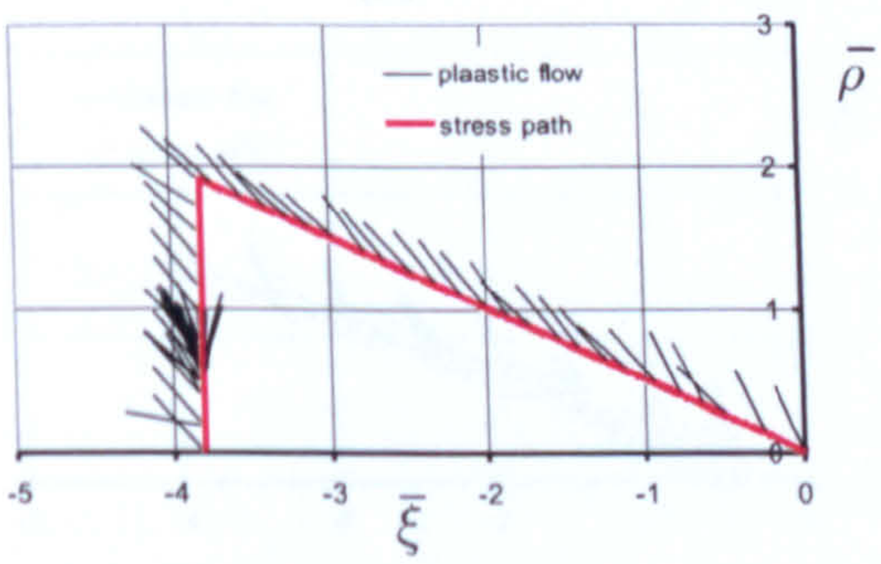

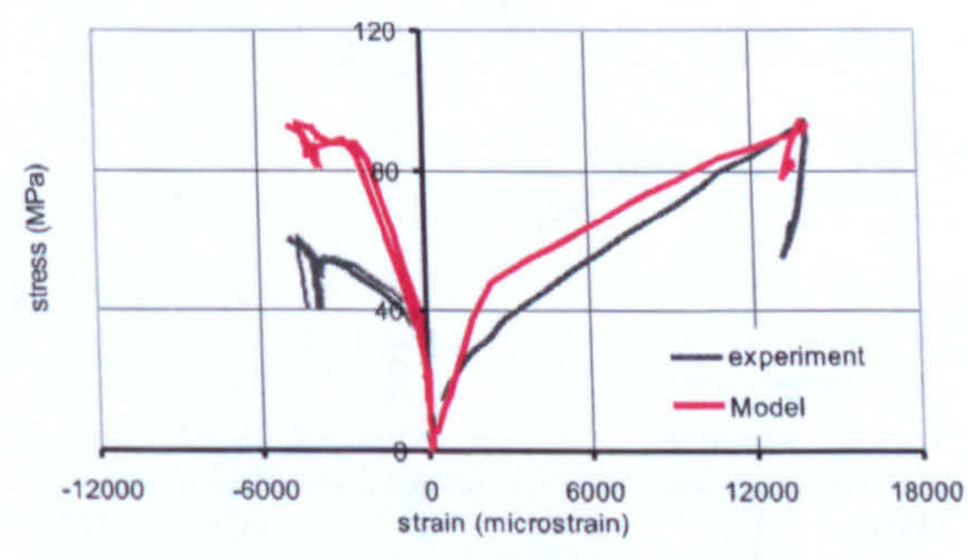

Figure 4.38: Plastic flow, stress paths and stress-strain simulations for Colorado tests, sample 4-12, 4-13, 4-14 and 4-15

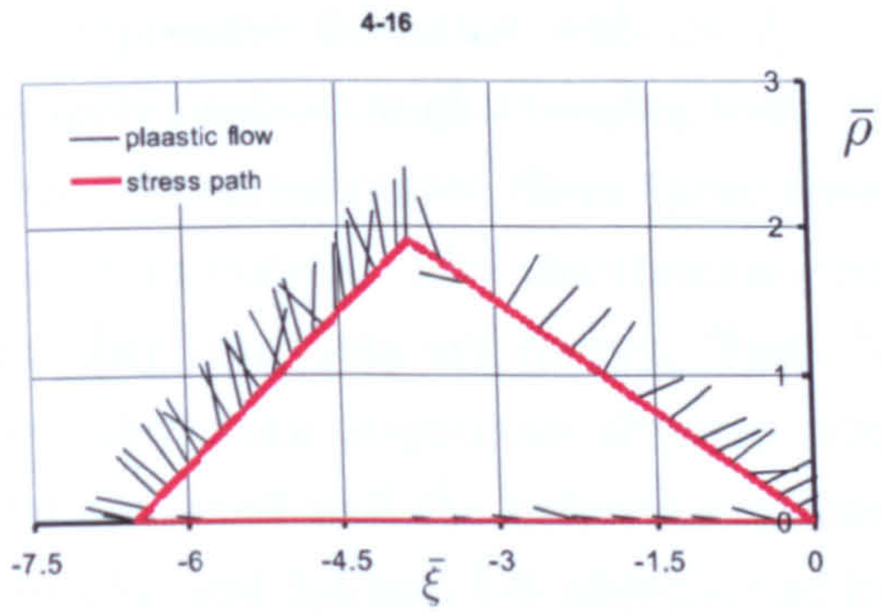

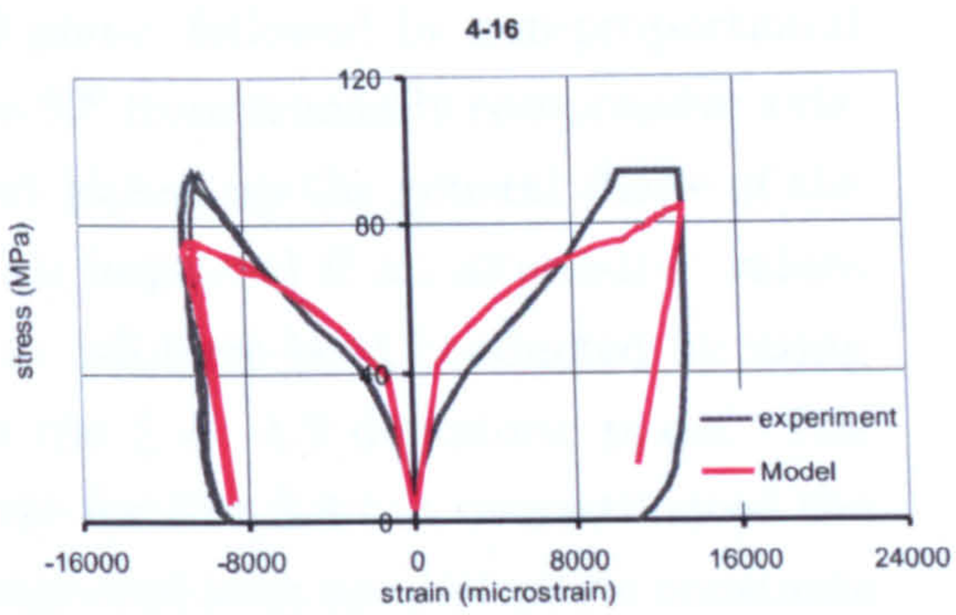

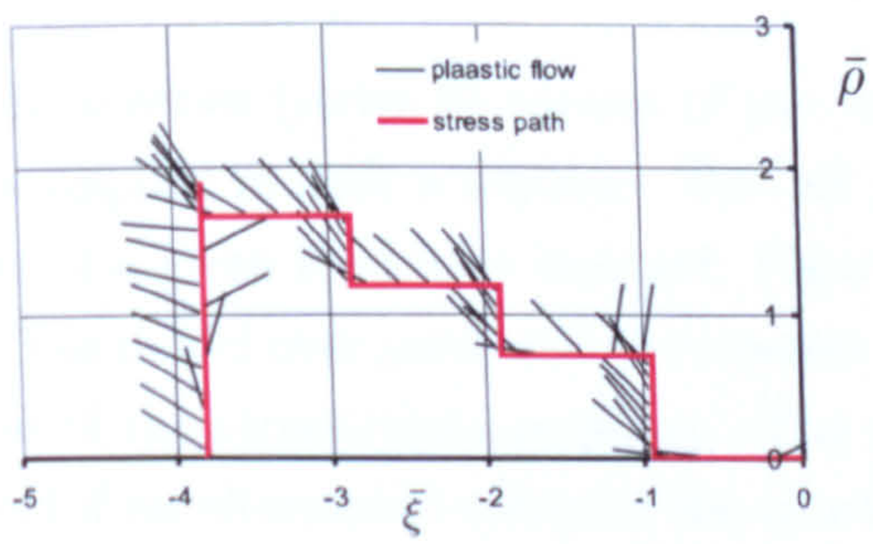

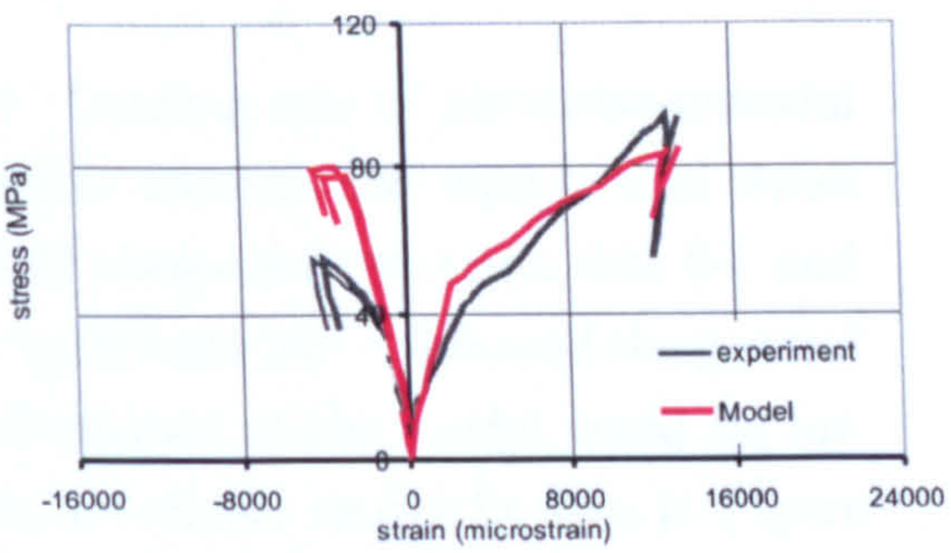

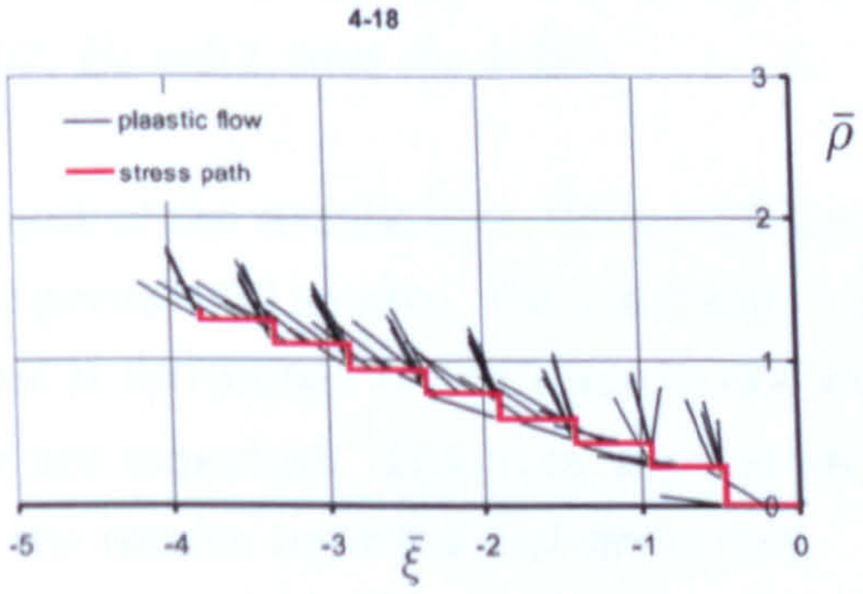

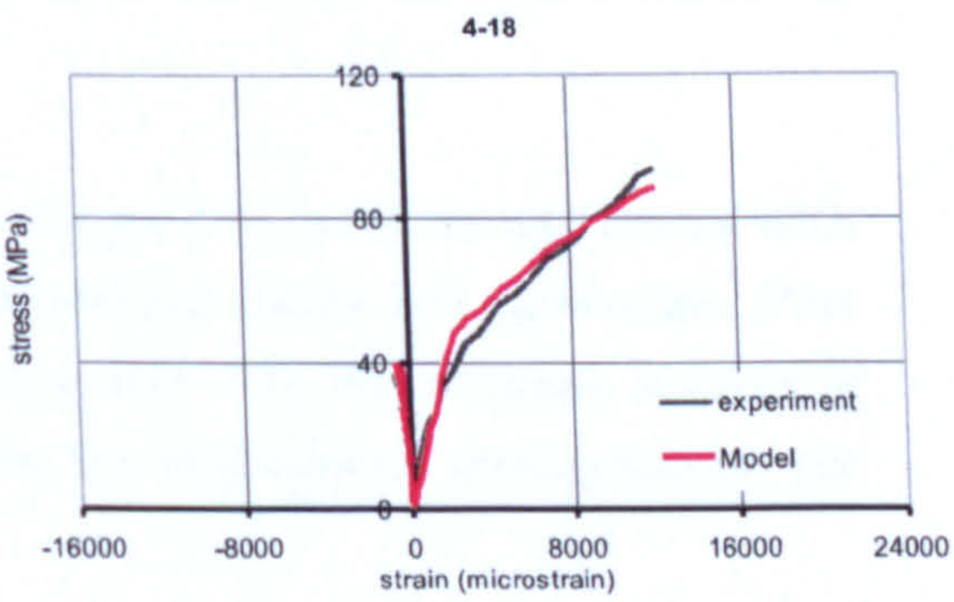

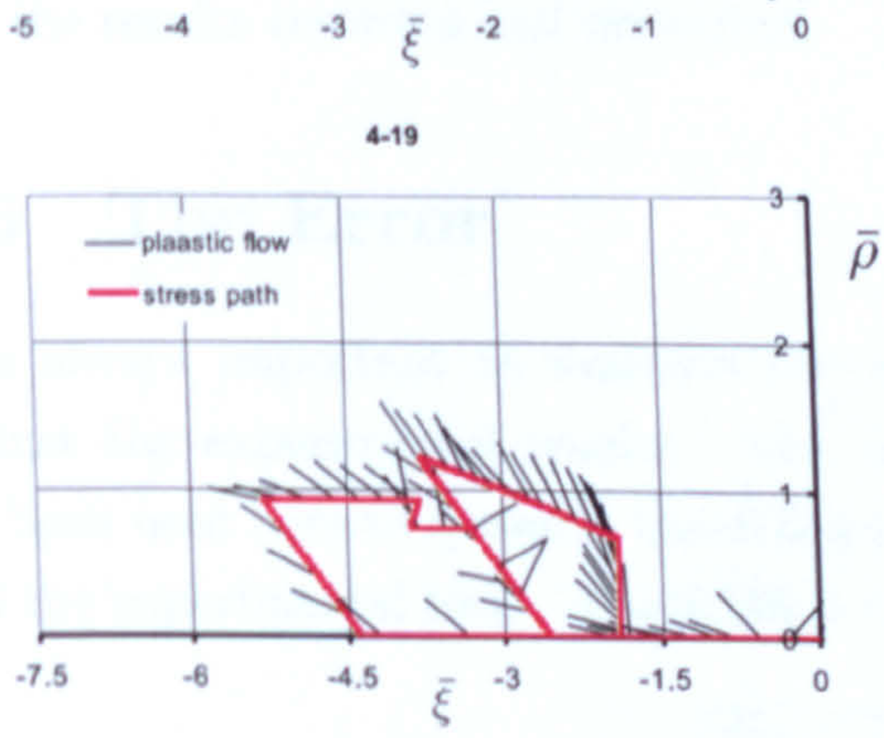

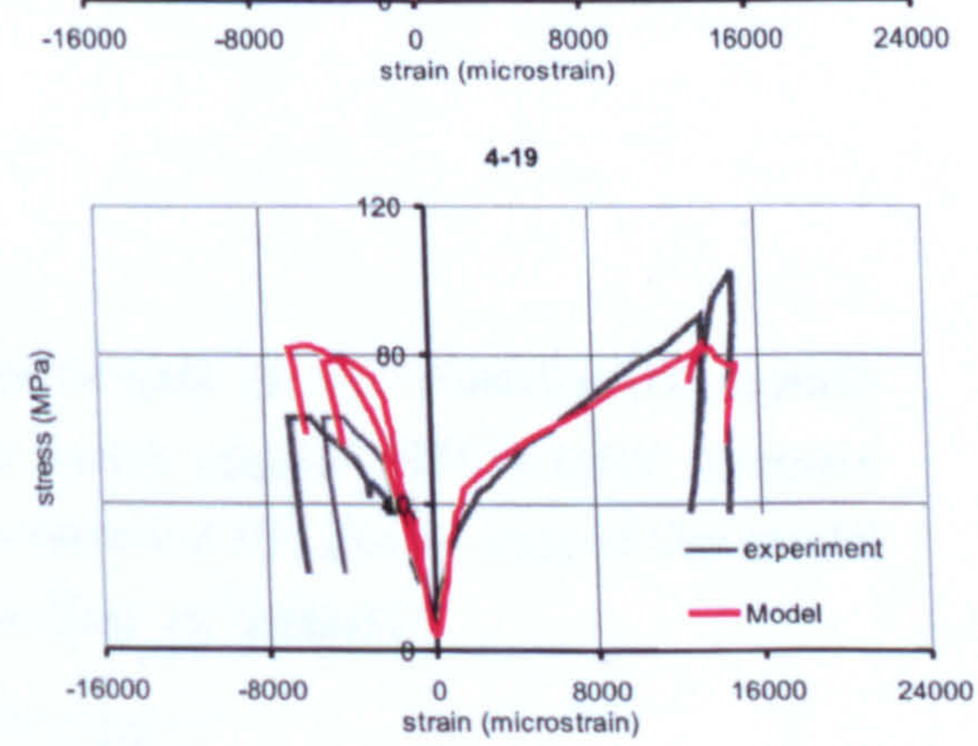

Figure 4.39: Plastic flow, stress paths and stress-strain simulations for Colorado tests, sample 4-16, 4-17, 4-18 and 4-19

sists of six tests from test 5-1 to 5-6. Test 5-2 to 5-5 are shown in Figure 4.41 and the final test 5-6 is shown in Figure 4.42. Tests 5-1 to 5-3 were subjected to triaxially compressive deviation with the $\bar{\xi}$ = -1.9 plane, followed by non-proportional stress increments at angles ranging from 30^0 to 90^0 from triaxially compressive axis. The model overestimated these three tests but picked up the general shape of the stress-strain curves. The simulations could be improved if an alternative values of ductility constants are chosen. Tests 5-4 to 5-6 have been conducted by using various deviatoric sequences of stress within the $\bar{\xi}$ = -1.9 deviatoric plane. The model predicted well the behaviour of concrete for test 5-4 but overestimated the stresses for test 5-5 and 5-6 which could be improved with an alternative constants values.

The final series (series 6) consist of two tests. Loading was of piecewise-uniaxial steps, applied in such a sequence that all possible uniaxial and equi-biaxial stress states of a given level were reached. Figure 4.42 shows the two tests, test 6-1 and 6-2. The model over predicted the stresses for both tests but it followed the general shape of the stress-strain response. The performance of the model could be improved if an alternative values of the constants are chosen as can be seen in Figure 4.42 test 6-1-b where A_h = 0.015, B_h =1 and A_k = 0.7, and test 6-2-b where A_h = 0.02, B_h =0.7, and A_k = 0.5.

For most of the simulations, the model has shown good to excellent agreement with the experimental results. For a few tests, the model has shown less agreement. Part of this is attributed to the error in the experimental data where many sources of error are expected. This may include error in the experiment arrangements, the way the results recorded and presented.

4.6 The Error

It is always important to evaluate the effectiveness of the constitutive models against the experimental results. The *root mean square* (RMS) error measure has been used here to quantify the difference between the predictions of the model and the experimental tests. The RMS is identified as follows:

$$RMS = \sqrt{\frac{\sum_{k=1}^{q}(\sigma_{ij}^{m} - \sigma_{ij}^{exp})^2}{\sum_{k=1}^{q}(\sigma_{ij}^{exp})^2}}.100\% \tag{4.9}$$

where σ_{ij}^{m} are the stresses calculated by the model and σ_{ij}^{exp} are the stresses reported by the experimental tests, q is the number of stress-strain readings in each test.

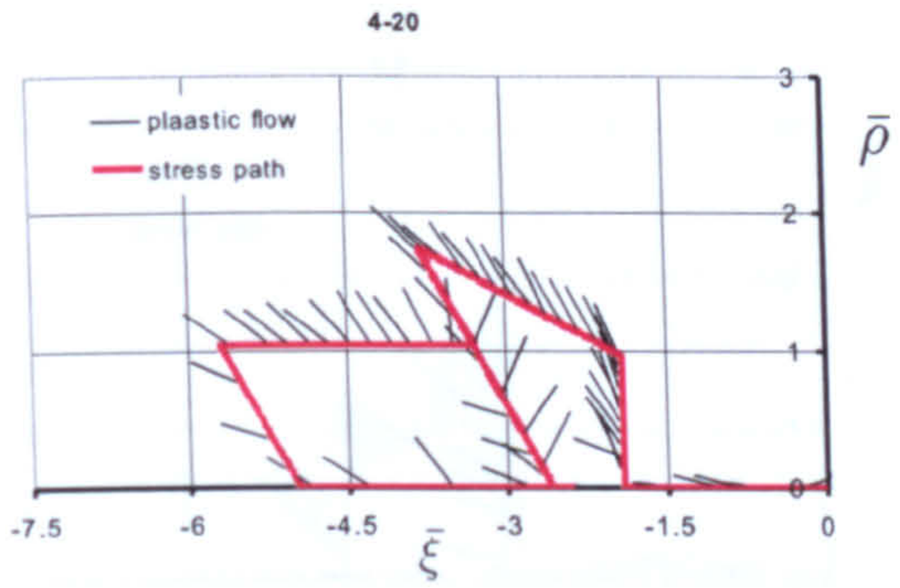

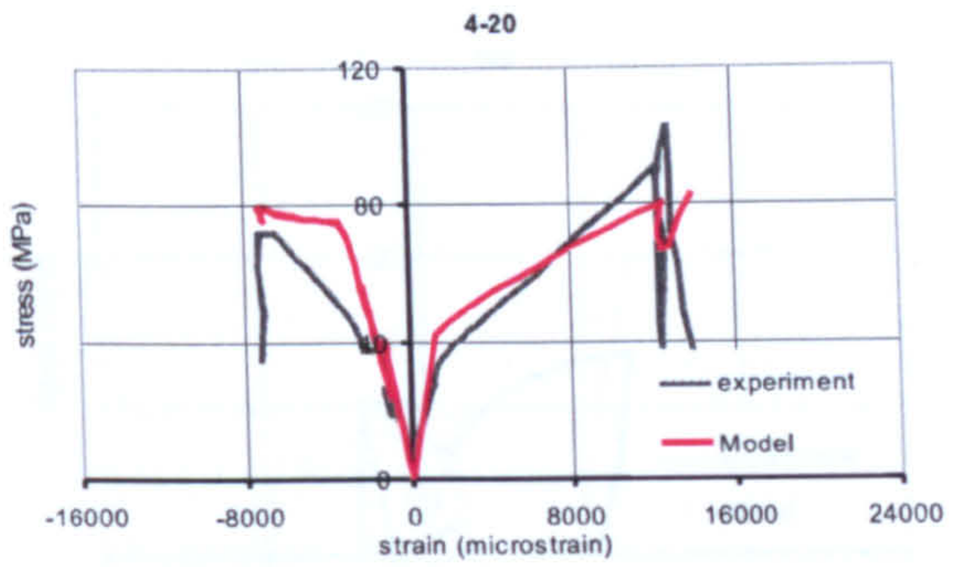

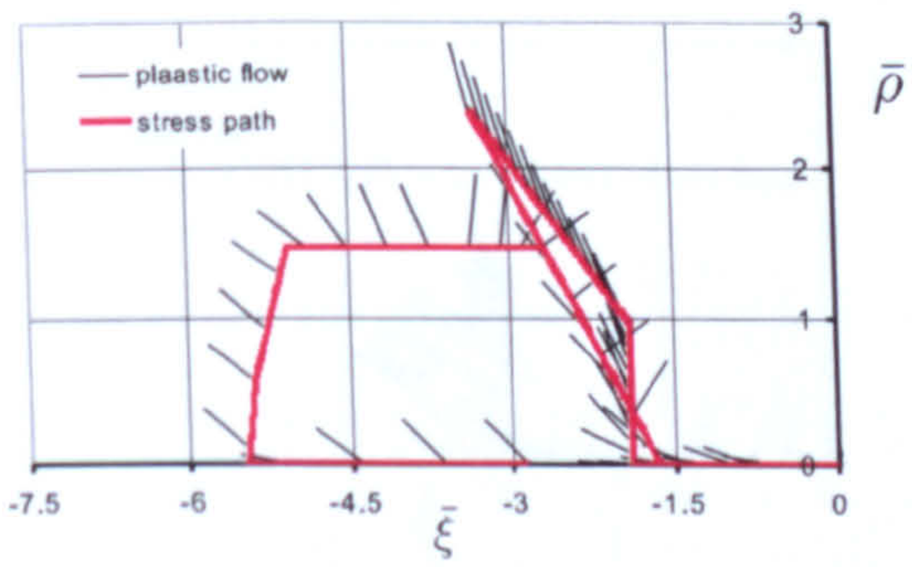

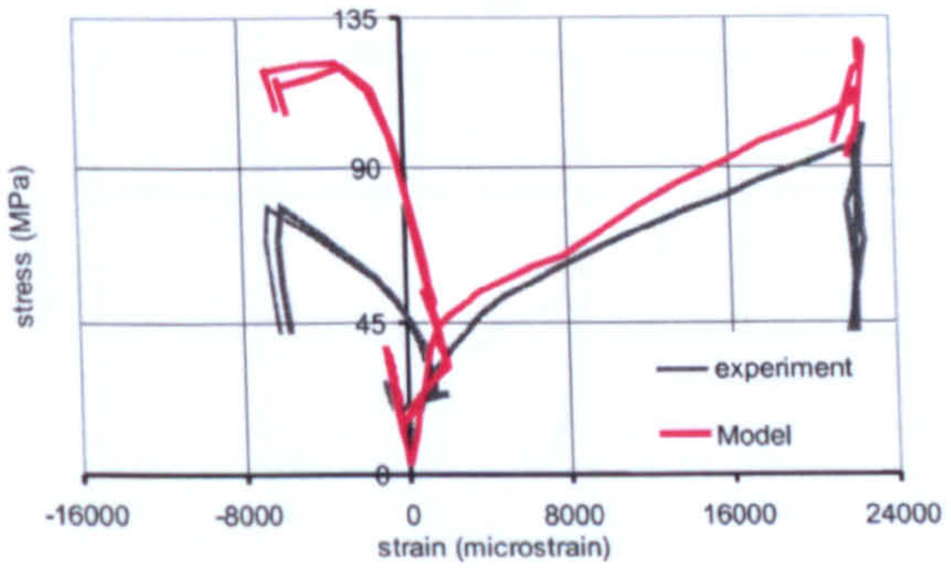

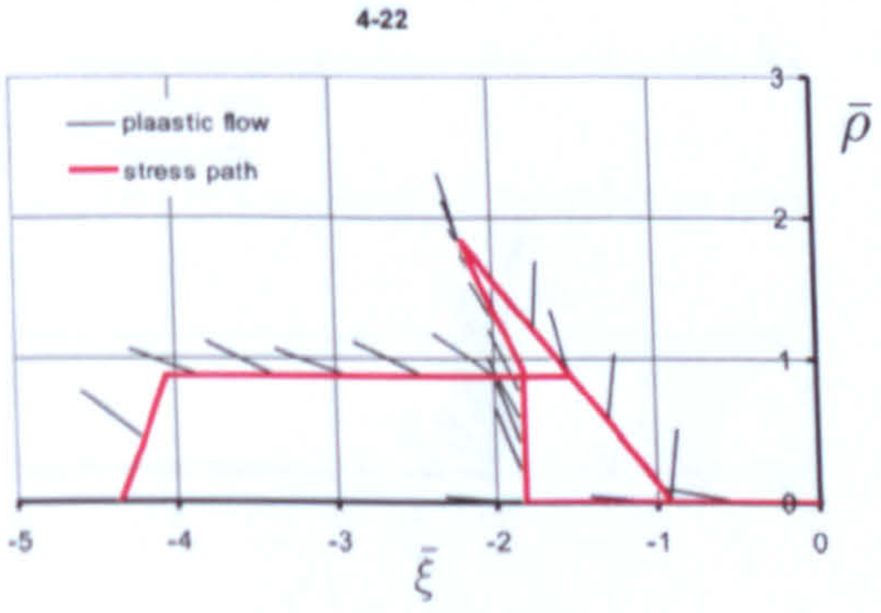

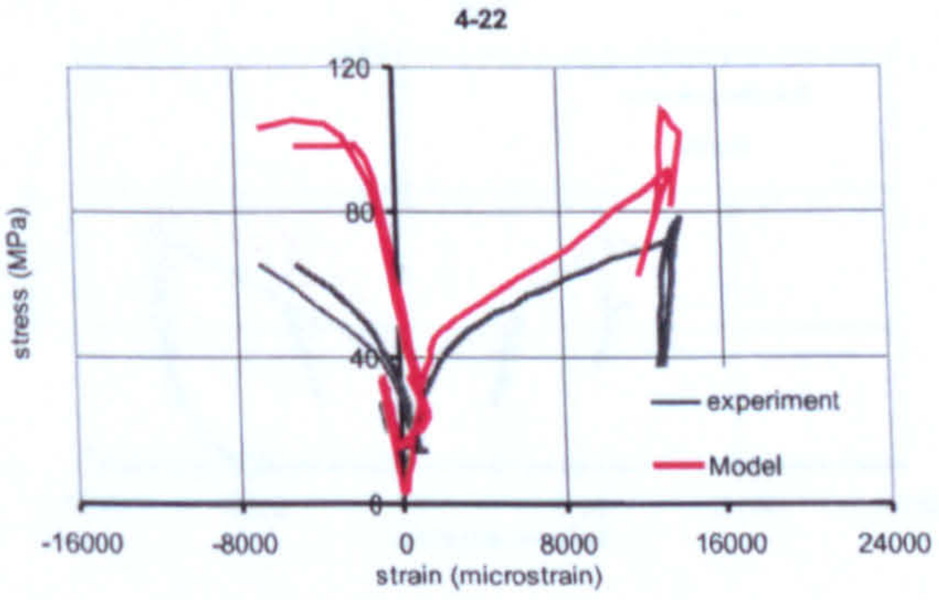

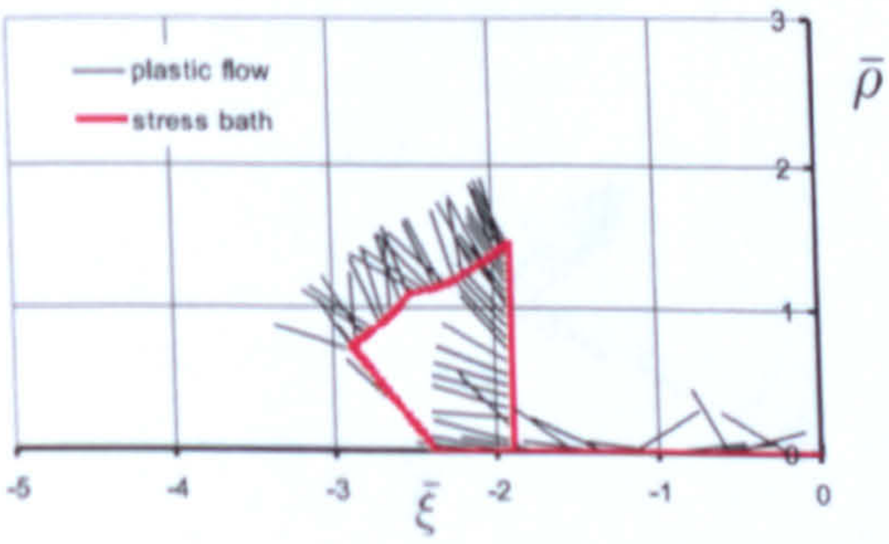

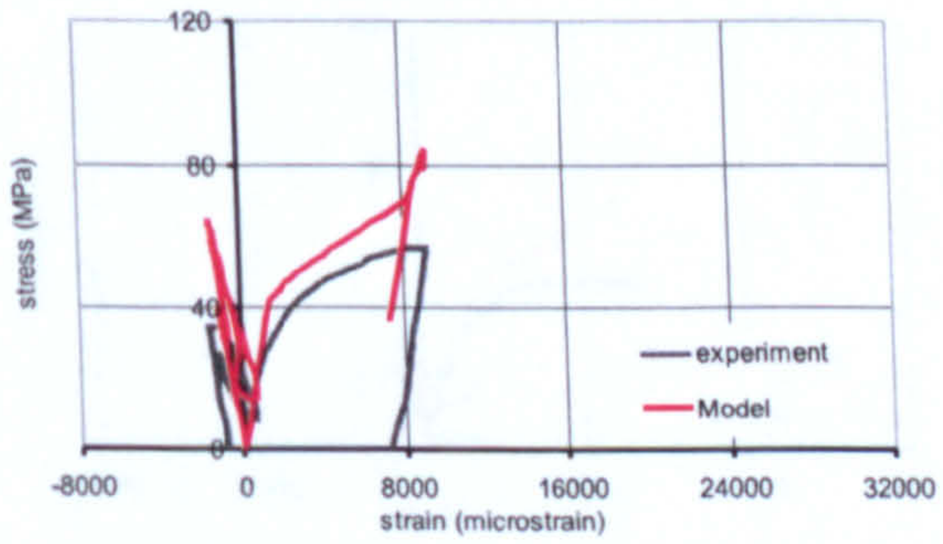

Figure 4.40: Plastic flow, stress paths and stress-strain simulations for Colorado tests, sample 4-20, 4-21, 4-22 and 5-1

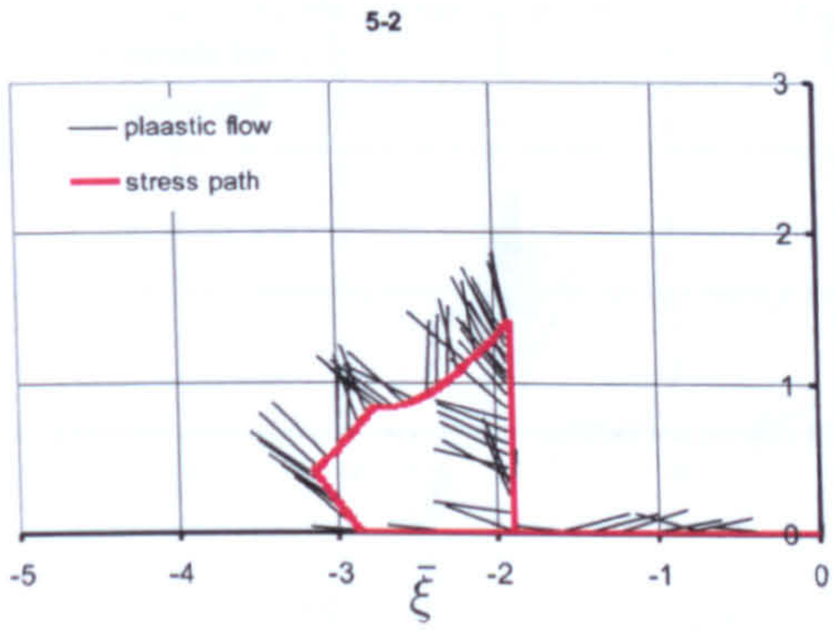

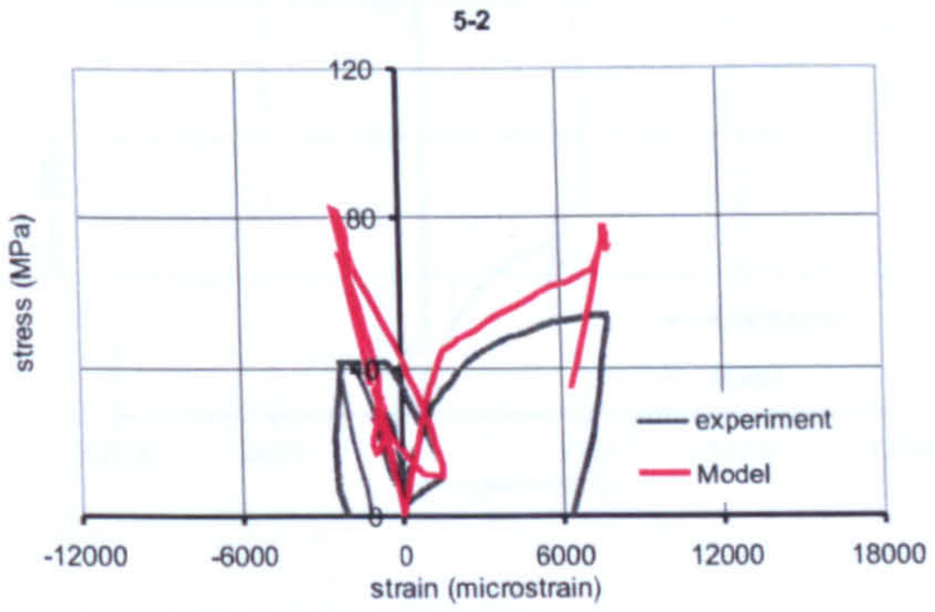

5-3

5-3

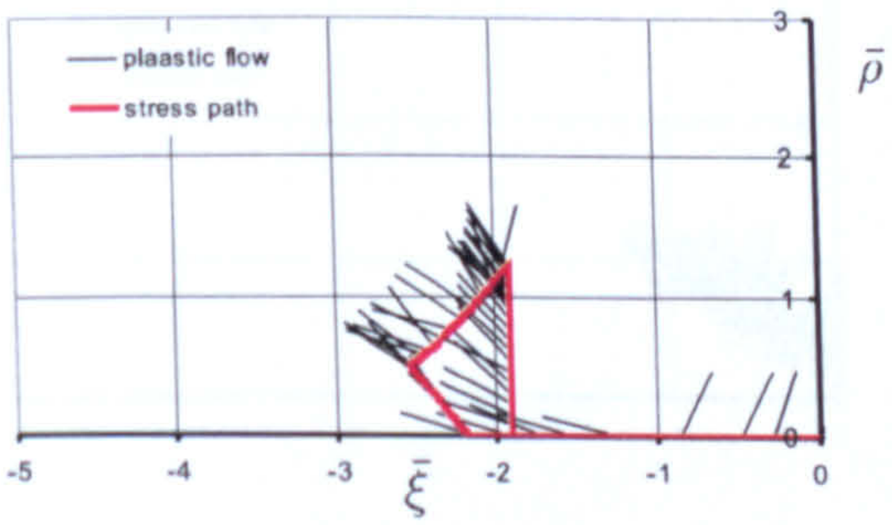

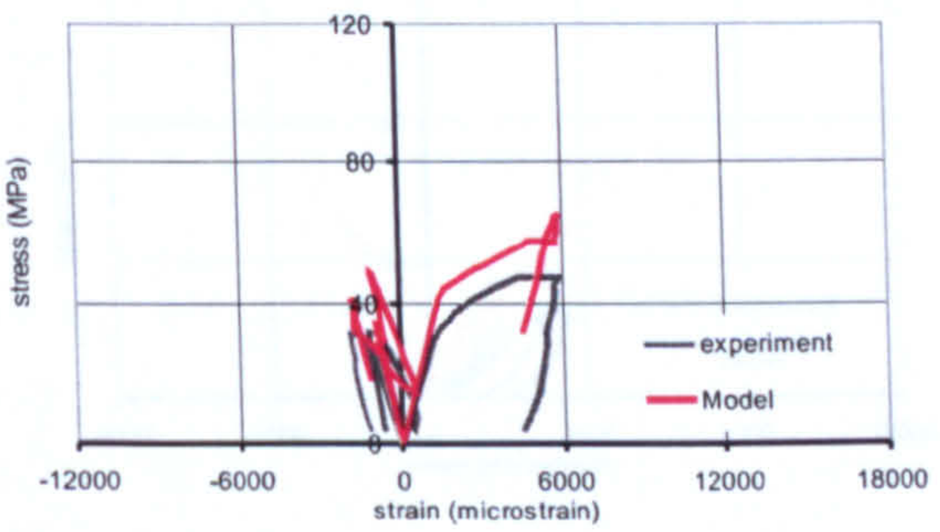

5-4

5-4

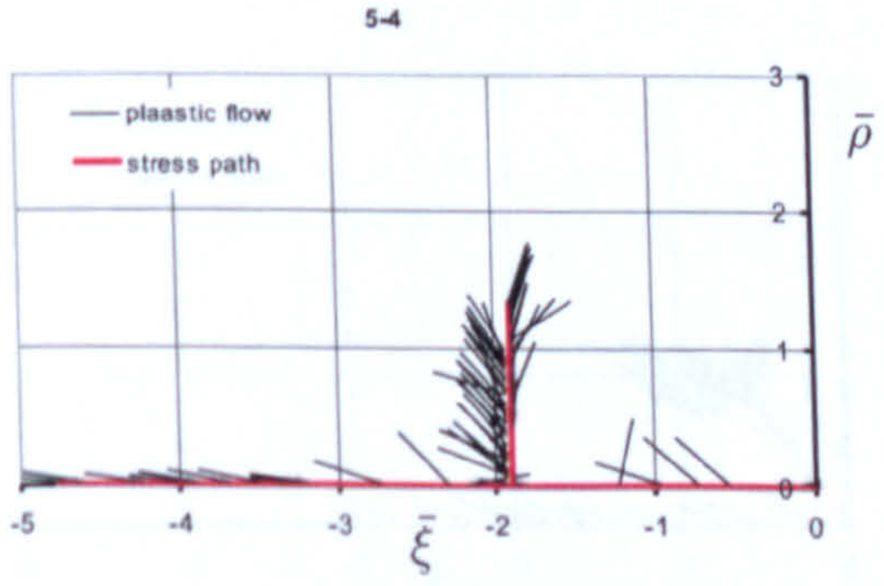

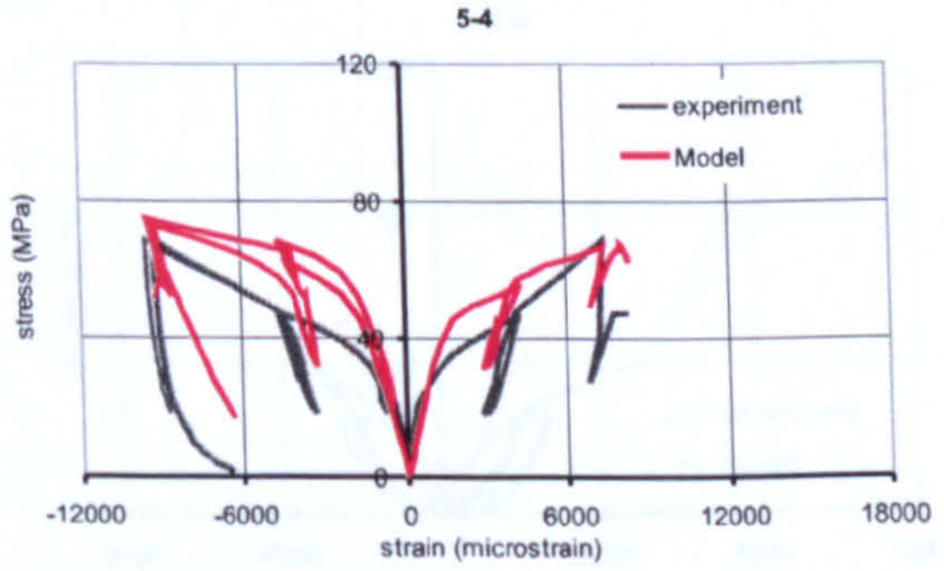

5-5

5-5

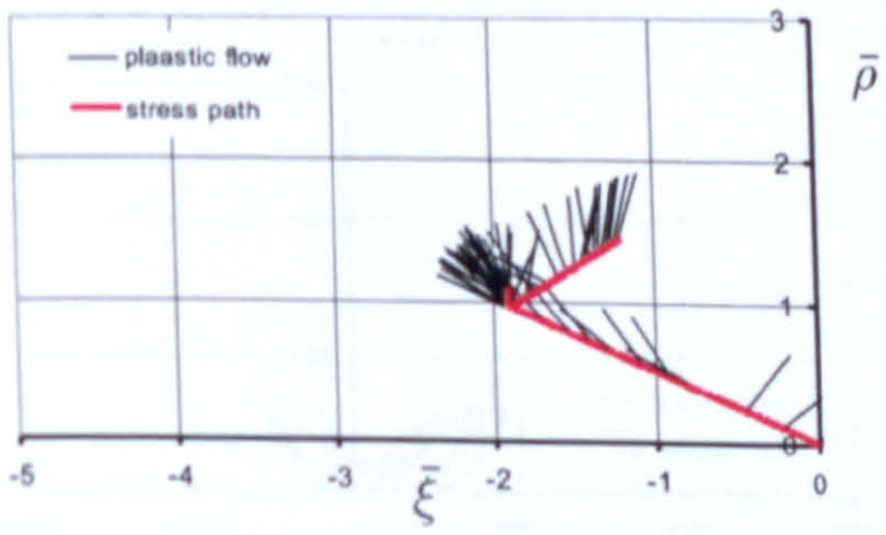

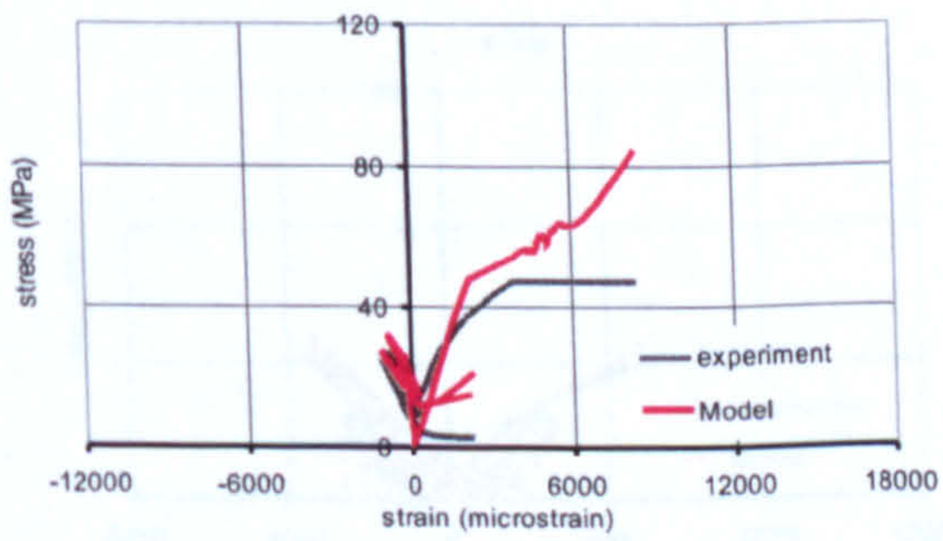

Figure 4.41: Plastic flow, stress paths and stress-strain simulations for Colorado tests, sample 5-2, 5-3, 5-4 and 5-5

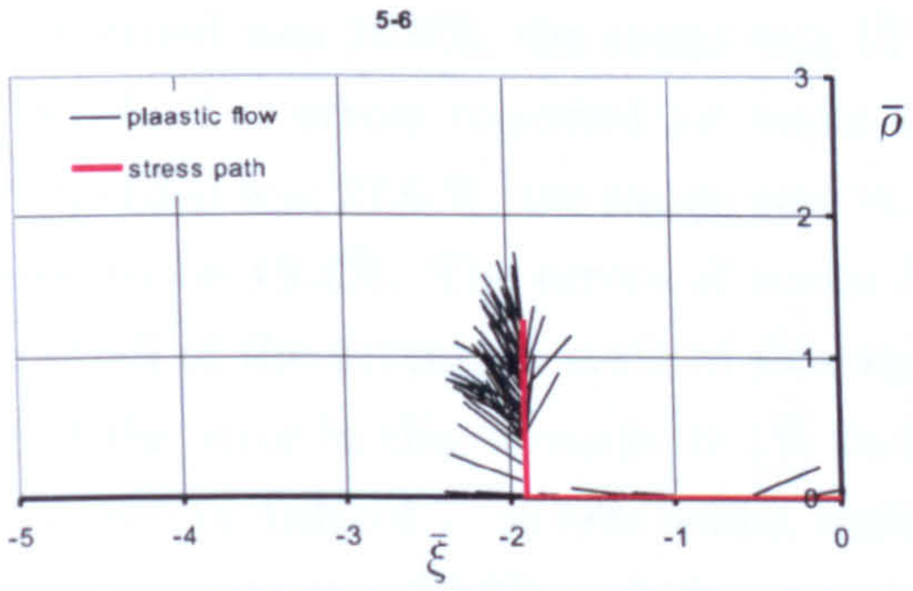

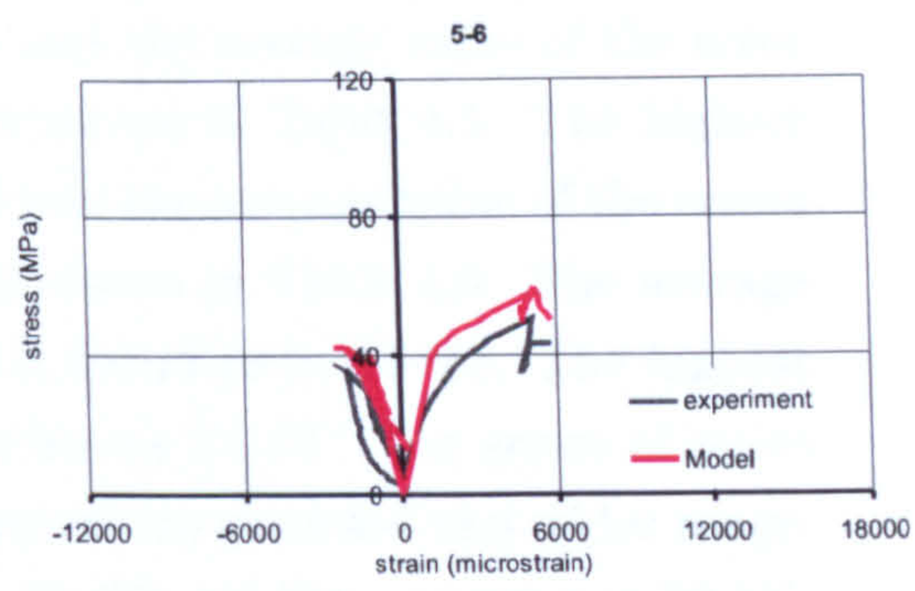

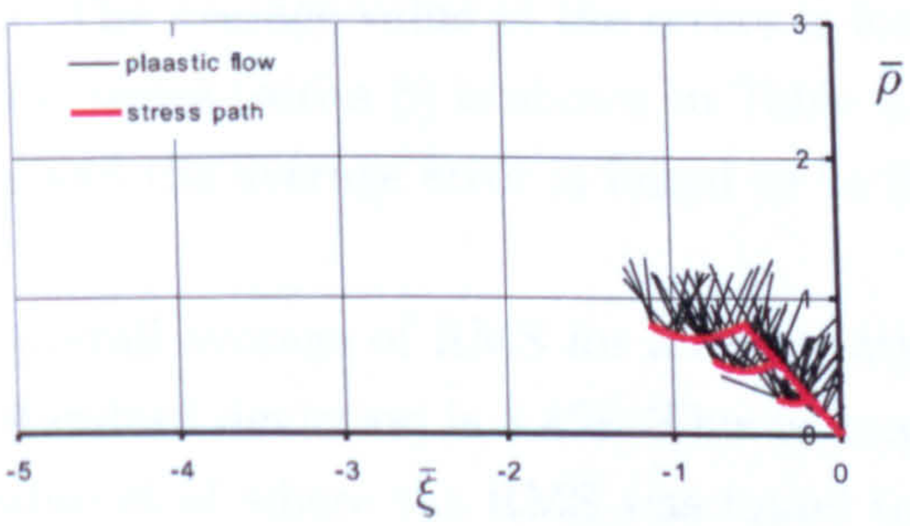

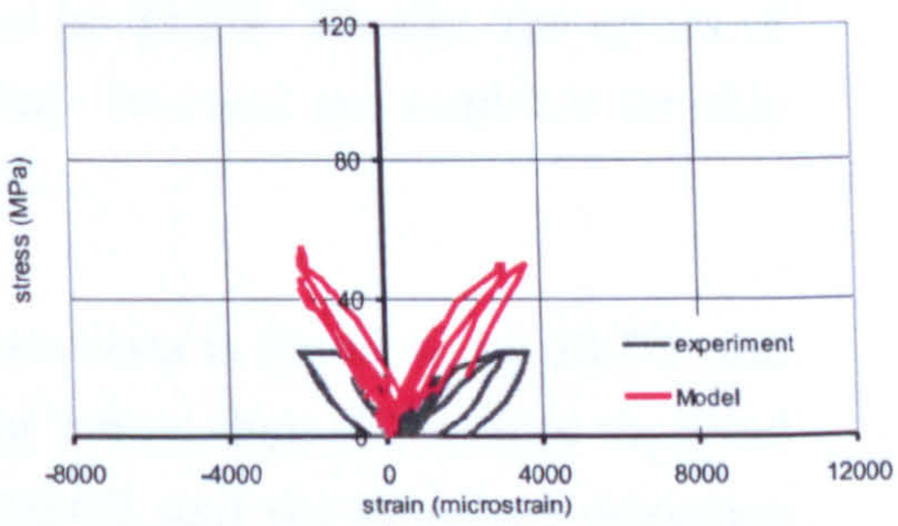

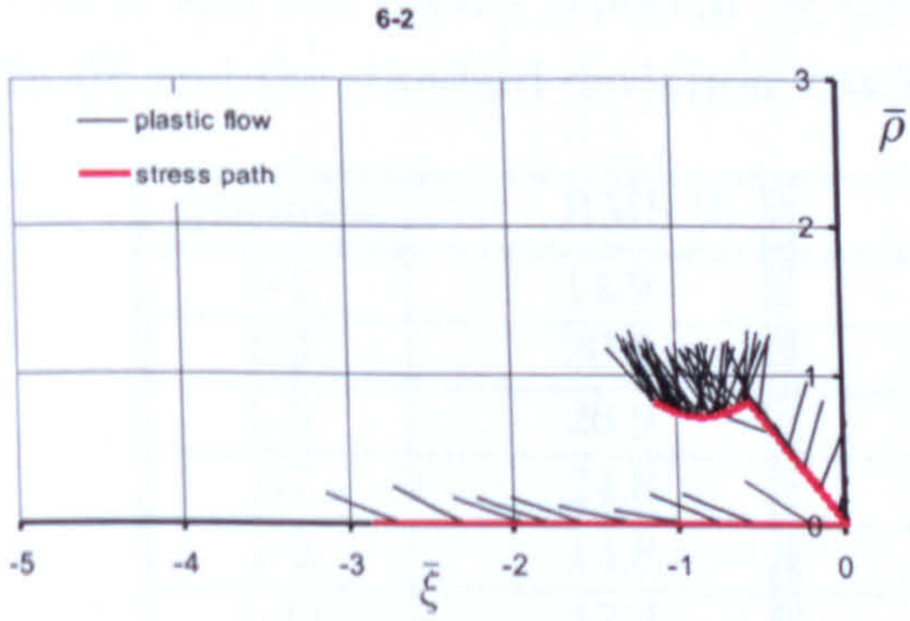

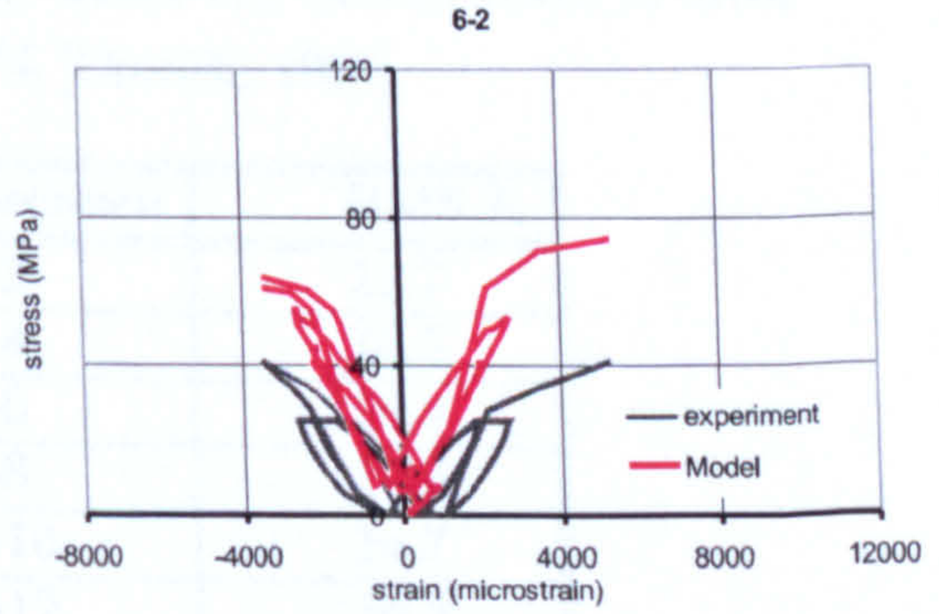

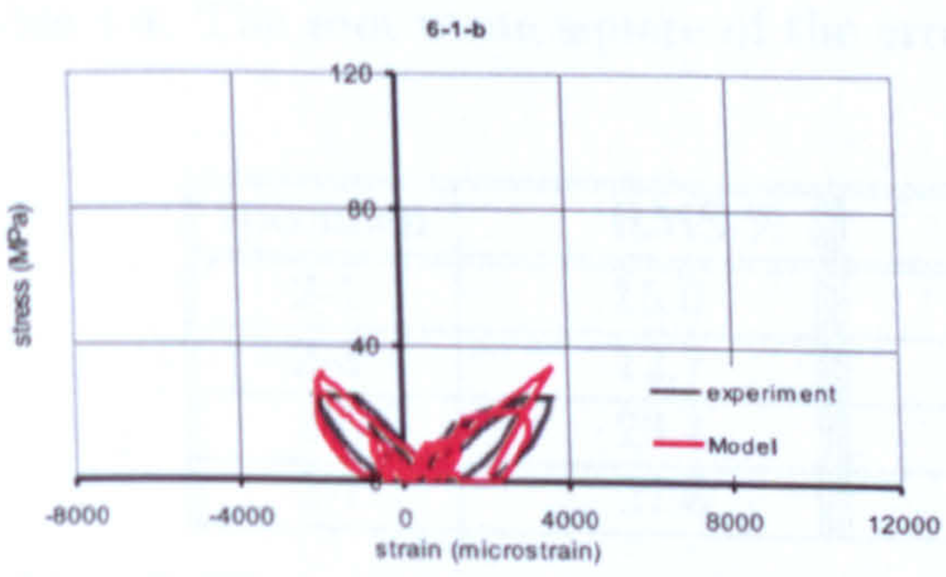

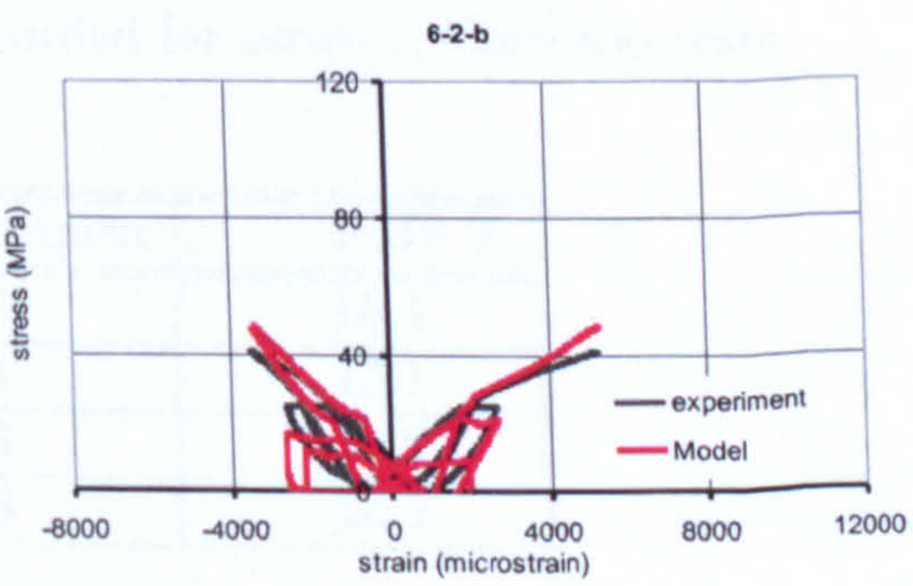

Figure 4.42: Plastic flow, stress paths and stress-strain simulations for Colorado tests, sample 5-6, 6-1 and 6-2

Table 4.4 shows the error values recorded for each of series 1 tests. The highest error recorded was 26.9%, the range was 12.2% and the average value of the error was 18.5%. The errors recorded for series 2 are shown in Table 4.5. The highest error recorded was 27.6 %, the range was 14.9 % and the average value of the errors is found to be 19.4%. The errors of series 3 are shown in Table 4.6. The average value of all of the seventeen tests of this series is found to be 19.6%. The highest value of the error in this series is 29.1% and the lowest 14.3%. The errors of series 4 are shown in Table 4.7. In this series, higher errors are recorded and wider range. The higher error was 37.3% and the range was 24.3% and the average was 23.1%. Table 4.8 shows the errors of series 5. Higher errors have been recorded for this series. The average value of the errors is found to be 33.2%. Finally, the errors of the last series (series 6) is shown in Table 4.9. Only two test are available for this series and the average error is found to be 85.35%.

The overall average of RMS for all the sixty seven tests is found to be 23.7% and the standard deviation is 8.4%. This is markedly better than the results reported by Simo *et al* where the RMS was found to be 26.6% and the standard deviation was 14.0%, and the results reported by Crouch, where the overall RMS of error was 29.4% and the standard deviation was 12.8% [Crouch, 1990].

specimen	RMS %	specimen	RMS %
1-1	14.9	1-2	18.7
1-3	20.6	1-4	16.5
1-5	26.9	1-6	18.9
1-7	24.8	1-8	17.6
1-9	14.8	1-10	14.7
1-11	17.4	1-12	16.3

Table 4.4: The root mean square of the error recorded for series 1, Colorado tests

specimen	RMS %	specimen	RMS %
2-1	15.0	2-2	16.1
2-3	12.7	2-4	13.1
2-5	23.1	2-6	22.9
2-7	27.6	2-8	24.7

Table 4.5: The root mean square of the error recorded for series 2, Colorado tests

specimen	RMS %	specimen	RMS %
3-1	24.7	3-2	21.6
3-3	29.1	3-4	15.0
3-5	23.7	3-6	19.5
3-7	25.7	3-8	15.8
3-9	14.5	3-10	21.6
3-11	15.6	3-12	14.3
3-13	23.8	3-14	15.1
3-15	16.6	3-16	18.3
3-17	18.4		

Table 4.6: The root mean square of the error recorded for series 3, Colorado tests

specimen	RMS %	specimen	RMS %
4-1	22.4	4-2	23.4
4-3	20.3	4-4	13.0
4-5	13.3	4-6	23.1
4-7	29.4	4-8	22.8
4-9	25.2	4-10	20.9
4-11	17.4	4-12	19.3
4-13	29.9	4-14	25.7
4-15	16.6	4-16	16.5
4-17	19.9	4-18	27.4
4-19	13.9	4-20	36.5
4-21	33.0	4-22	37.3

Table 4.7: The root mean square of the error recorded for series 4, Colorado tests

specimen	RMS %	specimen	RMS %
5-1	37.1	5-2	33.3
5-3	37.4	5-4	27.7
5-5	29.7	5-6	34.2

Table 4.8: The root mean square of the error recorded for series 5, Colorado tests

specimen	RMS %	specimen	RMS %
6-1	78.4	6-2	92.3

Table 4.9: The root mean square of the error recorded for series 6, Colorado tests

4.7 Concluding Remarks

In this chapter, the performance of the new constitutive model developed in Chapter 3 has been presented. This included the following:

1. In Section 4.2, each of the thirteen material constants were identified. Most of these can be assumed defaults.

2. In section 4.3, a complete calibration procedure (for all the constants) was developed.

3. In Section 4.4, the sensitivity of the model response to small changes in the material constants was determined. Some constants are found to have strong influence. These include, the uniaxial compression strength (f_c), the uniaxial tensile strength (f_t), the Young's modulus (E), and the ductility constants (A_h and B_h).

4. In Section 4.5, a series of comparisons between the model simulations and established experimental data was given. The data include triaxial and multiaxial compression tests.

5. In Section 4.6, the efficiency of the model was tested by determining the error for every simulated test. The overall error then compared with two previous results reported by other researchers. The model showed improvement in the results.

This chapter has shown that the new isotropic hardening elasto-plasticity formulation based on associated flow rule is capable of capturing all the basic deformation features under a wide range of triaxial and multi-axial compression stress states. Further work may be required to identify a more general hardening function.

4.8 References

ASTM Standards, ASTM C 39, Standard test method for compressive strength of cylindrical concrete specimens.

ASTM Standards, ASTM C 116, Standard test method for compressive strength of concrete using portions of beams broken in flexure.

ASTM Standards, ASTM C 496-90, Standard test method for splitting tensile strength of cylindrical concrete specimens.

British Standards Institution. BS 1881-117:1983 Testing concrete. Method for determination of tensile splitting strength.

British Standards Institution. BS 1881-118:1983 Testing concrete. Method for determination of flexural strength.

British Standards Institution. BS 1881-120:1983 Testing concrete. Method for determination of the compressive strength of concrete cores.

Chen W. F., and Saleeb A. F., 1994 b, Constitutive equations for engineering materials, Volume 1: Plasticity and Modelling, Elsevier.

Crouch R., 1990, Nonlinear deformation of concrete subjected to multiaxial compression, Doctoral thesis, The University of Manchester.

Crouch R. S., Petkovsi M. and Fernandez-Vega J., 2001, PCPV and PCCV materials behaviour under multiaxial loading conditioned with elevated temperature, CETWG BB/E/40835.

De Larrard F., Delloc A., Renwez S., Boulay C., 1994, Is the cube test suitable for high performance concrete, *Materials and Structures*, Vol. **27**, pp. 580-583.

Fumagalli M., 1991, Behaviour of concrete under multiaxial stress states: some observations on the state of the art, *Materials and Structures*, Vol. **24**, pp. 42-44.

Gyengo T., 1938, Effect of type of specimen and gradation of aggregate on compressive strength of concrete, *J. Am. Concr. Inst.* Vol. **34**, pp. 269-282.

Kupfer H., Hilsdorf H. K. and Rüsch H., 1969, Behaviour of concrete under biaxial stresses, *ACI Journal*, Vol. **66**, No. 8, pp. 656-666.

Neville A. M., 1995, Properties of Concrete, Forth edition, Longman.

Riisch H., 1960, Researches towards a general flexural theory for structural concrete, *J. Arner. Cone. Inst.*, Proceedings 57-1, pp. 1-28.

Scavuzzo, R., 1982, Behaviour of concrete under multiaxial load histories, M.S. Thesis, C.E.A.E Dept., University of Colorado, Boulder.

Stankowski, T., 1983, Concrete under multiaxial load histories, M.S. Thesis, C.E.A.E Dept., University of Colorado, Boulder.

Tahar B., 2000, C_2 Continuous hardening/softening elasto-plasticity model for concrete, Doctoral thesis, The University of Sheffield, UK.

Chapter 5

Investigations and Simulations of Concrete with Different Constituents

5.1 Introduction

Concrete is a heterogeneous material whose properties depend on the properties of its component phases and the interactions between them. Under the same configurations, concrete may perform differently because of material properties. Concrete constituents such as cement type, coarse and fine aggregates, water-cement ratio, additives, admixtures, temperature, mixing procedure, and mix proportions have a considerable contribution on the strength and strain experienced by a confined element of concrete.

It is intended in this chapter to investigate the effect of using different proportions of coarse aggregate on the behaviour of concrete under triaxial compression and to simulate the stress-strain response using the new developed model (see Chapter 4).

Coarse aggregate is a material that will pass the 3-inch (75 mm) screen and will be retained on the No. 4 sieve (e.g sieve size is 5 mm). Coarse aggregate occupies most of the volume of the concrete. The cement paste coats and binds the aggregates together. The composition, shape, and size of the aggregate all have significant impact on the workability, durability, strength, weight, and shrinkage of the concrete. The coarser the aggregate, the more economical the mix. Larger pieces offer less surface area of the particles than an equivalent volume of small pieces. Use of the largest permissible maximum size of coarse aggregate permits a reduction in cement and water requirements. One restriction usually assigned to

coarse aggregate is its maximum size. Larger pieces can interlock and form arches or obstructions within a concrete form. That allows the area below to become a void, or at best, to become filled with finer particles of sand and cement only. That results in either a weakened area or a cement-sand concentration that does not leave the proper proportion to coat the rest of the aggregate.

Since the aggregate is generally stronger than the paste, its strength is not a major factor for normal strength concrete. However, the aggregate strength becomes important in the case of higher-strength concrete or lightweight aggregate concrete. Surface texture and mineralogy affect the bond between the aggregates and the paste as well as the stress level at which microcracking begins. The surface texture, therefore, may also affect the modulus of elasticity, the shape of the stress-strain curve and, to a lesser degree, the compressive strength of concrete. Tensile strengths may be very sensitive to differences in aggregate surface texture and surface area per unit volume [Aitcin and Mehta].

The fine and coarse aggregates normally used for concrete are natural deposits of sand and gravel. Fine aggregate is defined as material that will pass a No. 4 sieve and will, for the most part, be retained on a No. 200 sieve (e.g. sieve 75 μm). The purpose of the fine aggregate is to fill the voids in the coarse aggregate and to improve the workability of the mix.

Beside testing the validity of the constitutive model developed in Chapter 3 against as many variations as possible, it is also important for some practical reasons to use concrete with no coarse aggregates. In desert regions, there are special problems associated with concreting. These problems concern the availability of the coarse aggregates, their cost, and the environment. On the other hand, concreting in such regions has an advantage due to the presence of fine aggregates almost everywhere [El-Ariss].

During 2003, at the Department of Civil and Structural Engineering of the University of Sheffield, a testing program was carried out to investigate the influence of coarse aggregates on the triaxial behaviour of plain concrete. Three mixes were used for this purpose; the first was normal mix similar in mix design to that presented in Chapter 2, the second was made with no coarse aggregates, the third with double coarse aggregates. Table 5.1 shows the mix proportions (by weight), for the three mixes, normalised with respect to cement content.

Constituents	Mix 1 (standard)	Mix 2 (mortar)	Mix 3 (double coarse agg.)
Cement	1	1	1
Water	0.56	0.56	0.56
Plasticiser	0.006	0.006	0.006
PFA	0.33	0.33	0.33
Sand	2.447	2.447	2.447
10 mm aggregate	1.39	0.0	2.78
20 mm aggregate	2.777	0.0	5.554

Table 5.1: The mix proportions (by weight), for the three mixes, normalised with respect to cement content

All samples were tested using a Hoek cell. The data contains six uniaxial tests for each mix and three tests for each of the six levels of confinements. There are six levels of confinement; 10, 20, 30, 40, 50, and 60 MPa. The data have been examined individually. Each test specimen had four strain gauges; two to measure the axial strains and two for the lateral strains. Readings were taken up to the peak stress. The average of the two readings from the strain gauges was adopted. If the strain gauge was broken before reaching the peak, the reading of that gauge was ignored. In such case only one reading was considered. In some tests there are no complete readings, and thus the entire test was ignored. The sign convention was chosen to be negative for compression and positive for expansion. However in some figures the stresses were assigned positive for the sake of illustration.

This chapter begins with section 5.2, where the examination of the uniaxial compression response of the three mixes is presented. This includes stress-strain response, the volumetric strain, peak stress, peak strain, Young's modulus, Poisson's ratio and the plastic flow vectors. In Section 5.3, the same topics are discussed with an additional study of the peak nominal stress envelope, the volume transition stress envelope and the yield surfaces. In Section 5.4, the simulations of the three mixes are presented. In Section 5.5 the yield surface for the three mixed are introduced. Finally, concluding remarks are listed in Section 5.6.

5.2 Uniaxial Response

5.2.1 Stress-strain Response

Figure 5.1 shows the uniaxial stress-strain response for three tests taken from six uniaxial tests for Mix 1, Sheffield tests. The first and second are taken from test M1A3_00_1 and M1C1_00_1 where the average values of the two strain gauges measuring the axial and lateral strains are taken. The third set of results are taken from test M1C9_00_1 where the results of only one strain gauge are taken because of the irregularities of the initial part of the curves of the other gauge and the large strain recorded prior to the loading. The other three samples are disregarded due to irregularities in the test results at the initial stage where large strain readings are recorded while the stress is still zero. Some strain gauges failed before reaching peak. The figure shows some concavity in the initial part of the tests. This could be due to some error in recording the stresses or the initial bedding of the platens. It seems that the latter is the most likely reason due to the repeated occurrence of the problem even with the normal concrete mixes.

Figure 5.2 shows the uniaxial stress-strain response for Mix 2. Only three out of six tests are presented here due to the same irregularities mentioned above. The behaviour of concrete seems to take almost a linear response for about 30% of the peak stress. This is then followed by a nonlinear response with an increasing rate until it reaches zero tangent at the peak.

The stress-strain behaviour for Mix 3 is presented in Figure 5.3 where three tests (M3A3A_00_1, M3A6_00_1 and M3A8_00_2) out of six tests are found to be useful. The average values of the two longitudinal and radial gauges are taken. Concavity in the initial part of some curves are again observed. This is due to some error in recording the stresses or the closure of the pre-existing cracks. The behaviour then changes into linear and gradually to nonlinear. The nonlinearity rate increases significantly whilst approaching the peak.

Figure 5.4 shows the variation of the stress-strain response of the three mixes mentioned above under uniaxial compression loading. It can be seen that the response is strongly influenced by the constituents proportions. The general behaviour of the axial response for the three mixes seems to have the same trend but with a significant reduction in the initial slope for Mix 2 and increase for Mix 3. The figure illustrates that Mix 2 seems to be the most ductile and Mix 3 is the most brittle.

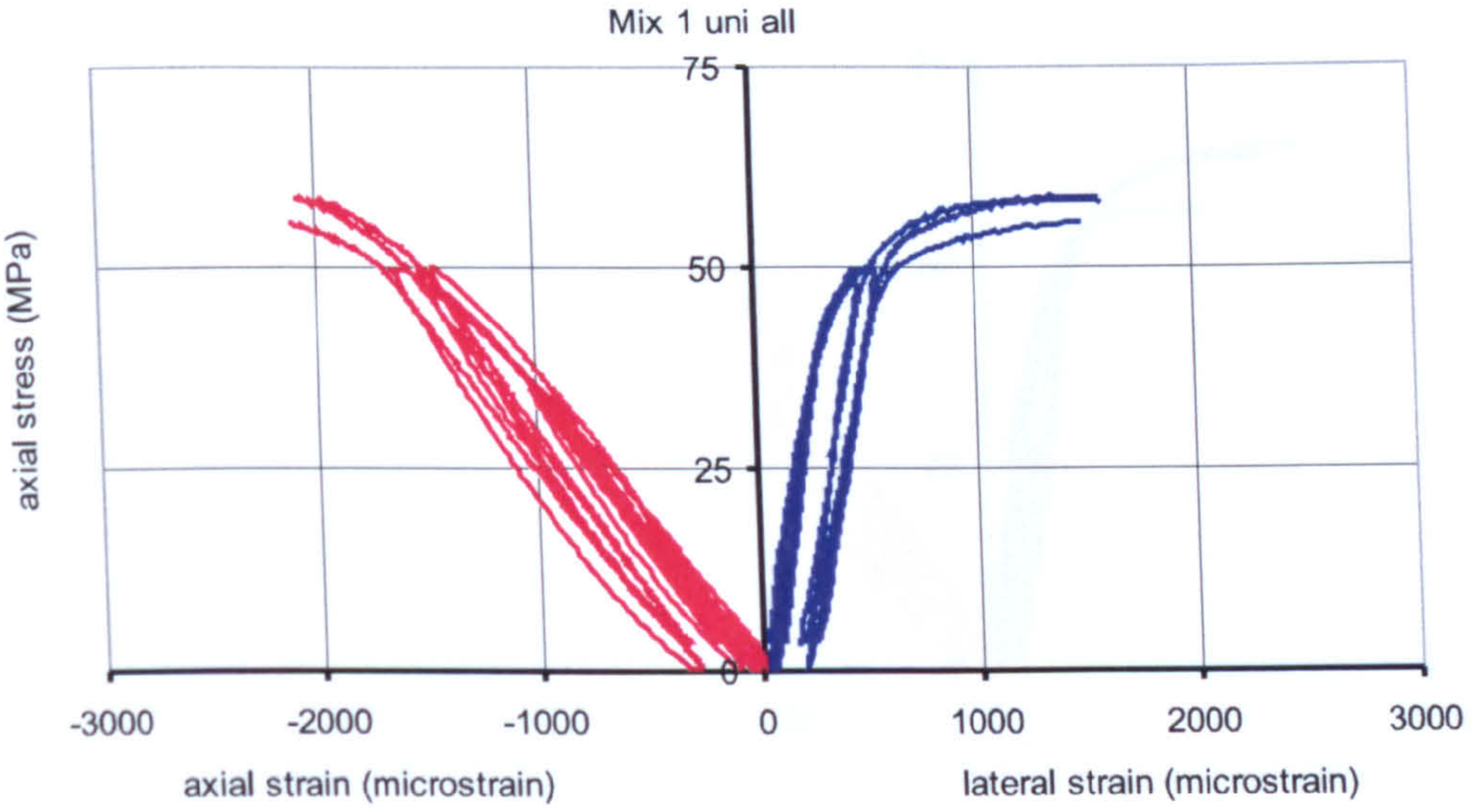

Figure 5.1: Three stress-strain curves for uniaxial compression test of Mix 1, Sheffield tests

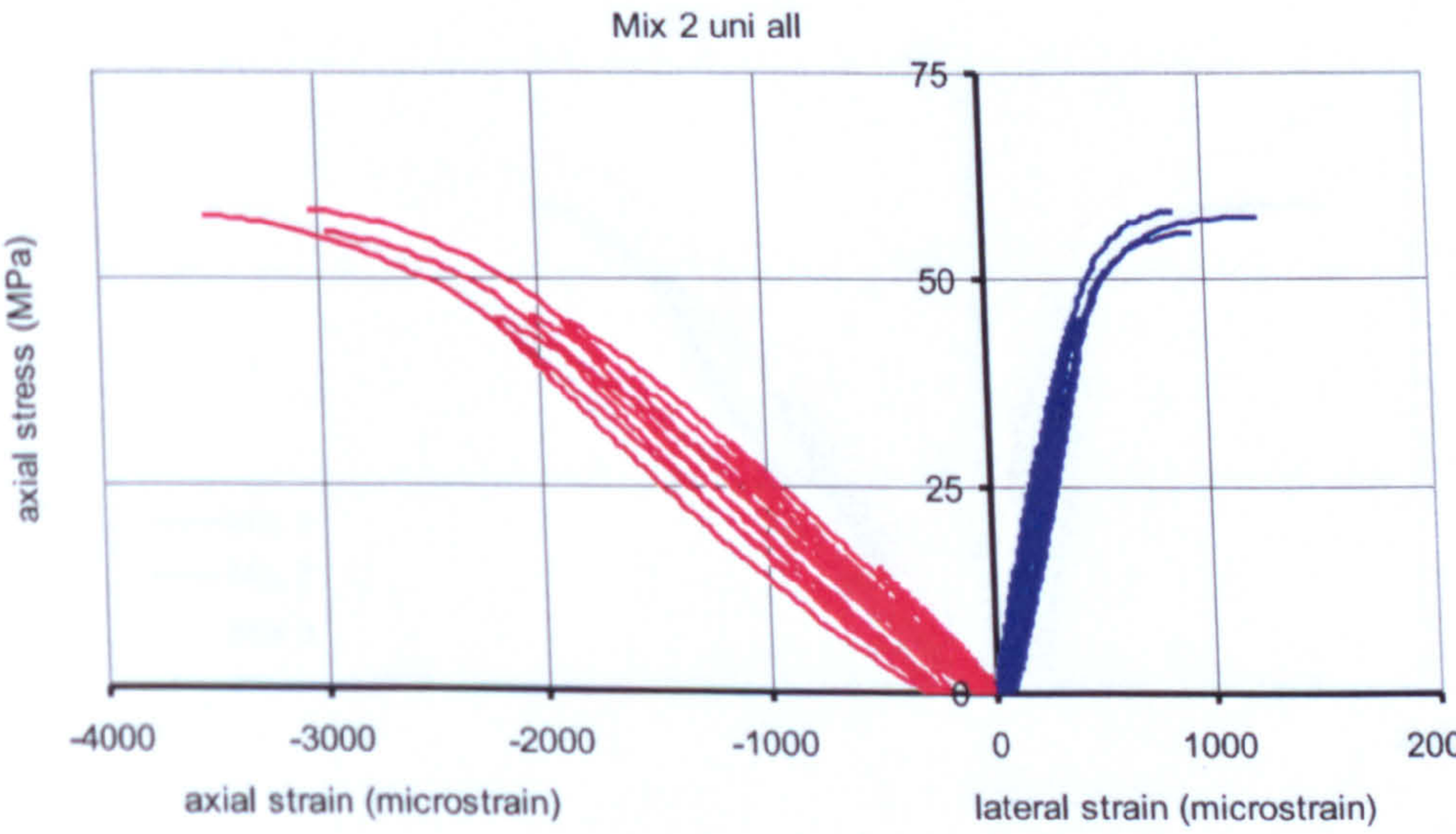

Figure 5.2: Three stress-strain curves for uniaxial compression test of Mix 2, Sheffield tests

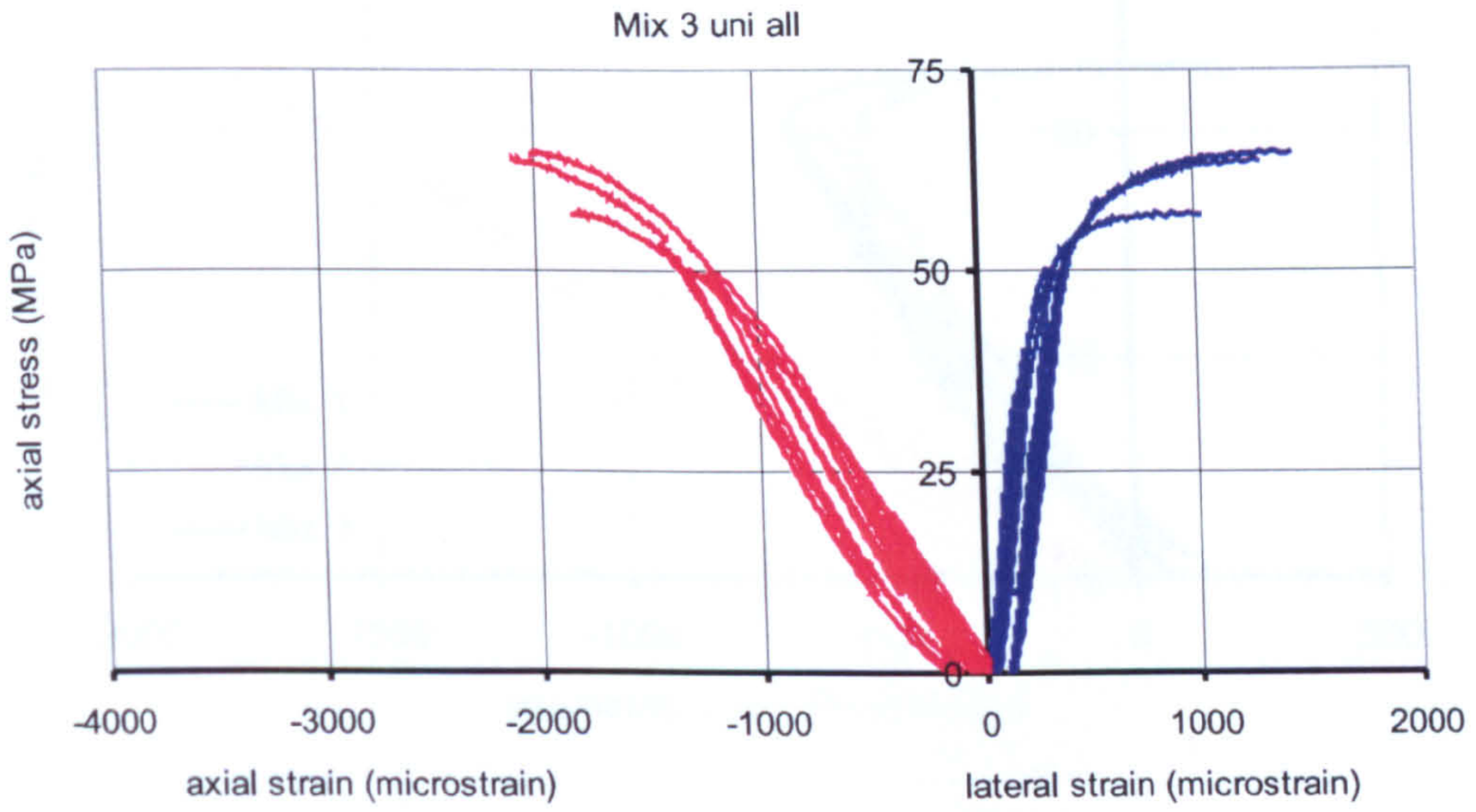

Figure 5.3: Three stress-strain curves for uniaxial compression test of Mix 3, Sheffield tests

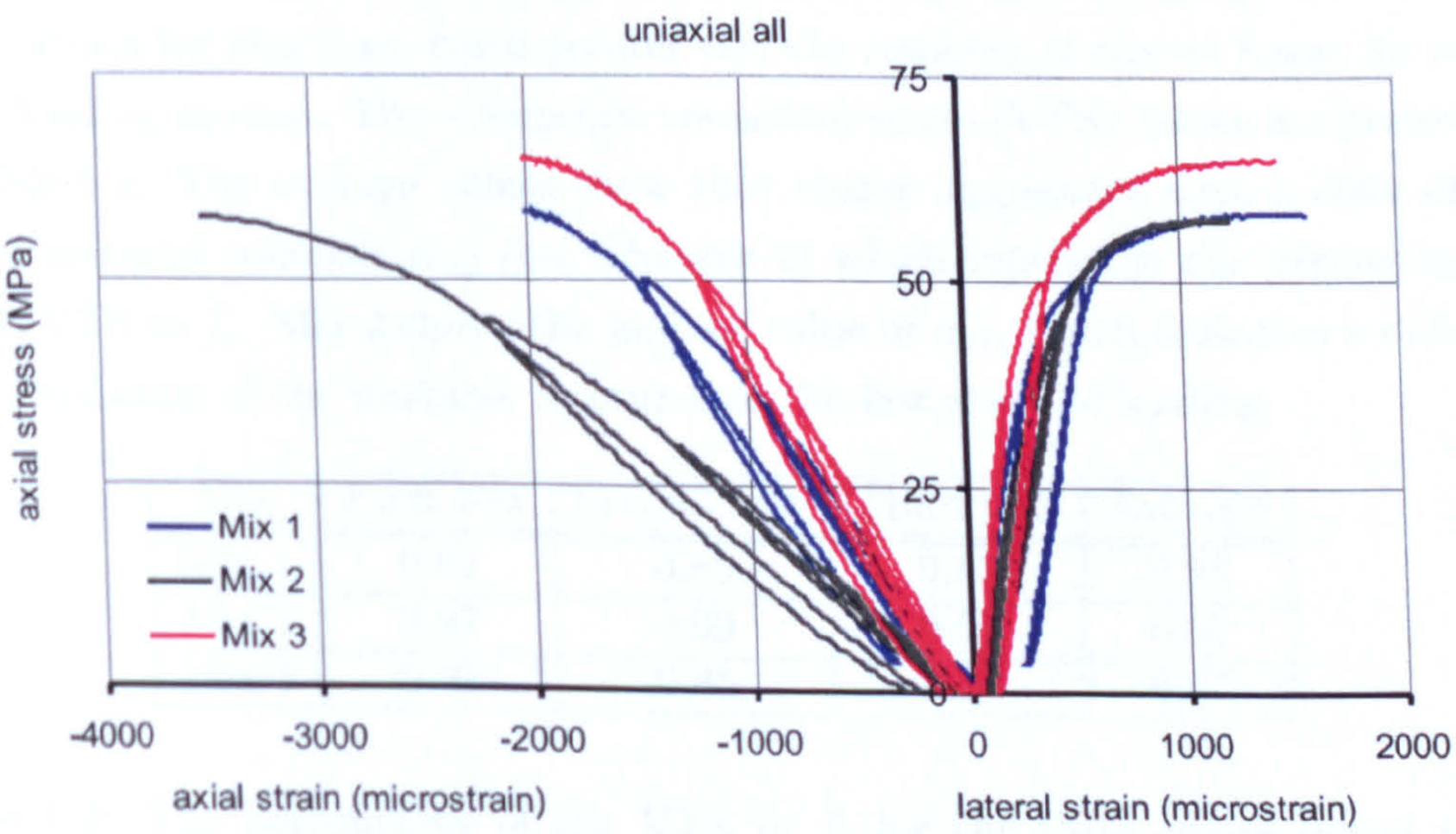

Figure 5.4: The variation of the stress-strain response of the three mixes under uniaxial compression loading

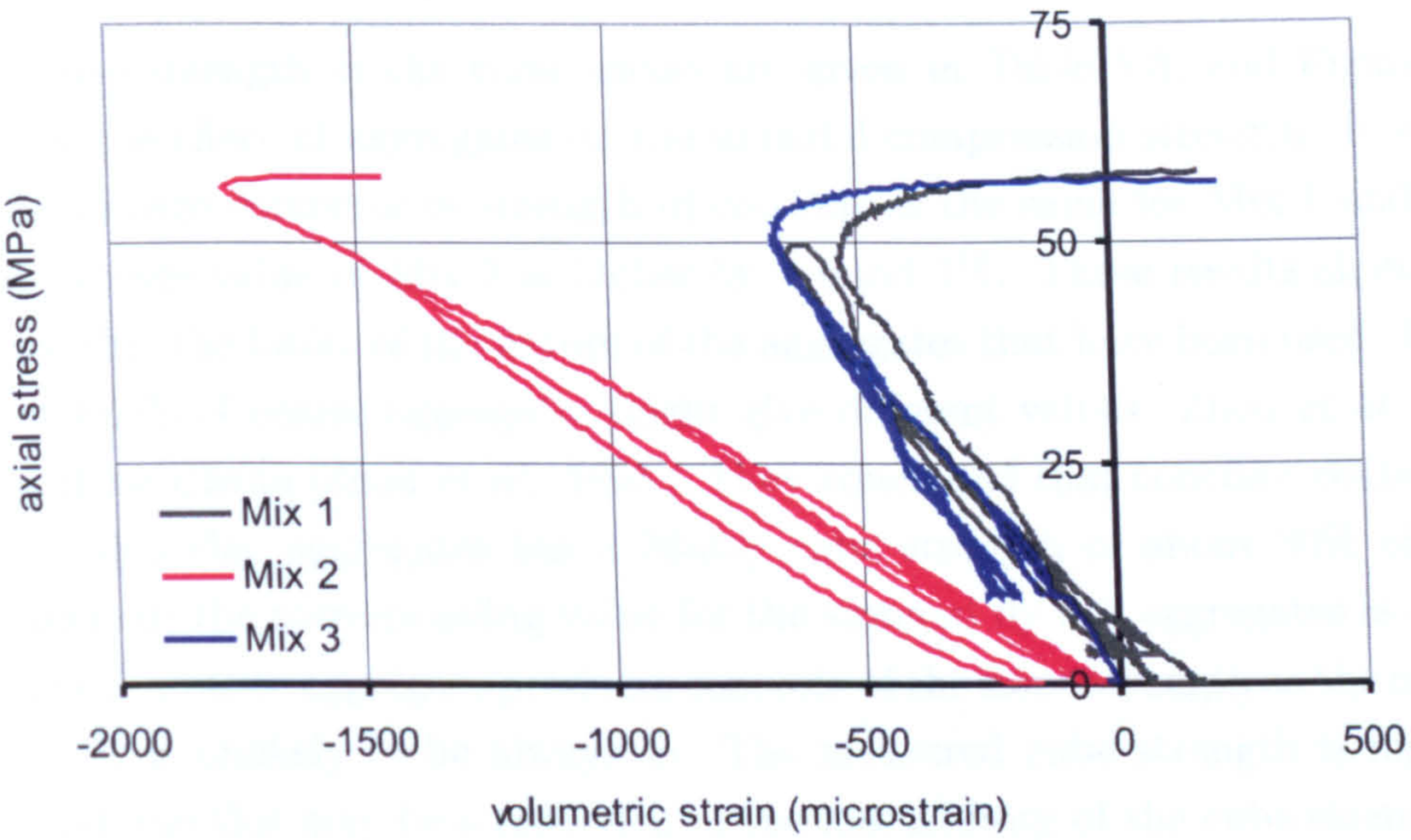

Figure 5.5: The volumetric strains versus the axial stresses for the three mixes

5.2.2 Volumetric strain

Figure 5.5 shows the volumetric strains for the three mixes. The volumetric behaviour of Mix 1 and Mix 3 seems to be similar to each other with some concavity in the initial part of the curves. This concavity is also notice in the stress-strain response and thought to be due to some technical error. The values of the volumetric strain for Mix 2 are much greater and the response is almost linear for most of the loading process. The volumetric transition stress (VTS) values are presented in Table 5.2. The average values show that coarse aggregates have a clear effect on the material constant α_{vts} (see Chapter 2) which represents the percentage of plastic VTS to f_c. Mix 2 shows the highest value of α_{vts} which indicates a delay in the formulation of the unstable fractures to the last stage of loading.

Mix	First test	Second test	Third test	Average
Mix 1	0.82	0.85	0.81	0.83
Mix 2	0.97	0.99	0.97	0.97
Mix 3	0.91	0.85	0.84	0.87

Table 5.2: The percentages of the VTS to f_c for the three mixes tested under uniaxial compression tests

5.2.3 Peak Stress, f_c

Compressive strength of the three mixes are given in Table 5.3, and Figure 5.4 illustrates the effect of aggregates on the uniaxial compression strength. It seems that the average compressive strength of concrete is the same for Mix 1 and Mix 2. The average value of Mix 3 is higher by around 7%. These results should be viewed within the limits of the nature of the aggregates that have been used. Using different kinds of coarse aggregates might give different values. Zhou *et al.* have studied these effects [Zhou *et al.*, 1995]. They concluded that concrete containing the expanded clay aggregates has a 28-day cube strength of about 30% of that of the mortar; the corresponding value for the sintered fly ash aggregates is about 80%. The limestone aggregate produces concrete of the same strength as the mortar although it is unlikely to be always so. The measured cube strength is high for glass bead and this may be a reflection of the insensitivity of the cube strength to aggregate mortar bond failure, which is certainly evident in this type of concrete. Too stiff aggregate, though improving modulus, may cause stress concentrations and initiate more microcracking causing a decrease in strength .

Mix	First test	Second test	Third test	Average
Mix 1	58.52	58.05	55.44	57.34
Mix 2	58.35	55.48	57.59	57.14
Mix 3	56.92	64.80	63.47	61.73

Table 5.3: The peak stresses for the three mixes tested under uniaxial compression tests

5.2.4 Strain at Peak Stress

Axial strains at peak stresses for the three mixes are given in Table 5.4 and the lateral strains in Table 5.5. Figure 5.4 shows the effect of coarse aggregates on the strain at peak stress. An increase of about 50% in the average value of the axial peak strain for Mix 2 is observed compared with Mix 1, whereas insignificant difference between Mix 3 and Mix 1. For the lateral strains, a decrease of around 30% for Mix 2 is noticed compared with Mix 1, while Mix 3 is less by around 15%.

5.2.5 Young's Modulus

The average values of Young's modulus for the three mixes are given in Table 5.6. The values suggested a decrease of about 35% of Young's modulus for Mix 2 compared with Mix 1 and an increase by an average value of about 13% for Mix 3. These values show that the coarse aggregates has significant effect on the stiffness.

Mix	First test	Second test	Third test	Average
Mix 1	-2097.13	-2003.17	-2122.10	-2074.13
Mix 2	-3039.59	-2974.72	-3524.31	-3179.54
Mix 3	-1841.45	-2017.66	-2101.15	-1986.75

Table 5.4: The axial strains at peak stresses for the three mixes tested under uniaxial compression tests

Mix	First test	Second test	Third test	Average
Mix 1	1576.73	1591.06	1493.06	1553.62
Mix 2	866.84	943.15	1239.12	1016.37
Mix 3	1030.24	1453.68	1297.60	1260.51

Table 5.5: The lateral strains at peak stresses for the three mixes tested under uniaxial compression tests

The absence of coarse aggregate causes a significant reduction in the stiffness of concrete.

Mix	First test	Second test	Third test	Average
Mix 1	38.35	43.3	42.6	41.42
Mix 2	27.97	25.17	28.5	27.21
Mix 3	51.0	43.93	45.93	46.95

Table 5.6: The average values of Young's modulus for the three mixes tested under uniaxial compression tests

5.2.6 Poisson's Ratio

The average values of Poisson's ratio for the three mixes are given in Table 5.7. It seems that the average value decreases by about 15% for Mix 2 and increases by about 7% for Mix 3. These are an average values of the Poisson's ratio but individual values of different tests might have the same values for different mixes. However, all these values do fall in the range of Poisson's ratio for concrete that have been reported in literature (see Chapter 2).

Mix	First test	Second test	Third test	Average
Mix 1	0.20	0.23	0.20	0.21
Mix 2	0.20	0.17	0.18	0.18
Mix 3	0.225	0.23	0.22	0.225

Table 5.7: The average values of Poisson's ratio for the three mixes tested under uniaxial compression tests

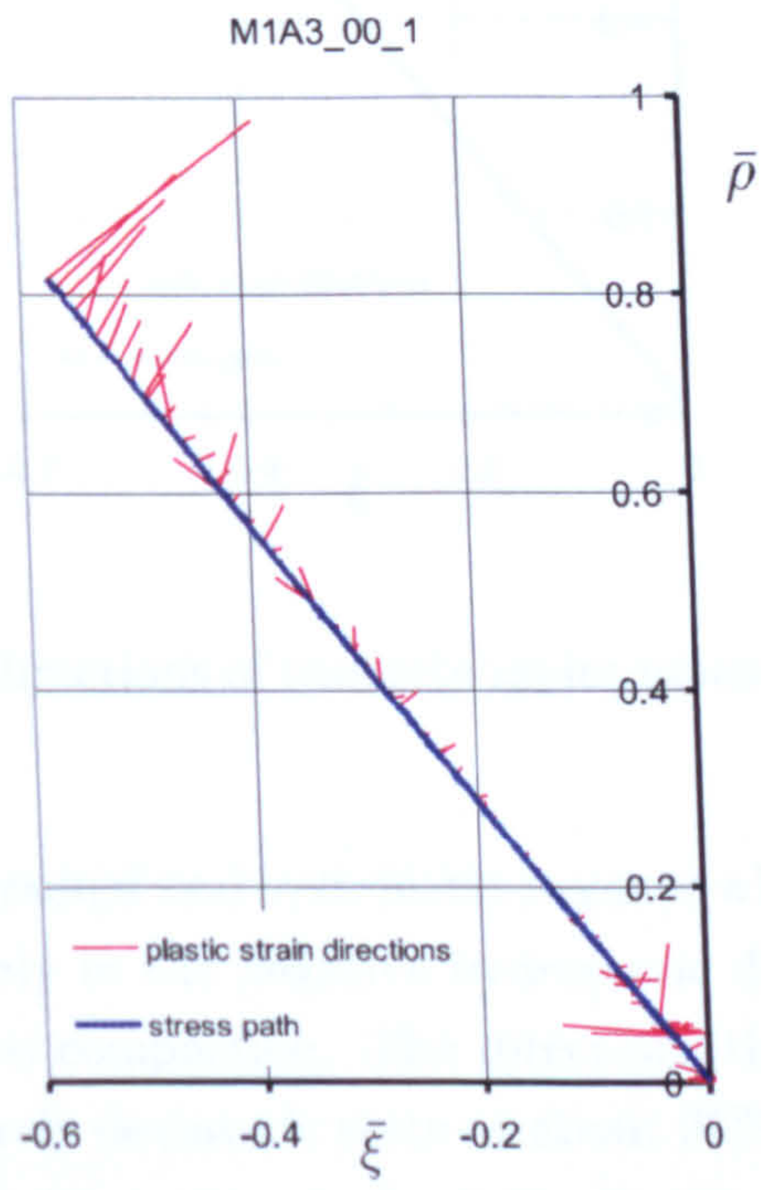

Figure 5.6: Plastic strain directions of concrete under uniaxial compression for Mix 1, sample M1A3_00_1

5.2.7 Plastic Flow

Figure 5.6 shows the plastic strain directions for Mix 1 under uniaxial compression. The plastic flow is scattered during the initial part of the loading process. This is due to the cyclic loading where some plastic strains have been recorded although theoretically, it should be totally elastic. Then, uniform and gradual plastic strains can be seen at about 80% of the peak stress. The directions in this region are mostly normal to the stress path which indicates that most of the plastic strains near the peak, are in the lateral direction.

The plastic strain directions of one uniaxial test of Mix 2 is shown in Figure 5.7.

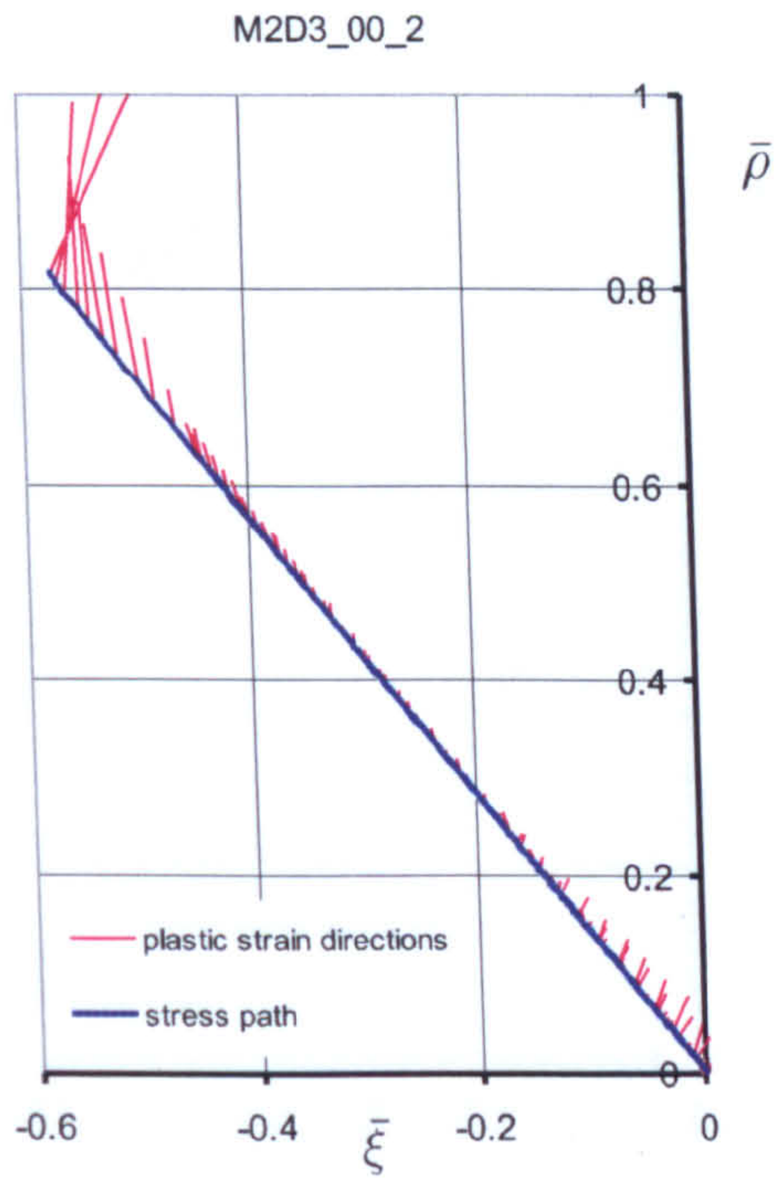

Figure 5.7: Plastic strain directions of concrete under uniaxial compression for Mix 2, sample M1D3_00_2

The plastic flow takes a gradual and systematic manner whereas the initial plastic strain directions are mainly in the negative hydrostatic direction. This indicates that the sample undergoes compaction. The directions then become more deviatoric until it reaches a purely deviatoric state at about 95% of the peak stress. The direction then changes to the positive hydrostatic direction which is an indication of plastic dilation. The directions remains increasingly positive until it becomes almost normal to the stress path at peak which is an indication of overwhelming lateral plastic deformation at this region. The overall behaviour illustrates the ductile behaviour of concrete without coarse aggregates. The plastic strains seen at the initial part of the test are thought to be the result of the cyclic loading and therefore, should not influence the general idea of the manner of the plastic flow.

Figure 5.8 shows the plastic flow of one of Mix 3 tests. It shows limited plastic strain during most of the loading process. Then, at about 90% of the peak stress, the plastic strains increase significantly. During the last part of the loading, the plastic strain directions are almost normal to the stress path. This indicates, as in the previous samples, that the lateral plastic deformation is dominant in this region. It should be noted that all the plastic strain vectors are normalised with respect to the peak equivalent plastic strain. So, the length of these vectors does

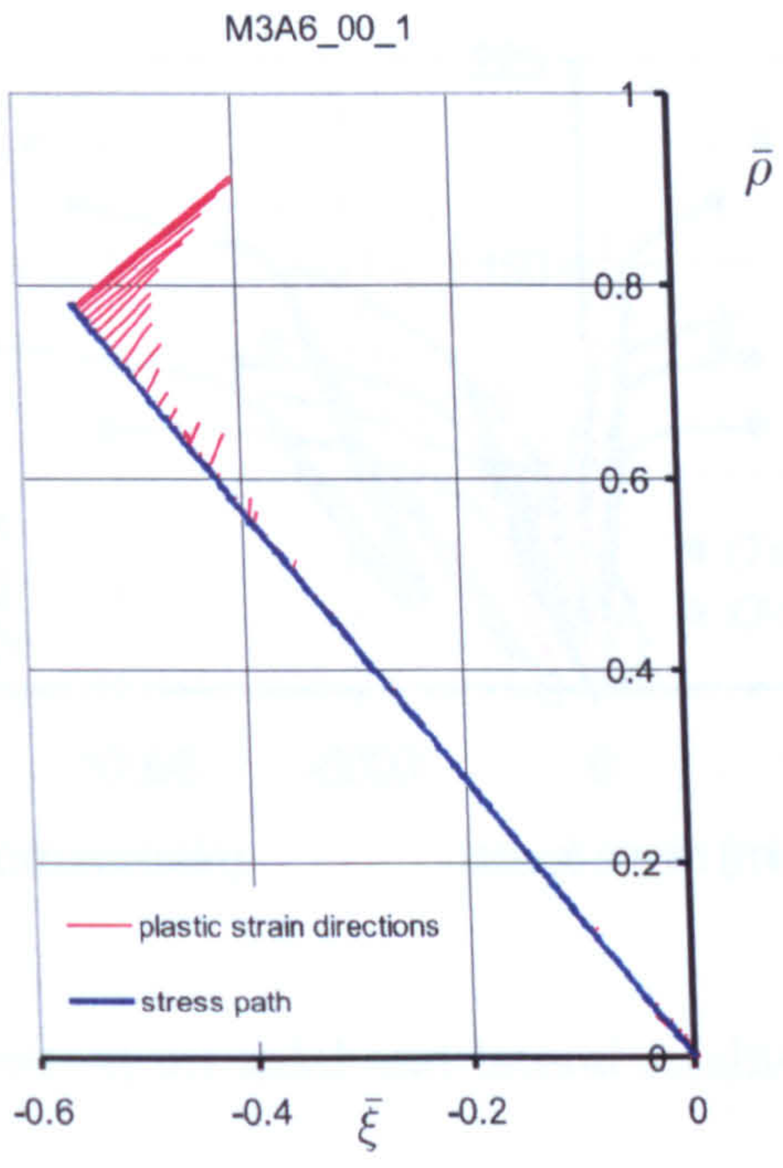

Figure 5.8: Plastic strain directions of concrete under uniaxial compression for Mix 3, sample M3A6_00_1

not reflect the actual value of the plastic strains.

5.3 Triaxial Response

The triaxial response for the three mixes is discussed in this section. This will help to observe the effect of the confinement on the mechanical properties of concrete with different constituents and draw a wider picture for the behaviour of concrete under various loading magnitudes. The same topics that have been discussed in the previous chapter are discussed here with additional discussions on the PNS, VTS and the yield surfaces.

5.3.1 Stress-strain Response

The stress strain behaviour for two levels of confinement (10 and 30 MPa) of the three mixes are shown in Figure 5.9. The peak axial stress of concrete increases significantly with the increase in confinement for all the three mixes, but with less proportion for Mix 2. The increase in confinement increases the ductility for all mixes, but this effect is the most prominent for Mix 2. The nonlinear response can be seen in all the mixes for most of the loading process. The peak lateral strain

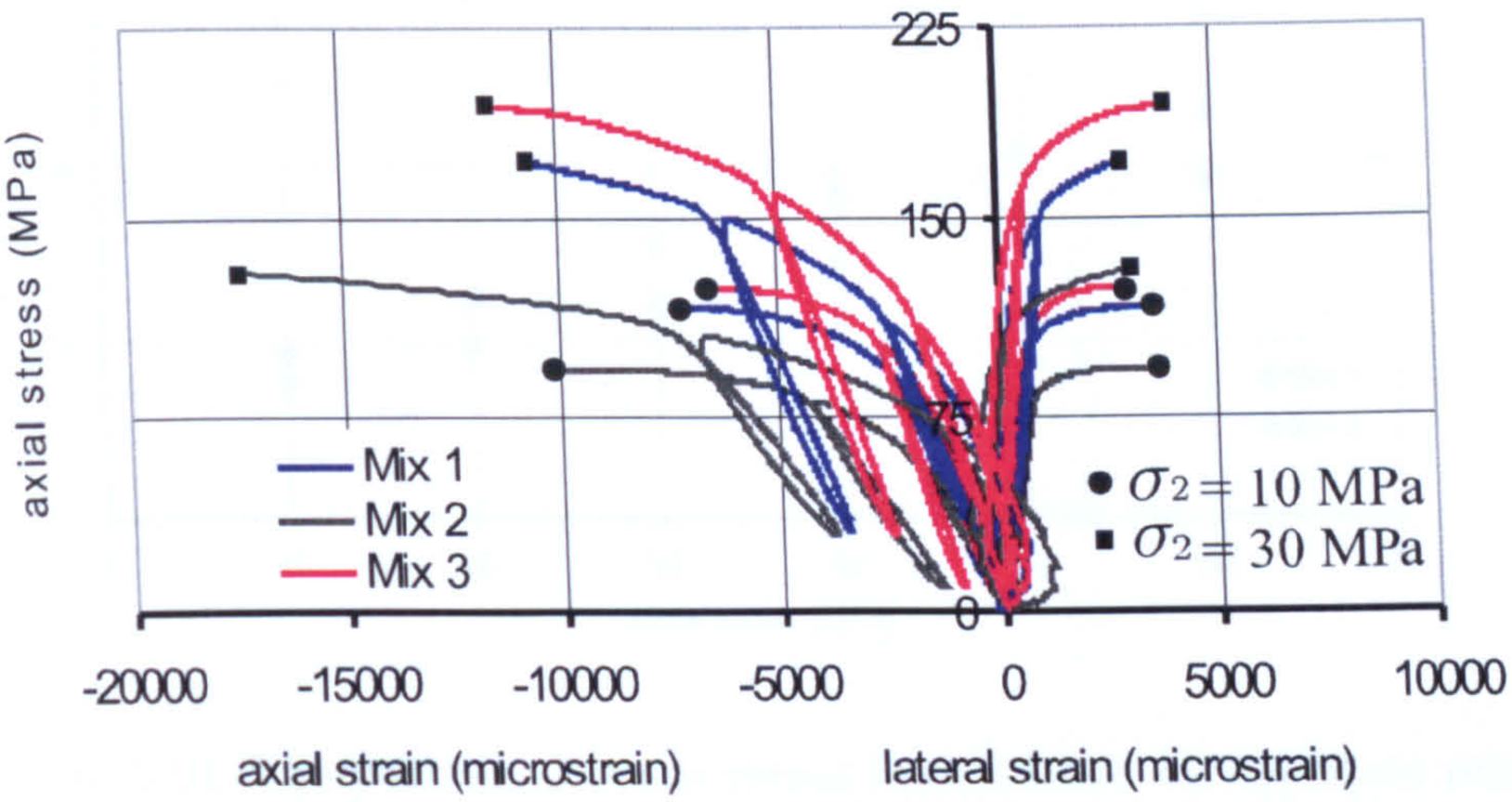

Figure 5.9: The axial stress versus axial and lateral strains for two levels of confinement

seems to be less for Mix 1 and Mix 2. However, these observations have been made with the limited data that have been studied. Only two complete sets of three tests under confinement are found in Sheffield's data. For other levels of confinement, the strain gauges have failed before reaching the peak.

5.3.2 Peak Axial Stress

Figure 5.10 shows the peak axial stress versus lateral stress for the three mixes. The response of all the three mixes seem to be almost linear. The effect of the coarse aggregates becomes more prominent with increasing confinement. The highest values of peak stresses are for Mix 3 followed by Mix 1 and the lowest are the values of Mix 2. At moderate to high level of confinement (30 MPa $\leq \sigma_2 \leq$ 60 MPa) the difference between the peak stresses of Mix 1 and Mix 2 seem to be maintained, while for Mix 3, the difference increases proportionately.

5.3.3 Young's Modulus

Figure 5.11 shows the values of Young's modulus for the three mixes. The values of Mix 2 are lower than that of Mix 1 and the values of Mix 3 are the highest. The average value for Mix 1 , Mix 2 and Mix 3 are 44.1, 27 and 52 GPa respectively. For Mix 1, the values increase slightly with the increase in confinement. There is no valid data for 40 MPa level of confinement and only one valid test for 20 and 30 level of confinement. For Mix 2, the data is available only for moderate level

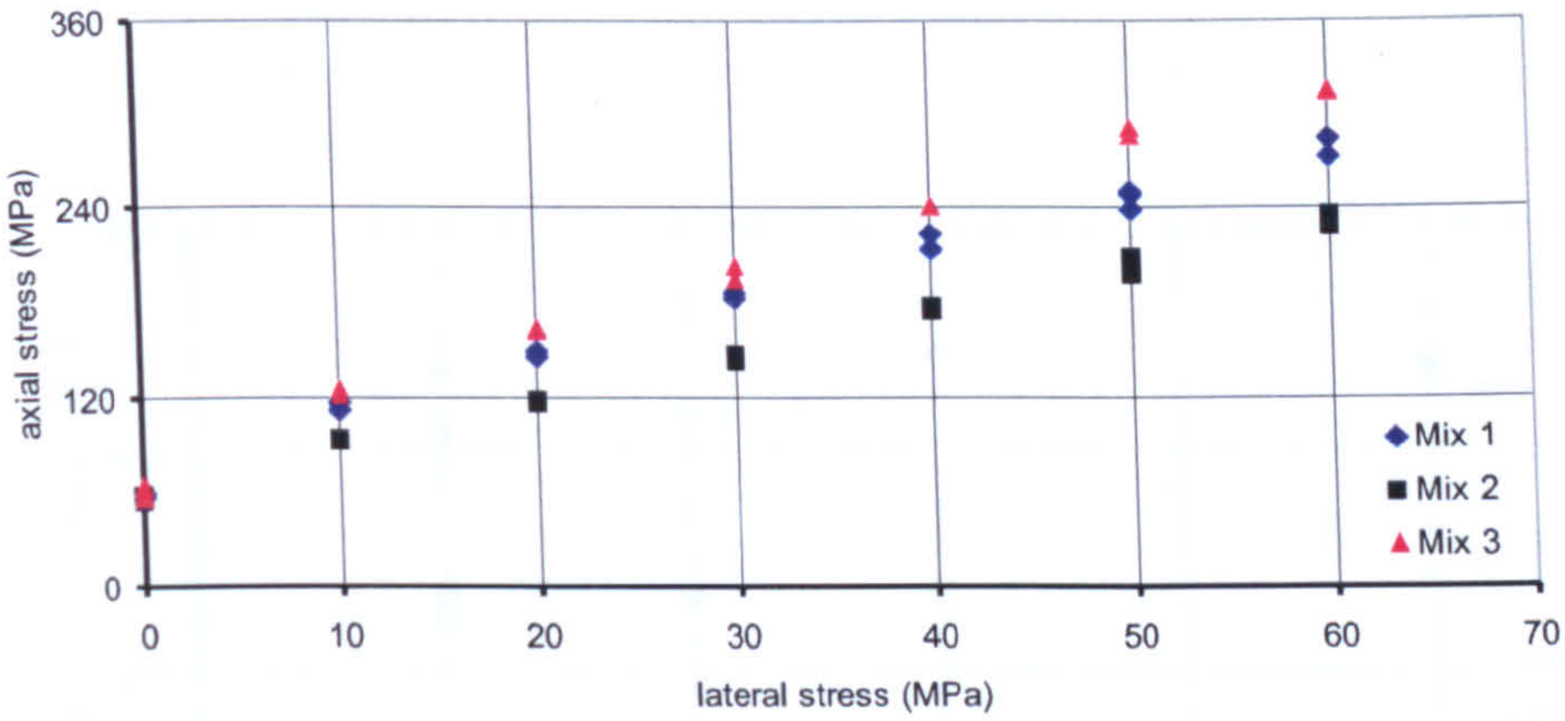

Figure 5.10: The peak axial stress versus lateral stress for the three mixes

of confinement ($\leq$ 30 MPa) and the modulus increases slightly with the increase of confinement. Finally, the modulus also increases slightly with the increase of confinement for Mix 3. For 10 MPa level of confinement, there is sharp increase in the modulus. This value is hard to verify due to the limited data for this level of confinement.

5.3.4 Poisson's Ratio

The average values of the Poisson's ratio for Mix 1, Mix 2 and Mix 3 are found to be 0.23, 0.22 and 0.23 respectively. Figure 5.12 shows Poisson's ratio for the three mixes with different levels of confinement. The values of Mix 1 (considering the experimental variations) seems to be independent of the ratio of coarse aggregates and the level of confinement. The same conclusion can be drawn for the other two mixes.

5.3.5 Plastic Strain at Peak Stress

Figure 5.13 shows the equivalent plastic strain at peak for the three mixes. The values of Mix 1 show the same trend that have been observed in Chapter 2. The limited number of complete data has restricted the detailed information on part of the behaviour, especially with high confinement where most tests have not reached the peak. The response is non linear with low values at zero level of confinement yet high values at high level of confinement. The response can be modelled by exponential function. Mix 2 has a similar shape of response but with a sharper increase with the increase in the level of confinement. As for Mix 3, the data seems

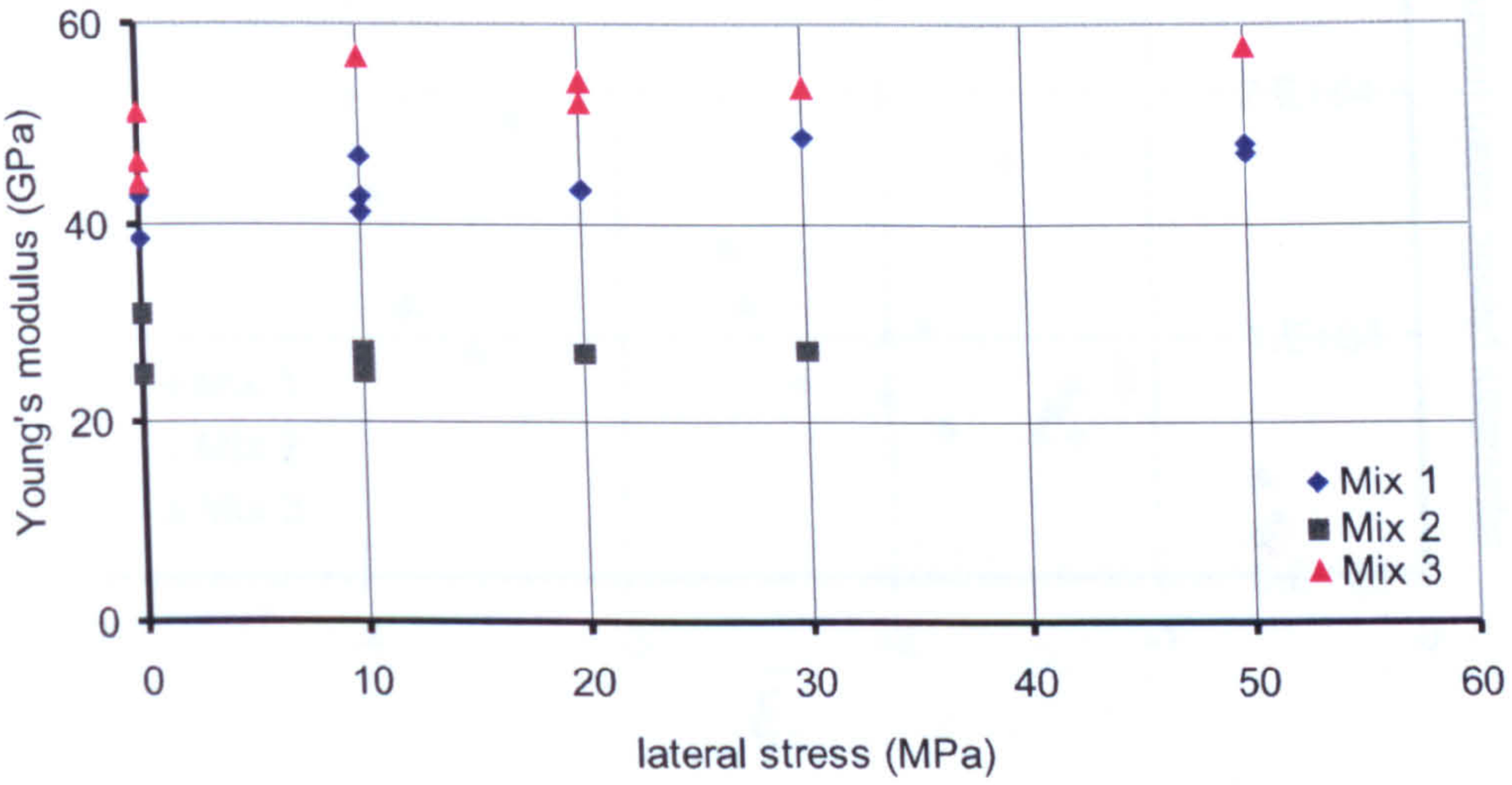

Figure 5.11: Young's modulus for the three mixes with different levels of confinement

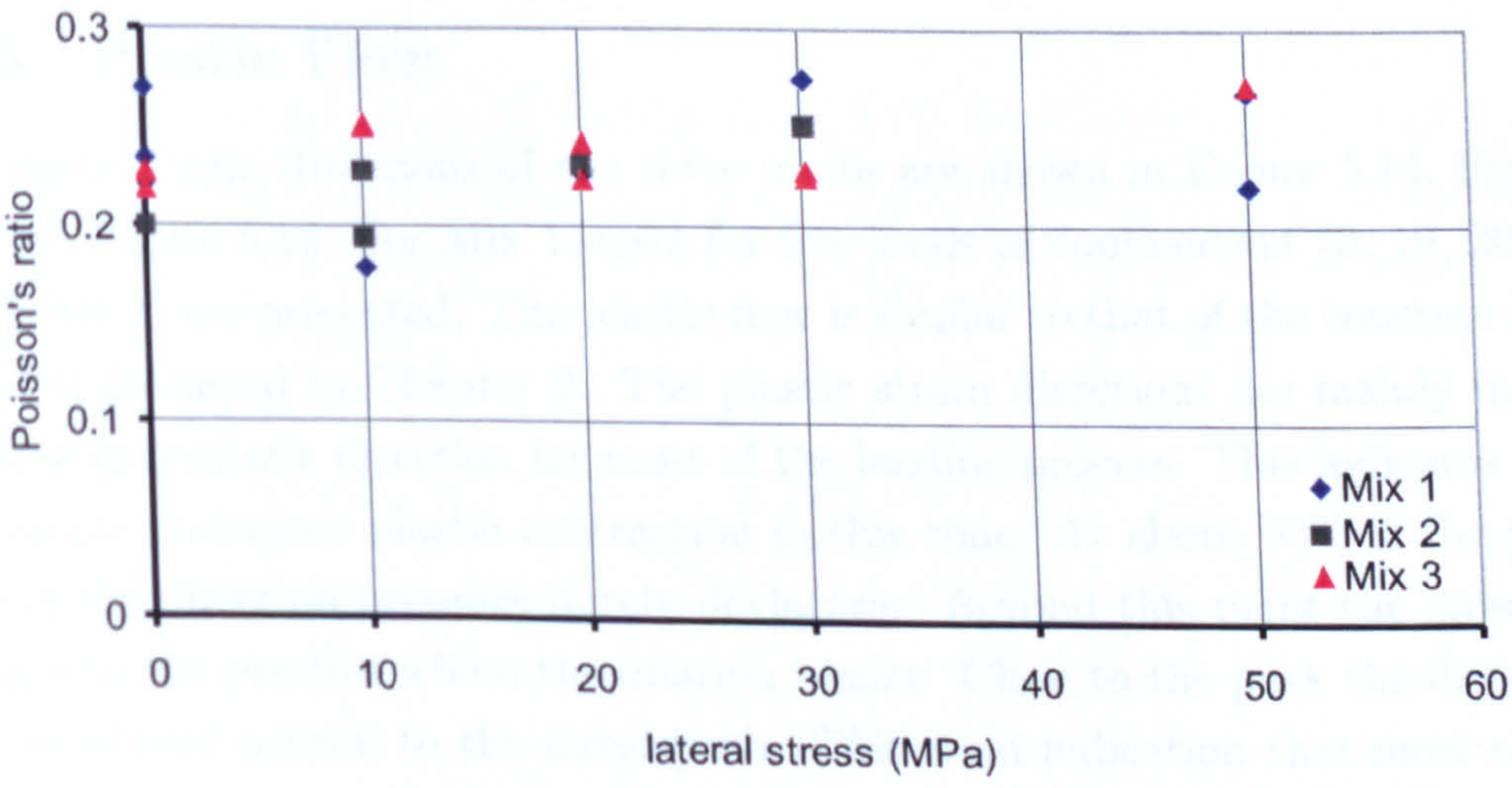

Figure 5.12: Poisson's ratio for the three mixes with different levels of confinement

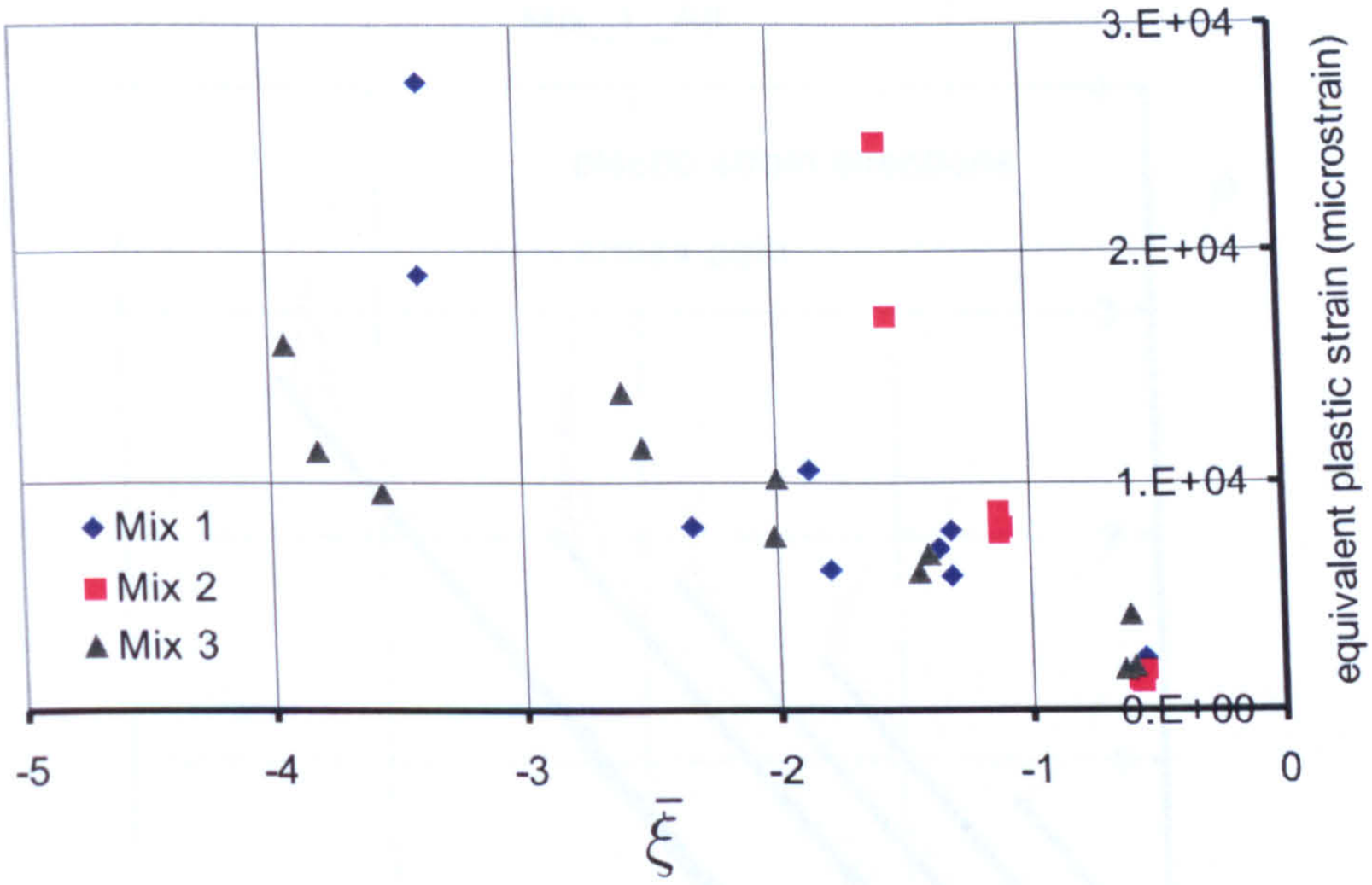

Figure 5.13: The equivalent plastic strain at peak stress for the three mixes

to be inconsistent, the response seems to increase almost linearly with the increase of the level of confinement for low and moderate level of confinement. The values of the equivalent plastic strains do not change significantly with high levels of confinement. These observations should be treated with caution because it seems that in most tests the strain measurement were interrupted before reaching the peak stress.

5.3.6 Plastic Flow

The plastic strain directions of the three mixes are shown in Figure 5.14, Figure 5.15 and Figure 5.16. For Mix 1, tests for five levels of confinement (0, 10, 20, 30 and 50 MPa) are presented. The plastic flow is similar to that of the concrete that has been discussed in Chapter 2. The plastic strain directions are mainly in the negative hydrostatic direction for most of the loading process. This indicates that the sample undergoes plastic contraction in this zone. At about 90% of the peak loading the direction becomes purely deviatoric. Beyond this point the direction changes to the positive where the dilation begins. Close to the peak the direction become almost normal to the stress path. This is an indication that most of the plastic strains at this point are in the lateral direction.

For Mix 2, the figure includes the results of four levels of confinements (0, 10, 20 and 30 MPa). For the 30 MPa level of confinement, it seems that the strain gauges

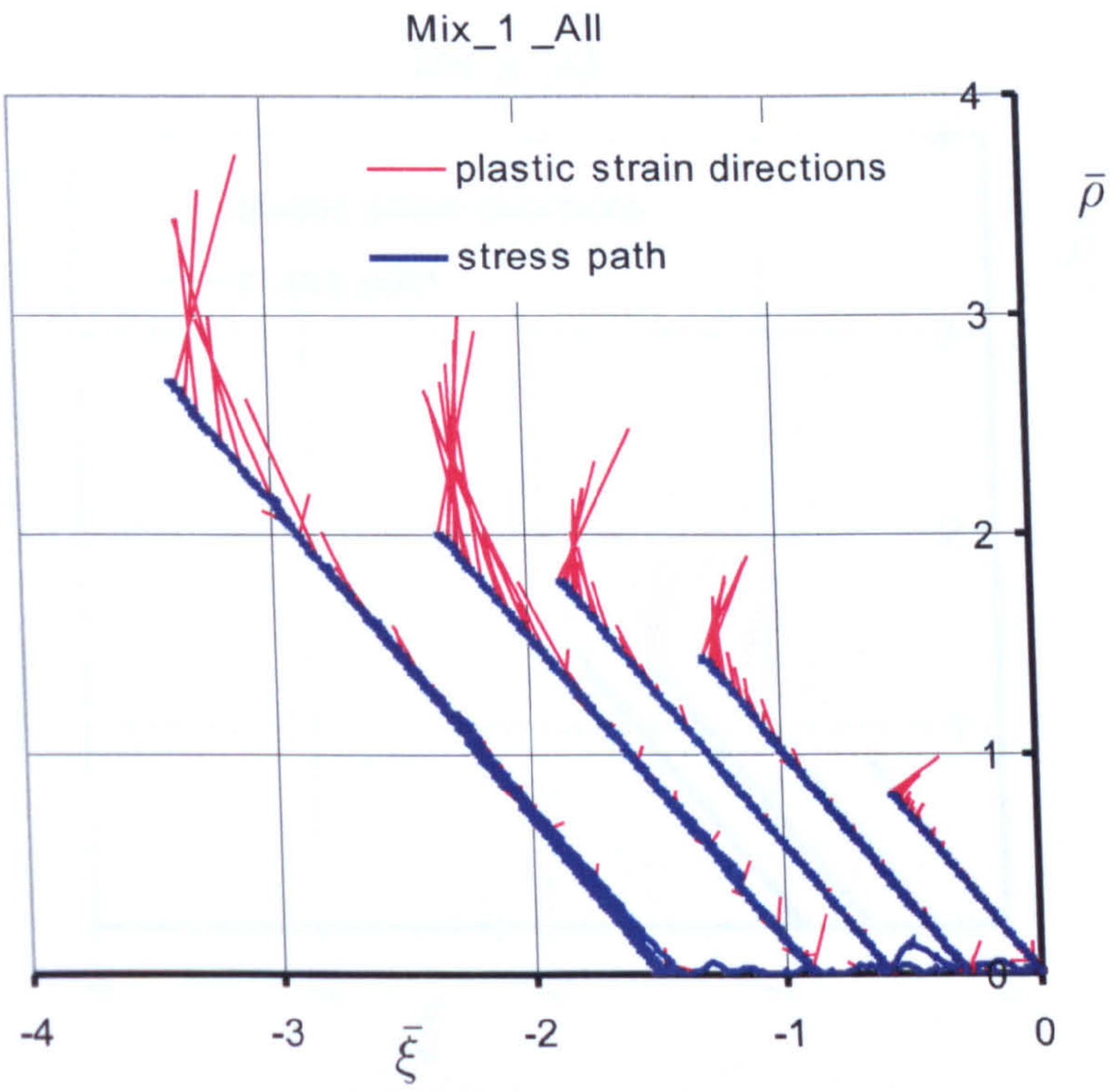

Figure 5.14: The plastic flow and stress path for Mix 1

have broken before reaching the peak. The plastic strain direction takes the same trend of Mix 1 but the volume transition stress (VTS) state is closer to the peak stress.

Six levels of confinement (0, 10, 20, 30, 40 and 50 MPa) are used to identify the plastic flow for Mix 3. The trend of the directions is similar to that of the other two mixes but the VTS state is relatively lower. The scattered directions at the initial zone are due to the cyclic loading.

5.3.7 Peak Nominal Stress, PNS

The peak nominal stresses (PNS) for the three mixes are shown in Figure 5.17. For Mix 2, where there are no coarse aggregates, the strength envelope is reduced in size. This shows clear reduction in strength for this mix. The PNS envelope for Mix 3 is increased in size, which indicates the increase in the strength of concrete with double coarse aggregates. The overall shapes of the PNS for the three mixes look similar to each other. That is, clear nonlinear behaviour with no or low level of confinement ($0 \leq \sigma_2 \leq 10$ MPa). The behaviour then becomes more linear with the increase in confinement.

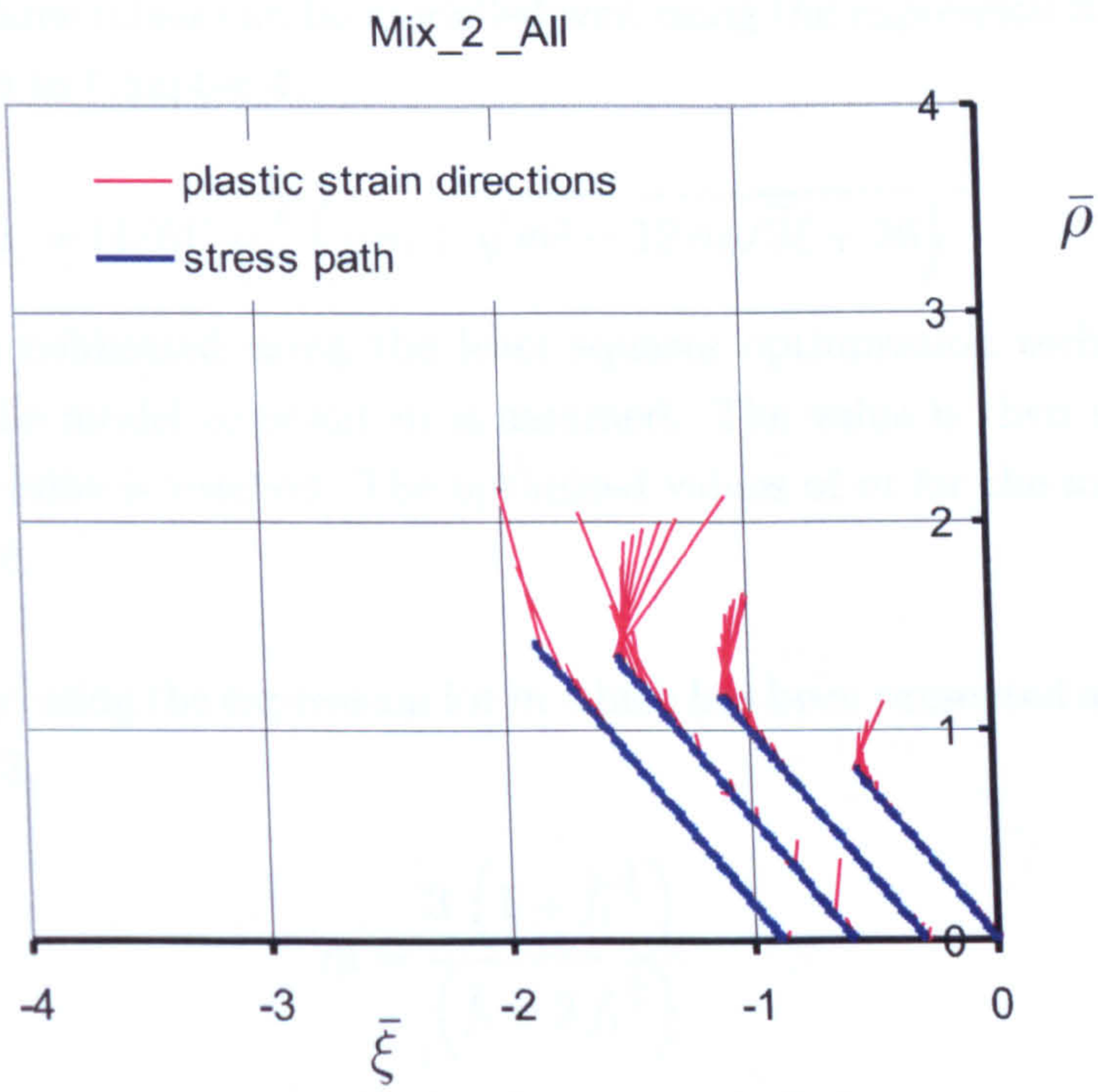

Figure 5.15: The plastic flow and stress path for Mix 2

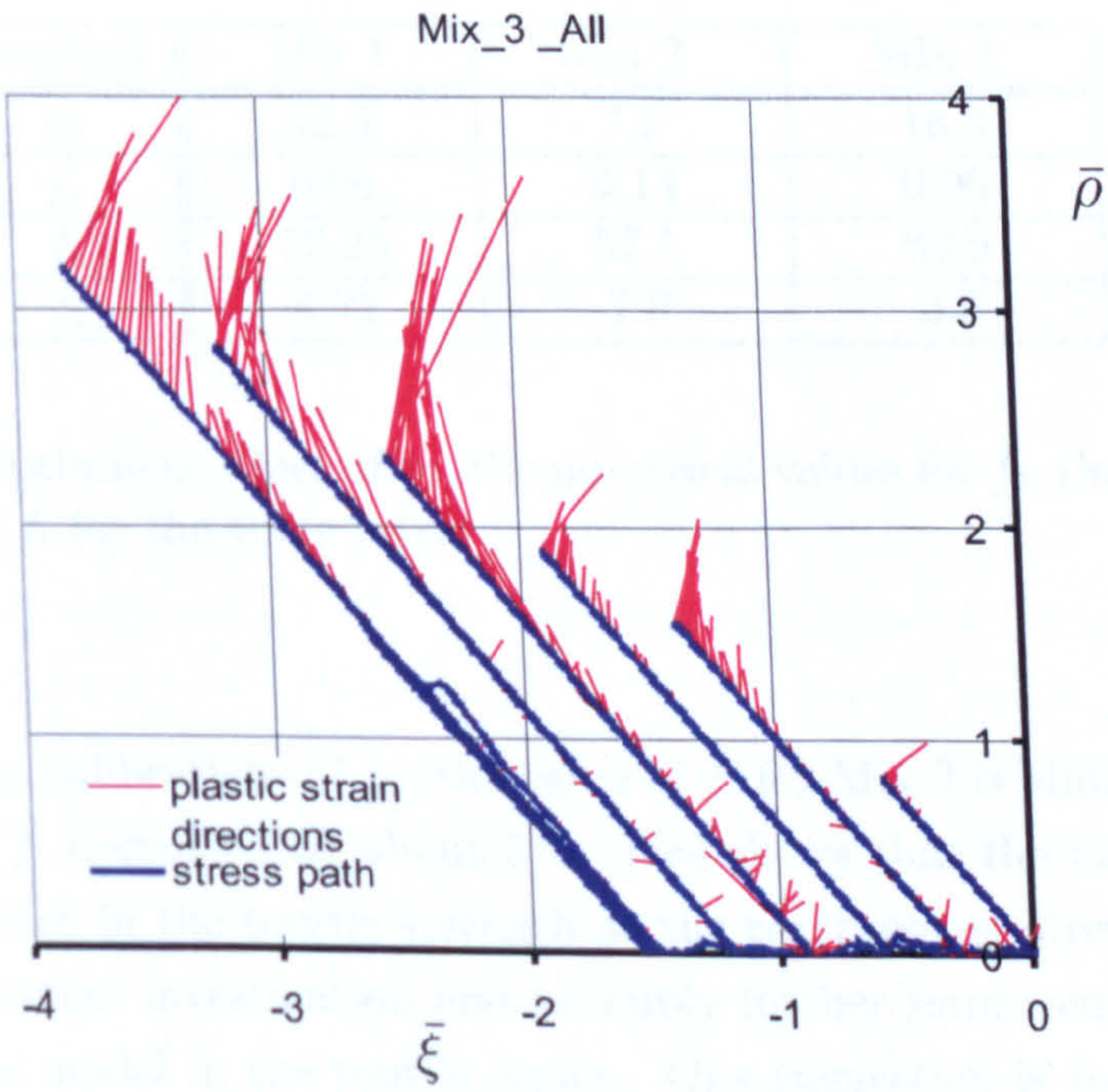

Figure 5.16: The plastic flow and stress path for Mix 3

The PNS for the three mixes can be modelled well using the expression for ρ_c which has been discussed in Chapter 4.

$$\rho_c = (1/6)^\gamma \sqrt{\frac{2}{3}} \left(-m + \sqrt{m^2 - 12\, m \sqrt{3} \bar{\xi} + 36} \right)^\gamma \tag{5.1}$$

Here ρ_c has been calibrated using the least squares optimisation technique. An initial value for the model constant m is assumed. The value is then varied until the least squares value is reached. The optimised values of m for the mixes can be found in Table 5.8.

We calculate $\bar{f}_t$ by using the expression for m which has been presented as a function of $\bar{f}_t$ in Chapter 3,

$$m = \frac{3 \left(1 - \bar{f}_t^{\frac{2}{\gamma}} \right)}{\left(\bar{f}_t + 2\, \bar{f}_t^{\frac{1}{\gamma}} \right)} \tag{5.2}$$

A numerical solution is used to identify the values of $\bar{f}_t$ for each mix. The values of f_c have been identified from the experimental data. Table 6.7 shows the values of m, $\bar{f}_t$, f_t and f_c for the three mixes.

constant	Mix 1	Mix 2	Mix 3
m	12.5	7.2	16.3
f_t	0.08	0.14	0.06
f_c	58.25	57.1	60.9
f_t	4.71	7.9	3.8

Table 5.8: The optimised values of m, the numerical values for $\bar{f}_t$, the experimental values of f_c and f_t for the three mixes

According to the calibrations of ρ_c, the value of f_t for Mix 2 is almost double that of Mix 1 while f_c decreased by about 5%. This shows that the model predicts a significant increase in the tensile strength as the compression strength decreases. This requires further investigation and probably further improvement of the performance of the model in the tensile region. One suggestion is to choose a third point in the confinement region beside f_c and f_t to formulate the PNS envelope expression.

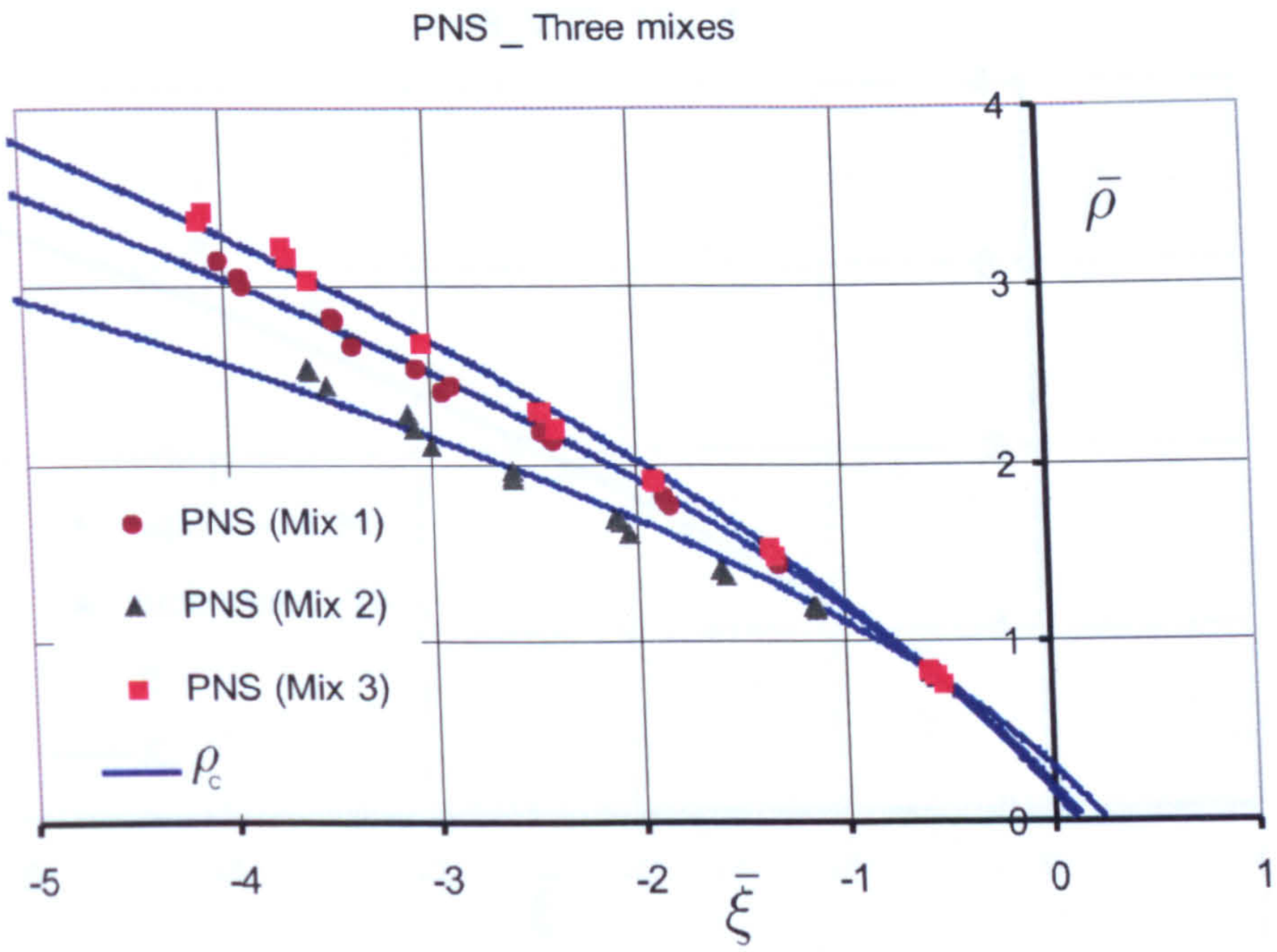

Figure 5.17: Experimental PNS and model fit for the three mixes

Figure 5.17 shows the experimental PNS and model fit for the three mixes. ρ_c formulation shows a good agreement with the experimental data for all mixes.

5.3.8 Volume Transition Stress (VTS)

The experimental values of VTS for the three mixes are shown in Figure 5.18, Figure 5.19 and Figure 5.20. The VTS envelopes for the three mixes have been simulated by the same equation for ρ_{vts} that have been used in Chapter 2

$$\rho_{vts} = \alpha_2 \ \rho_c \tag{5.3}$$

The material constant α_2 has been identified using the least squares optimisation technique. The values of the constant for Mix 1, Mix 2, and Mix 3 are found to be 0.93, 0.96, and 0.94 respectively. These values suggested that the uniaxial results for the VTS state may not be sufficient to identify α_2 for high level confinement cases. The figures also show the fit (5.3) with the experimental data for the three mixes. The fit seems to be good for all mixes.

As has been the case of concrete presented in Chapter 2, the shape of the VTS envelope is similar to that of the PNS but with reduced size. The value of the material constant α_2 seems to increase slightly for Mix 2 and more for Mix 3. This

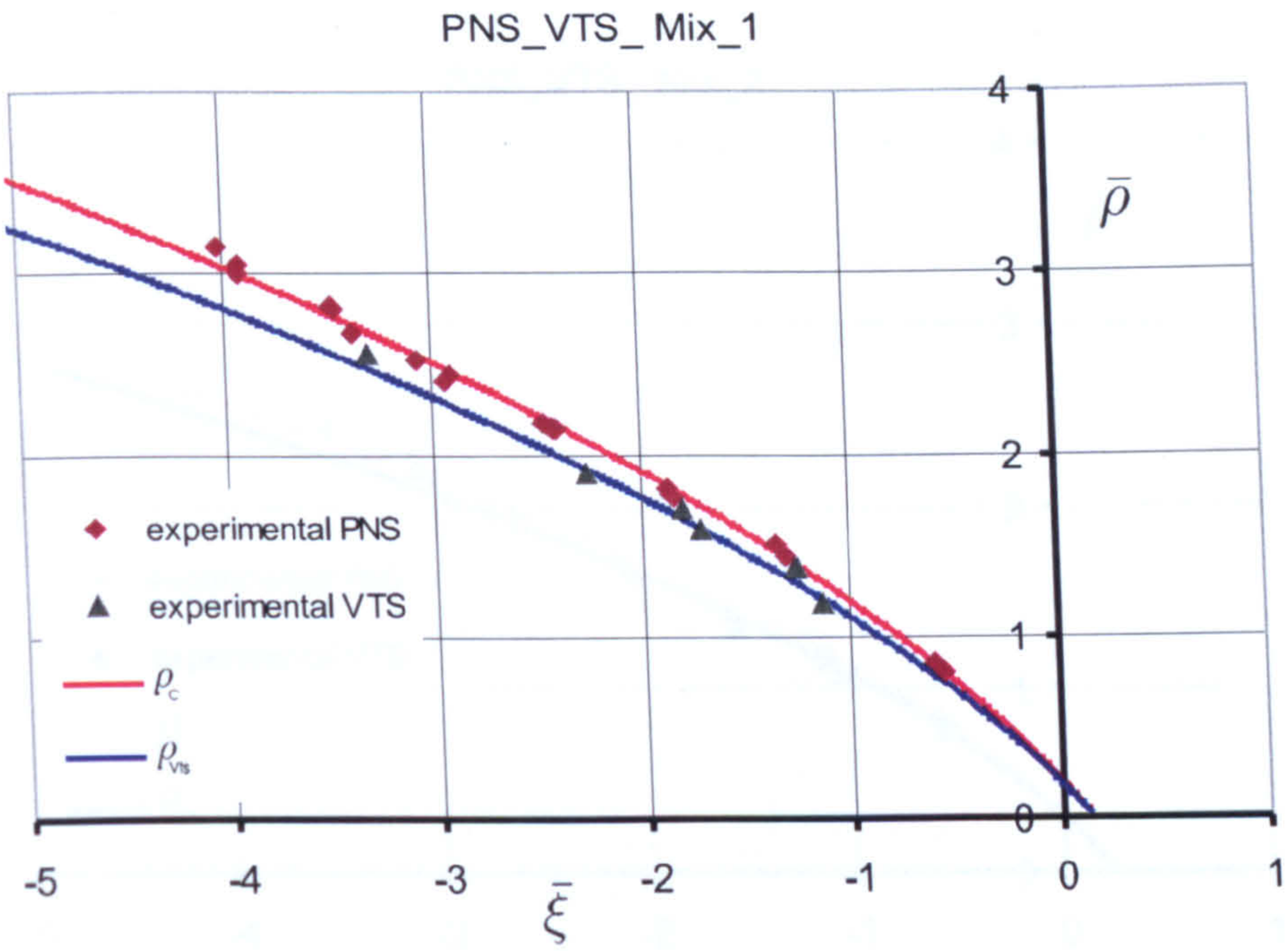

Figure 5.18: Experimental PNS and VTS, ρ_c and ρ_{vts} for Mix 1

suggests that dilation starts closer to the peak for both mixes.

5.4 Yield Surfaces

Following the identification of the plastic flow and the material constants (f_t, f_c, and α_2), the yield surfaces of the three mixes can be determined assuming associated flow rule in the same manner that has been discussed in Chapter 4. Figure 5.21, Figure 5.22 and Figure 5.23 show the yield surfaces for the three mixes. The yield surfaces pass horizontally through ρ_{vts} and intersect the hydrostatic axis normally at $\bar{\xi}_{ht}$ and $\bar{\xi}_{hc}$.

For Mix 1, the yield surfaces have the same shape and size of that of the normal concrete that have been simulated in Chapter 4. The plastic strain directions do seem to be normal to the yield surfaces even though the experimental data is limited. For Mix 2, few sets of data are found to be complete. Although the VTS is very close to the PNS, the model succeeded in fulfilling the requirements without crossing the PNS or encountering concavity. This shows the flexibility of the model and its capability of capturing the most extreme material variations. With the limited data available, the associated flow rule seems to to be valid for this test. Finally, the behaviour of Mix 3 can be also classified as associated flow.

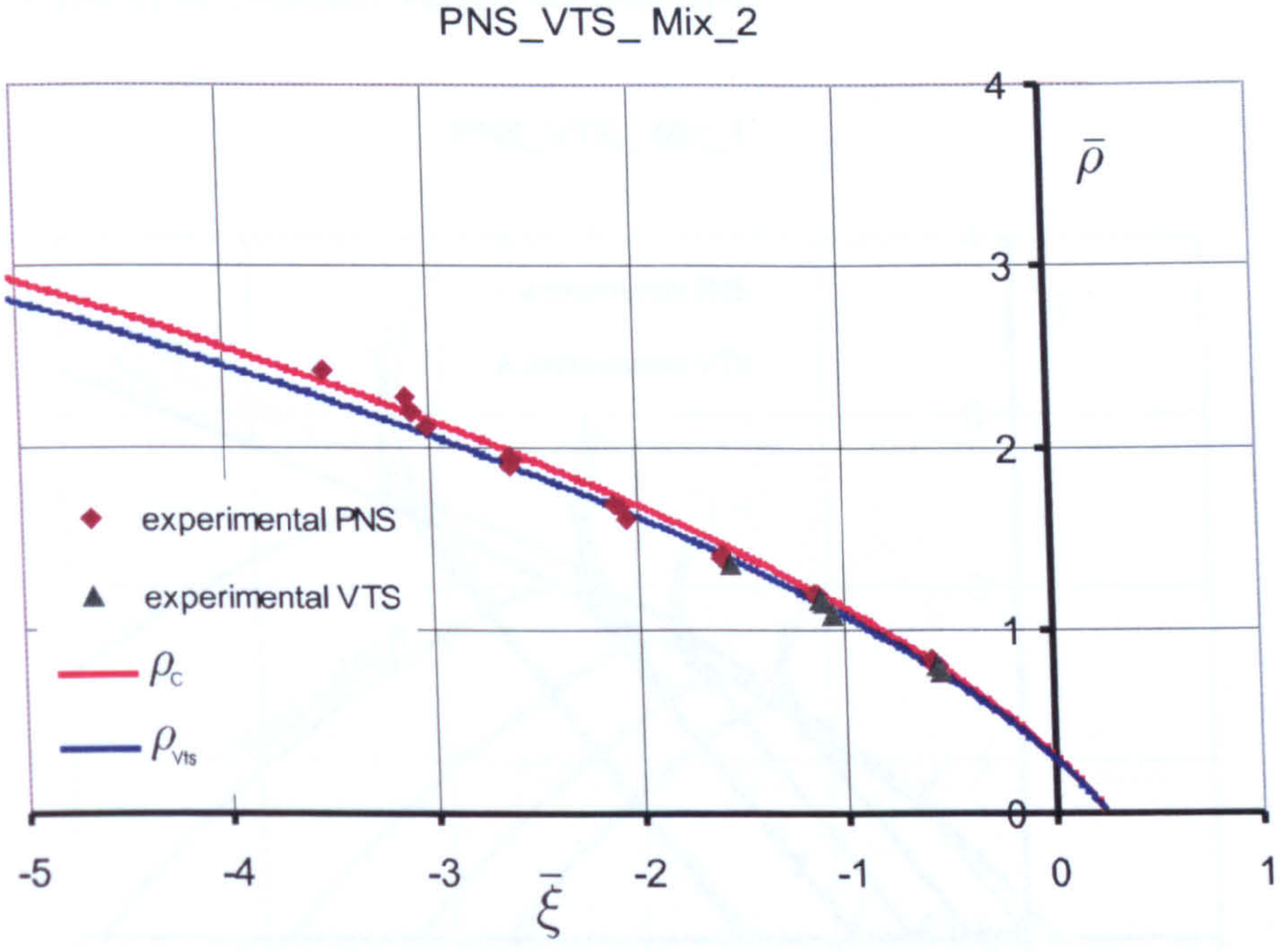

Figure 5.19: Experimental PNS and VTS, ρ_c and ρ_{vts} for Mix 2

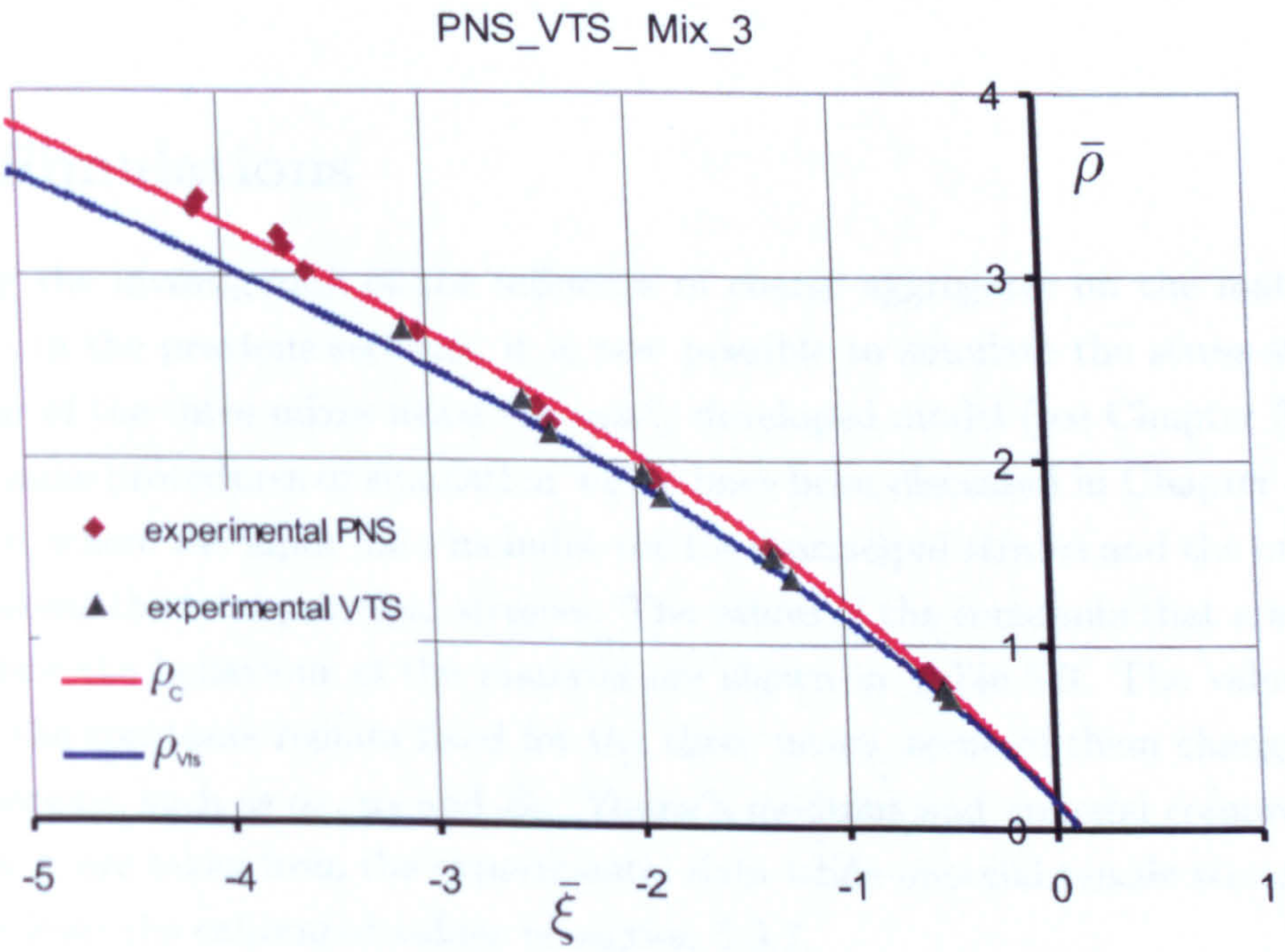

Figure 5.20: Experimental PNS and VTS, ρ_c and ρ_{vts} for Mix 3

The model seems to be capable of capturing the yield surface of all the mixes if an appropriate material constant values are selected.

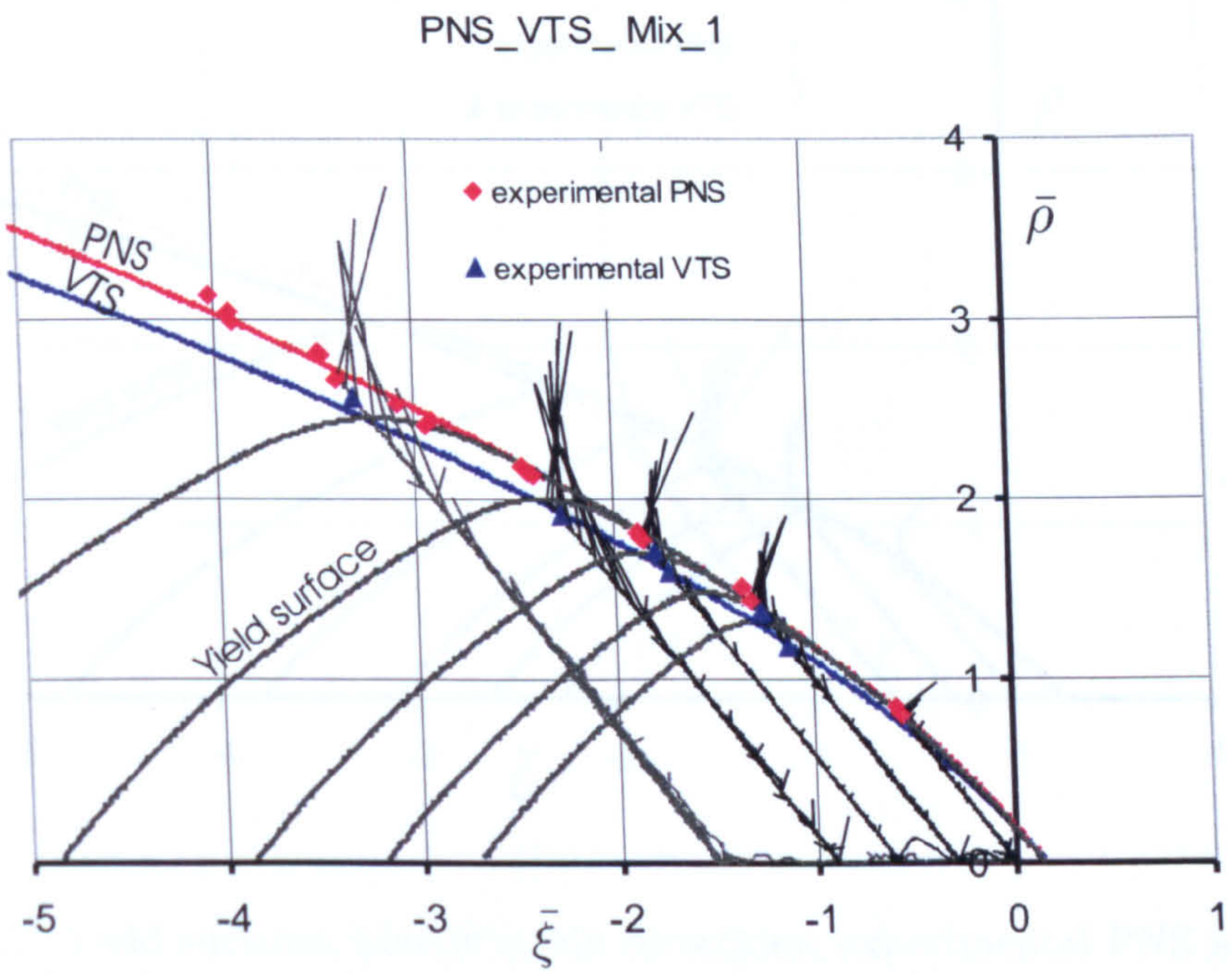

Figure 5.21: Yield surfaces, plastic strain directions, experimental PNS and VTS, ρ_c and ρ_{vts} for mix 1

5.5 Simulations

Following the investigation of the influence of coarse aggregates on the material constants in the previous sections, it is now possible to simulate the stress-strain behaviour of the three mixes using the newly developed model (see Chapter 3 and 4). The same procedures of simulation which have been discussed in Chapter 4 are used here, where the input data includes the total principal strains and the output data presents the total principal stresses. The values of the constants that are used to simulate the behaviour of the material are shown in Table 5.9. The values for most of the constants remain fixed for the three mixes, some of them changed by small margins, such as α_1, α_2 and B_h. Young's modulus and uniaxial compression strength f_c are taken from the experimental data while uniaxial tensile strength $\bar{f}_t$ is taken from the calibrated values in section 5.3.7.

Figure 5.24 shows experimental data and model predictions for stress-strain curves of Mix 1, with 0, 10, 20, 30 and 50 MPa confinement. The assigned value of Young's

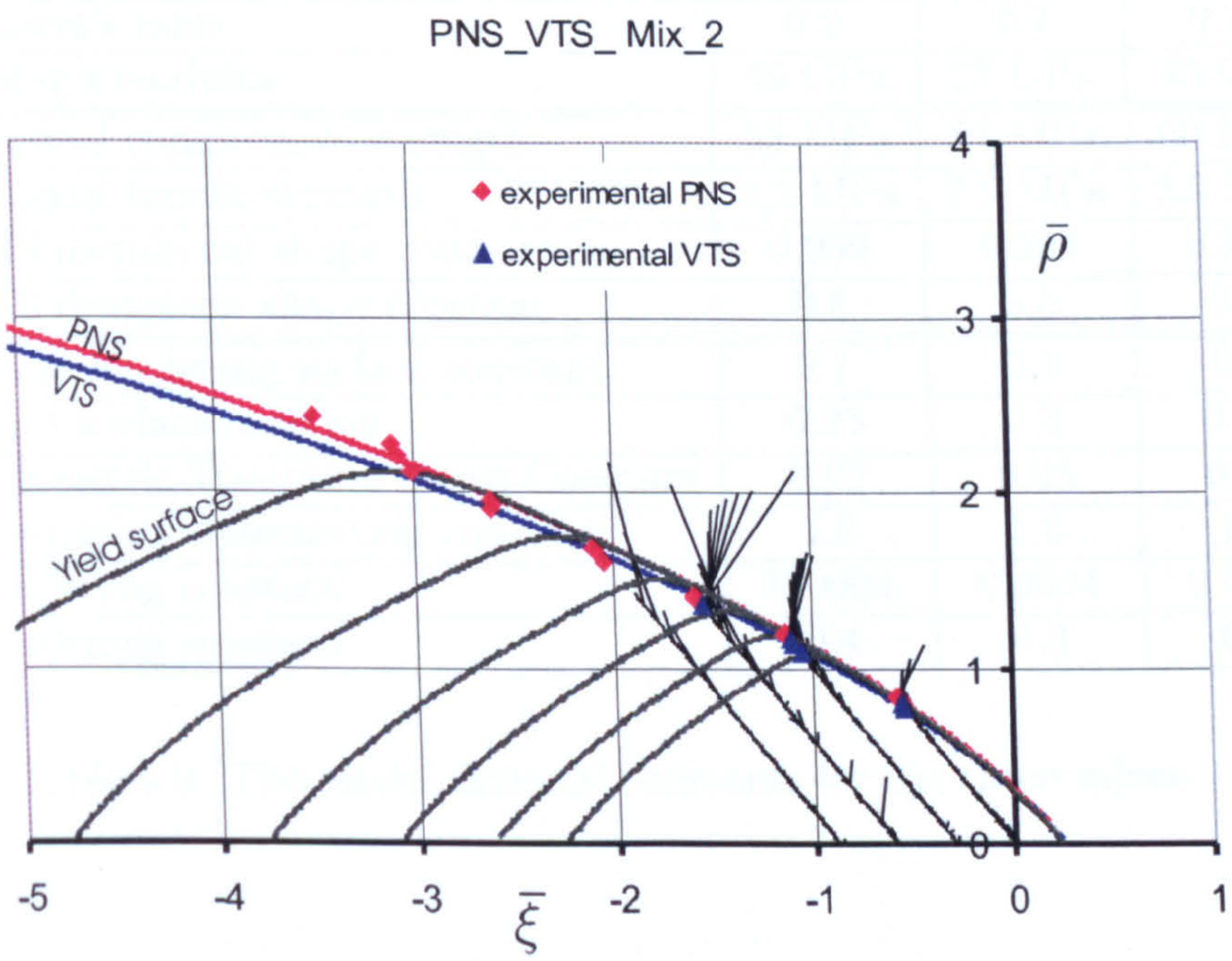

Figure 5.22: Yield surfaces, plastic strain directions, experimental PNS and VTS, ρ_c and ρ_{vts} for mix 2

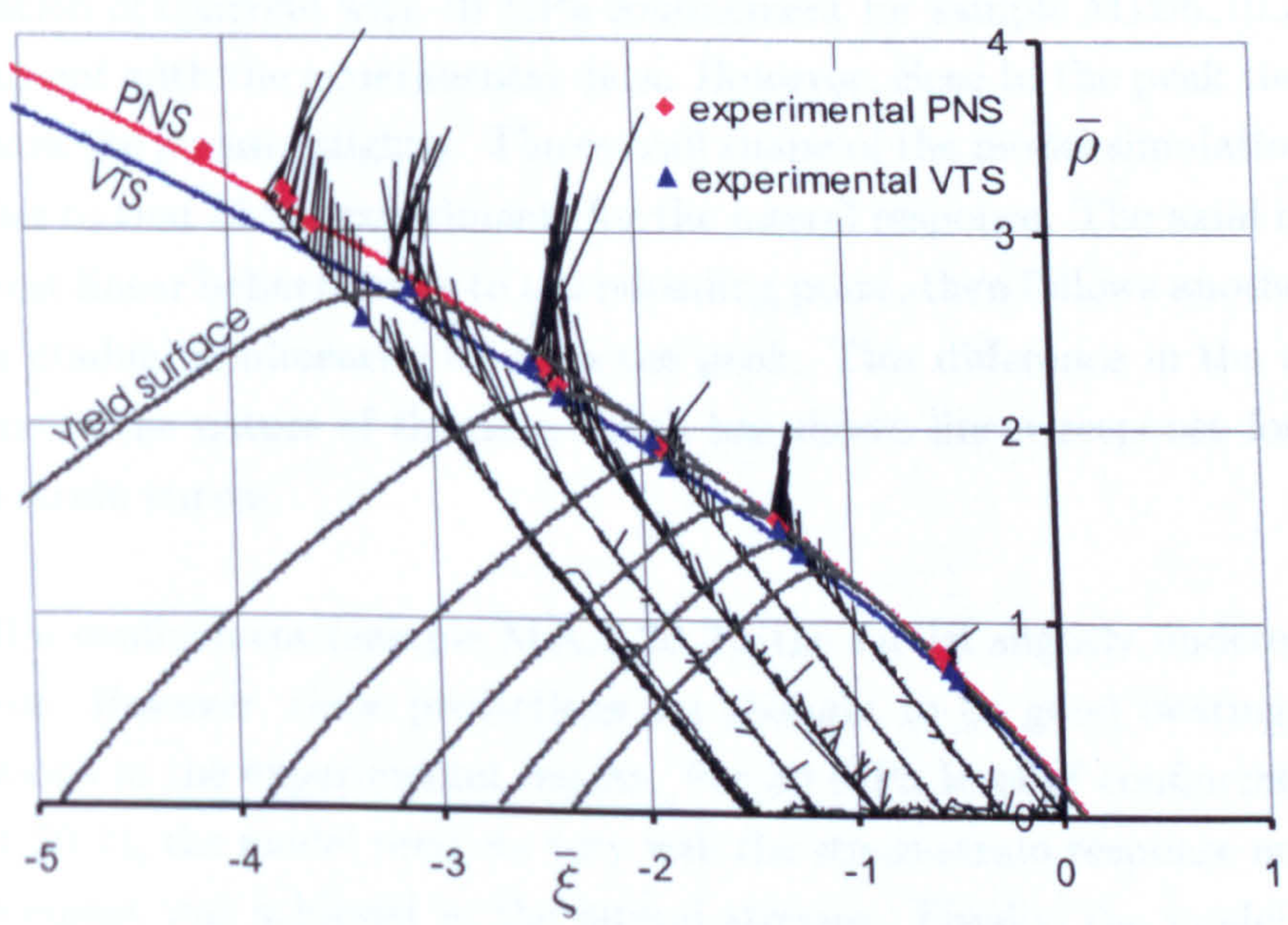

Figure 5.23: Yield surfaces, plastic strain directions, experimental PNS and VTS, ρ_c and ρ_{vts} for mix 3

	Constants	Mix 1	Mix 2	Mix 3
ν	Poisson's ratio	0.2	0.2	0.22
E	Young's modulus	40 GPa	27 GPa	45 GPa
f_c	Uniaxial compressive strength	58 MPa	57 MPa	60 MPa
f_t	Uniaxial tensile strength	4.3 MPa	7.9 MPa	5.5 MPa
γ	PNS meridional shape constant	0.999	0.999	0.999
α	PNS deviatoric shape constant	0.8	0.8	0.8
k_0	Initial hardening surface constant	0.1	0.1	0.1
α_1	Yield surface constant	0.25	0.3	0.25
α_2	Volumetric Transition Stress Constant	0.92	0.95	0.94
A_k	Hydrostatic intersection constant	1.5	1.5	1.5
A_h	Hardening constant	0.0004	0.0004	0.0004
B_h	Hardening constant	0.4	0.3	0.4

Table 5.9: The model material constants for the three mixes

modulus seems to be appropriate as can be seen from the unloading-reloading part of the curves. The model overestimated the stresses of the uniaxial compression test for sample M1C3_00. Another attempt has been made to simulate test (M1A3_00) with a reduction in the hardening constant B_h. The prediction of the model shows almost total agreement with the experimental results.

The simulation of concrete with 10 MPa confinement for sample M1B6_10_3 shows good agreement with the experimental data. However, close to the peak the model overestimates the stresses slightly. The overall shape of the model simulation seems to be similar to that of the experiments for the lateral response. The axial response shows almost linear behaviour up to the reloading point, then follows another linear state with gradual nonlinearity close to the peak. This difference in the response may be due to the nature of the data which has shown linear response for part of the stress-strain curves.

For 20 MPa confinement (sample M1C5_20_2), the model slightly underestimated the stresses. However, these predictions are thought to be good bearing in mind the variations in the experimental results. For 30 MPa level of confinement (sample M1B1_30_1), the model predicts very well the stress-strain response and almost total agreement was achieved in the lateral stresses. Finally, the model underestimates the stresses for the test with 50 MPa (sample M1B9_50_3). This can be improved if the value of the constant B_h is increased slightly.

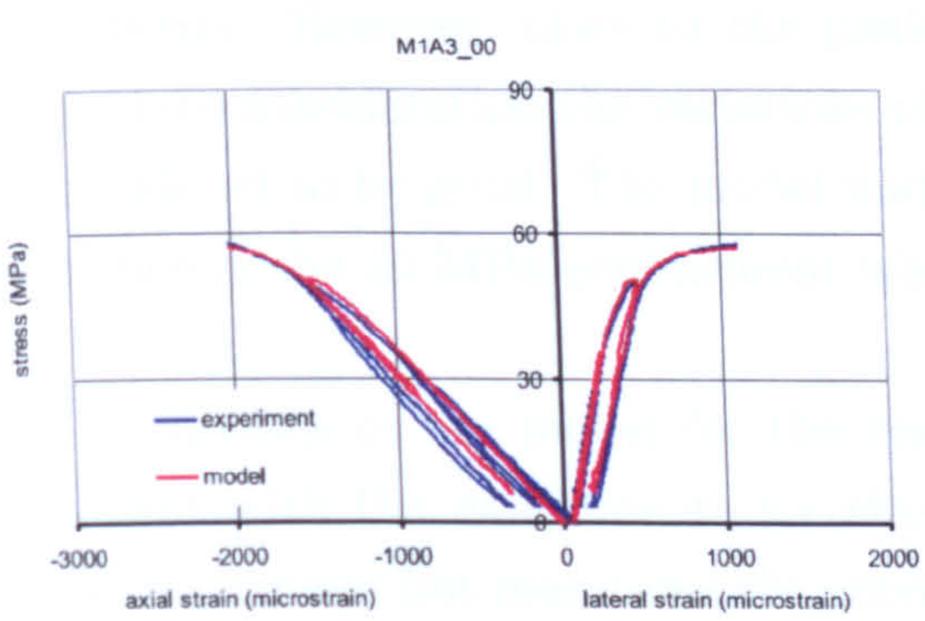

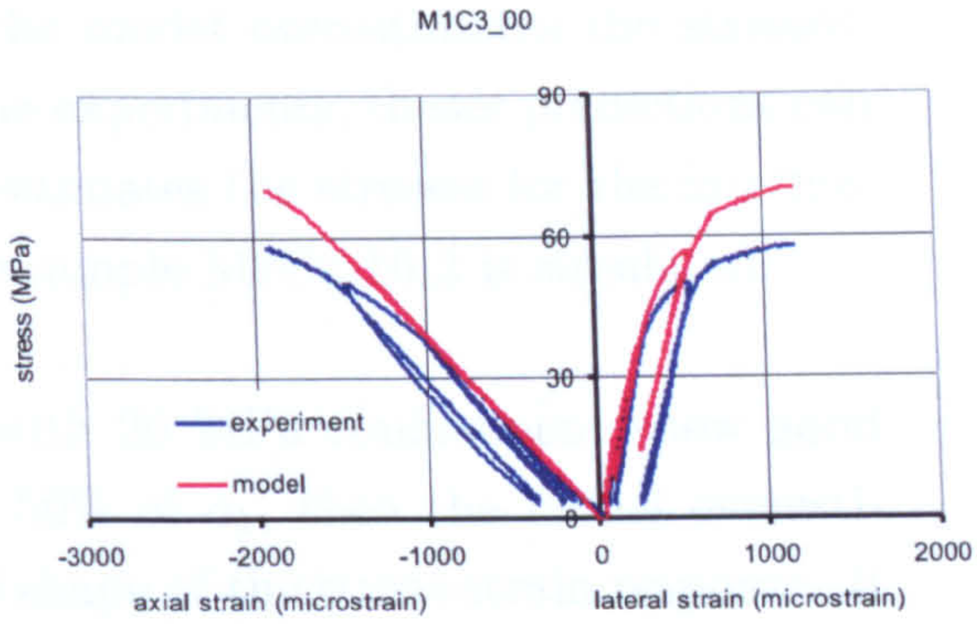

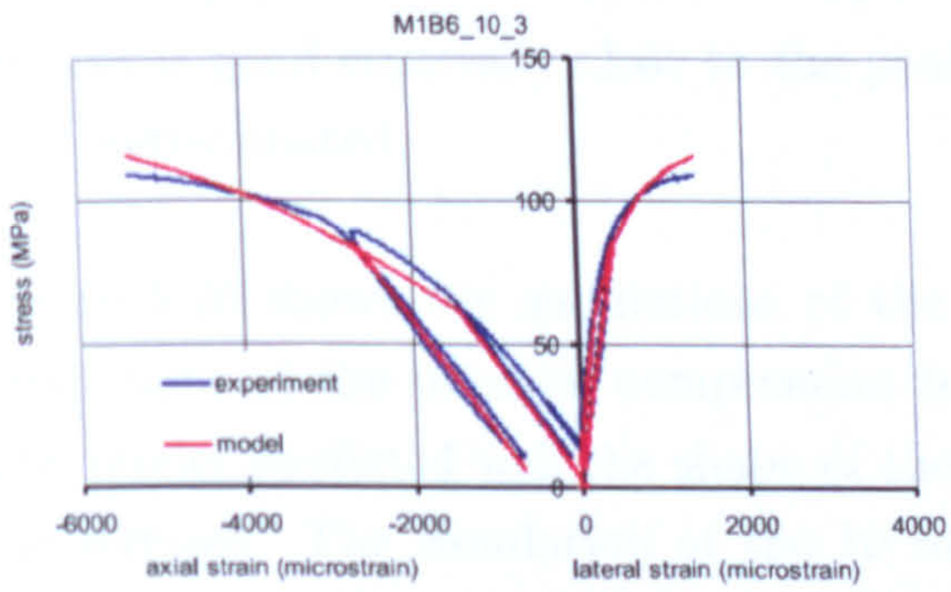

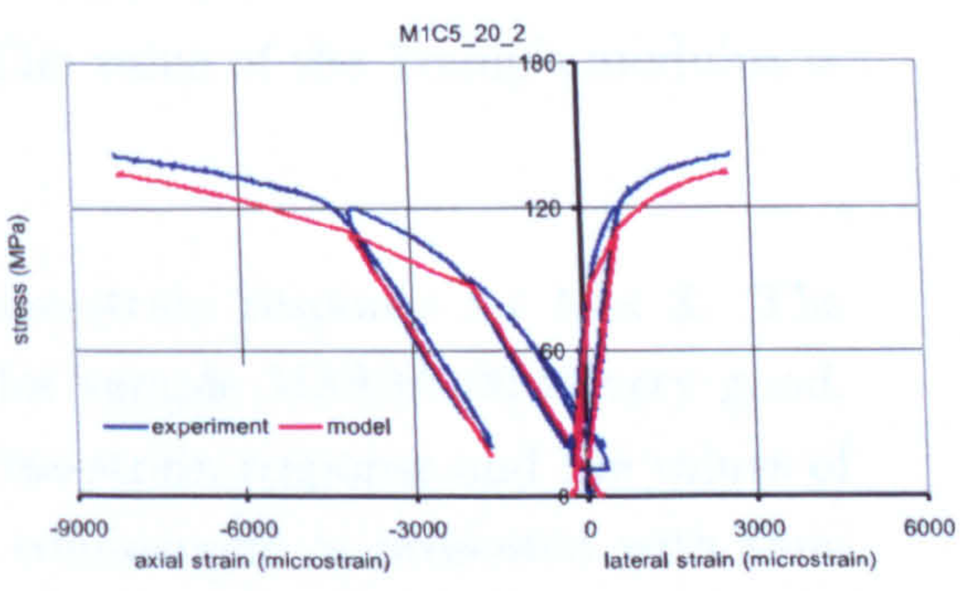

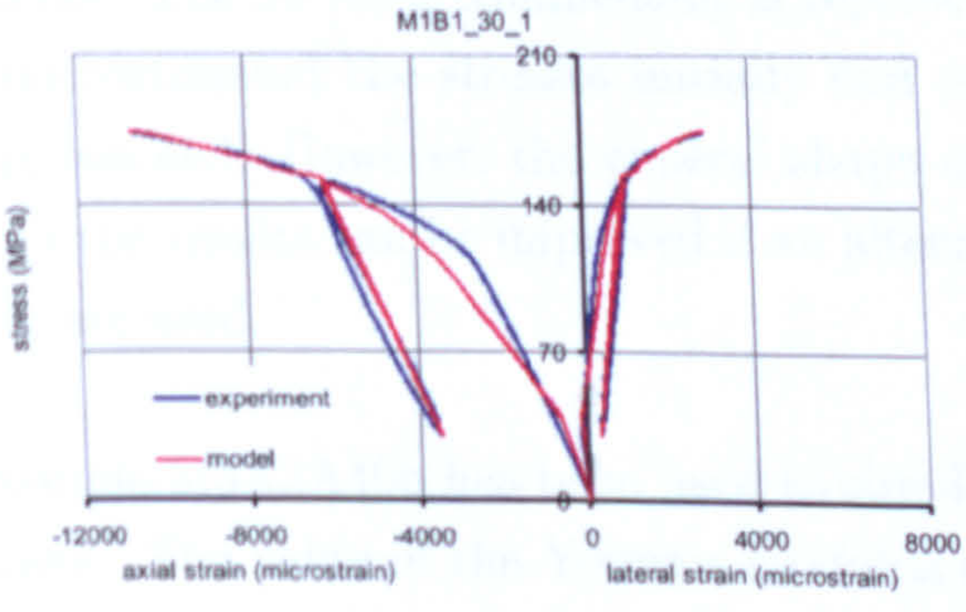

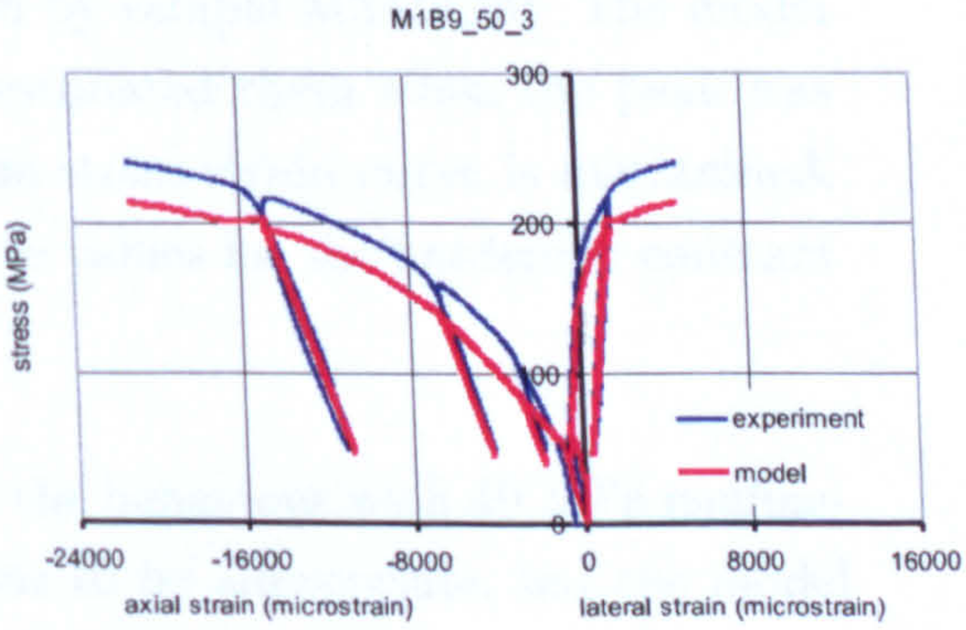

Figure 5.24: Experimental and model predictions for stress-strain curves of Mix 1, with 0, 10, 20, 30 and 50 MPa confinement

Figure 5.25 shows the experimental and model predictions for stress-strain curves of Mix 2 with 0, 10, 20 and 30 MPa confinement. Two uniaxial tests (M2D3_00_2 and M2D5_00_1) are simulated where the model shows good agreement with the experiments. However, close to the peak, the model overestimates the stresses. Taking into consideration the variations of the experiments, theses predictions can be considered to be good. The model underestimates the stresses for the intermediate zone of the 10 MPa confinement where sample M2C2_10_2 is simulated.

The predictions of the model for the test with 20 MPa confinement show good agreement with the experiments for about 50% of $\hat{\sigma}_1$, then the model overestimates the stresses but maintains the general shape of the stress-strain response. It can be seen from the unloading-reloading part that the value of the Young's modulus is overestimated. The reduction of its value might improve the predictions. Finally, a sample (M2F7_30_2) with 30 MPa confinement is simulated. The model successfully predicted the general shape of the response. The estimation of the stresses is good especially close to the peak. The value of the Young's modulus is also overestimated.

Figure 5.26 shows the simulations of the stress-strain response for Mix 3. The predictions of the uniaxial compression test for sample M3A3A_00 is very good. The model predicted well the shape of the stress-strain response and the values of the stresses. The simulation of the 10 MPa confinement is presented with sample M3A1_10. The model predicted well the stresses for up to about 90% of $\hat{\sigma}_1$, then significantly overestimated their values. For 20 MPa confinement, sample M3A3B20 is simulated. The predictions of the model are very close to the experiments. The 30 MPa confinement is represented by sample M3A9C30. The model underestimated the stresses initially and overestimated them when the peak was approached. However, the general shape of the stress-strain curve is maintained, and the results can be improved if an alternative values for the hardening constant B_h are used.

Sample M3A2A40b has been used to simulate the behaviour with 40 MPa confinement. The value of the Young's modulus seems to be appropriate, but the model underestimated the stresses. However the general shape of the response has been maintained. Finally, the simulation of sample M3C8_50_3b where 50 MPa confinement is used have been presented. The model simulated well the initial part of the test, but underestimated the stresses while the test was progressing. This could be improved if a higher value of B_h is used.

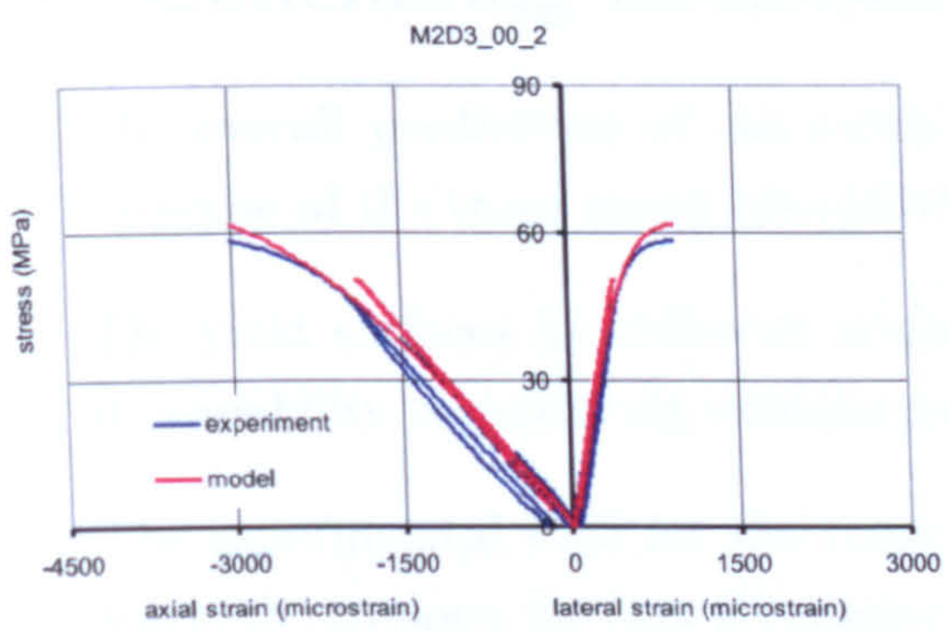

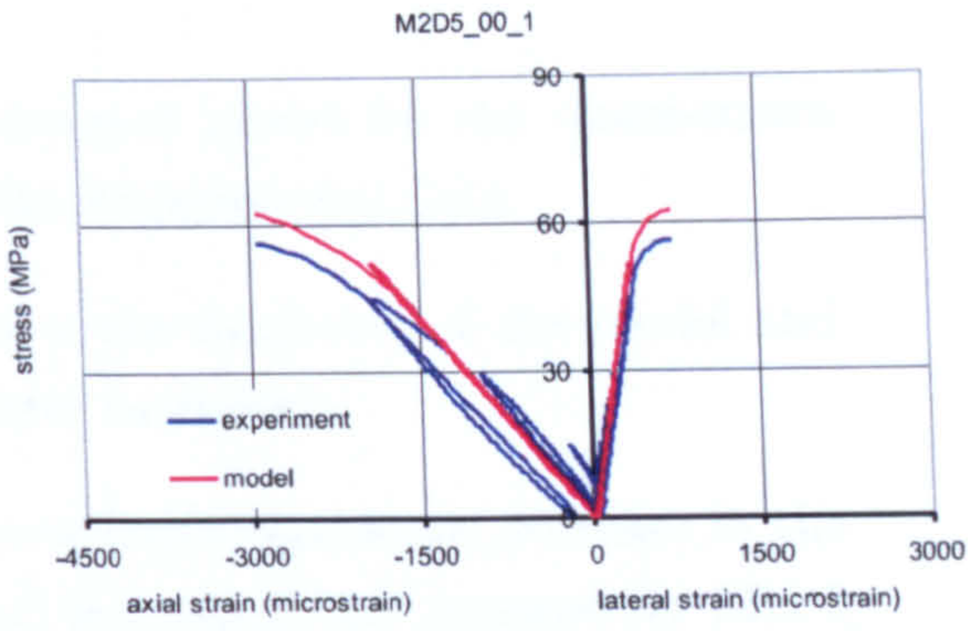

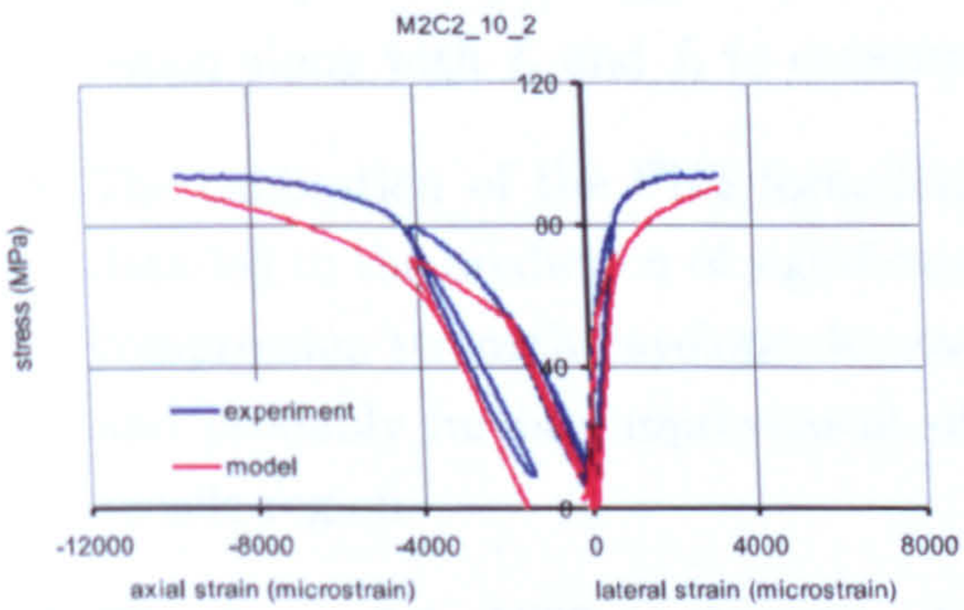

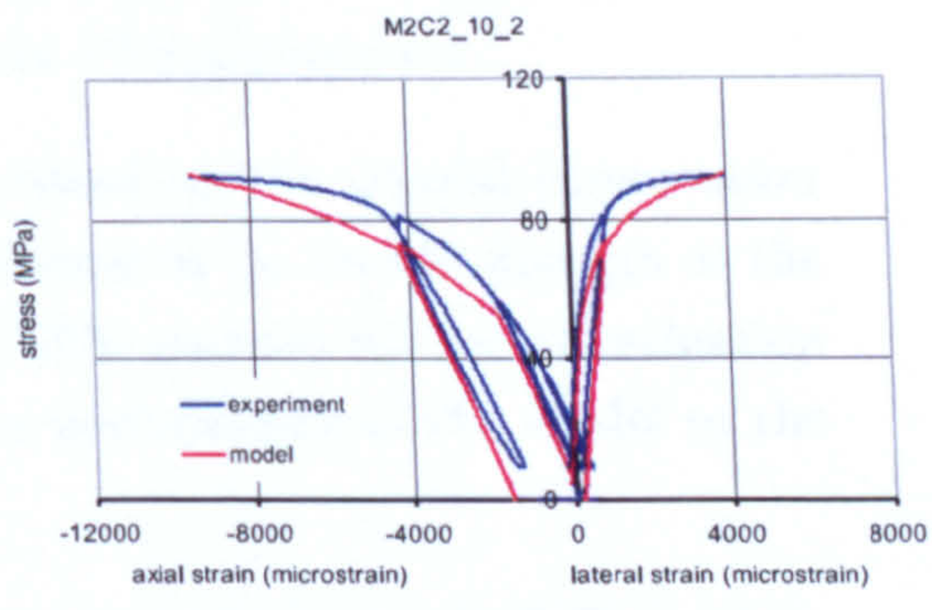

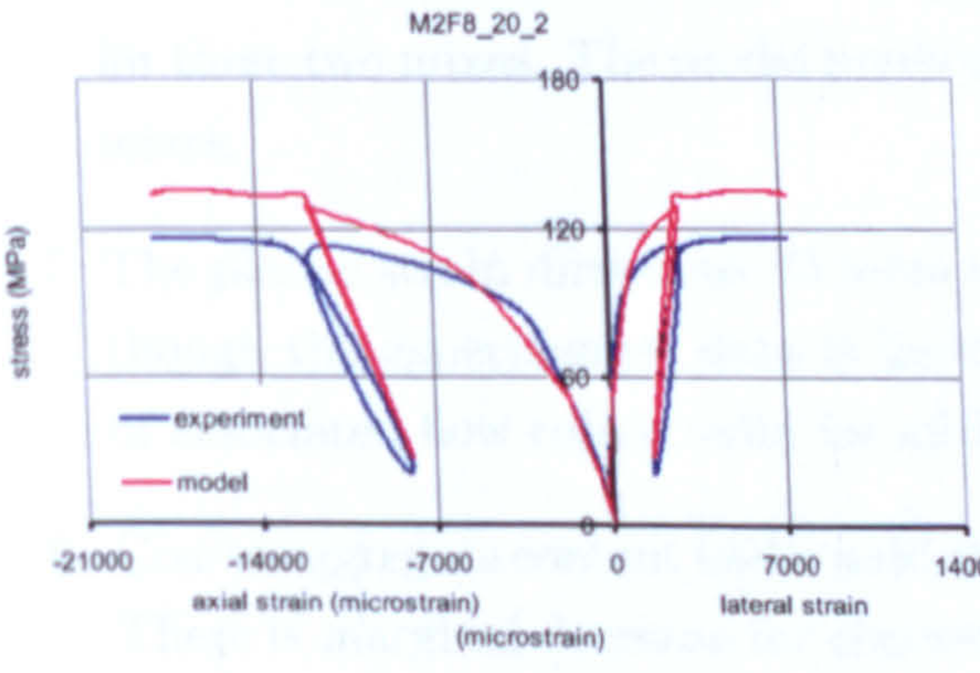

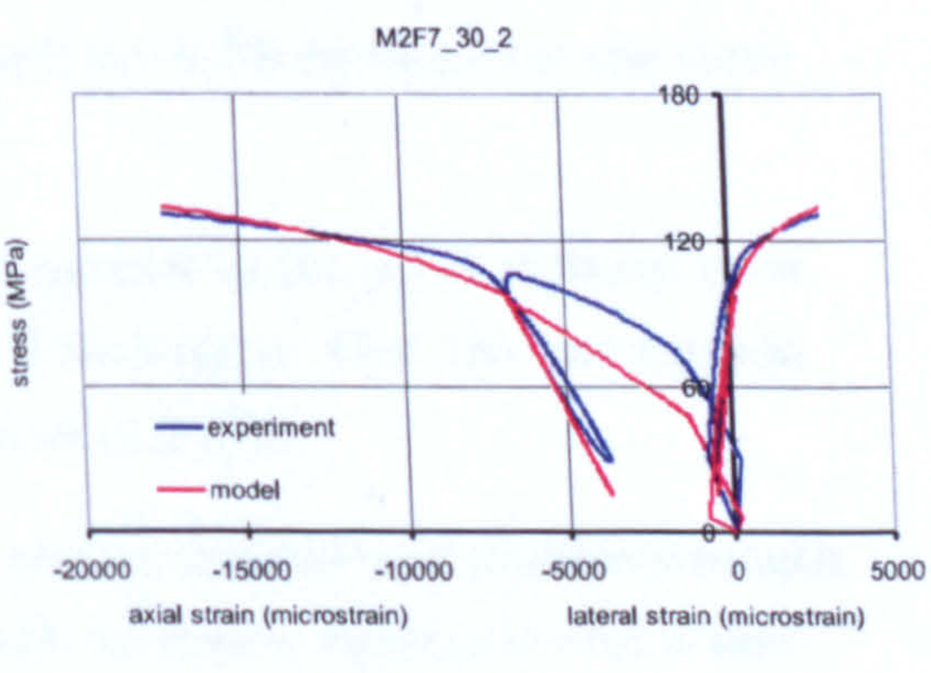

Figure 5.25: Experimental and model predictions for stress-strain curves of Mix 2, with 0, 10, 20 and 30 MPa confinement

5.6 Concluding Remarks

1. The overall predictions of the newly developed model for the stress-strain response of the three mixes are close to the experimental data.

2. The yield surfaces for different mixes show the flexibility of the model and its capability of capturing extreme material variations.

3. The experimental PNS for the three mixes shows significant decrease in the strength envelope for Mix 2 (mortar mix) and significant increase for Mix 3 (double coarse aggregate).

4. Further investigation and probably further improvement for the PNS formulation is required. One suggestion is to choose a third point in the confinement region along with f_c and f_t to construct the PNS formulation.

5. The calibration of the PNS formulation based on the triaxial compression data led to the prediction of significant increase in the tensile strength as the compression strength envelope decreases. This requires further investigation and probably further improvement of the performance of the model in the tensile region.

6. The shape of the VTS envelope for all the mixes is similar to the PNS envelope but with reduced size. The envelope is closer to the PNS envelope for Mix 2 and Mix 3. This indicates that the plastic dilation starts closer to the peak for these two mixes. The model predicted well the VTS envelope for the three mixes.

7. The plastic strain directions do seem to be normal to the yield surfaces even though the experimental data is limited. This suggest that the assumption of associated flow rule is valid for all kinds of concrete.

8. Coarse aggregate content had a mild effect on the uniaxial compressive strength. There is marginal decrease for concrete with no coarse aggregate and a marginal increase where double amount of coarse aggregate is used.

9. The content of coarse aggregate has mixed effect on the uniaxial strain at peak stress. Significant increase with no aggregate content was noticed and marginal decrease where double aggregates are used.

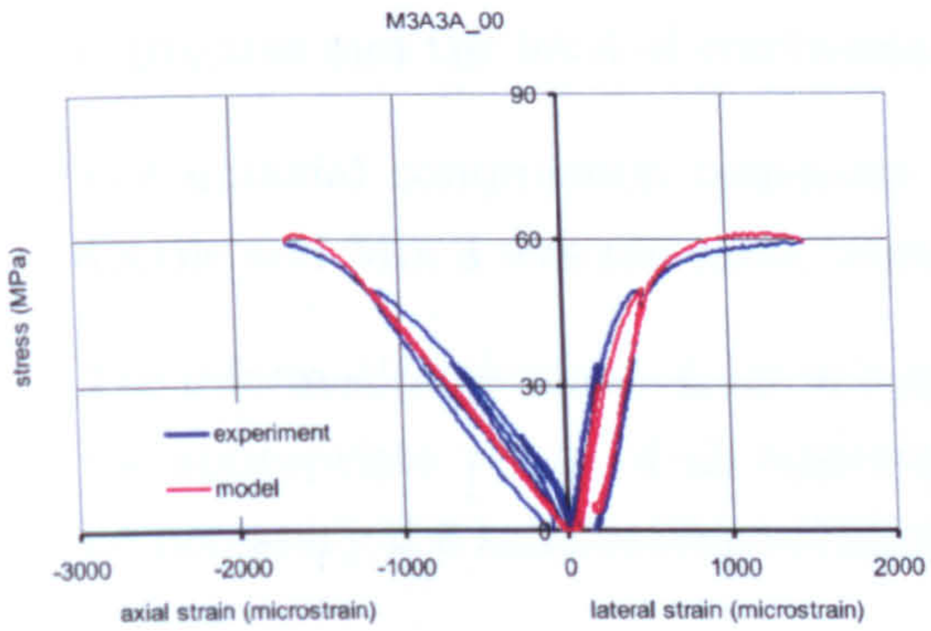

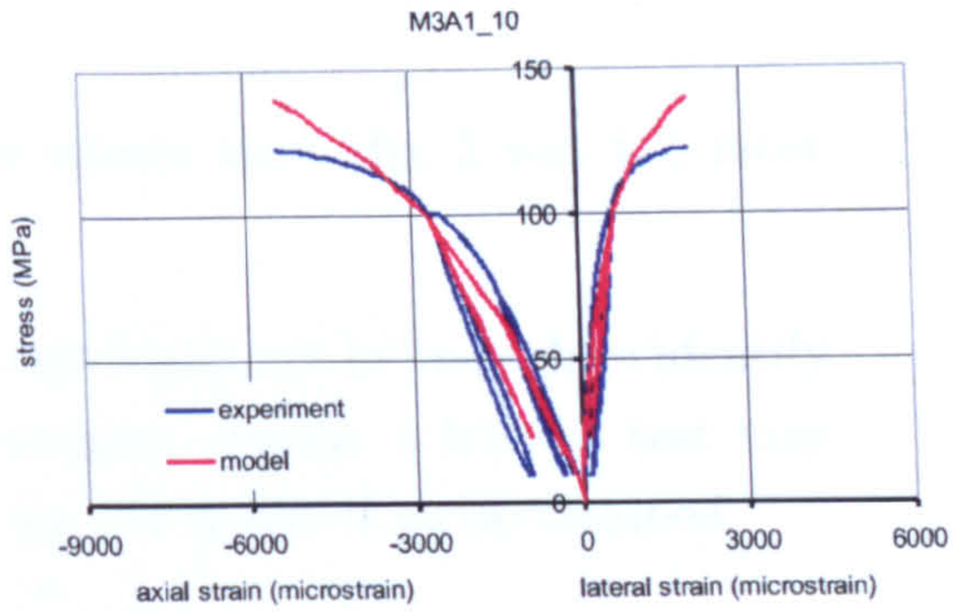

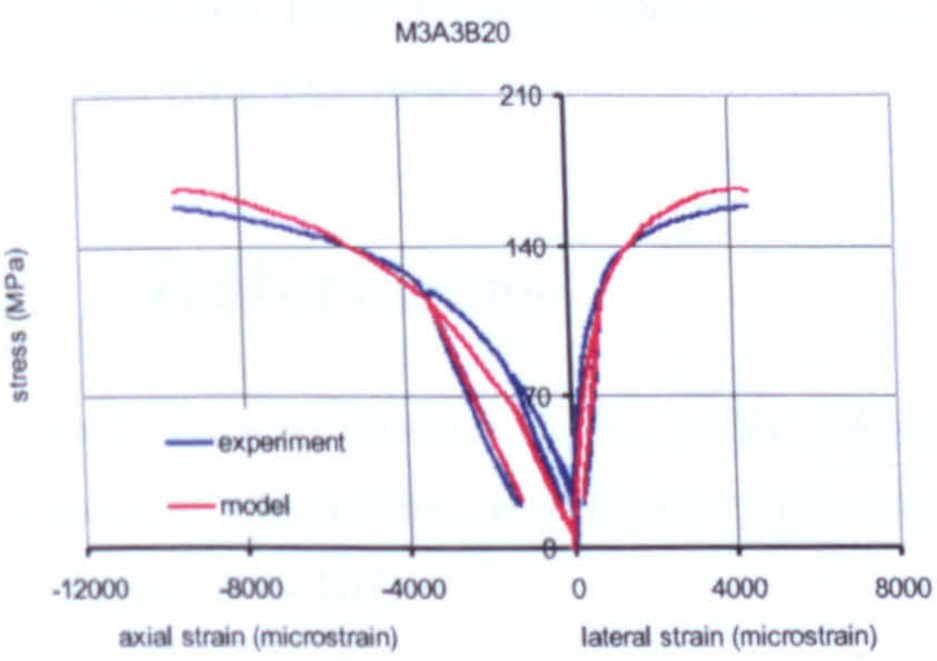

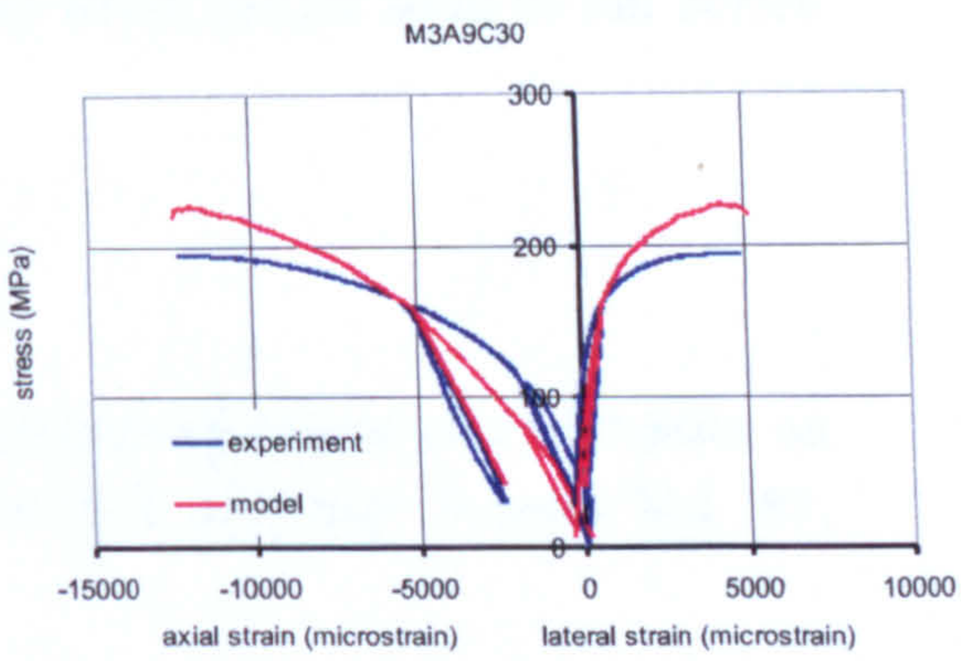

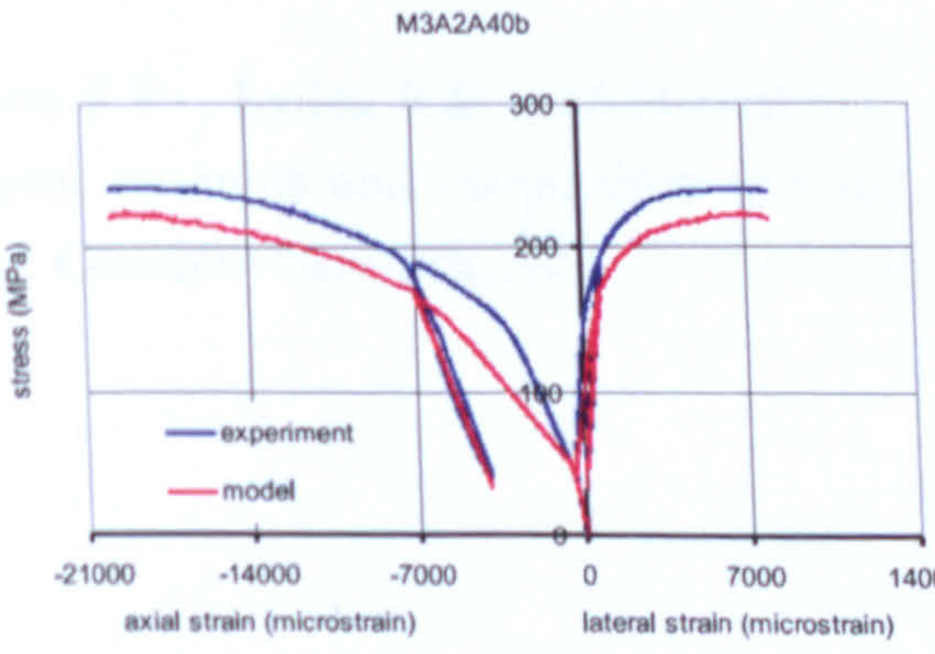

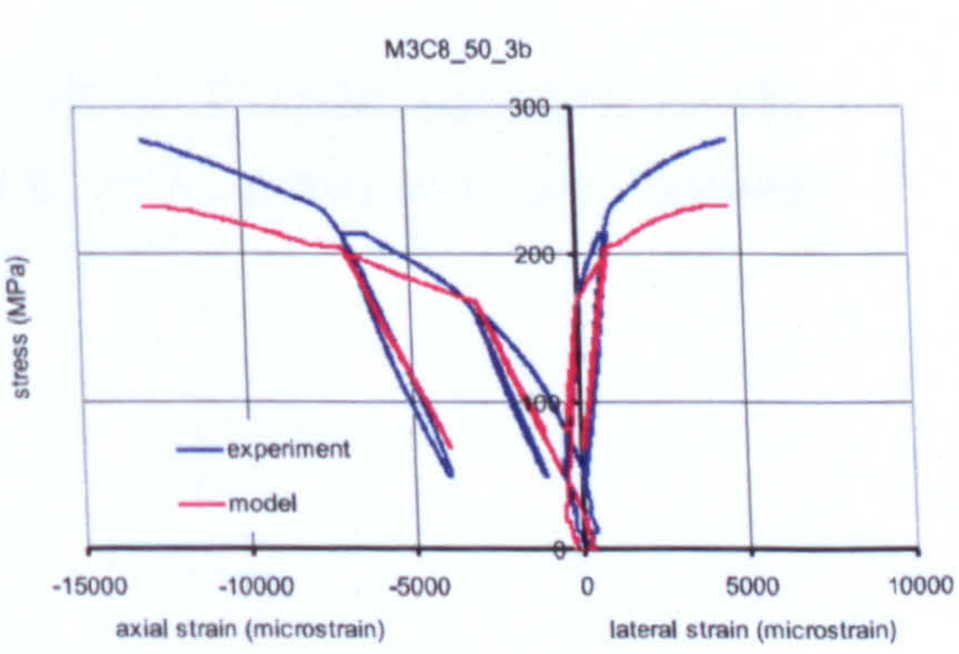

Figure 5.26: Experimental and model predictions for stress-strain curves of Mix 3, with 0, 10, 20, 30, 40 and 50 MPa confinement

10. Increasing coarse aggregate content significantly increased the modulus of elasticity.

11. The values of Poisson's ratio seems to be independent of the content of coarse aggregates and the level of confinement.

12. The uniaxial compression responses have shown that Mix 2 was the most ductile and Mix 3 was the most brittle.

13. The information available from uniaxial tests might not be enough to identify the appropriate values of all material constants. Hence, a triaxial test may be necessary if a satisfactory calibration for the model is to be attained.

14. The quality of the tests needs to be improved. Some errors have been noticed especially at the beginning of some tests where large values of strains are recorded prior to any loading. Also, many strain gauges seem to fail before reaching the peak.

5.7 References

Aitcin P-C. and Mehta P. K., 1990, Effect of coarse-aggregate characteristics on mechanical properties of high-strength concrete, *ACI Materials Journal*, Vol. **87**, No. 2, pp. 103-107.

El-Ariss Bilal, 2006, Effect of reducing coarse aggregates on concrete strength, *Construction and Building Materials*, Vol. **20**, No. 3, pp 149-157.

Zhou F.P. , Lydon F.D. and Barr B.I.G., 1995, Effect of coarse aggregate on the elastic modulus and compressive strength of high performance concrete, Cement and Concrete Research, Vol. **25**, No. 1, pp. 177-186.

Chapter 6

Numerical Verification and Simplification

6.1 Introduction

Large numbers of constitutive models have been proposed to simulate the behaviour of concrete under multiaxial loading. Many of these models stayed stored in the literature without any practical usage. The complexity of these models and the high number of material constants which causes difficulty to calibrate play a major role in the deterring of users.

Simple ideas without compromising the basic principle prove to be more effective. Therefore, for the model to be commercially accepted it has to be easy to understand, easy to calibrate and easy to use. One of the difficulties that we have encountered during the formulation of the new model, was the length of the analytical derivatives. This has been encountered because the newly developed model was built in four different stages with the introduction of a quartic polynomial function to fulfill the essential requirements of the yield surface, such as the conditions of continuity for the first and second derivatives. In other words, there are a number of dependent variables that have necessitated the use of long analytical derivatives.

Using numerical derivatives would significantly reduce the size of the derivatives and some derivatives of the internal variables can be avoided, thus much simpler derivatives could be produced. This will lead to a shorter code which makes it easier to understand and use. For example, the first derivative of the yield surface F with respect to $\{\sigma\}$ which has been presented in Chapter 3

$$\left\{\frac{\partial F}{\partial \sigma}\right\} = \bar{\rho}\left\{\frac{\partial r}{\partial \sigma}\right\} + r\frac{\partial \bar{\rho}}{\partial J_2}\left\{\frac{\partial J_2}{\partial \sigma}\right\} - \frac{\partial \rho_f}{\partial \bar{\xi}}\left\{\frac{\partial \bar{\xi}}{\partial \sigma}\right\} \tag{6.1}$$

requires the determination of eleven different analytical derivatives namely, $\left\{\frac{\partial r}{\partial \sigma}\right\}$, $\frac{\partial \bar{\rho}}{\partial J_2}$, $\left\{\frac{\partial J_2}{\partial \sigma}\right\}$, $\left\{\frac{\partial \bar{\xi}}{\partial \sigma}\right\}$, $\frac{\partial r}{\partial \xi}$, $\frac{\partial r}{\partial \theta}$, $\left\{\frac{\partial \theta}{\partial \sigma}\right\}$ and $\frac{\partial \rho_f}{\partial \xi}$ for four zones. These derivatives can be reduced to one single derivative if the numerical derivatives are to be used. Similarly, the twenty four derivatives required for $\left[\frac{\partial F}{\partial \sigma^2}\right]$, the fourteen derivatives required for $\frac{\partial F}{\partial k_p}$ and the fifteen derivatives required for $\left\{\frac{\partial^2 F}{\partial k_p \partial \sigma}\right\}$, each one of these analytical derivatives can be reduced to one numerical derivative.

In this chapter, the general formulation of the numerical derivatives is introduced in Section 6.2 along with Romberg's optimisation method. In the same section Ridder's algorithm is presented with a verification study to evaluate the algorithm performance and the calculations of the derivatives. In order to explore the performance of the model using numerical derivatives, the Colorado multiaxial data set is re-visited. The calibration of the model is discussed in Section 6.3 then the simulations of the number of tests are presented in Section 6.4. A comparative study about the time consumption for the numerical and analytical formulations is presented in Section 6.5. Finally, concluding remarks are presented in Section 6.6.

6.2 The Formulation of the Numerical Derivatives

The fact that differentiation (or equivalently, evaluation of Taylor coefficients) of analytical functions can be efficiently performed numerically was observed about fifty years ago. The earliest algorithm we know is the one described by Abate and Dubner in 1968 [Fornberg]. The algorithms to calculate the numerical derivatives are based on the expansion of Taylor's series in the vicinity of x which can be expressed as follows [Scheid]:

$$F(x+h) = F(x) + h\,.\,F'(x) + \frac{1}{2}h^2\,.\,F''(x) + \ldots \tag{6.2}$$

$$F(x-h) = F(x) - h\,.\,F'(x) + \frac{1}{2}h^2\,.\,F''(x) - \ldots \tag{6.3}$$

From equation 6.2 and 6.3 there are three well-known formulas that can be formulated to calculate the value of the first derivatives

$$y'(x) = \frac{y(x+h) - y(x)}{h} + 0(h) \tag{6.4}$$

$$y'(x) = \frac{y(x+h) - y(x-h)}{2\,h} + 0(h^2) \tag{6.5}$$

$$y'(x) = \frac{y(x) - y(x-h)}{h} + 0(h) \tag{6.6}$$

They are Newton Forward, Stirling and Newton Backward formulas respectively; in which only one term of the Taylor series is used.

In this chapter, the Stirling formula is used because it yields a more accurate approximation. Its error is proportional to square of the spacing. Its approximate second derivative is given by

$$y''(x) \sim \frac{y(x+h) - 2y(x) + y(x-h)}{h^2} \tag{6.7}$$

and for its mixed derivative

$$\frac{\partial^2 F}{\partial x \partial y} \sim \frac{[F(x+h, y+h) - F(x+h, y-h)] - [F(x-h, x+h) - F(x-h, y-h)]}{4\,h^2} \tag{6.8}$$

If the above equations are applied without critical consideration it is almost guaranteed to produce inaccurate results [Fornberg]. There are two sources of error in these equations; the truncation error and the roundoff error. The truncation error comes from discarding higher terms in the Taylor series expansion. The roundoff error has various contributors. First, there is a roundoff error in the stepsize h if it does not have an exact representation in binary. The other contributor is the machine accuracy which controls the lower value of h [Press *et al.*].

Therefore, an exploration of the functions derivative over a scale comparable to the point where the derivative required is needed, so that the high-order terms in a Taylor expansion have some meaning. Such methods also involve multiple evaluations of the function F, so their increased accuracy must be weighed against increased cost. For derivatives, one seeks to extrapolate, to $h \longrightarrow 0$, the result of finite-difference calculations with smaller and smaller finite values of h. One uses each new finite-difference calculation to produce both an extrapolation of higher order, and also extrapolations of previous, lower, orders but with smaller scales of h. Ridders has given a nice implementation of this idea which is based on Romberg's numerical integration [Ridders]. In the following subsection the method is presented followed by the algorithm.

6.2.1 Romberg's Method

The numerical differentiation that has been used here is based on extension to the numerical differentiation of Romberg's principle of sequence extrapolation, originally developed for numerical integration so that an algorithm can be developed which is capable of guaranteeing convergence to the actual optimal solution. This can be achieved bearing in mind that the functional form of the error of a numerical algorithm is known; the error can be estimated by evaluating the algorithm for two different increment sizes. The error estimate can be used both for error control and extrapolation [Ridders].

In order to approximate $F'(x)$ and $F'''(x)$ we use the Taylor expansion in the vicinity of x [Scheid], so

$$F'(x) \sim \frac{F(x+h) - F(x-h)}{2\,h} + e \tag{6.9}$$

with

$$e = -\frac{1}{3}\,h^2\,.\,F'''(x) + 0(h^3) \tag{6.10}$$

and

$$F''(x) \sim \frac{F(x+h) - 2\,F(x) + F(x-h)}{h^2} + d \tag{6.11}$$

with

$$d = -\frac{1}{12}\,h^2\,.F^{IV}(x) + 0(h^3) \tag{6.12}$$

When we put e = d = 0, we obtain the well-known and widely used approximation for the first and second derivative.

A serious drawback is the sensitivity of the accuracy of stepsize h. Machine precision imposes a lower boundary for h, so one never can be sure of the significant digits that are obtained.

From 6.10 and 6.12, we conclude the fact that the error e and d decrease quadratically with decreasing h. When we repeatedly halve the value of h, a series of corresponding values of $(F(x+h) - F(x-h))/2h$ are obtained, which we denote by A_1, A_2, A_3, ...

Now $F'(x) \sim A_1 + e_1 \sim A_2 + e_2$, furthermore $e_1/e_2 = 4$, so we get a better

proximation

$$F'(x) \sim \frac{4A_2 - A_1}{4 - 1} \tag{6.13}$$

which we denote by B_1.

This procedure leads us to the well known Romberg method. The entries can be represented in a so-called tableau:

	A_1	A_2	A_3	A_4	...
m = 1		B_1	B_2	B_3	...
m = 2			C_1	C_1	...
m = 3				D_1	...

with

$$B_n = \frac{A_{n+1} \cdot 4^m - A_n}{4^m - 1}, \quad m = 1 \tag{6.14}$$

$$C_n = \frac{B_{n+1} \cdot 4^m - B_n}{4^m - 1}, \quad m = 2 \tag{6.15}$$

and so on.

6.2.2 The Algorithm

To improve the accuracy in the computation of the derivatives of the model function (F), Ridder's algorithm which is based on Romberg's method is applied. The method gives fast convergence to an answer containing more significant digits than the usual method provides. The strategy is to evaluate equation 6.14 and 6.15 for a sequence of values of h tending to zero, stopping when the desired accuracy is reached. Input to the routine is a function (F), a position x, and a large stepsize h. Output is the returned value of the derivative, and an estimate of its error.

The following steps are to be carried out in sequence:

1. Estimate an initial stepsize (h); it need not be small and must be nonzero, but rather should be an increment in x over which $y(x)$ changes substantially.
2. Set an initial value for the permissable error in the derivative.
3. Set a value of the factor that the stepsize is decreased by in each iteration.
4. Set maximum value of the size of the tableau.

5. Calculate the initial derivative from $x - h$ and $x + h$

$$F'(x) = \frac{F(x+h) - F(x-h)}{2\ h} \tag{6.16}$$

6. Try a new, smaller stepsize.

7. Recalculate the derivative with the new stepsize.

8. Compute extrapolations of various orders, requiring no new function evaluations.

9. Compare each new extrapolation to one order lower, both at the present stepsize and the previous one. If the error is decreased, save the improved answer.

10. If the error is less or equal to the tolerance, save the derivative.

11. If the higher order is worse by a significant factor, then EXIT.

12. Go to step 6

6.2.3 The Derivatives of the Yield Function

Four groups of numerical derivatives are required to preform the numerical formulations. They are as follows:

1. The first derivatives of the yield function F with respect to the stresses

$$\frac{\partial F}{\partial \sigma_1} = \frac{F(\sigma_1 + h) - F(\sigma_1 - h)}{2\,h} \tag{6.17}$$

$$\frac{\partial F}{\partial \sigma_2} = \frac{F(\sigma_2 + h) - F(\sigma_2 - h)}{2\,h} \tag{6.18}$$

$$\frac{\partial F}{\partial \sigma_3} = \frac{F(\sigma_3 + h) - F(\sigma_3 - h)}{2\,h} \tag{6.19}$$

2. The first derivatives of the yield function F with respect to the internal hardening variable k_p

$$\frac{\partial F}{\partial k_p} = \frac{F(k_p + h) - F(k_p - h)}{2\,h} \tag{6.20}$$

3. The second derivatives of the yield function F with respect to the stresses

$$\frac{\partial^2 F}{\partial \sigma_1^2} = \frac{F(\sigma_1 + h) - 2\,F(\sigma_1) + F(\sigma_1 - h)}{h^2} \tag{6.21}$$

$$\frac{\partial^2 F}{\partial \sigma_2^2} = \frac{F(\sigma_2 + h) - 2\,F(\sigma_2) + F(\sigma_2 - h)}{h^2} \tag{6.22}$$

$$\frac{\partial^2 F}{\partial \sigma_3^2} = \frac{F(\sigma_3 + h) - 2\,F(\sigma_3) + F(\sigma_3 - h)}{h^2} \tag{6.23}$$

$$\frac{\partial^2 F}{\partial \sigma_1 \partial \sigma_2} = \frac{[F(\sigma_1 + h, \sigma_2 + h) - F(\sigma_1 + h, \sigma_2 - h)] - [F(\sigma_1 - h, \sigma_2 + h) - F(\sigma_1 - h, \sigma_2 - h)]}{4\,h^2} \tag{6.24}$$

$$\frac{\partial^2 F}{\partial \sigma_2 \partial \sigma_1} = \frac{\partial^2 F}{\partial \sigma_1 \partial \sigma_2} \tag{6.25}$$

$$\frac{\partial^2 F}{\partial \sigma_2 \partial \sigma_3} = \frac{[F(\sigma_2 + h, \sigma_3 + h) - F(\sigma_2 + h, \sigma_3 - h)] - [F(\sigma_2 - h, \sigma_3 + h) - F(\sigma_2 - h, \sigma_3 - h)]}{4\,h^2} \tag{6.26}$$

$$\frac{\partial^2 F}{\partial \sigma_3 \partial \sigma_2} = \frac{\partial^2 F}{\partial \sigma_2 \partial \sigma_3} \tag{6.27}$$

$$\frac{\partial^2 F}{\partial \sigma_1 \partial \sigma_3} = \frac{[F(\sigma_1 + h, \sigma_3 + h) - F(\sigma_1 + h, \sigma_3 - h)] - [F(\sigma_1 - h, \sigma_3 + h) - F(\sigma_1 - h, \sigma_3 - h)]}{4\,h^2} \tag{6.28}$$

$$\frac{\partial^2 F}{\partial \sigma_3 \partial \sigma_1} = \frac{\partial^2 F}{\partial \sigma_1 \partial \sigma_3} \tag{6.29}$$

4. The second mixed derivatives of the yield function F with respect to the stresses and the hardening internal variable

$$\frac{\partial^2 F}{\partial k_p \partial \sigma_1} = \frac{[F(k_p + h, \sigma_1 + h) - F(k_p + h, \sigma_1 - h)] - [F(k_p - h, \sigma_1 + h) - F(k_p - h, \sigma_1 - h)]}{4\,h^2} \tag{6.30}$$

$$\frac{\partial^2 F}{\partial k_p \partial \sigma_2} = \frac{[F(k_p + h, \sigma_2 + h) - F(k_p + h, \sigma_2 - h)] - [F(k_p - h, \sigma_2 + h) - F(k_p - h, \sigma_2 - h)]}{4\,h^2} \tag{6.31}$$

$$\frac{\partial^2 F}{\partial k_p \partial \sigma_3} = \frac{[F(k_p + h, \sigma_3 + h) - F(k_p + h, \sigma_3 - h)] - [F(k_p - h, \sigma_3 + h) - F(k_p - h, \sigma_3 - h)]}{4\,h^2} \tag{6.32}$$

6.2.4 Verification

A two-variable polynomial equation has been used to verify the derivatives by using arbitrary values for x, y and h. This has been introduced in order to verify the capability of the algorithm to calculate the derivatives of a simple function where its derivatives are already known. The algorithm has successfully calculated all derivatives and produced accurate results. All the numerical derivatives have been verified by comparing them with the analytical derivatives. The yield function then was introduced to the code and all its derivatives are calculated.

The error for all the derivatives is calculated using the following error measure

$$error = \frac{numerical\ derivative - analytical\ derivative}{analytical\ derivative} \times 100\% \tag{6.33}$$

For example, an arbitrary location on the yield surface is chosen from test 1-1 of the Colorado tests where $\bar{\xi}$ = -1.97. The same values of material constants are used for both analytical and numerical codes. The error of $\frac{\partial F}{\partial k_p}$ is found to be 2.23×10^{-11}%, for $\left\{\frac{\partial F}{\partial \sigma}\right\}$ is -0.0425 %, for $\left\{\frac{\partial^2 F}{\partial \sigma \partial k_p}\right\}$ is -0.423 % and for $\left[\frac{\partial^2 F}{\partial \sigma^2}\right]$ is 3.8 %. The values of these errors are thought to be within the acceptable range if we take in consideration that the values of the $\left[\frac{\partial^2 F}{\partial \sigma^2}\right]$ are in $10\times^{-17}$ range where the roundoff error can not be avoided.

6.3 The Model Calibration

The calibration of the model has been performed in the same manner that has been discussed in the analytical derivatives in Chapter 4 and 5 with an exemption of the hardening constants A_h and B_h and the hydrostatic intersection constantA_k.

These constants were calibrated through an automatic procedure where a modified version of the code has been introduced. The program is coded in a way which makes it possible to find the values of A_k, A_h and B_h which give the minimum error. The code is to freeze the value of two constants and vary the third and calculate the error. The same procedure is repeated for the other two constants. The values associated with the minimum error are to be chosen. The results were then re-examined where the minimum values of the errors are looked at in conjunction with a limited variation in the values of constants.

The range initial values has been selected from previous calibrations. These values were 0.5, 0.001 and 0.1 for A_k, A_h and B_h respectively. The optomised values were then used to simulate the stress-strain results. The peak uniaxial compression stress f_c, is reported to be 22.6 MPa and the tensile strength f_t, is assumed to be 10% of the peak compression stress.

The Modulus of elasticity E, is assumed to be 20.0 GPa. This value has been verified by examining the trend of the loading-unloading part of the stress strain curve. In previous chapters our study has shown that Young's modulus increases slightly with the increase of confinement. However, in this simulations the value of Young's modulus is assumed to be constant. The value of Poisson's ratio ν is assumed to be 0.2, the initial hardening constant k_0 is 0.1, the meridional shape constant γ is 0.999 and the merging constant α_1, is 0.35.

The VTS constant α_2 has been identified in the previous chapters through experimental investigations. During that investigation the value of this constant was found to be between 0.9 to 0.95. It was also observed that limited change in this constant does not have a significant effect on the general predictions of the model. The value of this constant in these simulations was set to 0.90.

The initial stepsize h has been selected according to the magnitude of the internal variables. For the stresses, the initial value is set to 100 Pa and for the internal hardening constant k_p the value is set to 0.1.

specimen	A_h	B_h	A_k	min error %
1-1	0.002	1.6	2.9	12.2
1-2	0.002	1.0	2.2	13.0
1-3	0.002	1.3	1.4	8.9
1-4	0.002	0.7	2.9	26.2
1-5	0.002	0.7	2.9	29.5
1-6	0.002	1.5	2.9	13.4
1-7	0.002	1.2	2.9	16.2
1-8	0.002	1.0	2.3	27.95
1-9	0.002	1.6	2.9	15.1
1-10	0.002	0.8	2.9	21.0
1-11	0.004	1.8	2.7	15.7
1-12	0.004	2.0	2.9	18.7

Table 6.1: The minimum error between experimental data and model predictions and the hardening constants A_h and B_h with the hydrostatic intersection constantA_k for series 1

6.4 The Simulations

Colorado test data [Scavuzzo *et. al.*] has been simulated in this section . All the sixty seven tests were simulated. The data includes three stress readings and three strain readings. Stresses are in psi and strains are microstrain x 1000 and the compression is taken positive.

The error measure for the simulations is as follows

$$error = \sqrt{\frac{\sum_{k=1}^{q}(\sigma_{ij}^{m} - \sigma_{ij}^{exp})^2}{\sum_{k=1}^{q}(\sigma_{ij}^{exp})^2}}.100\% \tag{6.34}$$

where σ_{ij}^{m} are the stresses calculated by the model and σ_{ij}^{exp} are the stresses reported by the experimental tests.

The minimum error values of series 1 with the hardening constants are shown in Table 6.1. The error values vary from around 10 % to 30%. The average error for the tests of this series is 19.8%. The values of A_h and A_k remains constant for most of the test while B_h changed in order to obtain the minimum values of error. The stress-strain curves for some tests of this series are shown in Figure 6.1. The performance of the model is similar to that of the analytical response with some improvement. The improvement is the result of the changing of the hardening constants.

The minimum error values of series 2 are shown in table 6.2 and the stress-strain

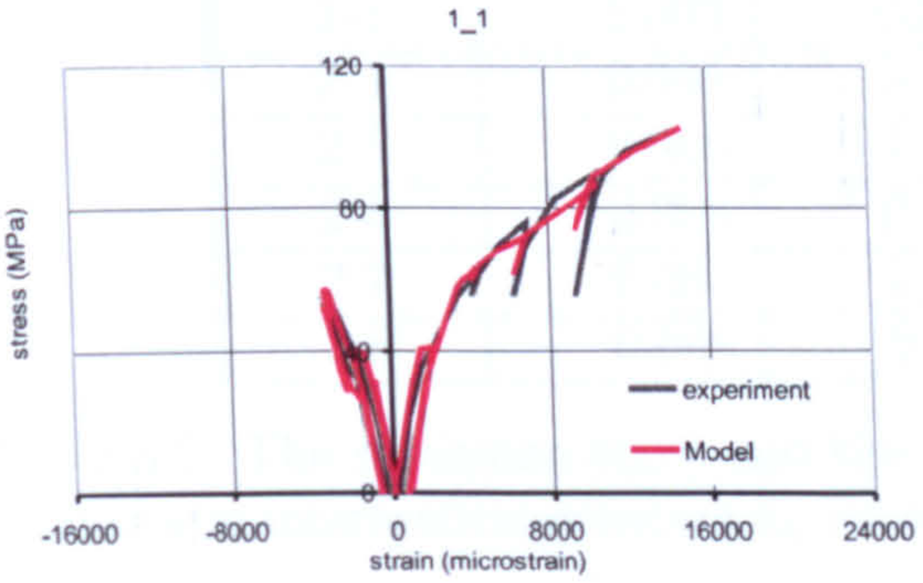

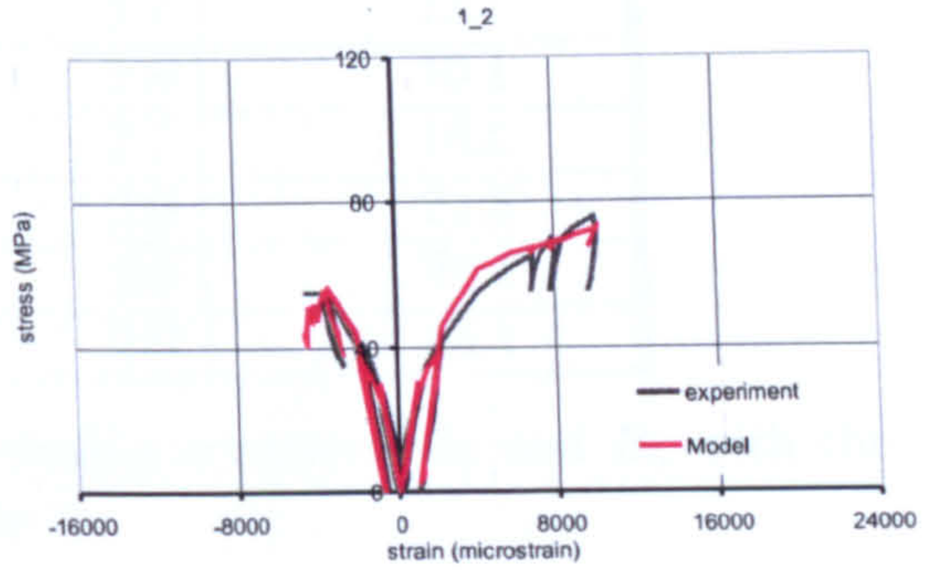

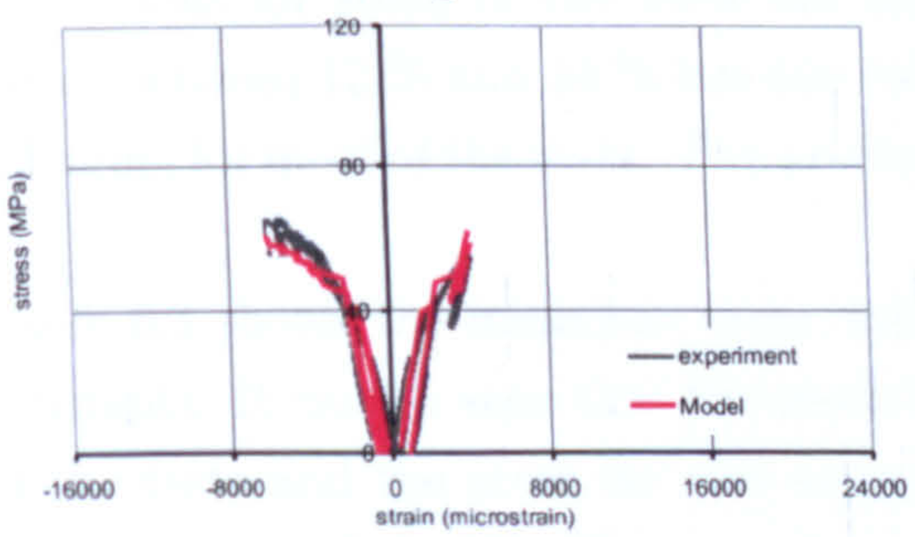

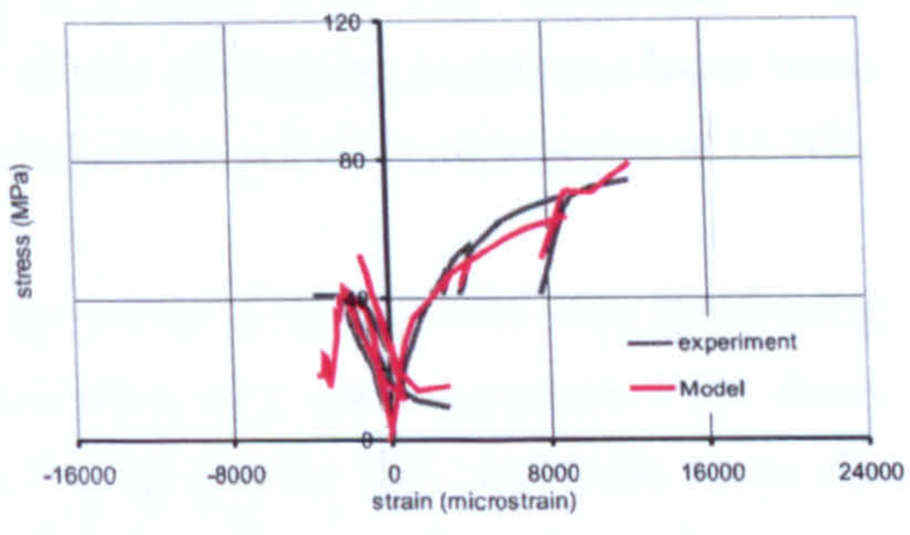

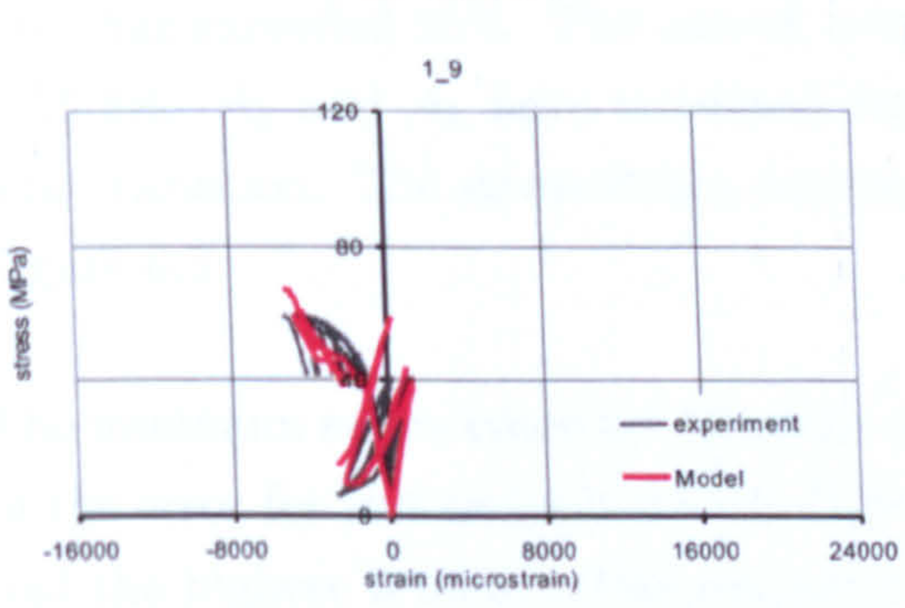

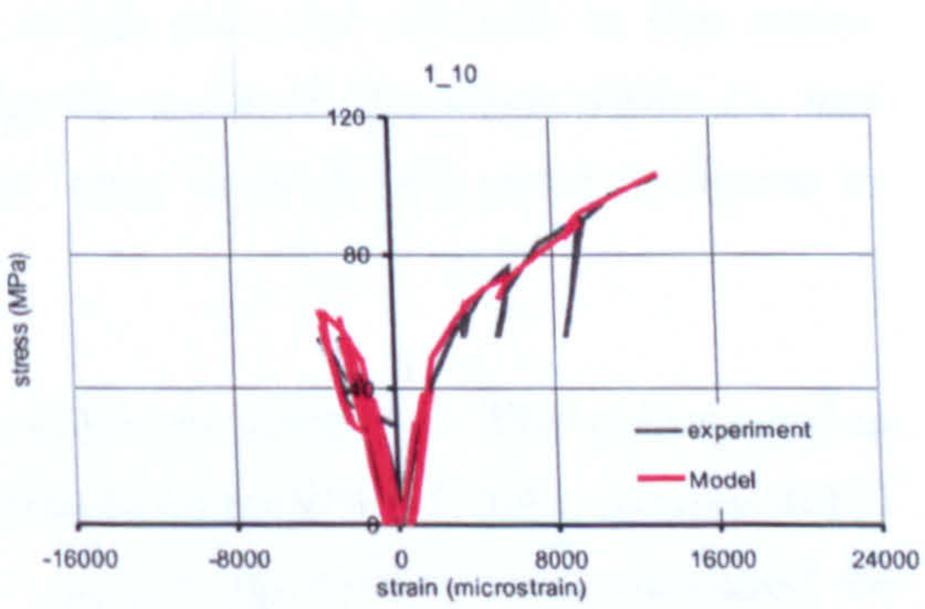

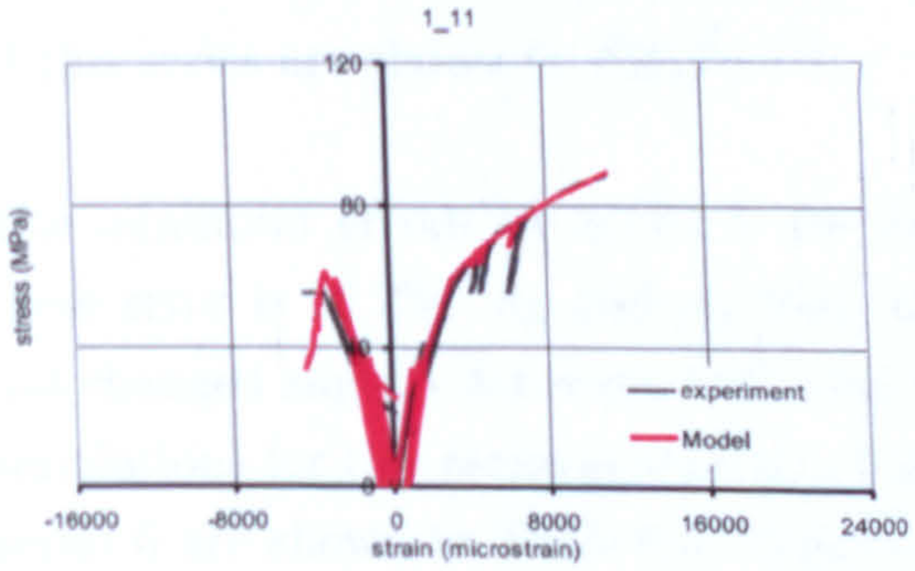

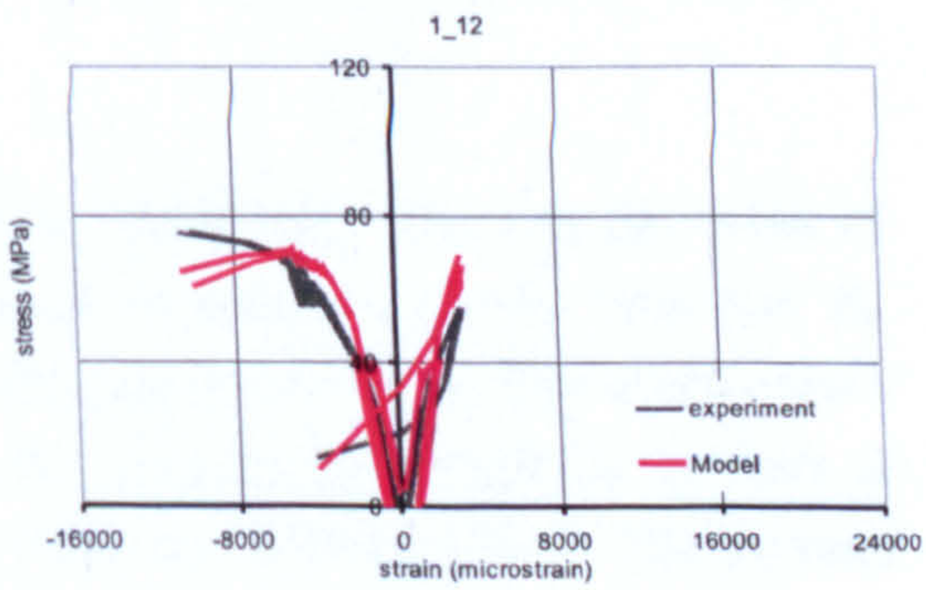

Figure 6.1: Experimental and model stress strain curves for the Colorado tests, Series 1

specimen	A_h	B_h	A_k	min error %
2-1	0.001	0.9	2.9	11.9
2-2	0.001	0.9	0.6	14.9
2-3	0.003	0.9	2.7	13.7
2-4	0.004	0.5	2.8	10.1
2-5	0.008	1.1	2.7	18.5
2-6	0.006	0.9	2.9	21.5
2-7	0.008	1.2	2.6	23.4
2-8	0.008	0.8	2.9	24.1

Table 6.2: The minimum error and the hardening constants A_h and B_h with the hydrostatic intersection constantA_k for series 2

simulations for some of the tests are shown in Figure 6.2. The minimum error varies between 12 % and 24 % but the values of the hardening constants have been changing for most of the tests. The average value of the error for this series is 15.3%.

Table 6.3 shows the minimum error values for series 3 along with the hardening constants. It can be seen that the model has shown very good agreement for most of the tests and the error for test sample 3-7 is as low as 7%. In some tests the error has exceeded 25%. The overall average of the error for all tests in this series is 15.4%. A_h and A_k have remained constant for most of the tests while B_h has some variation. The stress-strain response for some tests of this series is shown in Figure 6.3.

The minimum errors recorded for series 4 are shown in Table 6.4. The average value of the error for this series is 24.2%. The minimum error is 6.7% (test sample 4-17) and the highest is 36.8% (test sample 4-21). A_h and A_k have been maintained for most of the tests while B_h has been changed. Some of the stress-strain responses of this series are shown in Figure 6.4.

The minimum errors for series 5 are shown in Table 6.5. The average value of these error is 26.2%. A_h and A_k have remained constant for all the tests and B_h has changed slightly for some tests and significantly for test 5-4. The stress-strain simulations for this series is shown in Figure 6.5. Finally, the errors for the tests of series 6 are shown in Table 6.6. Significant error has been recorded. The average value of the errors is 35.8%.

The overall average error for all of the Colorado test data is 20.6%.

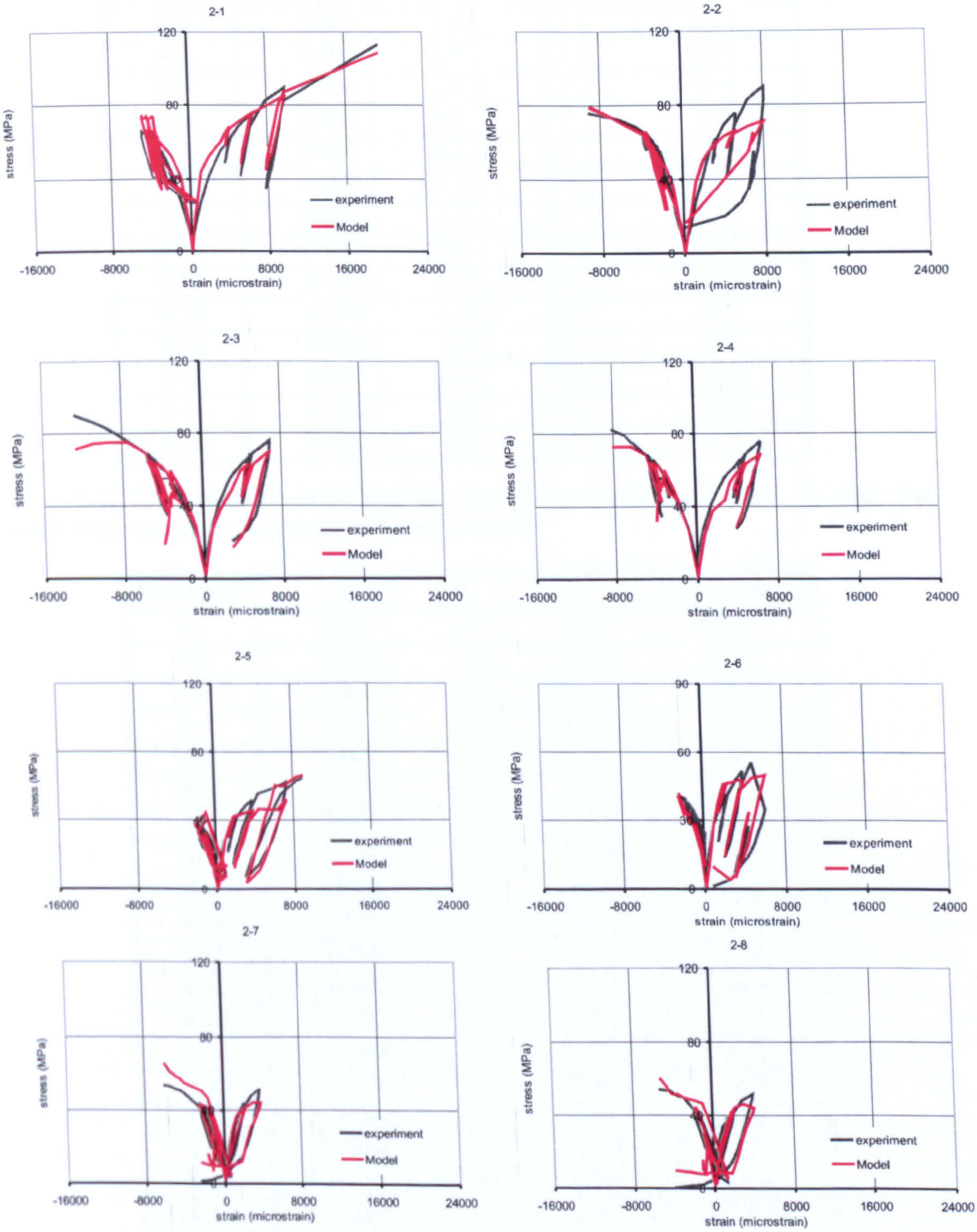

Figure 6.2: Experimental and model stress strain curves for the Colorado tests, Series 2

specimen	A_h	B_h	A_k	min error %
3-1	0.003	1.3	2.7	16.3
3-2	0.003	1.3	2.7	20.5
3-3	0.003	1.3	2.7	23.7
3-4	0.003	1.0	2.7	12.1
3-5	0.003	1.0	2.7	11.4
3-6	0.003	0.8	2.7	9.9
3-7	0.003	0.5	2.1	6.9
3-8	0.003	1.3	2.7	13.5
3-9	0.003	1.0	2.7	11.7
3-10	0.003	0.8	2.7	25.7
3-11	0.003	0.4	2.1	15.9
3-12	0.003	1.2	2.7	22.7
3-13	0.003	1.2	2.7	22.7
3-14	0.003	0.5	2.9	14.9
3-15	0.003	1.2	2.9	13.8
3-16	0.003	1.2	2.7	8.3

Table 6.3: The minimum error and the hardening constants A_h and B_h with the hydrostatic intersection constantA_k for series 3

specimen	A_h	B_h	A_k	min error %
4-1	0.003	1.0	2.7	20.5
4-2	0.003	1.0	2.7	22.8
4-3	0.003	1.3	2.7	17.8
4-4	0.003	0.7	2.8	11.7
4-5	0.003	0.7	2.9	14.6
4-6	0.003	0.7	2.9	25.9
4-7	0.005	0.8	2.8	20.2
4-8	0.003	1.0	2.7	20.7
4-9	0.003	1.1	2.7	19.8
4-10	0.003	1.1	2.9	20.4
4-11	0.002	1.0	2.9	17.4
4-12	0.002	0.8	2.7	18.4
4-13	0.003	0.7	2.7	27.5
4-14	0.003	0.9	2.7	25.7
4-15	0.003	1.4	2.9	35.2
4-16	0.003	0.8	2.7	32.8
4-17	0.003	1.1	2.7	6.7
4-18	0.003	1.4	2.7	12.5
4-19	0.003	1.1	2.7	30.1
4-20	0.003	1.1	2.7	32.4
4-21	0.003	0.7	2.7	36.8
4-22	0.003	0.6	2.7	31.4

Table 6.4: The minimum error and the hardening constants A_h and B_h with the hydrostatic intersection constantA_k for series 4

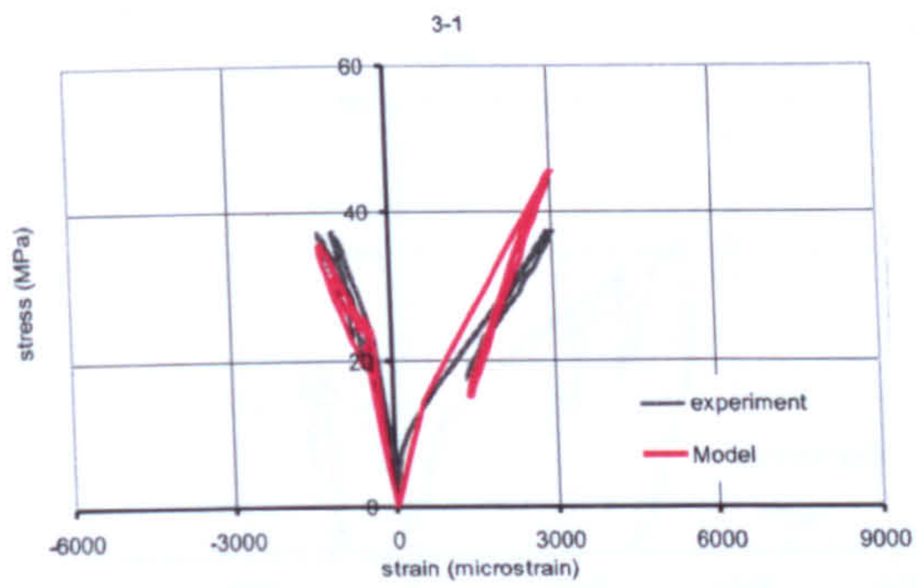

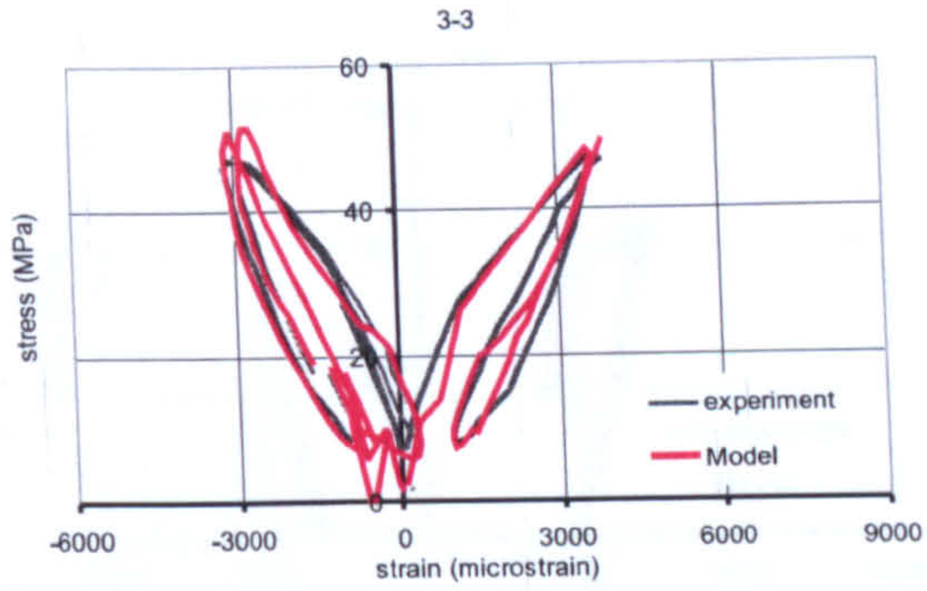

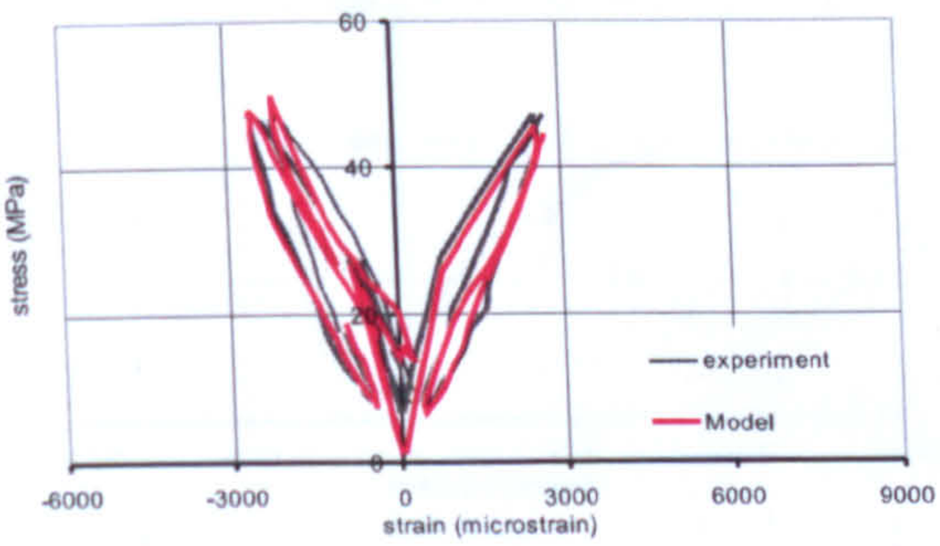

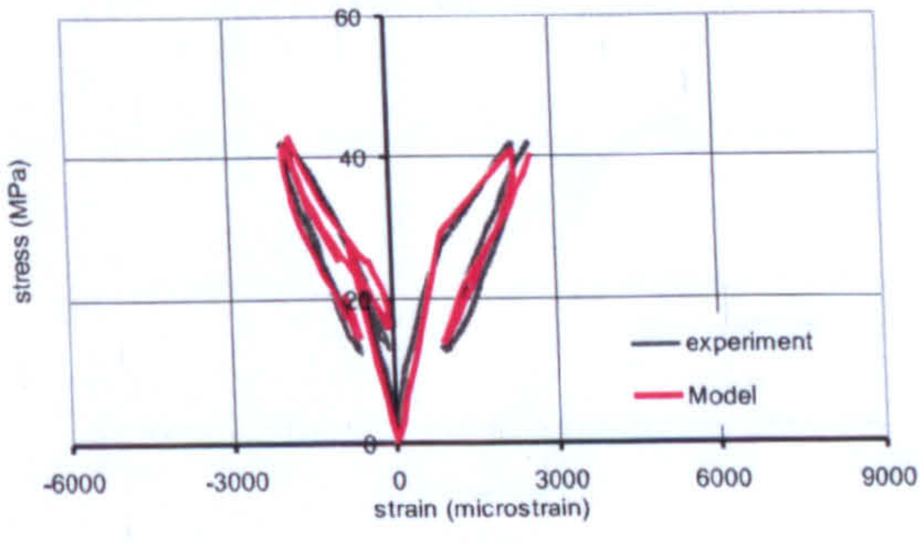

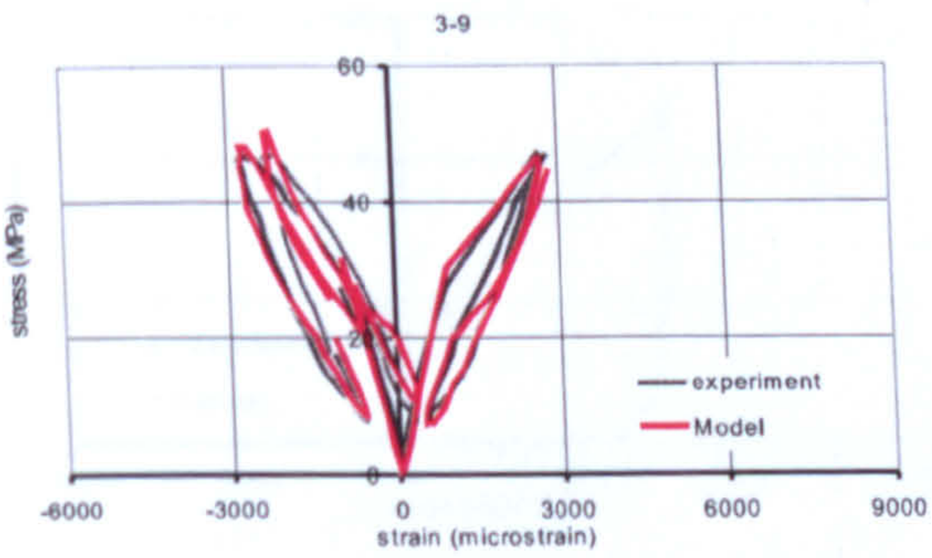

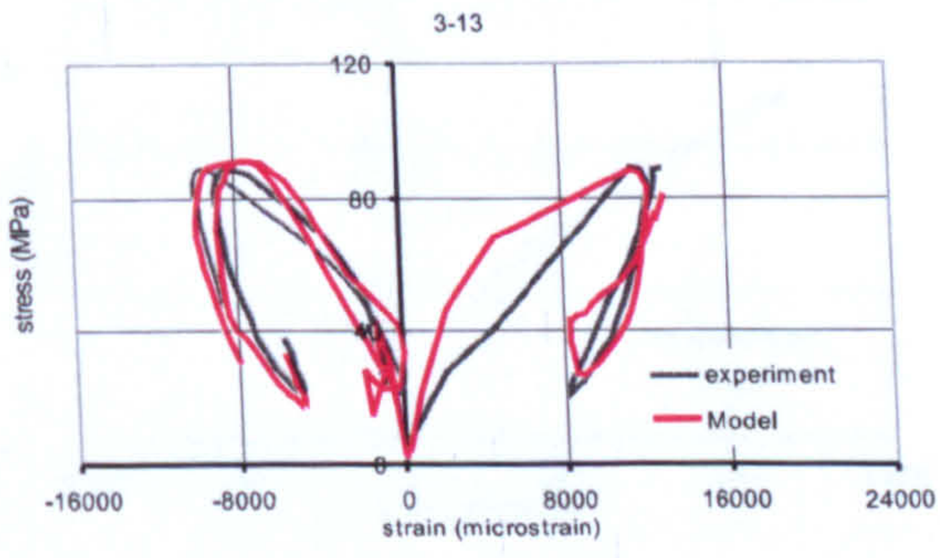

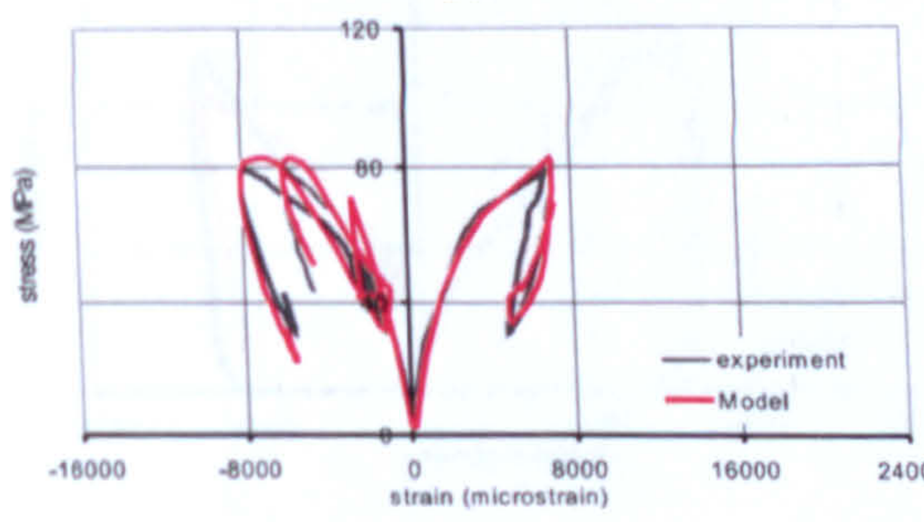

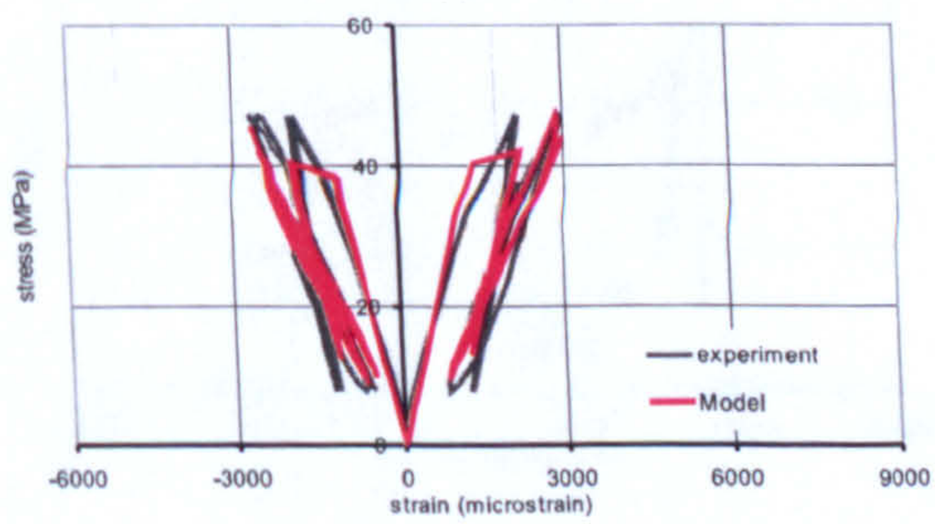

Figure 6.3: Experimental and model stress strain curves for the Colorado tests, Series 3

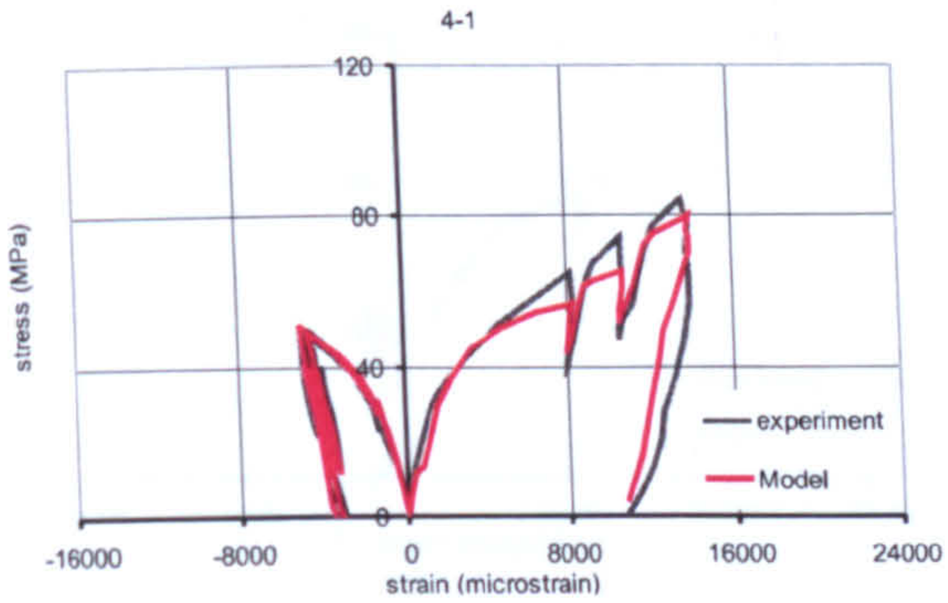

4-12

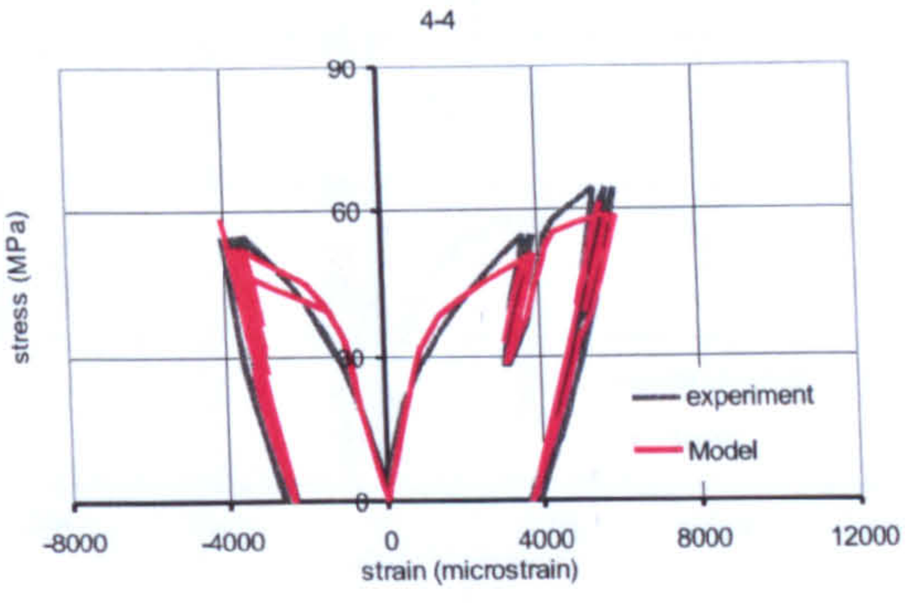

4-13

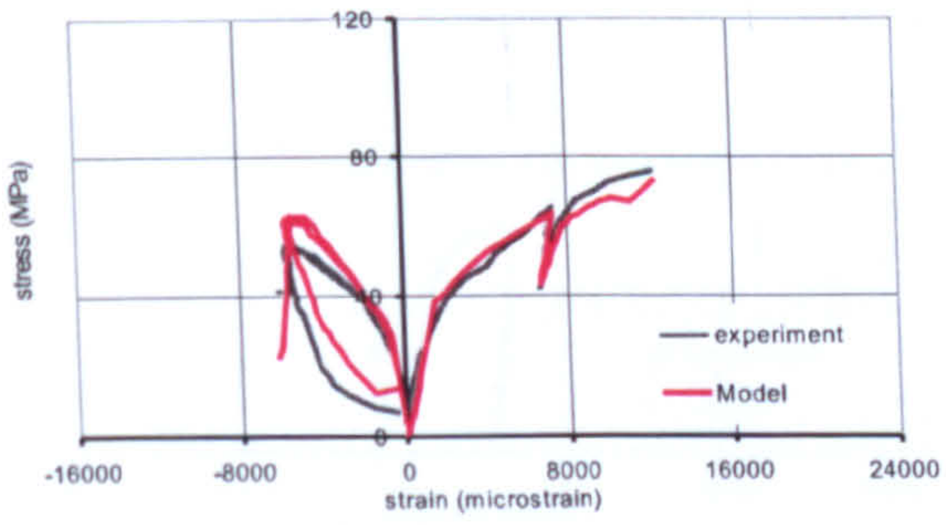

4-15

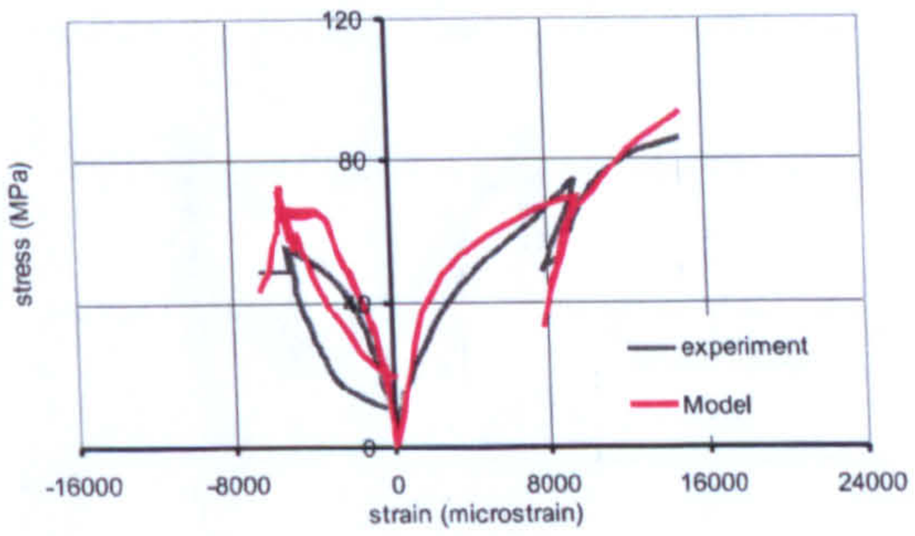

4-18

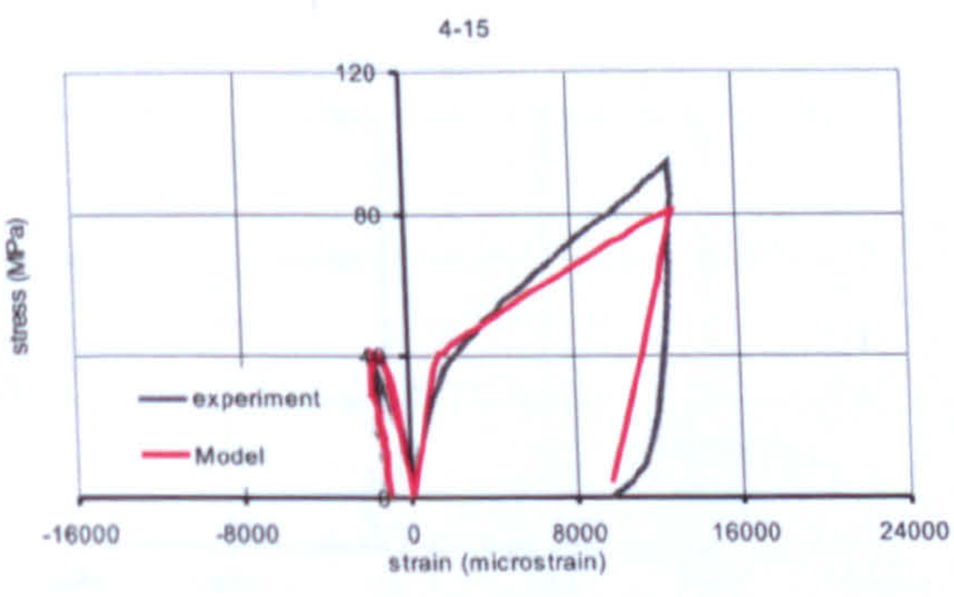

4-16

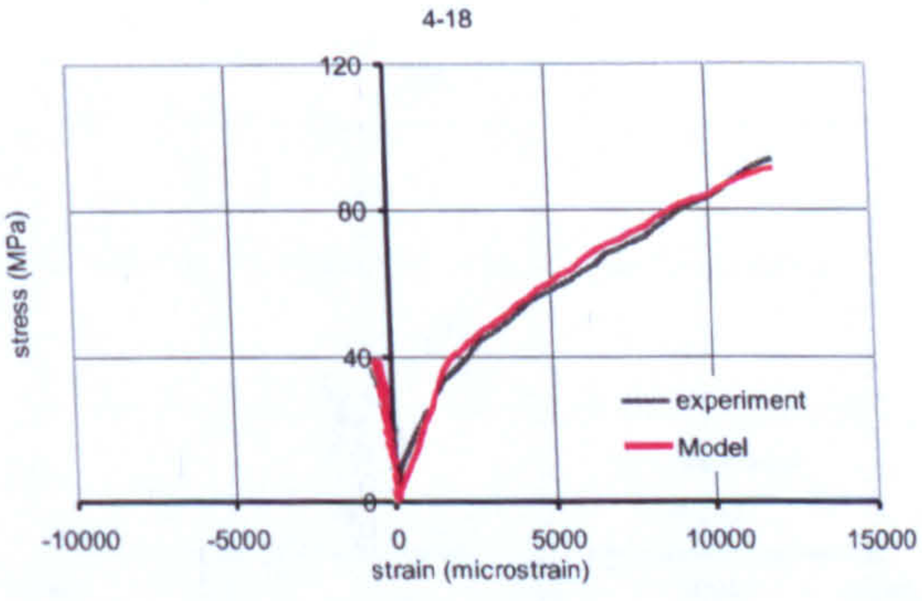

4-19

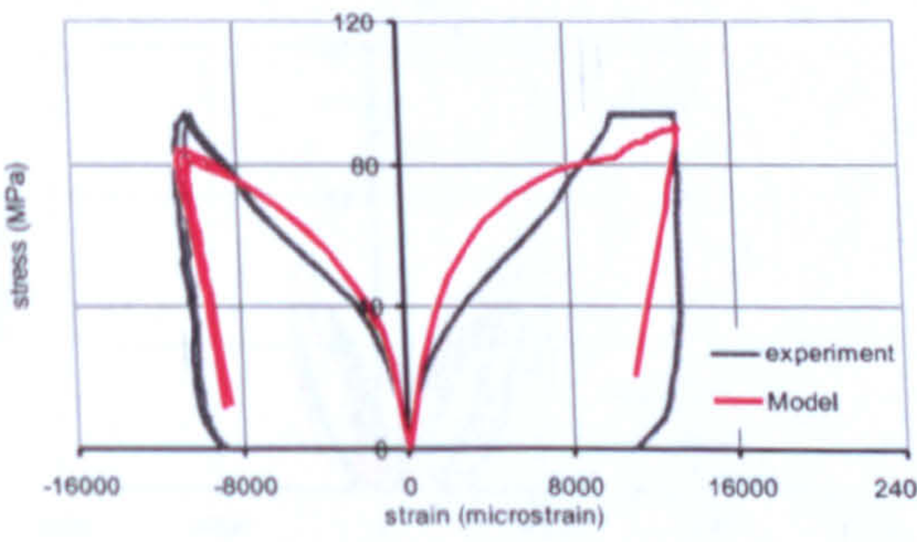

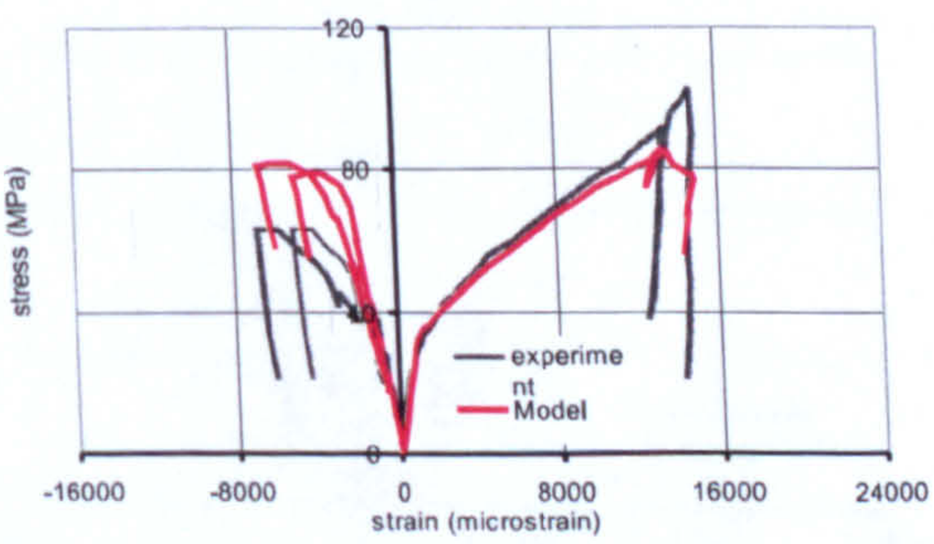

Figure 6.4: Experimental and model stress strain curves for the Colorado tests, Series 4

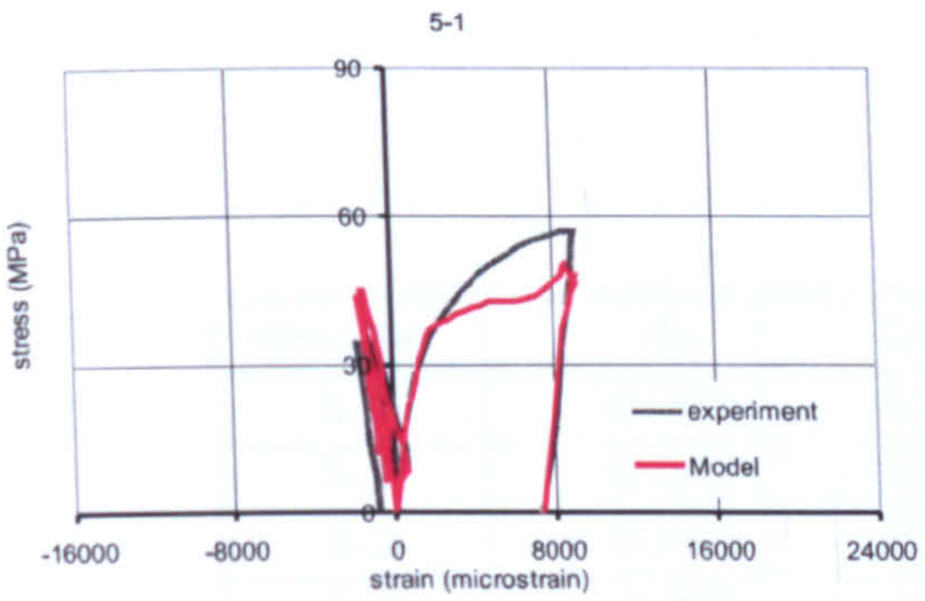

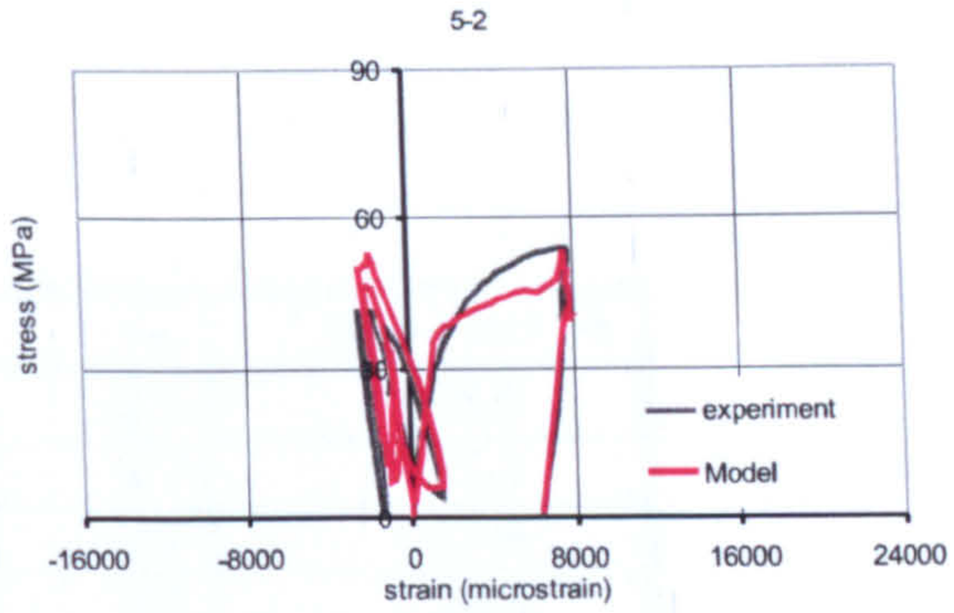

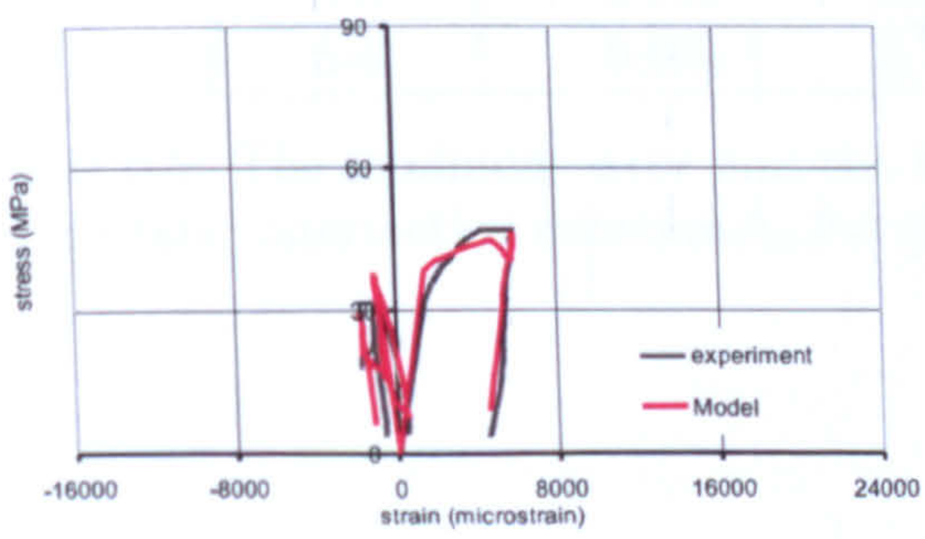

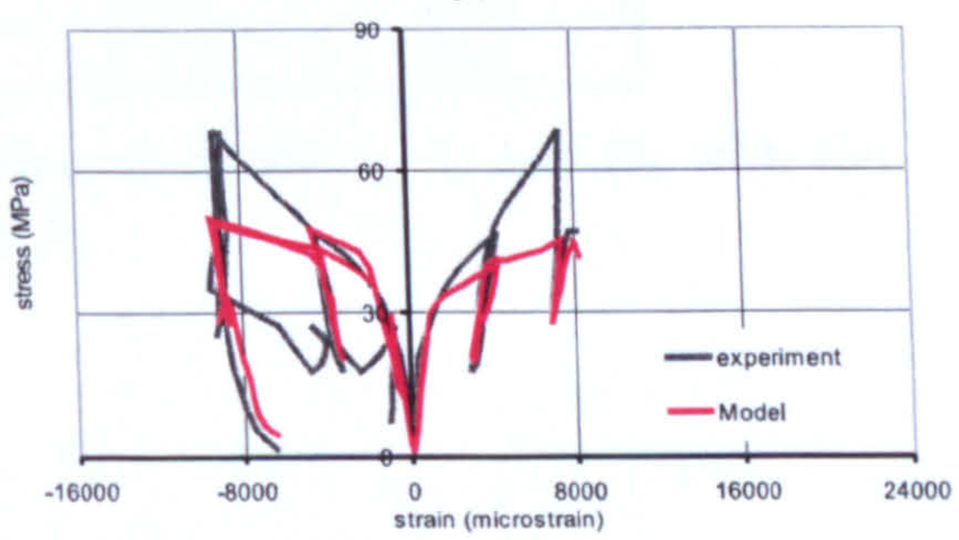

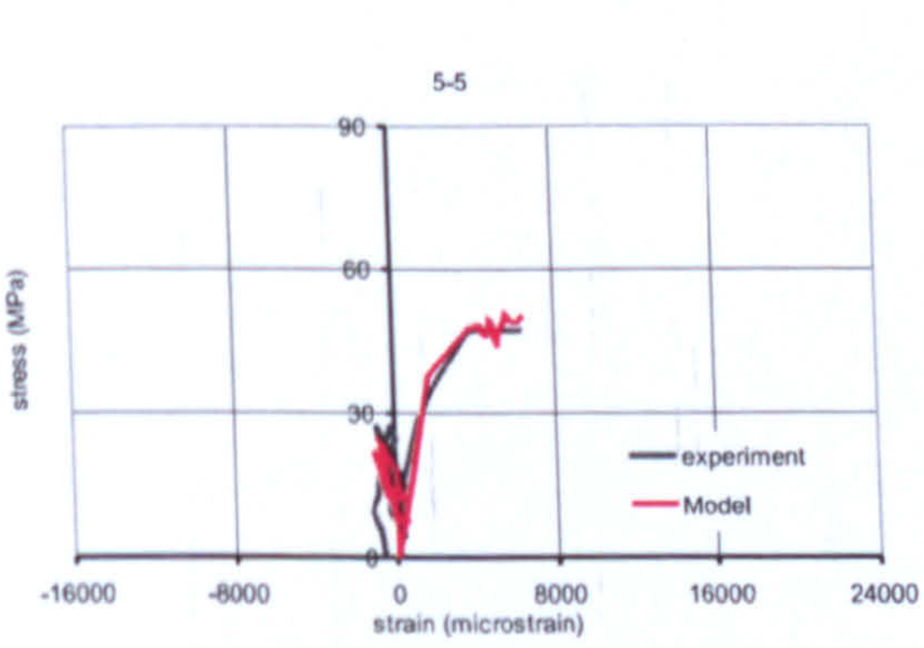

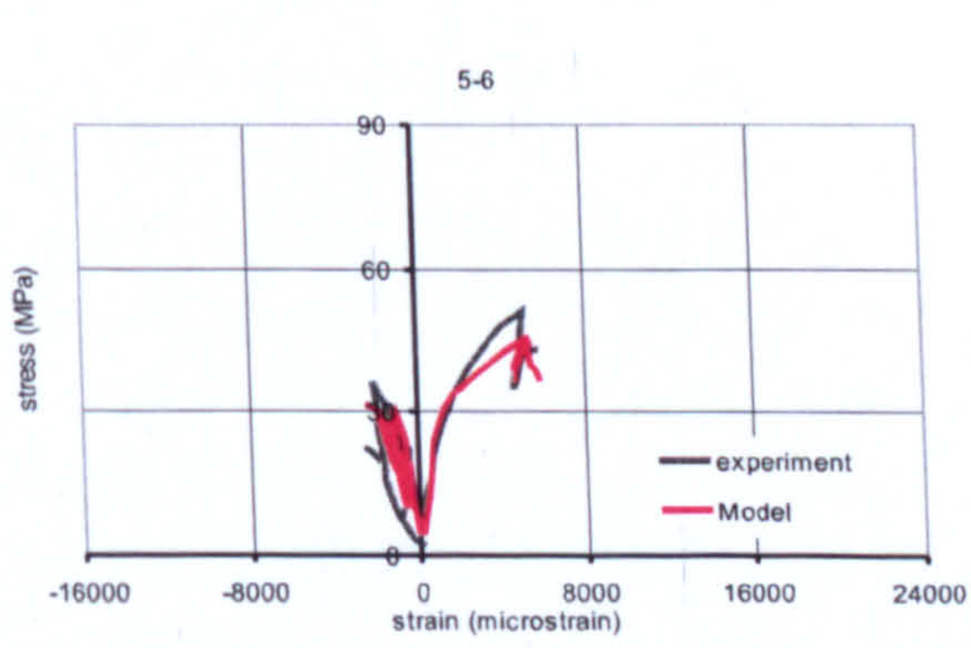

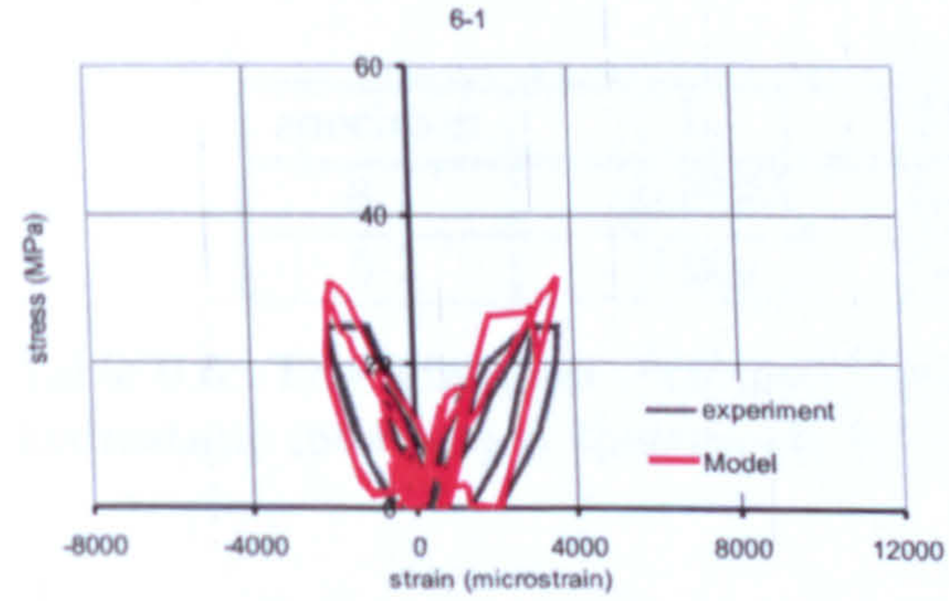

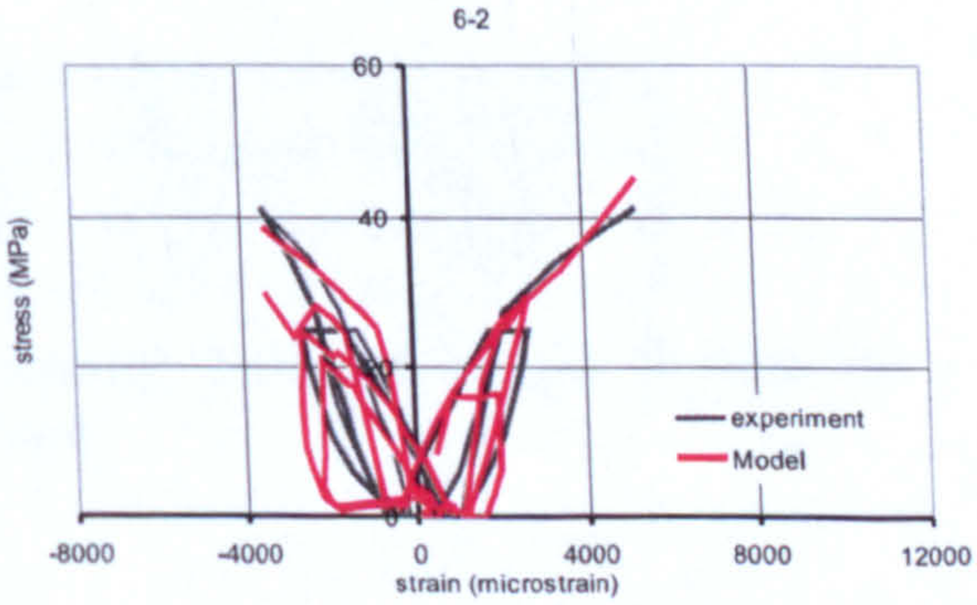

Figure 6.5: Experimental and model stress strain curves for the Colorado tests, Series 5 and 6

specimen	A_h	B_h	A_k	min error %
5-1	0.003	0.6	2.7	28.6
5-2	0.003	0.6	2.7	27.4
5-3	0.003	0.7	2.7	27.6
5-4	0.003	1.1	2.7	28.8
5-5	0.003	0.8	2.7	19.4
5-6	0.003	0.7	2.7	25.2

Table 6.5: The minimum error and the hardening constants A_h and B_h with the hydrostatic intersection constantA_k for series 5

specimen	A_h	B_h	A_k	min error %
6-1	0.003	0.2	1.0	33.0
6-2	0.008	0.4	1.0	38.6

Table 6.6: The minimum error and the hardening constants A_h and B_h with the hydrostatic intersection constantA_k for series 6

specimen	numerical (sec)	analytical (sec)	~ num/ana
1-1	0.531	0.047	11.3
1-2	0.656	0.043	15.3
1-3	0.578	0.062	9.3
1-5	0.614	0.046	13.3
1-6	0.391	0.047	8.3
1-7	0.469	0.047	10.0
1-8	0.640	0.047	13.6
1-9	0.484	0.031	15.6
1-10	0.531	0.078	6.8
1-11	0.547	0.062	8.8
1-12	0.625	0.063	9.9

Table 6.7: The time consumption of the analytical and numerical codes, series 1, Colorado tests

6.5 The Time Consumption

An important aspect - if the constitutive model is to be incorporated in finite element code - is the time consumption. Table 6.7 to Table 6.12 give the time consumption of both the numerical and analytical simulations for the Colorado tests. It can be seen clearly that the time consumed by the numerical simulations is much greater than the time consumed by the analytical ones. The average ratio between time consumption in the numerical and analytical simulations of series 1 is approximately 11 times, for series 2 approximately 15 times, for series 3 approximately 16 times, for series 4 approximately 12 times, for series 5 is approximately 13 times and for series 6 approximately 17 times. The overall average of the ratio of the time consumption between the numerical and analytical derivatives for all six series is approximately 15.

This significant increase in the time consumption of the numerical simulation is a result of the extrapolation and evaluation of the stepsize. This procedure involves two calculation loops in the Fortran program and therefore consumes more time. Changing the values of the tableau and the factor of safety could reduce the time consumption but does not eliminate the difference.

specimen	numerical (sec)	analytical (sec)	~ num/ana
2-1	0.531	0.031	17.1
2-2	0.594	0.078	7.6
2-3	0.536	0.046	11.7
2-4	0.500	0.032	15.6
2-5	0.469	0.031	15.1
2-6	0.375	0.016	23.4
2-7	0.516	0.031	16.6
2-8	0.469	0.031	15.1

Table 6.8: The time consumption of the analytical and numerical codes, series 2

specimen	numerical (sec)	analytical (sec)	~ num/ana
3-1	0.250	0.016	15.6
3-2	0.203	0.015	13.5
3-3	0.547	0.047	11.6
3-4	0.500	0.031	16.1
3-5	0.484	0.031	15.6
3-6	0.422	0.016	26.4
3-7	0.328	0.031	10.6
3-8	0.391	0.016	24.4
3-9	0.532	0.031	17.2
3-10	0.625	0.047	13.3
3-11	0.422	0.031	13.7
3-12	0.625	0.047	13.3
3-13	0.750	0.062	12.1
3-14	0.703	0.062	11.3
3-15	0.313	0.015	20.9
3-16	0.688	0.047	14.6
3-17	0.641	0.047	13.6

Table 6.9: The time consumption of the analytical and numerical codes, series 3

specimen	numerical (sec)	analytical (sec)	~ num/ana
4-1	0.485	0.046	10.5
4-2	0.515	0.047	10.9
4-3	0.500	0.047	10.6
4-4	0.391	0.031	12.6
4-5	0.407	0.032	12.7
4-6	0.516	0.031	16.6
4-7	0.578	0.047	12.3
4-8	0.578	0.047	12.3
4-9	0.672	0.062	10.8
4-10	0.562	0.047	11.9
4-11	0.641	0.062	10.3
4-12	0.797	0.063	12.7
4-13	0.782	0.079	9.9
4-14	0.656	0.047	13.9
4-15	0.641	0.063	10.2
4-16	0.703	0.062	11.3
4-17	0.625	0.047	13.3
4-18	0.610	0.078	7.8
4-19	0.656	0.063	10.4
4-20	0.859	0.063	13.6
4-21	0.813	0.062	13.1
4-22	0.610	0.047	13.0

Table 6.10: The time consumption of the analytical and numerical codes, series 4

specimen	numerical (sec)	analytical (sec)	~ num/ana
5-1	0.688	0.047	14.6
5-2	0.656	0.047	14.0
5-3	0.485	0.031	15.6
5-4	0.547	0.063	8.7
5-5	0.484	0.031	15.6
5-6	0.531	0.047	11.3

Table 6.11: The time consumption of the analytical and numerical codes, series 5

specimen	numerical (sec)	analytical (sec)	~ num/ana
6-1	0.641	0.031	20.7
6-2	0.469	0.032	14.7

Table 6.12: The time consumption of the analytical and numerical codes, series 6

6.6 Concluding Remarks

1. Numerical derivatives have been used in order to verify the analytical derivatives and reduce the size of the code for the newly developed model.

2. The numerical algorithm has successfully calculated the derivatives of the yield surface. The performance of the algorithm has been verified by comparing the results with the analytical solution.

3. The most critical issue associated with the numerical derivatives was the selection of the stepsize. Romberg's optimisation method which is developed originally for numerical integration has been used to reach an optimisated value for the stepsize.

4. The simulations using the numerical derivatives have similar results to that of the analytical derivatives.

5. Significant reduction in the size of the code and a simplification has been achieved.

6. The time consumption of the numerical derivative method is higher than that of the analytical method. This is attributed to the implementation of the extrapolation and optimisation technique of the stepsize.

There are benefits in producing a compact code for the potential new user. If that user is comfortable with the simulation capabilities of the model, then it is suggested that the full analytical derivatives be used to speedup the run time.

6.7 Reference

Fornberg B., 1981, Numerical differentiation of analytic functions, *ACM Transactions on Mathematical Software*, Vol. **7**, No. 4, pp.512-526.

Press W.H., Flannery, B.P., Teukolsky S.A. and Vetterling, W.T., 1992, Numerical Recipes in FORTRAN: The Art of Scientific Computing, 2nd ed. Cambridge, England: Cambridge University Press.

Ridders C J F, 1982, Accurate computation of $F'(x)$ and $F''(x)$, Technical note, Advanced Engineering Software, Vol. 4, 75-76.

Scavuzzo R, Stankowski T, Gerstle K H and Ko H-Y, 1983, Stress-strain curves for concrete under multiaxial load histories, Dept Civil, Environmental and Architectural Engineering, University of Colorado, Bounder, USA.

Scheid F, 1983, Theory and problems of numerical analysis, Schaum's Outline Series, McGraw-Hill Book Company, ch. 14, pp. 114-15.

Chapter 7

Conclusions and Suggestions for Further Research

7.1 Introduction

This study has been carried out in two parts. The first part dealt with the experimental observations and investigations of plain concrete under triaxial and multiaxial compression following cyclic loading and a variety of stress paths. The behaviour of concrete with different constituents was also investigated. The second part dealt with the modelling of the behaviour of concrete using the the theory of plasticity. In this part, a new constitutive model for plain concrete has been developed using the previous work in this field at the University of Sheffield. The new yield surface was developed as a combination of a reflection of part of the peak nominal stress surface (PNS) and a quartic function. The model was calibrated and the optimum values of the thirteen material constants are presented. A sensitivity study with simulations of a wide range of experimental data is presented. Finally, a comparative study between the analytical and numerical derivatives of the constitutive model is presented. This chapter contains the main experimental findings followed by the features of the new model. Finally, suggestions and recommendations for further studies are proposed.

7.2 Conclusions

7.2.1 Experimental Observations

In this section the main experimental findings are presented. These can be classified into three groups; the elastic, the pre-peak and the peak behaviour.

Elastic Behaviour

The elastic behaviour is concerned with determination of the elastic parameters namely Young's modulus, Poisson's ration and their influences on the plastic flow. These can be summarised as follows:

1. The values of Young's modulus in the second and subsequent loading cycles is less than the first cyclic loading. This degradation of stiffness is attributed to the damage that has been encountered during the cyclic loading.

2. The average values of Young's modulus seem to increase slightly with the increase of the confinement. This is due to the compaction of the material caused by closing of cracks and the collapse of voids.

3. Increasing coarse aggregate content significantly increased the modulus of elasticity.

4. Poisson's ratio is effectively independent of the loading path.

5. The values of Poisson's ratio seems to be independent of the content of coarse aggregates and the level of confinement.

6. The influence of the elastic parameters (E and ν) on the plastic flow is more evident in the elastic region.

Pre-peak Behaviour

The pre-peak observations are as follows:

1. The pre-peak behaviour of concrete under compression may be simplified into three levels of response:

   (a) Concrete initially responds as purely elastic material.

   (b) Under increased loading, distributed microcracking results in volumetric nonlinearity with contraction.

   (c) Eventually, further increase in compressive strain leads to development of multiple continuous crack systems resulting in a nonlinear volumetric dilation response.

2. The volumetric strain versus major principal stress seems to maintain an initial linear response regardless of the level of confinement. This linearity then turns to nonlinearity at a point referred to as the onset of stable fracture propagation (OSFP).

3. Concrete seems to be in a state of compaction throughout the compression loading but at peak stress, concrete sample retains its initial size.

4. At about 90% of the peak stress, where the volume of the sample reaches its minimum, the dilation response starts. The rate of dilation is significantly greater than the previous rate of contraction.

5. A loading surface can be identified from the minimum volumetric plastic strain. This is called the volume transition stress (VTS) surface.

6. At plastic VTS the directions of the plastic strain vectors are purely deviatoric.

7. Under high level of confinement, the total VTS and plastic VTS become closer to each other. This has been attributed to the fact that the plastic strain is dominant in this region.

8. It appears that the plastic strain vectors are normal to the plastic work contours. This gives further support to the assumption of associated flow for concrete.

Peak Behaviour

The experimental observations for concrete at peak loading can be summarised as follows:

1. The peak axial and lateral stresses and corresponding strains increase significantly with the increase of confinement. This supports the well known fact of the higher strain capacity of confined concrete.

2. With the increase in confinement, the axial strain capacity increases more than the lateral.

3. The equivalent plastic strain at peak stress increases significantly with the increase of confinement. The general relationship is nonlinear and follows an exponential form.

4. The values of peak plastic work increases significantly with the increase of confinement. The general relationship is nonlinear and follows an exponential form.

5. Increasing the coarse aggregate content increases the brittleness of concrete.

6. Coarse aggregate content had a mild effect on the uniaxial compressive strength. There is marginal decrease in concrete with no coarse aggregate and a marginal increase for concrete with double coarse aggregates.

7. The content of coarse aggregate has a mixed effect on the uniaxial strain at peak stress. Significant increase for no coarse aggregate concrete was noticed and a marginal decrease where double the amount of coarse aggregates were used.

8. The peak nominal stress (PNS) envelope is open-ended along the hydrostatic axis in the compression region. With no or low confinement, the surface is nonlinear but the shape becomes increasingly linear with the increase of confinement.

9. Increasing the coarse aggregates content significantly increases the strength envelope.

10. The shape of the VTS surface is similar to that of the peak nominal stress (PNS) surface but with a reduced size. For the same level of confinement, the ratio of the deviatoric component of the stresses at VTS and that at PNS is found to be constant ($\alpha_{vts} = \frac{\rho_{vts}}{\rho_c} = \text{constant}$).

11. The VTS envelope is closer to the PNS envelope for the mortar mix comparing with the normal and double coarse aggregates concrete mixes. This indicates that the dilation starts closer to the peak.

12. Plastic VTS and the intersection point of the PNS surface with the hydrostatic axis along with the plastic strain directions could be used to identify the shape of the yield surfaces.

13. At peak stress, the directions of the plastic strain increments appear to be normal to the PNS surface. This is an important point, since it suggests that the plastic flow for concrete at PNS is associated.

14. The directions of plastic strain vectors for concrete with different coarse aggregate contents seem to be normal to the yield surfaces. This suggests that the assumption of associated flow rule is valid for concrete with different constituents.

7.2.2 The New Constitutive Model

In this section the main features, the performance and efficiency of the new constitutive model are presented.

The Features

The main features of the new model can be summarised as follows:

1. The model is constructed within a classical isotropic elasto-plastic framework, based on the findings of experimental results.

2. It takes into consideration the physical behaviour of concrete and the effect of its constituents. Plastic VTS and the intersection points of the PNS surface with the hydrostatic axis along with the plastic strain directions have been used to identify the shape of the yield surfaces.

3. The new approach provides continuous loading surfaces, C_2 continuous and intersecting the hydrostatic axis normally in both tension and compression regions. These surfaces do not include any vertices. The geometric form of these surfaces provides considerable flexibility, allowing the surfaces to predict the plastic dilations.

4. It utilises one surface only for the yield and PNS.

5. It maintains the basic plasticity postulates such as normality and the convexity of the yield surface.

6. The deviatoric cross-sections of the yield surface have a general elliptic form which includes a control point on the shear meridian, in addition to control points on the compression and extension meridians.

7. The hardening function has been formulated with an introduction of control over the initial slope of the curve represents the relationship between the hardening parameter k and the internal hardening parameter k_p (k-k_p curve). This enables the nonlinear multiaxial deformation to be simulated in a realistic way.

8. The ductility measure is expressed using an exponential function using just two parameters.

9. An auxiliary stress surface has been introduced to deal with stress states which fall outside the zone where the yield function is defined.

10. The concept of the reflected yield surface and the ductility dependent hardening function could be introduced into other formulations with different PNS descriptions.

11. In total, thirteen material constants are available to calibrate the model. Most of these can take default values, if experimental data is not available for a particular concrete. A complete calibration procedure (for all the constants) was identified. The sensitivity of the model response to small changes in the constants was determined. Some constants are found to have strong influence. These include the uniaxial compression strength (f_c), the uniaxial tensile strength (f_t), Young's modulus (E), and the ductility constants (A_h and B_h).

The Efficiency

The efficiency of the new model has been tested against a large number of existing data. The following points summarise the main findings:

1. A series of comparisons between the model simulations and existing experimental data was given. The data includes triaxial and multiaxial compression tests.

2. The efficiency of the model was tested by determining the error for every simulated test. The overall error was then compared with two previous results reported by other researchers. The model showed better results.

3. The model describes the inelastic nonlinear behaviour of concrete in the pre-peak range in a realistic manner.

4. The new formulation captures the fundamental requirements of simulating plastic compaction and dilation.

5. The overall predictions of the newly developed model for the stress-strain response of the three mixes are close to the experimental data. This is a step forward in the development of a constituent dependent model.

6. The model predictions of the yield surfaces for different mixes show the flexibility of the model and its capability of capturing the most extreme material variations.

7. Numerical derivatives have been used in order to verify the analytical derivatives and reduce the size of the code used for the newly developed model. The numerical algorithm has successfully calculated the derivatives of the yield surface. The performance of the algorithm has been verified by comparing the results with the analytical solution. The most critical issue associated with the numerical derivatives was the selection of the stepsize. Romberg's optimisation method which was developed originally for numerical integration has

been used to reach an optimisation value for the stepsize. The simulations using the numerical derivatives have similar results to that of the analytical derivatives. Significant reduction in the size of the code and a simplification has been achieved when numerical derivatives are used. The time consumption of the numerical derivative method is higher than that of the analytical method. This is attributed to the implementation of the extrapolation and optimisation technique of the stepsize.

There are benefits in producing a compact code (using numerical derivatives) for the potential new user. If that user is comfortable with the simulation capabilities of the model, then it is suggested that the full analytical derivatives be used to speed up the run time.

8. The information available from uniaxial tests might not be enough to identify the appropriate values of all material constants hence, a triaxial test may be necessary if a satisfactory calibration for the model is to be attained.

7.2.3 Suggestions for Further Research

Some partially unsolved issues were encountered during this research. Other topics need to be added for further research programs. These can be classified into improvement of the existing model, extending it and further verifications and implementations.

Improving the Model

Two suggestions are proposed to enhance the efficiency of the model. These are:

1. The simulations of a variety of experimental data for different load paths have shown that the performance of the model is enhanced significantly when the values of the ductility constants A_h and B_h are changed with the change in confinement. Therefore, a new formulation to include this effect is recommended. One suggestion is to fix all the material constants and add a new formulation linking B_h with $\bar{\xi}$ through exponential function. This will increase the number of the material constants and it will require amendment of the hardening derivatives.

2. The calibration of the PNS surface based on the triaxial compression data led to the prediction of significant increase in the tensile strength as the compression strength envelope decreases. This requires further investigation and probably further improvement of the performance of the model in the

tensile region. One suggestion is to choose a third point in the compression region at any confinement along with f_c and f_t to construct the PNS surface.

Extending the Model

Some limitations have been introduced in this research. It is thought that it is appropriate to extend the model in the following directions:

1. Extensions of the model to include a continuum damage mechanics approach to anistropic stiffness degradation could be made to improve the simulation of the cyclic response and the stiffening encountered with a high level of confinement.

2. Further extensions of the model should be made to include a temperature dependency to enable modelling of accidental thermal loading of nuclear reactor vessels.

3. This study is focused on the response of concrete in multiaxial compression only. The model should be extended to the tension domain for applicability in finite element analysis of structures in which both brittle cracking and the frictional behaviour in compression play an important role. A promising approach might be a combination of a damage mechanics model, for the behaviour of concrete in tension, with the proposed plasticity model describing the compression behaviour.

4. The softening formulation needs to be introduced by linking the degradation of strength under progressive tensile straining to the dissipated fracture energy.

5. The model is time independent and further development is required to incorporate the loading rate effect.

Further Verification and Implementations

Further verification and implementations are proposed. These are:

1. Calibration of the model for different materials, such as rocks, using the PNS surfaces formulations for these materials.

2. Reformulating the hardening function using the plastic work as an internal hardening parameter instead of the equivalent plastic strain.

3. Coding the model using another language such as MATLAB.

4. The performance of the new constitutive model should be examined by implementing it in an advanced nonlinear finite element code such as *ya*FE*c* (Sheffield's finite element code).

5. High quality of experimental test data is needed. Some errors in existing test data have been noticed, especially at the beginning of some tests where large values of strains are recorded prior to any loading. Also, many strain gauges seem to fail before reaching the peak. Furthermore, experimental data for high performance concrete is needed in order to explore the capability of the model to simulate concrete with wider range of strengths.

Appendix A

Derivatives of the Stress Invariants and the Deviatoric Shape Function

In the formulation of the newly developed model, a set of new derivatives have appeared. These derivatives were fully defined and presented in Chapter 3. For completeness, here are presented the existing derivatives for the Haigh-Westergaard coordinates (ξ, ρ, and θ) and the shape function (r) which appeared in the yield surface formulation.

A.1 Derivatives of the Stress Invariants

Recall the Haigh-Westergaard coordinate of the stress space $\bar{\xi}$, $\bar{\rho}$, and θ:

The hydrostatic coordinate

$$\xi = \frac{I_1}{\sqrt{3}} \tag{A.1}$$

and the normalised hydrostatic coordinate

$$\bar{\xi} = \frac{\xi}{f_c} \tag{A.2}$$

The deviatoric coordinate

$$\rho = \sqrt{2\,J_2} \tag{A.3}$$

and the normalised deviatoric coordinate

$$\bar{\rho} = \frac{\rho}{f_c} \tag{A.4}$$

and Lode angle θ, where

$$cos\,(3\,\theta) = \frac{3\sqrt{3}}{2}\frac{J_3}{J_2{}^{\frac{3}{2}}} \tag{A.5}$$

or

$$\theta = \frac{1}{3}\arccos\left(\frac{3\sqrt{3}J_3}{2\,J_2{}^{3/2}}\right) \tag{A.6}$$

From equation (A.2)

$$\bar{\xi} = \frac{\sigma_1 + \sigma_2 + \sigma_3}{f_c} \tag{A.7}$$

thus

$$\left\{\frac{\partial\bar{\xi}}{\partial\sigma}\right\} = \left\{\frac{1}{\sqrt{3}f_c}\right\} \tag{A.8}$$

and

$$\left\{\frac{\partial^2\bar{\xi}}{\partial\sigma^2}\right\} = [0] \tag{A.9}$$

From equation (A.4)

$$\left\{\frac{\partial\bar{\rho}}{\partial\sigma}\right\} = \frac{\partial\bar{\rho}}{\partial J_2}\left\{\frac{\partial J_2}{\partial\sigma}\right\} \tag{A.10}$$

and

$$\left[\frac{\partial^2\bar{\rho}}{\partial\sigma^2}\right] = \frac{\partial^2\bar{\rho}}{\partial J_2^2}\left\{\frac{\partial J_2}{\partial\sigma}\right\}\left\{\frac{\partial J_2}{\partial\sigma}\right\} + \frac{\partial\bar{\rho}}{\partial J_2}\left[\frac{\partial^2 J_2}{\partial\sigma^2}\right] \tag{A.11}$$

The first and second derivatives of $\bar{\rho}$ with respect to second deviatoric stress invariant J_2 are given from:

$$\bar{\rho} = \frac{\sqrt{2J_2}}{f_c} = \frac{\sqrt{(\sigma_1-\sigma_2)^2 + (\sigma_2-\sigma_3)^2 + (\sigma_3-\sigma_1)^2}}{\sqrt{3}f_c} \tag{A.12}$$

thus

$$\frac{\partial\bar{\rho}}{\partial J_2} = \frac{1}{f_c\,\rho} \tag{A.13}$$

and

$$\frac{\partial^2\bar{\rho}}{\partial J_2^2} = \frac{-1}{f_c\,\rho^3} \tag{A.14}$$

The first and second derivatives of J_2 with respect to the stress tensor are as follows:

Since

$$J_2 = \frac{1}{6}[(\sigma_1 - \sigma_2)^2 + (\sigma_2 - \sigma_3)^2 + (\sigma_1 - \sigma_3)^2] \tag{A.15}$$

then the first derivatives with respect to the principal stresses are as follows:

$$\frac{\partial J_2}{\partial \sigma_1} = \frac{1}{3}(2\sigma_1 - \sigma_2 - \sigma_3) \tag{A.16}$$

$$\frac{\partial J_2}{\partial \sigma_2} = \frac{1}{3}(2\sigma_2 - \sigma_1 - \sigma_3) \tag{A.17}$$

$$\frac{\partial J_2}{\partial \sigma_3} = \frac{1}{3}(2\sigma_3 - \sigma_2 - \sigma_1) \tag{A.18}$$

and the second derivatives:

$$\left[\frac{\partial^2 J_2}{\partial \sigma^2}\right] = \left[\frac{2}{3}\right] \tag{A.19}$$

From (A.6) the first derivative of θ with respect to σ is

$$\left\{\frac{\partial \theta}{\partial \sigma}\right\} = \frac{\partial \theta}{\partial J_2}\left\{\frac{\partial J_2}{\partial \sigma}\right\} + \frac{\partial \theta}{\partial J_3}\left\{\frac{\partial J_3}{\partial \sigma}\right\} \tag{A.20}$$

and the second derivative

$$\left[\frac{\partial^2 \theta}{\partial \sigma^2}\right] = \frac{\partial^2 \theta}{\partial J_2^2}\left\{\frac{\partial J_2}{\partial \sigma}\right\}^2 + \frac{\partial \theta}{\partial J_2}\left[\frac{\partial^2 J_2}{\partial \sigma^2}\right] + \frac{\partial^2 \theta}{\partial J_3^2}\left\{\frac{\partial {J_3}^2}{\partial \sigma}\right\} + \frac{\partial \theta}{\partial J_3}\left[\frac{\partial^2 J_3}{\partial \sigma^2}\right] \tag{A.21}$$

where

$$\frac{\partial \theta}{\partial J_2} = \frac{3\sqrt{3}J_3}{2{J_2}^{5/2}\sqrt{4 - \frac{27{J_3}^2}{{J_2}^3}}} \tag{A.22}$$

and

$$\frac{\partial^2\theta}{\partial J_2^2} = \frac{3\sqrt{3}J_3\left(10\,{J_2}^3 - 27\,{J_3}^2\right)}{{J_2}^{7/2}\left(54\,{J_3}^2 - 8\,{J_2}^3\right)\sqrt{4 - \frac{27\,{J_3}^2}{{J_2}^3}}} \tag{A.23}$$

and

$$\frac{\partial\theta}{\partial J_3} = \frac{-\sqrt{3}}{{J_2}^{3/2}\sqrt{4 - \frac{27\,{J_3}^2}{{J_2}^3}}} \tag{A.24}$$

and

$$\frac{\partial^2\theta}{\partial J_3^2} = \frac{27\sqrt{3}\,J_3}{{J_2}^{9/2}\left(4 - \frac{27\,{J_3}^2}{{J_2}^3}\right)^{3/2}} \tag{A.25}$$

Since

$$J_3 = \frac{1}{27}(2\sigma_1 - \sigma_2 - \sigma_3)(2\sigma_2 - \sigma_1 - \sigma_3)(2\sigma_3 - \sigma_1 - \sigma_2) \tag{A.26}$$

then the first derivatives of J_3 respect to σ are

$$\frac{\partial J_3}{\partial \sigma_1} = \frac{1}{9}(4\sigma_2\sigma_3 - 2\sigma_2\sigma_1 - {\sigma_2}^2 - 2\sigma_1\sigma_3 + 2{\sigma_1}^2 - {\sigma_3}^2) \tag{A.27}$$

$$\frac{\partial J_3}{\partial \sigma_1} = \frac{1}{9}(4\sigma_1\sigma_3 - 2\sigma_2\sigma_3 - {\sigma_1}^2 - 2\sigma_2\sigma_1 + 2{\sigma_2}^2 - {\sigma_3}^2) \tag{A.28}$$

$$\frac{\partial J_3}{\partial \sigma_1} = \frac{1}{9}(4\sigma_2\sigma_1 - 2\sigma_2\sigma_3 - {\sigma_2}^2 - 2\sigma_1\sigma_3 + 2{\sigma_3}^2 - {\sigma_1}^2) \tag{A.29}$$

and the second derivatives are

$$\frac{\partial^2 J_3}{\partial \sigma_1^2} = \frac{1}{9}(4\sigma_1 - 2\sigma_2 - 2\sigma_3) \tag{A.30}$$

$$\frac{\partial^2 J_3}{\partial \sigma_2^2} = \frac{1}{9}(4\sigma_2 - 2\sigma_3 - 2\sigma_1) \tag{A.31}$$

$$\frac{\partial^2 J_3}{\partial \sigma_3^2} = \frac{1}{9}(4\sigma_3 - 2\sigma_2 - 2\sigma_1) \tag{A.32}$$

A.2 Derivatives of the Deviatoric Shape Function

The deviatoric shape function r (see subsection 3.4.2) follows from Bhowmik and Long and is formulated as

$$r = \frac{1}{g} = \frac{2d_0}{d_1 - \sqrt{((d_1)^2 - 4d_0d_2)}} \tag{A.33}$$

$$\frac{\partial r}{\partial \bar{\xi}} = \frac{\partial r}{\partial g}\frac{\partial g}{\partial \bar{\xi}} \tag{A.34}$$

$$\frac{\partial^2 r}{\partial \bar{\xi}^2} = \frac{\partial^2 r}{\partial g^2}\left(\frac{\partial g}{\partial \bar{\xi}}\right)^2 + \frac{\partial r}{\partial g}\frac{\partial^2 g}{\partial \bar{\xi}^2} \tag{A.35}$$

$$\frac{\partial^2 r}{\partial \bar{\xi}\partial \theta} = \frac{\partial^2 r}{\partial g^2}\frac{\partial g}{\partial \bar{\xi}}\frac{\partial g}{\partial \theta} + \frac{\partial r}{\partial g}\frac{\partial^2 g}{\partial \bar{\xi}\partial \theta} \tag{A.36}$$

$$\frac{\partial r}{\partial \theta} = \frac{\partial r}{\partial g}\frac{\partial g}{\partial \theta} \tag{A.37}$$

$$\frac{\partial^2 r}{\partial \theta^2} = \frac{\partial^2 r}{\partial g^2}\left(\frac{\partial g}{\partial \theta}\right)^2 + \frac{\partial r}{\partial g}\frac{\partial^2 g}{\partial \theta^2} \tag{A.38}$$

$$\frac{\partial r}{\partial g} = \frac{-1}{g^2} \tag{A.39}$$

$$\frac{\partial^2 r}{\partial g^2} = \frac{2}{g^3} \tag{A.40}$$

where

$$\begin{aligned} d_0 &= c_1\cos^2\theta - c_2\sin^2\theta + c_3\sin\theta\cos\theta \\ d_1 &= 2(c_4\sqrt{3}\cos\theta - c_5\sin\theta) \\ d_2 &= B_0(4 - 3B_0c_0) \end{aligned} \tag{A.41}$$

$$\begin{aligned} c_0 &= \frac{(2-\sqrt{3}B_1)(2B_0-\sqrt{3}B_1)}{(B_1(1+B_0)-\sqrt{3}B_0)^2} \\ c_1 &= 3 - c_0(1+B_0)^2 \\ c_2 &= 1 + 3c_0(1-B_0)^2 \\ c_3 &= 2c_0\sqrt{3}(1-{B_0}^2) \\ c_4 &= (1+B_0)(1-B_0c_0) \\ c_5 &= (1-B_0)(1-3B_0c_0) \end{aligned} \tag{A.42}$$

subject to the following restrictions

$$\begin{aligned} &\tfrac{1}{2} < B_0 \leq 1 \\ &\tfrac{\sqrt{3}B_0}{1+B_0} < B_1 < \tfrac{2B_0}{\sqrt{3}} \end{aligned} \tag{A.43}$$

where $B_0 = \frac{\rho_c}{\rho_c}$ and $B_1 = \frac{\rho_s}{\rho_c}$.

$$\bar{\rho}_e = (\frac{1}{3})^\gamma \sqrt{\frac{2}{3}} \left(-m + \sqrt{m^2 - 3\sqrt{3}m\bar{\xi} + 9c}\right)^\gamma \tag{A.44}$$

$$\bar{\rho}_c = (\frac{1}{6})^\gamma \sqrt{\frac{1}{6}} \left(-m + \sqrt{m^2 - 12\sqrt{3}m\bar{\xi} + 36c}\right)^\gamma \tag{A.45}$$

where γ is taken equal to 0.99 and m is controlled by the normalised uniaxial tensile strength, $\bar{f}_t = |f_t/f_c|$

$$m = \frac{3\left(1 - (\bar{f}_t)^{\frac{2}{\gamma}}\right)}{\bar{f}_t + 2(\bar{f}_t)^{\frac{1}{\gamma}}} \tag{A.46}$$

Carrying out the partial differentiation

$$\frac{\partial g}{\partial \theta} = \frac{v\frac{\partial u}{\partial \theta} - u\frac{\partial v}{\partial \theta}}{v^2} \tag{A.47}$$

where

$$u = d_1 - \sqrt{{d_1}^2 - 4d_0d_2} \tag{A.48}$$

$$v = 2d_0 \tag{A.49}$$

$$d_5 = \frac{\partial u}{\partial \theta} = \frac{\partial d_1}{\partial \theta} - \frac{\frac{\partial d_1^2}{\partial \theta} - \frac{\partial 4d_0d_2}{\partial \theta}}{2\sqrt{{d_1}^2 - 4d_0d_2}} \tag{A.50}$$

and

$$\frac{\partial d_1^2}{\partial \theta} = 2d_1\frac{\partial d_1}{\partial \theta} \tag{A.51}$$

where

$$d_3 = \frac{\partial d_1}{\partial \theta} = -2\left(c_4\sqrt{3}\sin\theta + c_5\cos\theta\right) \tag{A.52}$$

$$d_4 = \frac{\partial 4d_0d_2}{\partial \theta} = 4d_2\left(c_3(\cos^2\theta - \sin^2\theta) - 2(c_1 + c_2)\cos\theta\sin\theta\right) \tag{A.53}$$

$$d_4 = \frac{\partial 4 d_0 d_2}{\partial \theta} = 4 d_2 \left(c_3 (2\cos^2\theta - 1) - 2(c_1 + c_2)\cos\theta \sin\theta \right) \tag{A.54}$$

so that

$$d_5 = d_3 - \frac{d_1 d_3 - (d_4/2)}{\sqrt{((d_1^2) - 4 d_0 d_2)}} \tag{A.55}$$

and

$$\frac{\partial v}{\partial \theta} = \frac{\partial 2 d_0}{\partial \theta} = \frac{2}{4 d_2} \frac{\partial 4 d_0 d_2}{\partial \theta} \tag{A.56}$$

$$\frac{\partial g}{\partial \bar{\xi}} = \frac{\partial g}{\partial B_0} \frac{\partial B_0}{\partial \bar{\xi}} \tag{A.57}$$

The derivative of the function g is given as follows

$$\frac{\partial g}{\partial B_0} = \frac{v \frac{\partial u}{\partial B_0} - u \frac{\partial v}{\partial B_0}}{v^2} \tag{A.58}$$

where

$$u = d_1 - \sqrt{((d_1{}^2) - 4 d_0 d_2)} \tag{A.59}$$

$$v = 2 d_0 \tag{A.60}$$

$$\frac{\partial u}{\partial B_0} = \frac{\partial d_1}{\partial B_0} - \frac{\frac{\partial d_1^2}{\partial B_0} - \frac{\partial 4 d_0 d_2}{\partial B_0}}{2\sqrt{d_1{}^2 - 4 d_0 d_2}} \tag{A.61}$$

where

$$\frac{\partial d_1^2}{\partial B_0} = 2 d_1 \frac{\partial d_1}{\partial B_0} \tag{A.62}$$

$$\frac{\partial 4 d_0 d_2}{\partial B_0} = 4 \left(\frac{\partial d_0}{\partial B_0} d_2 + d_0 \frac{\partial d_2}{\partial B_0} \right) \tag{A.63}$$

$$\frac{\partial d_0}{\partial B_0} = \cos^2\theta \frac{\partial c_1}{\partial B_0} - \sin^2\theta \frac{\partial c_2}{\partial B_0} + \sin\theta\cos\theta \frac{\partial c_3}{\partial B_0} \tag{A.64}$$

$$\frac{\partial d_1}{\partial B_0} = 2 \left(\sqrt{3}\cos\theta \frac{\partial c_4}{\partial B_0} - \sin\theta \frac{\partial c_5}{\partial B_0} \right) \tag{A.65}$$

$$\frac{\partial d_2}{\partial B_0} = 4 - 3 B_0 \left(2 c_0 + B_0 \frac{\partial c_0}{\partial B_0} \right) \tag{A.66}$$

$$\frac{\partial c_5}{\partial B_0} = -(1 - 3B_0c_0) - 3(1 - B_0)(c_0 + B_0\frac{\partial c_0}{\partial B_0}) \tag{A.67}$$

$$\frac{\partial c_4}{\partial B_0} = (1 - B_0c_0) - (1 + B_0)(c_0 + B_0\frac{\partial c_0}{\partial B_0}) \tag{A.68}$$

$$\frac{\partial c_3}{\partial B_0} = -4\sqrt{3}B_0c_0 + 2\sqrt{3}(1 - B_0^2)\frac{\partial c_0}{\partial B_0} \tag{A.69}$$

$$\frac{\partial c_2}{\partial B_0} = 3(1 - B_0)\left(-2c_0 + (1 - B_0)\frac{\partial c_0}{\partial B_0}\right) \tag{A.70}$$

$$\frac{\partial c_1}{\partial B_0} = -(1 + B_0)\left(2c_0 + (1 + B_0)\frac{\partial c_0}{\partial B_0}\right) \tag{A.71}$$

From (A.42)

$$c_0 = \frac{(2 - \sqrt{3}B_1)(2B_0 - \sqrt{3}B_1)}{(B_1(1 + B_0) - \sqrt{3}B_0)^2} = \frac{s}{t} \tag{A.72}$$

$$\frac{\partial c_0}{\partial B_0} = \frac{t\frac{\partial s}{\partial B_0} - s\frac{\partial t}{\partial B_0}}{t^2} \tag{A.73}$$

where

$$\frac{\partial s}{\partial B_0} = -\sqrt{3}\frac{\partial B_1}{\partial B_0}(2B_0 - \sqrt{3}B_1) + (2 - \sqrt{3}B_1)(2 - \sqrt{3}\frac{\partial B_1}{\partial B_0}) \tag{A.74}$$

and

$$\frac{\partial t}{\partial B_0} = 2\left(B_1(1 + B_0) - \sqrt{3}B_0\right)\left((1 + B_0)\frac{\partial B_1}{\partial B_0} + B_1 - \sqrt{3}\right) \tag{A.75}$$

Note that B_1 is taken as

$$B_1 = (\frac{\sqrt{3}B_0}{(1 + B_0)}) + \alpha\left((\frac{2B_0}{\sqrt{3}}) - (\frac{\sqrt{3}B_0}{(1 + B_0)})\right) \tag{A.76}$$

where α ranges from 0 to 1

$$B_1 = \frac{\sqrt{3}(1 - \alpha)B_0}{(1 + B_0)} + \frac{2\alpha B_0}{\sqrt{3}} \tag{A.77}$$

$$\frac{\partial B_1}{\partial B_0} = \frac{(1 - \alpha)\sqrt{3}}{(1 + B_0)^2} + \frac{2\alpha}{\sqrt{3}} \tag{A.78}$$

The derivatives of the meridians $\bar{\rho}_e$ and $\bar{\rho}_c$ with respect to $\bar{\xi}$ are now given

$$\frac{\partial \bar{\rho}_e}{\partial \bar{\xi}} = -\gamma \left(\frac{-m + \sqrt{m^2 - 3\sqrt{3}m\bar{\xi} + 9c}}{3} \right)^{\gamma-1} \frac{m\sqrt{2}}{\sqrt{m^2 - 3\sqrt{3}m\bar{\xi} + 9c}} \tag{A.79}$$

$$\frac{\partial \bar{\rho}_c}{\partial \bar{\xi}} = -\gamma \left(\frac{-m + \sqrt{m^2 - 12\sqrt{3}m\bar{\xi} + 36c}}{6} \right)^{\gamma-1} \frac{m\sqrt{2}}{\sqrt{m^2 - 12\sqrt{3}m\bar{\xi} + 36c}} \tag{A.80}$$

The derivative of B_0 with respect to $\bar{\xi}$ is as follows

$$\frac{\partial B_0}{\partial \bar{\xi}} = \frac{\bar{\rho}_c \frac{\partial \bar{\rho}_e}{\partial \bar{\xi}} - \bar{\rho}_e \frac{\partial \bar{\rho}_c}{\partial \bar{\xi}}}{(\bar{\rho}_c)^2} \tag{A.81}$$

On the following, the second derivative with respect to the stress tensor are given.

and from (A.58)

$$\frac{\partial^2 g}{\partial \bar{\xi}^2} = \frac{\partial^2 g}{\partial B_0^2} \left(\frac{\partial B_0}{\partial \bar{\xi}} \right)^2 + \frac{\partial g}{\partial B_0} \frac{\partial^2 B_0}{\partial \bar{\xi}^2} \tag{A.82}$$

and

$$\frac{\partial^2 g}{\partial \theta^2} = \frac{\partial}{\partial \theta} \left(\frac{d_5 - g d_4/(2d_2)}{2d_0} \right) \tag{A.83}$$

From (A.51) and taking

$$p = d_5 - g d_4/(2d_2) \qquad \text{and} \qquad v = 2d_0 \tag{A.84}$$

$$\frac{\partial^2 g}{\partial \theta^2} = \frac{v \frac{\partial p}{\partial \theta} - p \frac{\partial v}{\partial \theta}}{v^2} \tag{A.85}$$

where

$$\frac{\partial p}{\partial \theta} = \frac{\partial d_5}{\partial \theta} - \left(\frac{d_4 \frac{\partial g}{\partial \theta} + g \left(\frac{\partial d_4}{\partial \theta} \right)}{(2d_2)} \right) \tag{A.86}$$

From (A.49)

$$\frac{\partial^2 g}{\partial \bar{\xi}^2} = \frac{\partial^2 g}{\partial B_0^2} \left(\frac{\partial B_0}{\partial \bar{\xi}} \right)^2 + \frac{\partial g}{\partial B_0} \frac{\partial^2 B_0}{\partial \bar{\xi}^2} \tag{A.87}$$

and

$$\frac{\partial^2 g}{\partial \theta^2} = \frac{\partial}{\partial \theta} \left(\frac{d_5 - g d_4/(2d_2)}{2d_0} \right) \tag{A.88}$$

From (A.51) and taking

$$p = d_5 - gd_4/(2d_2) \qquad \text{and} \qquad v = 2d_0 \tag{A.89}$$

$$\frac{\partial^2 g}{\partial \theta^2} = \frac{v\frac{\partial p}{\partial \theta} - p\frac{\partial v}{\partial \theta}}{v^2} \tag{A.90}$$

where

$$\frac{\partial p}{\partial \theta} = \frac{\partial d_5}{\partial \theta} - \left(\frac{d_4\frac{\partial g}{\partial \theta} + g\left(\frac{\partial d_4}{\partial \theta}\right)}{(2d_2)}\right) \tag{A.91}$$

From (A.49)

$$\frac{\partial d_5}{\partial \theta} = \frac{\partial d_3}{\partial \theta} - \left(\frac{\left(d_1\frac{\partial d_3}{\partial \theta} + d_3\frac{\partial d_1}{\partial \theta} - \frac{\partial d_4}{2\partial \theta}\right)(d_1 - u) - \left(\frac{\partial d_1}{\partial \theta} - \frac{\partial u}{\partial \theta}\right)(d_1 d_3 - d_4/2)}{(d_1 - u)^2}\right) \tag{A.92}$$

Replacing

$$\frac{\partial d_5}{\partial \theta} = \frac{\partial d_3}{\partial \theta} - \left(\frac{\left(d_1\frac{\partial d_3}{\partial \theta} + (d_3)^2 - \frac{\partial d_4}{2\partial \theta}\right)(d_1 - u) - (d_3 - d_5)(d_1 d_3 - d_4/2)}{(d_1 - u)^2}\right) \tag{A.93}$$

where

$$\frac{\partial d_3}{\partial \theta} = -2(c_4\sqrt{3}\cos\theta - c_5\sin\theta) = -d_1 \tag{A.94}$$

and

$$d_6 = \frac{\partial d_4}{2\partial \theta} = -4d_2\left(2c_3\cos\theta\sin\theta + (c_1 + c_2)(2\cos^2\theta - 1)\right) \tag{A.95}$$

Substituting the above into (A.88) and (A.87) we get

$$d_7 = \frac{\partial d_5}{\partial \theta} = -d_1 + \left(\frac{(d_1^2 - d_3^2 + d_6)(d_1 - u) + (d_5 - d_3)(d_1 d_3 - d_4/2)}{(d_1 - u)^2}\right) \tag{A.96}$$

$$d_8 = \frac{\partial p}{\partial \theta} = d_7 - \left(\frac{d_4\frac{\partial g}{\partial \theta} + 2d_6 g(\theta, B_0)}{(2d_2)}\right) \tag{A.97}$$

$$\frac{\partial^2 g}{\partial \theta^2} = \frac{d_8 - g_{,\theta}(d_4/2d_2)}{2d_0} \tag{A.98}$$

$$\begin{aligned}\frac{\partial^2 g}{\partial\xi\partial\theta} &= \frac{\partial}{\partial B_0}\left(\frac{v\frac{\partial u}{\partial\theta}-u\frac{\partial v}{\partial\theta}}{v^2}\right)\frac{\partial B_0}{\partial\xi}\\ &= \left(\left(v\frac{\partial^2 u}{\partial B_0\partial\theta}-u\frac{\partial^2 v}{\partial B_0\partial\theta}+\frac{\partial v}{\partial B_0}\frac{\partial u}{\partial\theta}-\frac{\partial u}{\partial B_0}\frac{\partial v}{\partial\theta}\right)/v^2\right.\\ &\quad \left.-2\frac{\partial v}{\partial B_0}\frac{\partial g}{\partial\theta}/v\right)\frac{\partial B_0}{\partial\xi}\end{aligned} \tag{A.99}$$

$$\frac{\partial^2 u}{\partial B_0\partial\theta}=\frac{\partial^2 d_1}{\partial B_0\partial\theta}-\frac{\left(d_1\frac{\partial^2 d_1}{\partial B_0\partial\theta}+d_3\frac{\partial d_1}{\partial B_0}-\frac{\partial d_4}{2\partial B_0}\right)-\left(\frac{\partial d_1}{\partial B_0}-\frac{\partial u}{\partial B_0}\right)(d_3-d_5)}{(d_1-u)} \tag{A.100}$$

where

$$\frac{\partial d_3}{\partial B_0}=\frac{\partial^2 d_1}{\partial B_0\partial\theta}=-2\left(\sqrt{3}\sin\theta\frac{\partial c_4}{\partial B_0}+\cos\theta\frac{\partial c_5}{\partial B_0}\right)=\frac{\partial^2 d_1}{\partial\theta\partial B_0} \tag{A.101}$$

and

$$\frac{\partial^2 v}{\partial B_0\partial\theta}=2\left(\frac{\partial c_3}{\partial_{B_0}}(2\cos^2\theta-1)-2\cos\theta\sin\theta(\frac{\partial c_1}{\partial B_0}+\frac{\partial c_2}{\partial B_0})\right)=\frac{\partial^2 v}{\partial\theta\partial B_0} \tag{A.102}$$

$$\begin{aligned}\frac{\partial^2 g}{\partial\theta\partial\xi} &= \frac{\partial}{\partial\theta}\left(\frac{v\frac{\partial u}{\partial B_0}-u\frac{\partial v}{\partial B_0}}{v^2}\right)\frac{\partial B_0}{\partial\xi}\\ &= \left(\left(v\frac{\partial^2 u}{\partial\theta\partial B_0}-u\frac{\partial^2 v}{\partial\theta\partial B_0}+\frac{\partial v}{\partial\theta}\frac{\partial u}{\partial B_0}-\frac{\partial u}{\partial\theta}\frac{\partial v}{\partial B_0}\right)/v^2\right.\\ &\quad \left.-2\frac{\partial v}{\partial\theta}\frac{\partial g}{\partial B_0}/v\right)\frac{\partial B_0}{\partial\xi}\end{aligned} \tag{A.103}$$

$$\begin{aligned}\frac{\partial^2 u}{\partial\theta\partial B_0} &= \frac{\partial}{\partial\theta}\left(\frac{\partial d_1}{\partial B_0}-\frac{\frac{\partial d_1^2}{\partial B_0}-\frac{\partial 4d_0d_2}{\partial B_0}}{2(d_1-u)}\right)\\ &= \frac{\partial^2 d_1}{\partial\theta\partial B_0}-\frac{\left(d_1\frac{\partial^2 d_1}{\partial B_0\partial\theta}+\frac{\partial d_1}{\partial\theta}\frac{\partial d_1}{\partial B_0}-\frac{\partial 4d_0d_2}{2\partial\theta\partial B_0}\right)}{(d_1-u)}\\ &\quad -\frac{1}{(d_1-u)}\left(\frac{\partial d_1}{\partial\theta}-\frac{\partial u}{\partial\theta}\right)\left(\frac{\partial d_1}{\partial B_0}-\frac{\partial u}{\partial B_0}\right)\end{aligned} \tag{A.104}$$

$$\frac{\partial^2 u}{\partial\theta\partial B_0} = \frac{\partial^2 d_1}{\partial\theta\partial B_0} - \frac{\left(d_1\frac{\partial^2 d_1}{\partial\theta\partial B_0} + d_3\frac{\partial d_1}{\partial B_0} - \frac{\partial^2 4d_0d_2}{2\partial\theta\partial B_0}\right) - \left(\frac{\partial d_1}{\partial B_0} - \frac{\partial u}{\partial B_0}\right)(d_3 - d_5)}{(d_1 - u)} \quad \text{(A.105)}$$

$$\frac{\partial^2 g}{\partial B_0^2} = \frac{\partial}{\partial B_0}\left(\frac{v\frac{\partial u}{\partial B_0} - u\frac{\partial v}{\partial B_0}}{v^2}\right)$$

$$= \left(v\frac{\partial^2 u}{\partial B_0^2} - u\frac{\partial^2 v}{\partial B_0^2}\right)/v^2 - \frac{2}{v}\frac{\partial v}{\partial B_0}\frac{\partial g}{\partial B_0} \quad \text{(A.106)}$$

$$\frac{\partial^2 u}{\partial B_0^2} = \frac{\partial^2 d_1}{\partial B_0^2} - \frac{\partial}{\partial B_0}\left(\frac{\frac{\partial d_1^2}{\partial B_0} - \frac{\partial 4d_0d_2}{\partial B_0}}{2(d_1 - u)}\right)$$

$$= \frac{\partial^2 d_1}{\partial B_0^2} - \frac{\left(\left(\frac{\partial d_1}{\partial B_0}\right)^2 + d_1\frac{\partial^2 d_1}{\partial B_0^2} - 2\frac{\partial^2 d_0d_2}{\partial B_0^2}\right) - \left(\frac{\partial d_1}{\partial B_0} - \frac{\partial u}{\partial B_0}\right)^2}{(d_1 - u)} \quad \text{(A.107)}$$

$$\frac{\partial^2 d_0d_2}{\partial B_0^2} = d_2\frac{\partial^2 d_0}{\partial B_0^2} + 2\frac{\partial d_0}{\partial B_0}\frac{\partial d_2}{\partial B_0} + d_0\frac{\partial^2 d_2}{\partial B_0^2} \quad \text{(A.108)}$$

$$\frac{\partial^2 d_0}{\partial B_0^2} = \cos^2\theta\frac{\partial^2 c_1}{\partial B_0^2} - \sin^2\theta\frac{\partial^2 c_2}{\partial B_0^2} + \sin\theta\cos\theta\frac{\partial^2 c_3}{\partial B_0^2} \quad \text{(A.109)}$$

$$\frac{\partial^2 d_1}{\partial B_0^2} = 2\left(\sqrt{3}\cos\theta\frac{\partial^2 c_4}{\partial B_0^2} - \sin\theta\frac{\partial^2 c_5}{\partial B_0^2}\right) \quad \text{(A.110)}$$

$$\frac{\partial^2 d_2}{\partial B_0^2} = -6c_0 - 3B_0\left(4\frac{\partial c_0}{\partial B_0} + B_0\frac{\partial^2 c_0}{\partial B_0^2}\right) \quad \text{(A.111)}$$

$$\frac{\partial^2 c_5}{\partial B_0^2} = 6\left(c_0 + B_0\frac{\partial c_0}{\partial B_0}\right) - 3(1 - B_0)\left(2\frac{\partial c_0}{\partial B_0} + B_0\frac{\partial^2 c_0}{\partial B_0^2}\right) \quad \text{(A.112)}$$

$$\frac{\partial^2 c_4}{\partial B_0^2} = -2\left(c_0 + B_0\frac{\partial c_0}{\partial B_0}\right) - (1 + B_0)\left(2\frac{\partial c_0}{\partial B_0} + B_0\frac{\partial^2 c_0}{\partial B_0^2}\right) \quad \text{(A.113)}$$

$$\frac{\partial^2 c_3}{\partial B_0^2} = -4\sqrt{3}\left(c_0 + 2B_0\frac{\partial c_0}{\partial B_0}\right) + 2\sqrt{3}(1 - B_0^2)\frac{\partial^2 c_0}{\partial B_0^2} \quad \text{(A.114)}$$

$$\frac{\partial^2 c_2}{\partial B_0^2} = 6c_0 - 12(1 - B_0)\frac{\partial c_0}{\partial B_0} + 3(1 - B_0)^2\frac{\partial^2 c_0}{\partial B_0^2} \quad \text{(A.115)}$$

$$\frac{\partial^2 c_1}{\partial B_0^2} = -2c_0 - 4(1 + B_0)\frac{\partial c_0}{\partial B_0} - (1 + B_0)^2\frac{\partial^2 c_0}{\partial B_0^2} \quad \text{(A.116)}$$

$$\frac{\partial^2 c_0}{\partial B_0^2} = \left(t\frac{\partial^2 s}{\partial B_0^2} - s\frac{\partial^2 t}{\partial B_0^2}\right)/t^2 - 2\frac{\partial t}{\partial B_0}\frac{\partial c_0}{\partial B_0}/t \qquad \text{(A.117)}$$

and

$$\frac{\partial^2 s}{\partial B_0^2} = -\sqrt{3}\left(2+2B_0-2\sqrt{3}B_1\right)\frac{\partial^2 B_1}{\partial B_0^2} - 2\sqrt{3}\left(2-\sqrt{3}\frac{\partial B_1}{\partial B_0}\right)\frac{\partial B_1}{\partial B_0} \qquad \text{(A.118)}$$

$$\frac{\partial^2 t}{\partial B_0^2} = 2\left(B_1(1+B_0)-\sqrt{3}B_0\right)\left(2\frac{\partial B_1}{\partial B_0}+(1+B_0)\frac{\partial^2 B_1}{\partial B_0^2}\right) + 2\left((1+B_0)\frac{\partial B_1}{\partial B_0}+B_1-\sqrt{3}\right)^2 \qquad \text{(A.119)}$$

where

$$\frac{\partial^2 B_1}{\partial B_0^2} = \frac{-2(1-\alpha)\sqrt{3}}{(1+B_0)^3} \qquad \text{(A.120)}$$

from (A.73)

$$\frac{\partial^2 B_0}{\partial \bar{\xi}^2} = \left(\bar{\rho}_c\frac{\partial^2 \bar{\rho}_e}{\partial \bar{\xi}^2} - \bar{\rho}_e\frac{\partial^2 \bar{\rho}_c}{\partial \bar{\xi}^2}\right)/(\bar{\rho}_c)^2 - 2\frac{\partial \bar{\rho}_c}{\partial \bar{\xi}}\frac{\partial B_0}{\partial \bar{\xi}}/\bar{\rho}_c \qquad \text{(A.121)}$$